A Computational and Experimental Study of Spark Ignition Engine Combustion

by

Timothy Hattrell

MEng

Submitted in accordance with the requirements for the degree of Doctor of Philosophy.

UNIVERSITY OF LEEDS

School of Mechanical Engineering

September 2007

Abstract

This work focuses on aspects of combustion in a spark ignition engine. A pent-roof research engine was used to generate an experimental data set which was combined with a preexisting data set from a disc-chamber research engine. The combined dataset was used to refine a thermodynamic spark ignition engine combustion code which could operate in either a three-zone entrainment and burn up, or a two-zone direct combustion, configuration.

The pent-roof engine was skip-fired to ensure residual gases were purged and care was taken to ensure that the thermodynamic state and chemical composition of the intake mixture were well defined. The combustion chamber, which featured near complete optical access, was illuminated using a sheet of laser light. Mie scattered laser light from fine seed particles was recorded allowing the position of the flame front to be tracked. These images were then ensemble averaged and combined to give a three-dimensional reconstruction of the mean combustion progress variable field for three different engine speeds.

As the flame approached the combustion chamber walls it was found to decelerate. A relationship between the burning velocity of an unconstrained flame and a flame approaching a wall was derived which agreed well with the experimental results. This relationship was incorporated into the engine simulation code and found to improve greatly the predictions of the two-zone combustion model.

New flame acceleration and laminar burning velocity submodels reported in the literature were added to the engine simulation code. The suitability of these models for simulating spark ignition engine combustion was evaluated using the disc and pent roof experimental data sets and model constants adjusted to optimise the performance of each submodel. Although there were substantial differences between the individual submodels, over the range of operating conditions for which experimental data was available changes to the submodel used had a negligible effect on the combustion model predictions.

The work concludes with an evaluation of the performance of the three-zone combustion model for simulating a pent-roof engine. The model was modified for the pent-roof engine to include suitable assumptions for turbulence and the position of the centre of the flame. Using constants which were chosen to fit data recorded in the disc chamber engine, the model predictions for the pent-roof engine were comparable in accuracy to predictions for the disc roof engine. The model was incorporated in a commercially available manifold gas dynamics simulation software to allow the predictive simulation of complete engine cycles.

Acknowledgements

Studying for a PhD has not been easy and there are a number of people who deserve a mention because they have worked hard to make my life easier. In no particular order...

- All at Cosworth Technology/Mahle Powertrain who supported this work, especially Alasdair Cairns, Jens Neumeister and Hugh Blaxill. Naturally the funding that came with the CASE studentship was useful; what really surprised me was that on top of this you were prepared to fly me to Detroit on the pretence of going to a conference, TWICE, put me up in the most pointlessly sumptuous hotel suites I'll probably ever get to stay in (the twelve seater dining table was a nice touch, thanks Carol) and then buy me beer all week!

- Further funding during the final year of study came from my employment as part of the government funded CCSPV project.

- Which brings me onto Dr Rob Woolley. Despite the fact that he put a lot of effort into helping me in the lab and teaching me little snippets of combustion wisdom over the first three years, he still found it within himself to resign from his position at Leeds with the CCSPV project just as I was running out of funding from Mahle. This brilliantly executed move by him (which was very fortunate for me) allowed me to step nicely into his shoes and provided funding for my last year. Thanks.

- Three other people who put a lot of effort into helping me out (and also made sure we went to the pub every Friday) are the technicians:

  - Mark Bachelor, thanks for all the mechanical things you sorted out, and the steam engine and Porsche chats.
  - Brian Leach, thanks for all the electrical things you sorted out, and all the farting and singing.
  - John Groves, thanks for keeping Mark and Brian in check (mainly Brian) when they started getting rowdy.

And let's not forget the combustion group secretaries, the lovely Simer, Fiona and Katie, who were always there to help.

- Ash, Dave, for the great illustrations, your names will now be immortalised forever in the Leeds University library. Bask in the glory.

- During my time at Leeds I was lucky enough to work with an entire room full of people who also showed a passing interest in burning things in a scientific way. My fellow PhD students (who I'm not going to name individually) contributed a lot to this thesis and also helped to make my time at Leeds enjoyable.

- My supervisors for the duration of PhD, and also for my undergraduate work, were Prof Chris Sheppard and Dr Alex Burluka. I think it's only fair to say that I couldn't have wished for any better. Thanks for giving me the chance to do this and all the support over the last four years. Sorry the thesis writing has somehow managed to turn into a rush job at the last minute, it seems to be my trademark.

Now comes the important bit...I would like to say thank you to my parents for always supporting me what ever direction I took. And most of all I would like to say thank you to Sarah. Whilst I've been writing this dreaded thesis, someone else has been cooking tea, listening to me drone on about boring science, putting up with a house where all the surfaces are covered with a scattering of books and papers, doing the shopping, doing the washing up, I could go on but the list would be endless. For everything. Thanks.

Declarations

Some parts of the work presented in this thesis have also been published in the following articles:

Abdi Aghdam, E. and Burluka, A. A. and Hattrell, T. and Liu, K. and Sheppard, C. G. W. and Neumeister, J. and Crundwell, N., Study of Cyclic Variation in an SI Engine using Quasi-Dimensional Combustion Model. *SAE Technical Paper*, 2007-01-0939, Society of Automotive Engineers, 2007.

Hattrell, T. and Sheppard, C. G. W. and Burluka, A. A. and Neumeister, J. and Cairns, A., Burn Rate Implications of Alternative Knock Reduction Strategies for Turbocharged SI Engines. *SAE Technical Paper*, 2006-01-1110, Society of Automotive Engineers, 2006.

Contents

List of Figures xxi

List of Tables xxii

Nomenclature xxiii

1 Introduction 1

1.1 Motivation and scope of the current work 1
1.2 Introduction to spark ignition engines 2
1.3 The nature of turbulent flow 3
1.3.1 The Reynolds decomposition and measures of the intensity of turbulence 5
1.3.2 Spatial velocity correlations 5
1.3.3 Characteristic turbulent length scales 7
1.3.4 Characteristic turbulent time scales 9
1.3.5 The spectrum of turbulence 10
1.3.6 Vortex stretching and dissipation 13
1.3.7 Scale relations 16
1.4 Turbulent flow in engines 16
1.4.1 Definitions of turbulence in engines 16
1.4.2 Measurements of turbulence in engines 18
1.5 Laminar and turbulent combustion 20
1.5.1 The effect of stretch on combustion 21
1.5.2 Combustion regimes 23
1.5.3 Laminar flame instabilities 24
1.5.4 Effect of turbulence on growing flames 25
1.6 Optical diagnosis of engine combustion 27
1.7 Simulation of combustion in spark ignition engines 28

2 Experimental Equipment **32**
2.1 Overview . . . 32
2.2 LUPOE2-P . . . 34
2.2.1 General information . . . 34
2.2.2 Intake air, fuelling, heating and exhaust systems . . . 35
2.2.3 Ignition system . . . 40
2.2.4 Dynamometer and control system . . . 41
2.2.5 Crank angle measurement . . . 41
2.2.6 In-cylinder pressure measurement . . . 43
2.2.7 Timing rack and triggering system . . . 44
2.3 Camera, laser, optics and seeding system . . . 45
2.3.1 Camera and scattered light optics . . . 45
2.3.2 Laser and sheet light optics . . . 49
2.3.3 Seeding system . . . 50
2.4 Data acquisition system . . . 51
2.4.1 Data acquisition system . . . 51
2.4.2 Electrical noise . . . 54
2.5 Experiment technique and procedure . . . 55
2.5.1 Morning routine . . . 55
2.5.2 Test procedure . . . 56
2.5.3 Window cleaning procedure . . . 59

3 Data Processing and Reduction **61**
3.1 Overview . . . 61
3.2 Analogue and digital signal processing . . . 62
3.2.1 Signal pre-processing . . . 62
3.2.2 Selection of representative cycles . . . 66
3.2.3 Reverse analysis using LUSIEDA . . . 66
3.3 Image processing . . . 71
3.3.1 Raw images . . . 72
3.3.2 Image pre-processing . . . 72
3.3.3 Binarising procedure . . . 73
3.3.4 Masking and noise removal . . . 75
3.3.5 Mean progress variable calculation and volume smoothing . 76
3.3.6 Isosurface generation and smoothing . . . 78
3.3.7 Flame curvature . . . 81

3.3.8 Local flame speed and burning velocity 83
3.3.9 Flame brush thickness 85
3.3.10 Flame volume 87
3.3.11 Flame surface area 88
3.3.12 Flame centre 89
3.3.13 Flame radius 92
3.3.14 Surface statistics 92

4 Combustion Simulation Software **94**
4.1 Overview 94
4.2 LUSIE 95
4.2.1 History of the LUSIE software 95
4.2.2 Overall operation of LUSIE 96
4.2.3 Model assumptions 98
4.2.4 Motoring simulation 98
4.2.5 Firing simulation 99
4.2.6 Heat transfer 99
4.2.7 Blowby and crevice flows 102
4.3 GT-LU 104
4.4 LUCoVe 106
4.5 Combustion, turbulence and thermodynamics routines common to all codes 107
4.5.1 Overview 107
4.5.2 Ignition 107
4.5.3 Two-zone model 107
4.5.4 Three-zone model 108
4.5.5 Laminar burning velocity 111
4.5.6 The effect of diluent on the laminar burning velocity 125
4.5.7 Turbulent burning velocity 127
4.5.8 Turbulent flame acceleration 129
4.5.9 Flame-wall interaction 133
4.5.10 Flame geometry 138
4.5.11 Pressure equalisation 140
4.5.12 Mixing burnt gas 140
4.5.13 Gas properties and chemical equilibrium 140
4.5.14 Turbulence 141

4.6 Software testing and changes to the code 143

5 Experimental and Numerical Results **153**

5.1 Overview 153
5.2 Experimental and data processing parameters 154
5.3 Experimental Results 159
5.3.1 Overall flame geometry 159
5.3.2 Centroid movement and in-cylinder flow 164
5.3.3 Measures of flame brush thickness 172
5.3.4 Flame brush thickness as flame approaches wall 176
5.3.5 Burning velocity as flame approaches wall 181
5.3.6 Turbulent flame acceleration 187
5.3.7 Flame sphericity 198
5.4 Combustion simulation 206
5.4.1 Parameters common to all simulations 208
5.4.2 Blowby and heat transfer model calibration 210
5.4.3 Combustion model calibration 214
5.4.4 Laminar burning velocity model calibration 216
5.4.5 Sensitivity analysis 223
5.4.5.1 Initial temperature and pressure 225
5.4.5.2 Laminar burning velocity 229
5.4.5.3 Integral length scale 232
5.4.5.4 Flame-wall interaction 235
5.4.5.5 Flame centre location 238
5.4.6 Performance of the two-zone model using different flame acceleration expressions 238
5.4.7 Performance of the three-zone model in a pent roof engine . 245
5.5 Error analysis 250
5.5.1 Error in pressure measurements 255
5.5.2 Error in optical measurements 256

6 Conclusions **261**

6.1 Conclusions to the current work 261
6.2 The future of SI engine combustion simulation and directions for further research 265
6.3 Recommended improvements to experimental and numerical facilities 271

A Summary of PProc routines **277**
A.1 PProc data structure 277
A.1.1 Data fields 277
A.1.2 Cycle statistics 278
A.1.3 Dataset statistics 278
A.1.4 Cycle lists 279
A.1.5 Dataset lists 279
A.1.6 Dataset parameters 279
A.1.7 Engine parameters 280
A.2 PProc routines 280

B Summary of IProc routines **282**

Bibliography **284**

List of Figures

1.1 Longitudinal and transverse spatial velocity correlations. 6
1.2 Sketch of a typical spatial autocorrelation function illustrating the definition of the Taylor scale λ. 8
1.3 Aliasing of high frequency turbulent structures in the one dimensional spectrum. Both the structures on the right of the illustration and the structures on the left are recorded as having the same wavelength despite the fact that the structures on the right have a shorter wavelength. After Tennekes and Lumley [1972]. 12
1.4 Generalised one and three-dimensional PSDs for isotropic turbulence at high Reynolds numbers. Note that $S(f)$ is larger than $E(f)$ at low frequencies because of the effect of aliasing in the one dimensional spectrum. 14
1.5 Variation in rms turbulent velocity with mean piston speed for different engines. Data sources are listed in Table 1.1 19
1.6 Turbulent combustion regimes, after Borghi and Destriau [1998]. . . 23
1.7 Dimensionless PSD of turbulence (left) and the effective rms turbulent velocity derived from it using Equation 1.46 (right). After Abdel-Gayed et al. [1987]. 26

2.1 Fuel and air control tower. 35
2.2 Schematic of the fuel and air control tower. Drawing by Mr Ashley Arundel. 36
2.3 Schematic of the engine intake and exhaust system. Drawing by Mr Ashley Arundel. 37
2.4 Shaft encoder TDC position dynamic alignment using a capacitive proximity sensor. 42
2.5 Timing rack and dynamometer inverter control panel. 45

2.6 Schematic showing the arrangement of the laser sheet, engine, scattered light optics and camera. Drawing by Mr David Cooper. . . . 46
2.7 Photographs of the experimental apparatus showing the arrangement of the camera, optics and engine. 47
2.8 Tool used to set the height of the laser sheet above TDC. 51
2.9 Data acquisition and timing rack wiring schematic. Drawing by Mr Ashley Arundel. 53
2.10 Scale images with the scale placed on the TDC plane (2.10a); parallel with the pent roof looking through the big window (2.10b); and parallel with the pent roof looking through the small window with the positions of the intake and exhaust ports indicated (2.10c). . . . 57

3.1 Typical raw data captured by the DAQ system. The bottom two graphs use a different scale to reveal detail around the time of ignition. 63
3.2 Flowchart showing the procedure used to process data recorded by the DAQ system. 64
3.3 Flowchart showing an overview of a single time step during a LUSIEDA reverse analysis. When the flow reaches *Solve to give equal experiment and model pressures* control transfers to the flowchart shown in Figure 3.4. 68
3.4 Flowchart showing the initial series of calculation steps taken to find Δm_b during a LUSIEDA reverse analysis. When the flow reaches *Iterate to find* Δm_b control transfers to the flowchart shown in Figure 3.5. 69
3.5 Flowchart showing the calculation steps used by LUSIEDA to determine Δm_b. 70
3.6 Stages in processing raw images. 73
3.7 Smoothing the first and last frames of a typical cycle using alternating sequential open close filtering. 75
3.8 The first 24 raw and processed images in a typical cycle. 77
3.9 Slices through the $\overline{c}$ field illustrating the effect of smoothing the volume data. 79
3.10 1-ring neighbourhood and smoothing algorithm applied to an arbitrary surface. After Taubin [1995a]. 80
3.11 Definition of angles α_{ij}, β_{ij} and θ. 82

3.12 Schematic of a turbulent flame front in the flamelet regime illustrating the flame brush thickness and the laminar flame thickness. . 86
3.13 Different definitions of δ_t applied to experimental $\overline{c}$ data. 86
3.14 Volume of burnt gas and corrections to Equation 3.21. 88
3.15 Regions of a $\overline{c} = 0.5$ isosurface identified as active and inactive; red shading denotes active surface, black shading denotes inactive surface. 90
3.16 Progression through a cycle of regions of the isosurface at $\overline{c} = 0.5$ identified as active and inactive; red shading denotes active surface, black shading denotes inactive surface. 91

4.1 Flowchart showing the sequence of events during a LUSIE simulation. 97
4.2 Flowchart showing the sequence of events during the simulation of a motoring cycle by LUSIE. 100
4.3 Flowchart showing the sequence of events during the simulation of a firing cycle by LUSIE. 101
4.4 Definition of distances used in calculating the area of a sector of a circle, Equation 4.1. 103
4.5 Flowchart showing the interaction between GT-Power and the LUSIE combustion routines during a single time step of a GT-LU simulation. 105
4.6 Flowchart showing a single time step during the simulation of constant volume adiabatic combustion using the LUCoVe software. . . 106
4.7 Flowchart showing a single time step during the simulation of combustion using the two-zone model. 109
4.8 Flowchart showing a single time step during the simulation of combustion using the three-zone model. 112
4.9 Variations of enhancement factor [dimensionless], burning velocity [m/s] and laminar burning velocity [m/s] with ϕ at 20 bar and 427 K for an iso-octane—air flame initially at 10 bar and 358 K. Reproduced from Al-Shahrany et al. [2005]. 119
4.10 Laminar burning velocity expressions and experimental data compared at 10 bar and 360 K across a range of equivalence ratios. Note that the data of Al-Shahrany [2004] is at 358 K. 121
4.11 Laminar burning velocity expressions and experimental data compared at 5 bar and 360 K across a range of equivalence ratios. 121

4.12 Laminar burning velocity expressions and experimental data compared at $\phi = 1$ and 5 bar across a range of temperatures. 122
4.13 Laminar burning velocity expressions and experimental data compared at $\phi = 1$ and 60 bar across a range of temperatures. 122
4.14 Laminar burning velocity expressions and experimental data compared at $\phi = 1$ and 360 K across a range of pressures. 123
4.15 Laminar burning velocity expressions and experimental data compared at $\phi = 1$ and 700 K across a range of pressures. 123
4.16 Laminar burning velocity expressions compared under isentropic compression from 1 bar and 300 K for a stoichiometric mixture. . . 125
4.17 Correction factors to give the laminar burning velocity of a fuel—air mixture combined with a diluent published by Metghalchi and Keck [1982] and Rhodes and Keck [1985]. 126
4.18 LUSIE predicted flame development models compared against crank angle for a typical LUPOE1-D 1500 rpm base condition cycle. . . . 133
4.19 LUSIE predicted flame development models compared against radius for a typical LUPOE1-D 1500 rpm base condition cycle. 134
4.20 LUSIE predicted flame development models compared against time for a typical LUPOE1-D 1500 rpm base condition cycle. 135
4.21 Mean progress variable profiles normalised with flame brush thickness [Lipatnikov and Chomiak, 2002]. The solid curve corresponds to Equation 4.33, the symbols show experimental data gathered by a number of authors. The key remains unchanged from the original publication. 137
4.22 The profile of the mean heat release rate $|\partial \bar{c}(x')/\partial x'|$ given by Equation 4.33 truncated in the presence of a wall. 137
4.23 Flame declaration in the presence of a wall for dimensionless flame brush thicknesses ranging from 1 to 4 as predicted by Equation 4.34. 138
4.24 Integral scale definitions used in LUSIE for disc and pent geometry combustion chambers. 143
4.25 Thermodynamic properties predicted by LUSIE and GT-Power. . . 146
4.26 Burnt gas equilibrium mole fractions predicted by LUSIE (solid lines) and GT-Power (dotted lines). As there is very little difference between the two codes the dotted lines fall almost directly on top of the solid lines. 147

4.27 A comparison of the pressure equalisation routines used in LUSIE and GT-Power. 148
4.28 Heat transfer rate using the Woschni [1967] correlation, cylinder temperature and pressure for a motoring cycle as calculated by LUSIE and GT-Power. 149
4.29 Piston ring pack pressure predicted by LUSIE and GT-Power. . . . 150
4.30 Top land crevice and piston ring orifice mass flow rates predicted by LUSIE and GT-Power. The numbers denote the piston ring gaps, 1 being closest to the piston crown and 3 closest to the crank case. 151
4.31 Cylinder pressures and temperatures predicted by LUSIE and GT-Power during a two-zone combustion simulation. 152
4.32 Cylinder pressures and temperatures predicted by LUSIE and GT-Power during a three-zone combustion simulation. 152

5.1 Isosurfaces of $\overline{c} = 0.5$ coloured to show the local mass burning velocity (m/s) at the 1500 rpm base condition. Figure continued on page 162. 161
5.2 Isosurfaces of $\overline{c} = 0.5$ coloured to show the local mass burning velocity (m/s) at the 750 rpm condition. Figure continued on page 164.163
5.3 Isosurfaces of $\overline{c} = 0.5$ coloured to show the local mass burning velocity (m/s) at the 1000 rpm condition. Figure continued on page 166.165
5.4 Isosurfaces of $\overline{c} = 0.5$ coloured to show the local mass burning velocity (m/s) at the 1500 rpm lean condition. Figure continued on page 168. 167
5.5 Binary images showing the locations of burnt and unburnt gas 7.5 mm above the TDC plane in ten different cycles for the 1500 rpm lean condition. The first image (left hand side) is at -9.3° aTDC, the last image (right hand side) is at 4.8° aTDC. 169
5.6 Slices showing the $\overline{c}$ field in the centre of the bore on the y-z plane. The engine conditions were: 1500 rpm base condition, -0.8–8.9° aTDC (left); 750 rpm stoichiometric, 2.0–11.8° aTDC (centre); 1000 rpm stoichiometric, -0.7–13.7° aTDC (right). 170
5.7 Location of the flame centroid defined as the barycentre (a) and active area centre (b) at different crank angle ° aTDC in the LUPOE2-P engine at 1500 rpm stoichiometric. 170

5.8 Location of the flame centroid defined as the barycentre 5.8a and active area centre 5.8b at different crank angle ° aTDC in the LUPOE2-P engine at 750 rpm stoichiometric. 171
5.9 Location of the flame centroid defined as the barycentre 5.9a and active area centre 5.9b at different crank angle ° aTDC in the LUPOE2-P engine at 1000 rpm stoichiometric. 171
5.10 Correlation between different measures of flame thickness for all crank angles at 1500 rpm. 173
5.11 Correlation between different measures of flame thickness for all crank angles at 750 rpm. 174
5.12 Correlation between different measures of flame thickness for all crank angles at 1000 rpm. 175
5.13 Isosurfaces of $\overline{c} = 0.1$,0.5 and 0.9 (green, blue and red respectively), illustrating the sensitivity of δ_{ts} to the angle of incidence of the surface normal vector to the $\overline{c} = 0.5$ isosurface. 176
5.14 Correlation between the distance from the wall and the flame brush thickness δ_{tg} at the 1500 rpm base condition. 178
5.15 Correlation between the distance from the wall and the flame brush thickness δ_{tg} at the 750 rpm condition. 179
5.16 Correlation between the distance from the wall and the flame brush thickness δ_{tg} at the 1000 rpm condition. 180
5.17 Correlation between the distance from the wall and the burning velocity at the 1500rpm base condition. 182
5.17 Correlation between the distance from the wall and the burning velocity at the 1500rpm base condition. 183
5.18 Correlation between the distance from the wall and the burning velocity at the 750rpm condition. 184
5.19 Correlation between the distance from the wall and the burning velocity at the 1000rpm condition. 185
5.20 Correlation between experimental flame deceleration in the presence of a wall and Equation 4.34 at the 1500 rpm base condition, 6.3° aTDC. 186
5.21 Correlation between experimental flame deceleration in the presence of a wall and Equation 4.34 calculated using $\delta_{t0} = 1.8/\delta_{tg0}$ at the 1500 rpm base condition, 6.3° aTDC. 187

5.22 Correlation between experimental flame deceleration in the presence of a wall and Equation 4.34 calculated using $\delta_{t0} = 1.8/\delta_{tg0}$ at the 750 rpm condition, 7.4° aTDC. 188
5.23 Correlation between experimental flame deceleration in the presence of a wall and Equation 4.34 calculated using $\delta_{t0} = 1.8/\delta_{tg0}$ at the 1000 rpm condition, 7.8° aTDC. 189
5.24 Variation in the LUSIEDA calculated turbulent mass burning velocity during three LUPOE1-D middle cycles at the 1500 rpm reference condition. 190
5.25 Variation in the LUSIEDA calculated turbulent mass burning velocity during three LUPOE2-P middle cycles at the 1500 rpm reference condition. 190
5.26 Flame acceleration during all the fast, middle and slow LUPOE1-D cycles reported by Abdi Aghdam [2003]. 191
5.27 Early flame development in LUPOE2-P with a stoichiometric mixture at 1500 rpm. The laser sheets are positioned at 9 (left), 10.5 (middle) and 12 mm (right) above the TDC plane, the spark gap is approximately 11.2 mm above the TDC plane. The first frame is taken at the moment of ignition, 7° bTDC, with 0.9° CA between frames. Each frame covers an area of 20 × 20 mm. Figure continued on page 195. 194
5.28 Flame acceleration during all the turbulent deflagrations reported by Ormsby [2005]. 196
5.29 Area weighted mean and standard deviation of the distance from the spark gap to active surface elements at the 1500 rpm base condition. 200
5.30 Area weighted PDF of the distance from the spark gap to active surface elements at 5.4° aTDC for the 1500 rpm base condition. . . . 201
5.31 Isosurfaces of $\bar{c} = 0.5$ coloured to show the local mass burning velocity at the 1500 rpm base condition showing the flame surface conforming the shape of the combustion chamber as it approaches the walls. 202
5.32 Area weighted mean and standard deviation of the distance from the flame barycentre to active surface elements at the 1500 rpm base condition. 203

5.33 Area weighted PDF of the distance from the flame barycentre to active surface elements at 5.4° aTDC for the 1500 rpm base condition. 203
5.34 Area weighted mean and standard deviation of the distance from the spark gap to active surface elements at the 750 rpm condition. . 204
5.35 Area weighted mean and standard deviation of the distance from the flame barycentre to active surface elements at the 750 rpm condition. 205
5.36 Area weighted mean and standard deviation of the distance from the spark gap to active surface elements at the 1000 rpm condition. 205
5.37 Area weighted mean and standard deviation of the distance from the flame barycentre to active surface elements at the 1000 rpm condition. 206
5.38 Flame active surface area plotted against flame volume derived from mean progress variable isosurfaces and LUSIEDA analysis of fast, middle and slow cycles at the 1500 rpm base condition. . . . 207
5.39 Flame active surface area plotted against flame volume derived from mean progress variable isosurfaces and LUSIEDA analysis of fast, middle, and slow, cycles at the 750 rpm condition. 208
5.40 Flame active surface area plotted against flame volume derived from mean progress variable isosurfaces and LUSIEDA analysis of fast, middle and slow cycles at the 1000 rpm condition. 209
5.41 Experimental (black) and LUSIE calculated (red) motoring pressure traces for the LUPOE2-P engine at 750 rpm with different intake pressures. The bottom pressure trace is the signal recorded by the absolute pressure transducer. 213
5.42 Experimental (black) and LUSIE calculated (red) motoring pressure traces for the LUPOE2-P engine at 1000 rpm with different intake pressures. The bottom pressure trace is the signal recorded by the absolute pressure transducer. 214
5.43 Experimental (black) and LUSIE calculated (red) motoring pressure traces for the LUPOE2-P engine at 1500 rpm with different intake pressures. The bottom pressure trace is the signal recorded by the absolute pressure transducer. 215
5.44 Surface showing the variation in G for different values of the combustion model constants A and C_{τ_b}. 217

5.45 Predicted (coloured lines) and experimental (black lines) pressure (top) and entrainment flame radius (bottom) for LUPOE1-D using different laminar burning velocity expressions at the base condition. The key to the coloured lines is given in Table 5.6. 219
5.46 Predicted laminar burning velocities for the LUPOE1-D simulations depicted in Figure 5.45. 220
5.47 Predicted (coloured lines) and experimental (black lines) pressure (top) and entrainment flame radius (bottom) for LUPOE1-D using different laminar burning velocity expressions at the 1500 rpm $\phi = 0.8$ condition. The key to the coloured lines is given in Table 5.6. . . 221
5.48 Predicted (coloured lines) and experimental (black lines) pressure (top) and entrainment flame radius (bottom) for LUPOE1-D using different laminar burning velocity expressions at 1500 rpm with a compression ratio of 10.2. The key to the coloured lines is given in Table 5.6. 222
5.49 Predicted (coloured lines) and experimental (black lines) pressure (top) and entrainment flame radius (bottom) for LUPOE1-D using different laminar burning velocity expressions at 1500 rpm with a compression ratio of 12.4. The key to the coloured lines is given in Table 5.6. 224
5.50 Sensitivity of the three-zone LUSIE model to small changes in intake pressure. 226
5.51 Sensitivity of the three-zone LUSIE model to small changes in intake temperature. 228
5.52 Sensitivity of the three-zone LUSIE model to small changes in laminar burning velocity. 230
5.53 Sensitivity of the two-zone LUSIE model to small changes in laminar burning velocity. 231
5.54 Sensitivity of the three-zone LUSIE model to small changes in integral length scale. 233
5.55 Sensitivity of the two-zone LUSIE model to small changes in integral length scale. 234
5.56 Sensitivity of the three-zone LUSIE model for a pent roof engine to changes in integral length scale model. Red lines show the integral scale decreasing in the eaves of the pent, Equation 4.39; black lines show no decrease, Equation 4.38 236

5.57 Sensitivity of the two-zone LUSIE model to different flame-wall interaction models. 237
5.58 Sensitivity of the three-zone LUSIE model to changes in ignition position when simulating a pent roof engine. Lines of different colours correspond to the ignition positions shown in the inset of the top graph. 239
5.59 LUSIE simulations of LUPOE1-D using different flame acceleration models at the 1500 rpm base condition. 242
5.60 LUSIE simulations of LUPOE1-D using different flame acceleration models at the 750 rpm operating condition. 243
5.61 LUSIE simulations of LUPOE1-D using different flame acceleration models at the 2000 rpm operating condition. 244
5.62 Cylinder pressure recorded in selected fast, middle and slow cycles compared with the LUSIE predicted pressure for LUPOE2-P at the 1500 rpm base condition. 246
5.63 Flame radius derived from mean progress variable isosurfaces (black crosses) compared with LUSIEDA calculated burnt flame radii for fast, middle and slow cycles, and the LUSIE predicted burnt flame radius for LUPOE2-P at the 1500 rpm base condition. Line colours correspond with those used in Figure 5.62. 246
5.64 Flame active surface area derived from mean progress variable isosurfaces (black crosses) compared with LUSIEDA calculated active surface areas for fast, middle and slow cycles, and the LUSIE predicted active surface area for LUPOE2-P at the 1500 rpm base condition. Line colours correspond with those used in Figure 5.62. . . . 248
5.65 Flame volume derived from mean progress variable isosurfaces (black crosses) compared with LUSIEDA calculated burnt gas volumes for fast, middle and slow cycles, and the LUSIE predicted burnt gas volume for LUPOE2-P at the 1500 rpm base condition. Line colours correspond with those used in Figure 5.62. 248
5.66 Cylinder pressure recorded in selected fast, middle and slow cycles compared with the LUSIE predicted pressure for LUPOE2-P at the 750 rpm operating condition. 251

5.67 Burnt flame radius derived from mean progress variable isosurfaces (black crosses) compared with LUSIEDA calculated burnt flame radii for fast, middle and slow cycles, and the LUSIE predicted burnt flame radius for LUPOE2-P at the 750 rpm operating condition. Line colours correspond with those used in Figure 5.66. 251
5.68 Flame active surface area derived from mean progress variable isosurfaces (black crosses) compared with LUSIEDA calculated active surface areas for fast, middle and slow cycles, and the LUSIE predicted active surface area for LUPOE2-P at the 750 rpm operating condition. Line colours correspond with those used in Figure 5.66. 252
5.69 Flame volume derived from mean progress variable isosurfaces (black crosses) compared with LUSIEDA calculated burnt gas volumes for fast, middle and slow cycles, and the LUSIE predicted burnt gas volume for LUPOE2-P at the 750 rpm base condition. Line colours correspond with those used in Figure 5.66. 252
5.70 Cylinder pressure recorded in selected fast, middle and slow cycles compared with the LUSIE predicted pressure for LUPOE2-P at the 1000 rpm operating condition. 253
5.71 Burnt flame radius derived from mean progress variable isosurfaces (black crosses) compared with LUSIEDA calculated burnt flame radii for fast, middle and slow cycles, and the LUSIE predicted burnt flame radius for LUPOE2-P at the 1000 rpm operating condition. Line colours correspond with those used in Figure 5.70. 253
5.72 Flame active surface area derived from mean progress variable isosurfaces (black crosses) compared with LUSIEDA calculated active surface areas for fast, middle and slow cycles, and the LUSIE predicted active surface area for LUPOE2-P at the 1000 rpm operating condition. Line colours correspond with those used in Figure 5.70. 254
5.73 Flame volume derived from mean progress variable isosurfaces (black crosses) compared with LUSIEDA calculated burnt gas volumes for fast, middle and slow cycles, and the LUSIE predicted burnt gas volume for LUPOE2-P at the 1000 rpm operating condition. Line colours correspond with those used in Figure 5.70. 254

5.74 Positions of P_{max} plotted against $\theta_{P_{max}}$ for ensemble averaged first, second, third etc. cycles from individual data sets recorded on LUPOE2-P at the 1500 rpm base condition. Numbers in Figure 5.74a denote the cycle number to which each point relates. Red points in Figure 5.74b correspond to the numbers in Figure 5.74a whilst blue points show the position of P_{max} against $\theta_{P_{max}}$ for all of the cycles in the data set. 257
5.75 Change in $\bar{c}$ calculated using increasing numbers of binary images 258
5.76 Flame thicknesses calculated from simulated spherical flames with and without data smoothing. 260

List of Tables

1.1 Data sources for Figure 1.5. 20

2.1 LUPOE2-P Engine dimensions. 34

4.1 Laminar burning velocity correlations, their range of applicability and experimental method used. 114
4.2 Constants for Equation 4.6 for iso-octane—air mixtures. 115
4.3 Constants for Equation 4.7 for iso-octane—air mixtures. 115
4.4 Constants for Equation 4.8 115

5.1 LUPOE2-P operating conditions. 158
5.2 LUPOE1-D operating conditions. 158
5.3 Camera and data acquisition system settings (1). 159
5.4 Camera and data acquisition system setting (2). 159
5.5 Data processing parameters. 159
5.6 LUSIE three-zone combustion model constants optimised for different laminar burning velocity models. The accuracy of all the constants is ± 0.1. 218

Nomenclature

Roman and Greek symbols

A	m^2, -	Area, turbulent burning velocity model constant
C	-	Constant
$\overline{c}$	-	Mean combustion progress variable
Da	-	Damköhler number
δ_l	m	Laminar flame thickness
δ_t	m	Turbulent flame brush thickness
δ_{tg}	m	Turbulent flame brush thickness defined using the gradient of the $\overline{c}$ field
δ_{ts}	m	Turbulent flame brush thickness defined as the distance between two $\overline{c}$ isosurfaces
E	W/kg	Three-dimensional turbulence PSD
$\overline{E}$	-	Dimensionless three-dimensional turbulence PSD
ε	W/kg	Turbulence specific dissipation rate
$\overline{F}$	-	Dimensionless frequency
f	Hz, -	Frequency, face
f_d	-	Flame acceleration/development factor
f_w	-	Flame-wall deceleration factor
$\mathcal{F}$	-	Set of faces

G	-	Goodness of fit in the least squares sense of LUSIE constants A and C_{τ_b} to experimental pressure and flame radius data
h_c	m	Combustion chamber clearance height
Ka	-	Karlovitz number
k	m^{-1}	Wavenumber
L	m	Turbulence integral length scale
λ	m	Turbulence Taylor scale
m	kg	Mass
P	Pa	Pressure
ϕ	-	Fuel-air equivalence ratio
R	-	Autocorrelation function
Re_L	-	Turbulence Reynolds number based on the integral scale
Re_λ	-	Turbulence Reynolds number based on the Taylor scale
r	m	Radius, distance
ρ	kg/m^3	Density
S	W/kg	One-dimensional turbulence PSD
$\overline{S}$	-	Dimensionless one-dimensional turbulence PSD
$\overline{S}_p$	m/s	Mean piston speed
$\mathcal{S}$	-	Set of faces and vertices defining a surface
T	K	Temperature
t	s	Time
τ_b	s	Characteristic burn-up time of entrained eddies
τ_L	s	Turbulence integral time scale
τ_λ	s	Turbulence Taylor time scale
θ	°CA	Crank angle
U	J, m/s	Total internal energy, total flow velocity
$\overline{U}$	m/s	Mean flow velocity
u	m/s	Burning velocity, turbulent velocity component
u'	m/s	Rms turbulent velocity

u'_k	m/s	Effective rms turbulent velocity
V	m^3	Volume
$\vec{v}$	m	Vertex, vector
$\mathcal{V}$	-	Set of vertices
x_b	-	Mass fraction burnt

Subscripts

b	Burnt
e	Entrained/entrainment
l	Laminar
r	Reaction (burnt)
t	Turbulent
u	Unburnt
$0, \infty$	Initial, final or asymptotic qualities

Acronyms and abbreviations

BDC	Bottom dead centre
CFD	Computational fluid dynamic
DAQ	Data acquisition (system)
DNS	Direct numerical simulation
°b/aBDC	Degrees of crank angle rotation before/after bottom dead centre
°b/aTDC	Degrees of crank angle rotation before/after top dead centre
°CA	Degrees of crank angle rotation
GT-LU	Gamma Technologies Leeds university (integrated engine simulation software)
HWA	Hot wire anemometry
LES	Large eddy simulation
LDV	Laser Doppler velocimetry
LUCoVe	Leeds university combustion vessel (simulation software)

LUPOE1/2-D/P	Leeds university spark ignition ported optical engine, Mk I/II, disc/pent configuration
LUSIE	Leeds university spark ignition engine (simulation software)
LUSIEDA	Leeds university spark ignition engine data analysis (reverse analysis software)
PDF	Probability density function
PIV	Particle image velocimetry
PSD	Power spectral density
PTV	Particle tracking velocimetry
RANS	Reynolds averaged Navier-Stokes
rms	Root mean square
SI	Spark ignition
TDC	Top dead centre
TTL	Transistor transistor logic

Chapter 1

Introduction

1.1 Motivation and scope of the current work

Almost all commonly used motive power sources ultimately derive their energy from fossil fuels. That reserves of fossil fuels, in particular oil, are finite and likely to be exhausted at some point in the not too distant future has been widely discussed and does not need to be elaborated further here. Despite the dwindling reserves and historically high price of oil at the time of writing, the gasoline fuelled spark ignition engine is still responsible for a significant proportion of automotive propulsion. Because of its compact size, relative ease of manufacture in large numbers and ability to burn with little modification a multitude of fuels this is likely to remain the case even if the often talked about switch to a hydrogen economy occurs.

The modern spark ignition engine is the product of over 100 years of research and development effort. Despite this expenditure of time and money there is still scope for improvement. Incremental engine development using prototypes has always been expensive because bespoke manufacturing of small numbers of parts is labour and capital intensive. Since the advent of digital computing attempts have been made to reduce the cost of engine development by performing some of the development work in a virtual environment. These attempts have had some success and certainly our understanding of the basic physics and chemistry in-

volved in combustion has improved remarkably over the last 50 years because of them. However, like the engine itself, there is significant scope for improvement in spark ignition engine combustion models.

This work presented in this thesis attempts to examine the suitability of a thermodynamic model of spark ignition engine combustion for simulating modern pent-roof car engines. The basic combustion code, which has previously been compared with data from a simple disc geometry spark ignition engine [Abdi Aghdam, 2003], is modified to interface with a commercially available gas dynamic code which is capable of simulating engine breathing. The code is extended by the addition of a number of submodels, the performance of which are evaluated against pressure and ensemble averaged three-dimensional flame position data recorded in an idealised pent-roof engine. Finally an attempt is made to draw conclusions from the research and provide direction for future work.

1.2 Introduction to spark ignition engines

A piston engine (either compression ignition or spark ignition) consists at the most basic level of a reciprocating piston connected to a crankshaft. These two elements form a crank-slider mechanism, which converts the linear motion of the piston to rotational motion. The piston moves within a cylinder closed at one end by the cylinder head to form the combustion chamber. Depending on the configuration of the engine the head may contain valves to facilitate engine breathing, or this may occur through ports or valves in the cylinder walls. In the case of a spark ignition (SI) engine, the motion of the piston compresses a premixed charge of fuel and air within the combustion chamber. The chemical energy stored in the fuel is then released by combustion which is initiated by a spark when the piston is close to top dead centre (TDC). The liberated energy is from the fuel is either converted to mechanical work through movement of the piston, rejected to the atmosphere as the exhaust gases are expelled when the piston reaches bottom dead centre (BDC), or lost through heat transfer to the cylinder walls. The cycle is completed by introducing a fresh charge to the combustion chamber.

In order to allow gas exchange at sensible engine speeds, the flows of gas into and out of the combustion chamber are necessarily turbulent. This turbulence persists during the compression stroke and combustion therefore all SI engine

combustion may be categorised as premixed[1] turbulent combustion. This chapter briefly summarises relevant topics in turbulence, laminar and turbulent premixed combustion, photographic diagnosis of combustion in engines and current combustion modelling techniques. A comprehensive treatment of the topics covered in this chapter may be found in the following references: Heywood [1988], Lumley [1999], Tennekes and Lumley [1972], Lipatnikov and Chomiak [2002], Borghi and Destriau [1998], Turns [1996].

1.3 The nature of turbulent flow

As combustion inside a spark ignition engine takes place in a turbulent environment, and the characteristics of the turbulence strongly influence the combustion, it is necessary to understand the features of turbulent flow before turbulent combustion can be understood.

Typical turbulent flows consist of a continuous spectrum of eddies.[2] The size of the largest eddies, which contain the majority of the energy, are determined by the dimensions of the container. The size of the smallest eddies, which are responsible for most of the dissipation, are determined by the viscosity of the fluid and the rate of dissipation of the turbulent energy. The presence of turbulent eddies increases the transport of heat and mass in the fluid well above the levels achieved by molecular diffusion alone [Tennekes and Lumley, 1972]. It is this enhanced mixing and transport which makes turbulence essential for combustion in spark ignition engines. The rate of burning in an equivalent laminar mixture would be around an order of magnitude slower making it impossible for the flame to travel across the combustion chamber in the time available at typical engine speeds. Turbulence is not only essential for enhancing the combustion in engines but also plays a large part in the preparation of the charge, ensuring that the fuel-air mixture which enters the cylinder, and any residual gases remaining

[1]There are instances where not all the fuel is premixed. This can occur for example during cold start conditions or when using a direct injection engine where, because of the operating condition, the injection takes place late in the cycle. As non-premixed combustion can lead to soot and unburnt hydrocarbon emissions this is usually not the intended operation of the engine.

[2]The term eddy, although commonly used when discussing turbulence phenomena, is perhaps misleading. The word eddy taken on its own implies a discreet rotating 'blob' of fluid where as the reality is a velocity field which, although almost certainly containing rotating structures identifiable as eddies in the traditional sense, will also probably contain many structures which do not conform to the traditional description of an eddy but still contribute to the characteristics of the turbulence none the less.

in the cylinder from the previous cycle, are homogeneous by the time combustion is initiated by the spark [Heywood, 1988].

Turbulence is by no means a simple phenomena and has been described as "The last great unsolved problem of classical physics" by Richard Feynman. One of the reasons turbulence is such a complex problem is that it involves a continuous spectrum of length and time scales and hence is only really vulnerable to attack from statistical techniques such as correlations or probability densities which reduce the amount of information required to describe the flow to manageable levels. The difficulty of producing analytical solutions to problems of turbulence requires that the following discussion deals mainly with the special case of homogeneous isotropic turbulence which is well studied theoretically and for which it is possible to arrive at certain general laws with a wide range of applicability. It should be noted that real flows are rarely either homogeneous or isotropic at the largest scales of turbulence but, owing to the difficulty in deriving laws to describe specific cases, it is common to apply the results given below to all turbulent flows.

In the study of turbulence it is customary to use certain terms to describe the nature of the flow:

- Homogeneous - Spatially uniform. Measurements taken in one position are statistically equivalent to measurements taken in any other position.
- Isotropic - With no preferential direction. Measurements taken with one particular probe orientation are statistically indistinguishable from measurements taken with any other probe orientation. Note that this is different to homogeneous. It is possible for turbulence to homogeneous without being isotropic and vice versa.
- Stationary - A function is said to be statistically stationary if its mean does not vary with time.
- Eulerian - Describes measurements or calculations which use a fixed frame of reference in space.
- Lagrangian - Describes measurements or calculations made with respect to individual moving fluid particles.

1.3.1 The Reynolds decomposition and measures of the intensity of turbulence

Following the methodology first proposed by O. Reynolds in 1895 it is usual to decompose the instantaneous velocity U in a turbulent flow field into a mean flow $\overline{U}$ and fluctuating "turbulent" component u such that

$$U = \overline{U} + u \tag{1.1}$$

where the time averaged mean of a, denoted with a bar, $\overline{a}$, over the period Δt starting at t_0 is defined as

$$\overline{a} = \lim_{\Delta t \to \infty} \frac{1}{\Delta t} \int_{t_0}^{t_0 + \Delta t} a \, \mathrm{d}t \tag{1.2}$$

and, by definition,

$$\overline{u} = 0 \tag{1.3}$$

The root mean square (rms) of the fluctuating velocity component, denoted u'

$$u' = \sqrt{\overline{u^2}} \tag{1.4}$$

is often used in studies of turbulence as a measure of the intensity of the fluctuations or as a characteristic speed of rotation for the largest eddies in a turbulent flow. The turbulent kinetic energy per unit mass of fluid e_k can be calculated by summing the contribution from each of the orthogonal components

$$e_k = \frac{1}{2}\left(u'^2 + v'^2 + w'^2\right) \tag{1.5}$$

where u', v' and w' denote the rms velocities in the directions of the x, y and z axes respectively. In the case of isotropic turbulence the rms velocity is the same regardless of the orientation of the measurement (i.e. $u' = v' = w'$) hence Equation 1.5 reduces to

$$e_k = \frac{3}{2}u'^2 \tag{1.6}$$

1.3.2 Spatial velocity correlations

As turbulence is by its very nature stochastic, any detailed analysis performed on a turbulent flow must use statistical methods such as correlations and probability

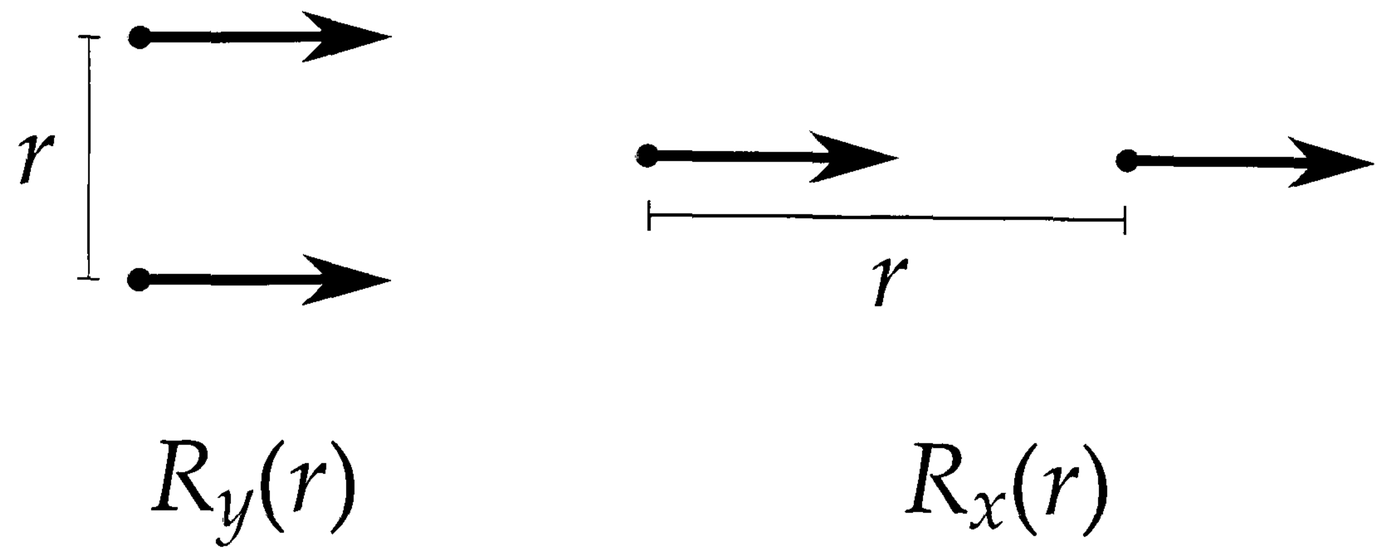

Figure 1.1: Longitudinal and transverse spatial velocity correlations.

density functions (PDFs). In order to gain a deeper insight into the nature of the fluctuating velocity component it is desirable to know how it varies in time or space and how the fluctuating component at one particular time or position is related to the fluctuating component at a different time or position. One way of investigating the relationship between the fluctuating velocity component u at position x, and position $x+r$ is to inspect the value of $\overline{u(x)u(x+r)}$ as r increases. If u changes only by a small amount as the point of measurement is moved then the product $\overline{u(x)u(x+r)}$ will remain approximately constant with increasing r and u is said to correlate well with itself. If u changes rapidly with position then the opposite is true. The distance over which u correlates well with itself is a measure of the size of the largest eddies or structures in the flow field.

The concept of an autocorrelation function can be used to give characteristic sizes for the eddies in a turbulent flow. In studies of turbulence a normalised spatial autocorrelation function $R(r)$ is often used.

$$R(r) = \frac{\overline{u(x)u(x+r)}}{u'^2} \tag{1.7}$$

Depending on the relative orientation of the vectors u and r the normalised autocorrelation function may be either longitudinal R_x or transverse R_y as illustrated in Figure 1.1. In isotropic turbulence the two correlations are related by [Batchelor, 1953, von Karman, 1937]

$$R_y = R_x + \frac{1}{2} r \frac{\partial R_x}{\partial r} \tag{1.8}$$

The easiest correlation to generate experimentally is the longitudinal correla-

tion which can be measured using just one probe providing there is an appreciable bulk flow velocity and Taylor's hypothesis[3] is applicable.

1.3.3 Characteristic turbulent length scales

The area under an autocorrelation function $R(r)$ gives an indication of the characteristic size of the energy containing eddies in a turbulent flow L, known as the integral scale [Tennekes and Lumley, 1972]

$$L = \int_0^\infty R(r)\,\mathrm{d}r \tag{1.9}$$

Depending on whether the longitudinal or transverse autocorrelation function is used to determine the integral length scale, the scale is refereed to as a longitudinal L_x or transverse L_y integral scale. By way of Equation 1.8 the two integral scales are related by [Hinze, 1959]

$$L_x = 2L_y \tag{1.10}$$

A further length scale can be defined using the curvature of the autocorrelation function at the origin. From the definition of $R(r)$ it is clear firstly that $R(0) = 1$ and secondly that $R(r)$ should decay to zero as r tends to infinity. When r is close to zero $R(r)$ can be expanded in a Taylor series as follows [Bernard and Wallace, 2002]

$$R(r) = 1 + r\frac{\mathrm{d}R}{\mathrm{d}r}\bigg|_{r=0} + \frac{r^2}{2!}\frac{\mathrm{d}^2R}{\mathrm{d}r^2}\bigg|_{r=0} + \ldots \tag{1.11}$$

If higher order terms are neglected then the terms given in Equation 1.11 form a parabolic approximation to R. The intersection of this parabola with the abscissa defines a length scale λ referred to as the Taylor microscale after G. I. Taylor who first derived it [Taylor, 1921].

$$0 = 1 + \lambda\frac{\mathrm{d}R}{\mathrm{d}r}\bigg|_{r=0} + \frac{\lambda^2}{2!}\frac{\mathrm{d}^2R}{\mathrm{d}r^2}\bigg|_{r=0} \tag{1.12}$$

$$\frac{1}{\lambda^2} = -\frac{1}{2}\frac{\mathrm{d}^2R}{\mathrm{d}r^2}\bigg|_{r=0} \tag{1.13}$$

[3] Taylor [1938] proposed that if $\overline{U} \gg u$ and $\overline{U}$ is constant then taking one measurement using a series of probes in the direction of the flow is equivalent to using a fixed probe and allowing the mean flow to convect the turbulence past the measurement point.

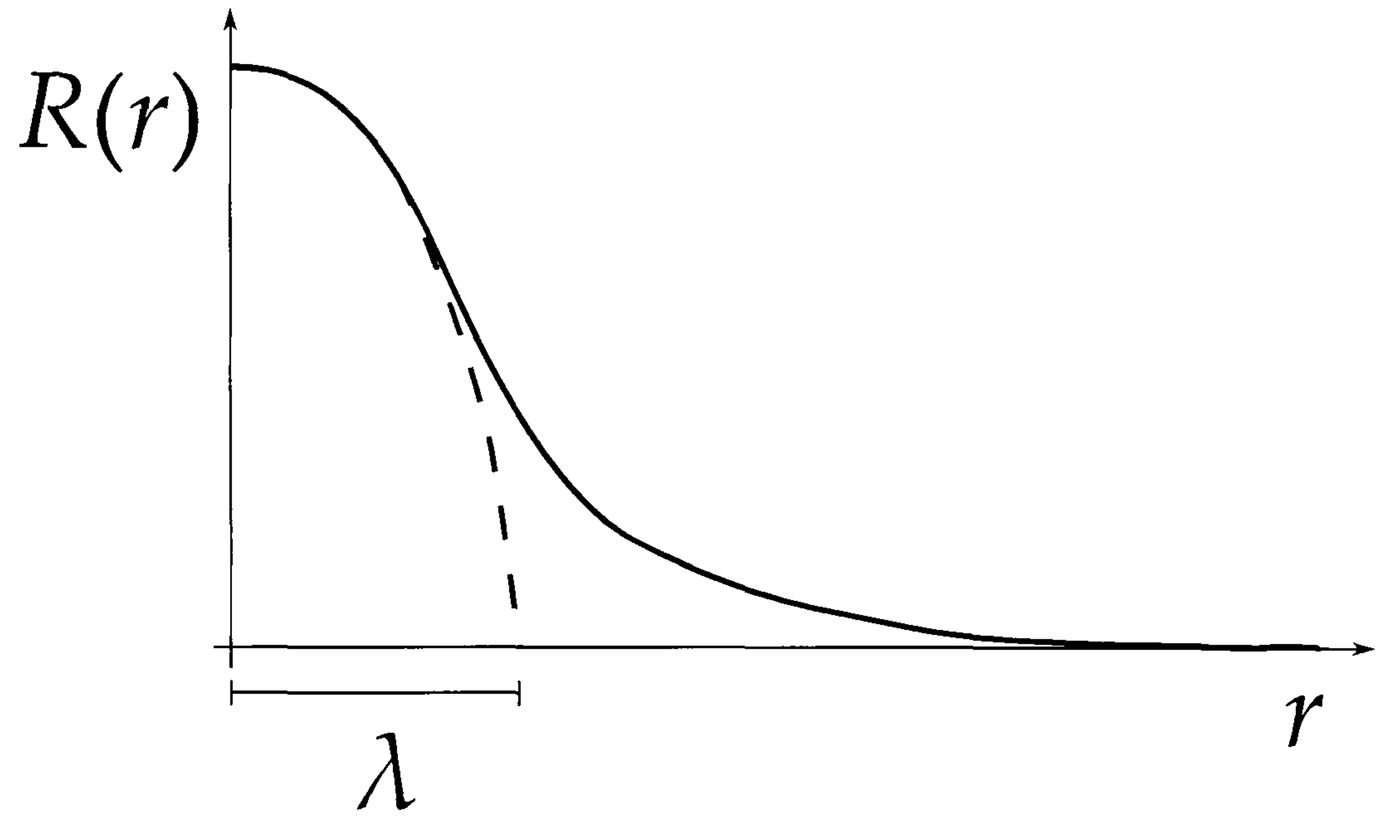

Figure 1.2: Sketch of a typical spatial autocorrelation function illustrating the definition of the Taylor scale λ.

The definition of λ is illustrated in Figure 1.2. In a similar fashion to the integral scale the longitudinal and transverse Taylor scales are related by [Hinze, 1959]

$$\lambda_x = \lambda_y \sqrt{2} \tag{1.14}$$

The Taylor scale is related to the rms fluctuating strain rate s' and the rate of dissipation ε (discussed in detail in Section 1.3.6) as follows [Taylor, 1935]

$$s' = \frac{u'}{\lambda} \tag{1.15}$$

$$\varepsilon = 15\nu s'^2 \tag{1.16}$$

where the rms fluctuating strain rate is defined as

$$s' = \sqrt{\overline{\left(\frac{\partial u}{\partial x}\right)^2}} \tag{1.17}$$

The Taylor microscale does not describe any particular class of eddies like the integral scale or Kolmogorov microscale (described in Section 1.3.6) however λ is often frequently used to describe turbulent flows as it is easily computed from the shape of the spatial autocorrelation function or the estimate $s' \sim u'/\lambda$. The

Taylor microscale has been described variously as:

- "a measure of the dimension of eddies which at the same intensity produce the same dissipation as the turbulence considered" Hinze [1959].
- "not a characteristic length of the strain-rate field and not representative of any group of eddy sizes in which dissipative effects are strong. It is not a dissipation scale, because it is defined with the assistance of a velocity scale which is not relevant for the dissipative eddies" Tennekes and Lumley [1972].
- "an intermediate length scale between the integral scale and the Kolmogorov microscale but weighted towards the smaller scales" Turns [1996].
- "a measure of the scales of motion at which turbulent energy dissipation takes place" Bernard and Wallace [2002].

From the variety of the above descriptions it is evident that, although widely used, the significance of the Taylor scale is not well understood.

Although both longitudinal and transverse correlations and length scales have been defined here, many turbulent combustion models make no distinction between the two. Unless otherwise stated, the symbols L and λ will be used to refer to the longitudinal length scales in the current work.

1.3.4 Characteristic turbulent time scales

In a fashion analogous to the spatial autocorrelation, the correlation between the turbulent velocity at two different instants in time can be expressed using a temporal autocorrelation

$$R(t) = \frac{\overline{u(t_0)u(t_0+t)}}{u'^2} \tag{1.18}$$

From this correlation an integral time scale τ_L and a Taylor time scale τ_λ can be defined [Tennekes and Lumley, 1972] as follows:

$$\tau_L = \int_{t=t_0}^{t=\infty} R(t)\,\mathrm{d}t \tag{1.19}$$

$$\tau_\lambda = -\frac{1}{2}\frac{\mathrm{d}^2 R}{\mathrm{d}t^2}\bigg|_{t=0} \tag{1.20}$$

These time scales are often interpreted as the characteristic time for an eddy revolution at the corresponding length scale. Where the mean velocity is zero the integral length scale and the integral time scale are related by:

$$L = u'\tau_L \tag{1.21}$$

1.3.5 The spectrum of turbulence

Spectral analysis of turbulence provides a method of analysing a turbulent flow in order to determine the relative importance of the contributions of each particular size or time scale of eddy. Turbulence spectra and temporal autocorrelations are related to one and other through the Fourier transform. There is no new information contained in a turbulence spectrum which is not already contained in the temporal autocorrelation, the spectrum is merely a different way of presenting the information. Different spectra can be formed using different autocorrelation functions as their starting point. A temporal autocorrelation will result in a spectrum which is a function of frequency f. A spatial autocorrelation will give a spectrum which is a function of wave number $k = 2\pi f/\overline{U}$ [Tennekes and Lumley, 1972].

The one dimensional[4] frequency power spectral density $S(f)$ is defined as [Tennekes and Lumley, 1972]

$$S(f) = \frac{1}{2\pi}\int_{-\infty}^{\infty} \exp(-itf)R(t)\,\mathrm{d}t \tag{1.22}$$

If $R(t)$ is odd the resulting spectrum will always contain an imaginary part. Spectra are always real provided $R(t)$ is an even function (i.e. turbulence is isotropic) hence it is often possible to simplify the definition of spectra for the special case of isotropic turbulence by replacing integrals between $-\infty$ and ∞ with integrals between 0 and ∞ and multiplying by a factor of two. Applying this procedure to Equation 1.22 gives

$$S(f) = \frac{1}{\pi}\int_{0}^{\infty} R(t)\cos(tf)\,\mathrm{d}t \tag{1.23}$$

The one dimensional power spectral density (PSD) shows how the turbulent kinetic energy is distributed among the different scales of the flow. The value of $S(f)$ at a particular frequency is proportional to the turbulent kinetic energy of eddies at that particular frequency. It follows therefore that the area under $S(f)$ is

[4] One dimensional because the measurements taken to generate $R(t)$ were one dimensional.

proportional to the total kinetic energy of the flow (compare with Equation 1.6).

$$\int_0^\infty S(f)\,\mathrm{d}f = \int_0^\infty S(k)\,\mathrm{d}k = u'^2 \tag{1.24}$$

Using the relationship given in Equation 1.24 the one dimensional PSD is often presented in dimensionless form as [Taylor, 1938]

$$\overline{S}(\overline{F}) = \frac{S(f)}{u'^2\tau_L} \tag{1.25}$$

where $\overline{F} = f\tau_L$ is the dimensionless frequency and $\int_0^\infty \overline{S}(\overline{F})\,\mathrm{d}f = 1$.

The one dimensional PSD of turbulence is susceptible to aliasing. This occurs because measurements are taken along a line (see Figure 1.1) and it is impossible to distinguish between the signal generated by turbulent structures which are aligned with the measurement direction and those which approach it at an angle. This situation is illustrated in Figure 1.3.5. At high frequencies where the size of the turbulent eddies is small aliasing is not a big problem [Tennekes and Lumley, 1972]. This is because, as discussed in Section 1.3.6, small eddies tend to local isotropy, they have a similar size in all directions. At low frequencies turbulence tends to be strongly anisotropic and aliasing of smaller eddies can influence the shape of $S(f)$: measured one-dimensional PSDs at a given frequency f_0 contain contributions from all frequencies higher than f_0.

Three-dimensional turbulence PSDs do not suffer from the problem of aliasing. In theory it is possible to generate a three-dimensional PSD by taking simultaneous measurements in all directions from an origin and producing a correlation, and hence PSD, which is a function of the vector from the origin to a point. There are two problems with this approach. Firstly, it is very difficult to make measurements simultaneously in all directions. Secondly, the resulting correlation and PSD would contain too much information to be of practical use. To overcome these difficulties, it is common integrate the three-dimensional PSD over spherical shells to give a spectrum which represents the amount energy at a particular distance from the origin point. The spectra in three orthogonal directions are then added together to give what is always referred to in the literature as the three-dimensional PSD [Tennekes and Lumley, 1972]. For the case of isotropic turbulence the one dimensional PSD is related to the three-dimensional

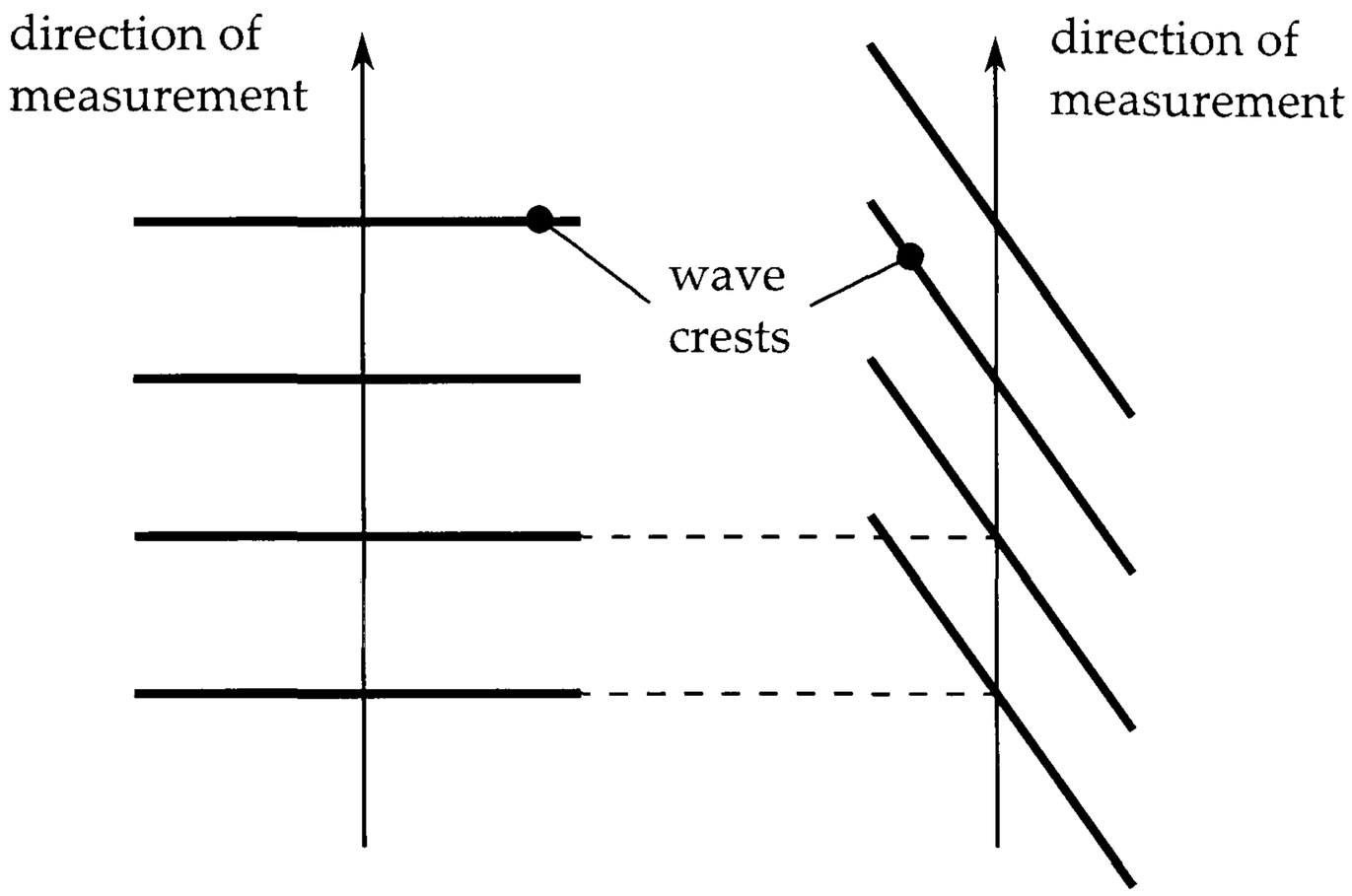

Figure 1.3: Aliasing of high frequency turbulent structures in the one dimensional spectrum. Both the structures on the right of the illustration and the structures on the left are recorded as having the same wavelength despite the fact that the structures on the right have a shorter wavelength. After Tennekes and Lumley [1972].

PSD by [Abdel-Gayed et al., 1987]

$$\overline{E}(\overline{F}) = \frac{\overline{F}^3}{2}\frac{\mathrm{d}}{\mathrm{d}\overline{F}}\left[\frac{1}{\overline{F}}\frac{\mathrm{d}\overline{S}(\overline{F})}{\mathrm{d}\overline{F}}\right] \tag{1.26}$$

Similar to the one-dimensional spectrum, the following relationships may be used to generate dimensionless PSDs

$$\overline{E}(\overline{F}) = E(f)/u'^2\tau_L \tag{1.27}$$

$$E(k) = \overline{U}E(f)/2\pi \tag{1.28}$$

and, in this case, the area under the PSD is exactly equal to the turbulence kinetic energy per unit volume of fluid:

$$\int_0^\infty E(f)\,\mathrm{d}f = \int_0^\infty E(k)\,\mathrm{d}k = \frac{3}{2}u'^2 \tag{1.29}$$

The shape of the turbulence spectrum has been widely studied. For two ranges of eddies well known power laws have been derived which apply to both

the one and three-dimensional spectra. For large Reynolds numbers there exists a range of eddies, the *inertial subrange* over which inertial forces dominate. These are the largest eddies within the equilibrium range (defined in Section 1.3.6), at the smaller scales dissipative viscous forces are dominant. Within the inertial subrange it can be shown [Kolmogorov, 1941] that

$$E(k) \sim k^{-5/3} \tag{1.30}$$

At the smallest scales, where dissipation takes place, the primary forces acting on the fluid are viscous hence this part of the turbulence spectrum is known as the *viscous subrange*. Here it has been demonstrated [Heisenberg, 1948] that

$$E(k) \sim k^{-7} \tag{1.31}$$

Given these two relationships a general shape of the PSD of isotropic may be sketched, shown in Figure 1.4.

1.3.6 Vortex stretching and dissipation

All turbulence is dissipative, without a constant source of energy turbulent motion will eventually die out and the flow will become laminar and then still. Conservation of angular momentum (Cauchy's equations) requires that the speed of rotation of an eddy must increase if it is deformed such that its diameter decreases. In a turbulent flow field eddies are constantly being strained and deformed by other turbulent eddies and it is this vortex stretching which produces the cascade of energy from the largest scales to the smallest scales.

It can be shown [Tennekes and Lumley, 1972] that rather than energy being transferred indiscriminately from one wavelength to all other wavelengths, eddies of a given wavelength receive most of their energy from eddies which are just slightly bigger than themselves and are most effective at transferring energy to eddies which are just slightly smaller than themselves. Eddies are literally "tuned" to receive energy from and donate energy to similar sized eddies. This implies that scales which are much larger than a given eddy have little effect on that eddy, hence, even if the turbulence is strongly anisotropic at the large scales,[5] by the time the energy has cascaded down to the smallest scales the tur-

[5]The largest eddies are induced by strain rates in the mean flow which for a typical situation such as flow through a pipe is not isotropic.

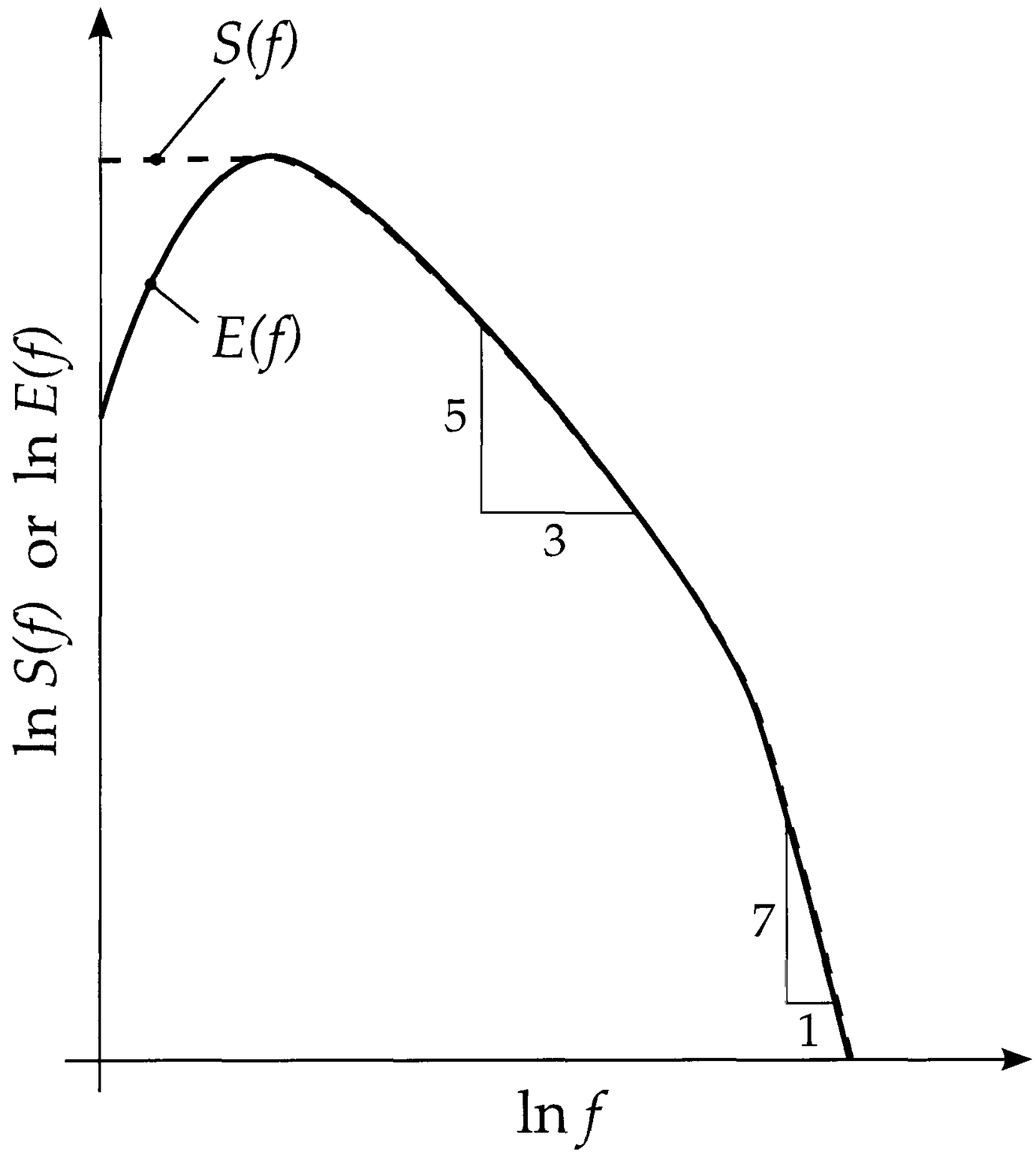

Figure 1.4: Generalised one and three-dimensional PSDs for isotropic turbulence at high Reynolds numbers. Note that $S(f)$ is larger than $E(f)$ at low frequencies because of the effect of aliasing in the one dimensional spectrum.

bulence will be locally isotropic. As the time scales of the eddies which are locally isotropic are small compared to those which exist in the mean flow these eddies respond quickly to macroscale changes. The responsiveness of the small eddies means that they are always in approximate equilibrium with the local conditions therefore the eddies of this scale are known as the *equilibrium range*.

The dissipation rate per unit mass ε of a turbulent flow field, that is the rate at which energy is passed from the mean flow to the largest eddies and on to smaller eddies until ultimately it is dissipated through viscosity into heat, can be calculated using

$$\varepsilon = \frac{u'^3}{L} \tag{1.32}$$

This equation can be understood as follows: if u'^2 is proportional to the kinetic energy of the turbulence (Equation 1.6) and L/u' is the characteristic time scale of the largest eddies (Equation 1.21) then $u'^3/L = u'^2(u'/L)$ can be thought of as the rate of change of turbulent energy with time [Lumley, 1999].

Given a mechanism for the dissipation of turbulent energy it is desirable to define a characteristic length scale at which the majority of the viscous dissipation of turbulent energy to heat takes place. It is to be expected that the length and time scales at which viscous dissipation occurs are finite but very small as it is only at small scales that viscosity is effective in entirely smoothing out turbulent velocity fluctuations. As viscosity is responsible for the ultimate conversion of turbulent kinetic energy to heat the viscosity of the fluid ν must influence the size of the scales at which this dissipation occurs. It is also reasonable to assume that the rate at which the dissipative scales are supplied with energy from the larger scales, that is the dissipation rate ε, should be influential. The characteristic size of the smallest eddies η is therefore a function of ν and ε. If this is so there is only one possible dimensionally correct expression for the size of the smallest eddies:

$$\eta = \left(\frac{\nu^3}{\varepsilon}\right)^{1/4} \tag{1.33}$$

This scale is commonly referred to as the Kolmogorov scale after A. N. Kolmogorov who first derived it in 1941. Scales smaller than η cannot exist because below this scale viscous effects dominate and the rotating eddies effectively grind to a halt.

1.3.7 Scale relations

It is often useful to be able to calculate one turbulent length scale given a different length scale and some properties of the fluid. If the integral scale, rms turbulent velocity and fluid viscosity are known, a Reynolds number for turbulent flow can be defined as

$$Re_L = \frac{u'L}{\nu} \tag{1.34}$$

This Reynolds number can be used to relate the different turbulent length scales, see for example Turns [1996]

$$\frac{L}{\eta} = Re_L^{3/4} \tag{1.35}$$

$$\frac{L}{\lambda} = Re_L^{1/2} \tag{1.36}$$

1.4 Turbulent flow in engines

Turbulence in an engine is generated by the shear in the jet-like flows of gas into the engine during the induction process [Tabaczynski, 1976]. Once the induction process is complete there is no further addition of kinetic energy to the fluid apart from the relatively slow movement of the piston hence the turbulence has a tendency to decay and u' decreases. The majority of modern automotive engines are designed such that the configuration of the intake(s) and cylinder head creates large scale bulk flow motions known as tumble[6] or swirl. As the piston approaches TDC these large structures break down and deposit their kinetic energy into the turbulent scales temporarily increasing u' [Arcoumanis et al., 1990, Hill and Zhang, 1994, Rui-Lin et al., 1996]. The phenomena of rapid distortion [Hunt, 1978, Wong and Hoult, 1979], whereby the eddies in turbulence which is compressed rapidly increase their rate of rotation in order to conserve angular momentum, may also slow the decay in u'. Given that the characteristic time scale for compression is much larger than typical turbulence time scales this effect is likely to be small in a SI engine.

1.4.1 Definitions of turbulence in engines

As discussed previously, the flow in the combustion chamber of an internal combustion engine is always turbulent at sensible engine speeds. Because of the pe-

[6]Sometimes referred to as barrel swirl.

riodic nature of the in-cylinder flow the turbulence equations given in Section 1.3 are often reformulated in terms of the engine crank angle θ and cycle number i hence the Reynolds decomposition (Equation 1.1) becomes

$$U(\theta,i) = \overline{U}(\theta,i) + u(\theta,i) \tag{1.37}$$

Often, similar large scale flow structures are observed every cycle. The ensemble average mean velocity $\overline{U}_{\mathrm{EA}}$ is given by

$$\overline{U}_{\mathrm{EA}}(\theta) = \frac{1}{N}\sum_{i=1}^{N} U(\theta,i) \tag{1.38}$$

and represents the "bulk" flow present in the combustion chamber. As turbulence is a chaotic phenomenon, these bulk flows do not repeat exactly every cycle but are subject to some cyclic variability $\hat{U}$ induced by small changes in intake and residual gas temperature, pressure, velocity and composition.

$$\hat{U}(\theta,i) = \overline{U}(\theta,i) - \overline{U}_{\mathrm{EA}}(\theta) \tag{1.39}$$

This secondary velocity is superimposed on the ensemble average velocity such that at a given crank angle in a particular engine cycle the instantaneous velocity may be thought of as being composed of an ensemble averaged component, an individual cycle mean velocity and a random "turbulence" component.

$$U(\theta,i) = \overline{U}_{\mathrm{EA}}(\theta) + \hat{U}(\theta,i) + u(\theta,i) \tag{1.40}$$

The above analysis is given by Heywood [1988] and is by no means universally accepted. There is great debate in the literature as to the correct method (if any) of separating low frequency cycle-to-cycle fluctuations $\hat{U}$ from high frequency turbulent fluctuations. Following this separation, calculation of the rms turbulent velocity requires that an average be taken, either time or ensemble, of u^2 (Equation 1.4). Again, there is no general consensus as to the correct approach. Some techniques for separating "turbulence" from the cyclicly varying mean flow discussed in the literature include: simple low pass filtering [Hall and Bracco, 1987]; minimising the difference between estimated and theoretical autocorrelation functions [Hilton et al., 1991]; and proper orthogonal decomposition [Aubry et al., 1988, Sirovich, 1987, Baby et al., 2002]. Previous experiments at Leeds University [Atashkari, 1997, Murad, 2006] have not attempted to distin-

guish between low frequency cycle-to-cycle variations and turbulence and have used an ensemble average to calculate the rms turbulent velocity u'. For the disc chamber LUPOE1-D where there is little bulk motion this approach is likely to be valid. The pent-roof LUPOE2-P has a significant bulk motion and it is probable that estimates of u' for this engine were influenced by this. Naturally, the definition of $\hat{U}$ has a large influence on the calculated value of u' and the many different definitions adopted in the literature greatly hamper comparisons of experimental data recorded by different research groups.

1.4.2 Measurements of turbulence in engines

Turbulence may be measured in the cylinder of an engine using one of three techniques: hot wire anemometry (HWA), laser doppler velocimetry (LDV) or particle image velocimetry (PIV). The earliest measurements conducted by Semenov used HWA [Semenov, 1958, 1963]. For measurements in engines this technique has the disadvantage that the probes are fragile, physically intrusive and require a complex calibration which changes markedly with temperature. One feature of HWA which other techniques do not posses is that the signal it provides is continuous which greatly simplifies the calculation of many of the parameters used to characterise a turbulent flow.

Later measurements used LDV (a point measurement which gives signals at random time intervals) or PIV (a planar measurement which gives signals at equally spaced intervals in space and time). Flow measurements have also been made using substances other than air as the working fluid have also been made, for example Jackson et al. [1995] and Choi and Guezennec [1998] used water. Measurements of u' using LDV and PIV reported by a number of different authors are shown plotted against mean piston speed in Figure 1.5. It is generally accepted [Heywood, 1988] that u' scales linearly with mean piston speed $\overline{S}_p$ at low to moderate engine speeds,[7] i.e.

$$u' \propto \overline{S}_p \tag{1.41}$$

The data presented in Figure 1.5 broadly confirm Equation 1.41 however it is evident that the constant of proportionality changes significantly with engine. Where low pass filtering has been applied to the data (open symbols) there is an

[7] This relationship has not been confirmed at high engine speeds because of the difficulty of taking measurements under these conditions.

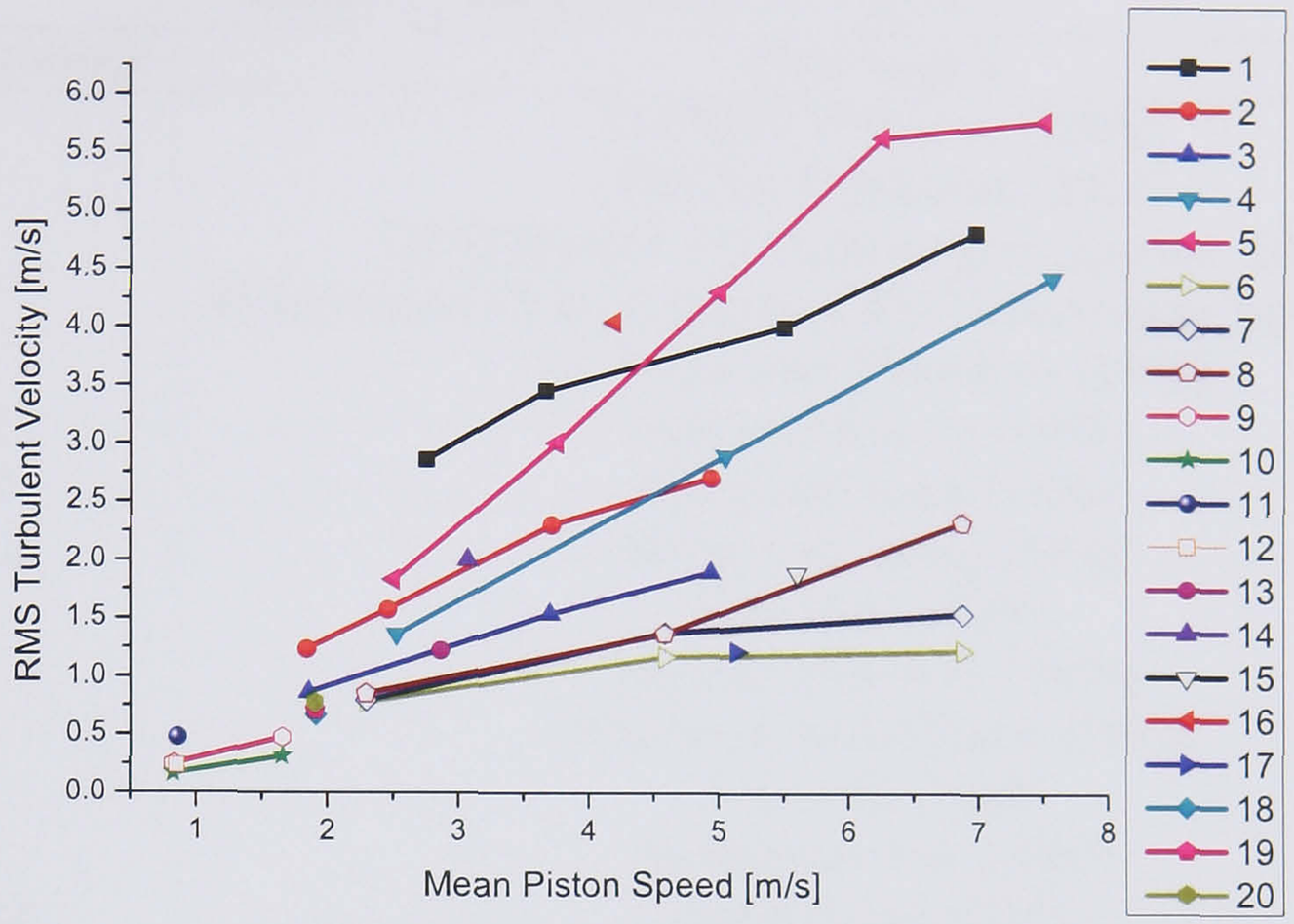

Figure 1.5: Variation in rms turbulent velocity with mean piston speed for different engines. Data sources are listed in Table 1.1

obvious tendency for the calculated u' to be lower for a given $\overline{S}_p$ than where other processing techniques where used. This discrepancy highlights the difficulty of separating the turbulent component of velocity from the mean flow discussed in Section 1.4.1.

Measurements of turbulent length scales in engines present even greater problems than measurements of u'. This is because, for reliable indication, data from two measurement locations are required to form a spatial velocity correlation. The low mean flow velocity during the period when the piston is close to TDC precludes the use of a temporal autocorrelation and Taylor's hypothesis to calculate the integral scale [Hill and Zhang, 1994]. Where data are recorded using LDV the intermittency of the signals from each measurement point creates an additional problem, a true spatial autocorrelation should be formed using measurements taken at exactly the same time from different locations. This is typically overcome by discarding measurements which do not occur within a certain time window of each other.

Despite the difficulties involved in making reliable measurements of L in engines, several research groups have made such measurements [Hong and Tarng, 1998, Breuer et al., 2005, Lee and Lee, 2003, Li et al., 2002, Fraser and Bracco, 1986, 1989, Klingmann and Johansson, 1999]. Because of the variety of different

Table 1.1: Data sources for Figure 1.5.

Caption number	Data source
1	LUPOE2-P Murad [2006]
2	LUPOE1-D Jakubík [2002]
3	LUPOE1-D CFD Volkswagon [approx. 2004]
4	Volkswagon Optical Engine CFD Volkswagon [approx. 2004]
5	Corcione and Valentino [1994]
6–8	Hall and Bracco [1987]
9–10	Kang and Baek [1998]
11–12	Hong and Tarng [1998]
13	Kim et al. [2000]
14	Arcoumanis et al. [1994]
15	Johansson and Olsson [1995]
16	Liu et al. [1999]
17	Nordgren et al. [2003]
18–20	Lee and Lee [2003]

techniques used to process the data, the different measurement locations, cylinder geometries and measurement crank angles, direct comparisons between the data are difficult. Broad conclusions may however be drawn. The data indicate that L is independent of engine speed and of the order of the clearance height. Individual measurements suggest that L falls in the range 1–13 mm when the piston is close to TDC for typical car engine geometries (bore $\sim$ 80, compression ratio $\sim$ 10).

1.5 Laminar and turbulent combustion

Combustion is the self-supported release of energy through the exothermic oxidation of fuel [Griffiths and Barnard, 1995]. Depending on the Reynolds number of the unburnt gas, combustion may be either laminar or turbulent. In industrial applications, combustion is almost always turbulent. Laminar combustion, widely studied because it is much simpler than turbulent combustion, does not have many practical applications.[8]

The rate of combustion, which ultimately determines the time taken for the flame to propagate across the cylinder in a spark ignition, can be measured using either a flame speed or a burning velocity. A flame speed is the rate of propaga-

[8]One notable exception is the humble candle flame.

tion of the flame front[9] relative to fixed coordinates in space and is not an intrinsic parameter as it depends on the configuration of the experiment. For example the flame speed of a spherically expanding flame in a combustion vessel is always finite whereas flame speeds measured on a bunsen burner are zero as the flame is not moving relative to the burner. Flame speeds will be denoted by the symbols S_l and S_t depending on whether the flame is laminar or turbulent.

A burning velocity is an intrinsic property of a given fuel-air mixture and provided that the differing gas flow velocities are accounted for, burning velocities from bunsen burners and expanding flames should be equal for the same mixture and turbulence. Burning velocities may be defined in one of two ways [Cheng and Shepherd, 1991], either as the rate of consumption of reactants by the flame front, or the rate of displacement of the flame front relative to the unburnt gas ahead of the flame. Historically, research conducted within the School of Mechanical Engineering at the University of Leeds has used the former definition. This is continued in the current work where a burning velocity will be denoted using the symbols u_l and u_t for the laminar and turbulent cases respectively.

1.5.1 The effect of stretch on combustion

Nearly all flames found in common applications are stretched[10] in some way, either through curvature of the flame surface or flow non-uniformity along the flame surface [Law, 1988]. Stretch affects flame behaviour, altering the ordinary heat and mass transfer processes by transporting heat and mass (reactants, products, free radicals) to other areas of the flame [Chomiak, 1989]. If a flame becomes sufficiently stretched the dissipation of heat and mass away from the flame front can become so great that the chemical reactions cease to become self-sustaining and the flame quenches. The growth rate of spherically expanding laminar flames is typically limited by geometric stretch when the flame is small as this is when the stretch rate is greatest. For this reason a laminar flame is most likely to quench mediately after ignition. The geometric stretch rate of a surface

[9]The flame front may be defined in a number of different ways, see Section 1.6. For the purpose of this discussion it suffices to say that the flame front represents some reference surface whose position is associated with the heat release and chemistry which define combustion.

[10]Flame stretch and flame strain are used interchangeably in the literature to describe the same property [Griffiths and Barnard, 1995].

α is defined as [Batchelor, 1953]

$$\alpha = \frac{1}{A}\frac{\mathrm{d}A}{\mathrm{d}t} \tag{1.42}$$

which, for spherically expanding flames, becomes

$$\alpha = \frac{2}{r}\frac{\mathrm{d}r}{\mathrm{d}t} \tag{1.43}$$

As the burning velocity of laminar flames is strongly affected by α care must be taken when calculating burning velocities from stretched flames to account for the effect of stretch. For a spherically expanding flame this is typically achieved by extrapolating the experimental measurements to zero stretch. A lack of understanding of, and failure to account for, the effects of stretch and instabilities (discussed in Section 1.5.3) is one of the main reasons why measured values of laminar burning velocity failed to converge for many years [Bradley, 2000].

Turbulent flames are subject to constant deformation through interaction with the flow field. A dimensionless expression for stretch in turbulent flames, the Karlovitz stretch factor first proposed by Kovasznay [1956], is often employed. The Karlovitz stretch factor Ka is defined as the quotient of a characteristic eddy lifetime λ/u' and the residence time in a laminar flame δ_l/u_l, hence [Griffiths and Barnard, 1995]

$$Ka = \frac{u'}{\lambda}\frac{\delta_l}{u_l} \tag{1.44}$$

where δ_l is the laminar flame thickness.

The Karlovitz stretch factor embodies the effect of turbulence on the flame. If the characteristic eddy lifetime is much larger than the residence time in a laminar flame then Ka will be less than one and it is likely that combustion will be complete before the flame structure is torn by the effect of turbulent motion. If, on the other hand, Ka is greater than one then it is likely that the flame surface will be significantly disrupted by the action of turbulence before combustion is complete. Unburnt material will be entrained behind the flame front and burnt in following eddies.

A related dimensionless number is the Damköhler number Da. This is defined as the ratio of a characteristic eddy time scale L/u' to the laminar chemical time scale δ_l/u_l [Turns, 1996]

$$Da = \frac{L}{\delta_l}\frac{u_l}{u'} \tag{1.45}$$

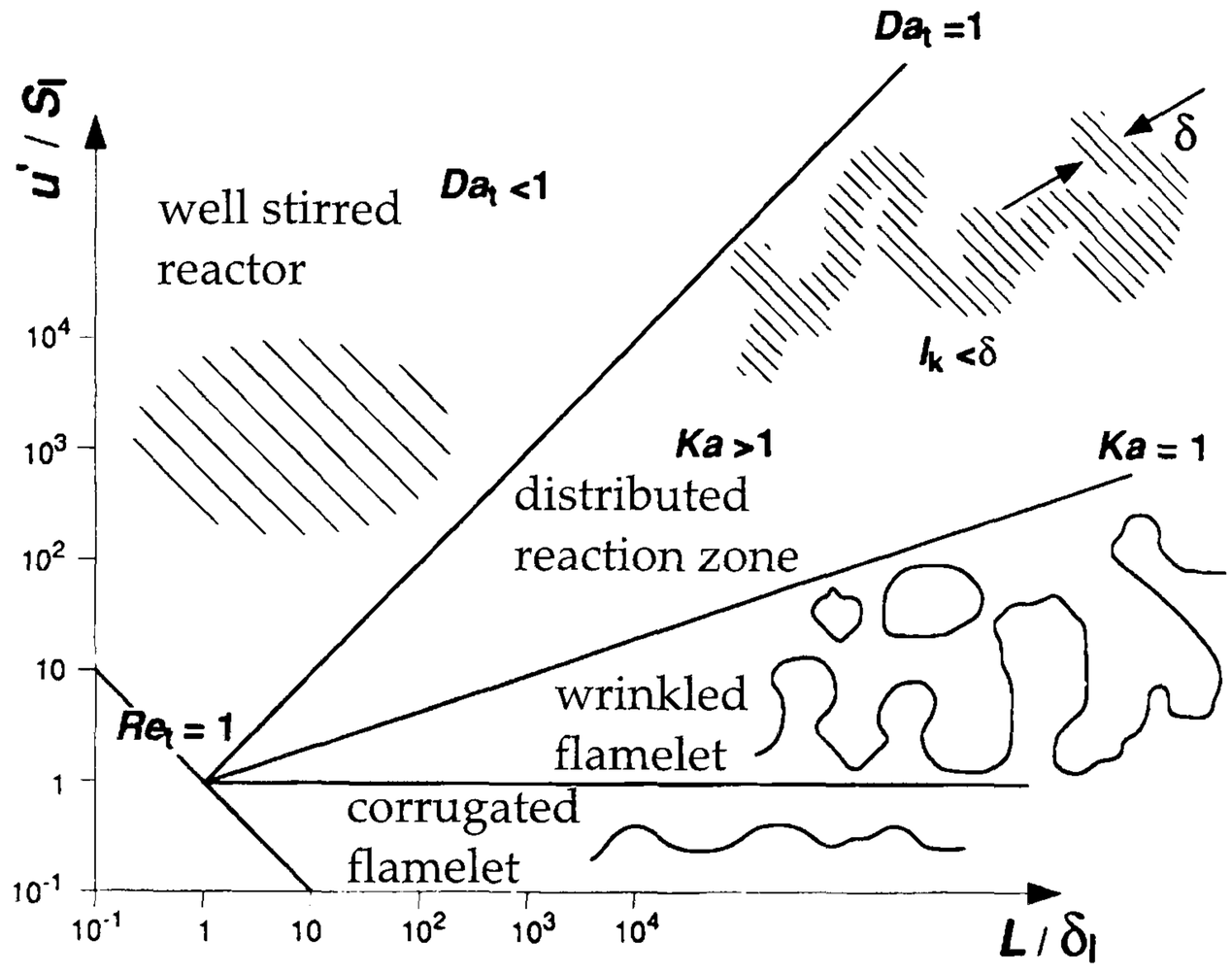

Figure 1.6: Turbulent combustion regimes, after Borghi and Destriau [1998].

The Karlovitz number is inversely related to the Damköhler number by Equation 1.36, see for example Cairns [2001].

1.5.2 Combustion regimes

Depending on the Reynolds number of the unburnt gas, combustion may be either laminar or turbulent. Premixed turbulent combustion may be further categorised depending on the ratios u'/u_l, a dimensionless turbulent velocity, and L/δ_l, a dimensionless turbulent length scale. These qualities are shown plotted against each other on logarithmic scales in Figure 1.6.

The thick lines in Figure 1.6 delineate the boundaries between different turbulent combustion regimes which are usually defined, although sometimes with different names, as follows [Griffiths and Barnard, 1995, Borghi and Destriau, 1998]

$Re_L < 1$ **Laminar combustion**

$Re_L > 1, Ka < 1, Da < 1$ **Well stirred reactor** Turbulence is fast compared to chemistry and combustion occurs without a distinct propagating flame front.

$Re_L > 1, Ka < 1, Da > 1$ **Distributed reaction zone** Chemistry is fast enough to form a distinct reaction front but this is thickened significantly by turbulence.

$Re_L > 1, Ka < 1, u' < u_l$ **Wrinkled flamelet regime** The flame surface is wrinkled and may be discontinuous but remains similar to a laminar flame in structure as chemical reactions occur quicker than they can be perturbed by turbulent fluctuations. Direct numerical simulations [Poinsot et al., 1990] suggest that the boundary of the flamelet regime lies above the line of $Ka = 1$ suggested by dimensional analysis alone.

$Re_L > 1, Ka < 1, u' > u_l$ **Corrugated flamelet regime** Similar to the wrinkled flamelet regime but with a continuous unbroken flame surface.

Combustion in a typical SI engine takes place either in the flamelet regime or the bottom half of the distributed reaction zone regime [Matthews et al., 1996] as, in an engine, the high pressures cause the laminar flame thickness to decreases therefore L/δ_l becomes large.

1.5.3 Laminar flame instabilities

The question of whether a laminar flame will propagate stably or unstably has been subject to much research, see for example Markstein [1964], Groff [1982], Zeldovich et al. [1985], and a complete discussion is outside the scope of this work. For the purpose of the current work it is sufficient to understand that a laminar flame may propagate either in a stable fashion, characterised by a smooth surface, or become cellular through the action of thermodiffusive and/or aerodynamic instabilities.

Whether a flame becomes unstable depends on the thermodynamic state of the unburnt mixture, the thermo-diffusive properties of the fuel and the rate of propagation of the flame front. For heavy hydrocarbons such as iso-octane the tendency to propagate unstably is most marked at high temperatures and pressures with rich mixtures. Under these conditions a flame may become cellular, with a consequent increase in surface area and flame speed, immediately after ignition. This immediate transition to cellularity makes the experimental measurement at conditions relevant to engine combustion of the laminar burning velocity, which is an input for many turbulent combustion models, extremely difficult [Hattrell et al., 2006]. Much of the laminar burning velocity data reported in

the literature for high temperatures and pressures has been determined from the pressure rise in a closed combustion vessel during the propagation of a spherical flame without photographic observation of the flame structure. In these cases the cellular nature of the flame is likely to be a significant source of error in the reported laminar burning velocities.

1.5.4 Effect of turbulence on growing flames

A flame growing from a point source, for example a spark kernel, in a turbulent environment will initially be smooth and laminar like. As the flame grows the flame front becomes wrinkled causing an increase in surface area, flame brush thickness and burning velocity [Lancaster et al., 1976, Beretta et al., 1983, Abdel-Gayed et al., 1987, Lipatnikov and Chomiak, 2002]. This phenomena is known as flame development and is governed by the time and length scales of the flame and turbulence as follows:

- The surface of a flame can only be wrinkled by eddies which are smaller than the flame, larger eddies merely convect the entire flame. As the flame increases in size it is exposed to a larger portion of the turbulence spectrum therefore the degree of wrinkling increases.

- As action of the turbulent eddies is not instant, the degree of wrinkling depends not just on the relative size of the flame but also on the amount of time the flame surface has been exposed to the turbulent field. An infinitely large smooth interface created instantaneously in a turbulent flow field will take some time before it becomes fully wrinkled.

Abdel-Gayed et al. [1987] attempted to quantify the effect of the turbulence spectrum on growing flames. They produced a normalised one-dimensional PSD of turbulence (Equation 1.25) based on LDV measurements of the flow field in a fan stirred combustion vessel, shown in Figure 1.7. They then reasoned that a flame which propagates from a point source and which has been in existence for a time t_k could only have been exposed to the portion of the turbulence spectrum with frequencies higher than t_k^{-1}. On their dimensionless PSD of turbulence the energy the growing flame has been exposed to is proportional to the area between $\overline{F}_k = t_k^{-1}\tau_L$ and infinity (infinite frequency is associated with zero time). For a particular flame lifetime an *effective* rms turbulent velocity, u'_k defined may

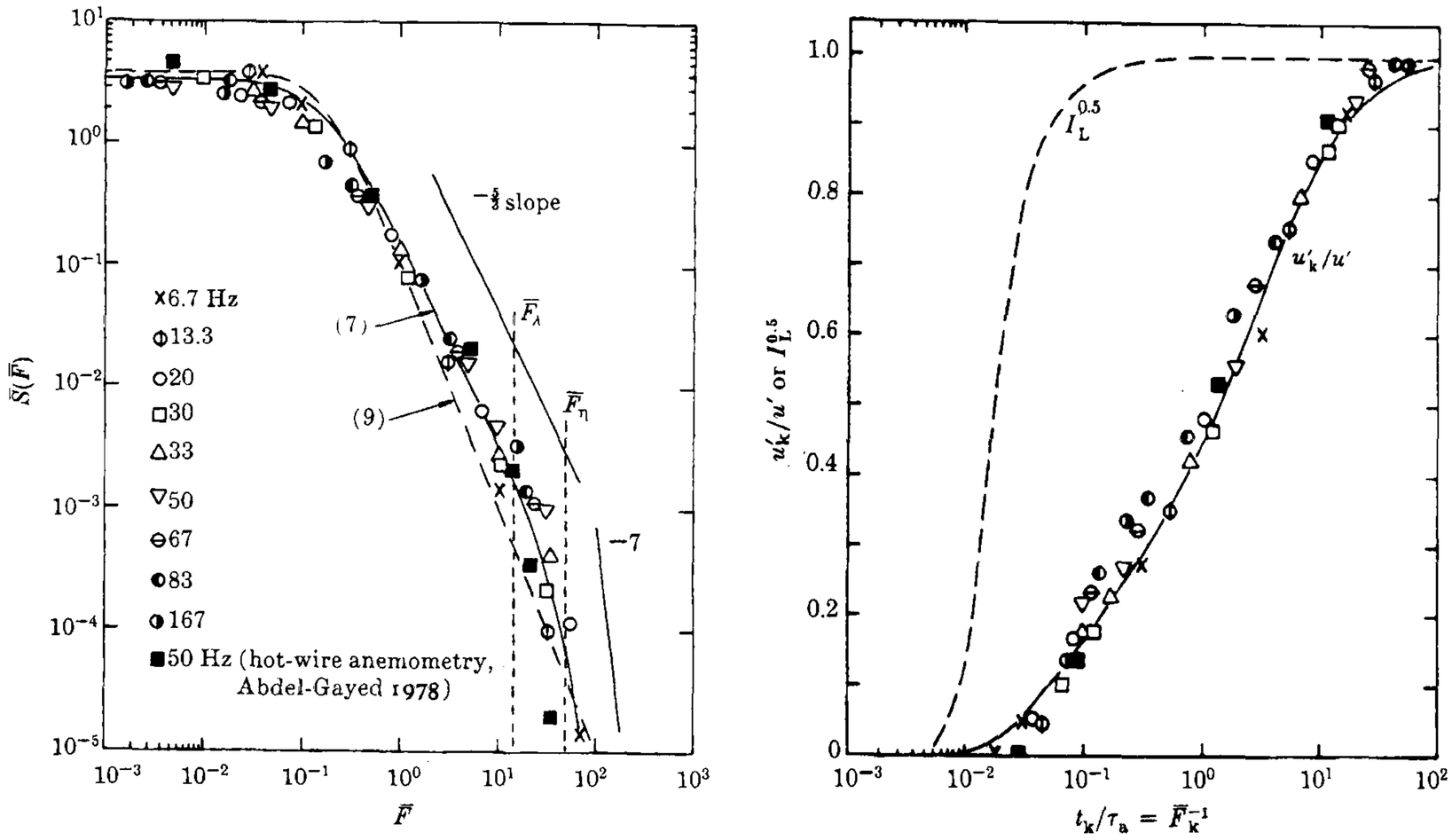

Figure 1.7: Dimensionless PSD of turbulence (left) and the effective rms turbulent velocity derived from it using Equation 1.46 (right). After Abdel-Gayed et al. [1987].

therefore be defined formally as:

$$u_k'^2 = u'^2 \int_{\bar{F}_k}^{\infty} \bar{S}(\bar{F})\, \mathrm{d}\bar{F} \tag{1.46}$$

Values of u'_k for different t_k are illustrated in Figure 1.7. It should be noted that Equation 1.46 applies only to an "average" flame; cycle-to-cycle variations in the turbulence in an engine can significantly affect the development of individual flames [Abdi Aghdam et al., 2007].

From the above discussion it is apparent that turbulent combustion is non-stationary. This greatly hampers the comparison of results from different research groups which are, for the most part, generated using different apparatus and recorded at different stages of flame development. Nonetheless, it is evident from the measurements of many workers [Lipatnikov and Chomiak, 2002] and theoretical studies going right back to the early work of Damköhler [1947] that the enhanced flame wrinkling and transport of heat and mass associated with increasing u' increases the turbulent burning velocity. This observation holds true for low to moderate values of Ka. At higher values of Ka the transport of heat and mass away from the reaction zone becomes so large that the chemical reaction is

no longer self sustaining and further increases in u' will quench the flame [Abdel-Gayed and Bradley, 1985].

The effect of changes to the turbulent length scale on combustion have been studied far less than the effect of changes in u'. This is because, experimentally, it is far harder to change the value of L, which requires a change in some fundamental dimension of the apparatus, than to change the value of u', which requires a change in the flow rate. Despite these difficulties, direct studies, for example the work of Leisenheimer and Leuckel [1996] which used two different sized turbulent combustion vessels, do exist. Their results suggest that u_t increases with L. This observation is supported by the meta-analysis of the largest databases of turbulent burning velocity undertaken by Lipatnikov and Chomiak [2002] although these authors caution that other contradictory measurements exist.

1.6 Optical diagnosis of engine combustion

There are many techniques for tracking the progress of a deflagration front in a spark ignition engine. Optical techniques include: natural light (chemiluminescent) photography, schlieren photography, and laser induced fluorescence (LIF) of, for example fuel molecules or OH radicals.

The technique used in this thesis is Mie scattering photography. Here the clearance volume of the engine is illuminated with a thin sheet of laser light and very fine (sub-micron) seed particles are added to the incoming fuel-air mixture. These particles cause elastic scattering of the laser light and a camera normal to the plane of the laser sheet records this scattered light. Because the seed particles have dimensions comparable to the wavelength of light the distribution of the scattered light is governed by Mie theory [Stratton, 1941], hence Mie scattering photography.

Given the correct seeding density, seed particles in the gas ahead of the flame front scatter sufficient laser light such that this region is luminous when recorded photographically. Behind the flame front the seed number density is lower (the burnt gases have expanded) and this region appears dark when recorded by the camera [Zhao and Ladommatos, 2001]. There is some debate in the literature, see for example Baritaud and Green [1986] and the other authors cited by Zhao and Ladommatos [2001], as to whether the change in seed number density is accompanied by changes to the actual particles which also reduce their ability to scatter light. Certainly, the temperature of the burnt gases is typically below

the melting point of the most commonly used seed material, titanium dioxide. It has however been conjectured that the increased temperature may be sufficient to reduce the angularity of the seed particles, removing sharp edges and therefore reducing their ability to scatter light.

The flame front recorded using Mie scattering laser sheet photography is generally interpreted as locating the interface between the unburnt and burnt gases [Bradley et al., 2003]. As the technique records only scattered light from the plane of the laser sheet the images obtained give information only on the plane of the laser sheet, effectively a "slice" of the flame. Recording images from a slice of flame in this way gives very detailed information about the structure of the flame front; the wrinkling action of large and small scale eddies can clearly be seen. Should the laser sheet fall through a different part of the flame than the one which was originally envisaged however, slices can be deceptive. This can occur when the experiment is configured to take a slice through the centre of the flame but the flame is convected and the laser sheet actually cuts through the periphery of the flame.

Flame visualisation techniques such as schlieren and natural light photography obscure much of the detailed wrinkling information as the outline of the flame is integrated along the line of sight. In contrast with Mie scattering photography, these techniques have the advantage that they record with no uncertainty the extents of the flame edges. There is some evidence that schlieren and natural light photography give flame edges which are very similar [Murad, 2006] and these techniques are typically interpreted as measuring the entrainment front of a turbulent flame, that is the leading edge of the flame brush [Bradley et al., 2003].

1.7 Simulation of combustion in spark ignition engines

Premixed turbulent combustion in spark ignition engines can be modelled using a number of different approaches. These are commonly split into two "families": fluid dynamic and thermodynamic [Heywood, 1988]. The fluid dynamic approaches, requiring the solution of some form of the Navier-Stokes equations, are the most complex. These models fall under the umbrella term of CFD (computational fluid dynamics) which includes all numerical flow simulation techniques, with or without combustion. The group of CFD models can be further

sub-divided [Candel et al., 1999] into direct numerical simulation, Reynolds averaged Navier-Stokes and large eddy simulations. The various fluid dynamic model formulations will first be described briefly, followed by the thermodynamic approaches employed in this thesis.

As discussed in Section 1.3, turbulence encompasses a wide range of length and time scales. The need to resolve all of these scales makes the direct numerical solution (DNS) of the Navier-Stokes equations under turbulent conditions a formidable challenge. The very fine temporal and spatial computational grids required to resolve the Kolmogorov length and time scales present a particular problem. Nevertheless, advances in computational power over the last decade have allowed the first DNS simulations of turbulent combustion to take place (for example Thévenin [2005]). These have typically been limited to low turbulent Reynolds numbers and small simulation volumes hence practical simulations which could be applied to spark ignition engines remain some way off.

A second fluid dynamic approach is termed large eddy simulation (LES). Here the larger scales of turbulence are solved numerically whilst the smaller scales, those in the equilibrium range (see Section 1.3.6), are represented using a submodel. Any anisotropy present in the macroscale eddies is removed by the process of vortex stretching hence the small scale eddies are isotropic. The energy spectrum of these small eddies has well defined characteristics (see Section 1.3.5) which makes them particularly amenable to description using a submodel. This simplification enables the spatial and temporal resolution of the computation to be increased significantly compared with a DNS simulation and hence much larger volumes, higher Reynolds numbers and longer times can be simulated using this approach. Several research groups are using LES to tackle problems in SI engine combustion which have previously been numerically inaccessible. See, for example, Vermorel et al. [2007].

The simplest of all fluid dynamic approaches is Reynolds averaged numerical simulation (RANS). A RANS approach employs time or ensemble averaged versions of the Navier-Stokes equations. Only the largest scales of fluid flow are solved numerically with all scales of "turbulence" included via a submodel, typically the well known k-ε model [Launder and Spalding, 1972] or one of its variants. This simplification allows accurate solutions to be generated using much coarser spatial and temporal resolution than possible with LES or DNS. With modern computing technology RANS solutions of spark ignition engine cycles can be calculated relatively easily. As RANS codes were the first to be

made commercially available, and because their computing requirements are relatively modest, they are the most widely used in the automotive industry. Despite this fact, the accuracy and predictive capability of the RANS approach is limited. [Hilbert et al., 2004].

Detailed chemical reaction schemes for even the simplest of mono-component hydrocarbon fuels, for example methane, comprise many hundreds of reactions with each reaction requiring a rate constant. At high temperatures and pressures three body reactions become important for which there are very little reaction rate data. The difficulties of employing full chemistry within laminar combustion simulations are therefore two fold: the reaction scheme or some of its rate constants may not be well defined, and the calculations required for its solution are demanding. Turbulence affects the transport of heat and mass hence the inclusion of detailed chemistry in a turbulent combustion simulation presents an even greater challenge. For this reason, until recently, most fluid dynamic models employed simple (often Arrhenius single-step) submodels for the burning velocity of the mixture. The advent of greater computing power and greater understanding has allowed the introduction of more detailed chemistry and transport models into turbulent combustion simulations. These are comprehensively reviewed in Hilbert et al. [2004].

A second family of SI engine combustion models are the thermodynamic models. These fall into two broad categories. Those where the charge is treated as a single lumped mass and the heat release rate is prescribed using a simple algebraic function, for example a Wiebe function, are known as zero dimensional models and are not predictive. A second category are the quasi-dimensional family of models such as the one employed in this thesis (see Chapter 4 and Blizard and Keck [1974]). These formulations use simple submodels for turbulence, flame geometry and burning velocity. A good review of the various submodels available is given by Heywood [1994]

Despite their relative simplicity compared to the fluid dynamic modelling approaches, thermodynamic models, in particular quasi-dimensional models, have a number of distinct advantages. They do not require the generation of a moving geometry mesh of the combustion chamber, their computational load is low and the results they generate are easily interpreted. Given the large uncertainties associated with input parameters such as the laminar burning velocity (see Section 4.5.5) it is doubtful whether the more detailed description of flow and combustion employed by fluid dynamic simulations enhances their predictive

capability significantly [Hattrell et al., 2006].

Chapter 2

Experimental Equipment

2.1 Overview

In order to improve the predictive capability of the Leeds University Spark Ignition Engine (LUSIE) code, described in detail in Chapter 4, it is necessary to compare the model output with data collected from real engines. In an ideal world, an experimental engine would allow perfect control over the mixture composition and in-cylinder flow and be capable of providing pressure and flame position information throughout the cycle whilst still being as close as possible in operation and geometry to a production engine. Modern pressure transducers are very compact and can typically be installed on a production engine without disturbing the normal operation of the engine; it is however difficult to provide unobstructed optical access to the entire bore in a conventional four valve poppet valved engine because of the location of the valves in the cylinder head.

By using an optical spark plug [Wu, 2005, Ikeda et al., 2005, Salvat et al., 1994] it is possible to measure flow or mixture properties in the region close to the spark plug. This technique has the advantage that it requires a minimum of modifications to the engine but does not provide a great deal of information other than during the very early stages of combustion. Greater optical access can be provided by adopting a windowed piston and mirror arrangement as pioneered by Bowditch [1961]. This requires extensive modifications to the piston and crank

case although crucially the cylinder head and valves can remain unchanged. If the modification of the piston required to facilitate the installation of the window is not too great the operation of the engine can remain similar to the production condition, save the slightly different heat transfer properties of the window in the piston and the inevitable change to the in-cylinder flow field. Modification of an engine in this fashion allows flame imaging and other optical techniques to be employed in an engine where, from a flow and combustion perspective, the engine is very close to the production condition. The major disadvantages of optical access provided in this way are that the later stages of flame propagation, during which time the majority of the mass is burnt, are not visible due to the need for a metal rim in which to mount the window and piston rings, and that for laser sheet work, as used in the current study, an access window must be provided in the cylinder head to allow the laser sheet to enter the combustion chamber.

The simplest practical method of providing full-bore optical access is to use a ported system of intake and exhaust similar to that used in two stroke engines. Although this modification moves the engine away from the overhead valve breathing arrangement which is the norm for car engines, it allows the head to be modified to incorporate windows covering the full extent of the bore. For combustion event validation, replication of production geometry is not necessary. By changing the angle(s) of the inlet port(s) this configuration affords a simple method of controlling the in-cylinder flow field not possible with an overhead valve arrangement where the ports are an integral part of the casting. As an additional advantage, it becomes possible to remove the head easily to facilitate the frequent window cleaning which is necessary when taking optical data and, because the head is of a relatively simple construction, the manufacture of heads with different geometries is much simpler than for an engine with a valved head.

For the purpose of this study two experimental engines were used to provide comparative data for LUSIE. Two of these, LUPOE1 and LUPOE2, acronyms for Leeds University Ported Optical Engine versions 1 and 2 respectively, were of the ported type with full-bore optical access as described above. Of the two engines, only LUPOE2 was actively used by the author to collect data for this study, data from LUPOE1 having been collected by previous authors. For further information regarding LUPOE1 see Abdi Aghdam [2003].

Table 2.1: LUPOE2-P Engine dimensions.

Bore [mm]	80
Stroke [mm]	110
Connecting-rod length [mm]	232
Geometric compression ratio	11.76
Effective stroke	83.7
Effective compression ratio	9.24
Pent roof angle [deg from horizontal]	21
Inlet port close [° aTDC]	-117.4
Exhaust port open [° aTDC]	115.7

2.2 LUPOE2-P

2.2.1 General information

The engine used in the current study was a pent-roof variant of LUPOE2 known as LUPOE2-P and is based on a single cylinder Lister Petter PH1 diesel engine crank case. Modifications to the original Lister Petter crank case were started by Butler [1999] and continued by Abdi Aghdam [2003] and Murad [2006]. The head, barrel and piston of the engine have been replaced by custom made parts manufactured in the University of Leeds Faculty of Mechanical Engineering workshop in order modify the engine for ported operation, provide a compression ratio suitable for spark ignition combustion and to allow optical access to the combustion chamber. The engine and associated systems comprised the following main components:

- Engine
- Dynamometer and inverter control unit
- Fuel and air control tower
- Ignition system and timing rack
- Heaters and control unit

These are described only in outline below to provide sufficient background for their use in later chapters; for full descriptions the reader is referred to earlier works by Murad [2006] and Abdi Aghdam [2003].

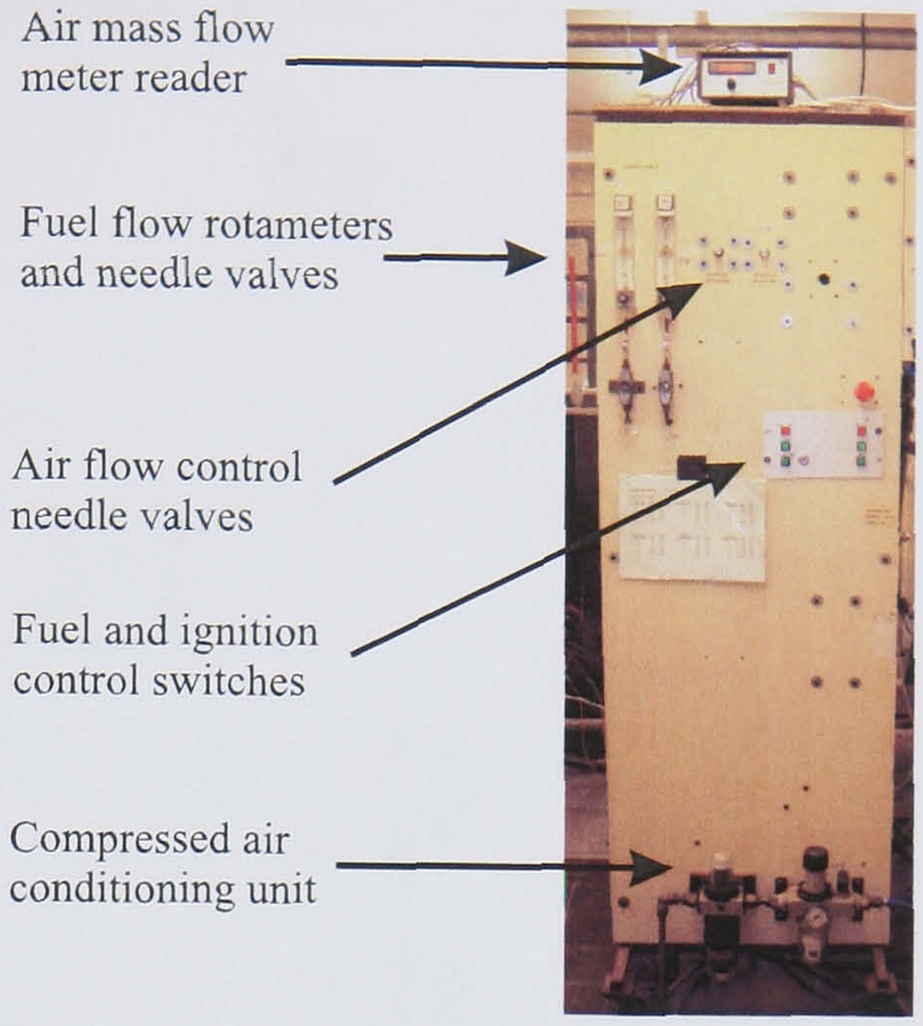

Figure 2.1: Fuel and air control tower.

2.2.2 Intake air, fuelling, heating and exhaust systems

A dedicated mobile unit referred to as the "tower", pictured in Figure 2.1, served the purpose of supplying and metering the air and fuel to the engine. Also mounted on the tower were switches for turning the ignition system on and off, but not the actual ignition system or any timing components, an emergency stop button, and the seeding system. Schematic diagrams of the systems described in this section are shown in Figures 2.2 and 2.3.

Intake air was supplied to the engine via the tower from the laboratory compressed air system after having first passed through a conditioning unit consisting of a filter, water trap and pressure regulator in series. This served to reduce the pressure of the air to 4 bar and remove any water or oil contamination from the supply. The pressure set on the regulator was not particularly accurate or repeatable but this was of little concern as experiments conducted with different air regulator pressures showed no discernable change in results provided the subsequently adjusted air mass flow rate remained constant. After having passed through the conditioning unit, the air line was divided into two separate supplies, the mass flow rate of which could be adjusted independently using needle valves. The mass flow rate of each supply was measured using Brooks model 5863 mass flow metres positioned downstream of the needle valves. To reduce the effect of pressure pulsations in the intake air system caused by the reciprocating motion of the engine, 5 litre surge tanks were fitted between the engine and the mass flow

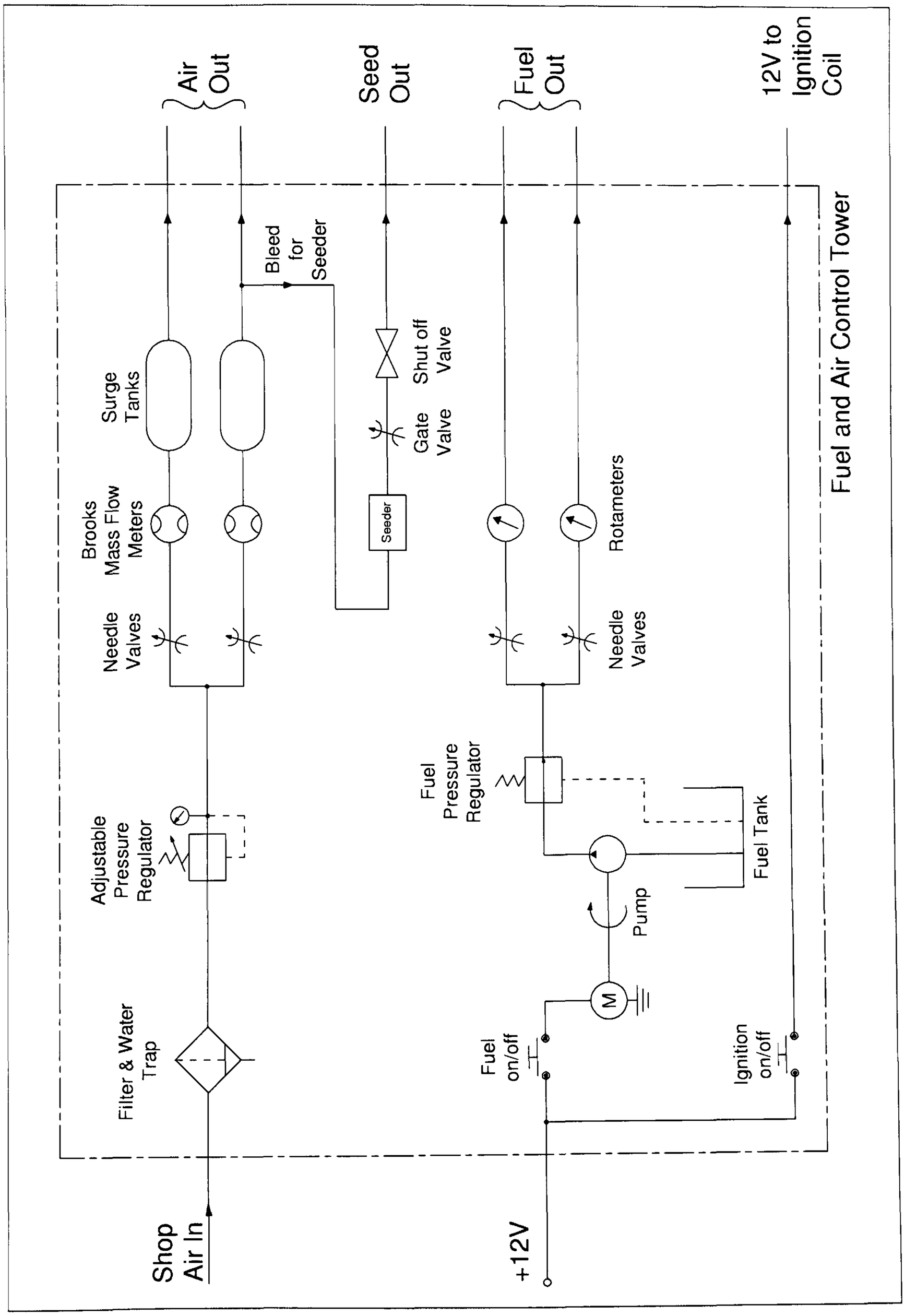

Figure 2.2: Schematic of the fuel and air control tower. Drawing by Mr Ashley Arundel.

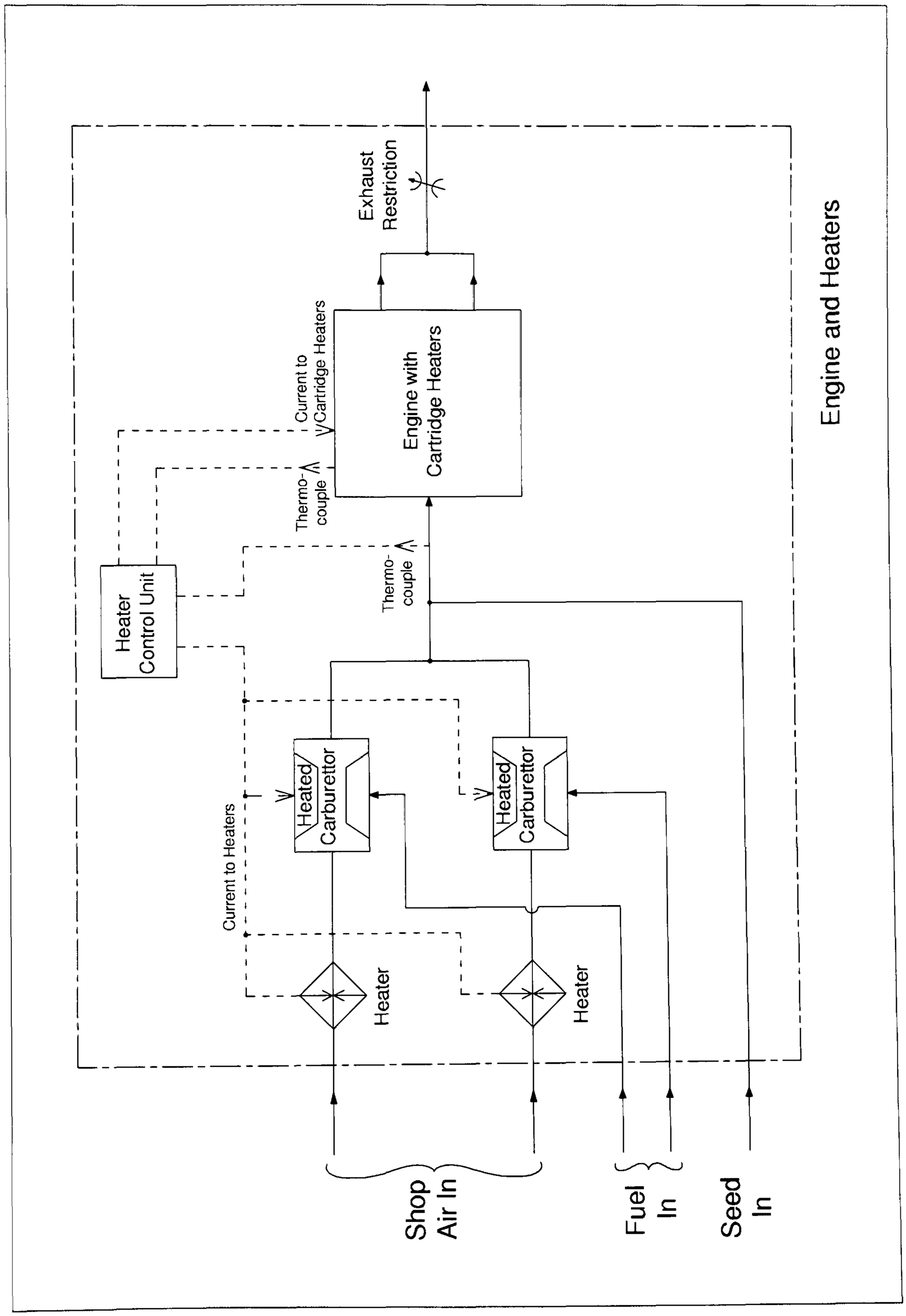

Figure 2.3: Schematic of the engine intake and exhaust system. Drawing by Mr Ashley Arundel.

metres.

Prior to the point of fuel addition the intake air temperature was increased using a series of three 200 W band heaters per air line to facilitate effective evaporation and mixing of the fuel. The intake air temperature was thermostatically controlled using a thermocouple positioned immediately upstream of the intake port and a commercial heater control unit, Digitron model 4801, available from RS Components. The accuracy of the temperature modulated by the control unit was checked using a mercury thermometer by allowing the intake air system to warm up to a steady state condition with the cylinder head removed. The thermometer was placed inside the barrel in the stream of air issuing from the intake port and was found to read the same as the set temperature of the controller with no noticeable fluctuations over time. When the fuel pump was activated before an experiment, the relatively high specific heat and latent heat of evaporation of the fuel introduced into the air line caused an inevitable drop in the temperature of the intake fuel-air mixture from that set on the temperature controller. This change in temperature was unavoidable with the current experiment configuration and is discussed further in Sections 2.2.2 and 5.4.5.

A heater system consisting of 12 $\times$ 20 W cartridge heaters, a thermocouple and a second heater control unit was used to maintain the temperature of the barrel and cylinder head. The accuracy of this system was checked in a similar way to that of the intake air heaters, again using a mercury thermometer. The engine was allowed to warm up with both the intake air and head/barrel heaters activated. With the head removed it was found that the barrel and cylinder head were at the set temperature and there was little variation in the temperature at different points on the engine. Inevitably, when the engine was motoring or firing during an experiment, the temperature of the internal surfaces of the head and barrel would increase either due to heat transfer from the hot combustion gases or friction induced heating. It was difficult to quantify the error introduced in this way but in order to minimise its effects care was taken to complete experiments in as short a time as possible.

Fuel was supplied from a tank mounted on the tower. This was delivered to the engine using a standard car fuel pump and pressure regulator. As with the air system, the fuel supply was split into two separate lines with each line supplying a corresponding air line. The fuel mass flow rates were controlled using needle valves and measured using a pair of Platon rotameters with a capacity of 25 cm^3/min of water. As the rotameters were designed for metering water it was

necessary to calibrate them for iso-octane by measuring the time for a given volume of fuel to flow for a particular rotameter setting. This had been previously undertaken by Murad [2006] and comparison with a calibration performed by the current author showed a negligible difference between the two results. For consistency with previous work, the calibration of Murad [2006] was adopted for the current study. Fuel was introduced to the air lines approximately 470 mm upstream of the intake port through brass venturis and atomising nozzles manufactured from hypodermic needles, see Cairns [2001] for a full description and diagrams of the venturis and nozzles.

The air-fuel mixtures from the two air lines were re-combined before the mixture entered the engine via the intake runner. The runner was inclined at 40°to vertical to promote the tumble flow commonly found in modern pent-roof engines. Metering the air and fuel in two separate supplies was not strictly necessary for the current study as the engine had only one intake port, this was an artefact from previous engine studies using LUPOE1 which had employed two separate intake ports and therefore individual air and fuel metering for each port. Dividing the air and fuel metering into two parts did however allow finer measurement and control of the air mass flow rate over a wider range of mass flow rates and stoichiometries than would otherwise have been possible given the flow capacities of the instruments used.

The exhaust port was composed of many small circular holes which discharged into an annulus which surrounded the barrel. The annulus itself was emptied into two larger exhaust runners before connection to the laboratory exhaust extraction system. This arrangement has been described by Murad [2006] in detail and was designed to reduce the influence of the gas motion during the exhaust phase of the cycle on the tumble flow imparted during the intake event.

The laboratory exhaust extraction system operated at slightly below atmospheric pressure, which improved the scavenging performance of the engine and helped to prevent run-on problems occurring. When evaluating the performance of the piston ring pack at high pressures, see Section 5.4.2, it was sometimes necessary to increase the exhaust back pressure. This was achieved using a ball valve in the exhaust line downstream of where the two exhaust lines were merged.

2.2.3 Ignition system

The ignition system consisted of a standard 12 V automotive coil connected to a spark plug mounted in the cylinder head. The spark plug was developed by Lee [1995] and Buran [1998] specifically for optical studies of flame propagation in engines and as such featured a body of reduced diameter and electrodes manufactured from thin gauge wire in order to reduce the projected area when viewed from above or the side. The spark was initiated from a trigger signal generated by the engine timing rack, see Section 2.2.7, which was variable in one degree increments between 99 °bTDC and 99 °aTDC. The trigger signal was fed to a Lucas solid-state contactless ignition unit which controlled the supply of current to the primary winding in the ignition coil. The 12 V supply to the coil and ignition unit was interrupted by a push switch located on the tower. This allowed the engine to be motored by the dynamometer without any spark discharges. In this way the fuel flow rate could be allowed to reach a steady state during testing before the spark was initiated.

Skip fired operation was adopted, with firing only occurring once for a set number of cycles; the intermediate cycles being motoring cycles. Operating the engine in this fashion allowed more time for scavenging to occur resulting in a cylinder charge essentially free of residual gas on firing cycles and removing any uncertainty as to the mixture composition to be used in simulation work.

The spark plug comprised a central anode located concentrically in an insulating alumina tube. The combined alumina tube and anode were situated in an outer brass tube which acted as the earth conductor. The earth electrode (cathode) was formed from a small length of wire brazed onto the outer tube and bent so as to form an L-shape in the manner of a standard car spark plug. Current was supplied to the anode using a carbon core high tension spark lead and flowed to earth after crossing the spark gap via a crocodile clip attached to the cathode on the outside the engine. Carbon was preferred to copper as the conductor in the spark lead because of its interference suppressing qualities. Occasional arcing between the spark lead and the cathode or crocodile clip could be prevented by increasing the length of insulation separating the anode from the cathode by sliding a length of rubber Hellerman tubing over the anode and over the top of the alumina insulation.

The spark gap was located slightly off-centre in the combustion chamber due to the placement of the windows in the cylinder head. The distance between the electrodes was set at manufacture at approximately 0.6 mm and was not adjusted

during the course of the experiments.

2.2.4 Dynamometer and control system

The speed of the engine was controlled using an electric dynamometer manufactured by Mawdsleys Ltd. coupled to an inverter and control system fabricated by Saftronics, pictured in Figure 2.5. The speed of the engine was monitored on an analogue gauge driven by a signal from the Saftronics control system, the calibration of which was checked using a hand-held optical tachometer. A potentiometer provided continuously variable adjustment to the set speed of the engine.

2.2.5 Crank angle measurement

A shaft encoder manufactured by Honer, model 1425-131R-1800, was coupled to the torque free end of the crankshaft, the signals from which were fed to the timing rack, see Section 2.2.7 and Figure 2.9. The shaft encoder produced 1800 pulses per revolution and a single reference pulse which was aligned with top dead centre. Accurate alignment of the reference pulse with the engine TDC is vital as this signal is used to time the ignition circuits and data recorded by the Data Acquisition (DAQ) system. The error in calculated IMEP for a one degree error in TDC position can be close to 5% [Douglas et al., 1997].

Coarse alignment of the shaft encoder was performed statically using an oscilloscope to monitor the signal from the shaft encoder and a dial indicator to measure the piston position. The crankshaft was rotated by hand until top dead centre was reached and the shaft encoder aligned by rotating the spindle relative to the crankshaft until the reference signal was visible on the oscilloscope. Once coarse alignment was completed a small grub screw on the rotating part of the shaft encoder was tightened to lock its position relative the crankshaft.

Fine alignment of the shaft encoder was done dynamically, using a capacitive proximity sensor mounted above the piston with the engine driven by the dynamometer at 1500 rpm. An oscilloscope was used to monitor both the signal from the proximity sensor and the signal from the shaft encoder. It was found that, especially at low engine speeds, the signal from the proximity sensor was susceptible to distortion caused by rocking of the piston close to TDC hence the maximum value recorded by the proximity sensor was not always at the top dead centre position. For this reason the shaft encoder was aligned by bisecting the

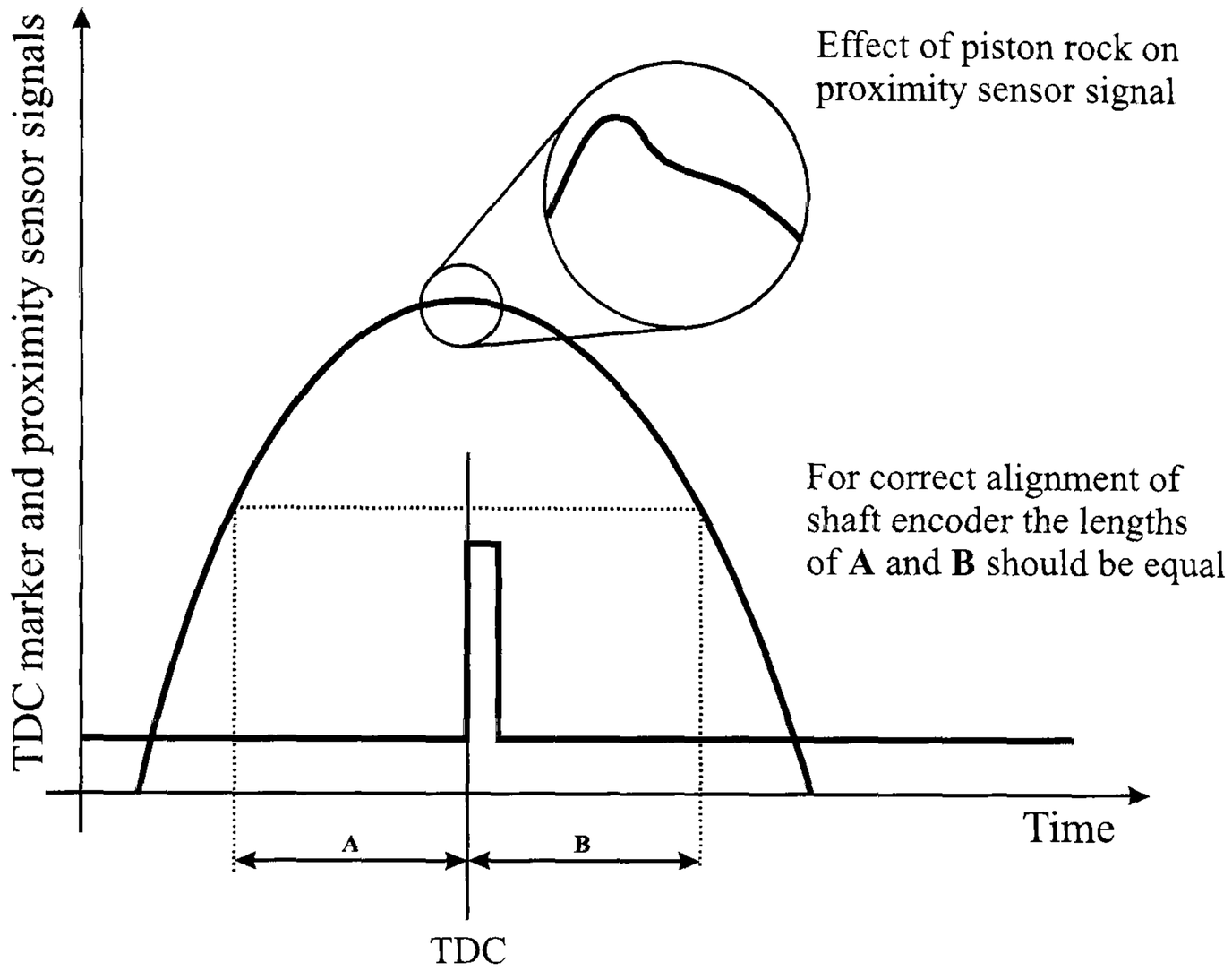

Figure 2.4: Shaft encoder TDC position dynamic alignment using a capacitive proximity sensor.

distance between two equal readings from the proximity sensor, one on the up stroke and one on the down stroke, as shown in Figure 2.4, rather than aligning with the maximum value from the proximity sensor.

The procedure described above is not the only method of determining the TDC position and it may be worthwhile for future workers to investigate other techniques. Douglas et al. [1997] recommend using a proximity sensor but also discusses the possibility of recording a motoring pressure trace with the engine running both forwards and backwards giving two pressure traces spaced equally either side of TDC. Many of the methods discussed in the literature, such as those described by Nilsson and Eriksson [2004], rely on measurements of cylinder pressure coupled with an estimation of the rate of heat transfer, which itself can be difficult to determine with any great accuracy. Leakage (blowby) from the combustion chamber should also be estimated accurately for a method of this class to be useful. For ported engines such as the LUPOE family measuring the mass flow rate in the piston ring-pack with enough precision to estimate the effect on the position of the peak cylinder pressure would be a very difficult undertaking.

The method of bisecting the distance between two equal readings as used here is similar to the method recommended by Plint and Martyr [1995] except

that here the alignment is adjusted whilst the engine is rotating. This technique is certainly more accurate than aligning with the peak cylinder pressure as recommended by Greene and Lucas [1969] although both authors state that achieving accurate alignment is extremely difficult. The torque required to turn the shaft encoder is very small, 0.03 Nm, it is unlikely that there is any error attributable to the flexing of the coupling between the crankshaft and the encoder. More likely is the possibility that torsional deflections in the crankshaft, which are always appreciable [Plint and Martyr, 1995], result in discrepancies between the crank angle as inferred by the piston position and that determined by the rotation of the flywheel.

2.2.6 In-cylinder pressure measurement

The engine was instrumented with two transducers for recording in-cylinder pressure. One, a Kistler 601A piezoelectric sensor (known as the *dynamic* pressure transducer), was mounted in the cylinder head. This transducer provided uninterrupted measurement of the cylinder pressure throughout the cycle, although because of the periodic exposure to high temperature products of combustion and the nature of piezoelectric pressure sensors the signal from this sensor was prone to drift over long periods of time. See for example Soltis [2005], Lee et al. [2005], Kuratle and Marki [1992], Douglas et al. [1997] or Zhao and Ladommatos [2001] for discussions on pressure measurement, thermal shock and transducer drift.

A second pressure sensor, a Kistler 4045A20 piezoresistive sensor (known as the *reference* or *absolute* pressure transducer) was mounted part way down the barrel. Here it was shielded from exposure to the majority of the high temperature gases and therefore drift in this transducer was minimal. The signal from this pressure sensor provided a reference absolute pressure against which the signal from the dynamic pressure sensor could be pegged. In practice, it was not necessary to use the reference pressure transducer at all times. As the engine was operated skip fired there was little chance of any prior cycle influence on the pressure at port closure hence for a given operating condition it was necessary to determine the pressure against which the dynamic transducer should be pegged only once.

The reference pressure transducer required calibrating before use by heating the engine to its operating temperature, removing the cylinder head, rotating the

crankshaft by hand to ensure that the sensor was exposed to the atmosphere and recording the voltage output from the piezoresistive amplifier. Atmospheric pressure measured using a mercury barometer could then be used to calculate the offset error in the signal from the reference pressure transducer.

The signals from the pressure transducers required conditioning before they could be recorded as voltage levels. The signal from the dynamic pressure transducer was converted into a voltage level using a Kistler type 5007 charge amplifier, the time base on the amplifier's built in filter was set to "long" for all tests. The reference pressure transducer signal was conditioned using a Kistler type 4601A piezoresistive amplifier. After conditioning the pressure traces were recorded by the DAQ system, see Section 2.4.1 and Figure 2.9.

2.2.7 Timing rack and triggering system

A programmable rack mount unit known as the timing rack was responsible for generating timing signals for the ignition, camera and DAQ systems given the TDC and external clock signals from the shaft encoder. The unit, shown in Figure 2.5, was modular, capable of a number of different configurations and designed and manufactured in the University of Leeds Mechanical Engineering Department.

Ignition was triggered with a Transistor-Transistor Logic (TTL) pulse which was generated at the programmed ignition crank angle by the timing rack. Where the timing rack was set to skip-fire the engine the ignition trigger was generated only on every firing cycle, the number of intermediate motoring cycles depending on the set skip-fire ratio. Data recording was initiated by the operator using a push switch mounted at the end of a trailing lead connected to the timing rack. Following the closure of the push switch the timing rack triggered the DAQ system at the BDC before the start of the next firing cycle. Trigger signals continued to be sent indefinitely at the BDC before firing until the timing rack was reset at the end of the experiment.

Triggering of the camera was achieved by adding an extra timing card to the timing rack in the *aux1* position. This card produced a TTL "high" signal once every cycle at its set crank angle. The *sample gate* signal, which is a standard output of the timing rack and takes the logic value "high" from BDC to BDC for the duration of each firing cycle, was combined with the *aux1* signal using an AND logic gate to give a trigger signal for the camera which occurred only on the

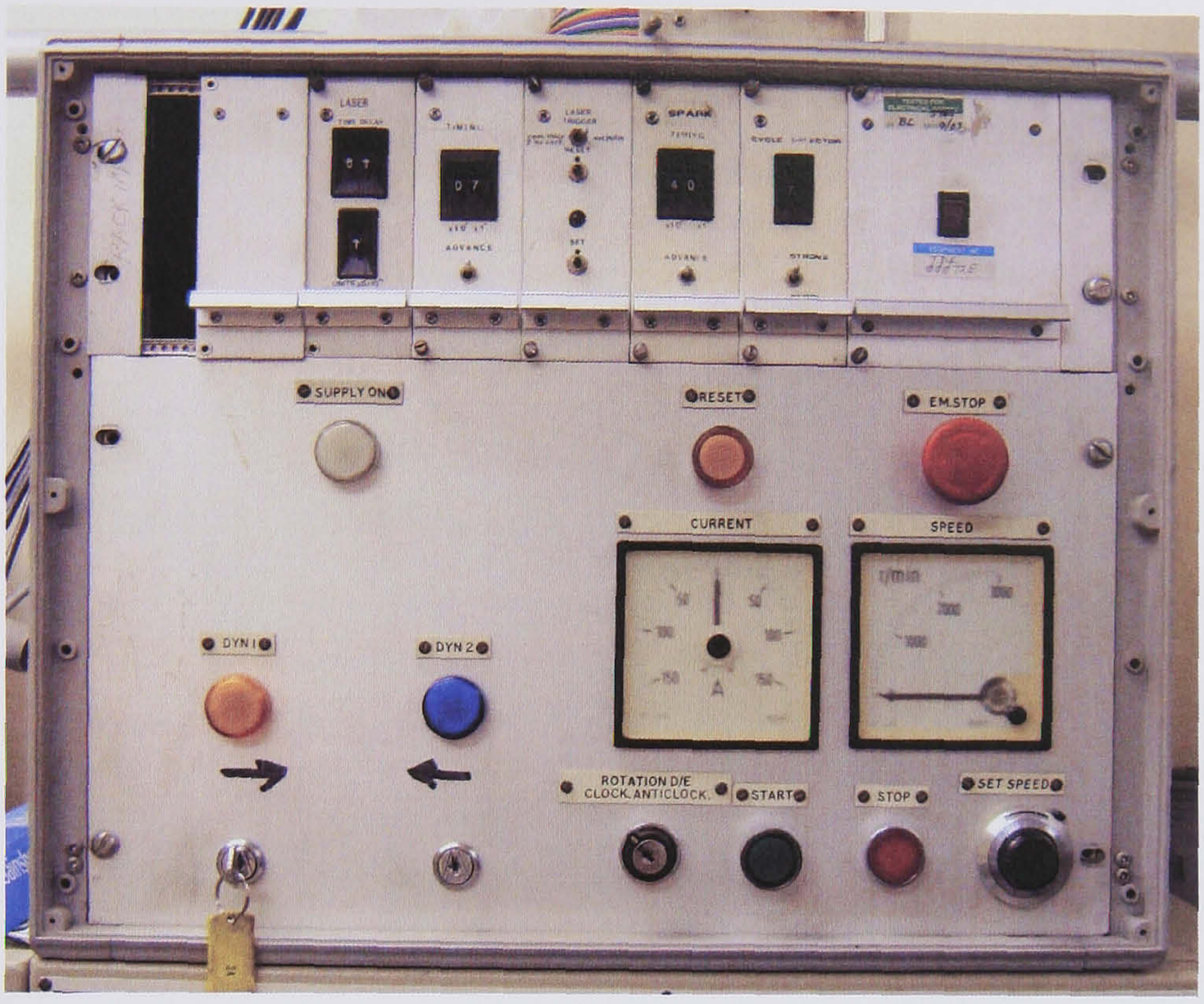

Figure 2.5: Timing rack and dynamometer inverter control panel.

firing cycles after data acquisition had been triggered on the timing rack.

2.3 Camera, laser, optics and seeding system

2.3.1 Camera and scattered light optics

Mie scattered light, generated by the interaction between the laser sheet and the titanium dioxide seed particles, indicates the position of the flame front during combustion (see Section 1.6 for an overview of the principals of Mie scattering photography). An arrangement of mirrors and a right angle prism with two mirror coated surfaces were used to form a single image from the scattered light leaving the two windows in the cylinder head, see Figures 2.6 and 2.7. This image was recorded using a Photron Ultima APX-RS 10 bit greyscale high speed video camera coupled to a computer running Photron's PFV software. The image was focused onto the camera sensor using a large aperture, $f/1.4$, Fujinon-TV 50 mm lens. The large aperture of the lens was essential for the high speed photography undertaken as the amount of light scattered from one laser pulse was very small.

In order to ensure the captured image had the maximum resolution, the recorded

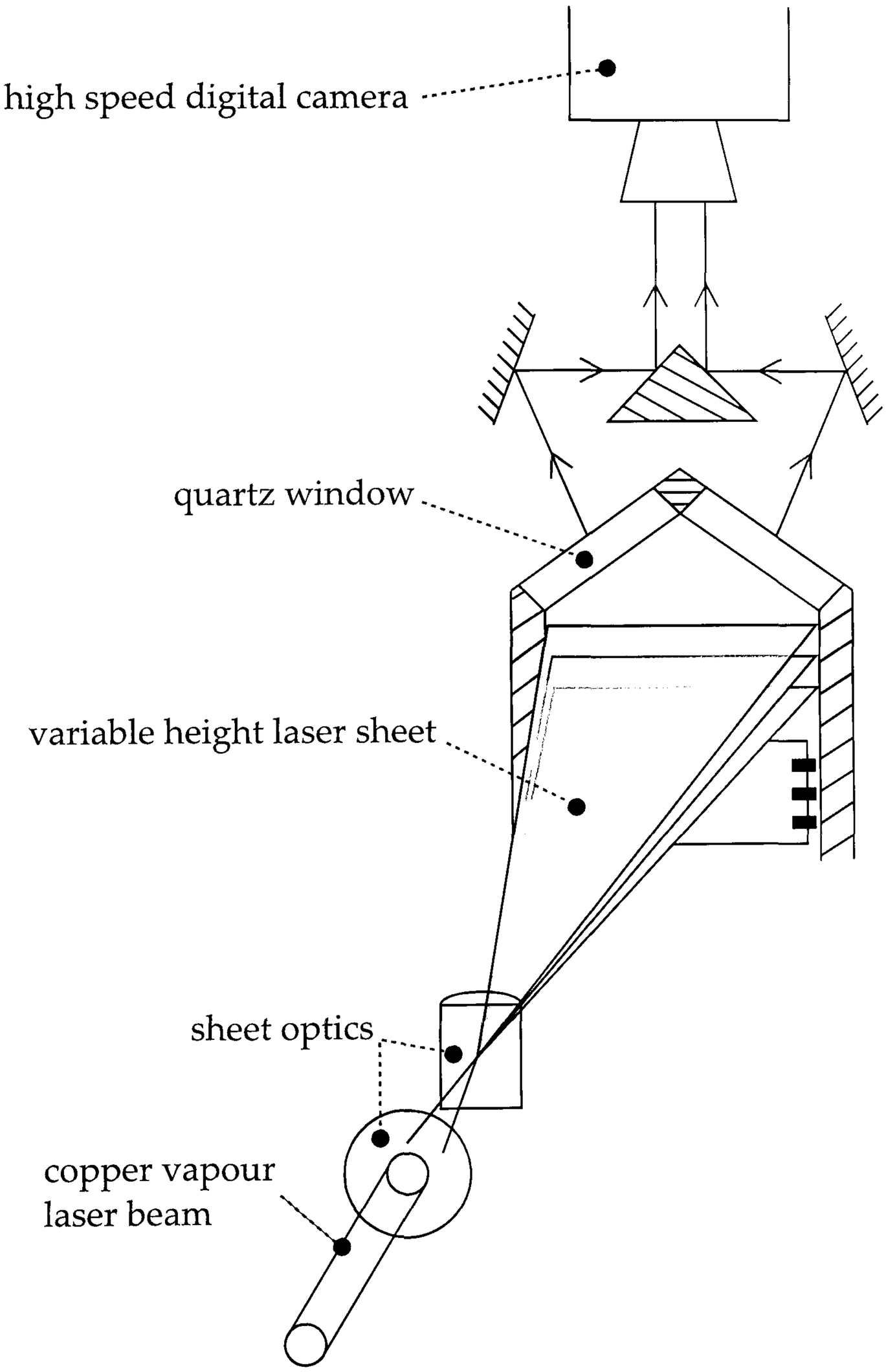

Figure 2.6: Schematic showing the arrangement of the laser sheet, engine, scattered light optics and camera. Drawing by Mr David Cooper.

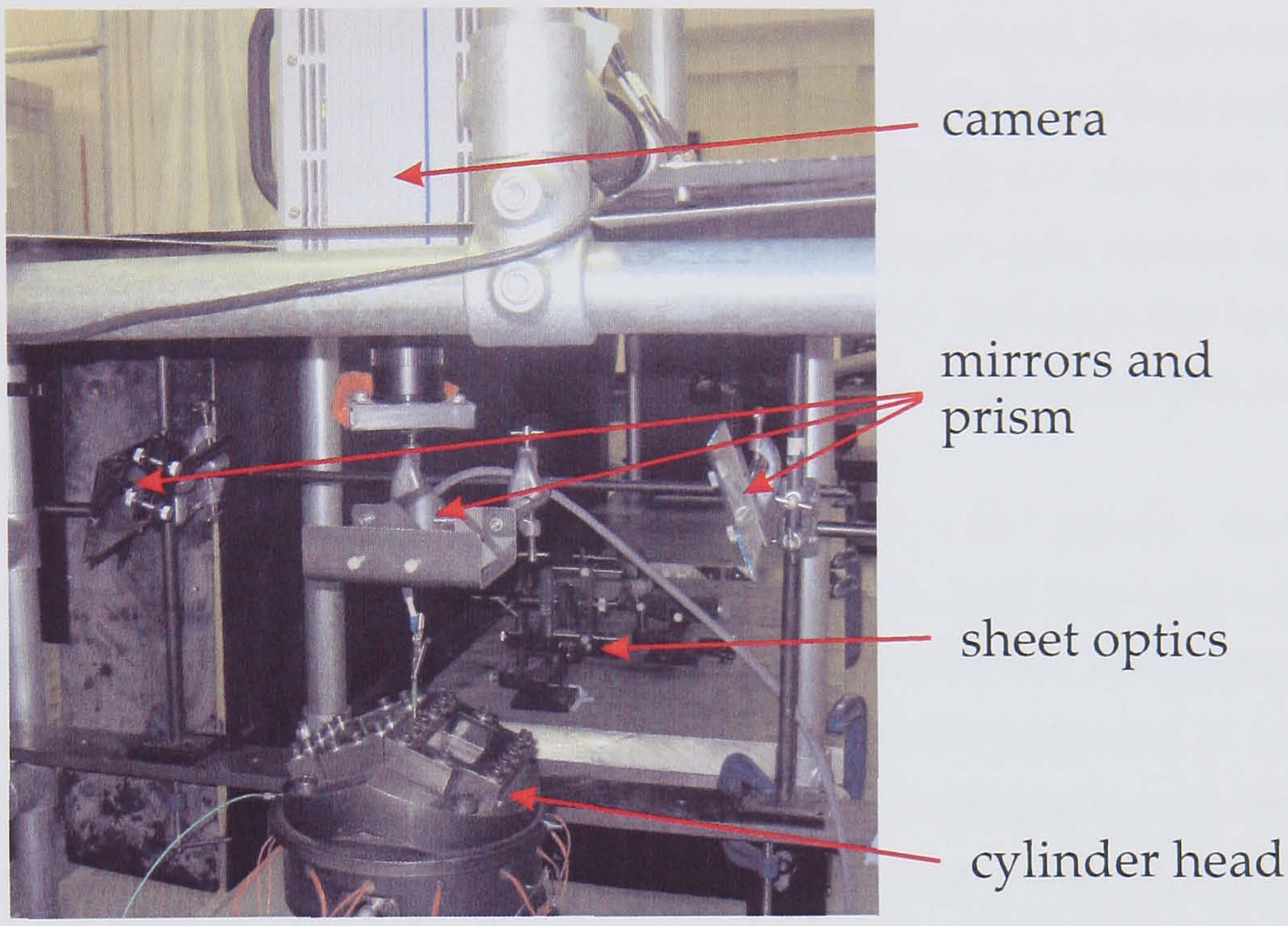

(a) Laser off.

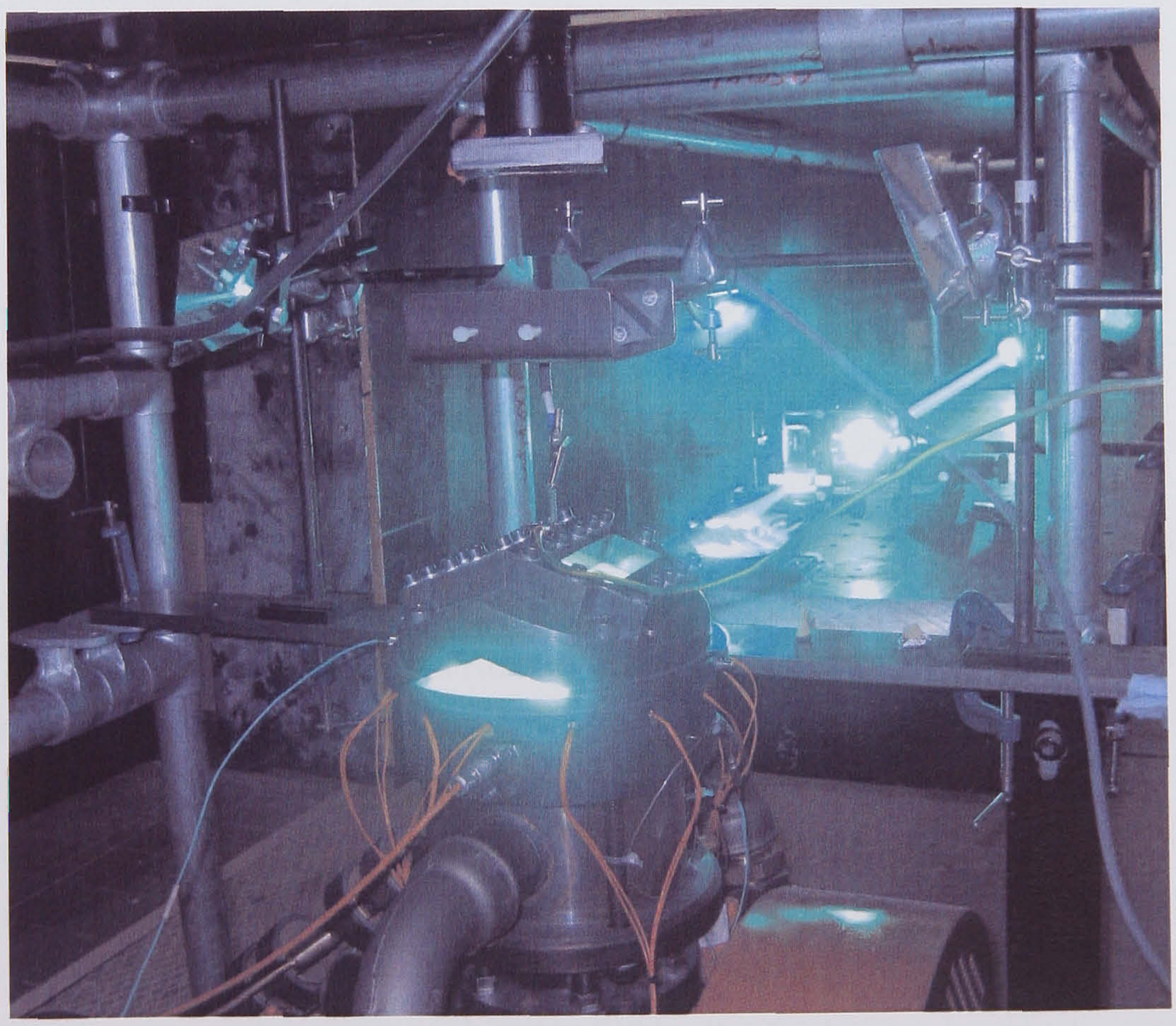

(b) Laser on.

Figure 2.7: Photographs of the experimental apparatus showing the arrangement of the camera, optics and engine.

image should appear as large as possible with little wasted area round the edges of the image. In order to achieve this it was necessary to place the camera quite close to the engine, outside the natural focal range of the lens. This problem was overcome by adjusting the back focus of the lens either by using an extension tube or by loosening the two grub screws on the camera lens mount and manually adjusting the camera back focus. As the distance between the lens and the camera imaging chip is increased it becomes possible to focus on objects closer to the camera.

The camera was operated at a resolution of 512×512 pixels. At this resolution the fastest available framing rate was 10 kHz and this was used for all experiments. An interference filter with a pass band of 511 nm, corresponding to the green light produced by the laser, was placed immediately in front of the camera lens to filter out luminous radiation from combustion and other extraneous light. As this filter was not completely efficient it was also necessary to minimise the exposure time of the camera to further reduce the amount of combustion related light recorded by the camera; the actual image exposure time was determined by the duration of the illumination provided by the laser pulse (see Section 2.3.2) rather than the camera exposure time. In practice the exposure time was set to 5 μs, as this proved the smallest period for which the laser could be reliably synchronised with the camera. The camera was configured to output a TTL "high" signal, the *frame signal*, when the shutter was open. This signal was recorded by the DAQ system along with the signals from the shaft encoder, see Section 2.4.1, to allow the crank angle of each camera frame to be extracted during later postprocessing.

The position of the two mirrors used to direct the image from each window onto the prism caused the resulting images to be taken at an angle to the bore axis. When the laser sheet was close to the TDC position the mirrors were situated directly above their respective windows, giving a degree of overlap between the two images. This overlap was a necessary feature of the experiment and allowed a reconstruction of the entire laser sheet during later postprocessing. As the sheet was moved up through the clearance volume it was necessary to move the two outer mirrors horizontally away from the engine in order to ensure that the recorded image from each of the windows maintained a degree of overlap. As this happened there was a tendency for internally reflected light from the top two windows to obscure part of the recorded image. This could be partially counteracted by adjusting the positions of the mirrors used to merge the images from the

two windows such that the viewing angle was more favourable, although there was usually a decline in image quality with the sheet in this position. Reflections from the piston crown were minimised by painting it black with Industrial Heat Shield Thermo Lack manufactured by Plasti-Kote, available from RS Components.

Rather than trigger the camera once per experiment and record all subsequent engine cycles, the camera was configured to multi-trigger such that only firing cycles were recorded (The triggering system is described in detail in Section 2.2.7). The camera mode referred to in the manual [Pho, 2003] as "random reset" was used for multi-triggering. With the triggering system typical of older cameras, recording would begin at the start of the next clock cycle after the trigger signal was received, resulting in an error in the timing of the first recorded image as discussed by Abdi Aghdam [2003]. The random reset mode forced the internal frame clock of the camera to reset with every trigger ensuring that the first recorded image after each trigger occurred at the same crank angle. The camera produced a trigger echo on receiving a trigger input and this signal was recorded by the DAQ system, see Section 2.4.1, to ensure that camera was triggering correctly.

2.3.2 Laser and sheet light optics

Laser light was provided by an Oxford Lasers LS20-50 copper vapour laser. This produced pulses of light with a single pulse occupying 25-30 ns, easily short enough to produce a flame image without any motion blur. The laser could be operated continuously at frequencies from 4.5 kHz to 20 kHz provided that the correct size of charging capacitors were installed. Burst operation from a single shot up to 50 kHz was also possible for short periods of time providing that the laser tube/cavity was at the correct operating temperature, something which could only be achieved if the laser was running continuously. For the current experiment, the laser was synchronised with the framing of the camera at 10 kHz. The camera frame signal was delayed slightly using a Thurlby Thandar Instruments TGP110 pulse generator to ensure that the emission from the laser occurred just after the camera shutter opened. The laser synchronisation signal was recorded by the DAQ system for later analysis, see Section 2.4.1.

The laser beam was formed into a horizontal sheet using a 1000 mm focal length plano-convex lens, which served to focus the light to a point in both the horizontal and vertical directions, followed by a 50 mm focal length plano-cylindrical

lens, positioned approximately 530 mm from the centre of the bore, which formed a sheet of light by expanding the beam in the horizontal direction. The window in the side of the cylinder head had a circular inner profile, the lensing effect of which helped to spread the sheet further inside the bore. Shown in Figures 2.6 and 2.7 are a schematic and photographs of the laser sheet and camera arrangement.

Basic alignment of the sheet optics was performed with the cylinder head removed. A spare cylinder head side window, positioned where the actual window would sit were the head in place, served as a useful tool to simulate the distorting effect of the head window on the sheet. It was also found to be useful during the alignment process to remove stray light from the edges of the beam using an adjustable diameter aperture just smaller than the beam located before any of the lenses. Vertical alignment of the laser sheet employed a purpose made alignment tool which screwed into two of the threaded holes on the barrel used for clamping the cylinder head during normal operation, see Figure 2.8. With the tool secured to the barrel, it was adjusted to the desired height with slip blocks used to measure the distance between the slit and the barrel top surface. Once the laser sheet position was adjusted to ensure that the beam passed through the slit the sheet was taken to be at the correct height. As the slit itself was 1 mm wide the accuracy of the height alignment was limited to ± 0.5 mm from the set position, although in practice finer alignment would not have been possible because of the difficulty in determining the exact sheet position by eye whilst wearing laser alignment goggles.

2.3.3 Seeding system

Seed was supplied to the engine using a fluidised bed which was formed from a porous sintered disc with a characteristic sinter particle size between 100 and 160 μm mounted at the bottom of a vertical tube, the tube being loaded with a small amount of seed material. After the mass flow rate had been measured a small amount of air was bled from the engine air supply which passed through the sintered disk and entrained seed particles before leaving the seeder at the top of the tube. The flow of seed was controlled using a ball valve mounted after the seeder which was kept closed until required for an experiment. In series with the ball valve was a gate valve which could be adjusted to control the amount of seed delivered to the engine, see Figure 2.2. Seed laden air was introduced to the

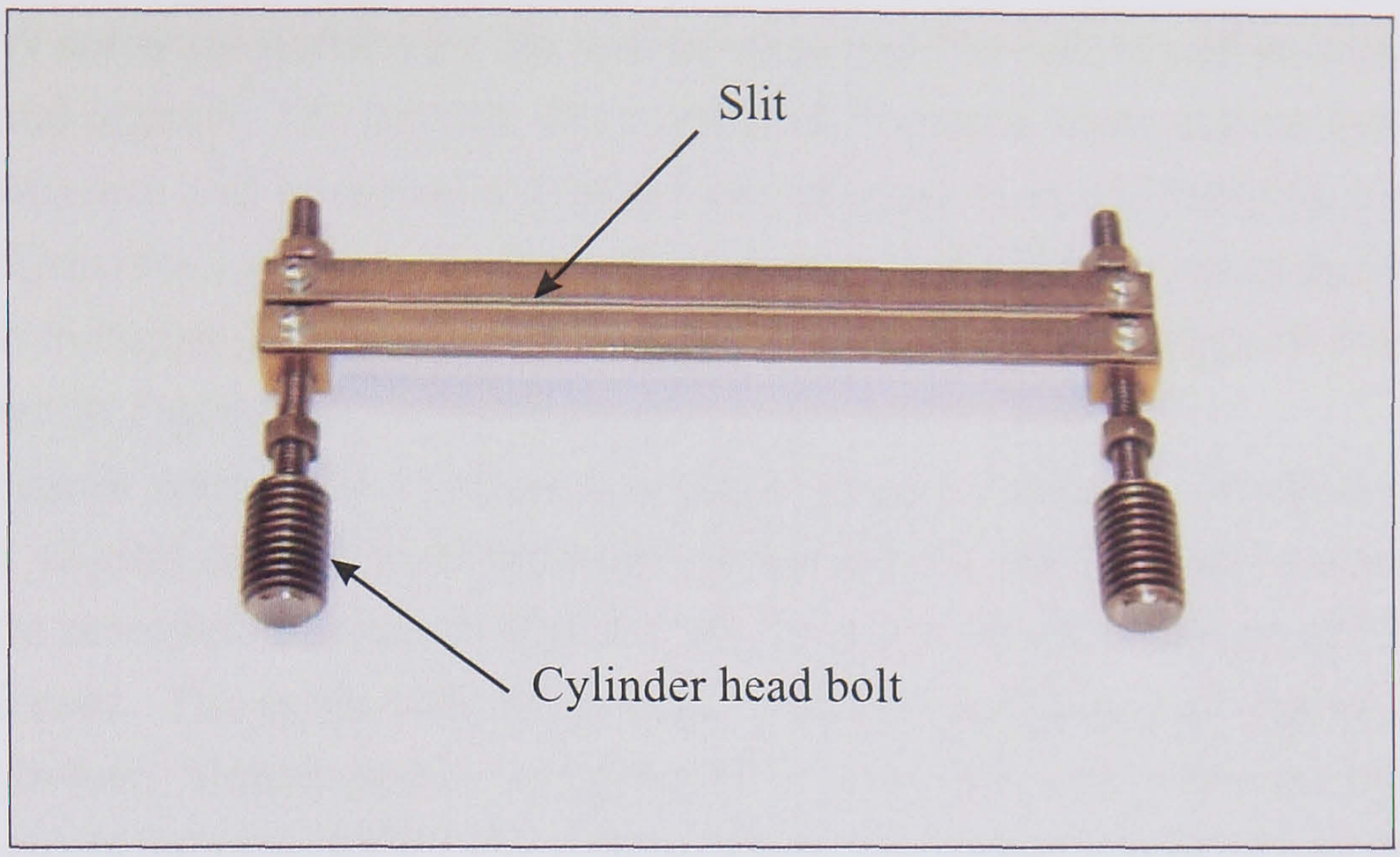

Figure 2.8: Tool used to set the height of the laser sheet above TDC.

main fuel and air supply through a tapped hole approximately 100 mm before the engine intake port.

The seed consisted of sub-micron titanium dioxide particles which were dried in an oven and stored in a desiccator prior to use to reduce the tendency of the seed to conglomerate. The fluidised bed functioned best when it was loaded with a small amount of seed, say 3 cm^3. When the seeder had not been used for a period of time or the amount of seed delivered started to fall it was found that removing the sintered disc and cleaning it, by forcing water through it and drying with compressed air, would often restore the performance of the seeder. If this proved insufficient the sintered disc was replaced.

2.4 Data acquisition system

2.4.1 Data acquisition system

The purpose of performing experiments on a real engine is to gather data which can be compared with model predictions. In order to cope with the large amounts of data generated and record all the signals from the engine simultaneously at a rate fast enough to provide crank angle resolved information, some form of computerised data logging system is necessary. For the purpose of the experiments undertaken during the current study two National Instruments data acquisition PCI cards, model numbers 6110 and DIO32-HS, and a personal computer running

LabVIEW software written by the author were used to collect and store analogue and digital signals. For brevity the combined National Instruments cards, LabVIEW software and personal computer are referred to as the DAQ (acronym for Data AcQuisition) system. A schematic diagram of the DAQ system and cameras is shown in Figure 2.9. A sample of the data recorded during a typical firing cycle are shown in Figure 3.1.

Two cards were used to allow true parallel data collection on each recorded channel. Digital signals were recorded on the DIO32-HS card and analogue signals were recorded as pseudo-differential signals with an accuracy of 12 bits on the 6110 card. The cards will be referred to as the analogue and digital cards in the text below. Simultaneous sampling of all channels was achieved by linking the two cards using an RTSI cable. This allowed the sample clock of one card to be synchronised with the other in a master-slave type configuration. The following analogue and digital signals were recorded:

- Absolute pressure transducer
- Dynamic pressure transducer
- Shaft encoder clock signal
- Top dead centre marker
- Bottom dead centre marker
- Ignition trigger
- Laser pulse signal
- Camera frame signal
- Camera trigger echo

Data recording was triggered at the instant of BDC before a firing cycle by the timing rack, see Section 2.2.7, and continued for a set number of samples as determined by the LabVIEW software. All DAQ data were recorded at a sampling rate of 200 kHz, equivalent to 22.2 samples per crank angle degree at 1500 rpm, the fastest engine speed used. Although it was not strictly necessary to sample at such a high rate to record the trace of the cylinder pressure sensors, doing so enabled a significant increase the signal to noise ratio by allowing the averaging of more than one recorded value as the signal was converted from the time domain to the crank angle domain during postprocessing, see Equation 3.3.

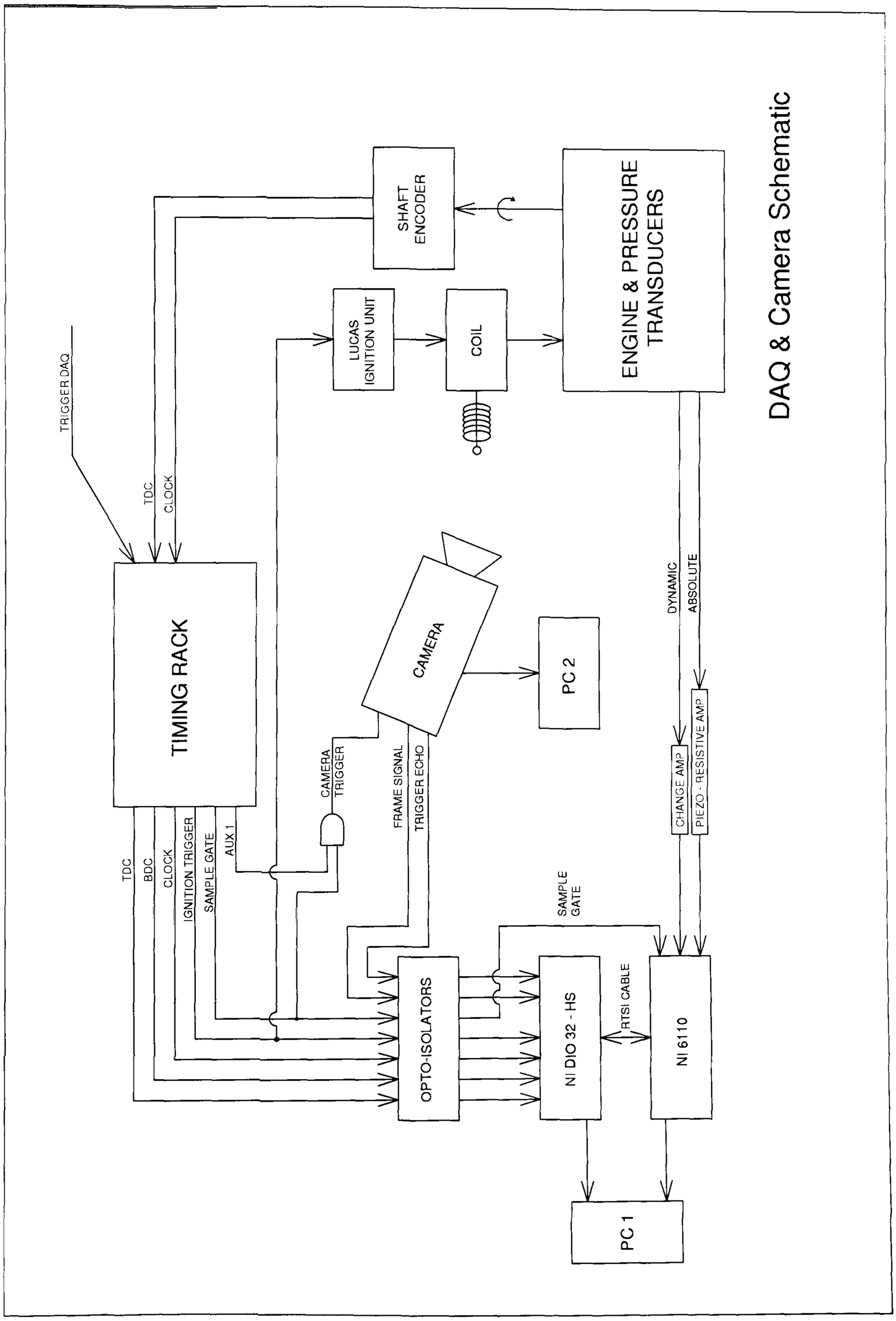

Figure 2.9: Data acquisition and timing rack wiring schematic. Drawing by Mr Ashley Arundel.

2.4.2 Electrical noise

The presence of equipment such as the ignition system, dynamometer and inverter in the laboratory in which the experiments were conducted meant that the environment was inherently electrically noisy. The most common problem with electrical noise was unwanted triggering of the DAQ hardware by the electrical interference emitted as the arc crossed the spark gap during ignition. This problem was compounded by the fact that the triggering circuits on the new National Instruments DAQ system proved to be much more sensitive to noise than the previously used Microlink system. Often, the system would work correctly during motoring tests or while there was no spark but would fail during firing tests, with data recording triggered as soon as the first spark discharge occurred rather than from the signal supplied from the engine timing rack.

Elimination of the problems caused by electrical noise proved to be something of a black art, however, several techniques were particularly effective including:

- Proper earthing of the spark plug using a crocodile clip connected directly to the spark plug cathode.
- The use of optical isolators, type P9001, manufactured by Sharp and available from RS Components, placed on all digital signal paths immediately before the DAQ inputs.
- Proper termination of all unused DAQ system inputs with 50 Ω BNC terminators.
- Careful routing of cables away from the path of the spark plug lead and associated wiring.
- The use of shielded cables, connectors and instrument cases where ever possible.

Both the analogue and digital DAQ cards possessed a trigger input and triggering of the DAQ system could be controlled by either card depending on which one was configured as the master and which one was configured as the slave. Initial experiments used the digital card as the master and hence the trigger signal was fed to the digital card. Despite the best efforts of the author it proved difficult to obtain reliable operation of the DAQ system using this configuration with the system being susceptible to false triggering caused by the electrical noise generated by the spark discharge. Later experiments employed the analogue card

as the master and hence triggering was controlled from the analogue card. The trigger input on this card was much less prone to false triggering and this configuration proved reliable.

Occasional noise in the digital signals recorded by the DAQ system could be removed by postprocessing the signal using a debouncing algorithm, see Section 3.2.1.

2.5 Experiment technique and procedure

Crucial to the collection of reliable and repeatable data was the consistent use of good experiment technique. To this end several aid-memoires were displayed in the laboratory which are reproduced with explanations below.

2.5.1 Morning routine

The text below details the routine followed in the mornings to ensure that all systems were sufficiently warmed up and the appropriate calibration images were taken.

- Laser on—*Set to internal triggering for warmup period. After the camera has warmed up and scale images have been taken the laser is changed to external triggering to synchronise with the camera.*
- Clean or replace seeder sintered disc (if necessary)— *Poor seeder performance could often be cured by cleaning or replacing the sintered disc, see Section 2.3.3.*
- Exhaust blower on—*Running without the exhaust blower on causes pour scavenging and a tendency for the engine to run on, besides having obvious safety implications.*
- Air supply on and check/adjust air mass flow rate.
- Heaters on—*Air and heaters were left on throughout the day to ensure that the engine was at a uniform temperature.*
- DAQ system, camera, timing rack, piezoresistive and charge amplifiers on—*All electronics systems were warmed up and allowed to stabilise at the start of the day.*

- Check fuel level—*Air locks in the fuel system caused by running the tank dry are time consuming to remove, daily fuel checks can help to avoid this.*

- Record motoring cycle—*A daily motoring test taken when the engine and DAQ system is fully warmed up but without fuel is a valuable tool for monitoring changes in the engine's performance over time and diagnosing faults. See Hountalas et al. [2006] for an excellent discussion on the causes of variations in motoring pressure.*

- Clean cylinder head windows.

- Take scale images—*Scale images, as shown in Figure 2.10, were taken at the start of every day with the camera interference filter removed. Scales were taken at the TDC plane and on the inside of each window using appropriately sized pieces of graph paper backed with stiff card used. In addition the orientation of the camera relative to the engine was recorded by taking an image of a piece of paper placed above the window on which the directions of the ports were labelled with arrows.*

- Calibrate camera—*Each sensor element on the camera imaging chip has an associated ambient noise level which is a function of the framing rate, resolution and exposure time. In order to remove this noise a black balance must be performed after the camera is fully warmed up. This allows the camera to record the ambient noise level of each pixel which is then automatically subtracted from the pixel value of recorded images by the camera hardware. A lens cap is placed over the lens and the calibrate option, accessed from the "More" button from the PFV software, is activated to achieve this.*

2.5.2 Test procedure

For a typical engine and dynamometer setup, the temperature of the cylinder head and barrel would be controlled by the coolant jacket and would usually be allowed to reach a steady state before data was collected. The arrangement for the LUPOE2 engine was a rather different, with the temperature being maintained by the cartridge heaters rather than by the action of combustion and friction. For this reason it was desirable to run the engine for as short a time as possible during testing to minimise the amount of drift from the set temperature. Given below is the procedure followed to record the simultaneous camera and pressure data used in this thesis.

- Laser beam-stop up.

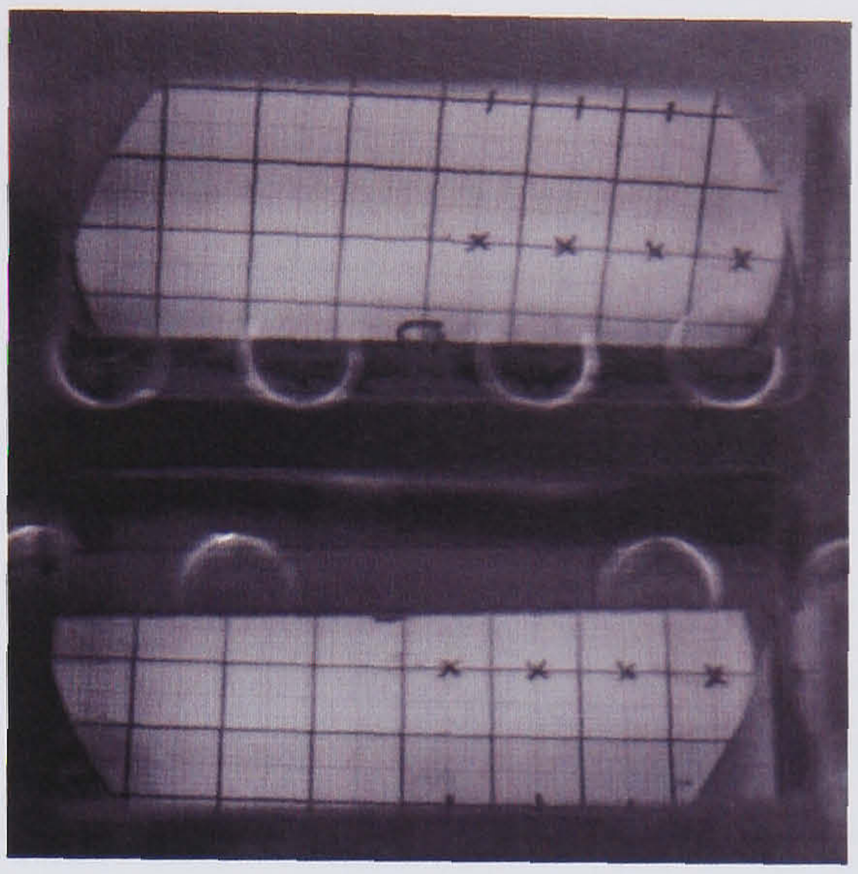

(a)

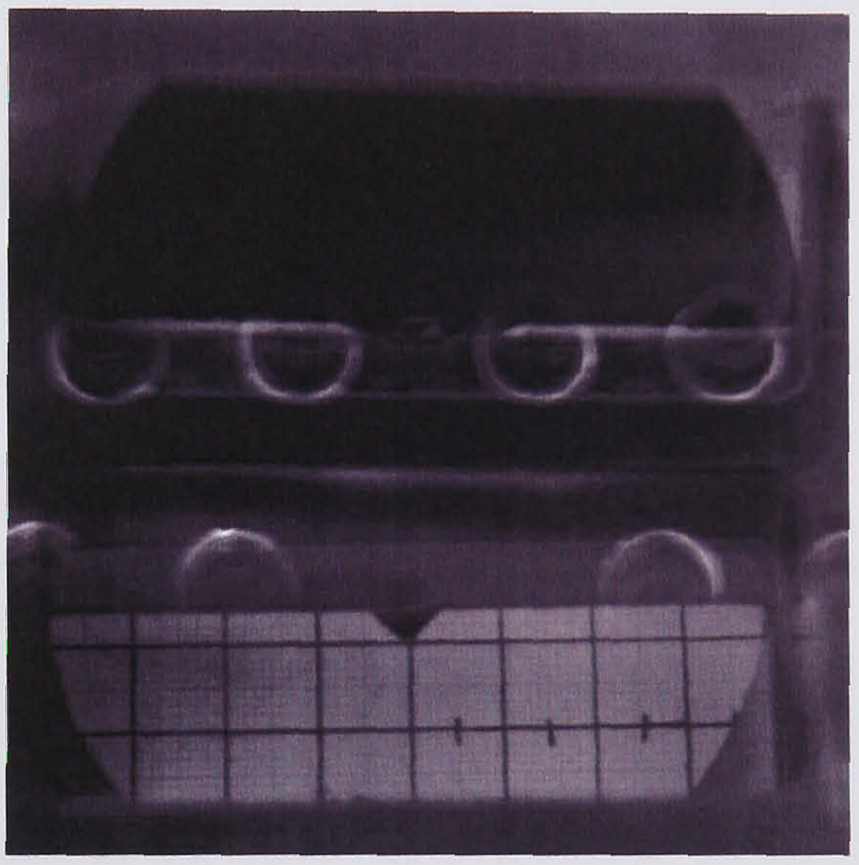

(b)

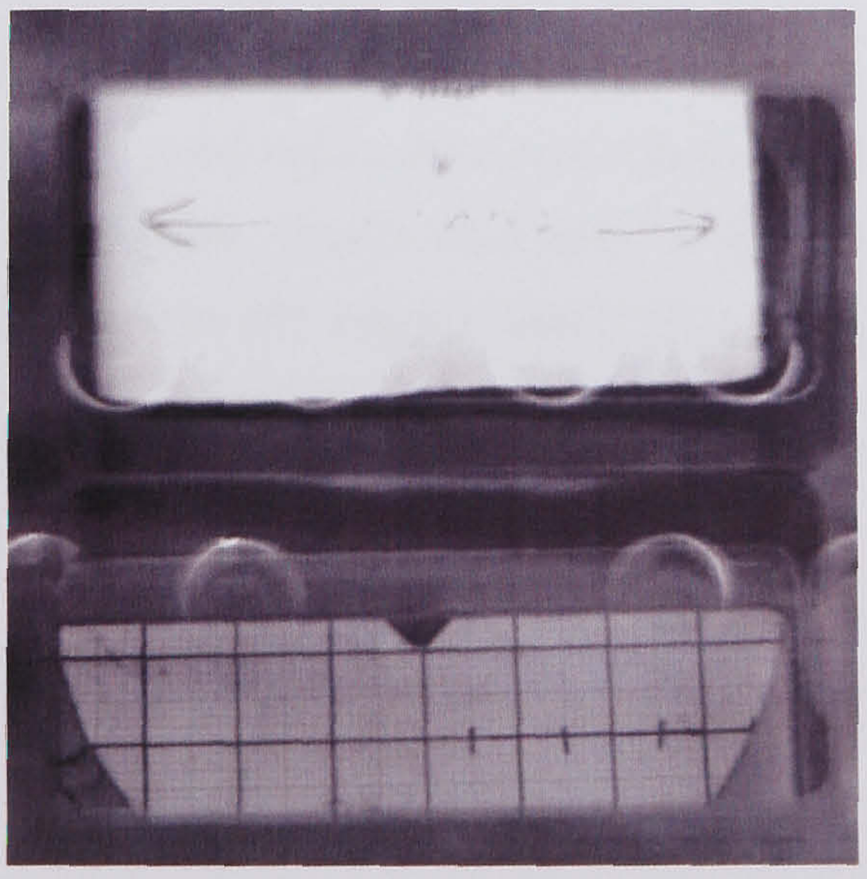

(c)

Figure 2.10: Scale images with the scale placed on the TDC plane (2.10a); parallel with the pent roof looking through the big window (2.10b); and parallel with the pent roof looking through the small window with the positions of the intake and exhaust ports indicated (2.10c).

- Check air mass flow rate and heater temperatures.
- Prepare camera and DAQ system for recording.
- Dynamometer inverter power on and reset.
- Opto-isolators on—*The opto-isolators were only turned on during testing as their battery life was short.*
- Arm camera and DAQ system—*The camera and DAQ system were armed after the dynamometer inverter was powered up to avoid electrical interference caused by the switching of the 3-phase power supply accidentally triggering data recording.*
- Begin low speed engine rotation using the dynamometer to drive the engine.
- Turn on fuel supply and open seed control valve—*As the fuel supply took a few seconds to reach its full flow rate the fuel system was activated before the engine was at full speed. The seeding system was turned on at this point for a similar reason.*
- Motor the engine to the desired speed using the dynamometer.
- Check the fuel flow rate and adjust if necessary.
- Activate ignition using the push switch on the tower.
- Begin data recording after approximately five firing cycles—*When the engine was running properly each firing cycle was audible as a distinct bang. Typically five firing cycles were allowed before data recording was started to allow the engine to settle into steady operation. It was also noted that the performance of the seeder improved significantly when the engine was firing, waiting for a couple of cycles gave time for seed to enter the chamber.*
- Wait until data recording is complete.
- Turn fuel pump off.
- Ignition off—*Turning the ignition system off causes the electric field in the coil to collapse resulting in an additional unwanted spark discharge. Turning the fuel supply off first reduces the risk of backfires down the intake or exhaust.*

- Dynamometer inverter power off—*The design of the dynamometer is such that current is supplied to the stator at all times hence the inverter should be turned off when the dynamometer is not rotating to prevent the possibility of overheating.*
- Opto-isolators off.
- Reset timing rack triggering system—*If the triggering system is not reset after a test trigger signals will continue to be sent out immediately the engine begins to rotate again.*
- Review captured data.
- Clean engine windows if necessary—*At high engine speeds the windows in the cylinder head needed cleaning after every test. At lower engine speeds fouling was less of a problem and it was possible to run the engine for two tests before cleaning the windows.*

2.5.3 Window cleaning procedure

During operation the engine windows inevitably became fouled with an opaque mixture of oil and titanium dioxide seed which reduced the quality of the recorded images. In order to restore the quality of the recorded images it was necessary to remove the cylinder head and clean the windows between tests. At low engine speeds, 750 or 1000 rpm, it was usually possible to record two or three tests before the image quality fell to an unacceptably low level. At 1500 rpm the window became fouled much quicker and the windows were cleaned after every test. The procedure followed when cleaning the windows is given below.

- Laser beam stop down.
- Remove Laser guarding.
- Set the charge amplifier to reset and disconnect dynamic pressure transducer—*Setting the amplifier to reset when disconnecting the pressure transducer short circuits the input circuit and precludes the possibility of damage to the instrument, for example, by static discharge.*
- Remove spark lead.
- Remove cylinder head.

- Clean windows using Ambersil glass cleaner available from RS Components—*Several different cleaning solutions were tried of which the afore mentioned glass cleaner proved the most effective. Crucial to the effective cleaning of the windows was that the cleaning tissue be not too dry and some cleaning solution be allowed to evaporate off the window after cleaning. Aggressive rubbing of the window with dry cleaning tissue, whilst appearing to remove marks, seemed to form a coating which oil and seed adhered to particularly readily. Occasionally after a couple of weeks of running a buildup of oily residue could form on the windows which was very difficult to remove. Several different aggressive solvents were used to remove this including toluene and xylene but none seemed particularly effective. Suggested but not tried were washing-up liquid, car windscreen cleaning products or unleaded petrol.*

- Wipe piston crown and bore to remove any accumulated oil film and seed.

- Replace cylinder head and tighten bolts to the correct torque using a torque wrench.

- Reconnect dynamic pressure transducer and set charge amplifier to operate.

- Reconnect spark lead.

- Replace laser guarding.

Chapter 3

Data Processing and Reduction

3.1 Overview

Raw data recorded by the data acquisition (DAQ) system and digital camera (see Chapter 2) consists primarily of time-based pressure and image information. In order to be useful for studies of SI engine combustion this data must be resampled to the crank angle domain and the images processed to remove noise and leave binary images showing only regions of burnt and unburnt gas. Many of the processing techniques used during the course of the current study are similar to those applied by Abdi Aghdam [2003], Murad [2006] and other previous students however, the Fortran programs and Adobe Photoshop commands used by these authors have been entirely replaced by routines written by the current author in the Matlab language.

Matlab is not a compiled language like Fortran hence data processing will always take longer using Matlab. This disadvantage is however more than outweighed by the depth and quality of the libraries included with Matlab which include routines for processing images, plotting data in two and three dimensions and constructing simple graphical user interfaces. The routines proved invaluable and allowed data processing to be almost entirely automated.

This chapter describes the procedure followed to convert raw data to a useful format. Further information on the precise nature of the raw data such as

sampling rates, exposure times, etc. can be found in Section 5.2 and Chapter 2.

3.2 Analogue and digital signal processing

3.2.1 Signal pre-processing

Raw data recorded by the DAQ system, a typical example of which is shown in Figure 3.1, was stored as columns of numbers in an ASCII text file. The text files were processed using a library of Matlab functions, `PProc`, written by the author. The library was designed in such a way that it could be used interactively, for example when processing an individual experiment to check the correct functioning of the DAQ system and transducers, or in a batch file when applying the same processing routine to a large number of data files. Central to the operation of the `PProc` routines is a Matlab data structure designed specifically to handle engine data. The field names of this structure and their intended use, along with a summary the `PProc` routines, is given in Appendix A.

The flowchart shown in Figure 3.2 shows the procedure adopted to process data recorded by the DAQ system. Raw text data was loaded into the Matlab workspace, appropriate scale factors applied to the pressure transducer signals and the data placed in a `PProc` data structure. Before beginning serious processing, the channels which encode the TDC and BDC signals were scanned to remove any noise introduced by electrical interference which would otherwise have caused processing to fail. In practice this routine was found to be unnecessary after opto-isolators were added to the digital input lines (see Section 2.4.2) to remove noise. Its use was continued as it provided a useful check on the quality of the recorded signals and did not incur a significant time penalty. Following glitch removal, the BDC marker signal was used to separate the continuous stream of data into individual cycles, which were then scanned to remove incomplete and skip-fired cycles.

Crank angle information, encoded by the shaft encoder signal, was now extracted. Starting at the beginning of each cycle, the pulse train recorded by the DAQ system from the shaft encoder was analysed to locate the significant going edges[1]. An output array of crank angles was generated by incrementing the crank

[1]Electronically, a digital signal may be represented in one of two ways: either a high voltage represents *true* and zero volts represents *false* or vice versa. For a signal where a high voltage encodes *true* a positive going edge, i.e. a transition from zero to five volts, is significant. For a signal where zero volts encodes *true* a negative going edge is significant.

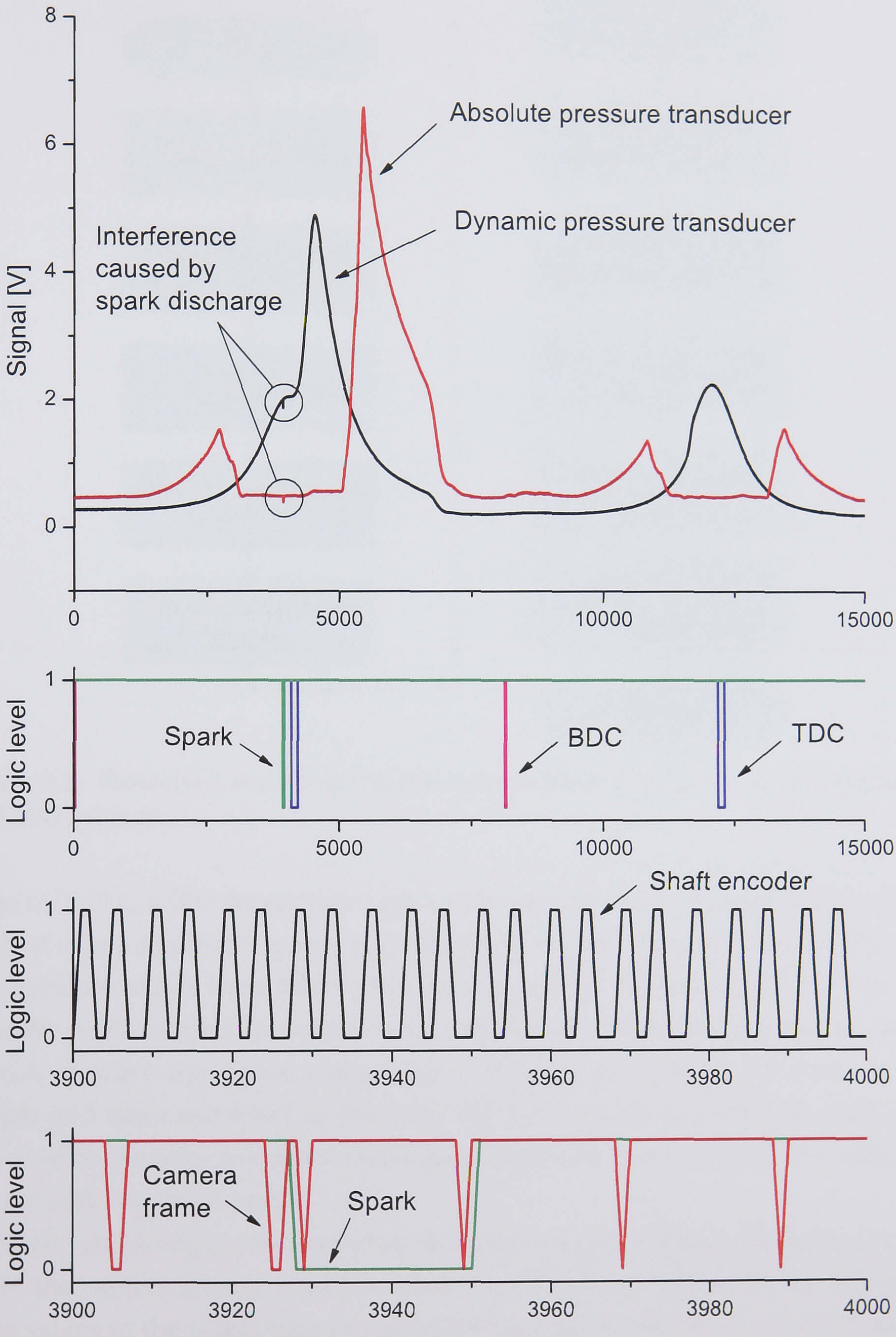

Figure 3.1: Typical raw data captured by the DAQ system. The bottom two graphs use a different scale to reveal detail around the time of ignition.

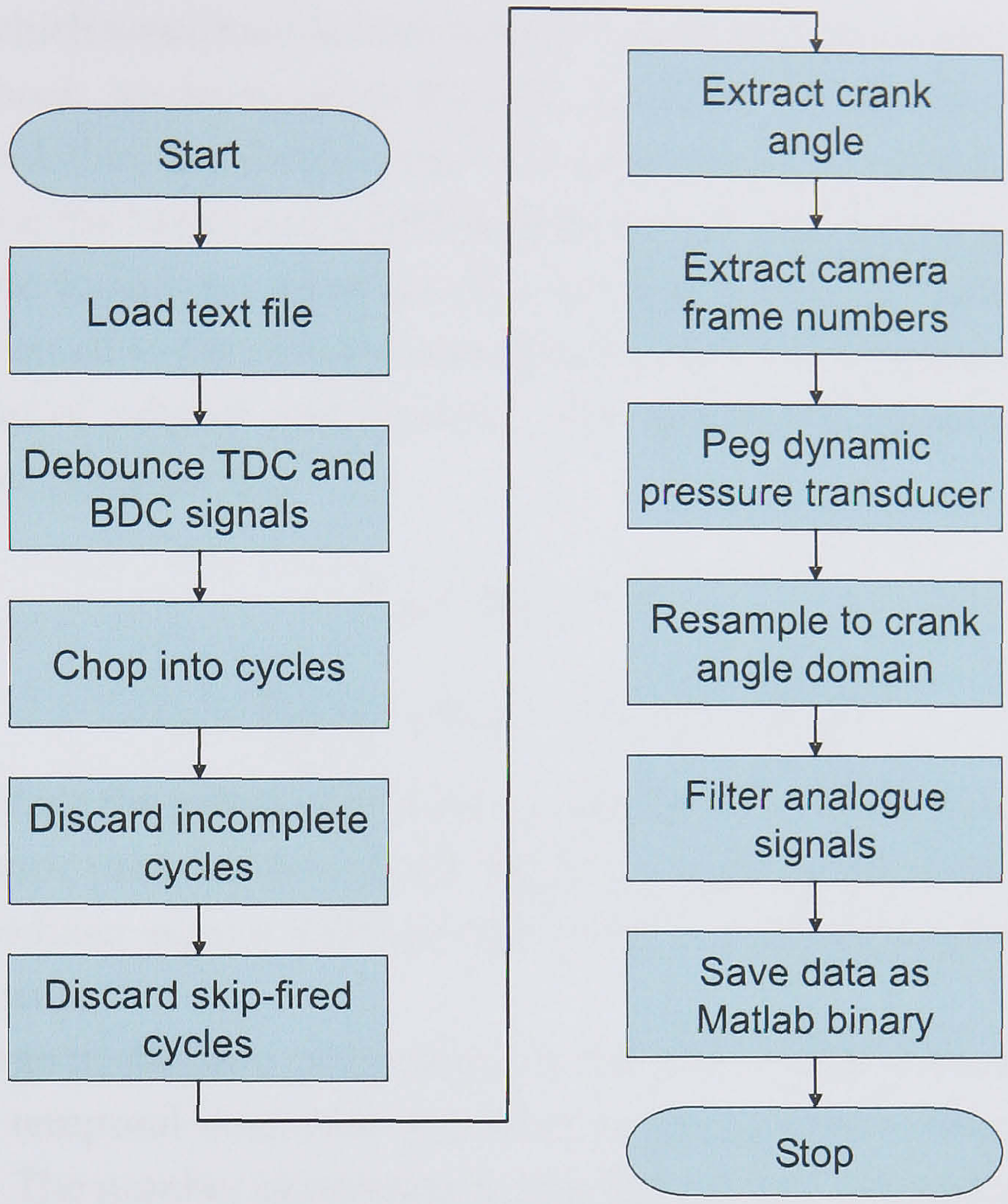

Figure 3.2: Flowchart showing the procedure used to process data recorded by the DAQ system.

angle by 0.2° CA (the separation between pulses for the particular shaft encoder used) at every significant going edge found in the shaft encoder signal. The samples between edges were filled with linearly spaced numbers such that for each cycle the crank angle information was continuous, began at 0° CA and advanced 0.2° CA at every significant going edge. Once the crank angle increase for each sample had been extracted in this way the TDC marker signal from each cycle was used to align the extracted crank angle data and ensure that 0° CA coincided exactly with top dead centre.

As the crank angle corresponding to each sample was now available the timing of the camera frames could be determined. The positions of the significant going edges in the pulse train encoded by the camera frame signal were used to ascertain the sample numbers corresponding to each camera frame; additionally, a list was generated giving the exact crank angle of each camera frame. Following this procedure the cylinder pressure recorded by the dynamic pressure trans-

ducer P_{dyn} (which was prone to both long term drift and short term errors caused by thermal shock, see for example Kuratle and Marki [1992]) was pegged to the pressure recorded by the absolute pressure transducer P_{abs} (which was mounted part way down the barrel and shielded from the hot combustion gases). The dynamic pressure transducer signal for the cycle was translated vertically such that its value was equal to the pressure recorded by the absolute pressure transducer at the moment of exhaust port closure.[2] The resulting pressure signal was the actual cylinder pressure P_{cyl}.

$$P_{\text{cyl}} = P_{\text{dyn}} + \varepsilon_P \tag{3.1}$$

$$\varepsilon_P = \overline{P}_{\text{abs}}(\theta = \theta_{\text{EPC}}) - \overline{P}_{\text{dyn}}(\theta = \theta_{\text{EPC}}) \tag{3.2}$$

In order to reduce the influence of noise or quantisation on the value used to correct the dynamic pressure transducer signal ε_P, both the absolute and dynamic pressure transducer signals were averaged over a small time period around exhaust port closure.

At this stage in the data processing procedure it was no longer necessary to maintain the temporal resolution provided by the high sampling rate used for data capture. The number of samples in the data set was reduced by resampling the data to the crank angle domain with a resolution of 0.2° CA. Signals were resampled by taking the mean of the samples within each 0.2° CA interval, for example the value calculated for TDC consisted of the mean of all those samples whose crank angles were in the range were $-0.1 \leq \theta < 0.1$. By adopting this procedure the rms noise in the resampled signal σ_{av} was reduced according to

$$\sigma_{\text{av}} = \sigma\sqrt{1/n} \tag{3.3}$$

where σ is the rms noise in the original signal and n is the number of samples over which the average is taken [Mihura, 2001]. To remove any remaining noise in the analogue signals a 5^{th} order low pass Butterworth filter was applied to the data using the Matlab built in functions `butter` to design the filter and `filtfilt` to filter the data with zero phase shift. The cutoff frequency used for filtering was $2°\,\text{CA}^{-1}$ in all cases. Finally the processed data set was saved in the Matlab binary file format (extension `.mat`) for later use.

[2] Here exhaust port closure is defined as occurring when the (flat) piston crown is level with the top of the exhaust port.

3.2.2 Selection of representative cycles

A typical data set recorded during the current study consists of 450 or more cycles. Rather than comparing the pressure traces of the whole data set to model predictions it is useful to work with a small number of cycles which represent the whole data set. Ensemble averaging a data set of experimental cycles recorded at the same operating condition reduces the data set to a single cycle. Although the IMEP of this cycle is equal to the mean IMEP of the entire data set, the shape of the pressure trace of the ensemble averaged cycle does not usually resemble any of the actual cycles in the data set [Abdi Aghdam, 2003]. This occurs because the distribution of pressures at a given crank angle is non-Gaussian [Abdi Aghdam et al., 2007]. Representative cycles were therefore selected on the basis of their peak pressure using the method advocated by Abdi Aghdam [2003]. The three cycles with a peak pressure closest to the mean peak pressure of the entire data set were designated "middle" or "mean" cycles. The three with peak pressures closest to the mean peak pressure plus two standard deviations were designated "fast" cycles whilst the three cycles with peak pressures closest to the mean minus two standard deviations were "slow" cycles.

3.2.3 Reverse analysis using LUSIEDA

A Fortran program known as LUSIEDA (Leeds University Spark Ignition Engine Data Analysis) was used to postprocess the pressure signals recorded by the DAQ system (see Sections 2.4.1 and 3.2.1 for detailed descriptions of the DAQ system and pressure pre-processing). The LUSIEDA code employs the subroutines used by the LUSIE simulation software (described later, see Section 4.2) to perform a reverse analysis on experimental cylinder pressure data, determining the mass fraction burnt and turbulent mass burning velocity u_{tr} at a given instant. It is also possible to supply experimental flame radius data to LUSIEDA to allow the calculation of the burning velocity u_t for the reference surface defined by the flame radii data. If the flame radii are determined using natural light or schlieren images the values of u_t calculated should be representative of burning velocity of the entrainment front (u_{te}) as used in three-zone LUSIE simulations. Flame radii derived from Mie scattering laser sheet studies such as the experiments reported in this thesis define a reference surface associated with the transition between burnt and unburnt gas. Values of u_t calculated using these radii should therefore be similar to the values of u_{tr} calculated from pressure records. Burning veloci-

ties are calculated with respect to the unburnt gas (see Gillespie et al. [2000]) at each time step after ignition. This requires values of the rate of consumption of unburnt gas, the unburnt gas density and the flame active surface area. These are provided from the estimate of the mass burnt during each time step Δm_b calculated by LUSIEDA, the thermodynamic property routines used by LUSIE and the LUSIE spherical flame routines respectively. The use of the LUSIE spherical flame routines implies that the flame in the experimental engine has the geometry of a truncated sphere. Any non-sphericity in the actual engine flame will therefore introduce errors in the estimated values of burning velocity.

The basic operation of LUSIEDA is similar to LUSIE in that a complete engine cycle is subdivided into a number of small time steps within which each cylinder process (e.g. heat transfer, blowby) is treated individually. Following every change in the thermodynamic state of the charge gas a pressure equalisation routine is called (see Section 4.5.11) which returns the burnt and unburnt zones to thermochemical equilibrium.[3] A LUSIEDA analysis initially proceeds in a similar fashion to a LUSIE simulation, following the flowcharts depicted in Figures 4.1, 4.2 and 4.3 and the assumptions given in Section 4.2.3. During the operation labelled *Combustion* in Figure 4.3 control switches to the flowchart shown in Figure 3.3, described below.

At the start of each time step after ignition the cylinder pressure is set to the value recorded experimentally from the preceding time step $P_{\mathrm{exp},i-1}$. The pressure between the burnt and unburnt zones is then equalised following piston movement and the amount of mass lost from the combustion chamber due to blowby (see Section 4.2.7) is calculated. Following blowby, control is passed to a second subroutine (Figure 3.4) which compares the pressure predicted after blowby and piston movement with the experimental cylinder pressure for the current time step to determine the amount of mass burnt (if any) during this time step Δm_b. Finally burning velocities are estimated using the parameters derived from the reverse analysis as described above.

Figure 3.4 shows the initial series of calculation steps taken to find Δm_b. The routine starts by saving the thermodynamic state of the charge gas (both burnt and unburnt zones) following the blowby calculations before computing the amount

[3]The process termed *Pressure equalisation* on the flowcharts shown in Figures 3.3, 3.4 and 3.5 refers to pressure equalisation between the burnt and unburnt gas as described in Section 4.5.11 rather than equalisation between the pressure calculated by LUSIEDA and the experimental pressure. As pressure equalisation is performed by LUSIEDA after every operation which causes a change in the thermodynamic state of the charge it is excluded from the description which follows for brevity.

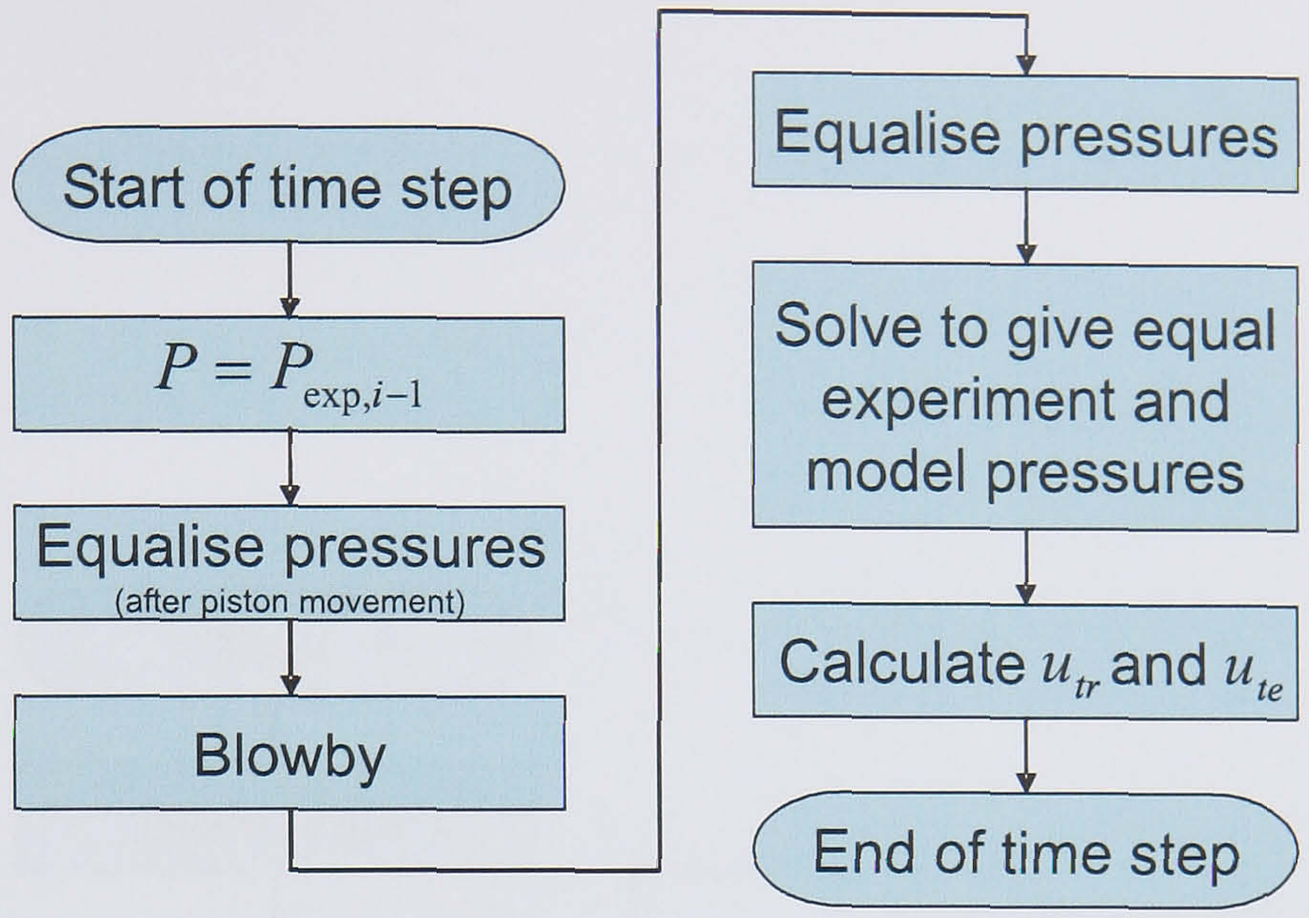

Figure 3.3: Flowchart showing an overview of a single time step during a LUSIEDA reverse analysis. When the flow reaches *Solve to give equal experiment and model pressures* control transfers to the flowchart shown in Figure 3.4.

of heat transfer between the charge and the cylinder walls (see Section 4.2.6). The calculated cylinder pressure following blowby and heat transfer is now compared with the experimental pressure recorded at this time step. If the experimental pressure is greater than the calculated pressure by more than a certain tolerance the deficiency is assumed to be due to an amount of mass which was burnt in the experimental engine. If the experimental pressure is less than the calculated pressure no mass is burnt during this time step and the code proceeds to the start of the next iteration.

Assuming the experimental pressure is higher than the pressure calculated following blowby and heat transfer the thermodynamic state of the charge is reset to its saved condition and the temperature, pressure and composition ($T_{b,i}$, $P_{b,i}$ and $Y_{b,i}$) of the fresh burnt gas this time step are computed assuming constant volume adiabatic combustion. The code now guesses upper and lower bounds to the amount of mass which has burnt this time step $\Delta m_{b,\max}$ and $\Delta m_{b,\min}$ and checks to ensure that they bracket the solution by calculating the cylinder pressures associated with them, $P_{\max}$ and $P_{\min}$. If $P_{\max}$ and $P_{\min}$ are above and below the experimental cylinder pressure $P_{\exp}$ then the actual amount of mass burnt this time step must lie between $\Delta m_{b,\max}$ and $\Delta m_{b,\min}$. If this is not the case the code iterates, widening the interval between $\Delta m_{b,\max}$ and $\Delta m_{b,\min}$ until $P_{\exp}$ is bounded by $P_{\max}$ and $P_{\min}$. Control then passes to the flowchart depicted in Figure 3.5.

The calculation of Δm_b employs the bisection method (see for example Press

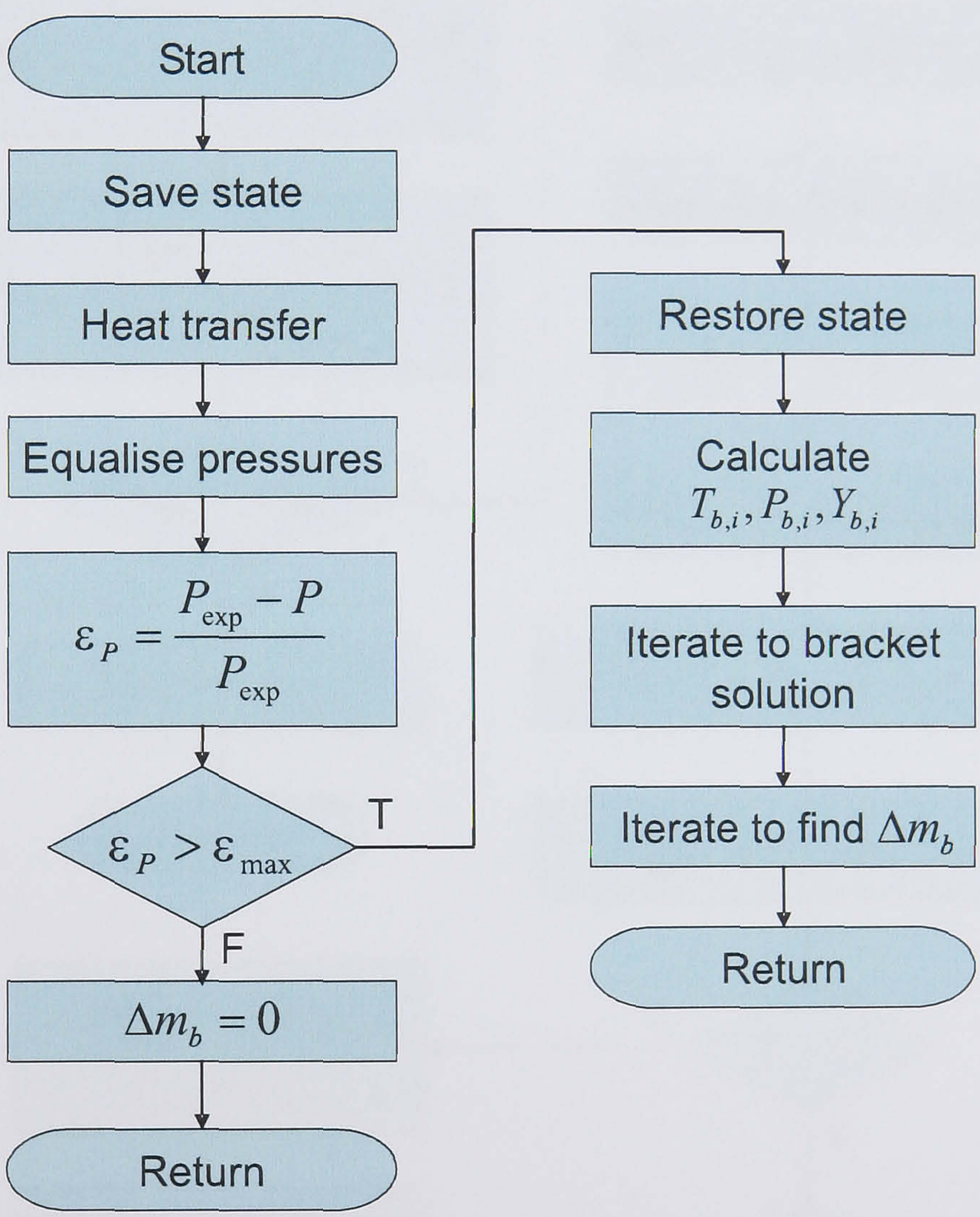

Figure 3.4: Flowchart showing the initial series of calculation steps taken to find Δm_b during a LUSIEDA reverse analysis. When the flow reaches *Iterate to find* Δm_b control transfers to the flowchart shown in Figure 3.5.

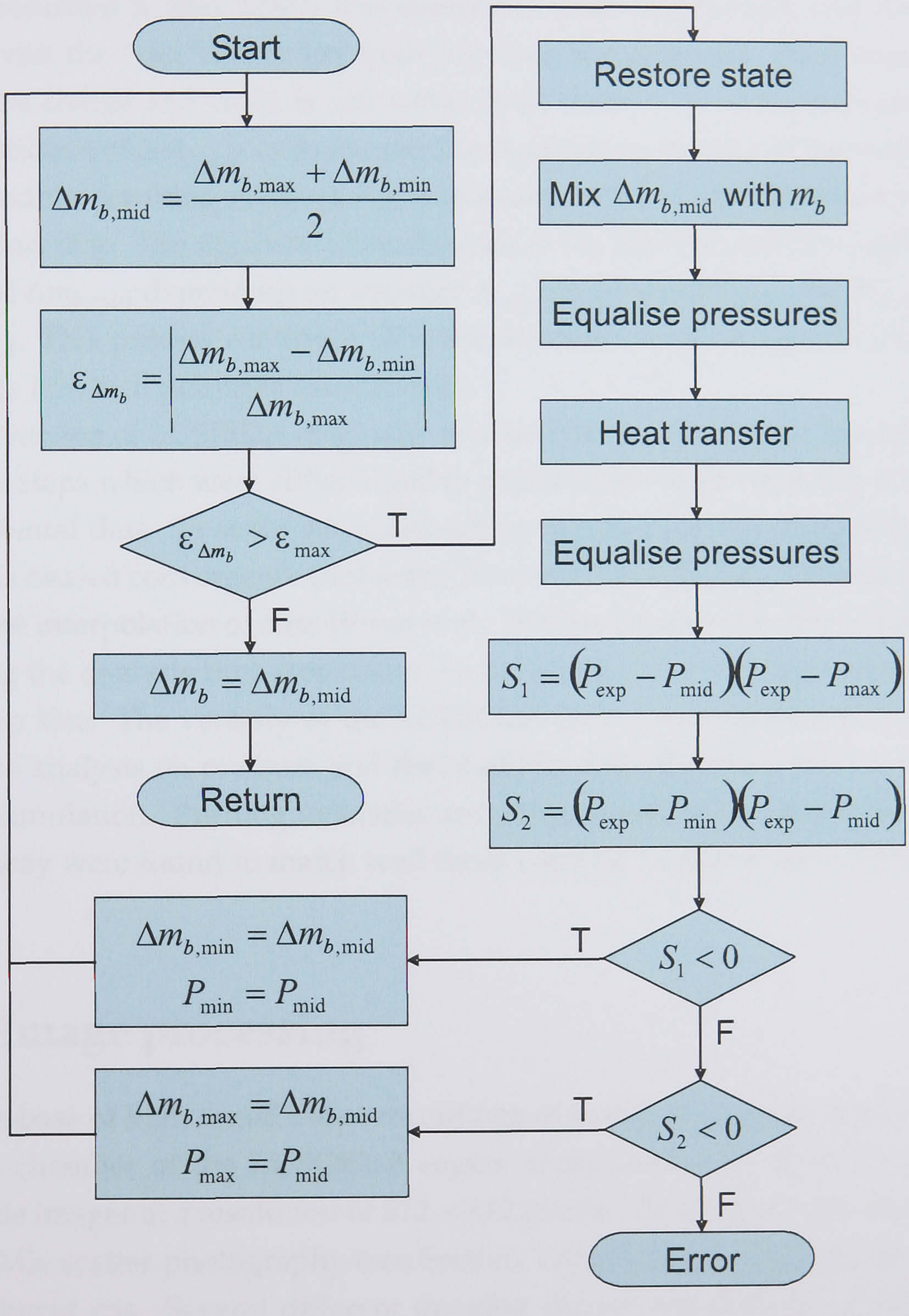

Figure 3.5: Flowchart showing the calculation steps used by LUSIEDA to determine Δm_b.

et al. [1992]) to narrow progressively the bounds $\Delta m_{b,\max}$ and $\Delta m_{b,\min}$ until a specified error tolerance is surpassed. Initially, a midpoint to the two bounds, $\Delta m_{b,\text{mid}}$ is calculated as the mean of $\Delta m_{b,\max}$ and $\Delta m_{b,\min}$. The state of the charge is then returned to that which was computed following blowby and $\Delta m_{b,\text{mid}}$ is mixed with the "old" burnt gas from previous iterations m_b. Heat transfer between the charge and walls is calculated (heat transfer must be recalculated for every estimate of $\Delta m_{b,\text{mid}}$ as its magnitude depends on the size of the wall wetted areas) and the resulting pressure P_{mid} compared with the experimental value P_{exp} at this time step. The upper or lower bounds of the solution are now replaced by P_{mid} and $\Delta m_{b,\text{mid}}$ depending on whether P_{exp} lies between $P_{\max}$ and P_{mid} or $P_{\min}$ and P_{mid}. This process continues until the solution has converged to a specified tolerance at which point the routine exits.

The version of LUSIEDA originally available to the author was limited to taking time steps which were either equal to or multiples of the time step size of the experimental data. In some situations where combustion was especially fast or slow this caused convergence problems. To remove this limitation routines for cubic spline interpolation of data [Press et al., 1992] were added to the original code allowing the analysis time step size to be decoupled from the experimental data time step size. The veracity of the LUDIEDA code was established by running a reverse analysis on pressure and flame radius data generated from a previous LUSIE simulation. Burning velocities and other predicted qualities determined in this way were found to match well those used by LUSIE in the original simulation.

3.3 Image processing

The database of high speed video recordings of combustion taken from the combustion chamber of the LUPOE2-P engine comprised over 140,000 individual greyscale images at a resolution of 512×512 pixels. The images were taken using planar Mie scatter photography (see Section 1.6) which records regions of burnt and unburnt gas. Several different imaging planes, the position of which was determined by the position of the laser sheet, were used to give close to full coverage of the clearance volume. In all cases the imaging plane was parallel to the piston crown. Given the large number of images manual image processing was impractical. All image processing used a Matlab library written by the author, `IProc`, (see Appendix B) which made used of the extensive built in image manip-

ulation and display functions provided with Matlab. Similar to the `PProc` library (see Section 3.2.1), the `IProc` library routines could be called individually from a script file or the Matlab command line, or used from within a graphical user interface.

3.3.1 Raw images

A typical unprocessed image recorded by the camera is shown in Figure 3.6a. The image consists of scattered light from the top two windows of the pent roof cylinder head which has been formed into a single image using two mirrors and a prism, see Figure 2.6. Individual raw images from each run were stored as a numbered series of binary files with the `.raww` extension by the camera software. A separate ASCII header file with the extension `.cih` which detailed the frame rate, exposure time, resolution and other camera settings accompanied each recording. The `.raww` format stored the 10 bit images recorded by the camera as a continuous string of 16 bit unsigned integers. Depending on the settings used when the images were saved, the 10 bit intensity of each pixel was encoded as either the first or last 10 bits of each 16 bit integer. A Matlab function was written by the author was used to read the `.raww` image files, discard the 6 null bits accompanying each 16 bit integer and store the resulting information in an array format compatible with other Matlab image processing functions. If necessary the images could also be loaded into Adobe Photoshop by changing the extension from `.raww` to `.raw`.

3.3.2 Image pre-processing

The first stage in the processing of raw images was to reduce the original greyscale images to binary images such that the areas of burnt and unburnt gas were represented by the pixel values zero and one, rather than a range of greyscales. The text below describes in detail the sequence of steps used to pre-process greyscale images.

Individual frames were loaded into the Matlab workspace and split into two halves which were rotated (slight misalignment of the mirrors and prism could cause the windows to appear tilted in the recorded image) and trimmed. This produced two images, one for each window, which contained only the pixels from the regions of interest from the original frame, see Figures 3.6b and 3.6c. The two images were then resized to remove the distortion caused by the oblique viewing angle and ensure that their widths were equal before being merged to

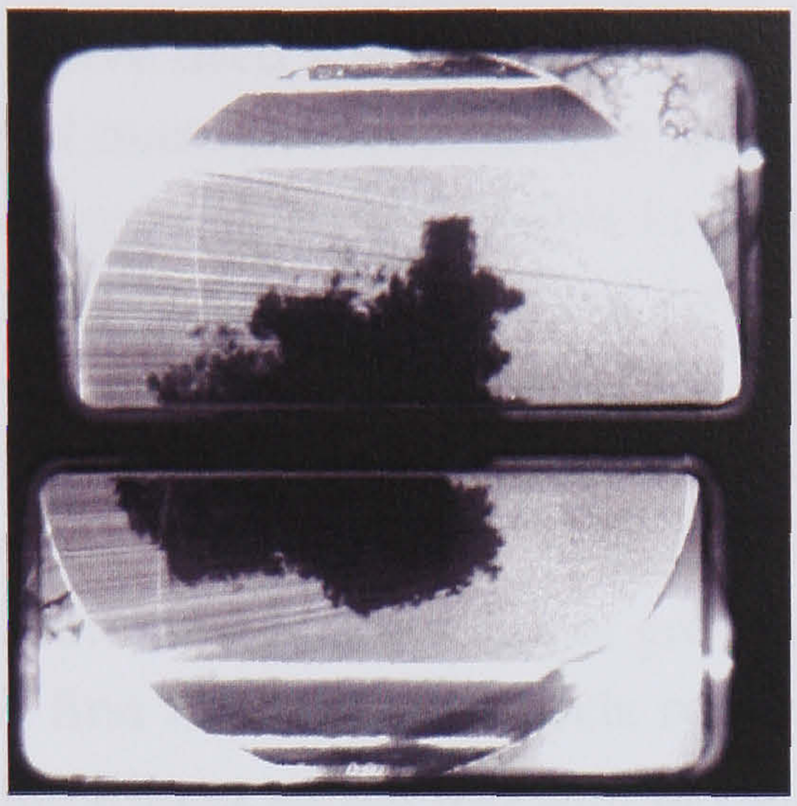

(a) A representative raw image.

(b) Top window.

(c) Bottom window.

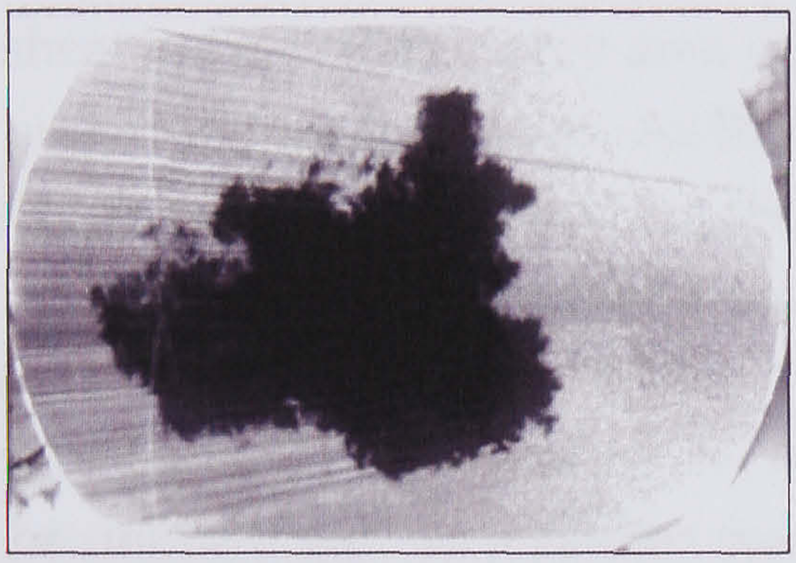

(d) Reconstructed laser sheet.

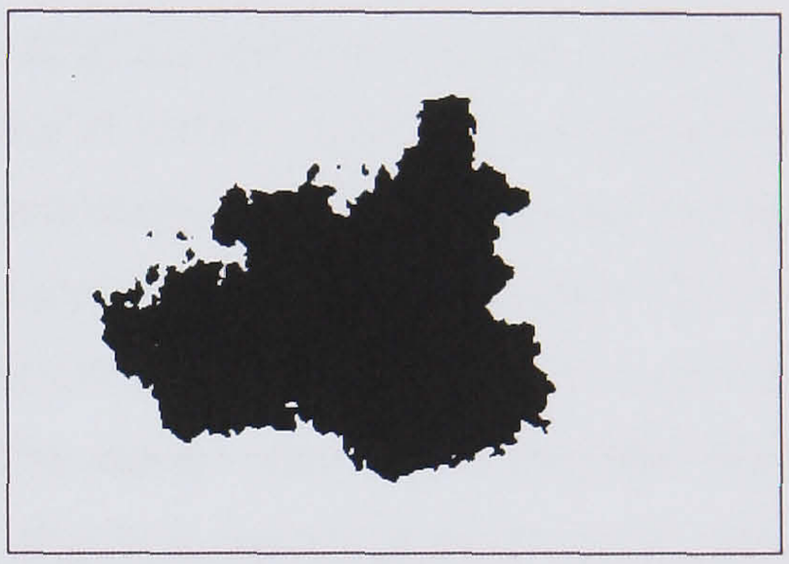

(e) Binarised image.

Figure 3.6: Stages in processing raw images.

produce an undistorted, reconstructed, view of the laser sheet, as shown in Figure 3.6d. To avoid any abrupt discontinuities in the merged image the two images were combined by fading one image into the other. The degree of overlap present in the two images, and hence the number of pixels which should be merged, was calculated trigonometrically using the scale images. Other parameters, for example the degree of rotation and trimming required for each image, were determined manually for each test (mirrors were occasionally knocked between tests when removing the cylinder head for cleaning). For this purpose, a graphical user interface to the `IProc` library was written to allow rapid determination of the relevant inputs.

3.3.3 Binarising procedure

Previous studies of flame propagation at the University of Leeds (for example Murad [2006], Abdi Aghdam [2003], Cairns [2001], Gillespie et al. [2000], Haq

[1998]) have used a simple thresholding operation, with the threshold level determined manually, to transform greyscale images of flame propagation into binary images. Although feasible for limited numbers of images, variations in the seeding level cycle-to-cycle and "streakiness" in the raw images, caused by the hot combustion gases distorting the laser sheet, rendered such a simple method unsuitable for processing the large number of images in the current data set. To combat this problem a novel thresholding technique was developed which allowed automated processing of greyscale images to binary images.

The first frame of each cycle recorded by the camera[4] was taken at the moment the trigger signal was sent to the ignition system. Regardless of the engine operating condition there was no evidence of combustion in this image hence the laser sheet appeared as a grey area with a slightly grainy texture caused by the finite size of the seed particles. As this frame showed only unburnt gas the pixel intensity at position ij, denoted $I_{ij,u}$, is representative of the luminous intensity of unburnt gas at that position in the combustion chamber in that cycle. This value specifies an upper bound for possible intensities at that position in later images where the flame is present; any pixel with the same intensity or brighter than $I_{ij,u}$ must be unburnt gas. In a similar way, in the last frame of each cycle, the pixel intensity $I_{ij,b}$ is representative of the intensity of burnt gas at that position for that cycle. Pixels darker than $I_{ij,b}$ must represent burnt gas. By thresholding each pixel in the intermediate frames between the representative values for unburnt and burnt gas for that cycle,

$$\frac{I_{ij} - I_{ij,b}}{I_{ij,u} - I_{ij,b}} > I_t \tag{3.4}$$

the binarising operation was adaptive to both local variations in image intensity, for example the intensity gradient caused by the attenuation of the laser sheet as it passed through the combustion chamber, and cycle-to-cycle or test-to-test variations in intensity caused by changes in the seeding level. The parameter I_t is the threshold level and should take a value between zero and one. For the current study, $I_t = 0.5$ for all the images processed.

In order to remove any graininess from the images and locally smooth the frames used to set $I_{ij,u}$ and $I_{ij,b}$ the first and last frames recorded for each cycle were first processed using alternating sequential open close filtering, see for example Gonzalez et al. [2004], as illustrated in Figure 3.7. This morphological pro-

[4]In practice the second frame was used as occasionally the laser failed to synchronise properly with the camera for the first frame. This is noticeable in the top left image of Figure 3.8 which is darker than the images which follow.

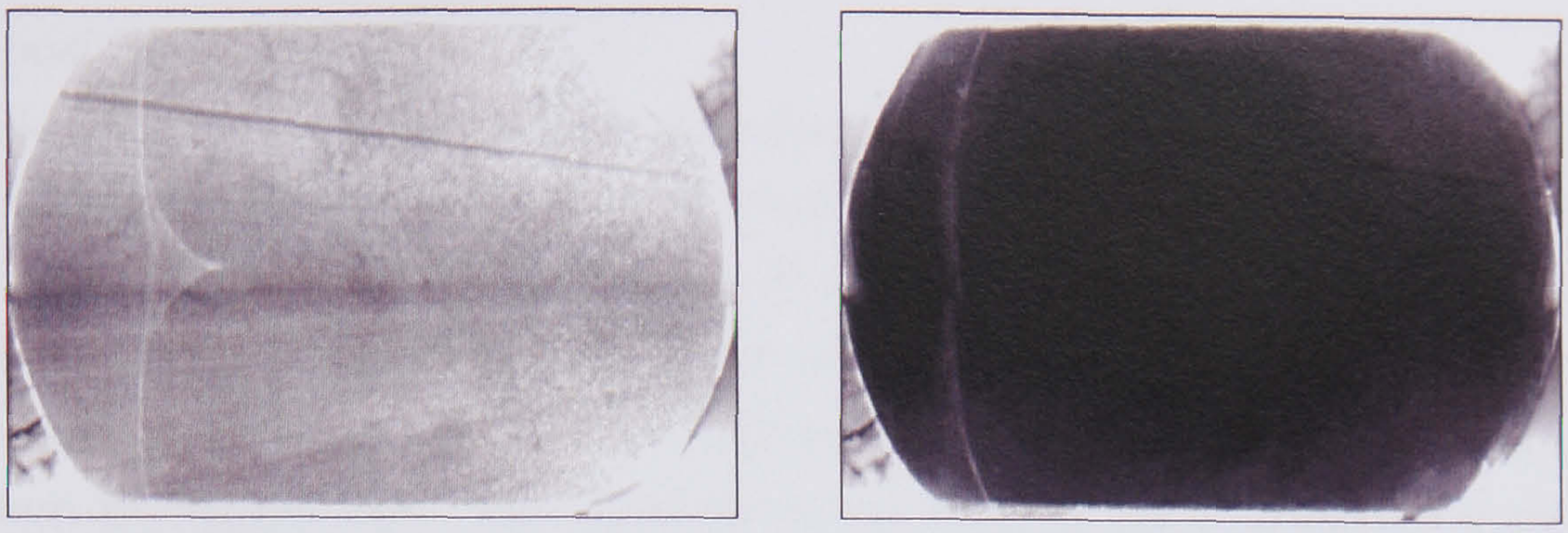

(a) First frame. (b) Last frame.

(c) Smoothed first frame. (d) Smoothed last frame.

Figure 3.7: Smoothing the first and last frames of a typical cycle using alternating sequential open close filtering.

cess uses structural elements of increasing size to alternately fill in any "holes" in the image and then crop any "peaks", resulting in an image in which the intensity of the pixels varies smoothly. The structural element employed for this filtering was a disc with a maximum diameter of 10 pixels.

3.3.4 Masking and noise removal

Once the original image had been converted to a binary representation of burnt and unburnt gas regions, any pixels from outside the combustion chamber were removed by applying a mask to the final image. The area to be masked for a particular laser sheet position was determined by loading an image into Adobe Photoshop and selecting the area inside the bore. The "magnetic lasso" tool was found to be particularly effective for this purpose as it snapped to regions of high contrast in the original image. After the area inside the bore had been selected, its interior was filled in white and its exterior was allowed to remain black resulting in a black and white mask which was saved for use in the Matlab automated processing routines. The same mask was reused for all images for a given laser

sheet position.

Following masking the images were filtered using Matlab to implement a two-dimensional median filter over a 3×3 pixel neighbourhood. This is similar to the "dust and scratches" filter available in Photoshop used by Abdi Aghdam [2003] and Murad [2006] and helped to remove any speckles from the image. A typical binarised image which has been through all the processing steps described above is shown in Figure 3.6e. Raw and binarised images for a complete cycles are shown in Figure 3.8.

3.3.5 Mean progress variable calculation and volume smoothing

Given a sufficient number of binary images it is possible to estimate the mean combustion reaction progress variable $\overline{c}$ at a particular position. For the purpose of this study the mean progress variable is defined as the probability of finding burnt gas at a particular position (similar to Chew et al. [1990], Knause et al. [1999], Renou et al. [2002] and others) and hence can be calculated by averaging the pixel values of a number of binary images at that location. If n images are combined where the intensity of the k-th image $I_{ij,k}$ at position ij ranges from zero to one then

$$\overline{c}_{ij} = \frac{1}{n} \sum_{k=1}^{n} I_{ij,k} \tag{3.5}$$

Conventionally, $\overline{c} = 1$ denotes burnt gas and $\overline{c} = 0$ denotes unburnt gas hence to conform to this convention the binary images were inverted before applying Equation 3.5. As the number of images used in the averaging procedure increases the resultant image gradually looses its binary quality and becomes a greyscale image where different levels of grey represent the probability of finding burnt gas at a particular position. This is illustrated in Figure 5.75a which shows the progression in $\overline{c}$ as different numbers of images are averaged.

A naïve implementation of Equation 3.5 where by all the images were loaded into the computer memory simultaneously before the mean was calculated resulted in memory problems because of the large number of images. To overcome this limitation each image was loaded into the memory individually, the average updated "online" and the image removed from the memory to make room for the next image. The algorithm suggested by Knuth [1998] who cites Welford [1962]

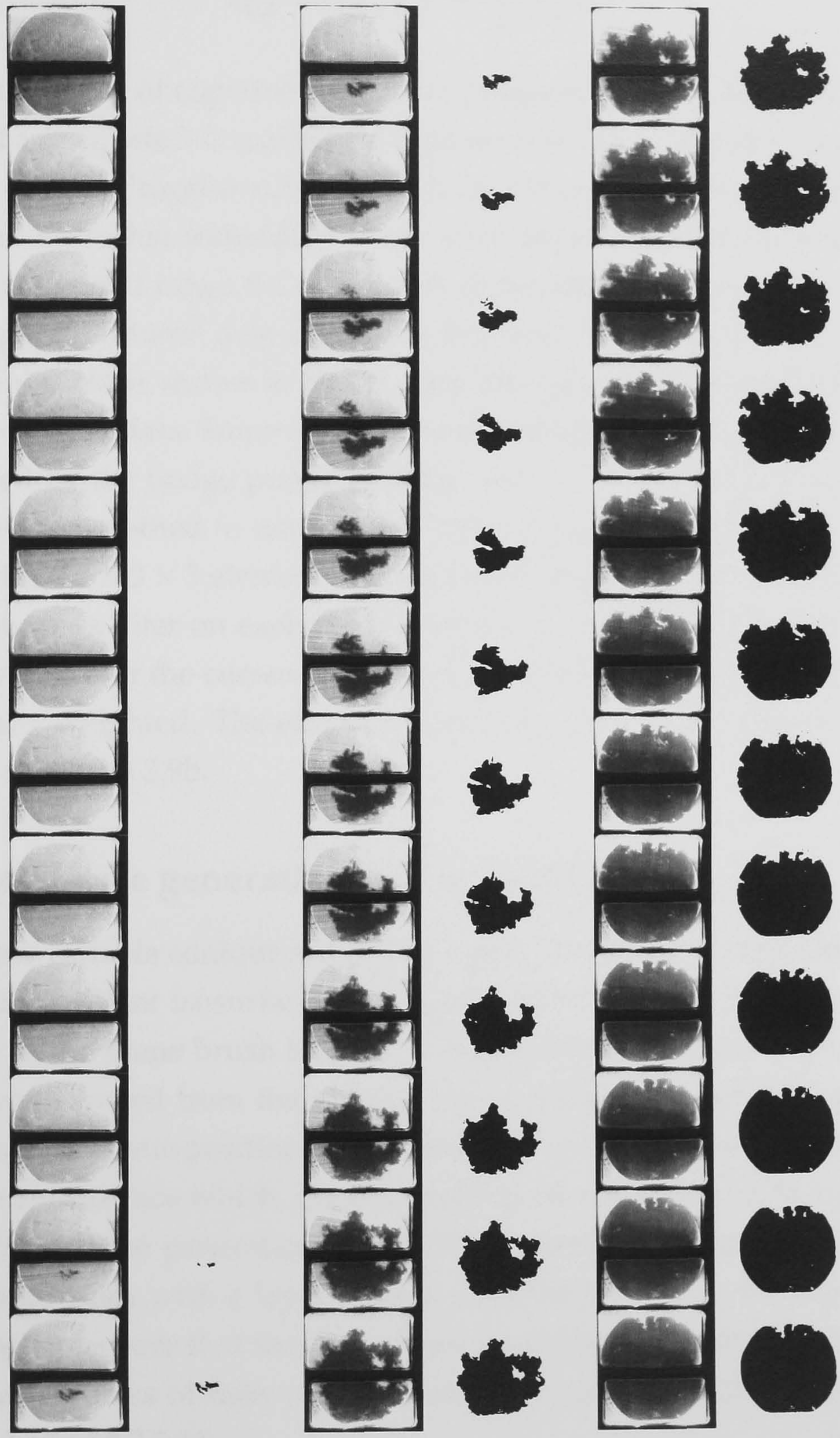

Figure 3.8: The first 24 raw and processed images in a typical cycle.

was used to update the average:

$$\overline{c}_{ij,k} = \overline{c}_{ij,k-1} + \frac{I_{ij,k} - \overline{c}_{ij,k-1}}{k-1} \tag{3.6}$$

Given a number of coplanar "slices" of progress variable data it is possible to reconstruct a complete 3-D scalar field representing the combustion progress variable in the engine. Progress variable fields for different laser sheet positions were interpolated such that individual slices were aligned on the same grid. Slices were then combined into a 4-D array, one dimension for time (crank angle) and three for space. Volume data created in this way contained abrupt steps along the pent roof surface, shown in Figure 3.9a, caused by the limited vertical resolution of the original data. Some regions of noise (mainly from spurious reflections) not removed by the image pre-processing were typically also present. The volume data was smoothed to remove this noise using the Matlab built in function `smooth3` with a $3 \times 3 \times 3$ element convolution kernel. This implements a moving average low pass filter on each voxel (volume pixel) with the new value calculated as the mean of the current voxel and its immediate neighbours, each voxel being equally weighted. The effect of smoothing the volume data in this way is illustrated in Figure 3.9b.

3.3.6 Isosurface generation and smoothing

The progress variable contour at $\overline{c} = 0.5$ is generally taken to represent the mean flame position. Other isosurfaces, for example at $\overline{c} = 0.1$ or 0.9 are useful in the estimation of the flame brush thickness, see Section 3.3.9. Isosurfaces at given $\overline{c}$ values were extracted from the volume data generated by combining the layers which define the flame position at a particular crank angle using the Matlab built in function `isosurface` which, given a scalar field, will extract a triangulated isosurface. Prior to the generation of the isosurfaces, the experimental data were padded on all sides with a layer of data with the value $\overline{c} = 0$. This procedure was adopted to ensure that the isosurfaces generated were always closed allowing reliable estimates of their surface area and enclosed volume as discussed in Sections 3.3.10 and 3.3.11.

Isosurfaces generated in this way were not always smooth because of the underlying "marching cubes" [Lorensen and Cline, 1987] procedure employed to create them. In order to remove this surface roughness the algorithm suggested

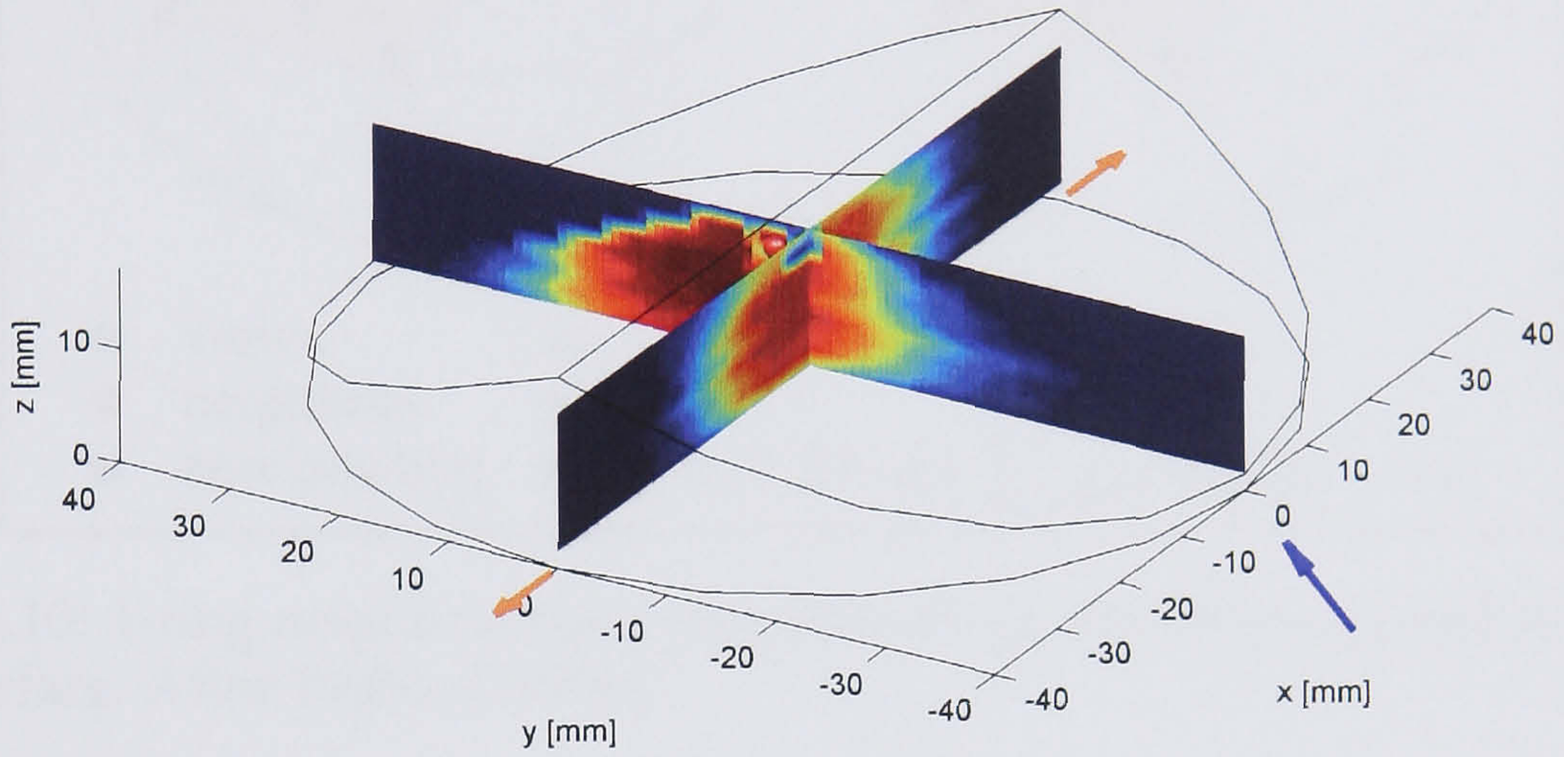

(a) Before smoothing.

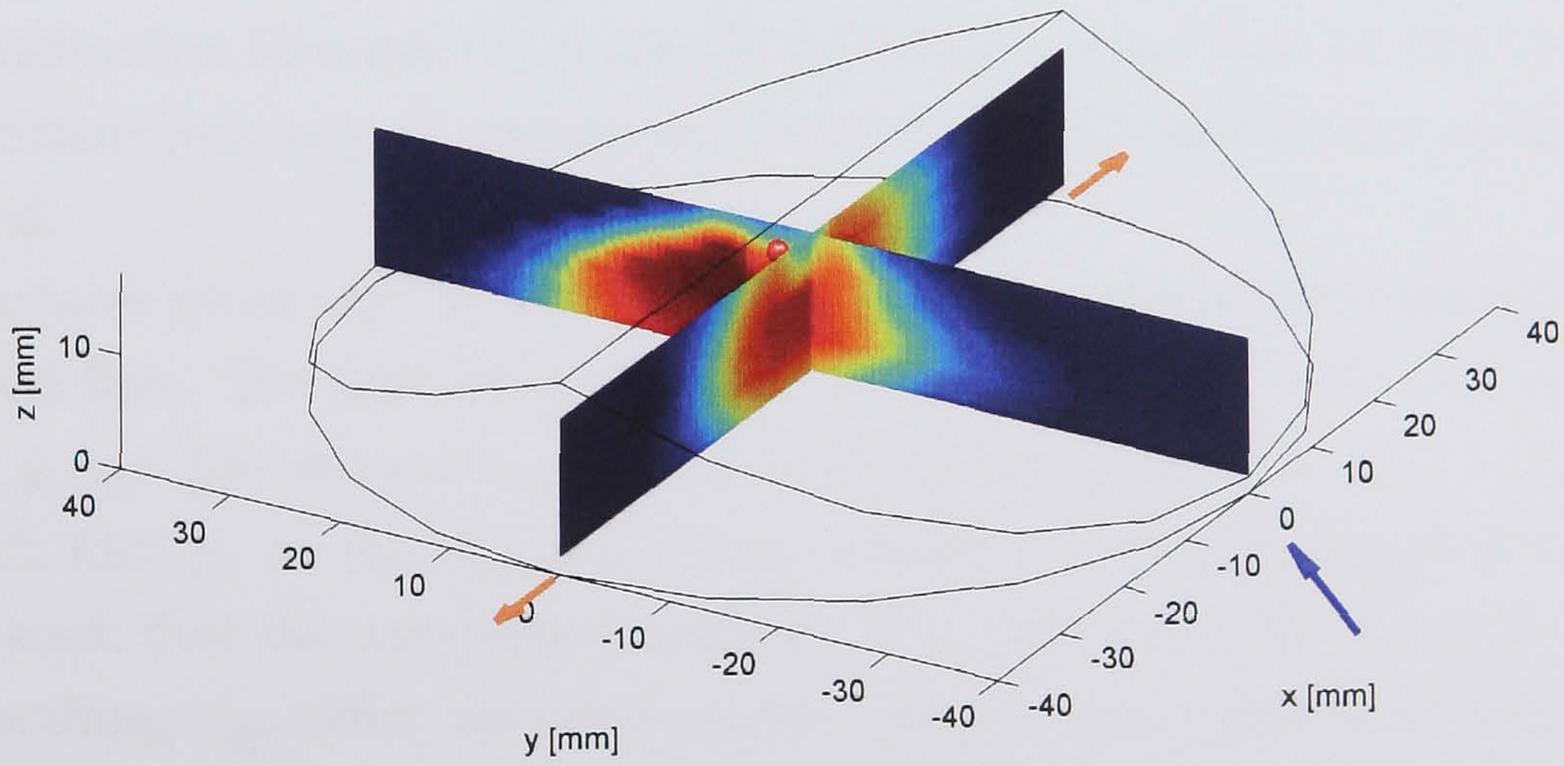

(b) After smoothing.

Figure 3.9: Slices through the $\overline{c}$ field illustrating the effect of smoothing the volume data.

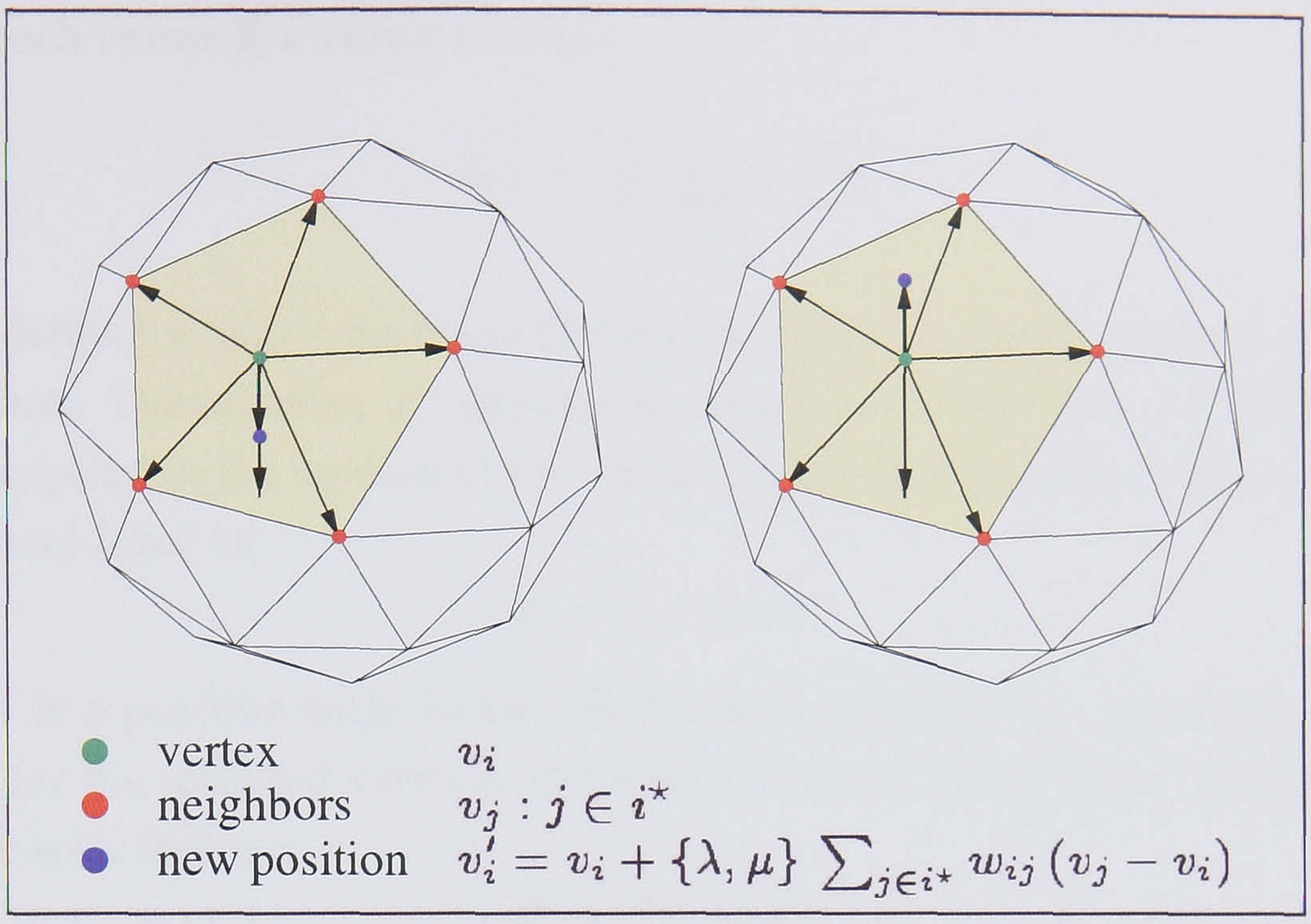

Figure 3.10: 1-ring neighbourhood and smoothing algorithm applied to an arbitrary surface. After Taubin [1995a].

by Taubin [1995a,b], which acts as a low pass filter on the surface curvature, was used. This particular algorithm was chosen from amongst the many available in the literature[5] as it is simple to implement, is used in several well known data visualisation libraries (for example the Visualisation Tool Kit [VTK]) and has the important property of preserving the volume enclosed by the surface being smoothed.

Isosurfaces generated by Matlab were stored as a structure comprising a pair of ordered lists. The first list is a list of vertices $\mathcal{V} = \{\vec{v}_i : 1 \leq i \leq n_\mathcal{V}\}$ where $\vec{v}_i = (x_i, y_i, z_i)$. The second list is a list of triangular faces $\mathcal{F} = \{f_k : 1 \leq k \leq n_\mathcal{F}\}$ with each face $f_k = (i_{1,k}, i_{2,k}, i_{3,k})$ being a sequence of non-repeated indices of vertices such that the complete isosurface $\mathcal{S}$ is defined as the set $\mathcal{S} = \{\mathcal{F}, \mathcal{V}\}$. The smoothing algorithm operates on the 1-ring neighbourhood of a vertex. For vertex $\vec{v}_i$ the 1-ring neighbourhood is the set i^* of indices of vertices $\vec{v}_j$ all of which share an edge or face with $\vec{v}_i$ as illustrated in Figure 3.10.

[5]The author is grateful to Professor Ken Brodlie and other members of the Visualisation and Virtual Reality Group, part of the School of Computing at the University of Leeds, for their helpful suggestions regarding surface smoothing.

For each vertex $\vec{v}_i$ a vector average

$$\Delta\vec{v}_i = \frac{1}{|i^*|}\sum_{j\in i^*}\vec{v}_j - \vec{v}_i \tag{3.7}$$

may be defined which is the mean of the vectors $\vec{v}_j - \vec{v}_i$ which extend from $\vec{v}_i$ to its neighbours. The notation $|i^*|$ denotes the number of members of i^*. Smoothing is now applied to the surface in two steps. In the first step the position of every vertex is updated as

$$\vec{v}'_i = \vec{v}_i + \lambda\Delta\vec{v}_i \tag{3.8}$$

where λ is a positive scale factor. In the next step the vector average is recalculated for the updated vertices and a second smoothing step is applied with a negative scale factor μ

$$\vec{v}''_i = \vec{v}'_i + \mu\Delta\vec{v}'_i \tag{3.9}$$

such that $(0 < \lambda < -\mu)$. Two idealised smoothing steps are illustrated in Figure 3.10.

For significant smoothing to occur the steps in Equations 3.7, 3.8 and 3.9 must be repeated a number of times, the scale factors λ and μ alternating with each iteration. The choice of values of λ and μ and the number of iterations necessary to achieve a desired level of smoothness requires the solution of a system of inequalities which were solved using the Microsoft Excel "solver" feature. Further detail on the choice of λ and μ can be found in references [Taubin, 1995a,b].

3.3.7 Flame curvature

The local curvature of the smoothed triangulated isosurfaces was calculated using the algorithm described by Meyer et al. [2002]. This algorithm was chosen from amongst the may in the literature as it is (relatively) easy to implement, is not strongly influenced by the quality of the triangulated mesh, is employed by other libraries, for example the GNU Triangulated Surface library [GTS], and does not require piecewise polynomial reconstruction of the surface with the associated problems of defining the local axis systems and the orders of polynomials to be used. A brief description of the algorithm is given below.

Calculation of the local surface curvature of the central vertex $\vec{v}_i$ of a 1-ring neighbourhood with neighbours $\vec{v}_j$ as shown in Figure 3.11 proceeded as follows.

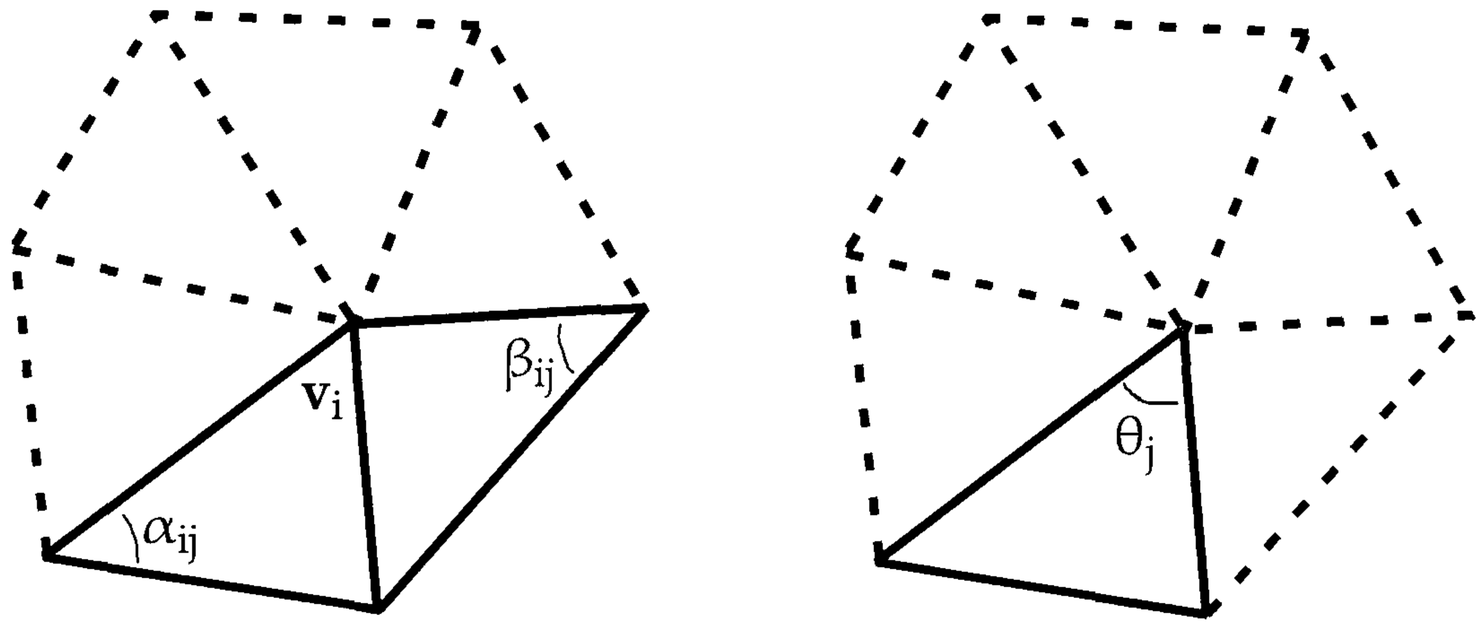

Figure 3.11: Definition of angles α_{ij}, β_{ij} and θ.

The mean curvature normal vector $\vec{K}$ was calculated using

$$\vec{K}(\vec{v}_i) = \frac{1}{2\mathcal{A}_{\text{mixed}}} \sum_{j \in i^*} (\cot \alpha_{ij} + \cot \beta_{ij})(\vec{v}_i - \vec{v}_j) \tag{3.10}$$

where $\mathcal{A}_{\text{mixed}}$ is the mixed area derived by Meyer et al. [2002] which is equal to either the sum of the areas of Voronoi regions surrounding $\vec{v}_i$ in the case where $\vec{v}_i$ is surrounded by acute angles or some hybrid area defined to give tight error bound in the case where some of the neighbouring angles are obtuse. Given $\vec{K}$ the magnitude of the mean curvature κ_H is easily calculated as:

$$\kappa_H = \frac{1}{2} \|\vec{K}(\vec{v}_i)\| \tag{3.11}$$

where $\|\vec{v}\|$ denotes the Euclidian norm of $\vec{v}$.

The magnitude of the maximum and minimum curvatures, κ_1 and κ_2 respectively, are now given by

$$\kappa_1(\vec{v}_i) = \kappa_H(\vec{v}_i) + \sqrt{\Delta(\vec{v}_i)} \tag{3.12}$$

$$\kappa_2(\vec{v}_i) = \kappa_H(\vec{v}_i) - \sqrt{\Delta(\vec{v}_i)} \tag{3.13}$$

where $\Delta(\vec{v}_i) = \kappa_H^2(\vec{v}_i) - \kappa_G(\vec{v}_i)$ and the Gaussian curvature κ_G is equal to an average of the interior angles of the 1-ring neighbourhood:

$$\kappa_G(\vec{v}_i) = (2\pi - \sum_{j \in i^*} \theta_j) / \mathcal{A}_{\text{mixed}} \tag{3.14}$$

here θ_j is the angle formed at $\vec{v}_i$ by the two sides of the face which meet at $\vec{v}_i$ as shown in Figure 3.11.

The algorithm described above was implemented as a Matlab function by the author. Tests carried out with perfect spheres and cylinders (see Harker et al.) of different dimensions and mesh resolutions showed it to be very robust even for surfaces with poor mesh resolution.

3.3.8 Local flame speed and burning velocity

Once isosurfaces representing the flame surface were available it was possible to estimate the local flame speed by measuring the local distance between two isosurfaces consecutive in time (i.e. taking the forward difference) and dividing by the elapsed time. The global flame speed, which was estimated through a reverse analysis of the cylinder pressure data as described in Section 3.2.3, does not reveal detailed information about the effect of, for example, the proximity of the cylinder walls on the flame propagation. Calculating the local flame speed allowed a detailed investigation into effects which would have been masked by the integrating effect of a reverse analysis.

Given the local flame speed at the i-th vertex $S_{t,i}$, the local burning velocity is easily calculated (assuming that the densities of the burnt and unburnt gas regions are uniform) by multiplying the flame speed by the ratio of burnt to unburnt gas density, which was estimated using LUSIEDA (see Section 3.2.3).

$$u_{t,i} = \frac{\rho_b}{\rho_u} S_{t,i} \tag{3.15}$$

The algorithm[6] employed involved generating surface normal vectors for every vertex on the first isosurface $\mathcal{S}_1$ and then testing for intersection of the surface normal vectors with the triangular faces of the second isosurface $\mathcal{S}_2$. If a normal vector from $\mathcal{S}_1$ was determined to have intersected with a surface element from $\mathcal{S}_2$ the distance between the vertex associated with the normal vector and the point of intersection on $\mathcal{S}_2$ was calculated using Pythagoras' theorem. In the case where there is more than one intersection (there will always be at least two intersections for two concentric flame surfaces, one at the closest face and one on the face diametrically opposite) the smallest distance was taken.

[6]The following books: Hearn and Baker [2004], Foley et al. [1996], Hill [2001] were found to be useful sources of information when designing the function to calculate the local separation between two isosurfaces.

As testing for intersection between a line (a surface normal vector) and a polygon (a triangle) is computationally expensive the problem was first reduced to the mathematically much simpler problem of testing for intersection between a normal vector and a sphere which bounds the triangle. Bounding spheres were generated by first calculating the positions of the triangle centroids the as mean of the three vertex positions. The radius of the bounding sphere is then the largest distance between the centroid and any of the triangle vertices. It is possible to find a smaller bounding sphere by positioning the centre of the sphere at the triangle circumcentre in the case of an acute triangle or at the midpoint of the longest side in the case of an obtuse triangle. For the current application the added computational complexity of finding such a sphere was not justified.

Given bounding spheres for each surface element of S_1 the problem of determining intersection can be reduced to that of calculating the discriminant of a quadratic equation. If the point $\vec{s}_0$ and scalar r define the centre and radius of a sphere respectively, and the points $\vec{l}_1$ and $\vec{l}_2$ define a line, then two further vectors, $\vec{p} = \vec{s}_0 - \vec{l}_1$ and $\vec{q} = \vec{l}_2 - \vec{l}_1$ may be defined. Given $\vec{p}$ and $\vec{q}$ the question of whether the line intersects the sphere can be answered by calculating the following discriminant.

$$(2\vec{q}\cdot\vec{p})^2 - 4(\vec{q}\cdot\vec{q})(\vec{p}\cdot\vec{p} - r^2) = \begin{cases} -1 & \text{no intersection} \\ 0 & \text{line touches sphere surface} \\ 1 & \text{line intersects sphere} \end{cases} \tag{3.16}$$

When the bounding spheres (if any) which intersect a particular surface normal vector have been identified the more computationally intensive task of determining which surface elements are intersected by the surface normal vector my be undertaken. To determine whether a line intersects a triangle defined by vertices $\vec{t}_1$, $\vec{t}_2$ and $\vec{t}_3$ first the position $\vec{p}$ where the line intersects the infinite plane which passes through $\vec{t}_1$, $\vec{t}_2$ and $\vec{t}_3$ is calculated using following determinant equation

$$a = -\frac{\det\begin{pmatrix} 1 & 1 & 1 & 1 \\ \vec{t}_1^{\,T} & \vec{t}_2^{\,T} & \vec{t}_3^{\,T} & \vec{l}_1^{\,T} \end{pmatrix}}{\det\begin{pmatrix} 1 & 1 & 1 & 0 \\ \vec{t}_1^{\,T} & \vec{t}_2^{\,T} & \vec{t}_3^{\,T} & (\vec{l}_2 - \vec{l}_1)^T \end{pmatrix}} \tag{3.17}$$

$$\vec{p} = \vec{l}_1 + a(\vec{l}_2 - \vec{l}_1) \tag{3.18}$$

where a is a parametric variable and $\vec{t}^T$ represents the transpose of $\vec{t}$ etc. The question of whether $\vec{p}$ is bounded by the triangle $\vec{t}_1, \vec{t}_2, \vec{t}_3$ can now be resolved by discarding one of the dimensions, reducing the problem to two dimensions, and using the Matlab built in function `inpolygon` to test whether the point is inside the triangle. To reduce errors associated with the finite precision of floating point arithmetic the dimension to be discarded was chosen to give the largest possible projected area of the resultant triangle.

3.3.9 Flame brush thickness

The flame brush thickness δ_t is a macroscopic parameter which is representative of the distance between the leading and trailing edges of the flame, see Figure 3.12, as opposed to the laminar flame thickness which is presumably similar in magnitude to the local reaction front in the flamelet regime. It may be defined variably as:

1. The distance between two $\overline{c}$ contours or isosurfaces. For example Gouldin and Miles [1995] use $\overline{c} = 0.1$ and $\overline{c} = 0.9$; Renou et al. [2002] suggest $\overline{c} = 0.05$ and $\overline{c} = 0.95$. In the current work the former pair of isosurfaces are adopted hence

$$\delta_{ts} = |x_{0.1} - x_{0.9}| \tag{3.19}$$

   where $\overline{c}(x_{0.1}) = 0.1$ and $\overline{c}(x_{0.9}) = 0.9$ as shown in Figure 3.13a.

2. The distance between the intercepts at $\overline{c} = 0$ and $\overline{c} = 1$ of the tangent to the $\overline{c}$ field at $\overline{c} = 0.5$ as shown in Figure 3.13b.

$$\delta_{tg} = \left| \frac{1}{\nabla \overline{c}} \right|_{\overline{c}=0.5} \tag{3.20}$$

   This is similar to Namazian et al. [1986] who used the intercepts at $\overline{c} = 0$ and $\overline{c} = 1$ of $|\mathrm{d}\overline{c}/\mathrm{d}x|_{\max}$ to estimate the flame thickness using $\overline{c}$ data with one spatial dimension. Obviously for data with more than one dimension this definition breaks down and some reference surface must be adopted as in Equation 3.20.

3. The rms deviation of the flame edge from some suitably defined mean flame position, typically given the notation a'. This method has been used by previous authors at Leeds, see for example Hicks et al. [1994], Gillespie et al. [2000], Cairns [2001].

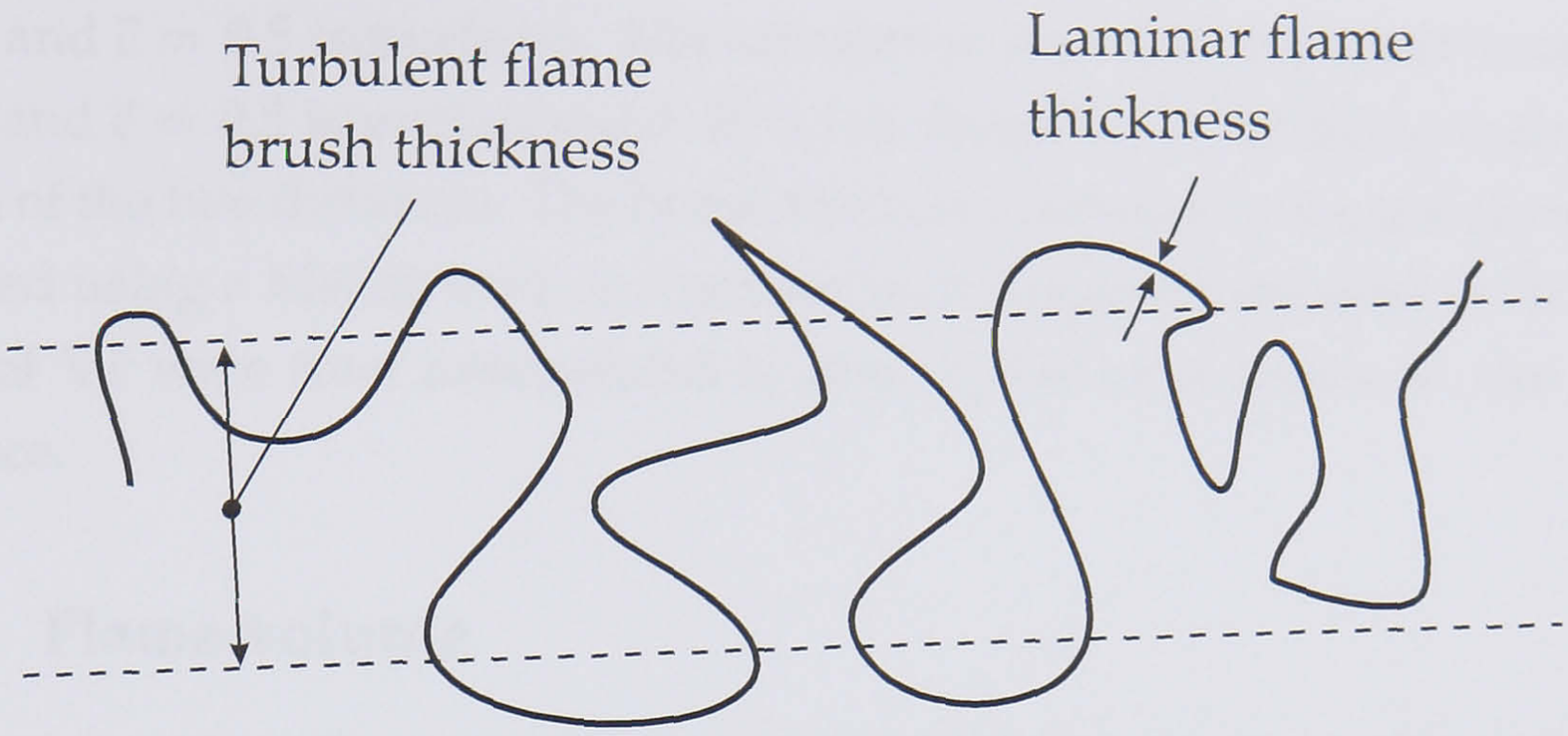

Figure 3.12: Schematic of a turbulent flame front in the flamelet regime illustrating the flame brush thickness and the laminar flame thickness.

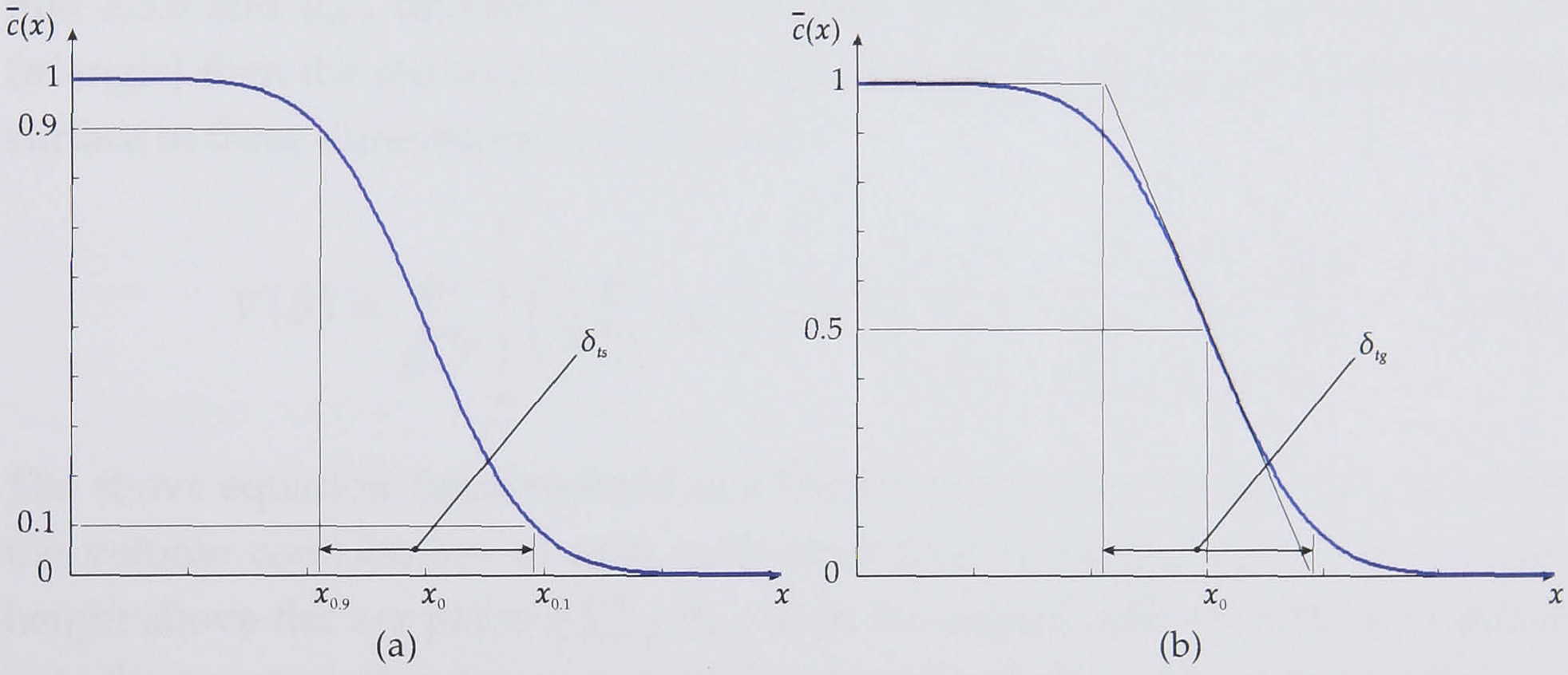

Figure 3.13: Different definitions of δ_t applied to experimental $\bar{c}$ data.

Of the three definitions described above, δ_{tg} is preferred as it does not rely on either the choice of arbitrary values of $\bar{c}$ to represent the leading and trailing edges of the flame (δ_{ts}) or the choice of cutoff frequency used to low pass filter the flame edge when determining the mean flame position (a'). Interestingly, the availability of progress variable contours in the current data set suggests an alternative mean flame position, the isosurface at $\bar{c} = 0.5$, which could be used to calculate a'. Due to the limited time available the viability of this modification was not investigated further.

In order that their equivalence may be evaluated δ_{ts} and δ_{tg} were calculated. To find δ_{ts} the algorithm for finding the distance between two concentric isosurfaces, described in Section 3.3.8, was used to calculate the distance between the

$\overline{c} = 0.1$ and $\overline{c} = 0.5$ isosurfaces. The calculation was then repeated between the $\overline{c} = 0.9$ and $\overline{c} = 0.5$ isosurfaces and the local flame brush thickness estimated as the sum of the two distances. The brush thickness defined by the gradient δ_{tg} was calculated using a Matlab built in function to evaluate the gradient of the $\overline{c}$ field. Values of $\nabla\overline{c}$ were then interpolated to give δ_{tg} for each vertex on the $\overline{c} = 0.5$ isosurface.

3.3.10 Flame volume

The volume enclosed by an isosurface was calculated using the general formula for the volume of a closed surface in any number of dimensions given by Allgower and Schmidt [1986]. If the surface is defined using the notation of Section 3.3.6 and $\vec{v}_{ik,x}$ denotes the x-coordinate of the i-th vertex of the k-th face (triangle) then the reduced version of this formula for the case of a triangulated surface in three dimensions is as follows:

$$V(\mathcal{S}) = \sum_{f_k \in \mathcal{F}} \left[\left(\frac{1}{3} \sum_{i=1}^{3} \vec{v}_{ik,z} \right) \frac{1}{2} \det \begin{pmatrix} 1 & 1 & 1 \\ \vec{v}_{1k,x} & \vec{v}_{2k,x} & \vec{v}_{3k,x} \\ \vec{v}_{1k,y} & \vec{v}_{2k,y} & \vec{v}_{3k,y} \end{pmatrix} \right] \tag{3.21}$$

The above equation, implemented as a Matlab function by the author, calculates the volume contribution of each individual face as the product of its average height above the x-y plane $\frac{1}{3}\sum_{i=1}^{3} \vec{v}_{ik,z}$ with the signed area of its base projected onto the x-y plane (the determinant term). In order for the sign of the volume contribution for each face to be correct the vertices comprising each triangle should be oriented in a clockwise direction relative to the outward facing surface normal vector. As the vertices of the isosurfaces generated by Matlab were not oriented by default the code checked the orientation of each face during execution and changed the sign of its volume contribution if necessary.

The proportion of the clearance volume which was accessible to the laser sheet was limited by the size of the windows in the top and side of the cylinder head. It was not possible to record data below the TDC plane or very close to the roof of the pent for this reason. The inaccessible volume between the bottom laser sheet and the piston crown was estimated as the area of the burnt region ($\overline{c} \geq 0.5$) on the bottom progress variable layer multiplied by the distance between the piston crown and the bottom layer (as calculated using the crank-slider equation). Where there was no data in the roof region of the pent the missing volume was

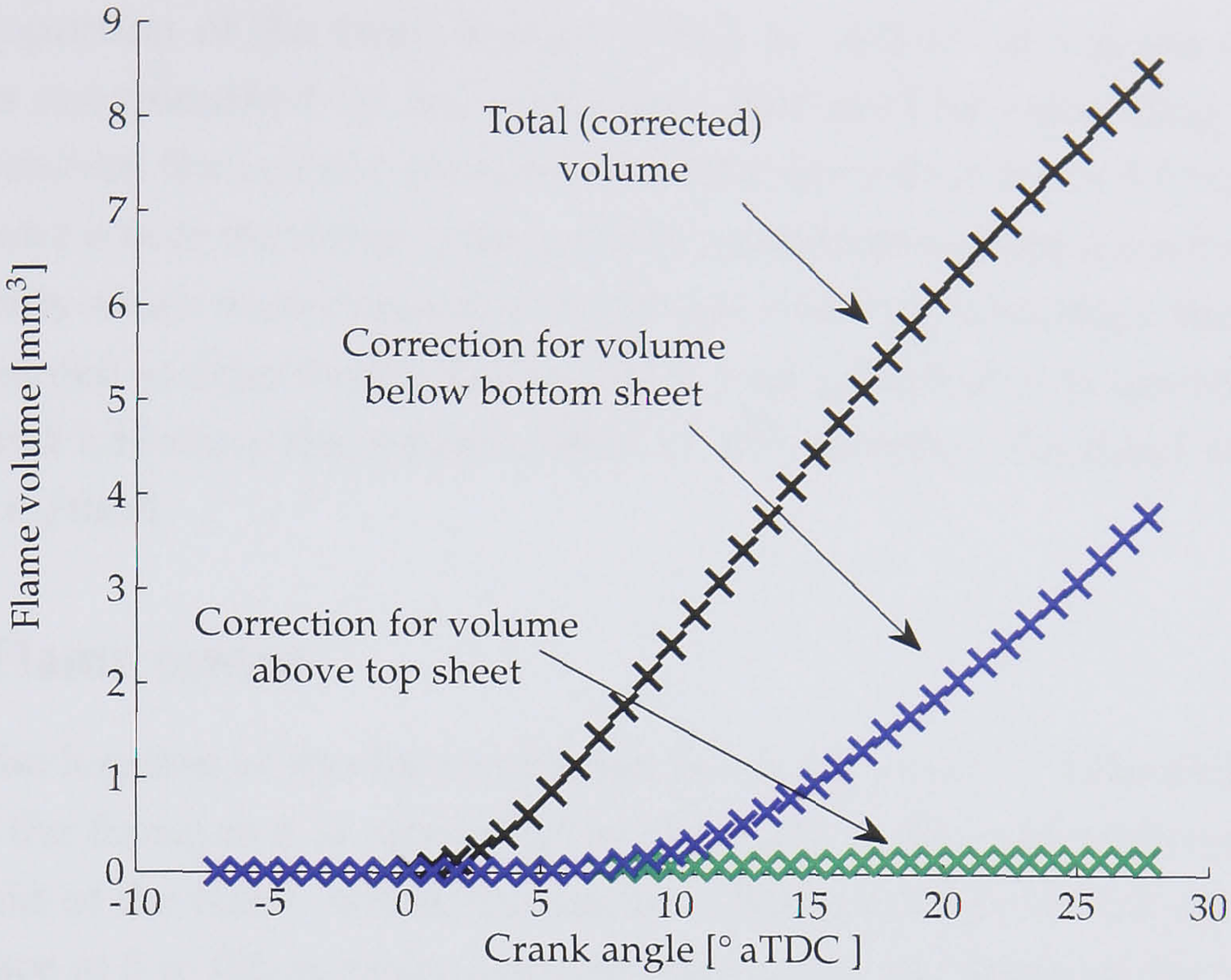

Figure 3.14: Volume of burnt gas and corrections to Equation 3.21.

estimated as the triangular area between the plane of the top laser sheet and the pent roof, multiplied by an equivalent length calculated by dividing the area of the burnt region on the top progress variable layer by the distance between the two pent roof walls on that plane. These two corrections were added to the volume calculated using Equation 3.21 to give an estimate of the total volume of burnt gas at a particular crank angle. The graph illustrated in Figure 3.3.10 shows the burnt volume and the magnitude of the corrections calculated.

3.3.11 Flame surface area

Given that isosurfaces generated by Matlab were composed entirely of triangular elements the total surface area can be calculated by summing the contribution of individual faces. The area of a triangle in three-dimensional space well known and is equal to half the Euclidean norm of the sum of the cross products of each of the three vertices with the other. The surface area of an isosurface is therefore given by

$$A(\mathcal{S}) = \sum_{f_k \in \mathcal{F}} \left[\frac{1}{2} \left\| \vec{v}_{1k} \times \vec{v}_{2k} + \vec{v}_{2k} \times \vec{v}_{3k} + \vec{v}_{3k} \times \vec{v}_{1k} \right\| \right] \tag{3.22}$$

where $\|\vec{v}\|$ is the Euclidean norm of $\vec{v}$.

The proportion of the flame surface which is "active" at a given crank angle, that is not quenched by the walls, was estimated by calculating the local distance between the current isosurface and the isosurface formed from the last camera frame where the entire contents of the combustion chamber is burnt. Surface elements which were closer than 1.5 mm to this final isosurface, the distance being calculated as described in Section 3.3.8, were assumed to be quenched. Figures 3.15 and 3.16 show the region of the $\bar{c} = 0.5$ isosurface identified as inactive using this method.

3.3.12 Flame centre

Tracking the location of the flame centroid is a simple way of following the migration of the flame as it is convected by the flows in the combustion chamber. The centroid of the flame, where the flame is defined as the volume enclosed by an isosurface at $\bar{c} = 0.5$, is easily calculated by taking the mean of the x, y and z coordinates of all the elements of the scalar field where $\bar{c} \geq 0.5$. The scalar field of $\bar{c}$ was generated as discussed in Section 3.3.5.

For modelling work, for example with LUSIE, a more relevant metric for the location of the centre of the flame is the point $\vec{x}_e$ which is equidistant from all the active surface area. The location of $\vec{x}_e$ may be found by solving the following least-squares minimisation problem

$$\min_{\vec{x}_e} \left(f(\vec{x}_e) \right) \tag{3.23}$$

where

$$f(\vec{x}_e) = \sum_{k \in a} A(f_k) \left\| \vec{C}(f_k) - \vec{x}_e \right\|^2 \tag{3.24}$$

Here a is the set of all faces which are active and $A(f_k)$ is the area of face f_k. The area weighting is used to ensure that the calculated value of $\vec{x}_e$ is not unduly influenced by one or two faces with large areas. Both a and $A(f_k)$ were calculated as described in Section 3.3.11. The centroid of a face, given by the function $\vec{C}(f_k)$, is found from the mean of the x, y and z coordinates of the three vertices which define the face. Equations 3.23 and 3.24 were solved iteratively using the Matlab function `lsqnonlin`, part of the optimisation toolbox.

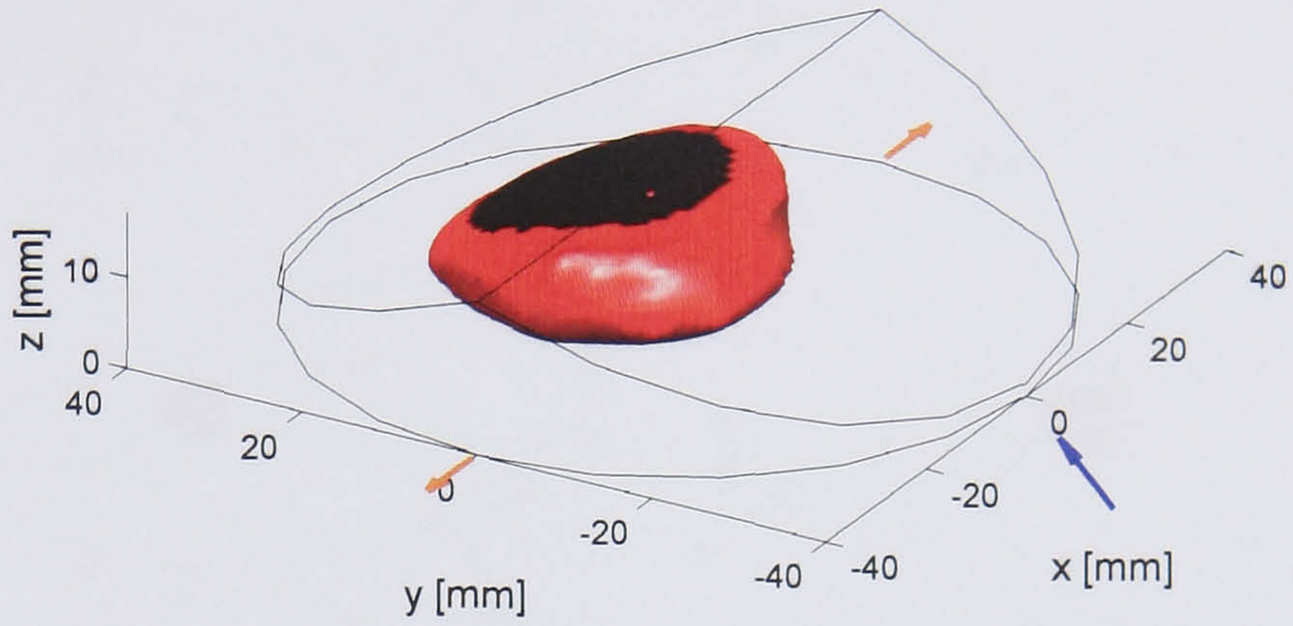

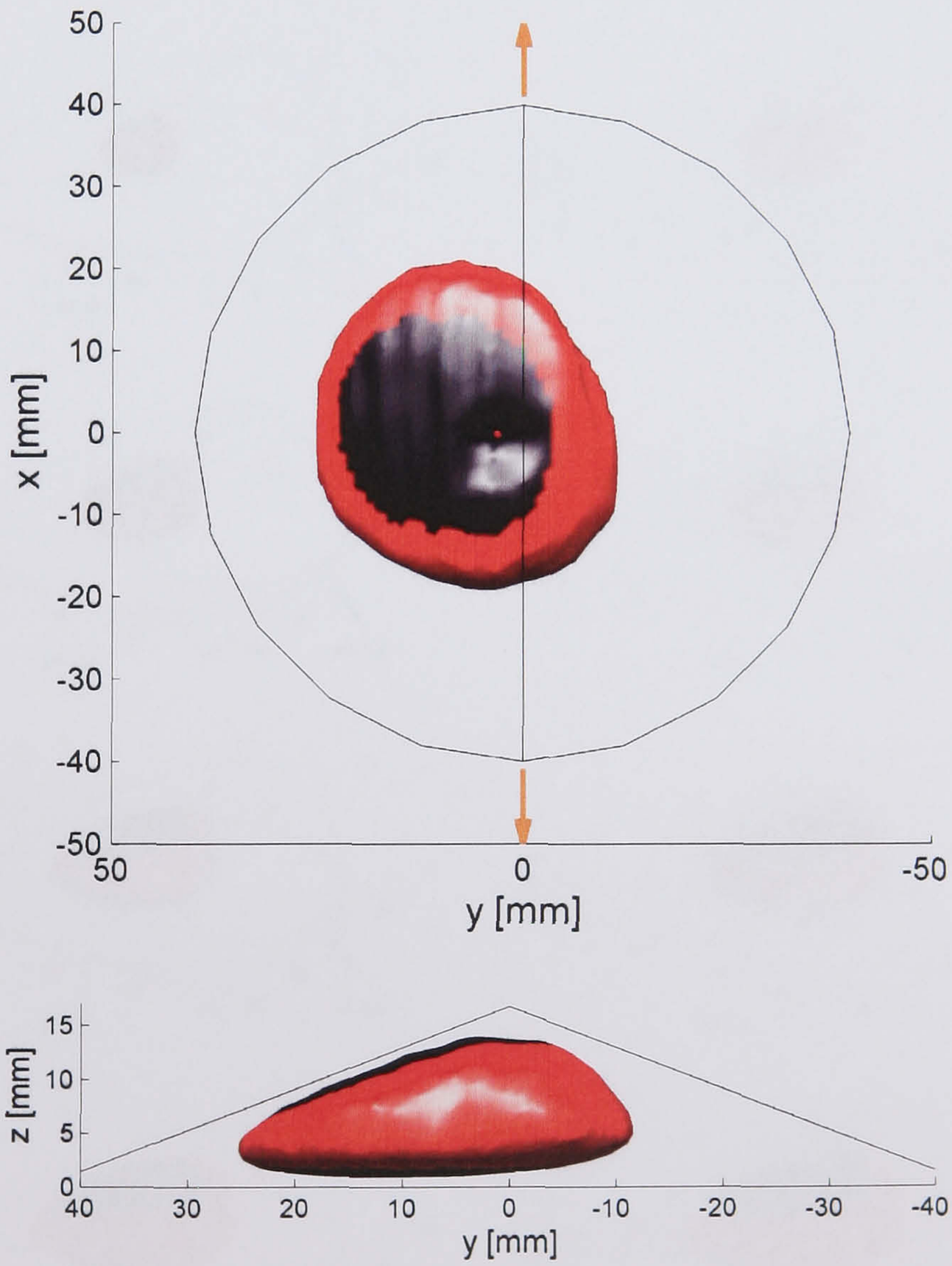

Figure 3.15: Regions of a $\bar{c} = 0.5$ isosurface identified as active and inactive; red shading denotes active surface, black shading denotes inactive surface.

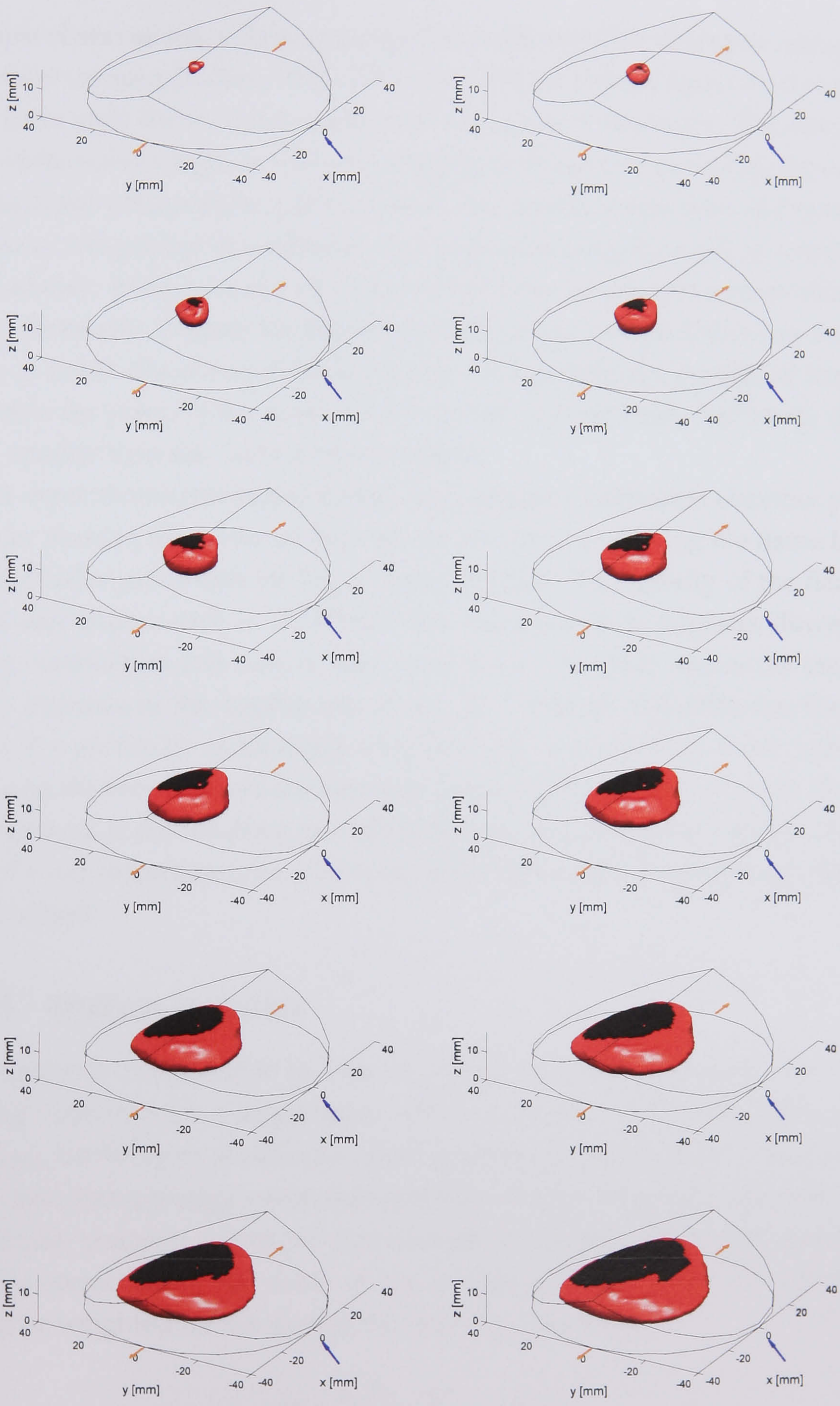

Figure 3.16: Progression through a cycle of regions of the isosurface at $\overline{c} = 0.5$ identified as active and inactive; red shading denotes active surface, black shading denotes inactive surface.

3.3.13 Flame radius

Previous observations of flame propagation in the LUPOE1-D engine using either laser sheet imaging [Cairns, 2001, Gillespie, 1998] or natural light [Abdi Aghdam, 2003] have used flame radii to monitor the progress of the flame. The integrating effect of the natural light or schlieren imaging techniques ensures that the ensuing images capture the periphery of the flame. Flame radii were calculated from these images by computing the enflamed area and calculating the radii of a circle with an equal area. Images produced using the laser sheet technique used in this thesis do not necessarily capture the flame periphery as parts of the flame may be either above or below the plane of the laser sheet. If a substantial portion of the flame is outside the plane of the sheet a flame radius derived from that image may be much smaller than the "actual" flame radius.

For experiments conducted using a disc shaped combustion chamber placing the laser sheet in the centre of the clearance volume (assuming the flame is close to spherical) ensures that the sheet passes through the majority of the flame. In a pent roof engine such as LUPOE2-P the flame naturally migrates downwards during combustion and no one laser sheet plane antiquely represents the flame for the duration of the combustion event. To overcome this difficulty, the flame radius at a particular crank angle was calculated by summing in the z-direction (i.e. along the bore axis), all the elements of the $\overline{c}$ field for which $\overline{c} \geq 0.5$. The non-zero elements in the resulting two-dimensional matrix represented the silhouette of the $\overline{c} = 0.5$ isosurface from which the flame radius of an equivalent circle could be calculated.

3.3.14 Surface statistics

On occasion it is helpful to be able to describe a surface property such as the burning velocity with a single mean value or using a PDF (probability density function). As the faces of isosurfaces of $\overline{c}$ (generated as described in Section 3.3.6) are defined using triangles with different sizes simply taking the arithmetic mean of a surface property calculated per triangle would give misleading results. To give the correct mean the value of the surface property χ for the k-th face χ_k should be weighted for the area of the face $A(f_k)$ such that

$$\overline{\chi} = \frac{1}{A(\mathcal{S})} \sum_{f_k \in \mathcal{F}} \chi_k A(f_k) \tag{3.25}$$

where $A(\mathcal{S})$ is the area of the entire surface calculated as described in Section 3.3.11. A surface weighted standard deviation may be calculated in a similar way as

$$\sigma_\chi = \sqrt{\frac{1}{A(\mathcal{S})} \sum_{f_k \in \mathcal{F}} (\chi_k - \overline{\chi})^2 A(f_k)} \tag{3.26}$$

Calculation of a PDF requires that the data should be "binned", that is all values within a certain range are grouped together in a single bucket or bin. Typically several non-overlapping bins are used the ranges of which cover the extent of the data. For a normal PDF the height of each bar is then proportional to the count in that bin. Generating the PDF of a surface property requires that the count in each bin be multiplied by the sum of the areas of the faces whose values have been placed in that bin. To generate a surface PDF bin values are then normalised such that the integrated area function when plotted is equal to one.

Chapter 4

Combustion Simulation Software

4.1 Overview

Iterative spark ignition engine development using prototypes is inherently expensive as the economies of scale which make mass produced powertrain components affordable are lost when manufacturing small numbers of prototypes. The prospect of virtual engine design using computer models is appealing as computer run time is generally much cheaper than the manufacture of prototypes. Currently available computer models of premixed turbulent combustion may be classified as either thermodynamic or fluid dynamic (see Section 1.7) of which thermodynamic models, such as the ones used in the current study, are attractive because of their simplicity and relatively low computational cost.

Combustion simulation was undertaken during the currently reported study in order to: 1) Better understand the actions of the many phenomena which influence SI engine combustion and 2) Employ this knowledge to improve the performance of the combustion model such that it may be better employed as a design tool. All the combustion simulations used a thermodynamic code based on the LUSIE (Leeds University Spark Ignition Engine) software, an in-house code written in Fortran described in Sections 4.2 and 4.5. From this original code two further codes were derived: GT-LU, a hybrid code comprising the LUSIE combustion routines and a commercial engine breathing simulation package GT-

Power [Gam, 2004], described in Section 4.3; and LUCoVe (Leeds University Combustion Vessel), a code developed to simulate constant volume combustion, described in Section 4.4. This chapter describes the formulation of the above models and modifications made to them during the course of the study.

The contents of this chapter are organised as follows. Initially, an overview of the LUSIE, GT-LU and LUCoVe codes is given. At this point any routines which are particular to each individual software package are detailed. All of the codes share the same library of thermodynamics, flame geometry and burning velocity routines. The functions of the important routines are described individually. Finally the procedures undertaken to verify the numerical accuracy of the software are reported.

4.2 LUSIE

4.2.1 History of the LUSIE software

Engine cycle simulation has a long history at The University of Leeds beginning with the equilibrium cycle code of Desoky [1981] and Al-Mamar [1983]. This code was later modified by Hynes [1986] to incorporate a variable rate of combustion controlled either by an empirical law, such as the well known Wiebe function, or a turbulent burning velocity expression coupled with the entrainment and burn-up model postulated by Blizard and Keck [1974]. The code written by Hynes, with many later modifications, forms the basis of the modern LUSIE code, the descendants of which have been used in many studies of engine combustion, for example Bradley et al. [1988], Abdel-Salam [1992], Merdjani and Sheppard [1993], Langridge [1995], Cairns [2001], Abdi Aghdam [2003].

The original turbulent burning velocity expressions employed by Hynes, based on the work of Damköhler [1947], Groff and Matekunas [1980] and Hamid [1986], were updated with the addition of the Leeds *Ka* and *KaLe* turbulent burning velocity correlations, [see Abdel-Gayed et al., 1987, Bradley et al., 1992], by Merdjani and Sheppard [1993]. Until this point any changes in the amount of trapped mass available for combustion caused by blowby had been neglected, functions to account for the mass flow through the top land crevice and piston ring pack were incorporated by Abdel-Salam [1992] and later Langridge [1995]. In order to allow the simulation of more realistic engines, routines to calculate flame volume and surface area for non-disc combustion chambers were added by Merdjani [1996].

The software was further improved by Abdi Aghdam [2003] with the incorporation of the burning velocity expression proposed by Lipatnikov and Chomiak [2002], some refinement to the blowby model, and the correction of a number of errors in its thermodynamic formulation.

Recently the LUSIE software has been incorporated with the commercial software Ricardo WAVE [Sheppard et al., 2005] to allow complete engine cycle simulation including breathing effects. As the code incorporated, by this stage in its history, a large number of modifications by various users, Dr Kexin Liu rewrote much of the code inherited from Abdi Aghdam in order to simplify its operation and improve the flame geometry routines. This rewritten code, incorporating some modifications discussed below, forms the basis of the LUSIE code used for the current study. The description given here is not complete, for further information the reader should refer to Abdi Aghdam [2003], Hynes [1986] or the excellent manual of Liu [2004].

4.2.2 Overall operation of LUSIE

Combustion in a spark ignition engine is a complex phenomena with many different processes taking place simultaneously. The LUSIE software simplifies the simulation of these processes by breaking a complete engine cycle down into a number of much smaller time steps. Within each time step the code uses different specialised subroutines called in series to calculate changes in the thermodynamic state and chemical composition of the charge caused by piston motion, combustion, heat transfer etc. assuming conservation of mass and energy, and conformance to the second law of thermodynamics.

The code takes as its input text files which define the engine and running conditions to be simulated. After the input files have been parsed and variables initialised, each cycle consists of a motoring simulation followed by a firing simulation, the output from both simulations being recorded to text files for later analysis and comparison with measured cycles. The initial motoring cycle simulation is necessary for the correct simulation of a firing cycle even if the user is not interested in the output as the Woschni heat transfer model, see Section 4.2.6, requires as an input values of motoring pressure. When the simulation of one cycle is complete the software checks for further input files and continues until no further input is found. A flowchart illustrating the above sequence is shown in Figure 4.1.

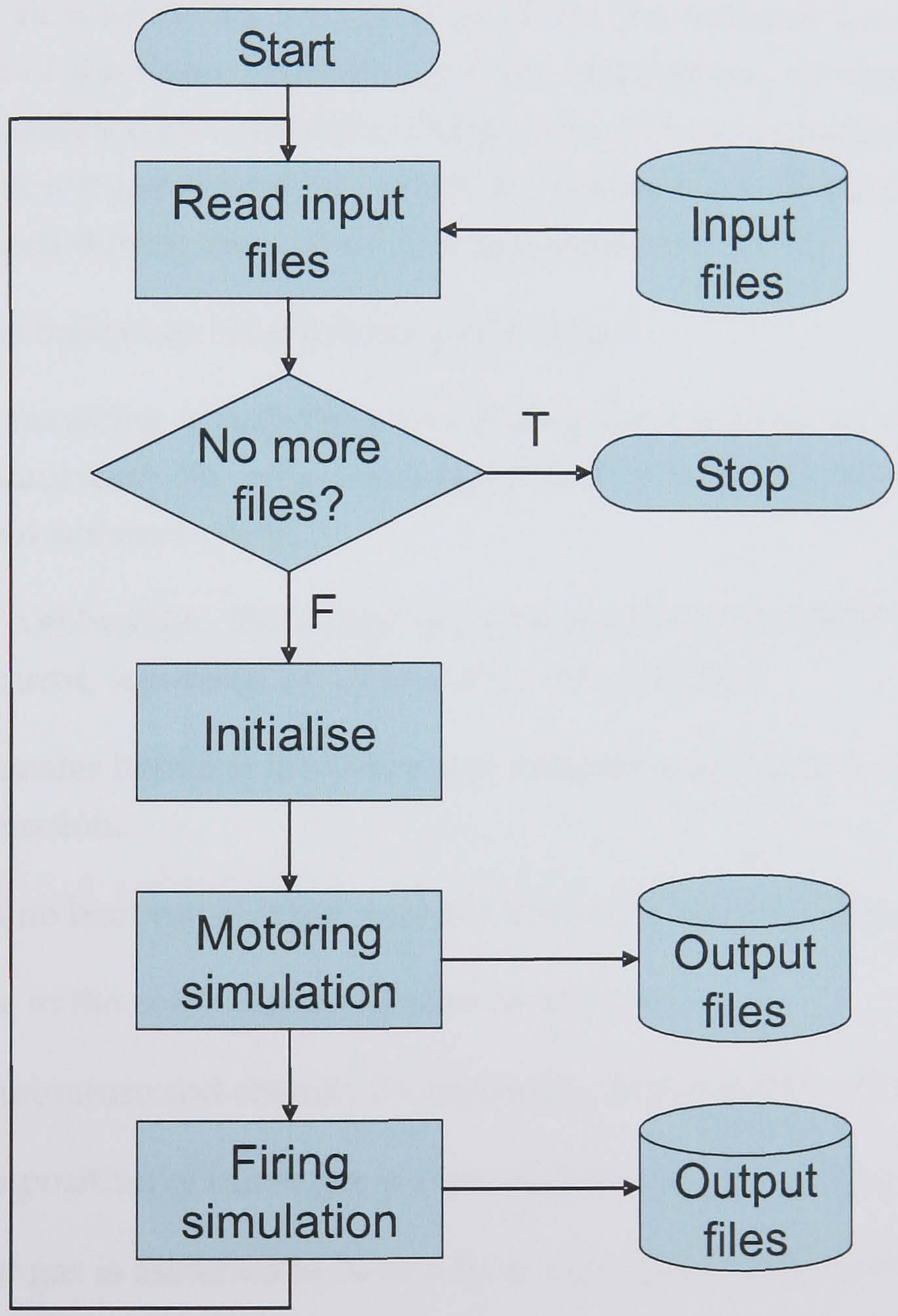

Figure 4.1: Flowchart showing the sequence of events during a LUSIE simulation.

4.2.3 Model assumptions

The LUSIE code falls within the thermodynamic class of engine combustion simulation models, see Section 1.7, in that the model equations have their foundations in the laws of thermodynamics rather than fluid-dynamics. Within the class of thermodynamic models LUSIE can further be sub-classified as quasi-dimensional, as it separates the burnt gas from the unburnt gas and incorporates features of the flame geometry into the calculations, as opposed to zero-dimensional models where the entire charge is treated as a homogeneous lumped mass. The following assumptions, which are common for all quasi-dimensional models, are used during the calculations performed by LUSIE.

- All gases behave as ideal but not perfect gases.
- During motoring simulations and during compression or expansion in a firing simulation, the cylinder charge is fully mixed and not separated into burnt and unburnt zones.
- During combustion, the charge is partitioned into two zones of gas, burnt and unburnt, separated by an infinitely thin interface.
- Mass transfer between the burnt and unburnt zones only occurs as a result of combustion.
- There is no heat transfer between the burnt and unburnt zones.
- Pressure in the combustion chamber is uniform.
- The temperature and chemical composition within a zone are homogeneous.
- The composition of burnt gas is maintained in chemical equilibrium.
- Unburnt gas is assumed to have a frozen chemical composition.

4.2.4 Motoring simulation

Motoring operation of an engine is simulated using a number of discrete subroutines which are called sequentially each time step, with each subroutine calculating changes to the charge gas thermodynamic state caused by different engine phenomenon. The calculation for a single time step, shown in the flowchart in Figure 4.2, proceeds as follows. At the start of every time step the crank angle is

advanced by a small amount and a new piston position and chamber volume calculated. The temperature and pressure of the charge are then updated assuming that the compression/expansion of the gas is isentropic and the mixture composition is frozen. Finally, heat transfer and blowby are simulated as described in Sections 4.2.6 and 4.2.7.

4.2.5 Firing simulation

The simulation of a firing cycle proceeds in a similar way to that of a motoring cycle whereby each time step is broken down into a number of discrete processes which are simulated sequentially as shown in Figure 4.3. At the start of every time step the crank angle is advanced by a small amount and a new piston position and chamber volume are calculated. If the current crank angle is before the ignition timing θ_{sp} the simulation proceeds to compress the charge gas using the same procedure as for motoring simulations, outlined in Section 4.2.4 and Figure 4.2. If the crank angle is later than the ignition timing, one of two subroutines, for the 2 and three-zone combustion models, is called. The first call to either subroutine is used to create a spark kernel. During subsequent calls combustion proceeds according to the prescription of either the 2 or three-zone models, see Sections 4.5.3 and 4.5.4.

Whilst combustion is being simulated, the cylinder charge is partitioned into separate burnt and unburnt zones. Any process which causes the pressure in one zone to differ from the other is immediately followed by a procedure to equalise the pressure between the two zones and return the system to thermodynamic equilibrium as described in Section 4.5.11. When the mass fraction burnt, x_b, exceeds 99% combustion is assumed to be complete. Expansion is simulated in a similar way as for a motoring simulation, assuming isentropic expansion followed by blowby and heat transfer, except that now the chemical composition of the burnt gas is maintained in equilibrium. A complete description of the combustion and turbulence routines used by LUSIE can be found in Section 4.5.

4.2.6 Heat transfer

Accurate description of engine heat transfer is important for the correct prediction of gas pressures and temperatures. Many heat transfer models have been proposed in the literature, see for example the review of Borman and Nishiwaki [1987]. Quasi-dimensional models (including LUSIE) typically neglect any heat

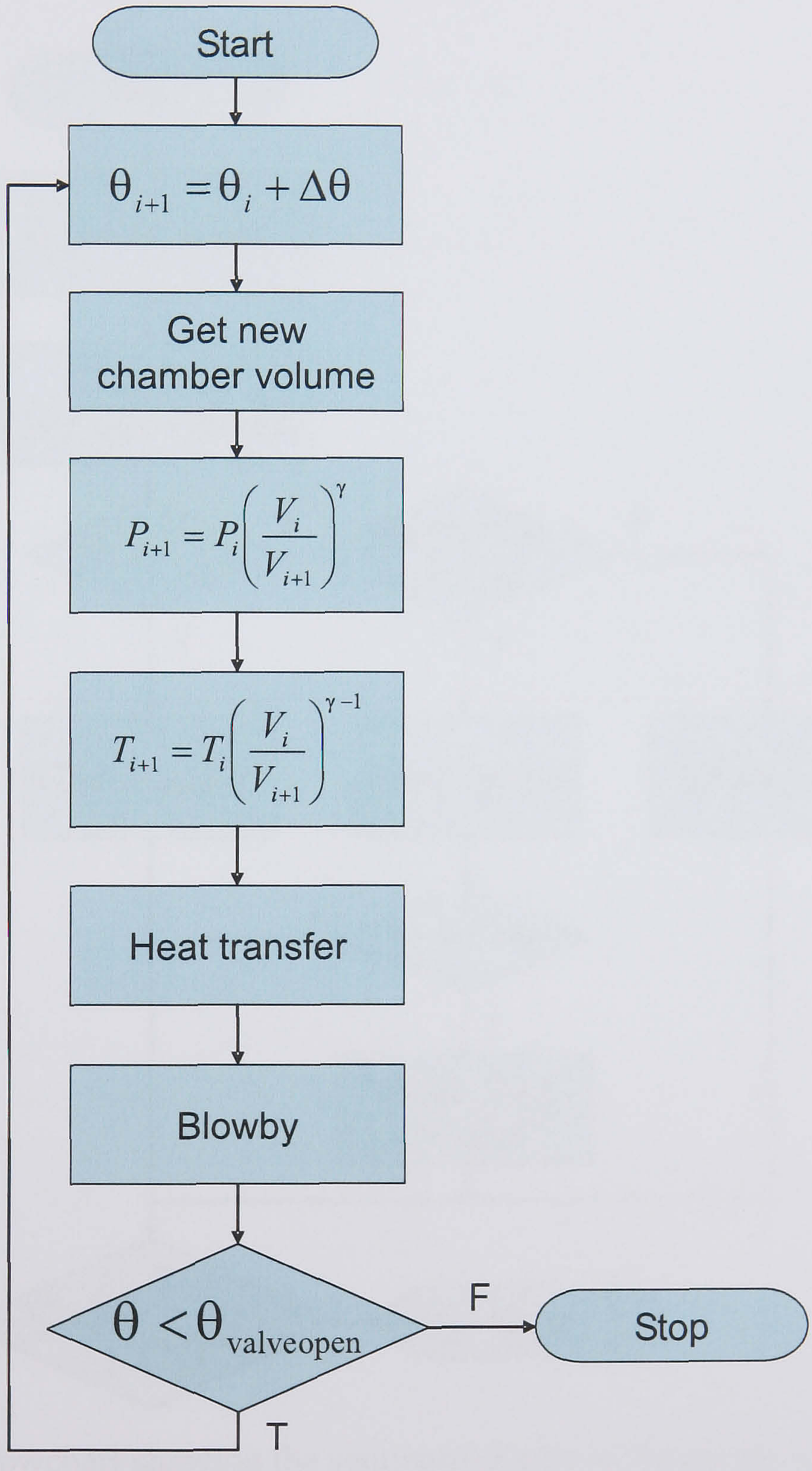

Figure 4.2: Flowchart showing the sequence of events during the simulation of a motoring cycle by LUSIE.

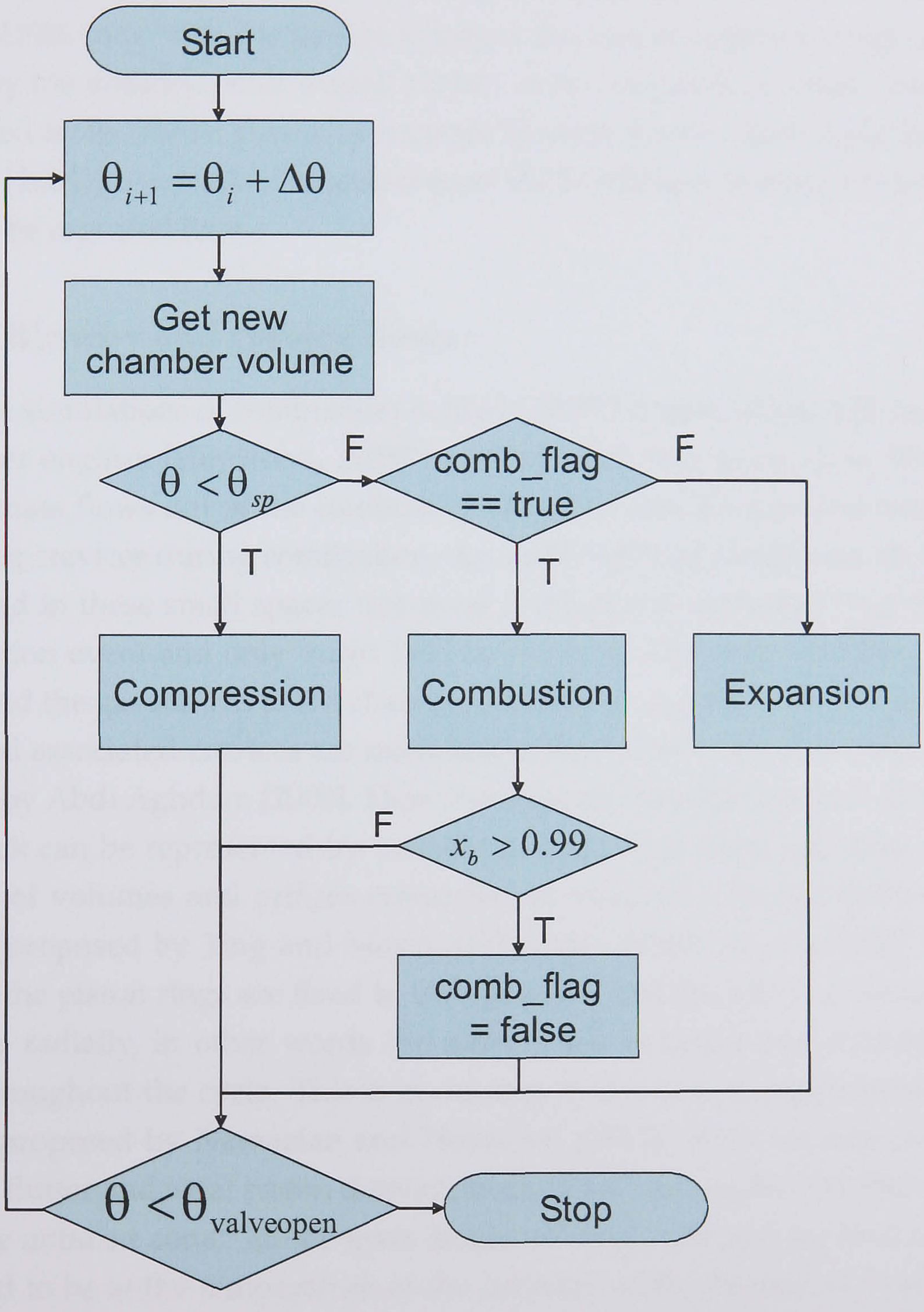

Figure 4.3: Flowchart showing the sequence of events during the simulation of a firing cycle by LUSIE.

transfer between the burnt and unburnt gas and employ a Nusselt—Reynolds number correlation such as that which may be derived for steady turbulent flows in pipes [Blumberg et al., 1979] to predict the gas—wall heat transfer rate. Two such correlations, proposed by Woschni [1967] and Annand [1963] are included in the LUSIE code with the facility to adjust the model constants originally proposed by the authors. Wall wetted surface areas, required as model inputs, are calculated by the flame geometry routines (Section 4.5.10). Abdi Aghdam [2003] and Liu [2004] give detailed descriptions of the LUSIE heat transfer models which will not be repeated here.

4.2.7 Blowby and crevice flows

Previous simulations of combustion in the LUPOE1 engine [Abdi Aghdam, 2003] and other engines [Heywood, 1988] have indicated that as much as 10% of the charge mass flows out of the combustion chamber into the top land crevice and inter-ring crevices during combustion. As, under normal conditions, the flame is quenched in these small spaces this mass is effectively excluded from the main combustion event and only burns later in the cycle when the cylinder pressure drops and the gas returns to the chamber. Blowby and gas flow in the piston ring pack and associated crevices are modelled in the LUSIE software using routines written by Abdi Aghdam [2003]. Here it is assumed that the top land crevice and ring pack can be represented by inviscid compressible isentropic flow through a series of volumes and orifices connected in series in a similar fashion to the models proposed by Ting and Mayer [1974] and Ruddy et al. [1981]. In these models the piston rings are fixed in their grooves and the piston is assumed not to move radially, in other words the sizes of the volumes and orifices remain fixed throughout the cycle. This is in contrast to the more complex models such as that proposed by Namazian and Heywood [1982] which include provisions for ring flutter and axial piston displacement. Mass leaving the chamber is taken from the unburnt zone;[1] all the mass inside the ring pack and top land crevice is assumed to be at the temperature of the cylinder walls, the rate of heat transfer presumably being very large given the large surface area to volume ratio of the crevices [Furuhama and Tada, 1961, cited by Abdi Aghdam [2003]], [Namazian

[1]The assumption that blowby gases are unburnt is only really valid if the spark plug is approximately central. For the engines studied in this thesis this is indeed the case. Where ignition is not central, mass should be taken in appropriate proportions from the burnt and unburnt zones depending on the ratio of areas in contact with the top land gap from each zone.

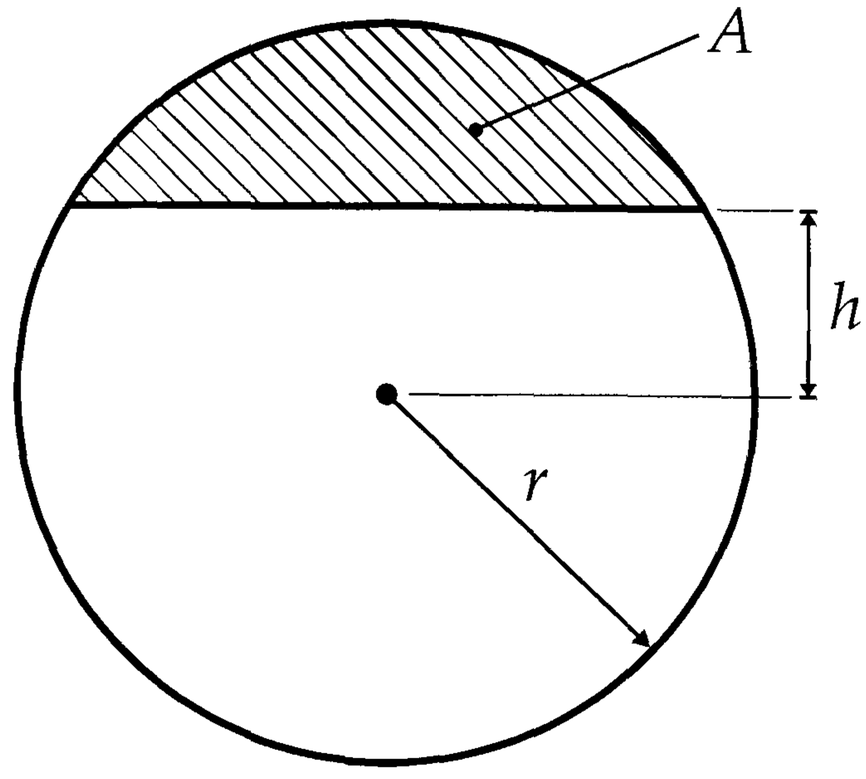

Figure 4.4: Definition of distances used in calculating the area of a sector of a circle, Equation 4.1.

and Heywood, 1982].

As the LUPOE family of engines are ported the pressure in the top-land and inter-ring crevices is set to that of the intake port during those periods in the cycle when the crevices are exposed to the port. The crank case pressure is assumed to remain constant through the cycle. The existing blowby routines assumed square ports, as used on LUPOE1, when calculating the mass flow rate between the port and crevices. The exposed area of the port was then easily calculated by multiplying its width by the exposed height. The LUPOE2 exhaust port was composed of multiple small circular holes as described in Section 2.2.2. To allow the calculation of the exposed area of the LUPOE2 exhaust port the original LUSIE blowby routines were modified by the present author to accept an arbitrary number of ports with either rectangular or circular geometry. The area of a sector of a circle, used in the calculation of the exposed area of a circular port, is given by

$$A = \frac{r^2}{2}\left[2\cos^{-1}\frac{h}{r} - \sin\left(2\cos^{-1}\frac{h}{r}\right)\right] \tag{4.1}$$

where h is the distance from the centre of the circle, r is the radius of the circle and A is the area of the sector of the circle as shown in Figure 4.4.

4.3 GT-LU

The combustion and burning velocity routines used in LUSIE (see Section 4.5) were integrated with the commercial engine manifold simulation software GT-Power to give a hybrid code GT-LU. This work was undertaken by the author as part of the sponsorship by Cosworth Technologies/Mahle Powertrain to enable predictive combustion simulation for commercial engine development. The resulting GT-LU code has been used to successfully simulate two engines to date, see Hattrell et al. [2006] and Abdi Aghdam et al. [2007].

The integration used the "usermodel" feature of the GT-Power software whereby the user may substitute for the default GT-Power model their own model for certain parts of the simulation, for example: in-cylinder turbulence, turbulent combustion, turbocharger performance, fuel injection etc. The user written models are placed in a Fortran library which is called by GT-Power whenever necessary. In this configuration GT-Power retains overall execution control and solves for the flow in the manifolds to provide boundary conditions at the moment of valve/port closure. After this point GT-Power passes to the LUSIE combustion routines the mass, composition and state of the unburnt and burnt zones during each time step. The LUSIE routines return to GT-Power an amount of mass which is to be burnt during the current time step; GT-Power removes this mass from the unburnt zone and places it in the burnt zone, solving for thermodynamic and chemical equilibrium as shown in Figure 4.5. The simulation continues in this fashion until valve/port opening at which point full control is returned to GT-Power.

The turbulence routines used by LUSIE were integrated with GT-Power in a similar way to the combustion routines and can optionally be used to calculate values of u' and L for use in the combustion calculations. Although it is possible to construct a volume and orifice blowby model using GT-Power, see Section 4.6, it is not possible to use this model for firing simulations as any mass which is removed from the combustion chamber comes in equal proportions from the burnt an unburnt zones. This is a limitation of the GT-Power software rather than GT-LU. For simulation of production engines the lack of blowby model should be of little consequence as, in general, blowby rates and top land crevice volumes are much smaller than for the LUPOE family of engines.

The GT-LU software has been used to successfully simulate combustion in two production engines. These simulations are not presented as part of this thesis

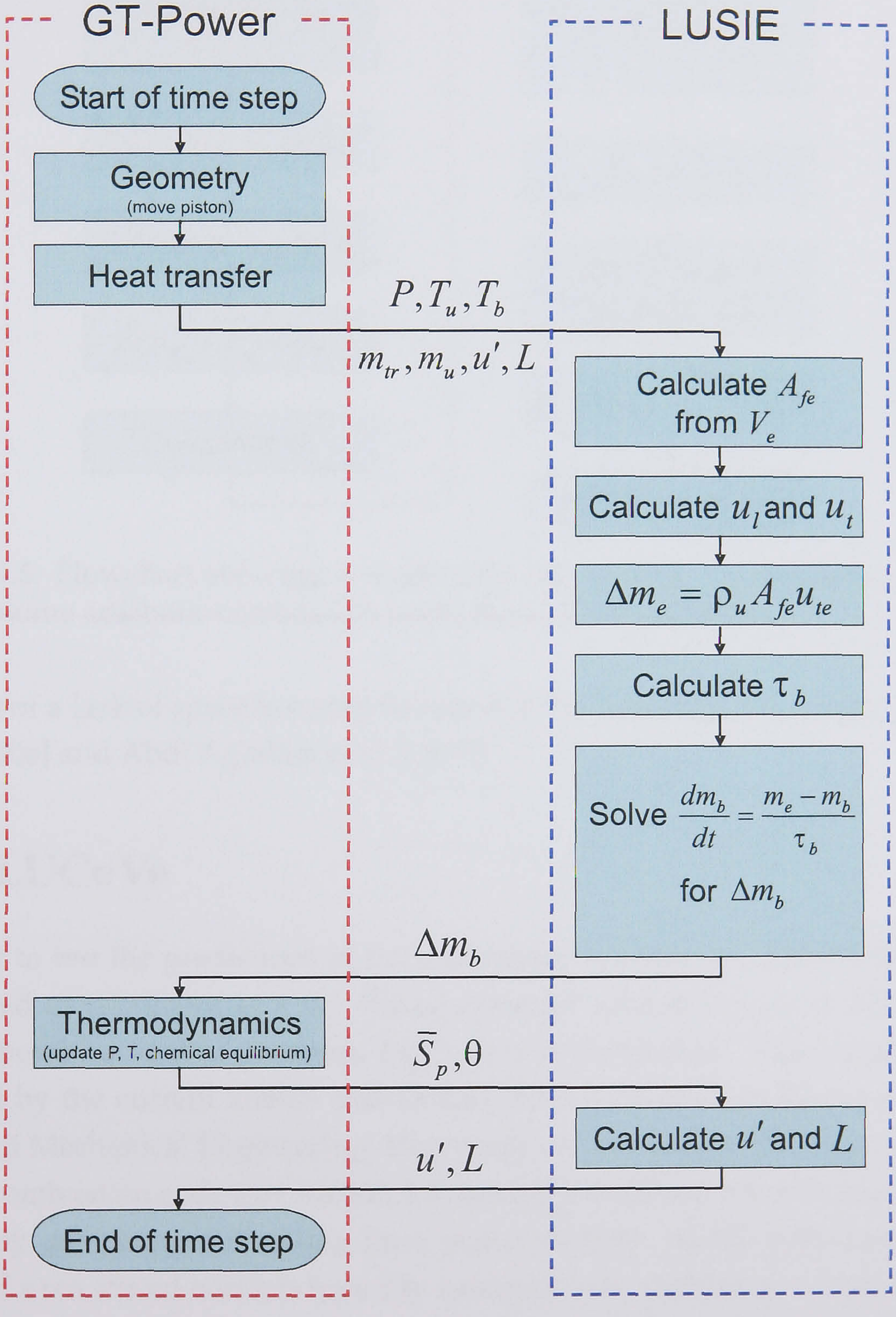

Figure 4.5: Flowchart showing the interaction between GT-Power and the LUSIE combustion routines during a single time step of a GT-LU simulation.

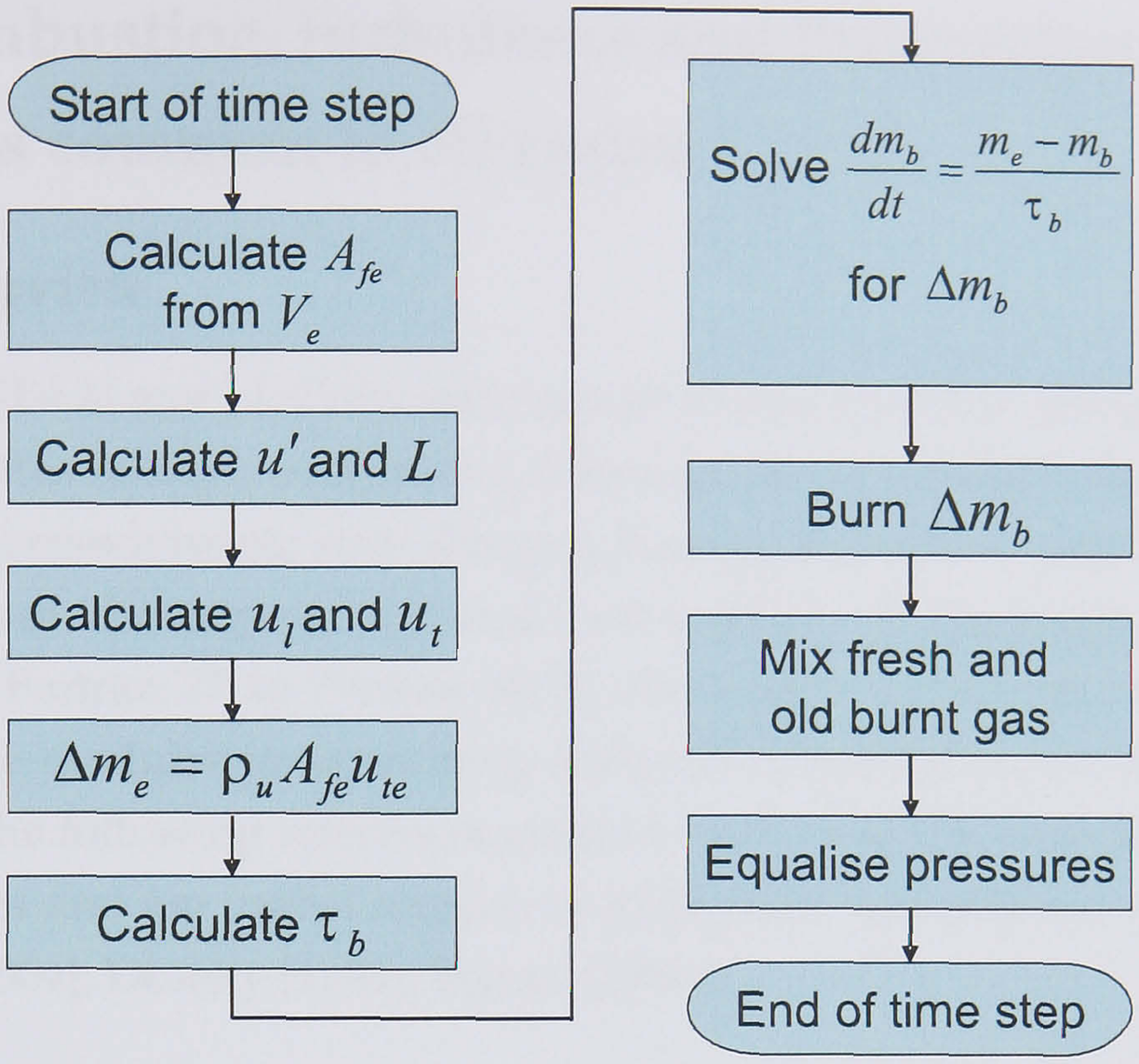

Figure 4.6: Flowchart showing a single time step during the simulation of constant volume adiabatic combustion using the LUCoVe software.

because of a lack of space but may be found in the following references: Hattrell et al. [2006] and Abdi Aghdam et al. [2007]

4.4 LUCoVe

In order to test the predictions of the combustion routines used by LUSIE in the simplified environment of a fan stirred constant volume turbulent combustion vessel (bomb) a further program, LUCoVe was developed. This program, developed by the current author and Dr Liu of the Combustion Research Group, School of Mechanical Engineering, University of Leeds, used the majority of the LUSIE combustion code (see Section 4.5) but neglected heat transfer, blowby, and obviously any changes resulting from piston motion. As the turbulence in the centre of a fan stirred bomb is typically assumed to be stationary, values of u' and L are prescribed at ignition an left unchanged for the duration of the simulation. Figure 4.6 shows the sequence of events in a single time step during the operation of the three-zone version (a two-zone version is also available) of LUCoVE.

4.5 Combustion, turbulence and thermodynamics routines common to all codes

4.5.1 Overview

The LUSIE, GT-LU and LUCoVe software all share a common library of routines, described in this section, comprising subprograms to calculate thermodynamic properties, thermodynamic state changes, burning velocities, combustion, chemical equilibrium, flame geometry and heat transfer. These routines have been moved from Fortran 77 to Fortran 90 by the current author and now take advantage of the modular programming framework offered by the newer version of Fortran. The following references contain more detailed descriptions of some of the routines and are useful sources of additional information: Abdi Aghdam [2003], Liu [2004], Desoky [1981], Hynes [1986].

4.5.2 Ignition

Ignition is treated as an abrupt discontinuity with a spherical flame kernel of a prescribed radius created after a delay period from the spark crank angle. The temperature and pressure of the spark kernel are calculated assuming constant volume adiabatic combustion of the enveloped unburnt gas, followed by equalisation of pressures between the spark kernel and the unburnt zone, see Section 4.5.11. The heat transfer (to calculate heat flux between the unburnt gas and the walls) and blowby subroutines described in Sections 4.2.6 and 4.2.7 are now employed to calculate further changes to the charge before combustion proceeds according to either the two or three-zone model.

4.5.3 Two-zone model

The two-zone model is the simplest of the predictive combustion models available in LUSIE. Here the code attempts to predict directly the amount of gas burnt each time step based on an expression for the turbulent mass burning rate u_{tr}.[2] As there is no entrainment, in the sense of the three-zone model, the development of the predicted pressure curve depends strongly on the expressions used for u_{tr}

[2]LUSIE also incorporates a Wiebe function model (see for example Heywood [1988]) from which a burning velocity can be derived using the truncated spherical flame assumption described in Section 4.5.10.

and flame development. Further discussion on the merits and disadvantages of the two-zone model formulation can be found in Sections 5.4.5 and 5.4.6.

Shown in the flowchart in Figure 4.7 is the sequence of computations carried out during one time step when using the two-zone model for combustion prediction. Each time step begins by equalising the pressures between the burnt and unburnt zones following the change in chamber volume caused by piston movement. Any mass lost to, or returning from, the top land crevice is accounted for using the blowby subroutines, and the active area of the burnt gas flame front is calculated by the flame geometry routines. The turbulence and burning velocities of the mixture are now calculated according to the equations given in Sections 4.5.5, 4.5.7 and 4.5.14 and the amount of fresh gas to be burnt this time step Δm_b is determined according to

$$\Delta m_b = \rho_u A_{fr} u_{tr} \tag{4.2}$$

where ρ_u is the density of the unburnt gas, A_{fr} is the active area of the burnt (reacted) gas front and u_{tr} is the turbulent mass burning velocity.

The temperature and pressure of the small amount of fresh gas to be burnt is calculated assuming constant volume adiabatic combustion before mixing with the previously burnt gas takes place according to conservation of energy and chemical equilibrium, see Section 4.5.12. Finally heat transfer between the charge gas and combustion chamber walls is calculated using wall wetted areas supplied by the flame geometry routines (Section 4.5.10).

4.5.4 Three-zone model

Under typical SI engine conditions the chemical time scale is much smaller than the turbulent time scale and therefore combustion takes place in the quasi-laminar "flamelet" regime, see Section 1.5.2. Apart from the period immediately after ignition when the flame kernel is smooth and laminar-like, the flame front itself is wrinkled and convoluted by the flow field to such an extent that combustion may be thought of as taking place across a thick "flame brush". The three-zone model formulation, based on the ideas of Blizard and Keck [1974], is an extension of the basic two-zone model which attempts to improve the simulation accuracy by accounting for the existence of this thick flame brush. The basic premise of the model is that fresh gas is first entrained at the leading edge of the flame brush, which moves at the turbulent entrainment burning velocity u_{te}, before being con-

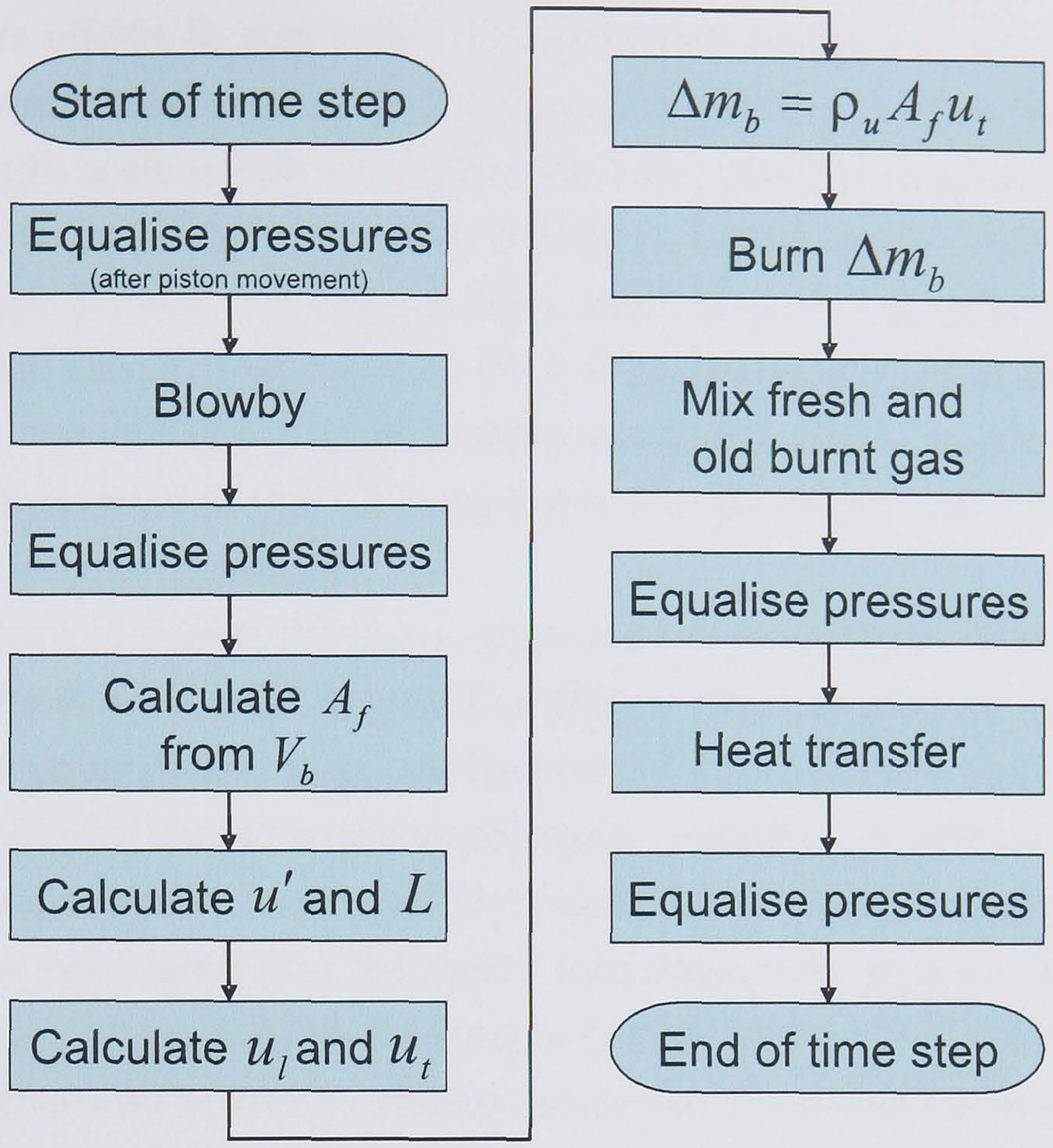

Figure 4.7: Flowchart showing a single time step during the simulation of combustion using the two-zone model.

verted to burnt gas at a rate determined by a characteristic time τ_b. The characteristic time is typically based on the assumption that, once entrained, individual eddies burn as discrete units at a rate proportional to the laminar burning velocity.

Whilst, superficially, the three-zone model appears to offer the advantage of a more realistic treatment of the combustion event, the model is now much more sensitive to the value of laminar burning velocity and the assumed scale of the entrained eddies than the two-zone model. For example, three-zone simulations of LUPOE1-D [Abdi Aghdam, 2003, Section 5.4.5] have shown that a $\pm 10\%$ variation in the laminar burning velocity results in a $\pm 7\%$ change in the value of peak pressure whilst a $\pm 10\%$ variation in the integral length scale gives a $\mp 5\%$ change in peak pressure. The laminar burning velocity of a fuel-air mixture is a parameter which is difficult to determine by measurement with any accuracy at engine conditions because of the rapid onset of instabilities at high temperature and pressure.

At the same time, the uncertainty of chemical kinetics data at these condi-

tions hampers efforts to determine the laminar burning velocity computationally [Al-Shahrany et al., 2005]. To the best of the current author's knowledge, a turbulent length scale inside an engine has been directly measured, as opposed to inferred from measurements of a turbulent time scale, by only a handful of research groups [Fraser and Bracco, 1986, 1989, Breuer et al., 2005, Lee and Lee, 2003, Hong and Tarng, 1998, Li et al., 2002, Klingmann and Johansson, 1999]. For these reasons, the seemingly more realistic treatment of the combustion event offered by the three-zone model vis-à-vis the two-zone model may be more difficult to realise accurately in practice.

The sequence of events during a single time step using the three-zone model is shown in the flowchart in depicted in Figure 4.8, each process being followed by a pressure equalisation step, see Section 4.5.11. The time step begins by returning the cylinder charge to thermodynamic equilibrium following the change in volume caused by the motion of the piston. Mass transfer across the top land crevice is now calculated and the active entrainment front area A_{fe} is deduced from the volume of gas behind the entrainment front by the flame geometry routines. Turbulence and burning velocity values for the current time step are determined according to the equations given in Sections 4.5.5, 4.5.7 and 4.5.14 and the amount of gas entrained this time step Δm_e is calculated according to

$$\Delta m_e = \rho_u A_{fe} u_{te} \tag{4.3}$$

where ρ_u is the unburnt gas density, A_{fe} is the active area of the entrainment front and u_{te} is the turbulent entrainment burning velocity. Gas which is behind the entrainment front but has not yet been burnt is assumed to remain in the same thermodynamic state as the unburnt gas.

The code now proceeds to calculate, given the mass of gas behind the entrainment front m_e and the mass of burnt gas m_b, the amount of gas which should be burnt this time step Δm_b according to the second order Runge-Kutta solution [see Abdi Aghdam, 2003] of the following differential equation.

$$\frac{\mathrm{d}m_b}{\mathrm{d}t} = \frac{m_e - m_b}{\tau_b} \tag{4.4}$$

where the characteristic time for combustion τ_b is defined as

$$\tau_b = C_{\tau_b} \frac{L}{u_l} \tag{4.5}$$

Here L is the integral length scale, u_l is the unstretched laminar burning velocity and C_{τ_b} is a constant. It is important to note that the characteristic size of the entrained eddies L_c is not necessarily equal to L and in the literature a number of different scales based on the valve lift, the Taylor scale, the integral scale or some combination of the above have been used.[3] [Cairns, 2001] In the current work it is assumed that $L_c \propto L$, the constant C_{τ_b} accounts for this proportionality and any proportionality arising from the assumption that $\tau_b \propto 1/u_l$.

During the final part of the time step the new temperature, pressure and composition of the small amount of gas removed from the unburnt zone Δm_b is calculated assuming constant volume adiabatic combustion. This freshly burnt gas is now mixed with the "old" burnt gas assuming constant internal energy and chemical equilibrium for the burnt zone, see Section 4.5.12. The time step is completed by the calculation of heat transfer between the gas and walls as described in Section 4.2.6.

4.5.5 Laminar burning velocity

A value of the unstretched laminar burning velocity u_l is required as an input for both the three-zone model, where it controls the rate of combustion behind the entrainment front, Equation 4.5, and for the calculation of the turbulent burning velocity, Equations 4.17 and 4.18. As highlighted by Wallesten et al. [1998] and Hattrell et al. [2006], there is substantial scatter in the published values of u_l at engine-like temperatures and pressures. Furthermore, the precise determination of u_l at elevated temperatures and pressures remains difficult experimentally because of the tendency of flames of hydrocarbons heavier than CH_4 to become cellular immediately after ignition [Gillespie et al., 2000].

As the model, especially when using the three-zone formulation, is very sensitive to the value of u_l used, several alternative u_l data sets (the work of Al-Shahrany et al. [2005], Ormsby [2005], Muller et al. [1997], Ryan and Lestz [1980] and Rhodes and Keck [1985]) were identified by the current author and added to the LUSIE code in addition to the previously employed correlation of Metghalchi and Keck [1982]. The range of applicable temperatures and pressures for each data set, show in Table 4.1 are typically smaller than the range of conditions found during SI engine combustion. With the possible exception of the correla-

[3]The LUSIE software allows the user to select either the integral scale L or the Taylor scale λ as the characteristic size of the entrained eddies. In keeping with the previous work of Abdi Aghdam [2003], only L was used in the current study.

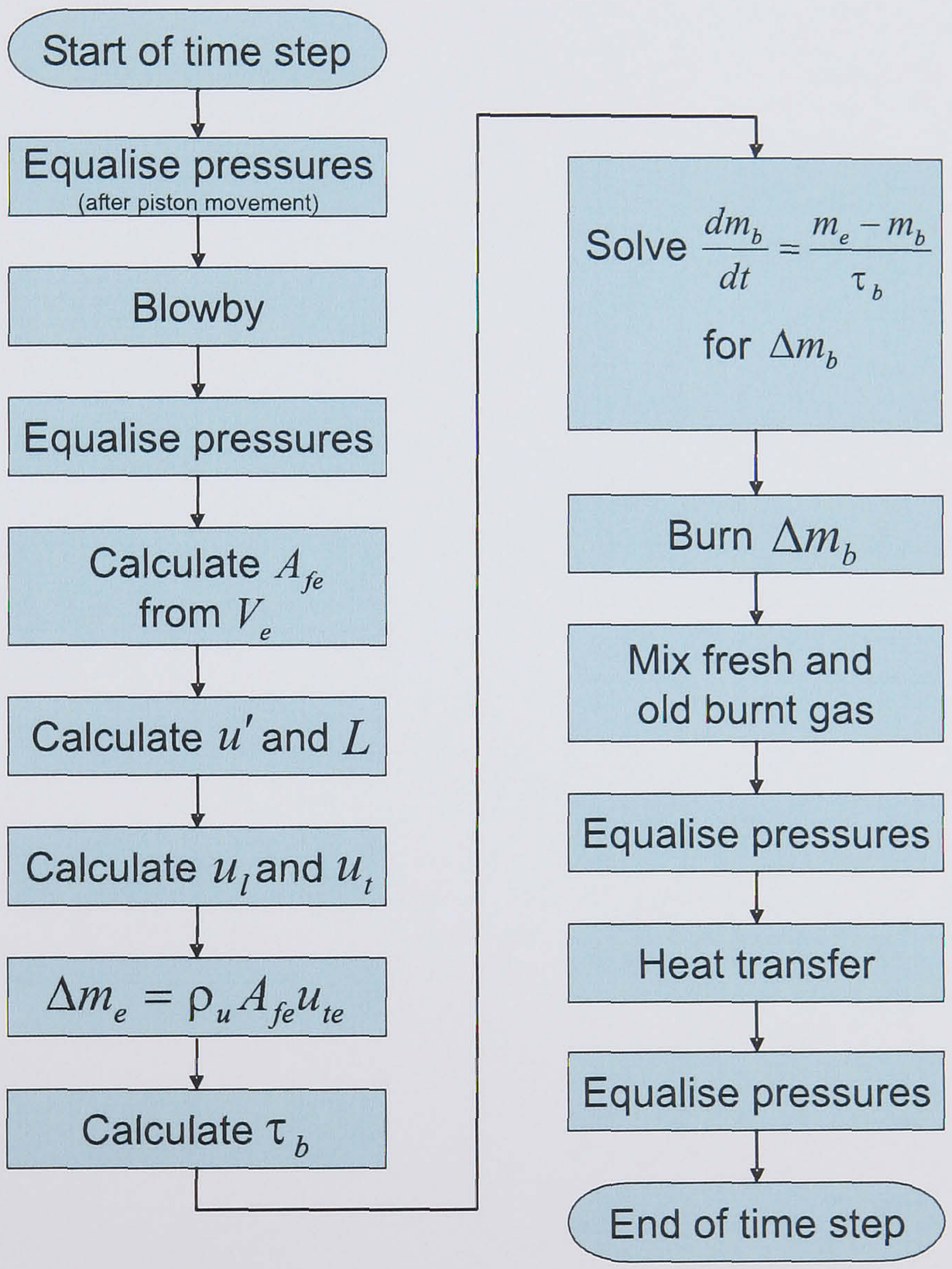

Figure 4.8: Flowchart showing a single time step during the simulation of combustion using the three-zone model.

tion of Metghalchi and Keck, all of the u_l expressions must be extrapolated to simulate "wide open throttle" conditions for typical car engine compression ratios. If the engine to be simulated employs any form of pressure charging the situation is undoubtedly worse.

Table 4.1: Laminar burning velocity correlations, their range of applicability and experimental method used.

Investigator(s)	Pressure	Temperature [K]	Equivalence ratio	Method, see below
Metghalchi and Keck [1982]	0.4–50 atm	298–700	0.8–1.5	1
Rhodes and Keck [1985]	0.4–12 atm	350–500	0.7–1.6	1
Ryan and Lestz [1980]	4–18 bar	470–600	0.7–1.3	1
Bradley et al. [1998]	1–10 bar	358–450	0.8, 1.0	2
Ormsby [2005][a]	1–10 bar	360	0.8–2.0	2
Al-Shahrany [2004][b]	5–30 bar	358–470	0.8–1.4	3
Muller et al. [1997]	1–40 bar	298–800	0.6–1.0	4

[a] see also Lawes et al. [2005].
[b] see also Al-Shahrany et al. [2005].

1. A fuel-air mixture was ignited in the centre of an constant volume combustion vessel and the laminar burning velocity determined by application of the laws of thermodynamics to measurements of the pressure-time history during combustion in a bomb.

2. A fuel-air mixture was ignited at a single point in the centre of a constant volume combustion vessel and the progress of the propagating flame recorded using schlieren photography. The laminar burning velocity was determined by inspection of the schlieren images.

3. A fuel-air mixture was ignited at two diametrically opposite points in a constant volume combustion vessel and the closure of the two inwardly propagating flames recorded using schlieren photography. The laminar burning velocity was inferred from the rate of change of flame radii with time, an attempt to mimic the effect of instabilities on the burning velocity was incorporated for using linear instability theory.

4. Values of the unstretched laminar burning velocity were calculated based on a reduced chemical reaction scheme and used to determine the constants of an analytical expression derived using an asymptotic analysis.

Table 4.2: Constants for Equation 4.6 for iso-octane—air mixtures.

Investigator(s)	α	β	P_0	T_0
Metghalchi and Keck [1982]	$2.18 - 0.8(\phi - 1)$	$-0.16 + 0.22(\phi - 1)$	1 atm	298 K
Rhodes and Keck [1985][a]	$2.4 - 0.271\phi^{3.51}$	$-0.357 + 0.14\phi^{2.77}$	1 atm	298 K
Bradley et al. [1998] $\phi = 1.0$	1.01	-0.282	1 bar	358 K
Bradley et al. [1998] $\phi = 0.8$	1.07	-0.348		
Bradley+Ormsby	1.04	$-0.34 + 0.47(\phi - 1)$	5 bar	360 K
Bradley+Ormsby+Al-Shahrany	$1.16 - 3.33(\phi - 1)$	$-0.30 + 0.42(\phi - 1)$	5 bar	360 K

[a]These constants are for indolene, see the discussion in the text.

Table 4.3: Constants for Equation 4.7 for iso-octane—air mixtures.

Investigator(s)	B_m [m/s]	B_2 [m/s]	ϕ_m
Metghalchi and Keck [1982]	2.632	-8.472	1.13
Rhodes and Keck [1985][a]	3.05	-5.49	1.21
Bradley et al. [1998] $\phi = 1.0$	0.48	0	-
Bradley et al. [1998] $\phi = 0.8$	0.40		
Bradley+Ormsby	0.31	-1.04	1.11
Bradley+Ormsby+Al-Shahrany	0.32	-1.07	1.11

[a]These constants are for indolene, see the discussion in the text.

Table 4.4: Constants for Equation 4.8

ϕ	b_1	b_2	b_3
0.85	66.026	-0.479	2106.1
1.0	29.655	-0.051	2008.0
1.15	73.606	-0.466	2130.2

The correlations of Metghalchi and Keck, Rhodes and Keck, and Ryan and Lestz were all generated from values of u_l derived from the pressure-time history of a deflagration initiated from a point source in a constant volume combustion vessel. The correlation of Rhodes and Keck was generated using indolene as a fuel but is included here as previous studies have found little difference between a correlation of iso-octane and a 10% n-heptane 90% iso-octane gasoline analogue [Bradley et al., 1998] or values of α and β (see Equation 4.6) for a wide range of different fuels [Metghalchi and Keck, 1982].

A thermodynamic analysis of the pressure rise was employed to calculate the flame surface area, rate of mass consumption and unburnt mixture state, from which the laminar burning velocity was derived. No visual record of the flame was recorded, hence during analysis of the experimental data no attempt was made to account for the effects of flame stretch or the instabilities which would typically be present at the elevated temperatures and pressures under which the measurements were taken. As data were taken for the entire duration of the deflagration, the compression of the unburnt mixture during the later stages of the combustion event allowed values of u_l to be determined along an isentrope with a single deflagration. This method therefore allows data to be collected over a range of conditions with a single experiment, albeit with the caveat that the structure (cellular or otherwise) of the flame, and any deviation of the flame from sphericity, remain unknown.

The data of Bradley et al. and Ormsby were determined from schlieren records of the propagation of a laminar flame and hence can be considered to be direct measurements of the unstretched laminar burning velocity, albeit at temperatures and pressures which are too low to be useful for the full range of SI engine combustion. A fuel-air mixture was ignited at a single point in the centre of a constant volume combustion vessel and the progress of the propagating flame recorded using schlieren photography. The laminar burning velocity was inferred from the rate of change of flame radius with time, the flame radius being determined from the inspection of the schlieren images. An appropriate number of images immediately after ignition were excluded from the analysis to ensure that the effect of the spark on the propagation velocity was negligible. Where the flame was unstable, only those images before the onset of cellularity were used. Appropriate steps were taken to account for the effects of flame stretch rate and burnt gas expansion.

A commonly used expression to correlate experimentally derived laminar

burning velocities is the simple power law given in Equation 4.6. Here, the basic shape of the u_l—ϕ curve at a reference temperature and pressure T_0 and P_0 is described by a quadratic function for u_{l0} in terms of equivalence ratio ϕ, Equation 4.7 The effects of temperature and pressure are determined by exponents α and β respectively. The experimental data of Metghalchi and Keck, Rhodes and Keck, and Bradley et al. are all correlated using an expression of this form, derived values α, β, $_0$, P_0, B_m, B_2 and ϕ_m are given in Tables 4.2 and 4.3 for mixtures of iso-octane and air.

$$u_l = u_{l,0} \left(\frac{T}{T_0} \right)^{\alpha} \left(\frac{P}{P_0} \right)^{\beta} \tag{4.6}$$

$$u_{l,0} = B_m + B_2(\phi - \phi_m)^2 \tag{4.7}$$

The experimental data of Ryan and Lestz are fitted to an Arrhenius type expression, Equation 4.8, with the constants b_1, b_2 and b_3 assigned the values given in Table 4.4. Although no citation is given by Ryan and Lestz for the origin of the expression, Metghalchi and Keck [1982] cite Lavoie [1978] for a similar expression.

$$u_l = b_1 P^{b_2} \exp\left(\frac{-b_3}{T} \right) \tag{4.8}$$

The correlations of Metghalchi and Keck, Rhodes and Keck and Ryan and Lestz, being derived without reference to the flame structure, must all be considered unreliable at the temperatures and pressures relevant to SI engine combustion. The correlation of Bradley et al., derived from measurements of u_l where the effects of flame stretching and cellular flame instabilities have been accounted for, should provide more accurate values of u_l at the low temperatures and pressures under which the experiments were conducted. This correlation can be extrapolated and used with LUSIE at the two equivalence ratios for which data values are available ($\phi = 0.8$ and 1) however, it is not suitable for use with GT-LU which includes a full breathing simulation and therefore precludes fixing precise values of ϕ.

Ormsby [2005] measured the laminar burning velocity of iso-octane at a single temperature using the same technique as Bradley et al. [1998] but over a wider range of equivalence ratios. Using these data a new correlation was developed using a least squares fitting method [Metghalchi and Keck, 1982] which covers a continuous equivalence ratio range $\phi = 0.8$–1.2, see Tables 4.2 and 4.3. Data for richer mixtures, although available, were not included in the correlation as they are not especially relevant for SI engine combustion and the rapid onset of

cellularity under these conditions reduces the accuracy of the derived u_l values. As all the data were recorded at a single temperature it was not possible to calculate a value for α. The correlations of Metghalchi and Keck and Rhodes and Keck suggest that α changes significantly with equivalence ratio. This is likely to be an erroneous finding however as the propensity for a particular flame to turn cellular, with a consequent increase in burning velocity,[4] is strongly influenced by pressure (and hence temperature in the constant volume combustion technique used) and mixture strength [Gaydon and Wolfhard, 1953, Bradley et al., 1998, 2000]. The correlation of Bradley et al. shows a much weaker dependence of u_l on temperature than most other published correlations however, the temperature range over which measurements were taken was quite narrow. The mean of the two values for α published by Bradley et al. was used in the correlation of Ormsby's data.

Al-Shahrany [2004] used schlieren photography to record the closure of two flames ignited at two diametrically opposite points in a constant volume fan stirred combustion vessel bomb, with the fans at rest. The laminar burning velocity was then inferred from the rate of change of the flame radii with time, the flame radii being determined from the inspection of the schlieren images. The compression of the unburnt gas in the final stages of the deflagration allowed observation of the propagating flames at much higher temperatures and pressures than possible during a conventional single kernel deflagration where the flame front moves out of view of the window before the mixture is compressed significantly. As the flames were inevitably cellular during the measurements, allowance was made for the enhancing effect of instabilities on the propagation velocity using linear instability theory [see Bechtold and Matalon, 1987, Bradley et al., 1998, Bradley, 1999] to calculate an "enhancement factor" which expresses the ratio of the burning velocity enhanced by instabilities to the laminar burning velocity at any instant, see Figure 4.9. This factor was then applied to the measured (enhanced) burning velocity to give an estimate of the stable, unstretched laminar burning velocity.

When calculating u_l using double kernel experiments, the enflamed volume must somehow be estimated as the flame kernels come together. As the combustion vessel is not perfectly spherical, and in particular the (stationary) fans will have been engulfed by the flame, this estimate is non-trivial and likely to cause

[4]Cellularity not only increases the laminar burning velocity but actively accelerates the flame with time after it has turned cellular.

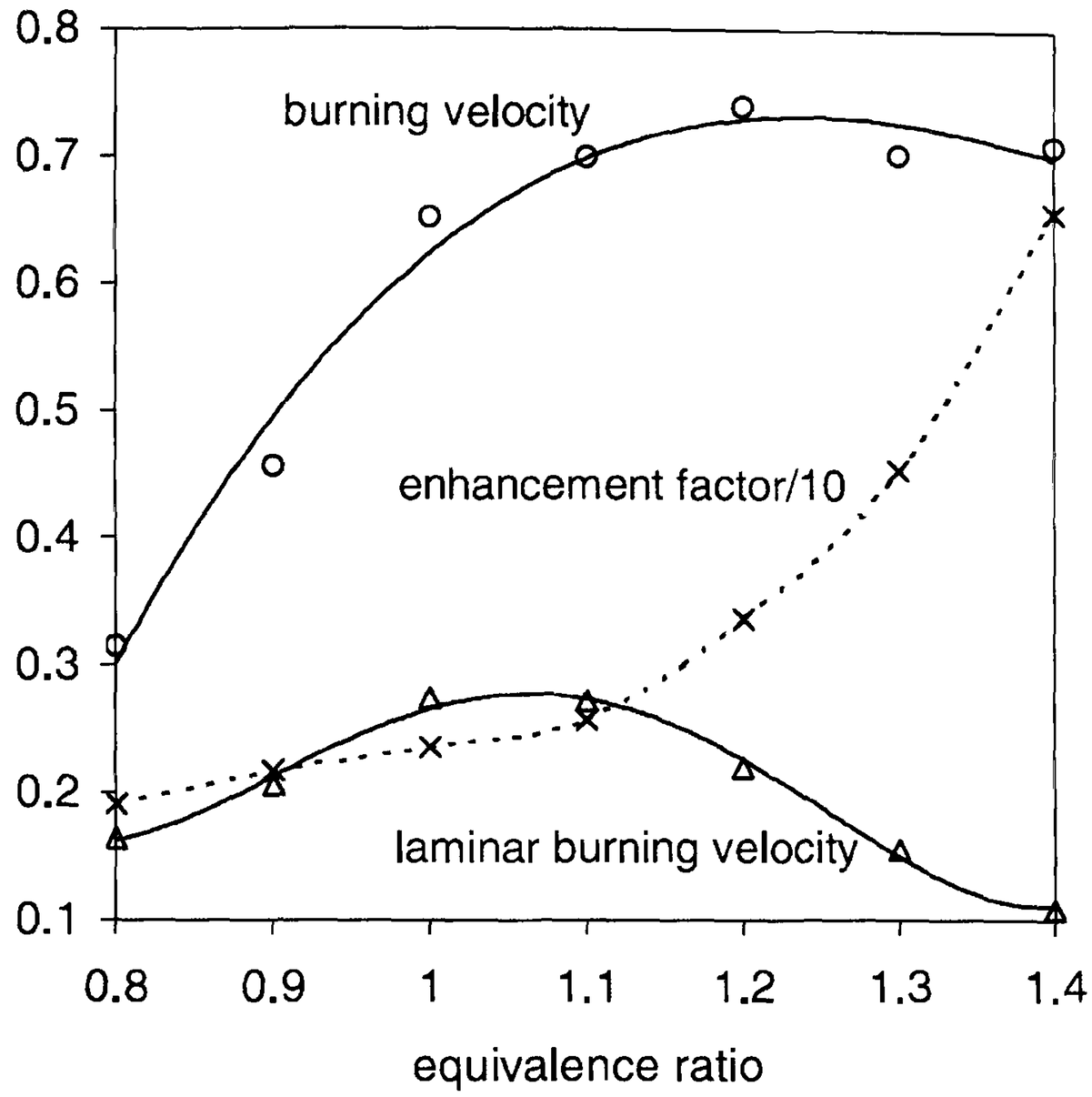

Figure 4.9: Variations of enhancement factor [dimensionless], burning velocity [m/s] and laminar burning velocity [m/s] with ϕ at 20 bar and 427 K for an iso-octane—air flame initially at 10 bar and 358 K. Reproduced from Al-Shahrany et al. [2005].

significant errors in the derived values of u_l. Heat transfer to the fans and other effects outside the field of view, coupled with application the rather complex correction for cellularity discussed above, mean that the values of u_l calculated by Al-Shahrany [2004] should naturally be treated with some caution.

The data of Ormsby [2005] and Al-Shahrany [2004] are compared at their only common condition, 10 bar and 358/360 K, in Figure 4.10. At this condition the agreement between the two data sets is good, especially considering the rather indirect analysis which must be used for double kernel deflagrations. A second correlation was developed using the combined data sets of Ormsby and Al-Shahrany in the range $\phi = 0.8$–1.2. As the combined data sets include a wider range of experimental measurements than the data of Ormsby taken on its own, this correlation encapsulates the effects of temperature, pressure and mixture strength. The constants for this correlation are given in Tables 4.2 and 4.3

Computer simulations of iso-octane—air flames [Muller et al., 1997], valid for stoichiometric and lean mixtures, and based on elementary reaction mechanisms comprising a few hundred reactions, have been used to determine values of the unstretched laminar burning velocity over a range of temperatures, pressures and lean or stoichiometric equivalence ratios. An asymptotic analysis [Peters and Williams, 1987] then provides the framework for an approximation formula for the laminar burning velocity Equations 4.9, 4.10, and 4.11, the constants of which are adjusted iteratively to minimise the difference between the approximation formula and the computed laminar burning velocity values. For iso-octane, the constants B, E, F, G, m and n have been assigned the values 3.8×10^7 bar, 20906 K, 29.26 m/s, -25.6 K, 0.5578 and 2.5214 respectively.

$$u_l = A(T_0) Y_F^m \frac{T}{T_0} \left(\frac{T_b - T_0}{T_b - T} \right)^n \tag{4.9}$$

$$P = B \exp\left(-\frac{E}{T_0} \right) \tag{4.10}$$

$$A(T_0) = F \exp\left(-\frac{G}{T_0} \right) \tag{4.11}$$

Here Y_f is the fuel mole fraction and T_0 is the inner layer temperature. The adiabatic flame temperature at chemical equilibrium T_b, is approximated for lean flames as a function of equivalence ratio by the following polynomial

$$T_b = aT_u + b + c\phi + d\phi^2 + e\phi^3 \tag{4.12}$$

where the coefficients a, b, c, d and e are assigned the values 0.61, 936.0 K, -1127 K, 5326 K and -3044 K respectively for iso-octane—air flames.

The four published and two new laminar burning velocity expressions are compared over a range of equivalence ratios in Figures 4.10 and 4.11. Also included in the figures are the experimental data of Ormsby and Al-Shahrany. Agreement between the expressions and measured data is good apart from for the correlation of Ryan and Lestz which is consistently low, and the correlation of Rhodes and Keck which appears to be inaccurate for rich mixtures.

Shown in Figures 4.12 and 4.13 are comparisons of the different laminar burning velocity expressions at 5 and 60 bar for different temperatures with a stoichiometric mixture. The two pressures were chosen to allow comparison first at a pressure close to atmospheric where none of the correlations are extrapo-

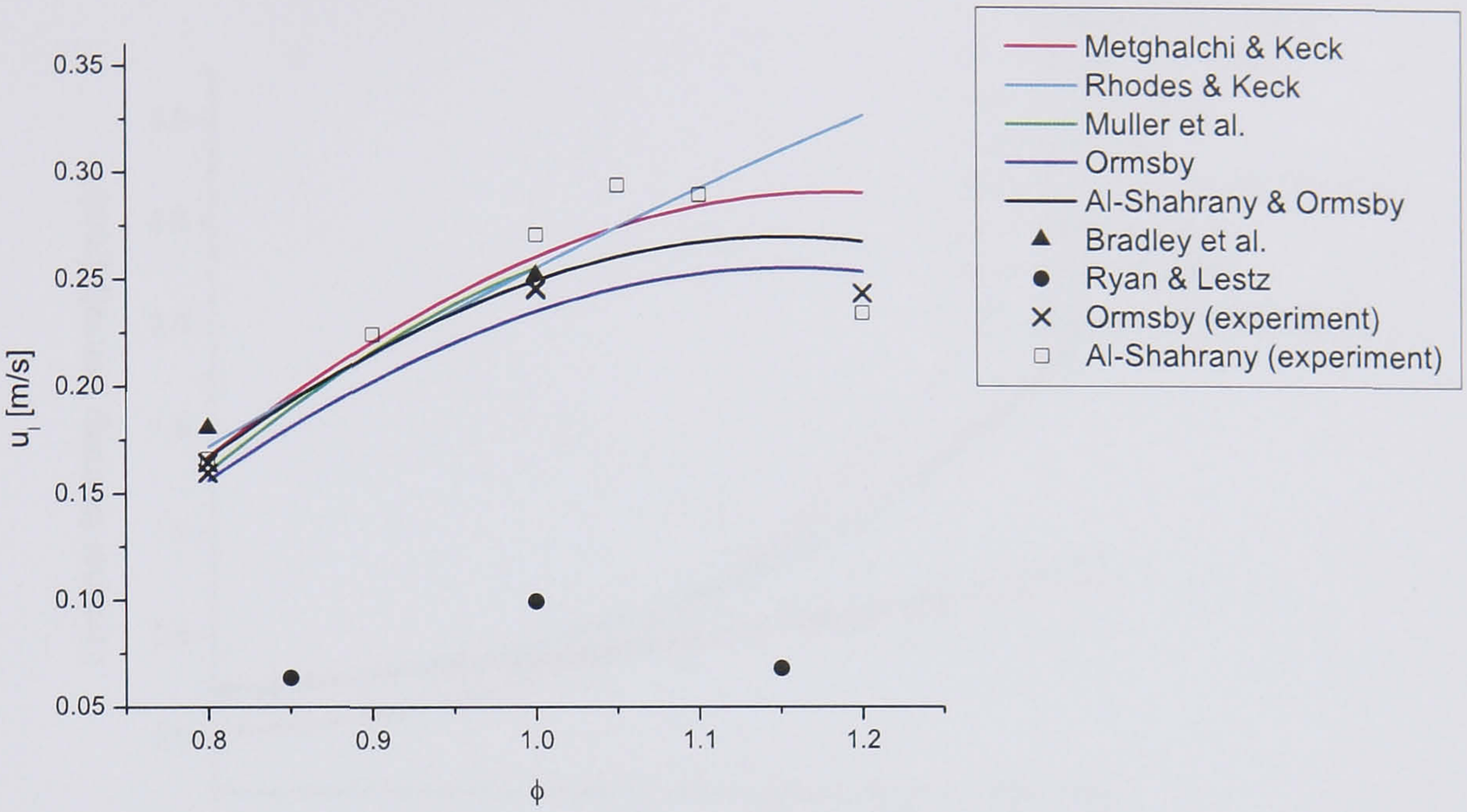

Figure 4.10: Laminar burning velocity expressions and experimental data compared at 10 bar and 360 K across a range of equivalence ratios. Note that the data of Al-Shahrany [2004] is at 358 K.

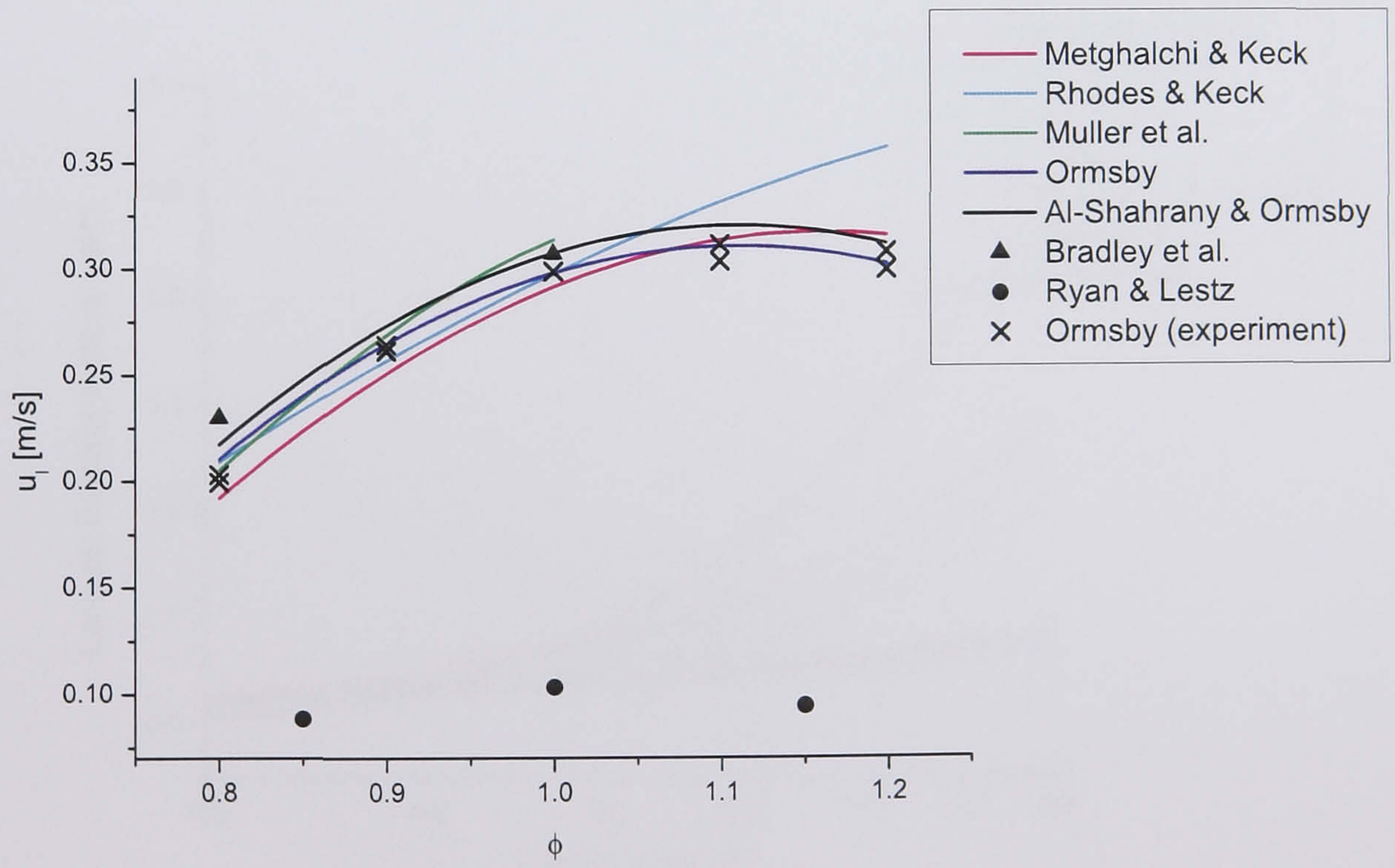

Figure 4.11: Laminar burning velocity expressions and experimental data compared at 5 bar and 360 K across a range of equivalence ratios.

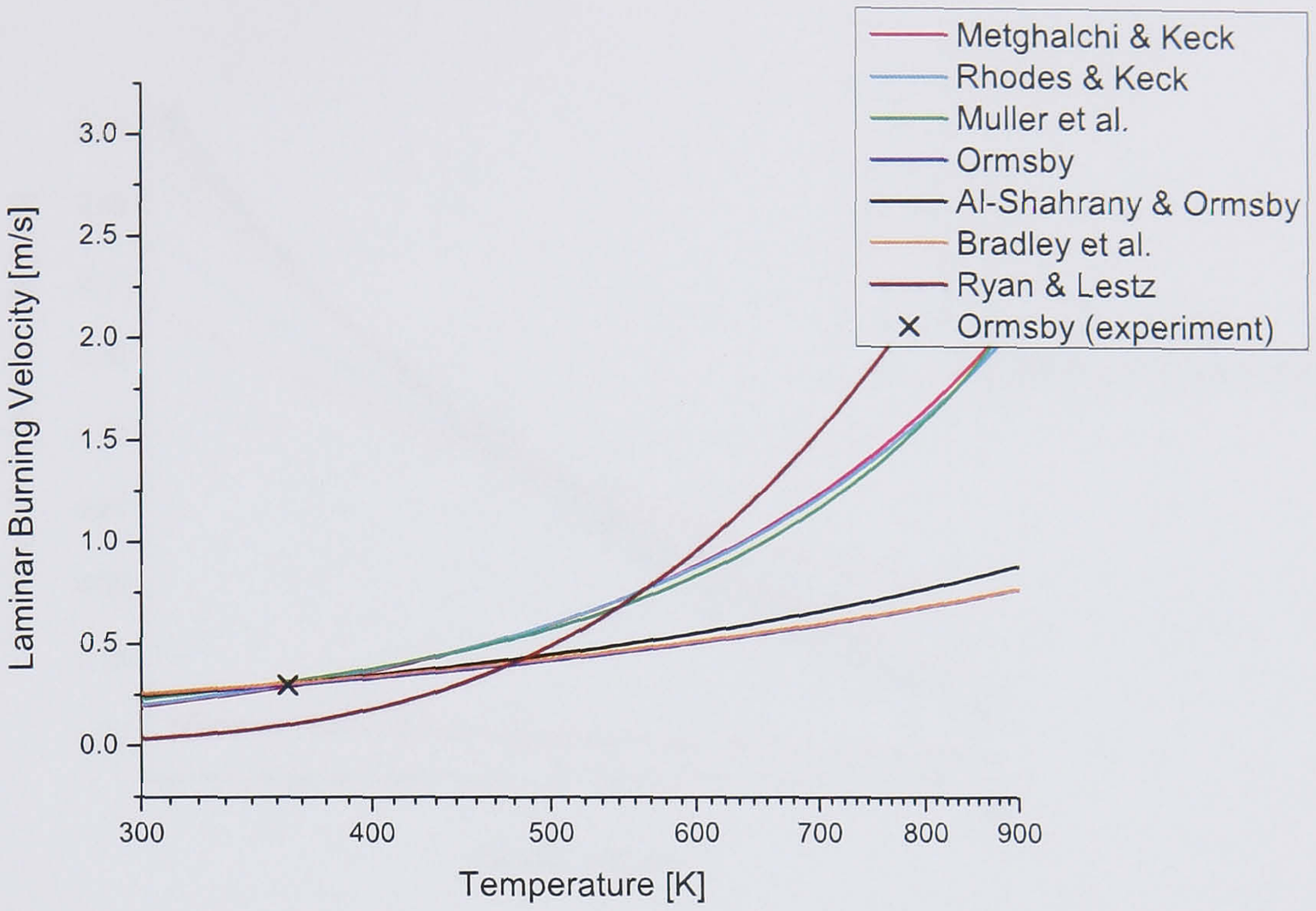

Figure 4.12: Laminar burning velocity expressions and experimental data compared at $\phi = 1$ and 5 bar across a range of temperatures.

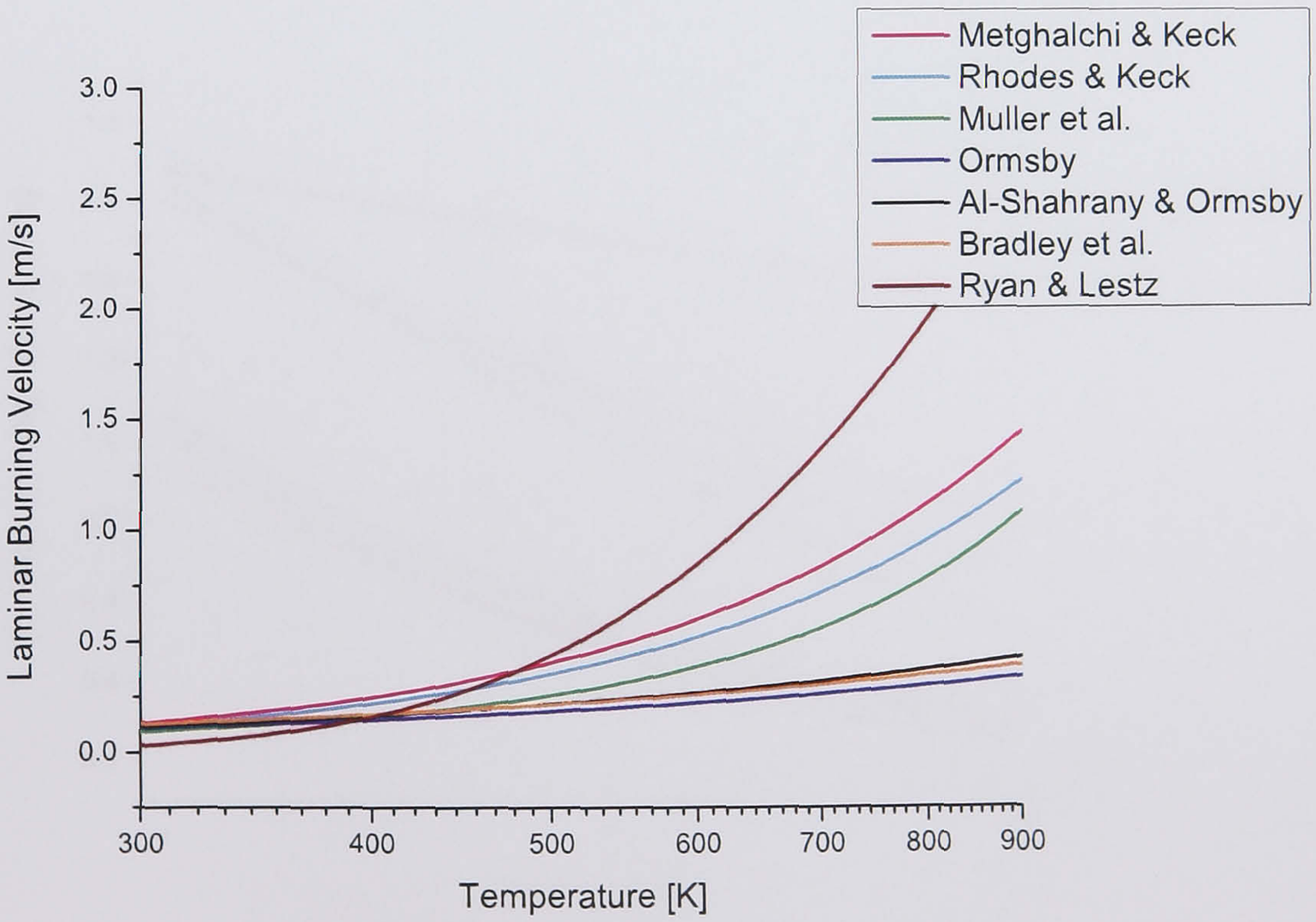

Figure 4.13: Laminar burning velocity expressions and experimental data compared at $\phi = 1$ and 60 bar across a range of temperatures.

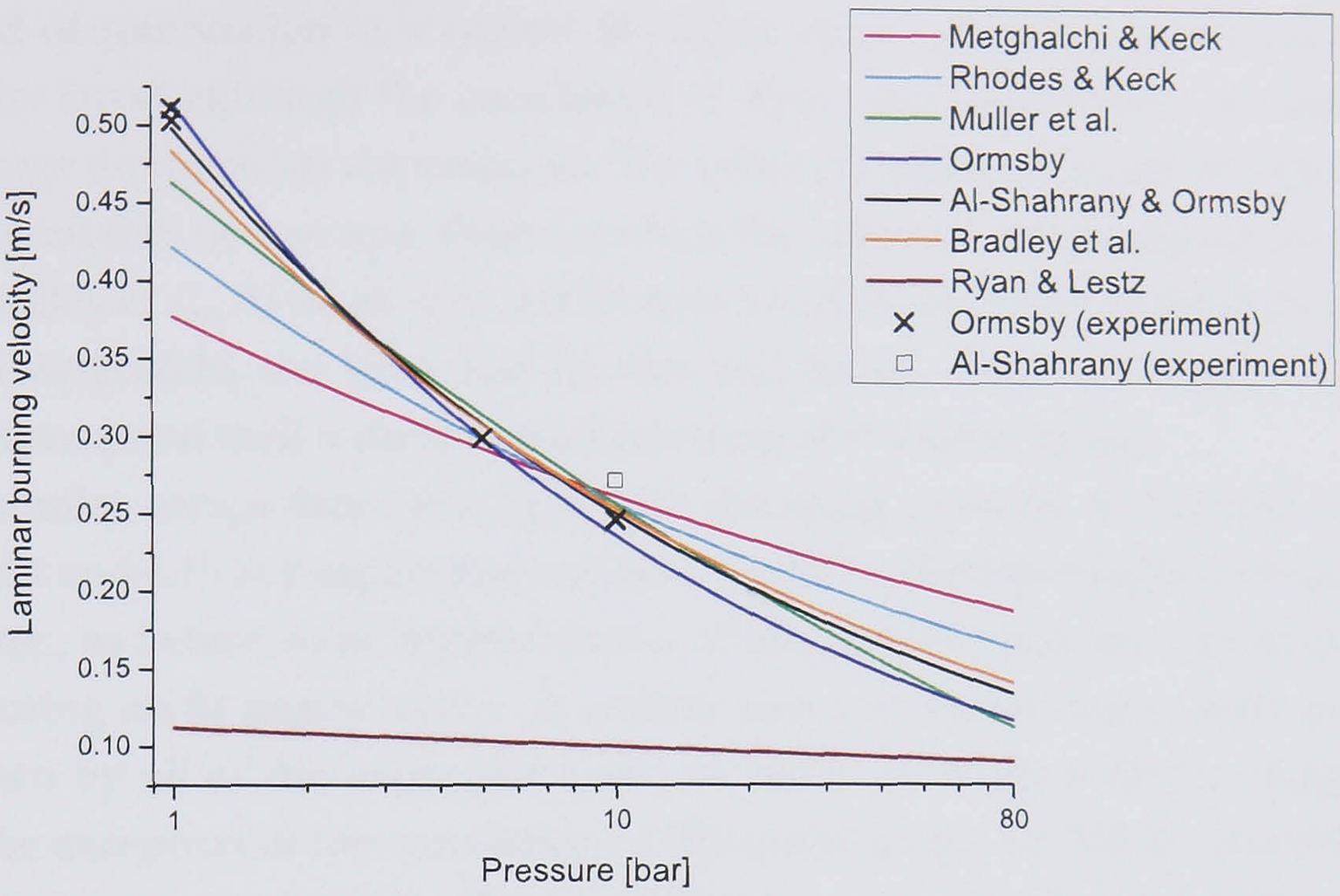

Figure 4.14: Laminar burning velocity expressions and experimental data compared at $\phi = 1$ and 360 K across a range of pressures.

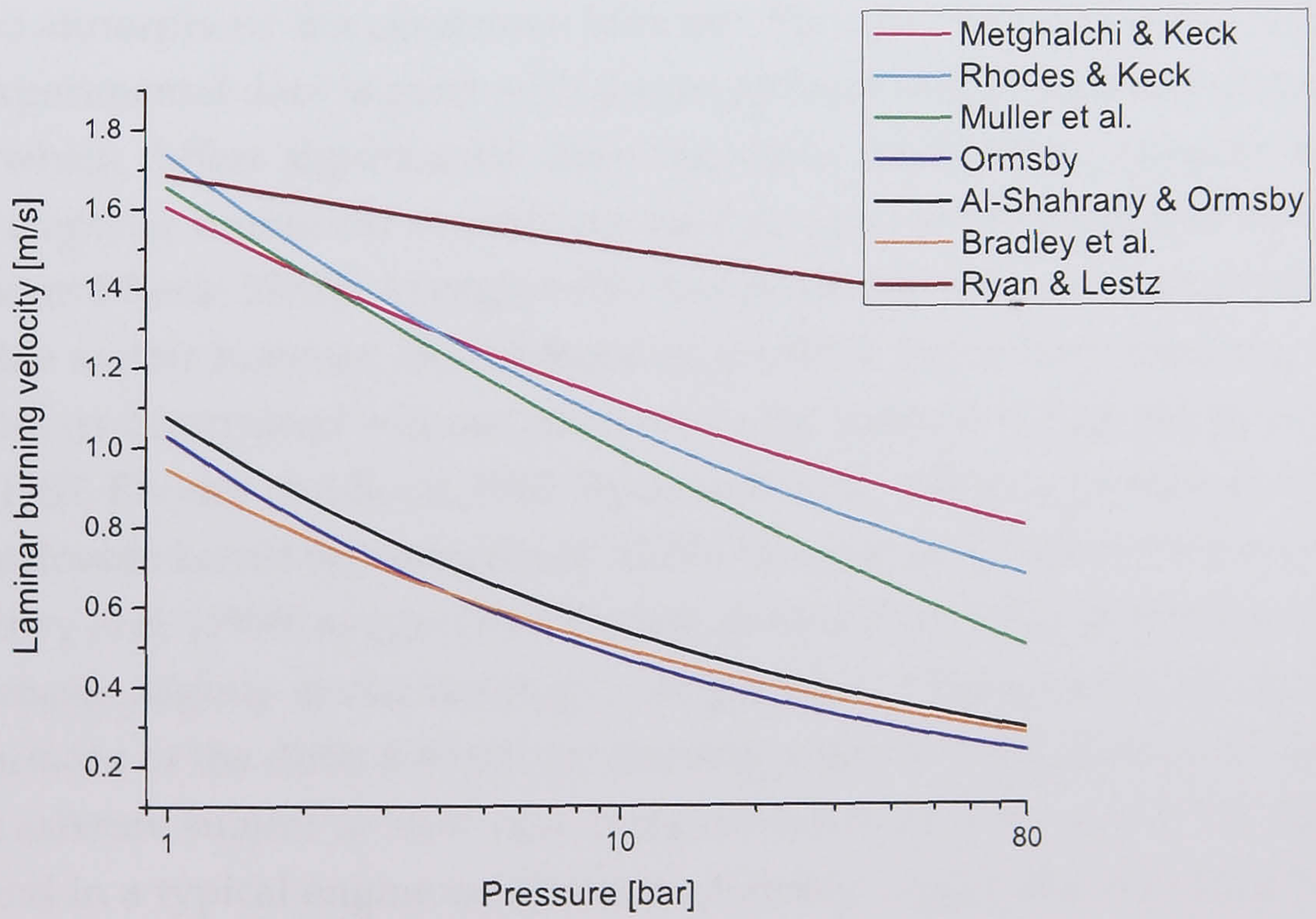

Figure 4.15: Laminar burning velocity expressions and experimental data compared at $\phi = 1$ and 700 K across a range of pressures.

lated and second at a pressure representative of the conditions present close to the end of combustion in a typical SI engine cycle. All the expressions exhibit a similar trend although the correlation of Ryan and Lestz shows an unrealistically large temperature dependence. The other correlations based on experimental data fall into two groups, those in which the effects of cellularity are accounted for (Bradley et al., Al-Shahrany and Ormsby) and those based on pressure records alone (Metghalchi and Keck and Rhodes and Keck). The calculations of Muller et al. correspond well with the measurements of the latter group.

A similar comparison, this time with changing pressure is displayed in Figures 4.14 and 4.15 at temperatures of 360 and 700 K. Here the highest temperature is chosen, as before, to be representative of the conditions at the end of combustion during an SI engine cycle. A similar trend of decreasing u_l with pressure is shown by all of the expressions and at 360 K all show a similar magnitude with the exception of the correlation of Ryan and Lestz. At 700 K the previously discussed grouping between those correlations determined without reference to the flame structure and those determined with reference to the flame structure is again evident.

In summary, all of the previously discussed expressions show the same trends for temperature, pressure and equivalence ratio. At temperatures and pressures close to atmospheric the agreement between the different expressions and available experimental data is good with the exception of the correlation of Ryan and Lestz which differs significantly from the other expressions, possibly because of the stepwise numerical procedures used to process the measured data [Metghalchi and Keck, 1982]. At engine-like temperatures and pressures there is considerable scatter between the different expressions and a clear tendency for the correlations determined without reference to the flame structure [Metghalchi and Keck, 1982, Rhodes and Keck, 1985, Ryan and Lestz, 1980] to give larger values of u_l. The double kernel experiments of Al-Shahrany et al. [2005] and the correlation of Bradley et al. [1998] suggest that the laminar burning velocity remains constant or decreases slightly under isentropic compression. Displayed in Figure 4.16 are comparisons of the different laminar burning velocity expressions for a stoichiometric mixture subject to isentropic compression from 1 bar and 300 K as would be found in a typical engine combustion chamber. Again the grouping between those expressions developed without reference to the flame structure and those formulated through inspection of schlieren images is clearly visible.

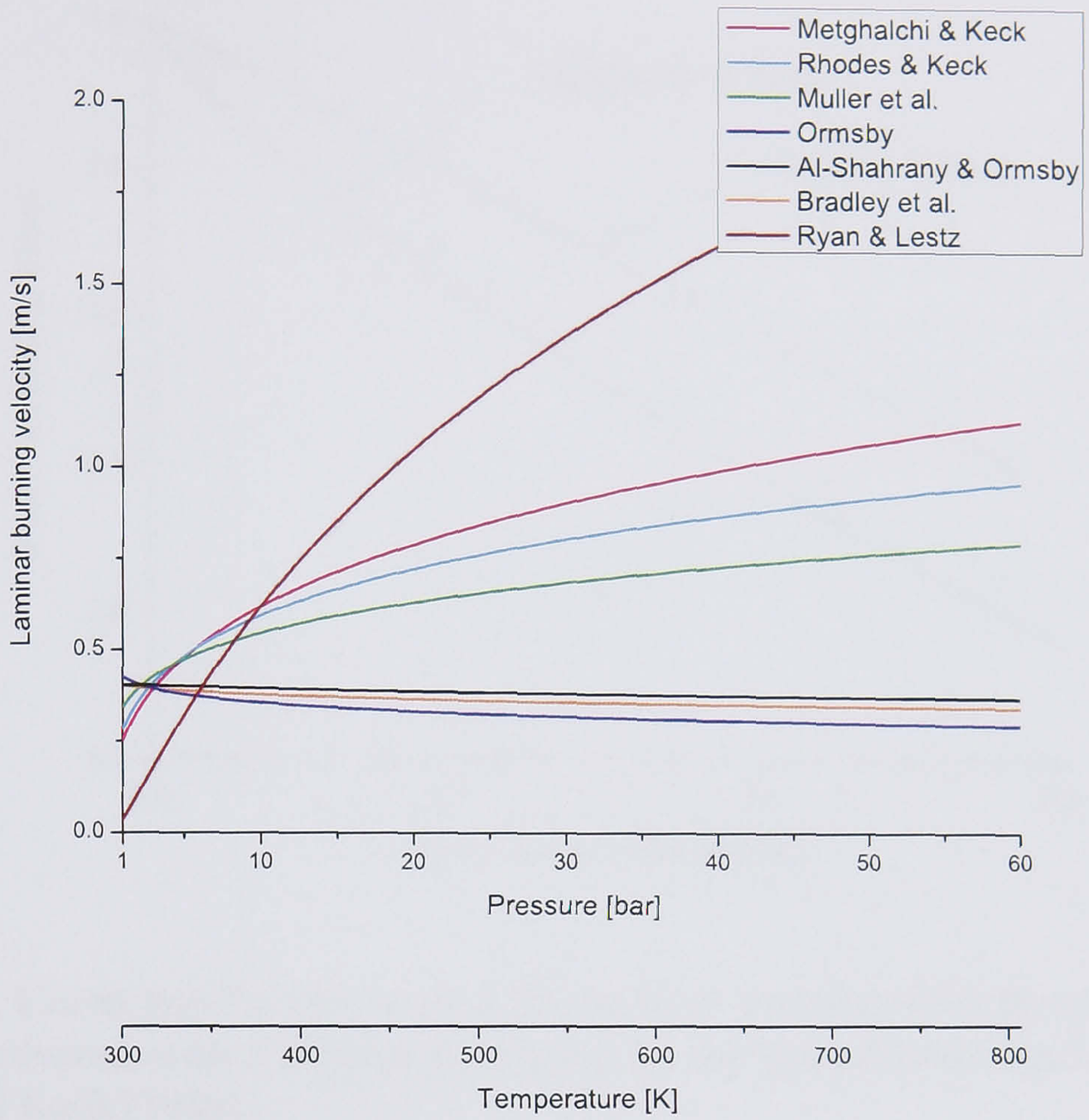

Figure 4.16: Laminar burning velocity expressions compared under isentropic compression from 1 bar and 300 K for a stoichiometric mixture.

4.5.6 The effect of diluent on the laminar burning velocity

The LUPOE family of engines are typically skip fired to enable the complete purging of all residual gas from the combustion chamber before ignition. Where residual gases are required, for example for studies of autoignition, they are supplied from bottles of gas and added to the incoming mixture as required [Smallbone, 2004]. All practical engines operate with some diluent present in the combustion chamber, either recirculated exhaust gas deliberately added to the incoming fuel—air mixture or combustion products remaining from a previous cycle. The influence of a diluent on the laminar burning velocity of a mixture has been studied by Metghalchi and Keck [1982] (Equation 4.14) and Rhodes and Keck [1985] (Equation 4.15) who published simple correction factors based on the mole fraction (Y_b) or mass fraction (x_b) which could be applied to a value of u_l for a pure

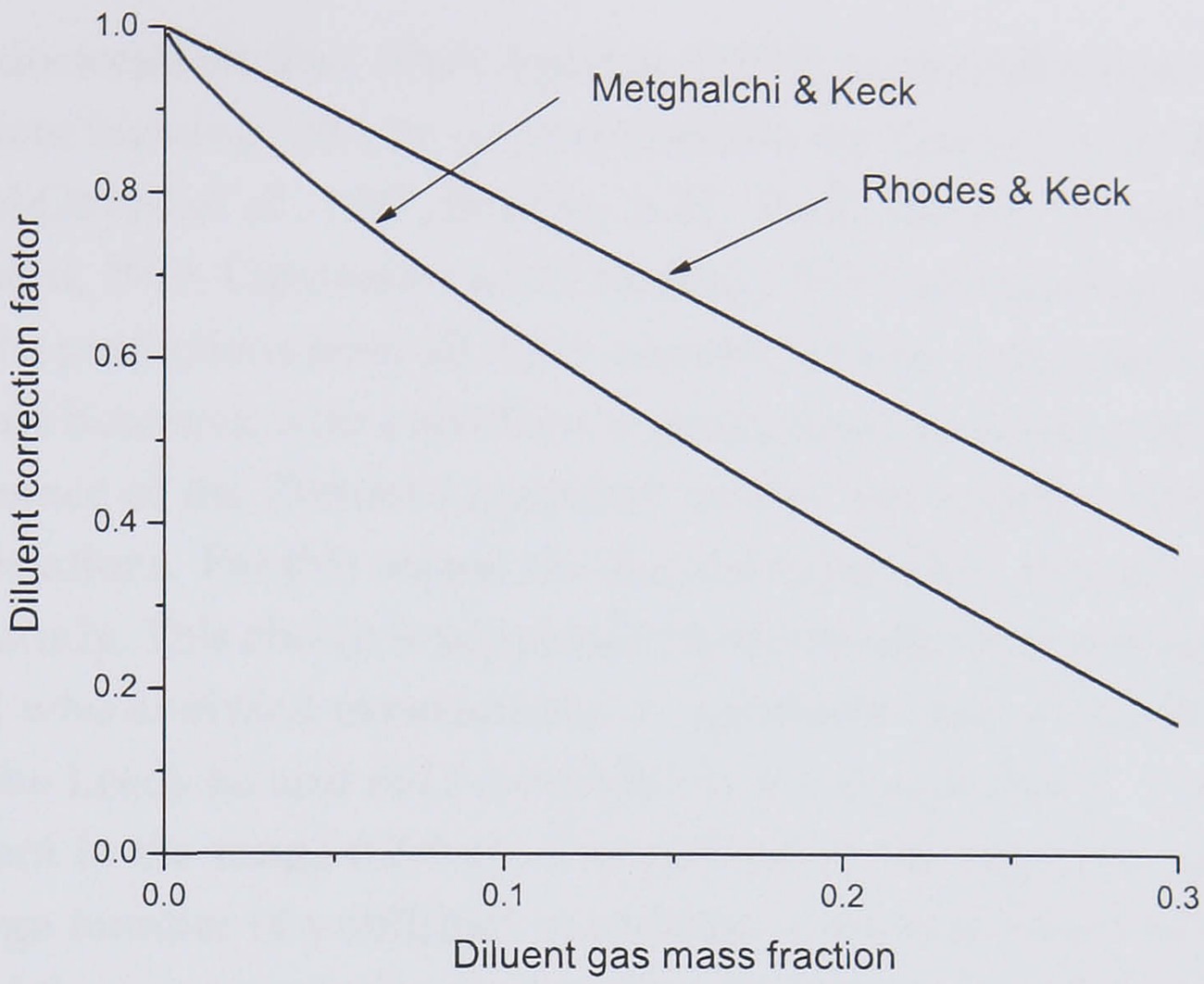

Figure 4.17: Correction factors to give the laminar burning velocity of a fuel—air mixture combined with a diluent published by Metghalchi and Keck [1982] and Rhodes and Keck [1985].

fuel—air mixture to give values of u_l in the presence of residual gas $u_{l,r}$.

$$u_{l,r} = u_l f_r \tag{4.13}$$

$$f_{r,\mathrm{RK}} = 1 - 2.1 x_b \tag{4.14}$$

$$f_{r,\mathrm{MK}} = 1 - 2.06 Y_b^{0.773} \tag{4.15}$$

Both diluent expressions have been included in the LUSIE code, their values and are compared in Figure 4.17. Apart from the difference at low concentrations of diluent, both expressions show a similar rate of change of u_l with the difference between the two expressions close to static for residual gas mass fractions greater than 0.1. Naturally, with very high concentrations of diluent, both expressions will become negative. Presumably at these concentrations a laminar flame will not ignite and the concept of a laminar flame speed becomes meaningless.

4.5.7 Turbulent burning velocity

During his doctorial studies, Abdi Aghdam [2003] compared the performance of three turbulent burning velocity (u_t) expressions, the Leeds *Ka* and *KaLe* correlations [Abdel-Gayed et al., 1987, Bradley et al., 1992] and the Zimont-Lipatnikov model [Zimont, 1979, Lipatnikov and Chomiak, 1997]. He concluded that the reliability of the predictions from all three expressions was comparable for different engine speeds however, with variations in equivalence ratio or compression ratio the performance of the Zimont-Lipatnikov model was superior to either the *Ka* or *KaLe* correlations. For this reason the Zimont-Lipatnikov model is adopted for the current study. This choice is supported by the review of Lipatnikov and Chomiak [2002] who analysed experimental u_t databases from a number of sources (including the Leeds *Ka* and *KaLe* correlations) and found that $u_t \sim u' Da^a$ where a is a constant in the range 0.2-0.44. Comparison of the experimental databases with the large number of published models for u_t revealed that only four could predict all of the experimentally observed trends in turbulent flame propagation, including the decrease in u_t with pressure. These four models were: the expression due to Zimont [1979]; an expression based on the G-equation developed by Peters [2000]; the pair-exchange model of Kerstein [1988] and the coherent flame model Duclos et al. [1993].

Zimont [1979] based his model on an assumption that the turbulent burning velocity of a flame surface element is given by the product of the local, quasi-laminar, burning velocity $u_{n,t}$ of a thickened flamelet, and the ratio of the wrinkled surface area of the thickened flamelet to the projected surface area normal to the direction of propagation:

$$u_{t,\infty} = u_{n,t} \overline{\left(\frac{\delta S}{\delta S_0} \right)} \tag{4.16}$$

where δS is the area of the thickened flamelet surface area and δS_0 is the area projected onto a plane normal to the propagation direction of the flame. By considering the condition whereby the local flame thickness expands with the entrainment of larger and larger vortices until an equilibrium is established between convection, conduction and chemical reactions, an expression for the local burning velocity was established. In this work, this expression is used for the fully developed turbulent burning velocity $u_{t,\infty}$ below:

$$u_{t,\infty} = A u' Da^{1/4} = A u'^{3/4} u_l \kappa^{-1/4} L^{1/4} \tag{4.17}$$

Here A is a constant, Da is the Damköhler number ($= \tau_L / \tau_c$ where $\tau_L = L/u'$ is the integral time scale and $\tau_c = u_l^2 / \kappa$ is the characteristic laminar chemical time scale) u' is the rms turbulent velocity and κ is the molecular thermal diffusivity. The original expression derived by Zimont was intended to represent the rate of turbulent mass burning u_{tr} rather than the rate of entrainment u_{te}. In the current LUSIE code it is used, with different values of A, to give predictions the fully developed values of both u_{tr} and u_{te} depending on whether the two or three-zone combustion model is employed.

Lipatnikov and Chomiak [1997] developed an expression for the developing turbulent burning velocity u_t using Equation 4.17. Lipatnikov and Chomiak accounted for the fact that in a real engine, for a significant portion of the cycle, the flame is not statistically stationary, rather the flame brush thickness is increasing and the flame is accelerating. They added a further term f_d to describe the development of the flame front as it is wrinkled by an increasing amount of the turbulent spectrum. The expression proposed for f_d by Lipatnikov and Chomiak is discussed in Section 4.5.8 along with expressions proposed by other authors. In addition to this, they reasoned that as $\lim_{u' \to 0} u_{t,\infty} = 0$, Zimont's original expression should be modified to include a laminar term to give accurate predictions in low turbulence situations.

Finally, Abdi Aghdam [2003] observed that as the flame approaches the wall the active flame surface area was reduced as parts of the flame brush contact the wall. This effect was accounted for by reducing the active spherical flame surface area predicted by the model by an experimentally derived factor. Given the form of Equations 4.2 and 4.3 this is mathematically equivalent to reducing the burning velocity. Here this effect is incorporated into the turbulent burning velocity expression proposed by Lipatnikov and Chomiak using a factor f_w, discussed further in Section 4.5.9, giving the final expression below:

$$u_t = (u_l + u_{t,\infty} f_d) f_w \tag{4.18}$$

In his original work, Zimont intended Equation 4.17 to predict the turbulent *reaction* burning velocity u_{tr} In this work, as with previous studies at Leeds, Equation 4.17, together with Equation 4.18, are used, with different values of A, to calculate values of both u_{te} for three-zone simulations and u_{tr} for two-zone simulations.

4.5.8 Turbulent flame acceleration

Combustion in an SI engine is a transient phenomenon. The flame kernel produced by the spark discharge is initially laminar-like. As it grows it becomes wrinkled by successively larger turbulent eddies, increasing its surface area, propagation velocity and brush thickness [Lancaster et al., 1976, Beretta et al., 1983, Abdel-Gayed et al., 1987, Lipatnikov and Chomiak, 2002]. This is known as flame development.

The flame acceleration aspect of flame development is particularly important for modelling SI engine combustion using a quasi-dimensional model. In order to account for this behaviour, Equation 4.18 includes a term f_d which encapsulates flame acceleration and may be interpreted either as the ratio u'_k/u' where u'_k is the effective rms turbulent velocity (see Section 1.5.4) or as a multiplying factor to $u_{t,\infty}$.

Verhelst [2005] identified several models for flame acceleration in the literature. These included an empirical expression given by Dai et al. [1995] used in the Ford Motor Company in-house code GESIM; an expression proposed by Wu et al. [1993] intended for use in fractal combustion models which considered the increasing range of turbulent scales available to wrinkle the flame as it grew (see also Baratta et al. [2006] for an alternative fractal development model); the expression proposed by [Lipatnikov and Chomiak, 1997] and an expression based the integral of the dimensionless turbulence PSD [Abdel-Gayed et al., 1987]. Apart from the models of Lipatnikov and Chomiak and Abdel-Gayed et al. which were already present in the code, all of the above models and one other, based on the work of Scott [1992] were added to the LUSIE code by the current author.

As pointed out by Verhelst, the expressions of Dai et al. (Equation 4.19) and Wu et al. (Equation 4.20) are quite similar and both predict $\lim_{r_f \to \infty} f_d = \infty$, i.e. a turbulent flame will accelerate indefinitely:

$$f_d = \left[1 - \exp\left(\frac{-r_f}{r_c}\right)\right]\left(\frac{r_f}{r_c}\right)^{1/3} \tag{4.19}$$

$$f_d = \left(\frac{r_f}{L}\right)^{1/3} \tag{4.20}$$

here r_f is the flame radius, L is the integral scale of turbulence and r_c is a "critical" radius, assumed to be of a similar magnitude to the integral scale.

Two acceleration expressions which have been previously employed in SI en-

gine simulations at Leeds are those due to Lipatnikov and Chomiak [1997] which was used in the study of Abdi Aghdam [2003] and a curve fit [Merdjani, 1996] to values of u'_k (see Section 1.5.4) which was used in the previous study by Cairns [2001]. Lipatnikov and Chomiak developed their expression by considering the development of the normal and tangential length scales of the propagating flame front, Σ and Λ respectively. They assumed that $u_t = u_{t,\infty}\delta S \approx \Sigma/\Lambda$ where δS is the relative increase of the flame surface area as compared to the laminar case. By assuming that Σ is controlled by turbulent diffusion in much the same way as the flame brush thickness (see Section 4.5.9) and that a regime of fully developed Λ occurs much faster than a regime of fully developed Σ they derived the following expression

$$f_d = \left\{1 + \frac{\tau'}{t}\left[\exp\left(-\frac{t}{\tau'}\right) - 1\right]\right\}^{1/2} \tag{4.21}$$

Here τ' is a turbulent time scale which, by application of the k-ε turbulence model constants used by Lipatnikov and Chomiak, is given by

$$\tau' = \frac{1}{u'^2}\lim_{t\to\infty} D_t(t) = \frac{D_{t,0}}{u'^2} = 0.55\tau_L \tag{4.22}$$

where u' is the rms turbulent velocity, D_t is the transient turbulent diffusivity, $D_{t,0}$ is the asymptotic turbulent diffusivity predicted, for example by the k-ε turbulence model and τ_L is the integral time scale ($= L/u'$).

The integral of the dimensionless PSD of turbulence [Abdel-Gayed et al., 1987] to give a value of u'_k, the *effective* rms turbulent velocity appears to have been introduced by Merdjani [1996] as an alternative to the original u'_k curve fit proposed by Abdel-Gayed et al. [1987]. Although this particular fit is mentioned by Cairns [2001], Merdjani does not include it in his LUSIE manual. It would appear that the curve fit is implemented for computational convenience, avoiding the need to calculate an integral numerically at run time. In its dimensionless form it is equal to

$$f_d = 1 - \exp\left(-0.0113\left[\log t + 3\right]^{3.7}\right) \tag{4.23}$$

The dimensionless PSD correlation $\bar{S}(\bar{F})$ used in the derivation of Equation 4.23 was based on LDA measurements of velocity in single vessel, the Leeds Mk I fan stirred bomb. Here $\bar{F}$ is dimensionless frequency ($= f\tau_L$). Scott [1992] later generated an improved correlation based on the velocity measurements of many authors in locations as diverse as tidal channels, wakes behind cylinders and grid turbulence. This correlation employed a dimensionless wave number $\bar{k}_\eta = k\eta$

where k is the wave number and η is the Kolmogorov length scale [Scott, 1992, Haq, 1998]

$$\bar{S}(\bar{k}_\eta) = \frac{0.01668Re_\lambda^{2.5} + 3.74Re_\lambda^{0.9} - 70Re_\lambda^{-0.1}}{1 + \left(0.127Re_\lambda^{1.5}\bar{k}_\eta\right)^{5/3} + \left(1.15Re_\lambda^{0.622}\bar{k}_\eta\right)^4 + \left(1.27Re_\lambda^{0.357}\bar{k}_\eta\right)^7} \tag{4.24}$$

where Re_λ is the turbulent Reynolds number defined using the Taylor length scale $Re_\lambda = u'\lambda/\nu$ and Re_λ and λ are related to the integral scale by $\lambda/L = A/Re_\lambda$ [Tennekes and Lumley, 1972]. The Kolmogorov scale η may be calculated using $\eta = LRe_L^{-3/4}$ [Tennekes and Lumley, 1972]. The constant A is typically assigned the value 15 [Tennekes and Lumley, 1972] which is in line with the work of Scott who found $A = 16 \pm 1.5$. Further discussion on turbulence relationships can be found in Section 1.3.7.

A wave number k $(= f/c)$ denotes a number of cycles per unit length and is defined as the quotient of a frequency f and a speed c. Given this definition it is possible to define a wave number relevant to the propagation of a turbulent flame either in terms of a time elapsed since ignition $k = 2\pi/st$ where $s = u'\sqrt{8/\pi}$ [Abdel-Gayed et al., 1987] or a characteristic flame size ℓ which may be either a radius or a diameter, $k = 2\pi/\ell$, hence

$$\bar{k}_\eta(t) = \frac{2\pi}{tu'\sqrt{8/\pi}}\eta = \frac{\pi^{3/2}}{tu'\sqrt{2}}\eta \tag{4.25}$$

or

$$\bar{k}_\eta(\ell) = \frac{2\pi}{\ell}\eta \tag{4.26}$$

For environments with statistically stationary turbulence, for example a fan stirred bomb, a value of f_d for a given time or characteristic length can be calculated with a simple integration of Equation 4.24

$$f_d = \left[\frac{\sqrt{A}}{Re_\lambda}\int_{\bar{k}_\eta}^{\infty}\bar{S}(\bar{k}_\eta)\,\mathrm{d}\bar{k}_\eta\right]^{1/2} \tag{4.27}$$

In an engine the turbulence is decaying and the integral length scale is a function of the piston position hence the former assumption of stationary turbulence is no longer valid. This situation requires that Equation 4.27 is calculated as a sum of contributions from previous time steps, taking into account the changing u' and L. Numerically in the LUSIE code the value of f_d at the n-th time step

(where $n > 1$) is calculated using the following sum

$$f_{d,n} = \left[\sum_{i=2}^{n} \int_{\bar{k}_{\eta,i}}^{\bar{k}_{\eta,i-1}} \frac{\sqrt{A}}{Re_\lambda} \bar{S}(\bar{k}_\eta)\, \mathrm{d}\bar{k}_\eta \right]^{1/2} \tag{4.28}$$

where values of $\bar{k}_\eta$ at the n-th time step are calculated using

$$\bar{k}_{\eta,n}(\ell) = \left[\sum_{i=1}^{n} \frac{1}{\bar{k}_\eta(\Delta\ell)} \right]^{-1} \tag{4.29}$$

if f_d is evaluated using a characteristic flame length or

$$\bar{k}_{\eta,n}(t) = \left[\sum_{i=1}^{n} \frac{1}{\bar{k}_\eta(\Delta t)} \right]^{-1} \tag{4.30}$$

if f_d is evaluated using the time elapsed since ignition. Here $\Delta\ell = \ell_i - \ell_{i-1}$ and $\Delta t = t_i - t_{i-1}$

At the first time step the upper limit of the integral of the PSD is infinite hence

$$f_{d,n=1} = \left[\int_{\bar{k}_{\eta,i=1}}^{\infty} \frac{\sqrt{A}}{Re_\lambda} \bar{S}(\bar{k}_\eta)\, \mathrm{d}\bar{k}_\eta \right]^{1/2} \tag{4.31}$$

As the value of $\bar{S}(\bar{k}_\eta)$ is effectively zero for large $\bar{k}_\eta$ this is achieved in the code by setting the upper limit of the integral to a number chosen to be large enough such that any further increase does not change the result of the integration.

The integral in Equations 4.28 and 4.31 is evaluated iteratively using Simpson's rule with the step size halving between iterations. When the error between two consecutive iterations falls below a specified tolerance the evaluation is judged to be accurate and the calculation halts.

The curves plotted in Figures 4.18, 4.19 and 4.20 compare the evolution of f_d with crank angle, dimensionless time (t/τ_L) and dimensionless distance (r_f/L), calculated using Equations 4.19, 4.20, 4.21, 4.23 and 4.28 during the simulation of a middle cycle of the LUPOE1-D engine operating at the 1500 rpm base condition. Regardless of the abscissa used there is little difference in the curves produced by any of the equations based on the integral of the turbulence PSD (Equations 4.23 and 4.28) although the expression proposed by Scott gives higher values than the curve fit of Merdjani [1996]. Despite being derived from a very different premise,

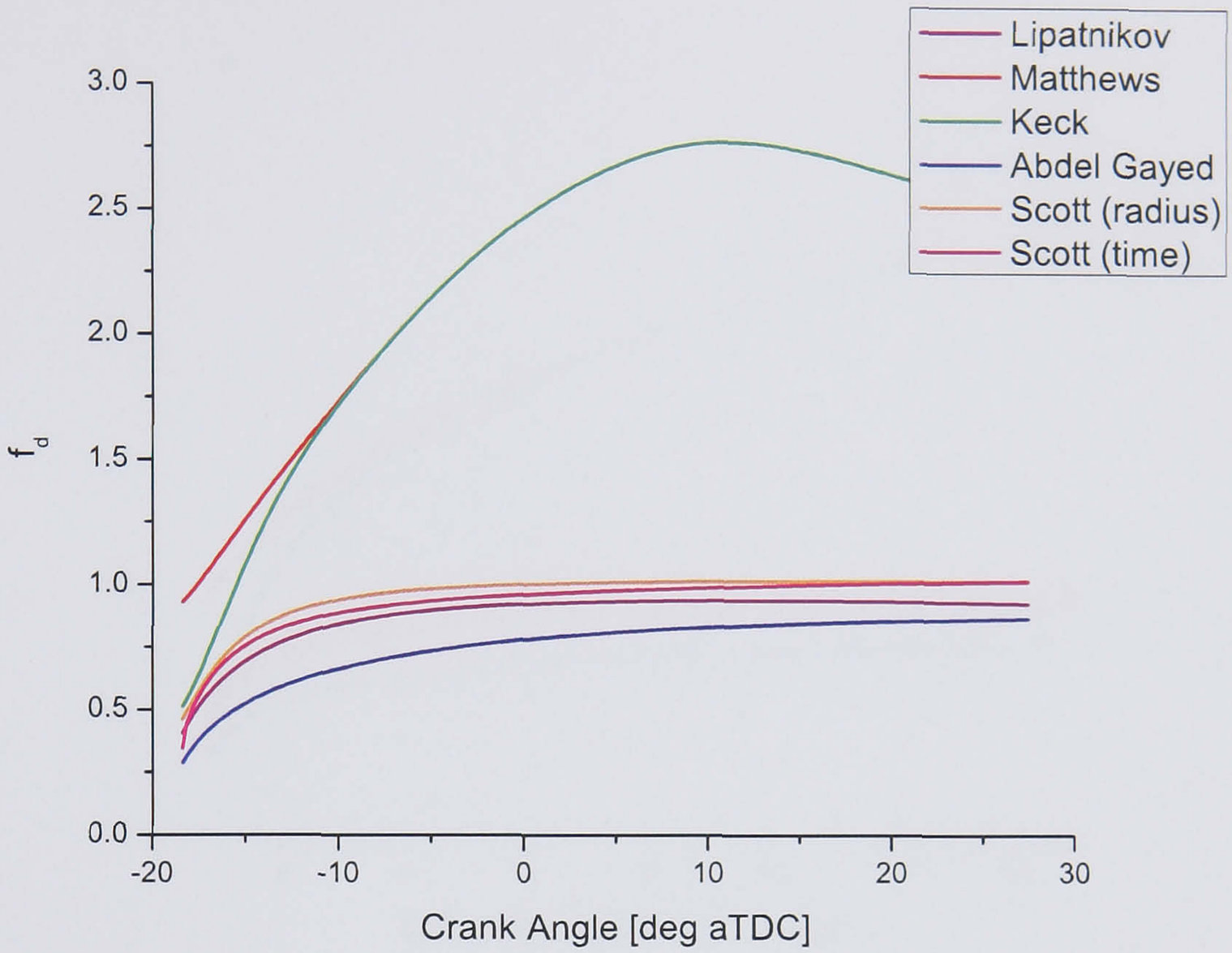

Figure 4.18: LUSIE predicted flame development models compared against crank angle for a typical LUPOE1-D 1500 rpm base condition cycle.

the expression of Lipatnikov and Chomiak is remarkably similar to the family of u'_k expressions. The expressions of Dai et al. and Wu et al. both give much higher values of f_d than the previously discussed expressions. This is likely to be due to the value of C_L (Equation 4.38) used to calculate the integral scale. In the later stages of the simulation the value of f_d calculated using Equations 4.19 and 4.20 begin to fall. This is clearly non-physical and is caused by the assumption that L scales linearly with h_c.

4.5.9 Flame-wall interaction

During the final stages of combustion in an SI engine as the flame approaches the walls the active flame surface area decreases as the wrinkled flame front is truncated by the walls. This also occurs where the flame contacts the head and piston, as well as the cylinder bore. In reality, even flames in the LUPOE1-D engine, which possesses a disc geometry combustion chamber with little large scale gas motion, are not spherical [Cairns, 2001], hence the flame does not meet the

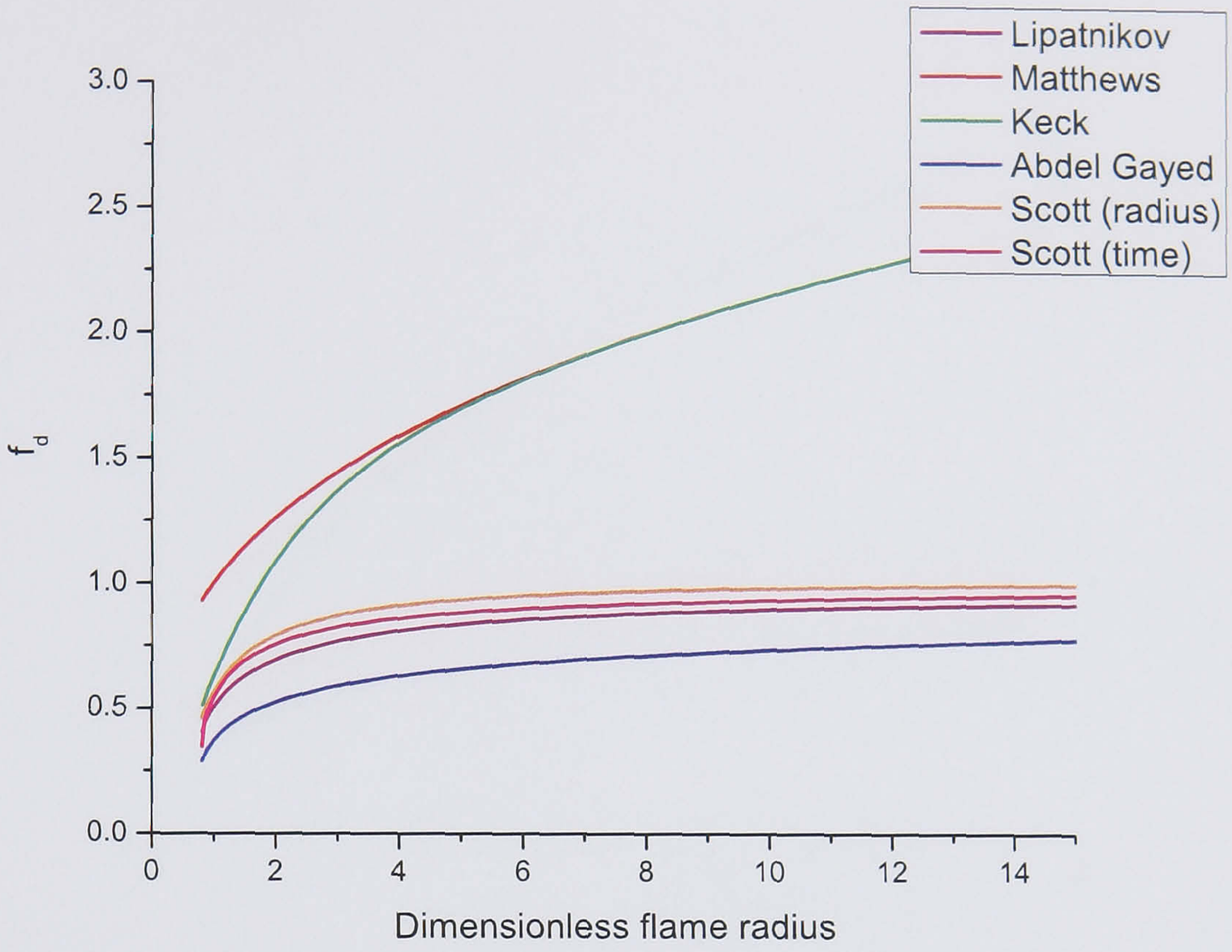

Figure 4.19: LUSIE predicted flame development models compared against radius for a typical LUPOE1-D 1500 rpm base condition cycle.

walls evenly. Contact with the walls causes the rate of heat release to fall until finally the entire flame surface is quenched and the combustion ends. When SI engine pressure traces are processed to give the mass fraction burnt at a particular crank angle (for example using the method of Rassweiler and Withrow [1938] or LUSIEDA, see Section 3.2.3) this effect is evident in the rounding of the S-shaped curve as the flame approaches the wall. When engine simulation is undertaken using the two-zone model it is important that a submodel is present which accounts for the reduction in burning rate as the flame approaches the wall. Without such a feature combustion ends abruptly (especially in the case of central ignition) and the resulting pressure curve lacks the rounding in the region of peak pressure exhibited by a real engine. This is clearly exhibited in the pressure curves shown in Figure 5.57. As the governing equations for the three-zone model (Equations 4.4 and 4.5) naturally give rise to an exponential decay in the rate of burning during the final stages of combustion [Heywood, 1988], predictions of mass fraction burnt and pressure will be of the correct form even without

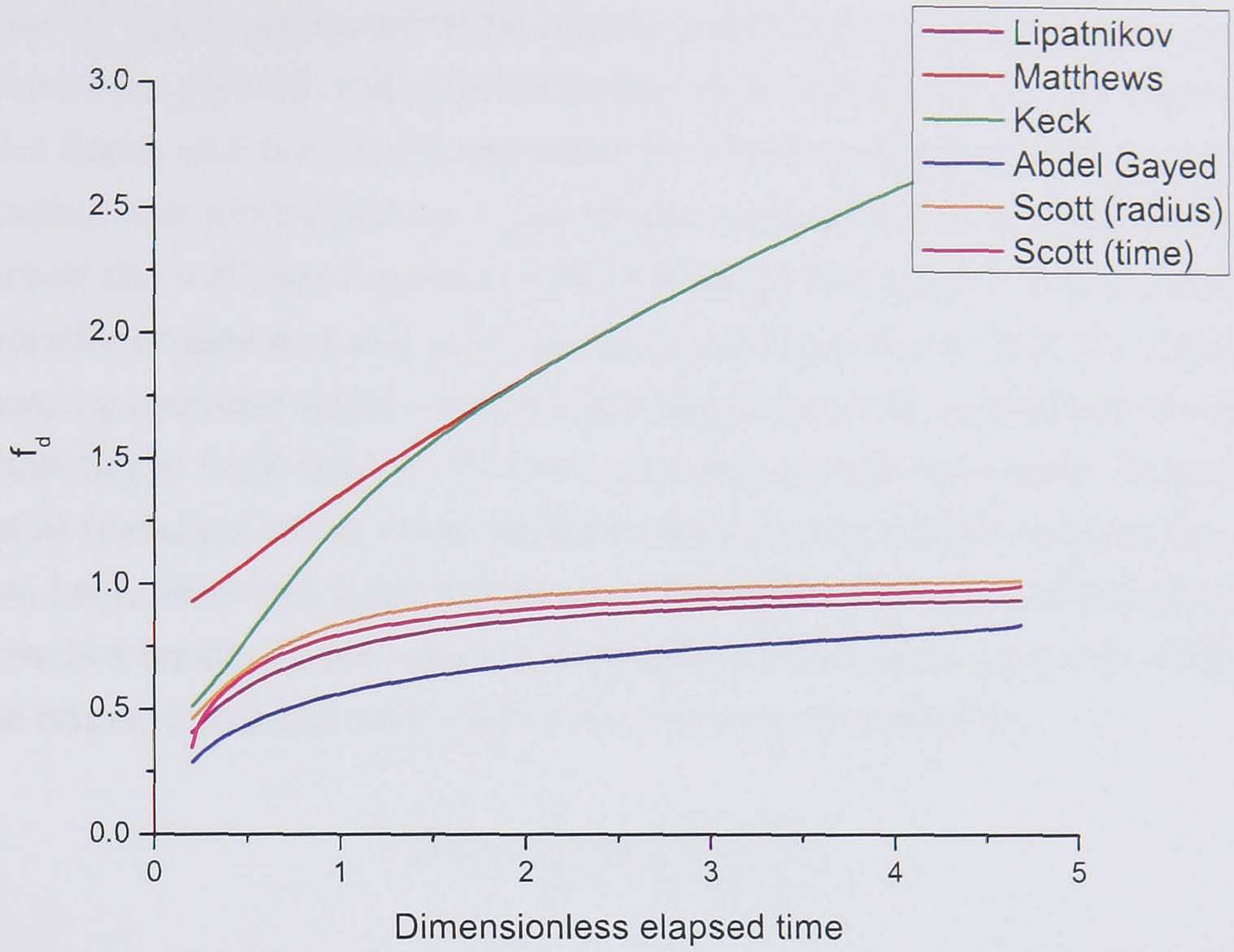

Figure 4.20: LUSIE predicted flame development models compared against time for a typical LUPOE1-D 1500 rpm base condition cycle.

the inclusion of a flame-wall interaction submodel. The results of Abdi Aghdam [2003] show however that the entrainment front does decelerate as it comes in contact with the wall. For realistic predictions then of the position of the entrainment front (three-zone model) or burnt gas front (two-zone model), some form of flame-wall interaction submodel must be included in order to model the deceleration of the flame in the wall region.

In a previous version of LUSIE [Abdi Aghdam, 2003] the deceleration of the flame in the wall vicinity was accounted for using the active perimeter fraction (APF) of the flame derived from natural light images of flame propagation viewed along the bore axis in LUPOE1-D

$$f_{d,\mathrm{APF}} = p_a / p_t \tag{4.32}$$

where p_a is the "active" flame perimeter in a particular image, the perimeter which is not in contact with the cylinder bore; and p_t is the total flame perimeter, the sum of the active perimeter and the perimeter which has been quenched after

contact with the cylinder bore [Abdi Aghdam, 2003].

Values of $f_{d,\mathrm{APF}}$ appeared to be largely independent of the engine operating condition when plotted with dimensionless flame radius ($= r_f/r_b$) where r_f and r_b are the flame and bore radii respectively. The burning velocity at a particular flame radius was multiplied by $f_{d,\mathrm{APF}}$ to give a suitable deceleration as the flame approached the wall, see Equation 4.18. Although this approach was effective for the particular engine tested it is not general as it does not include the flame brush thickness, a parameter which would affect the distance from the bore at which the truncation flame front begins. To overcome this deficiency a new dimensionless expression (detailed below) was added to the existing LUSIE code by the author.

It has been observed [Lipatnikov and Chomiak, 2000, and references therein] that there is a tendency for measured profiles of the mean progress variable $\bar{c}$ to collapse onto a universal curve which is well approximated by

$$\bar{c}(x) = \frac{1}{2}\mathrm{erfc}\left(\frac{x - x_0}{\delta_t(t)}\right) \tag{4.33}$$

where x_0 is the position of the centre of the flame ($\bar{c}(x) = 0.5$), δ_t is the flame brush thickness and $\mathrm{erfc}(x)$ is the complementary error function. Experimental data points from a wide range of conditions and values of $\bar{c}(x)$ generated with Equation 4.33 are compared in Figure 4.21. The heat release rate at a particular position x' is proportional to $|\partial\bar{c}(x')/\partial x'|$. When in the case of a planar flame the profile of $\left|\partial c(\bar{x}')/\partial x'\right|$ is truncated by a wall located at x_w, shown in Figures 4.22 and 4.23, the rate of combustion is decreased by the following factor

$$f_w = \int_{-\infty}^{x_w} \left|\frac{\partial\bar{c}(x')}{\partial x'}\right| \mathrm{d}x' = \mathrm{erf}\left(\frac{x_w - x'}{\delta_t(t)}\right) \tag{4.34}$$

In the coordinate system relevant to engine combustion Equation 4.34 can be recast as [Abdi Aghdam et al., 2007]

$$f_w = \frac{1}{2}\mathrm{erf}\left(\frac{r_b - r_f}{\delta_t(t)}\right) \tag{4.35}$$

where r_b is the bore radius and r_f is the flame radius.

In order to use Equation 4.35 in a LUSIE simulation a value of the flame thickness δ_t is required.[5] This may be approximated for the three-zone model as the

[5]The flame brush thickness has a tendency to decrease in the presence of a wall as shown in Section 5.3.4. The flame brush thickness required by Equation 4.34 is the "unconstrained" flame

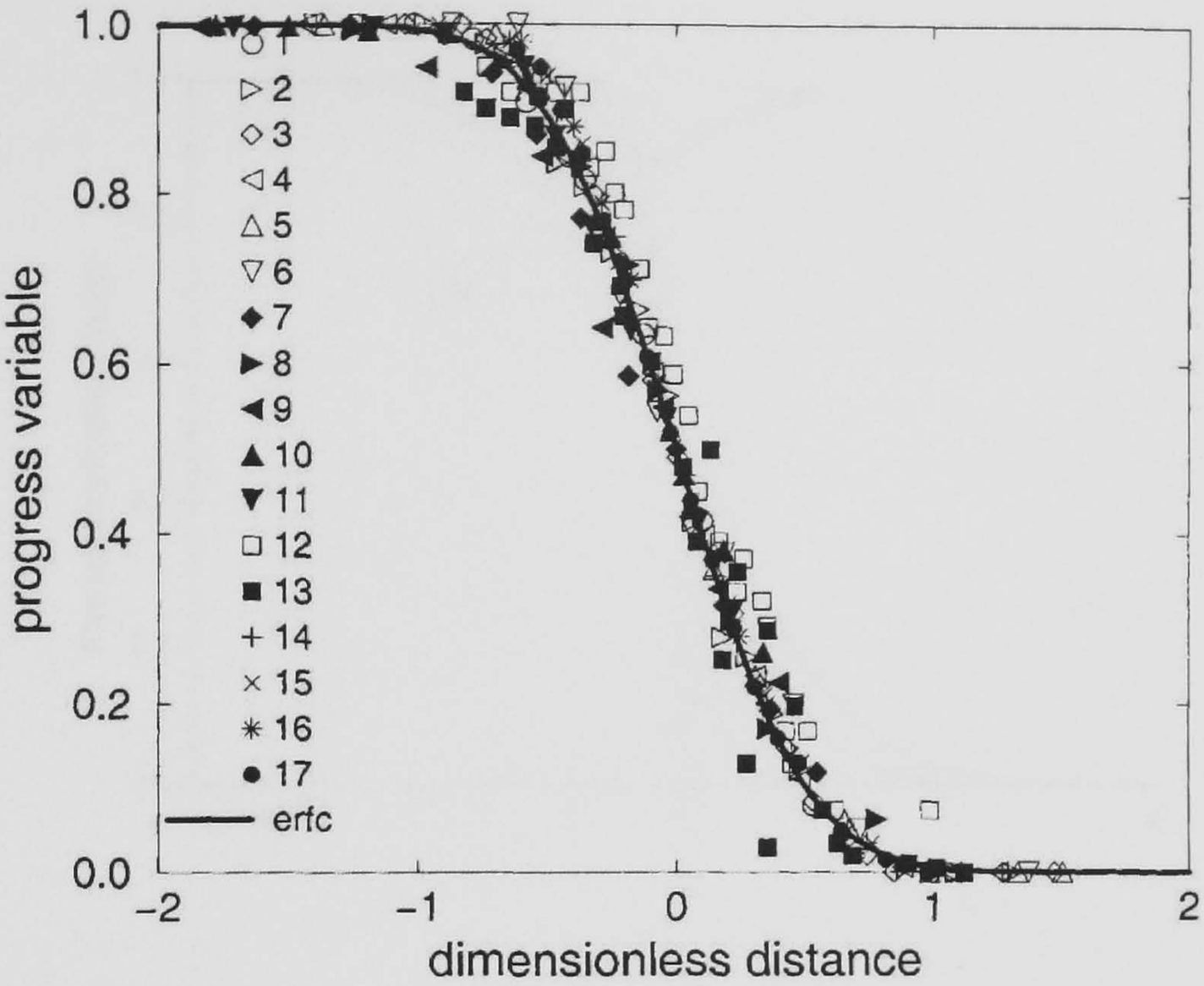

Figure 4.21: Mean progress variable profiles normalised with flame brush thickness [Lipatnikov and Chomiak, 2002]. The solid curve corresponds to Equation 4.33, the symbols show experimental data gathered by a number of authors. The key remains unchanged from the original publication.

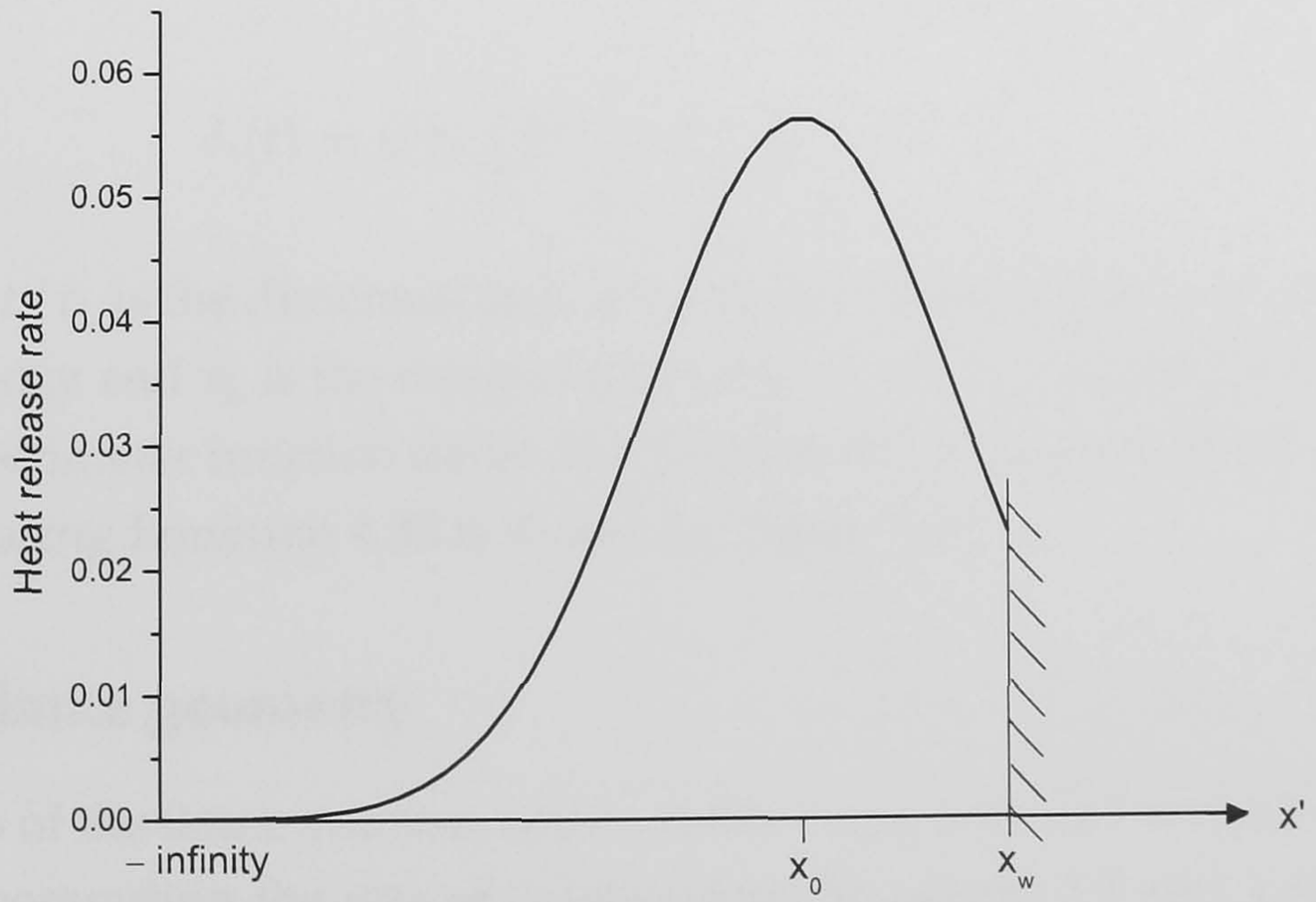

Figure 4.22: The profile of the mean heat release rate $|\partial \bar{c}(x')/\partial x'|$ given by Equation 4.33 truncated in the presence of a wall.

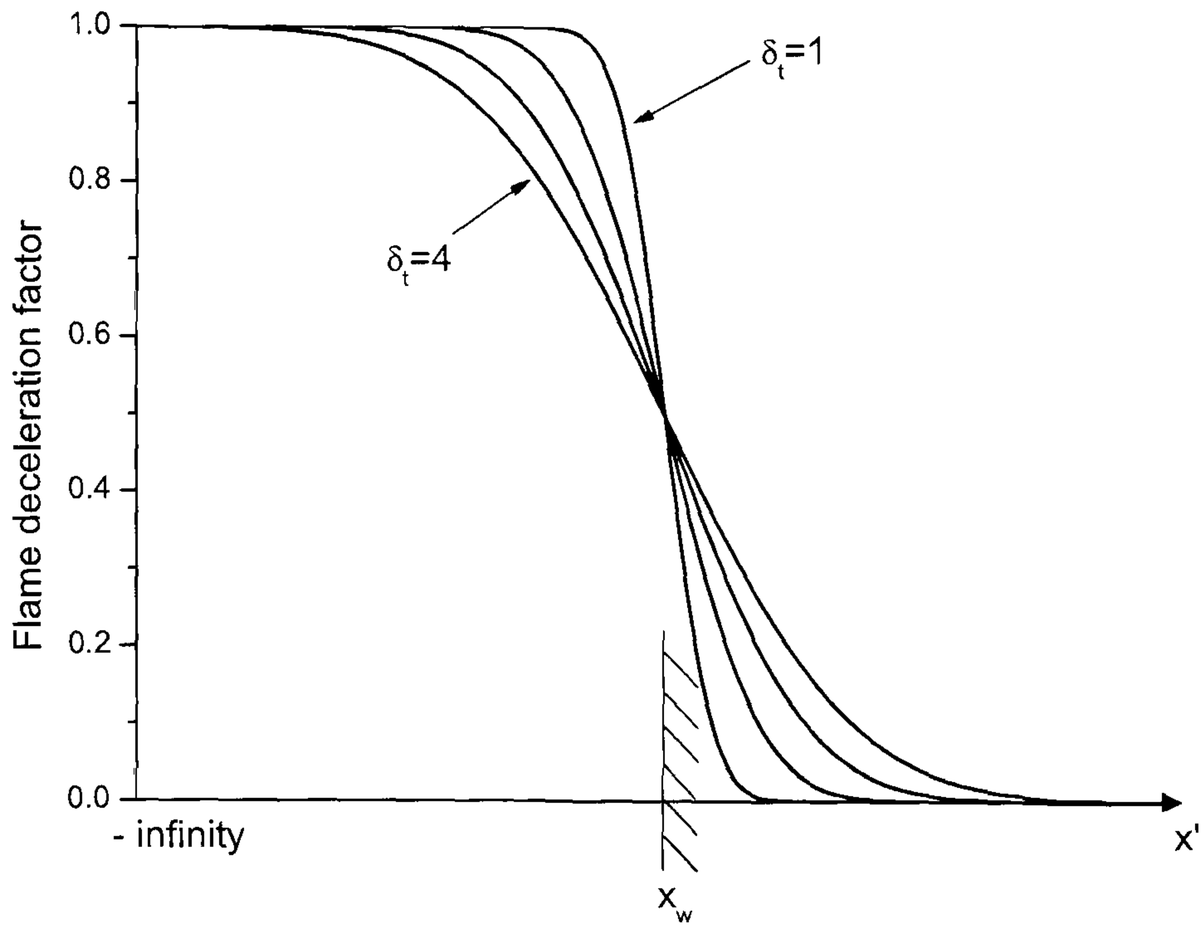

Figure 4.23: Flame declaration in the presence of a wall for dimensionless flame brush thicknesses ranging from 1 to 4 as predicted by Equation 4.34.

distance between the entrained and burnt gas fronts ($\delta_t = r_{fe} - r_{fb}$). Alternatively, it can be assumed that the growth of the turbulent flame brush is mainly controlled by turbulent diffusion [Lipatnikov and Chomiak, 2000]:

$$\delta_t(t) = u'\tau_L \left\{ 2t' \left[1 - \frac{1}{t'} \left(1 - e^{-t'} \right) \right] \right\}^{1/2} \tag{4.36}$$

where $t' = t/\tau_L$ is the dimensionless elapsed time since ignition, u' is the rms turbulent velocity and τ_L is the integral time scale ($= L/u'$). A comparison between the active perimeter function flame deceleration factor and the flame deceleration calculated using Equation 4.35 is shown in Figure 5.57.

4.5.10 Flame geometry

Calculation of the flame volume, active surface area and wall wetted areas is necessary for computing the rate of combustion (Equations 4.2 and 4.3) and gas to wall heat transfer (Section 4.2.6). The propagating flame is assumed to take the form of a sphere, possibly truncated by the combustion chamber walls. For the

thickness which a freely propagating flame with the same history and age would possess.

case of central ignition in a disc chamber engine such as LUPOE1-D the calculation of flame volume, active flame front area and wall wetted areas is possible using simple analytical expressions [Hynes, 1986]. If ignition is not central or the chamber is not cylindrical, numerical triangulation must be resorted to. Here the relevant volumes and areas are calculated by dividing the chamber and flame into many smaller regular elements for which the volume and area is easily calculated analytically.

The original flame geometry routines for non-disc chambers or off-centre ignition [Merdjani, 1996] represented the combustion chamber surface with a number of triangular elements. The flame was then divided into a number of concentric hexahedral (tetrahedral at the poles and the centre) volume elements along the longitude and latitude of the sphere. By determining, for a flame of a given radius, which volume elements lay inside or outside the combustion chamber the flame volume and wall wetted areas were estimated. Where a volume element intersected the chamber walls a weighting was applied to the volume and surface area associated with it in order to estimate the contribution of that element.

The original numerical flame geometry routines were found to contain some significant errors [Liu, 2004] and were replaced with simpler routines as part of the GET-CO2 project [Sheppard et al., 2005, Liu, 2004]. Here the chamber walls are divided into a number of discrete triangular surface elements in a similar fashion to the original flame geometry routines. The flame is then divided into polyhedral elements, one vertex of each element located at the centre of the flame with the outer face (representing the flame surface) of each element having a one-to-one correspondence with the projected area of an element of the chamber wall. The flame volume and area are now calculated as the sum over all the flame elements of the volume and area of each element. Where a flame element intersects the chamber walls or piston crown it is subdivided into a number of smaller polyhedral elements, the volume and area of which are calculated in a similar manner. As the calculation of flame volume and area using the methods described above is computationally demanding, at run time LUSIE employs a previously generated lookup table of flame volumes and areas for given flame radii and piston positions. The LUSIE manual written by Liu [2004] contains a more detailed description of the flame geometry routines.

4.5.11 Pressure equalisation

During combustion simulation the chamber contents are partitioned into burnt and unburnt zones. When the equilibrium between the two zones is disturbed, for example when fresh gas is burnt and mixed with the previously burnt gas, it is necessary to equalise the pressures of the burnt and unburnt zones and return the chamber contents to thermodynamic equilibrium. This is achieved with isentropic compression/expansion of the unburnt gas as appropriate followed by expansion/compression of the burnt gas with the constraints that the internal energy of the entire system remains constant, the combined volume of the two zones is equal to the volume of the combustion chamber and the burnt gas remains in chemical equilibrium. The operation of the pressure equalisation algorithm is discussed in detail by Abdi Aghdam [2003].

4.5.12 Mixing burnt gas

Following combustion the burnt gas exists in two separate zones, a zone of "old" burnt gas which remains from previous time steps and a zone of "fresh" burnt gas which has been burnt during the current time step. These zones are mixed adiabatically using an iterative procedure with the constraint of constant volume of the two zones and thermochemical equilibrium of the mixed gas. Once mixing of the burnt gas is complete the chamber contents are returned to equilibrium using the pressure equalisation routines, Section 4.5.11.

4.5.13 Gas properties and chemical equilibrium

Thermodynamic properties of gas mixtures are calculated according the prescriptions of Prothero [1969] using two sixth order polynomials for the molar specific heat at a constant pressure $\tilde{c}_p$ covering the temperature range 300–6000 K. Other gas properties are derived from these polynomials using standard relationships, e.g [Rogers and Mayhew, 1992]. Chemical equilibrium for the burnt gases is calculated using the routines implemented by Desoky [1981] which assume infinitely fast chemistry. Molecular thermal diffusivity of species is calculated using the methods described by Bird et al. [1960] and mixture viscosities are determined using the polynomials of Watson [1972] for common species and where necessary by theoretical means using the methods given by Hirschfelder et al. [1964]. For further detail see the theses of Hynes [1986] or Desoky [1981], or the manual of

Liu [2004].

4.5.14 Turbulence

The flow field, and hence combustion, in an engine is always turbulent at sensible engine speeds by nature of the fact that in order to inhale sufficient fresh charge during the limited time available for gas exchange the flow of the incoming gas must be at a high Reynolds number. The properties of the in-cylinder turbulence, in particular the rms turbulent velocity u', although difficult to define unambiguously in an engine (see Section 1.4), strongly influence the rate of combustion [Damköhler, 1947, and many other authors] and therefore any engine simulation must include an accurate description of the nature of the turbulent flow field. For the quasi-dimensional model described in this chapter, expressions for u' and L are required by Equations 4.5 and 4.17. In the LUPOE1-D engine the flow was found to be quiescent [Atashkari, 1997] however in a real engine the properties of the turbulent field undoubtedly vary spatially and are non-isotropic, see for example the measurements of Li et al. [2002], Fraser and Bracco [1989]. Regardless of any inhomogeneity, given the spherical flame assumption employed by LUSIE it is only possible to use either bulk turbulence quantities or to permit variation radially from the centre of the flame.

Atashkari [1997] found during cold tests in the LUPOE1-D engine that u' was approximately proportional to the mean piston speed $\bar{S}_p$ and that in the region -20 to 20 °aTDC the decay of turbulence was approximately linear with crank angle. A number of different authors using different engines and measurement techniques have found a similar result [Semenov, 1963, Murad, 2006, Liu et al., 1999, Arcoumanis et al., 1994, Hall and Bracco, 1987, Nordgren et al., 2003, Hilton et al., 1991, Johansson and Olsson, 1995, Jakubík, 2002] which can be summarised as follows

$$u' = C_1 + C_2\bar{S}_p + C_3\theta \tag{4.37}$$

here C_1 and C_3 are constants with units m/s and m/s °CA respectively and C_3 is a dimensionless adjustable constant. Atashkari postulated that C_1 is associated with turbulence generated by flow through the inlet ports and C_2 accounts for turbulence generation by the motion of the piston. This explanation is plausible for the LUPOE family of engines where the intake air mass flow rate remains constant regardless of the engine's rotational speed. For conventional engines where the velocity of the intake air depends on the engine speed this explanation

is clearly nonsensical as $\lim_{\bar{S}_p \to 0} u' = C_1$. In this case C_1 may serve as a correction factor which accounts for any nonlinearity in $u' \propto \bar{S}_p$.

Direct determination of the integral length scale L in an IC engine is difficult experimentally because of 1) its small magnitude, 2) the necessity of taking simultaneous measurements at two spatially distinct points in order to generate the correlation function and 3) cycle-to-cycle variations in the mean flow pattern. Indirect determination using the temporal autocorrelation of a single point measurement is equally difficult and often gives erroneous results as the magnitude of the mean velocity close to TDC is not typically large enough for Taylor's hypothesis to be valid [Hill and Zhang, 1994]. Nevertheless, direct measurements by a number of authors [Hong and Tarng, 1998, Breuer et al., 2005, Lee and Lee, 2003, Li et al., 2002, Fraser and Bracco, 1986, 1989, Klingmann and Johansson, 1999] indicate that L is of the order of the clearance height h_c when the piston is close to TDC hence in the LUSIE code the following expression is adopted for disc shaped chambers:

$$L = C_L h_c(\theta) \tag{4.38}$$

where C_L is a constant, typically $C_L \approx 0.2$.

The integral scale is generally assumed to be a strong function of the vessel dimensions [Tennekes and Lumley, 1972] and for a steady flow in a vessel of constant volume it is likely that this is true. Interestingly, the results of Fraser and Bracco [1989] suggest that in the environment of an internal combustion engine combustion chamber where the flow is non-stationary and the volume is subject to constant flux, C_L does not scale strongly with compression ratio (i.e. vessel dimensions), in other words the idea of a universal value of C_L is questionable.

Equation 4.38 is plausible for engines in which the combustion chamber is cylindrical or close to cylindrical. Modern four valve engines typically employ a pent geometry combustion chamber where the TDC clearance height is much larger in the centre of the chamber than in the "eaves" of the pent. For engines such as these the integral scale was related to the local distance between the piston crown and the cylinder head h_f for a given flame radius r_f, see Figure 4.24. In order to accurately model engines such as these the expression below was added to the existing LUSIE code by the author:

$$L = C_L h_r(r_f) \tag{4.39}$$

Equation 4.39 is supported by particle tracking in LUPOE2-P [Sheppard et al.,

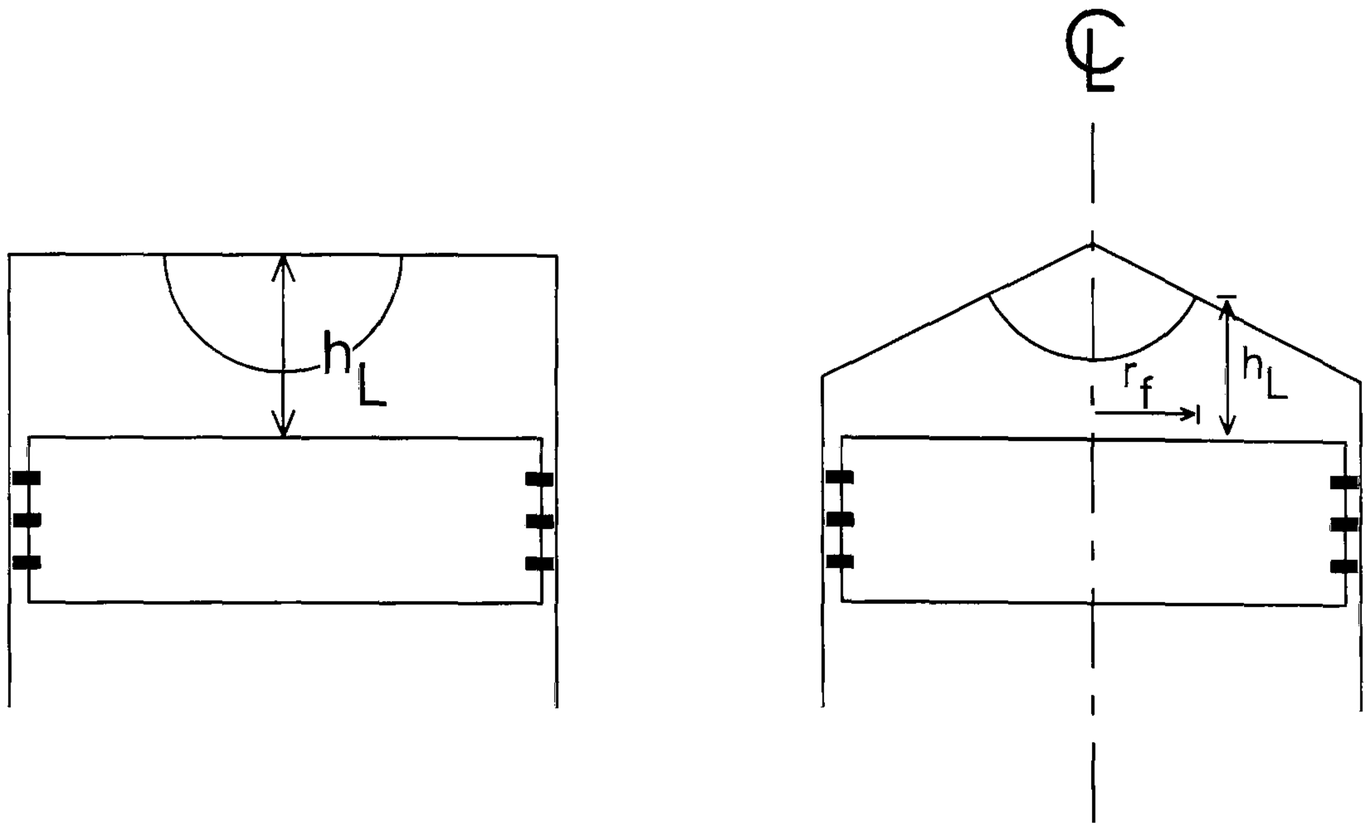

Figure 4.24: Integral scale definitions used in LUSIE for disc and pent geometry combustion chambers.

2005, Murad, 2006], CFD data supplied by Volkswagon for a production pent roof engine [Volkswagon, approx. 2004] and, to some extent, by the finding that its use allows the three-zone model to reproduce the pressure traces observed experimentally on LUPOE2-P.

4.6 Software testing and changes to the code

The inherited version of the LUSIE code and the other software written during the course of the study (GT-LU and LUCoVE) were rigourously tested for errors by checking for conservation of mass and energy and ensuring that changes in entropy did not contravene the second law of thermodynamics. This was achieved by inserting additional statements into the code to store the mass, total internal energy and total entropy of the unburnt and burnt zones before and after every calculation which caused a change in the thermodynamic state of the charge. By monitoring the changes in mass, energy and entropy during each calculation and referring to the intended mode of operation for each subroutine, (for example, compression/expansion of the unburnt gas should always be isentropic) some small errors in the code were discovered and corrected:

- Examination of the blowby routines revealed that the calculated mass flow rates through the ring-gaps and top land crevice were erroneous. Mass flow

rates were calculated using a second order Runga-Kutta solution method [Abdi Aghdam, 2003] whereby the flow rate is predicted at the current time step and one step in advance using the appropriate differential equations for flow through an orifice. The final solution is taken as the arithmetic mean of the two predicted flow rates. The original blowby routines used only the solution from the first time step rather than the mean to update the crevice masses leading, in some cases, to "negative" crevice masses. This deficiency was corrected in the current version of LUSIE. Figures 4.29 and 4.30 show a comparison between the predictions of the corrected LUSIE blowby routines and blowby predicted by a GT-Power model (described in Section 5.4.2) of an identical engine.

- Immediately after the ring pack flow was calculated a second routine was called to update the pressure and temperature of the unburnt gas (blowby losses were assumed to always come from the unburnt zone) prior to pressure equalisation between the burnt and unburnt zones. This routine assumed constant internal energy of the unburnt gas hence

$$m_{\text{new}}u_{\text{new}} = m_{\text{old}}u_{\text{old}} + \Delta m h_{\text{TLC}} \tag{4.40}$$

where u_{new} and m_{new} are the specific internal energy and mass of the unburnt gas following blowby; u_{old} and m_{old} are the specific internal energy and mass of the unburnt gas prior to blowby; Δm is the mass gained through the top land crevice and h_{TLC} is the specific enthalpy of the gas flowing through the top land crevice. New values of unburnt gas temperature and pressure were now calculated based on the total internal energy of the unburnt gas ($m_{\text{new}}u_{\text{new}}$). In the inherited version of the code the value of m_{old} used in the subroutine was the total trapped mass rather than the mass of unburnt gas. This error resulted in an incorrect pressure and temperature calculated for the unburnt gas post-blowby which also lead to errors in the subsequent pressure equalisation step.

- The first process in a firing iteration is the calculation of temperatures and pressures for the burnt and unburnt zone following compression/expansion caused by piston movement. The inherited version of the code mistakenly employed the original isentropic compression—isentropic expansion algorithm for this purpose rather than the new isentropic compression—

constant internal energy routines, (see [Abdi Aghdam, 2003]). This error was corrected by implementing the revised pressure equalisation routines and calculating the total internal energy of the system (which the pressure equalisation routines use to update the temperature and pressure of the gases) as

$$U_{s,\text{new}} = U_{r,\text{old}} + U_{p,\text{old}} - \int_{V_{\text{old}}}^{V_{\text{new}}} P \, \mathrm{d}V \tag{4.41}$$

where U denotes total internal energy, V denotes volume and P denotes pressure. The subscripts old and new indicate values before and after piston movement and the subscripts s, r and p indicate system, reactant (unburnt) and product (burnt) values respectively. The integral in Equation 4.41 is evaluated using the trapezium rule.

Other additions to the code include new output routines designed to simplify the production of formatted column-based ASCII files suitable for import into spread sheet software; new input routines which allow a flexible and extensible input file format with error checking and new message handling routines. The majority of the code has been moved to Fortran 90 enabling improved data encapsulation using modular programming and better error checking at compile time

Further testing of the code was possible by comparing the output of identical models run using LUSIE, GT-Power and GT-LU or comparing the performance of individual subroutines in the three codes. A comparison of the unburnt gas thermodynamic properties calculated by LUSIE and GT-Power for a simulated LUPOE1-D 1500rpm base condition cycle is shown in Figure 4.25. The graphs in this figure were generated by writing the temperature, pressure and mixture composition at each time step of the LUSIE simulation to a text file. A GT-LU simulation was then started and the GT-Power property routines (accessible to the user from inside the GT-Power user-programmable routines) were then called using values read from the text file generated by LUSIE. The two sets of property routines show little difference through the cycle, justifying the continued use of the property routines of Prothero [1969] in LUSIE. A similar exercise was undertaken to test the correspondence between the LUSIE and GT-Power chemical equilibrium calculations, see Figure 4.26 which again showed a negligible difference between the two codes.

The correspondence between the pressure equalisation algorithms (see Section 4.5.11) employed by LUSIE and GT-Power was compared by running an

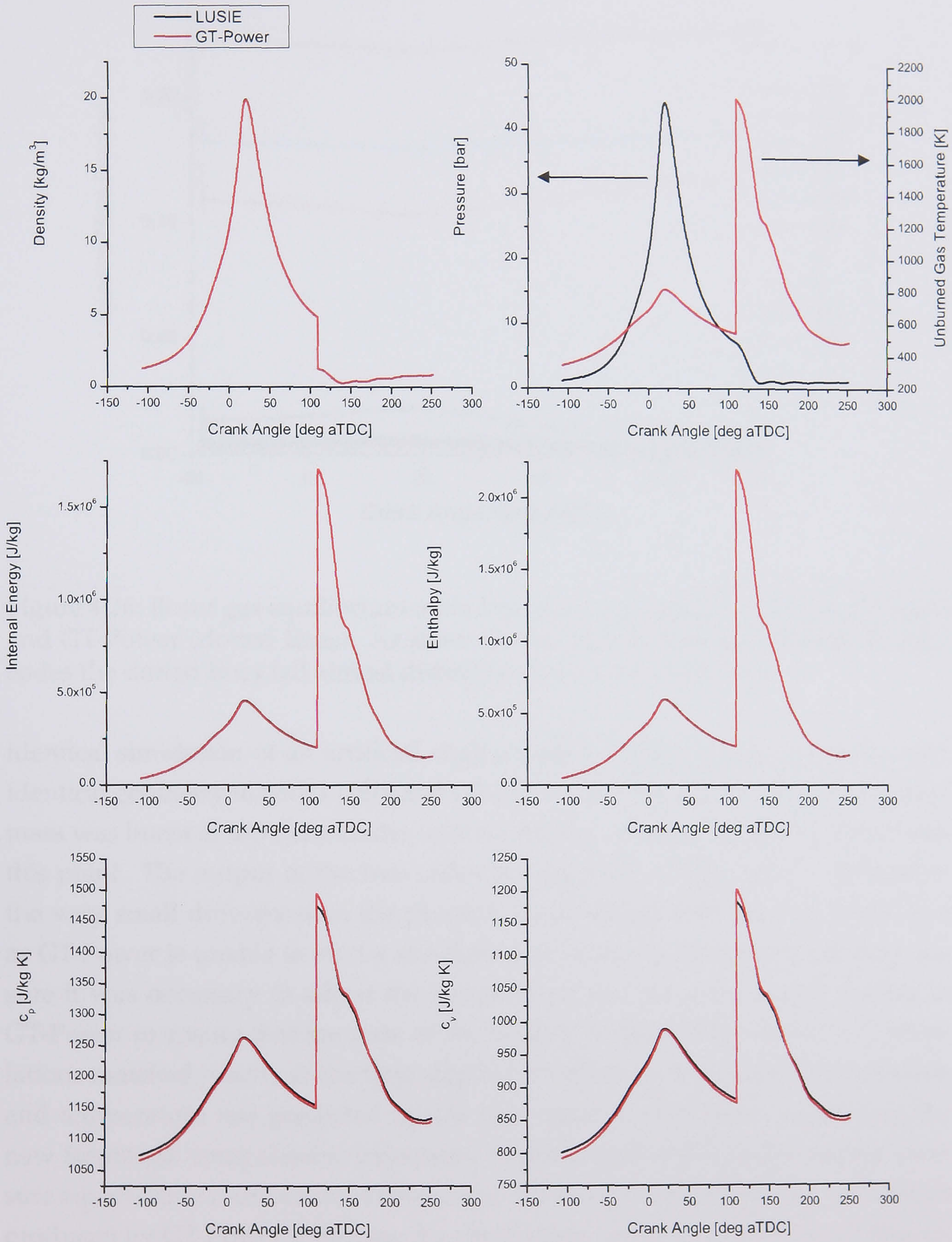

Figure 4.25: Thermodynamic properties predicted by LUSIE and GT-Power.

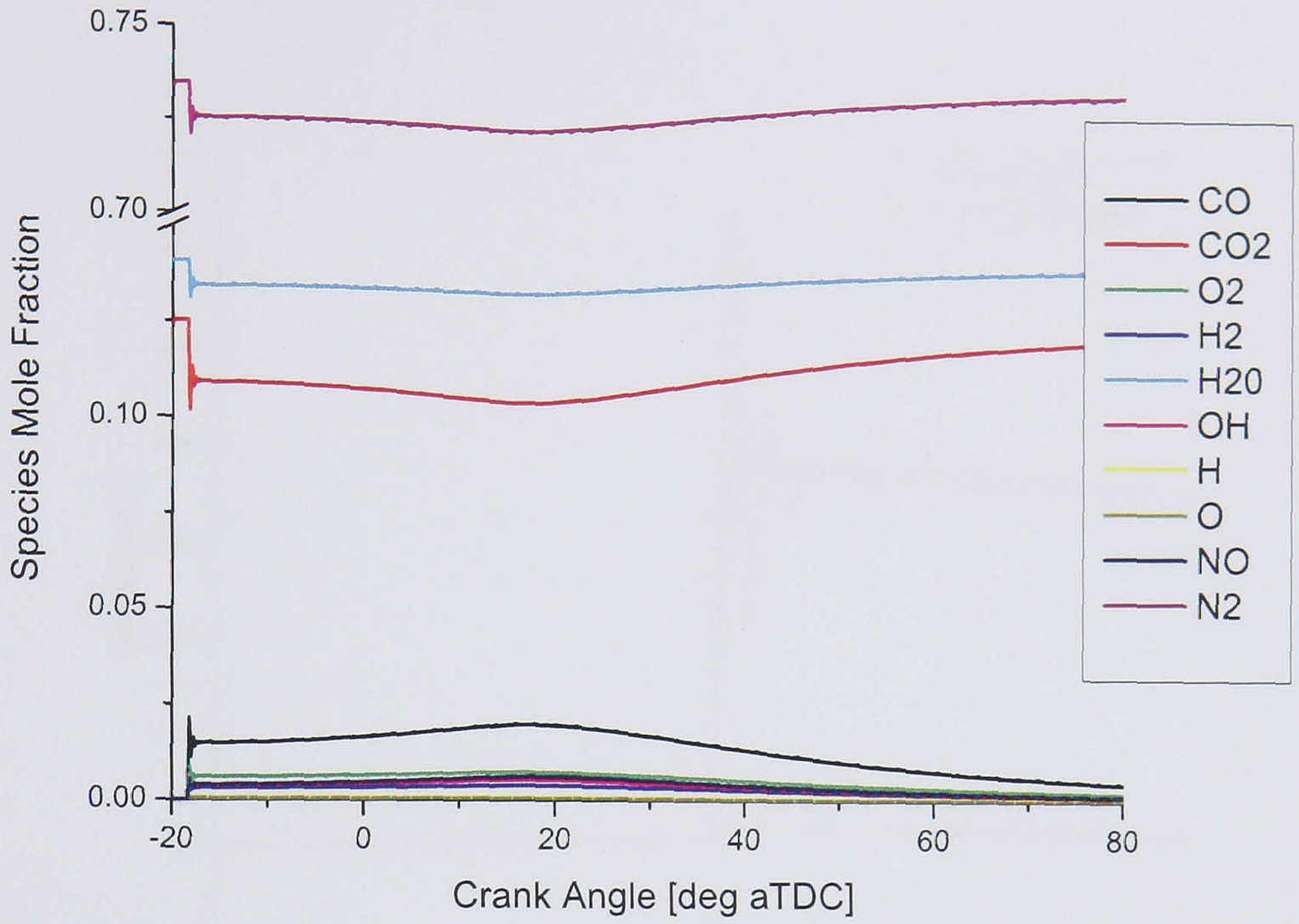

Figure 4.26: Burnt gas equilibrium mole fractions predicted by LUSIE (solid lines) and GT-Power (dotted lines). As there is very little difference between the two codes the dotted lines fall almost directly on top of the solid lines.

identical simulation of an artificial engine with no heat transfer or blowby and identical geometry in both LUSIE and GT-LU. In each simulation 1% of the charge mass was burnt at top dead centre with no further combustion taking place after this point. The output of the two codes is compared in Figure 4.27. Because of the very small differences in the property routines between the two codes and as GT-Power is unable to start a simulation at precisely the moment of port closure it was necessary to adjust the temperature and pressure at port closure in GT-Power to ensure that the state of the mixture in the LUSIE and GT-LU simulations matched exactly at the time step before the mass was burnt. The pressure and temperature rise predicted by the two codes is very close vindicating the new isentropic compression/expansion—constant overall internal energy pressure equalisation routines implemented by Abdi Aghdam [2003]. The oscillations produced by GT-Power following the combustion event indicate that, for this artificial test, the numerical stability of the routine used by GT-Power is inferior to the LUSIE routine.

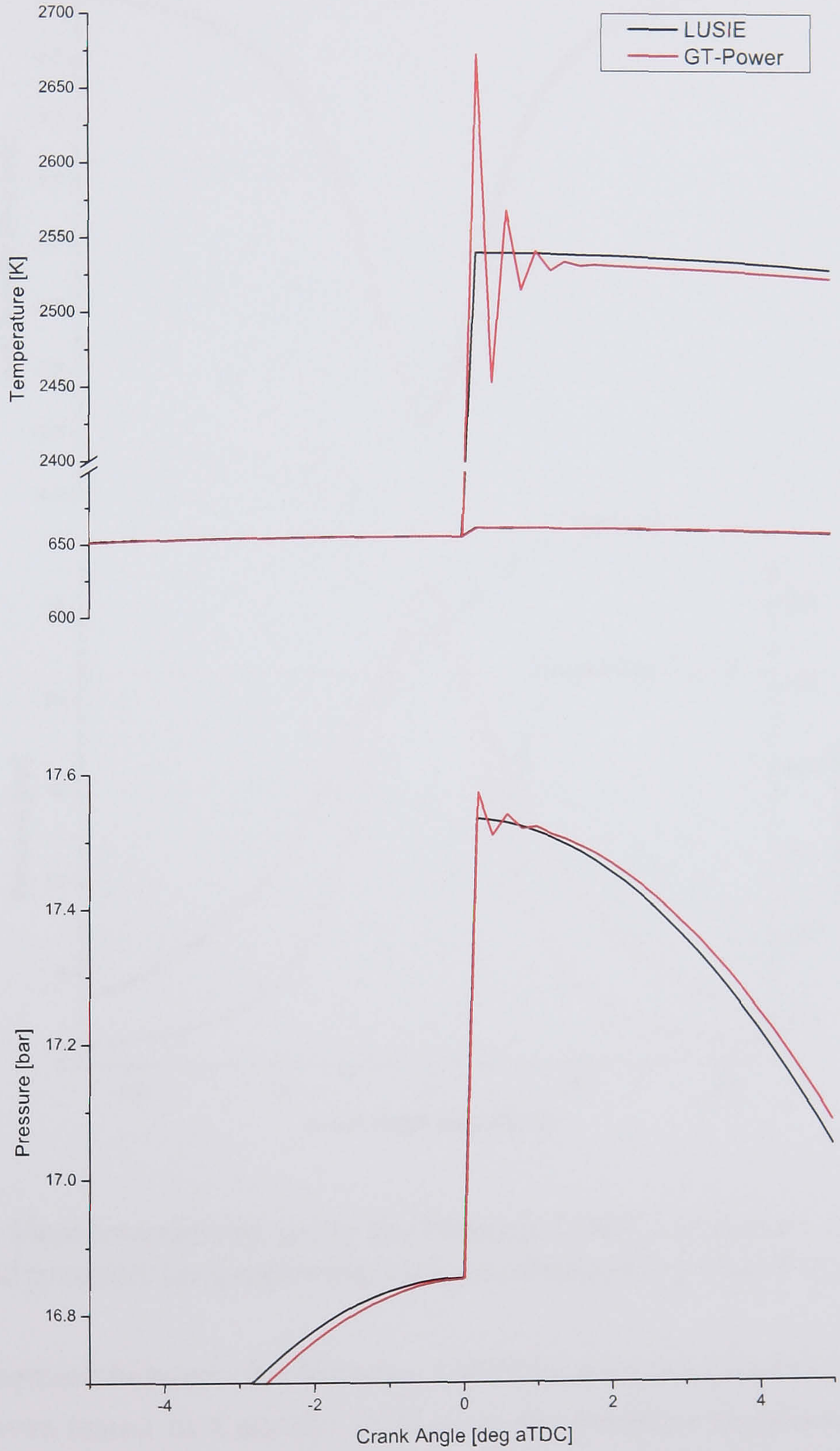

Figure 4.27: A comparison of the pressure equalisation routines used in LUSIE and GT-Power.

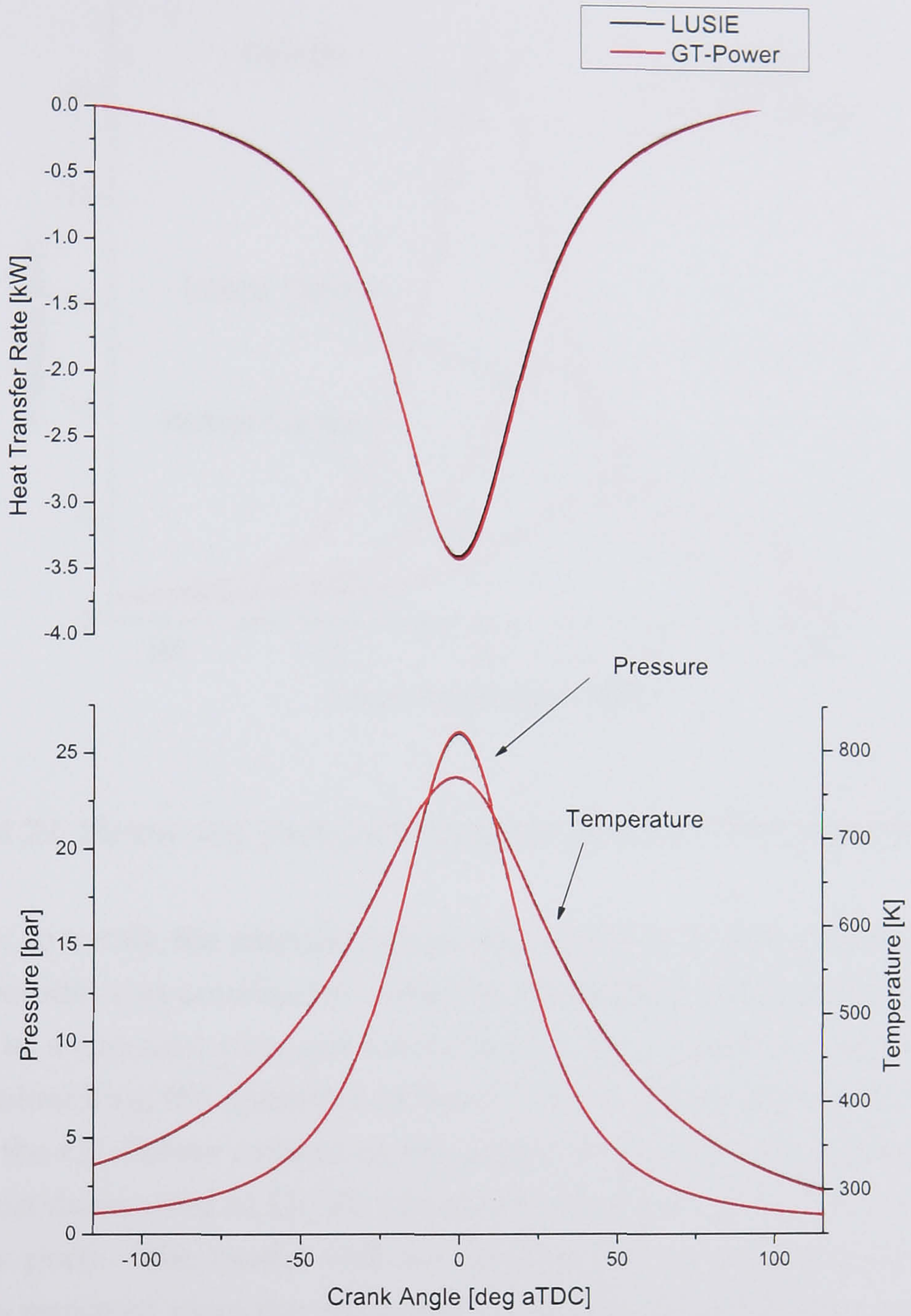

Figure 4.28: Heat transfer rate using the Woschni [1967] correlation, cylinder temperature and pressure for a motoring cycle as calculated by LUSIE and GT-Power.

The agreement between the Woschni [1967] heat transfer routines used by the two codes was tested in a similar fashion to the pressure equalisation routines using identical simulations of a hypothetical engine. In this case the simulation was of a motoring cycle with no blowby. The predicted temperature, pressure and heat transfer rates of the two codes is shown in the graphs in Figure 4.28, the difference between the two codes is again very small.

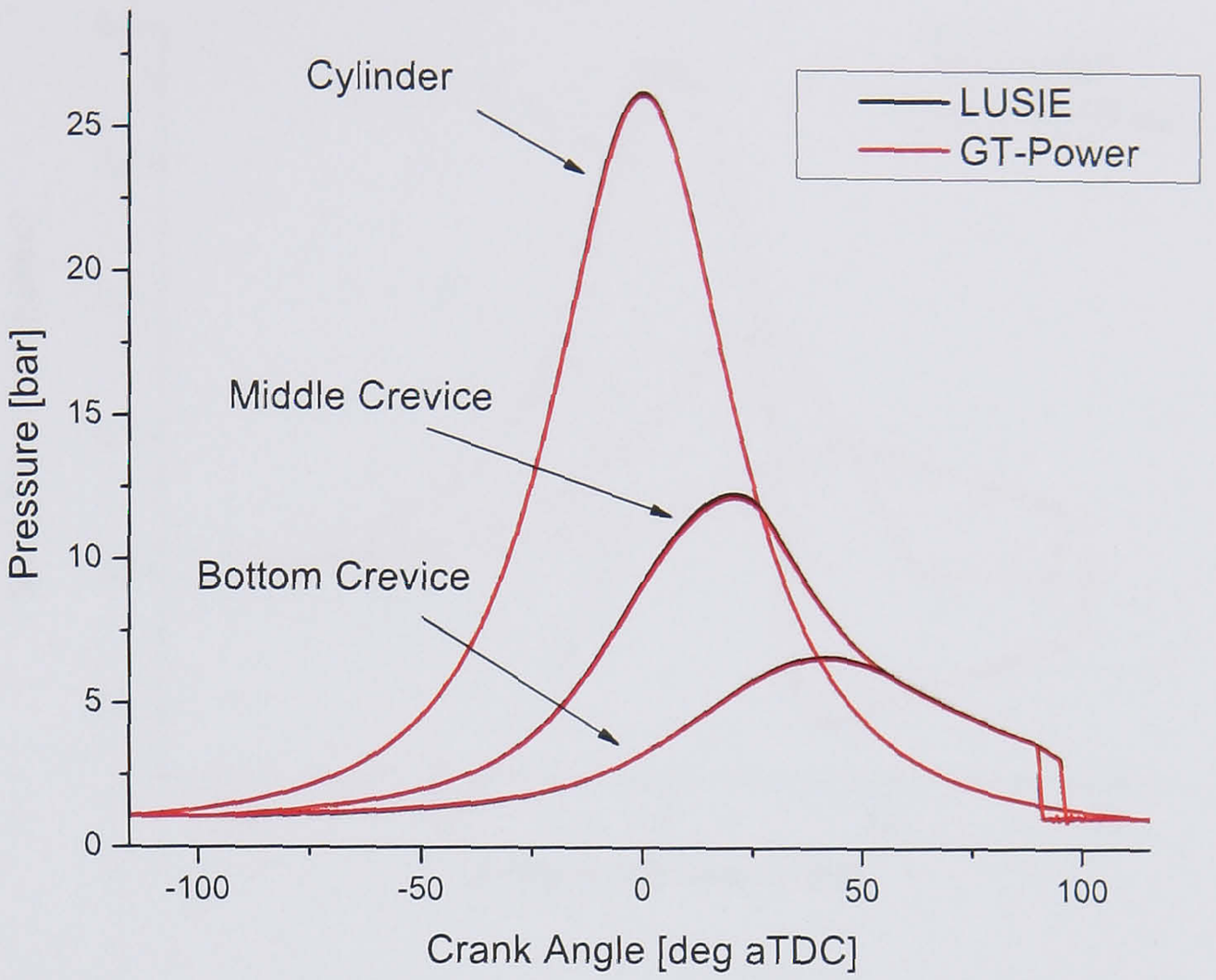

Figure 4.29: Piston ring pack pressure predicted by LUSIE and GT-Power.

In order to verify the calculations of the corrected LUSIE blowby routines a GT-Power model was constructed whereby the engine combustion chamber was connected to a constant pressure environment via a series of volumes and orifices thus mimicking the operation of the blowby routines used by LUSIE. Valves connected the GT-Power orifices to the constant pressure environment to replicate the procedures used in LUSIE to simulate the effect of the inter-ring crevices passing the ports. The model was not appropriate for simulating firing cycles as the mass removed from the combustion chamber by GT-Power is assumed to come in equal proportions from the unburnt and burnt trapped gas; the mass flow across the top land crevice in a real engine is mostly unburnt gas during a the majority of the combustion event. A comparison of the crevice pressures and orifice mass flow rates predicted by LUSIE and GT-Power two identical models without heat transfer is shown in the graphs in Figures 4.29 and 4.30. The two codes show little difference in their output for the duration of the cycle.

A final test of the software used in this thesis was performed by building identical LUSIE and GT-LU models which featured no blowby or heat transfer and comparing the predictions of the two codes during firing cycle simulations. Calculated temperatures and pressures for LUSIE and GT-LU using both the two

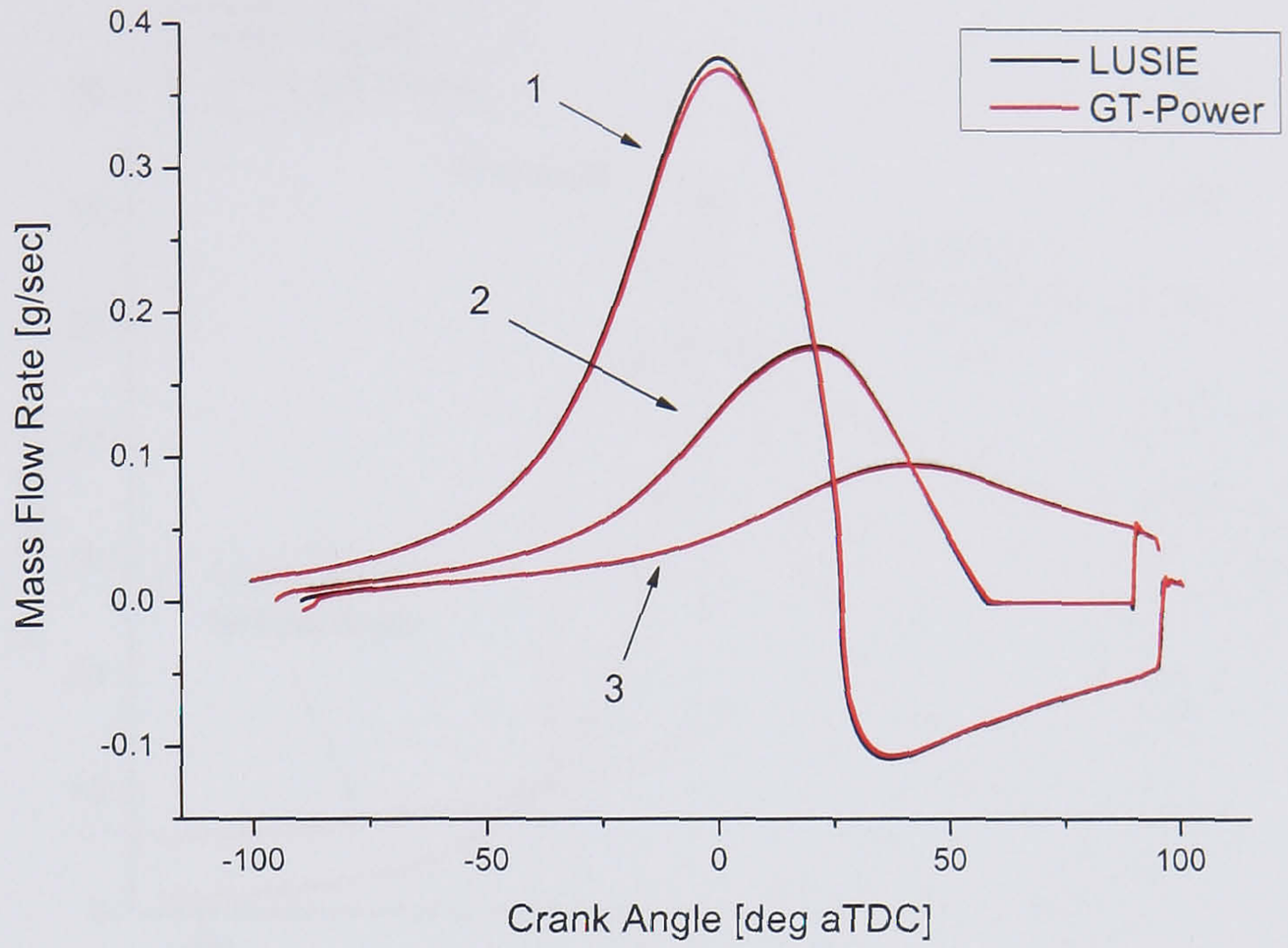

Figure 4.30: Top land crevice and piston ring orifice mass flow rates predicted by LUSIE and GT-Power. The numbers denote the piston ring gaps, 1 being closest to the piston crown and 3 closest to the crank case.

and three-zone models are shown in the graphs in Figures 4.31 and 4.32. Again the agreement between the two codes is good, a feature which hopefully confirms that the calculations made by the revised LUSIE code are error free.

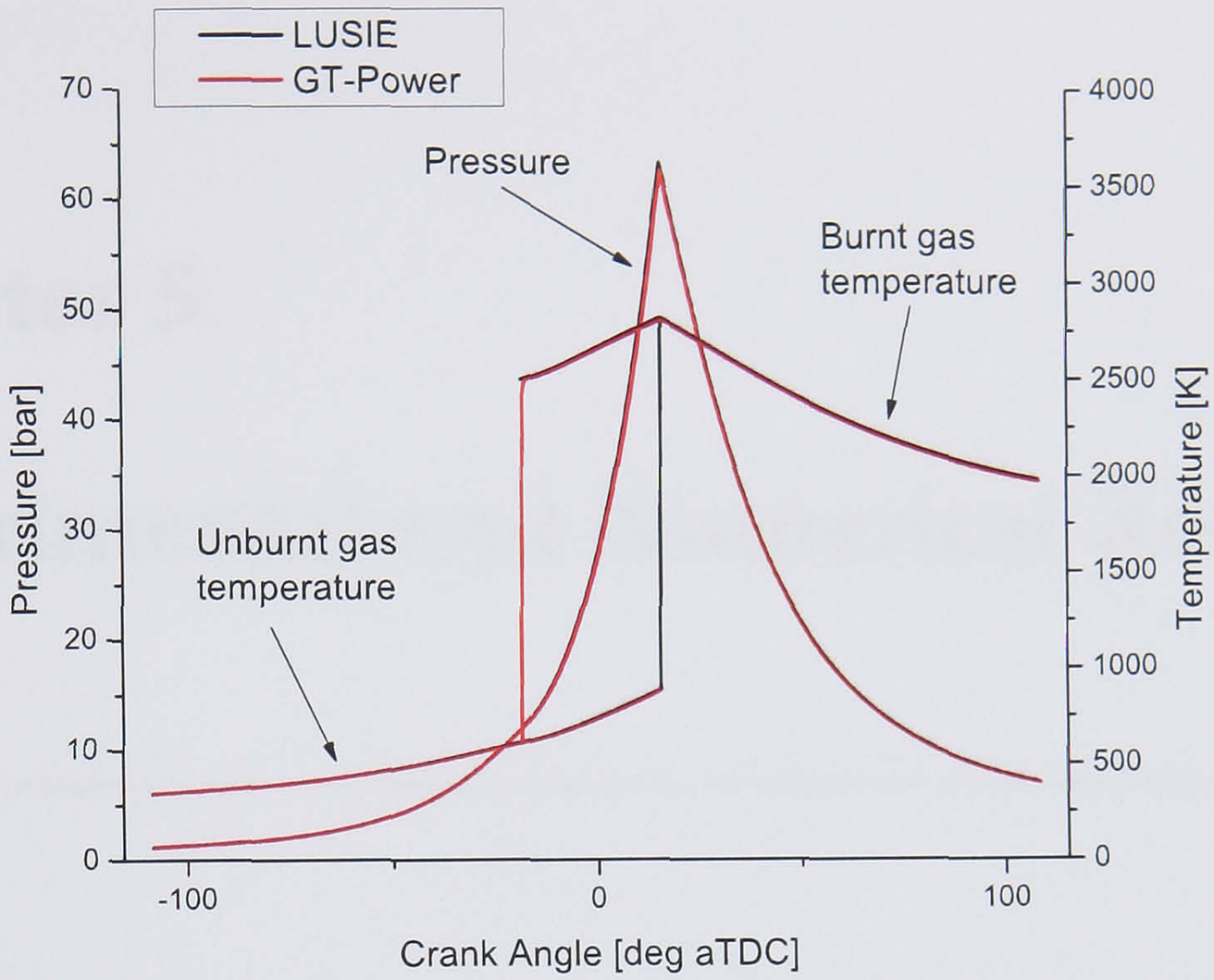

Figure 4.31: Cylinder pressures and temperatures predicted by LUSIE and GT-Power during a two-zone combustion simulation.

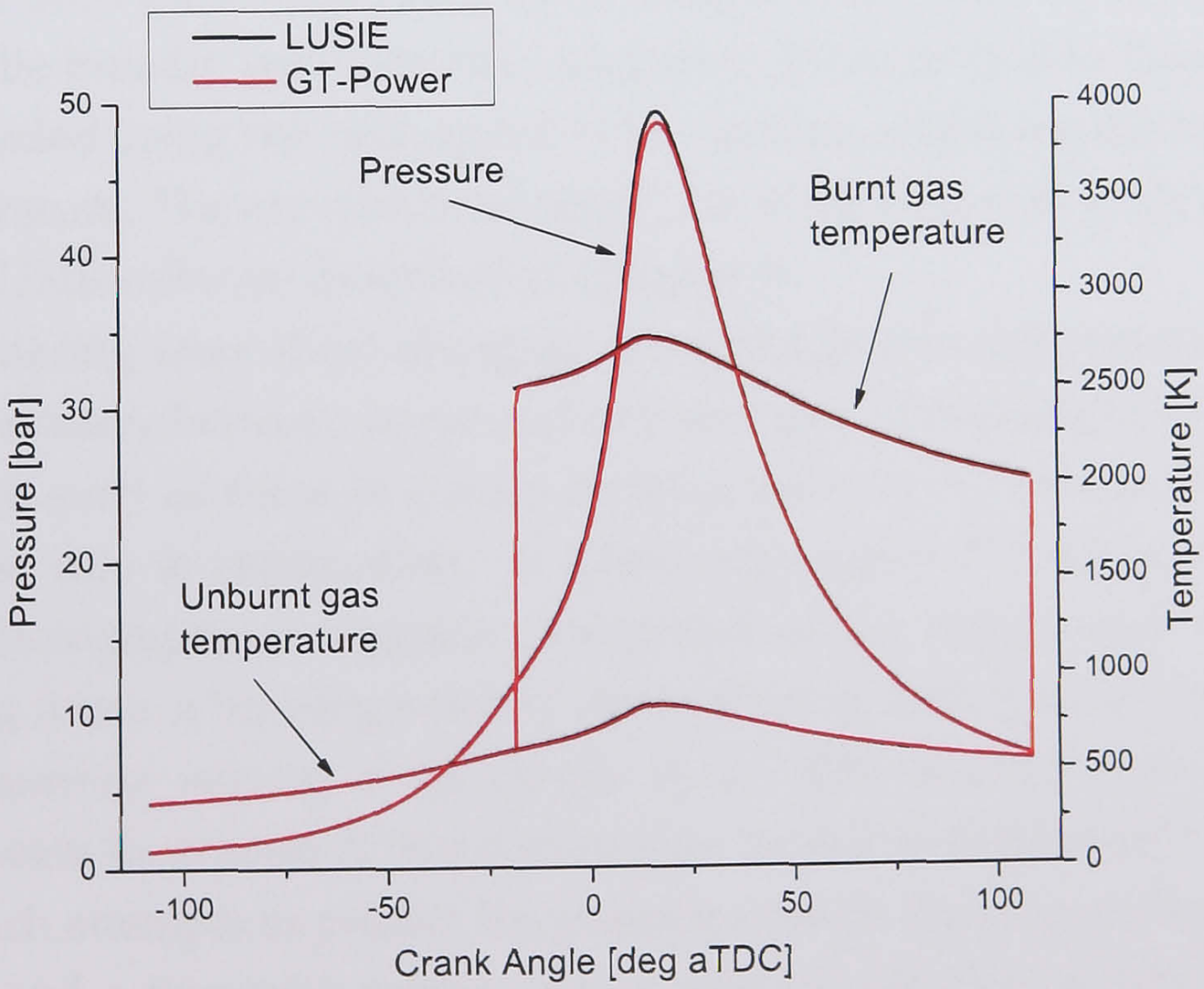

Figure 4.32: Cylinder pressures and temperatures predicted by LUSIE and GT-Power during a three-zone combustion simulation.

Chapter 5

Experimental and Numerical Results

5.1 Overview

This chapter presents experimental results recorded for the LUPOE2-P engine which have been processed using the techniques described in Chapter 3. The results can be broadly split into two categories: those related to flame propagation as recorded using the high speed video camera, and those related to the in-cylinder pressure. The experimental results are compared with cycle simulations using the LUSIE software described in Chapter 4.

Mie scattering laser sheet imaging, as undertaken in the current study, defines the boundary between burnt and unburnt gas. A burning velocity derived from images such as these is a mass burning velocity u_{tr} and is related to the pressure rise due to combustion. A flame edge derived from natural light or schlieren photography is typically interpreted as the entrainment front of the propagating flame, a burning velocity derived using such data would be the entrainment burning velocity u_{te} [Gillespie et al., 2000, Bradley et al., 2003]. The LUSIE software incorporates two combustion model formulations: A three-zone model, which attempts to predict the position of both the entrainment and burnt gas fronts, and a two-zone model, which seeks to directly predict the location of the burnt gas front. The images and associated progress variable isosurfaces presented for LUPOE2-P are derived from Mie scattering laser sheet photogra-

phy and are therefore more relevant to the two-zone model formulation than the three-zone model.

As the LUSIE software is a thermodynamic code and hence typically used to predict "mean" cycles, the majority of the analysis in this chapter is confined to discussion of the mean or most frequently occurring cycle. By definition, the mean progress variable, see Section 3.3.5, which is used to characterise the visual observations of flame propagation, is an ensemble average statistic, representative of a mean cycle. Ensemble averaging flames growing in a cyclicly varying flow field will undoubtedly influence the mean progress variable analysis attempted in this thesis by "smearing" the data leading to, for example, a thickening of the perceived flame brush thickness. Previous analysis of the bulk flow in the LUPOE2-P engine [Murad, 2006] suggests that for a given engine speed the flow (and hence combustion) is not entirely repeatable and alternates between two "modes". For the 750 and 1500 rpm conditions tested the most frequently occurring flow pattern was present in 75–80% of the observed cycles. That the most frequently occurring flow mode was present in 75–80% of cycles should hopefully keep the distortion in the experimental results to an acceptable level.

With the current arrangement of intake and exhaust ports the presence of this cycle-to-cycle variability in the experimental engine is unavoidable. One possible solution is conditional sampling of the experimental data after it has been recorded on the basis of the flow pattern of each cycle. A second solution is the alignment of individual flames on their centroid as used by Renou et al. [2002]. These experiments were however conduced in a wind tunnel where the flame did not contact any walls. In an engine configuration the application of this technique is problematic as images of flames which have been quenched by the wall should be aligned on the wall plane to give a sharp edge to the mean progress variable field at the wall. For the three-dimensional reconstruction technique used here a further difficulty arises in that, even if the flame centroids are aligned in the imaging plane, alignment in the direction normal to the imaging plane is not possible.

5.2 Experimental and data processing parameters

Four engine running conditions, selected from those used previously by Murad [2006] with the LUPOE2-P engine, were used during the experimental program. The conditions were chosen such that the experiments would capture the effect of different rms turbulent velocities and mixture strengths on flame propagation.

One condition, 1500 rpm stoichiometric, was selected as the reference condition with low, 750 rpm, and middle, 1000 rpm, engine speeds used to provide different levels of in-cylinder turbulence. The effect of a fuel lean mixture was studied by running the engine at $\phi = 0.8$ at 1500 rpm. Details of the four operating conditions are given in Table 5.1 For the fuel lean mixture the air mass flow rate was increased by 30% over that used by Murad to improve scavenging and prevent autoignition occurring in the skip-fired cycles. This problem was not reported by Murad and is probably linked to the movement of the engine to a different position in the laboratory, discussed below.

For the currently reported experiments, the piston was moved to BDC and heated air was blown through the intake system between experiments. The air was heated using the band heaters on the intake system (Section 2.2.2) and ensured that the intake, head and barrel remained in thermal equilibrium at the desired temperature. During firing the fuel pump was activated immediately prior to triggering the ignition system. Experiments with a thermocouple which was stripped of its protective sheath revealed that the addition of fuel to the intake air stream caused $\sim 10^{\circ}$C drop in the intake temperature. This figure agrees with an estimate of the temperature drop calculated using the latent heat of evaporation of the fuel and the fuel and air flow rates. As the intake system possessed considerable thermal inertia the heaters were unable to restore the temperature of the mixture to the temperature set on the thermostat within the time scale of an experimental run. For this reason the intake air temperatures stated in Table 5.1 should be reduced by approximately 10°C. It is likely that, although not discussed in thesis', previous experimental data recorded on the LUPOE family of engines at Leeds suffer from a similar inaccuracy The implications of an error in intake temperature of this magnitude are investigated in Section 5.4.5.

The ignition timings chosen by Murad were selected to give the maximum IMEP for the engine speed and mixture strength employed and can therefore be considered to be maximum brake torque (MBT) ignition timings. Following the completion of experiments using LUPOE2 by Murad the engine was moved to a different dynamometer to enable easier access for the copper vapour laser beam necessary for the Mie scattering imaging technique used in this thesis. During initial testing and setting up of the current experiments the combustion performance of the engine in the new position, as indicated by cylinder pressure traces, was observed to have altered when compared with results recorded with the engine in its previous position. A substantial amount of investigation revealed that

this change in behaviour was linked to the proximity of the engine in the new position to the exhaust blower used to evacuate burnt gases from the laboratory exhaust extraction system. With the engine now closer to the exhaust blower the pressure in the exhaust runner was reduced by ~ 0.1 bar. As the exhaust port is the last port to close on a two stroke engine such as LUPOE2 the pressure in the exhaust runner determines the pressure at the start of the cycle. Simple Wiebe function simulations using LUSIE demonstrated that a change in initial pressure of this magnitude was sufficient to cause the drop in peak pressure during firing cycles at 1500 rpm observed with the engine in the new position.

For the reasons discussed above, the results presented in this thesis should not be considered directly comparable to the results recorded by Murad. It should be noted however that for the most part the performance of the engine remains very similar and that the trends, for example in flame centroid migration, reported by Murad remain similar to those presented here. Flow velocities measured by Dawood [2007] using LDV with the engine in the new position suggest that, despite some difference during the intake and exhaust periods, the flow field during the combustion period has not been substantially altered by the change in pressure at port closure. The rms velocities reported by Murad are therefore used as inputs for the LUSIE simulations reported in this thesis.

For all running conditions experimental data were recorded with the laser sheet parallel to the TDC plane[1] at distances of 1.5–13.5 mm above TDC. The spacing between sheet positions (the vertical resolution) was 1.5 mm. For each laser sheet position when running the engine at the reference condition, 100 firing cycles per laser sheet position were recorded. For other running conditions, 50 firing cycles were recorded per laser sheet position. The choice of the number of firing cycles, and the accuracy of the progress variable field calculated when averaging different numbers of images is discussed in Section 5.5.

The resolution of the camera optics for images in the sheet plane was evaluated using a USAF test pattern purchased from Edmund Optics and found to be 2 line pairs per millimetre (0.5 mm) in the worst case. The camera resolution was 512×512 pixels therefore the per pixel resolution, assuming the bore filled the entire image, was approximately $80/512 = 0.15$ mm. As the original images were later resampled to match the vertical resolution (1.5 mm) the high resolution of the original laser sheet images was unnecessary. The full resolution of

[1]Here the TDC plane, or simply TDC, is defined as the plane of the flat piston crown when it is positioned at TDC. The position of the laser sheet is defined in terms of distances along the bore axis from the TDC position.

these images may however be useful to other investigators in future studies. Relevant details of the settings for the camera and data acquisition (DAQ) system are given in Tables 5.3 and 5.4. Data processing was performed using the same parameters regardless of the engine operating condition. Parameters used for data processing are detailed in Table 5.5.

A significant amount of the analysis in this chapter uses the results of Abdi Aghdam [2003] recorded on the LUPOE1-D engine. These results were preferred to data from LUPOE2-P in some cases as the LUPOE1-D combustion chamber has a disc geometry and there is little large scale fluid motion close to TDC. This simple geometry, coupled with comprehensive measurements of turbulence [Atashkari, 1997, Jakubík, 2002] was ideal for analysis and basic testing of the LUSIE combustion models as it ensures that results are not obscured by non-spherical experimental flame geometry or inhomogeneous turbulence such as those present in LUPOE2-P. A summary of the LUPOE1-D operating conditions used by Abdi Aghdam for which data have been presented in this thesis is given in Table 5.2.

Table 5.1: LUPOE2-P operating conditions.

Condition	Engine speed [rpm]	ϕ	θ_{sp} [° aTDC]	T_{air} [° C] [a]	T_{head} [° C]	$\dot{m}_{air}$ [g/sec] [b]	Skip-fire ratio
Base condition	1500	1.0	-7	55	55	8.61	7
Low engine speed	750	1.0	-2	55	55	8.61	7
Medium engine speed	1000	1.0	-4	55	55	8.61	7
Lean mixture	1500	0.8	-12	55	55	11.19	7

[a] This is the temperature of the intake air without fuel. The addition of fuel caused ~10° C drop in the intake temperature, discussed in the text above and Section 5.4.5.

[b] The air mass flow metres were supplied calibrated in standard litres of air per minute (0° C, 1.013 bar). Full scale deflection (100%) was equal to 400 l/min, 8.61 g/sec.

Table 5.2: LUPOE1-D operating conditions.

Condition	Engine speed [rpm]	r_v	ϕ	θ_{sp} [° aTDC]	T_{air} [° C] [a]	$\dot{m}_{air}$ [g/sec]	Skip-fire ratio
Base condition	1500	7.6	1.0	-20	70	6.9	5
Lean mixture	1500	7.6	0.8	-31	70	6.9	5
Low engine speed	750	7.6	1.0	-10	70	6.9	5
High engine speed	2000	7.6	1.0	-31	70	6.9	5
Medium compression ratio	1500	10.2	1.0	-20	70	6.9	5
High compression ratio	1500	12.4	1.0	-20	70	6.9	5

[a] Cylinder head and barrel temperatures were 80 and 72° C respectively. It is likely that the intake air temperatures reported are inaccurate because of temperature drop caused by fuel addition as per LUPOE2 although this is not discussed by Abdi Aghdam [2003].

Table 5.3: Camera and data acquisition system settings (1).

Condition	Firing cycles captured for a given laser sheet position	Frames captured per cycle
Base condition	100	50
Low engine speed	50	80
Medium engine speed	50	70
Lean mixture	50	60

Table 5.4: Camera and data acquisition system setting (2).

DAQ system sample rate [kHz]	200
Firing cycles captured per test	10
Camera frame rate [kHz]	200
Camera exposure time [μsec]	5
Camera resolution [pixels]	512×512

5.3 Experimental Results

5.3.1 Overall flame geometry

Presented in this section are ensemble three-dimensional flame surfaces defined as the isosurface of $\overline{c} = 0.5$ reconstructed from laser sheet slices as described in Section 3.3.6. Figures 5.1, 5.2, 5.3 and 5.4 show the ensemble average position of the burnt gas front in the LUPOE2-P engine for the base condition, low speed, middle speed and lean conditions respectively. The large arrows indicate the orientations of the ports with respect the pent roof. The blue arrow represents the intake port, the two orange arrows represent the exhaust runners which emptied the annulus behind the multiple small exhaust ports as described in Section 2.2.2.

Table 5.5: Data processing parameters.

Threshold level I_t	0.5
Median filter region [pixels]	3×3
Voxel resolution [mm]	$1.5 \times 1.5 \times 1.5$
Volume smoothing filter region [voxels]	$3 \times 3 \times 3$
Surface smoothing λ	0.33
Surface smoothing μ	-0.331
Number of surface smoothing iterations	20
Analogue signal downsample rate [$^\circ$CA^{-1}]	0.2
Analogue signal filter cutoff frequency [$^\circ$CA^{-1}]	1

The actual vertical positions of the ports was much lower than shown in the figures. A red sphere in the centre of the chamber shows the location of the spark gap and the black lines indicate the extents of the clearance volume. The surface of the flame is coloured to indicate the local mass burning velocity u_{tr} where the scale in the upper left image applies to all the images in the figure.

In all cases apart from for the lean images, discussed later, the early flame propagation appears from visual inspection to be close to spherical. As the cycle progresses the flame is convected either towards or away from the intake port depending on the engine speed. The position of the isosurface later in the cycles, see in particular the last image in Figure 5.3, shows the extents of the clearance volume imaged. Although the flame is not fully grown in this image the missing regions in the "eaves" of the pent, clipped by the windows because of the off-axis viewing angle of the camera are evident. Early in the cycle the small region obscured by the spark is evident, see for example the top right images in Figure 5.3.

Results for the lean condition, Figure 5.4 are very poor compared to the results from the other engine conditions. In particular, early in the cycle there appears to be little coherence between the behaviour of the flame on different sheet planes as evidenced by the split flame kernel in the first couple of images. This is clearly nonphysical, in order for burnt gas to be present at the top and bottom of the clearance volume there should be burnt gas somewhere in the middle of the clearance volume.

It is possible that, as the engine is much more sensitive to variations in fuelling when running away from stoichiometry small changes in the engine fuelling for this condition could have adversely affected the results. To minimise the number of adjustments to the laser sheet position, both stoichiometric and lean tests for a particular sheet position were recorded together. For this reason the fuel mass flow rate was re-adjusted for every laser sheet position and some small variability in fuelling should be expected different sheet positions.

A second possibility, that the increased fragmentation of the flame under lean conditions requires a larger number of images to be averaged to give representative $\overline{c}$ contours, is also possible. Shown in Figure 5.5 are binary images of depicting the location of burnt and unburnt gas on the plane 7.5 mm above TDC for ten individual cycles in the lean condition. The flames are noticeably more disrupted, with a greater proportion of unburnt close to the centre of the flame, than similar flames with stoichiometric fuelling. Consequently, values of $\overline{c}$ in the centre of the flame will be lower and, as mentioned above, more images should be averaged to

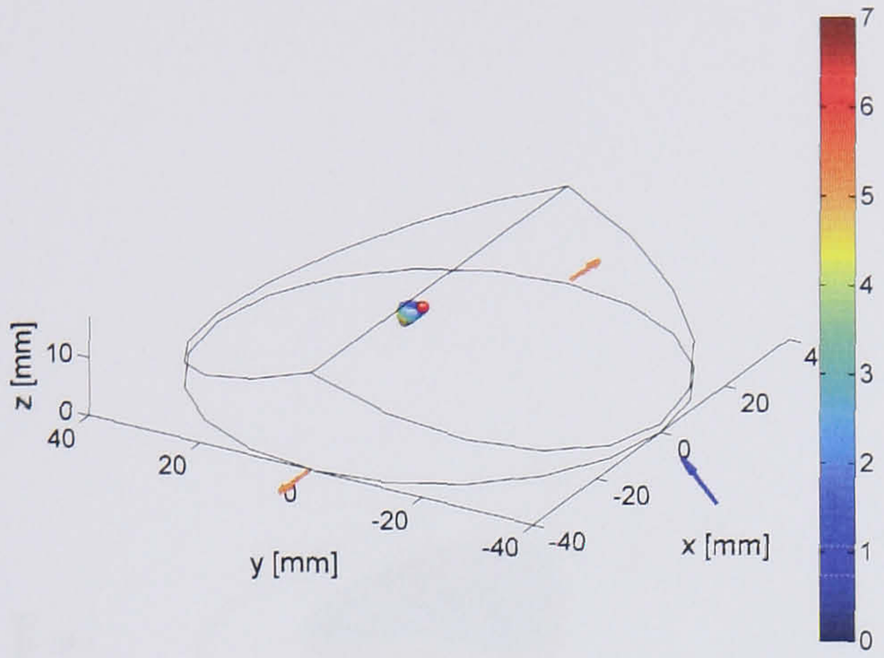

(a) -0.8° aTDC

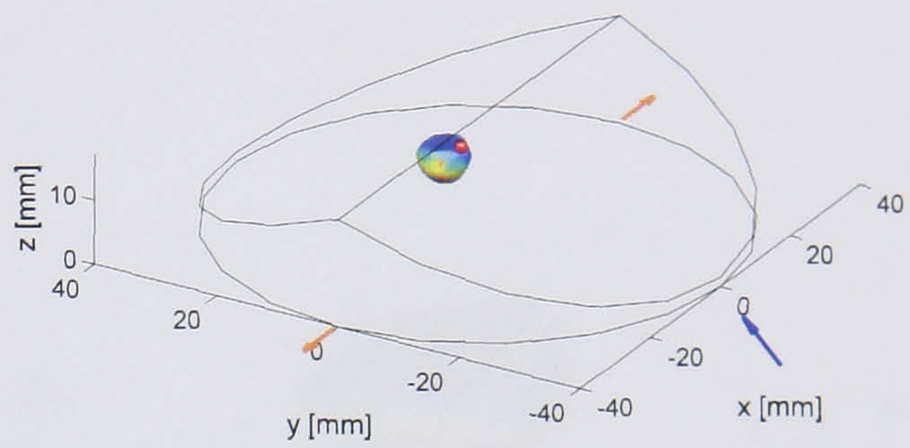

(b) 0.1° aTDC

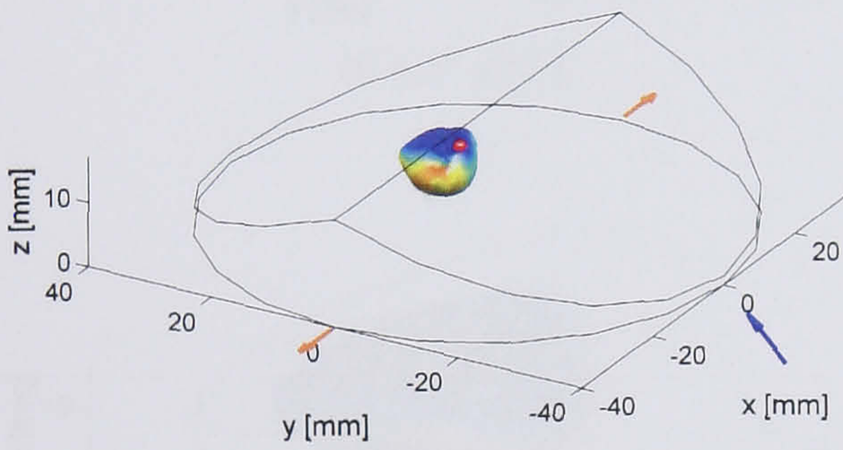

(c) 1.0° aTDC

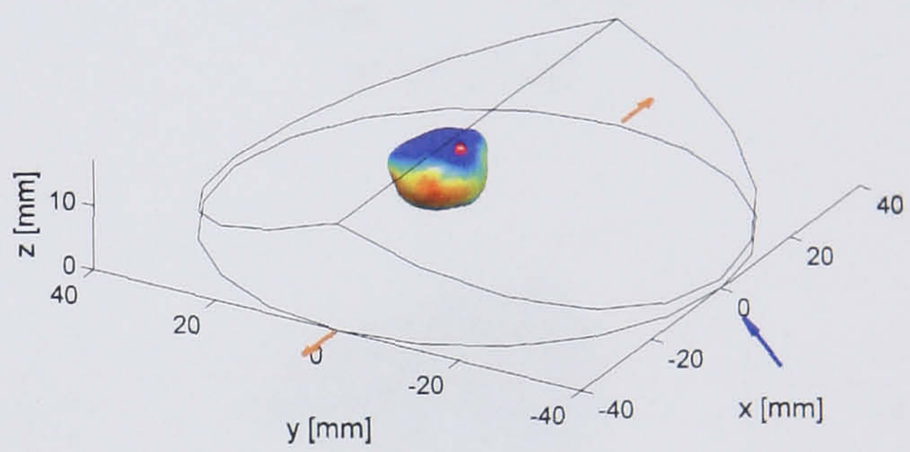

(d) 1.9° aTDC

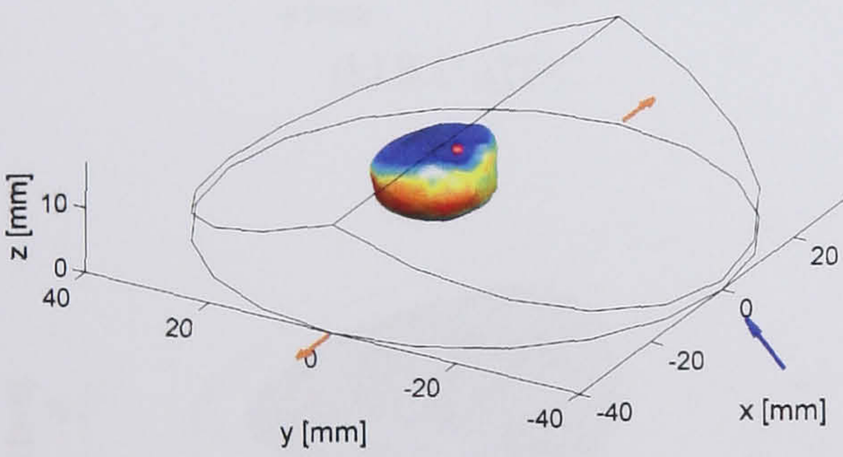

(e) 2.8° aTDC

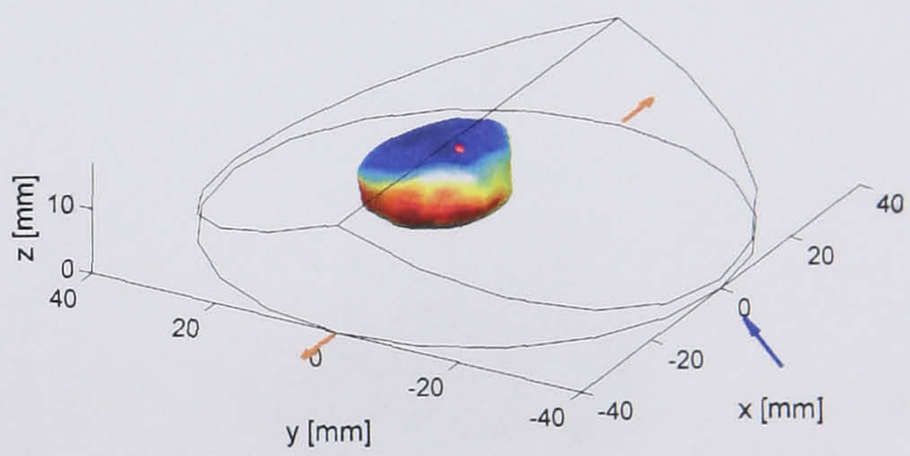

(f) 3.6° aTDC

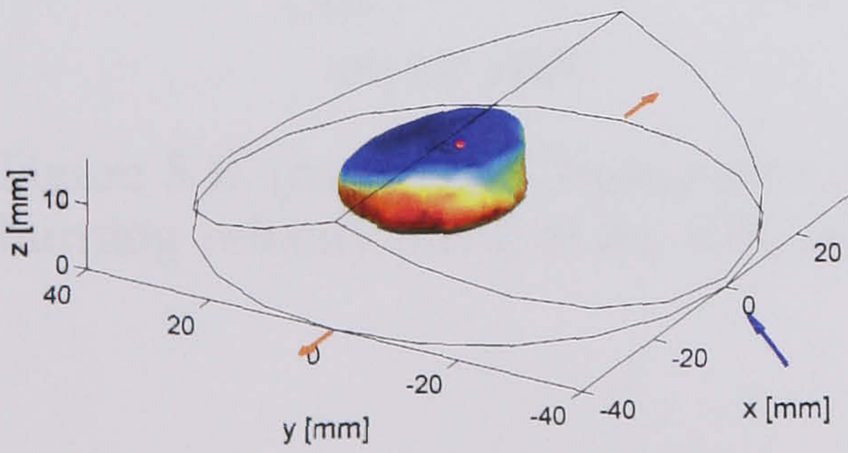

(g) 4.5° aTDC

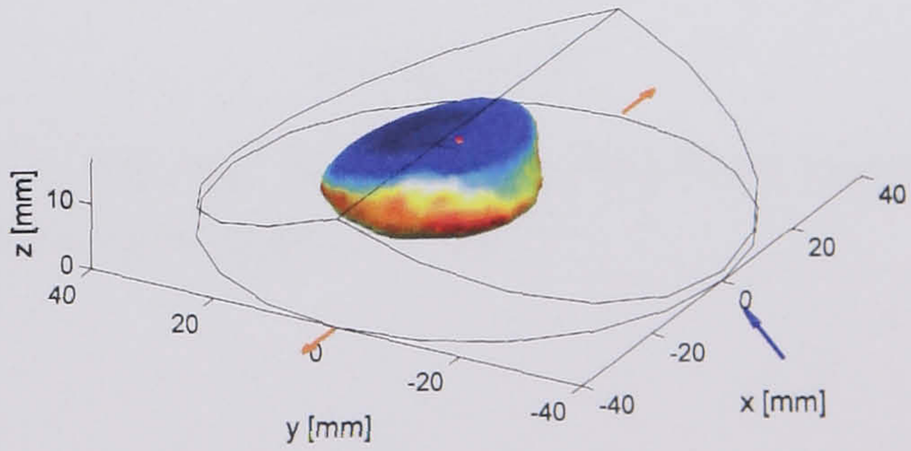

(h) 5.4° aTDC

Figure 5.1: Isosurfaces of $\bar{c} = 0.5$ coloured to show the local mass burning velocity (m/s) at the 1500 rpm base condition. Figure continued on page 162.

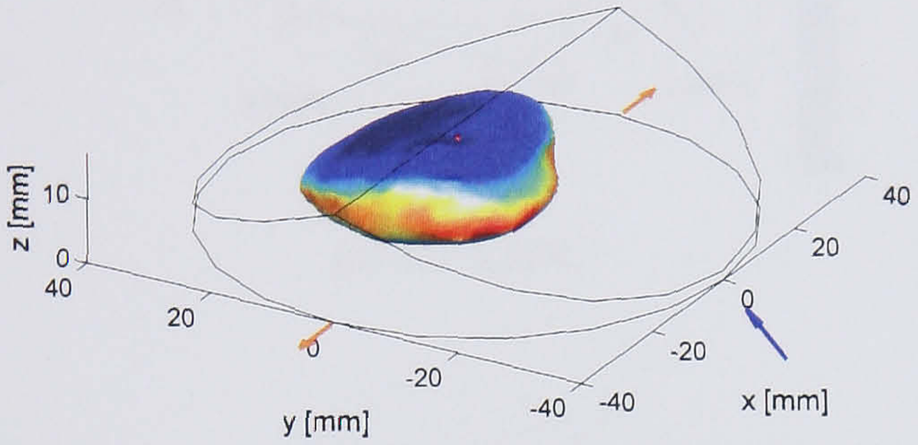

(i) 6.3° aTDC

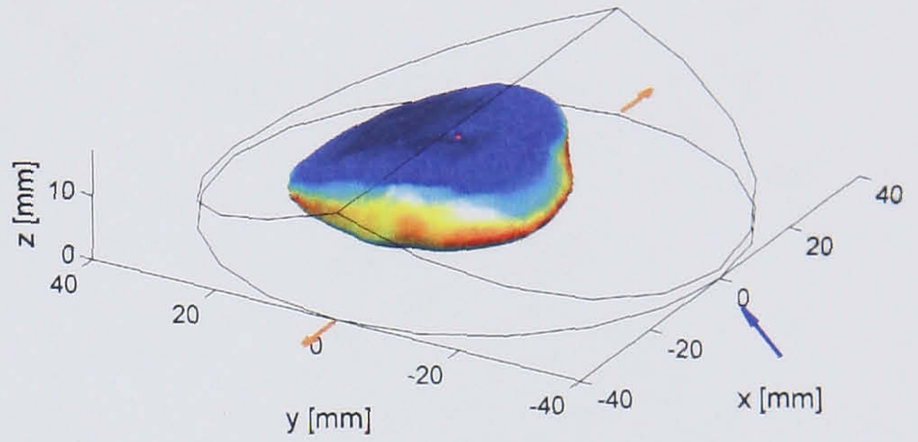

(j) 7.2° aTDC

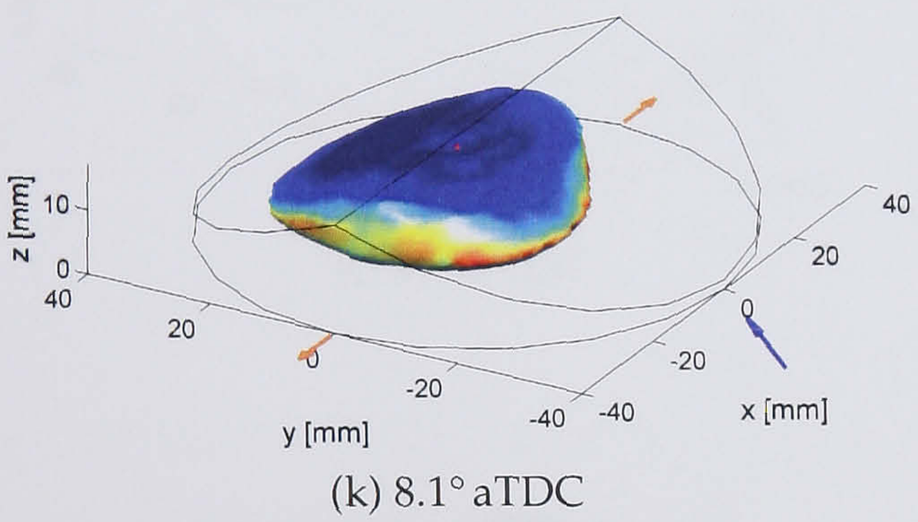

(k) 8.1° aTDC

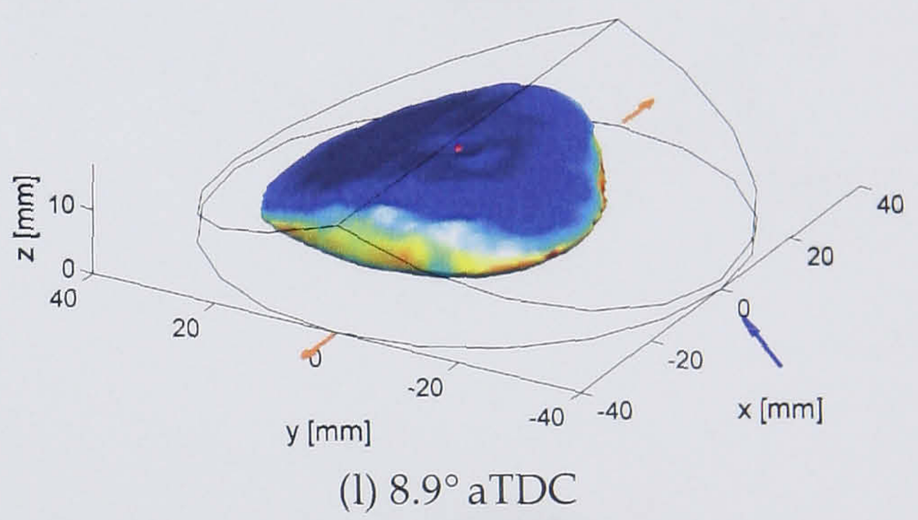

(l) 8.9° aTDC

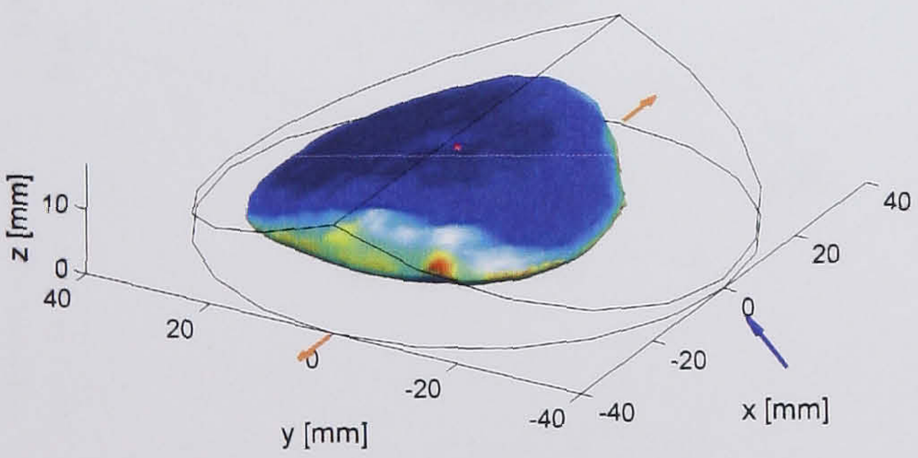

(m) 9.8° aTDC

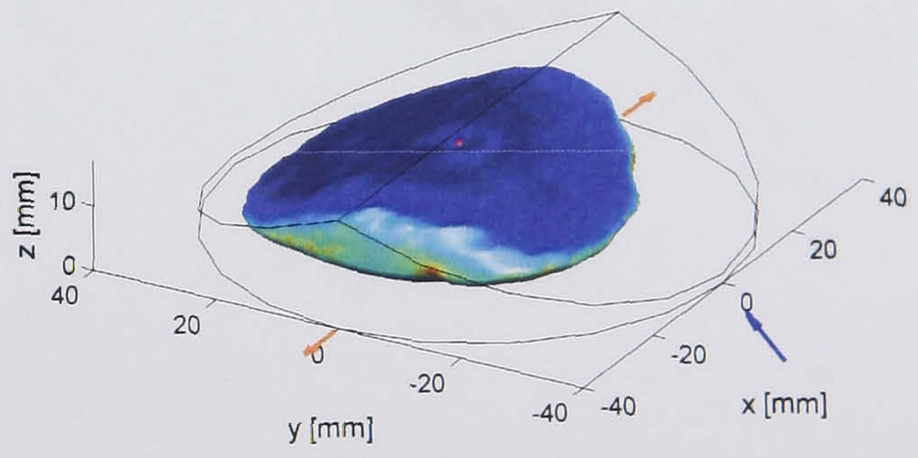

(n) 10.7° aTDC

Figure 5.1: (continued) Isosurfaces of $\overline{c} = 0.5$ coloured to show the local mass burning velocity (m/s) at the 1500 rpm base condition.

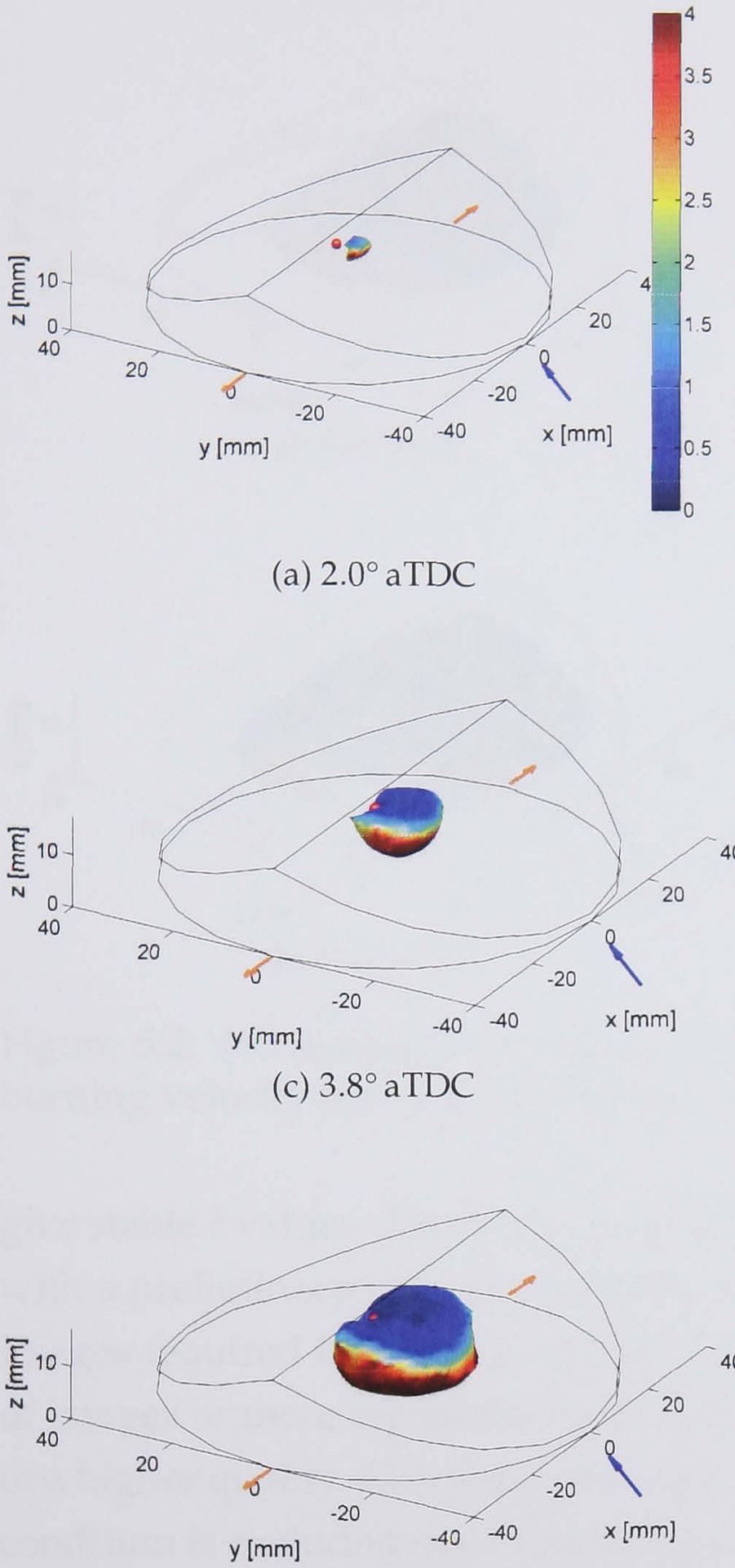

(a) 2.0° aTDC

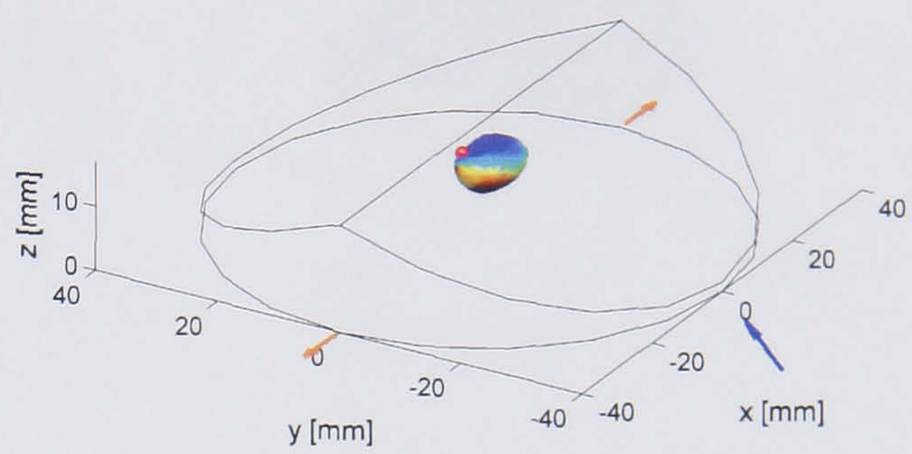

(b) 2.9° aTDC

(c) 3.8° aTDC

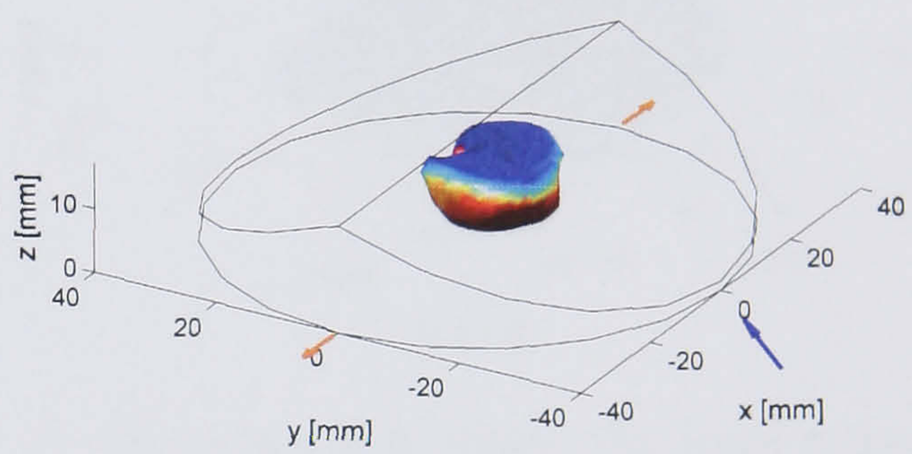

(d) 4.7° aTDC

(e) 5.6° aTDC

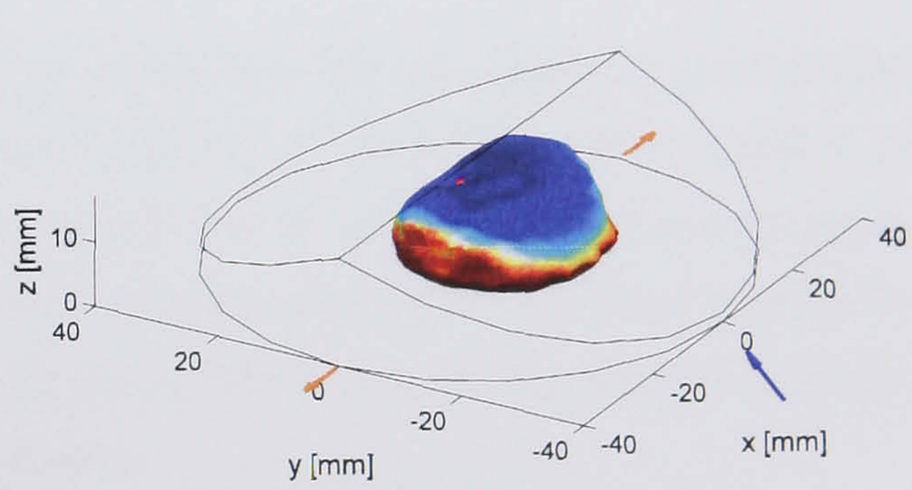

(f) 6.5° aTDC

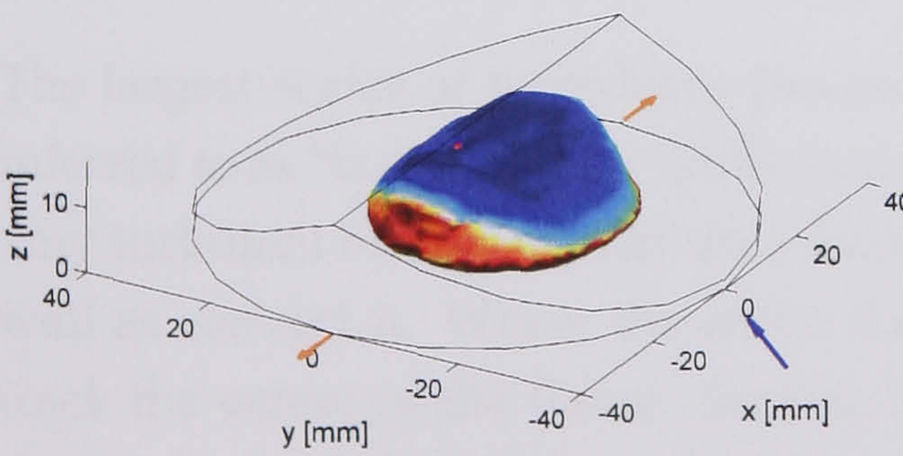

(g) 7.4° aTDC

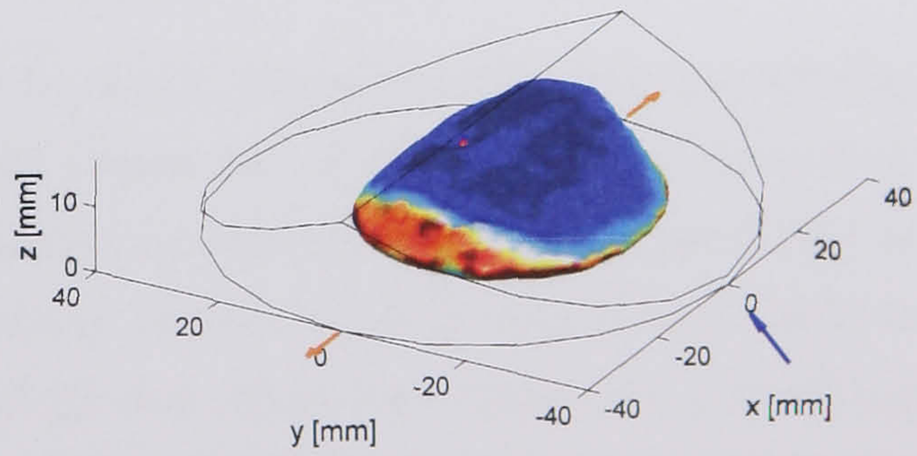

(h) 8.2° aTDC

Figure 5.2: Isosurfaces of $\overline{c} = 0.5$ coloured to show the local mass burning velocity (m/s) at the 750 rpm condition. Figure continued on page 164.

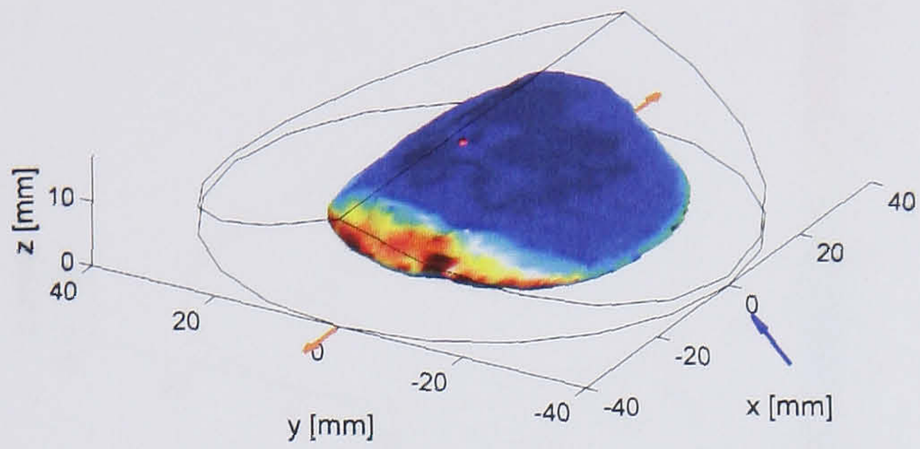

(i) 9.1° aTDC

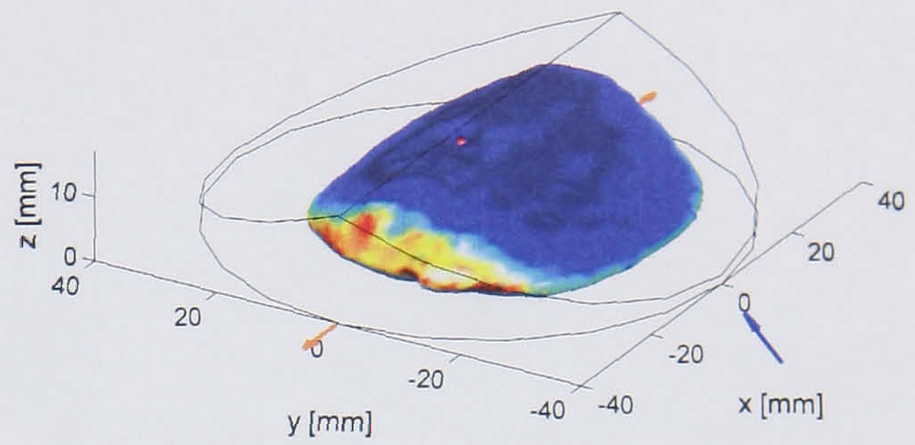

(j) 10.0° aTDC

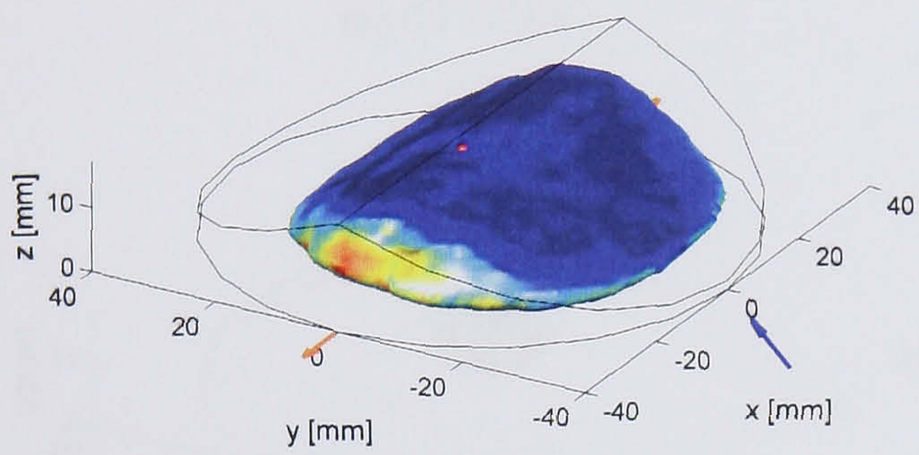

(k) 10.9° aTDC

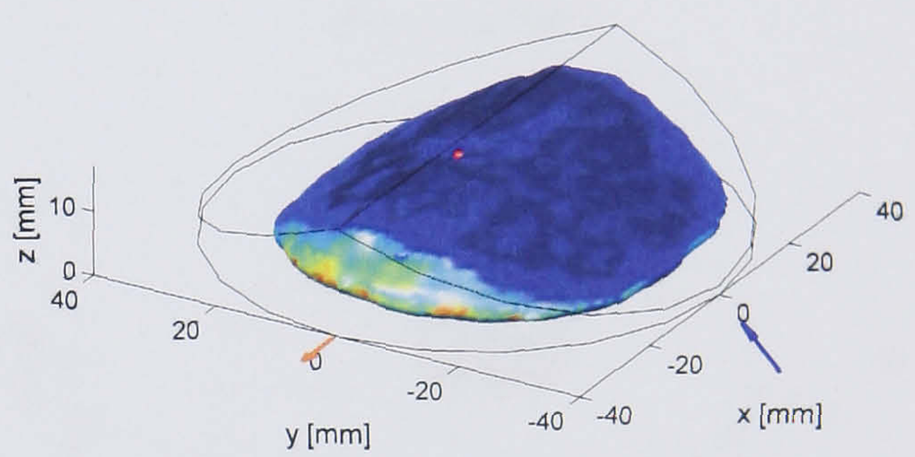

(l) 11.8

Figure 5.2: (continued) Isosurfaces of $\overline{c} = 0.5$ coloured to show the local mass burning velocity (m/s) at the 750 rpm condition.

give stable $\overline{c}$ values. The analysis described in Section 5.5 was initially performed with a preliminary data set of stoichiometric flames to determine the number of images required for the experiment. It is possible that with an increased number of images or more repeatable fuelling the results for the lean condition would be of a higher quality. Given the obvious problems with the imaging results the lean condition is excluded from further discussion.

5.3.2 Centroid movement and in-cylinder flow

The largest scales of turbulence present in the combustion chamber, sometimes referred to as "bulk flow" or "bulk motion" cause the entire flame to be convected. Any turbulent eddies smaller than the flame can potentially wrinkle the flame as well as convect it. Where the entire flame is convected it is useful to be able to track the centre of the flame. Section 3.3.12 described two methods of tracking the location of the centre of the flame; either tracking the centre of mass, the barycentre, or tracking the point which is equidistant, in the least squares sense, from the active flame front.

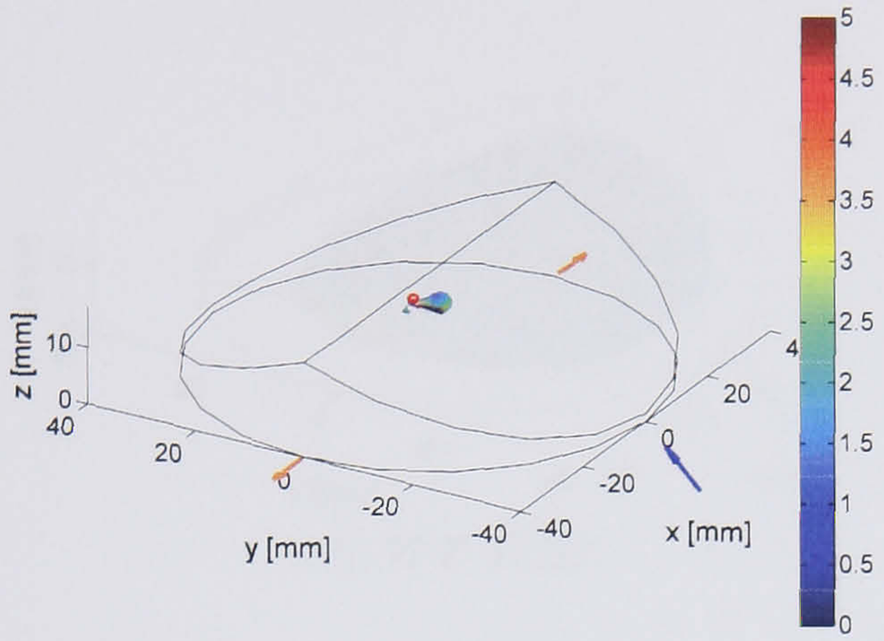

(a) 0.7° aTDC

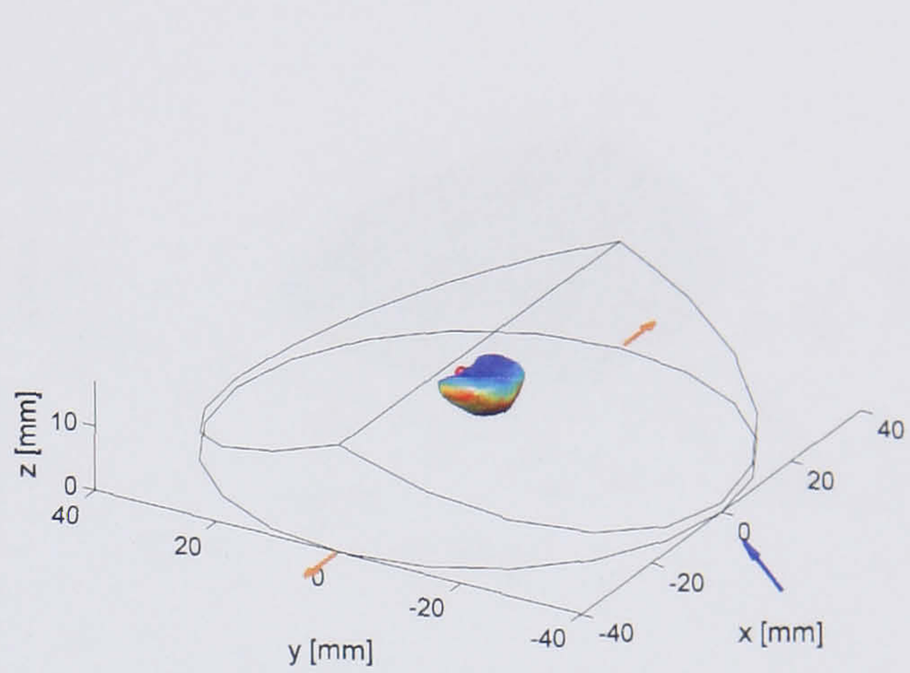

(b) 1.9° aTDC

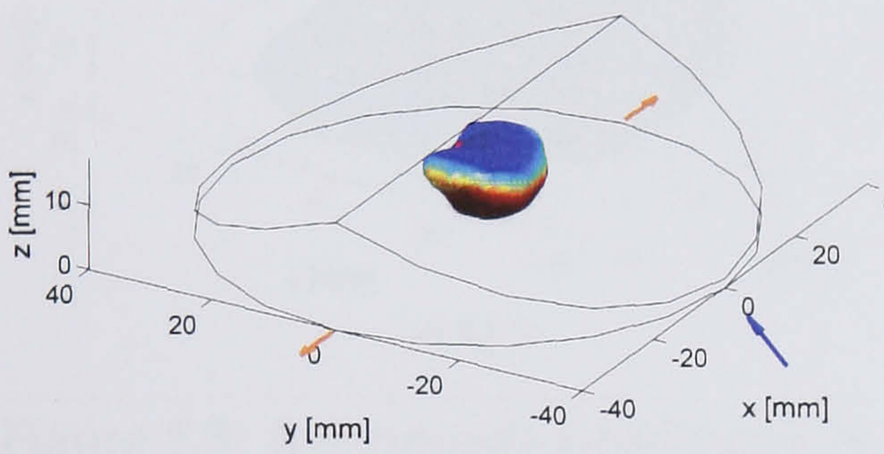

(c) 3.1° aTDC

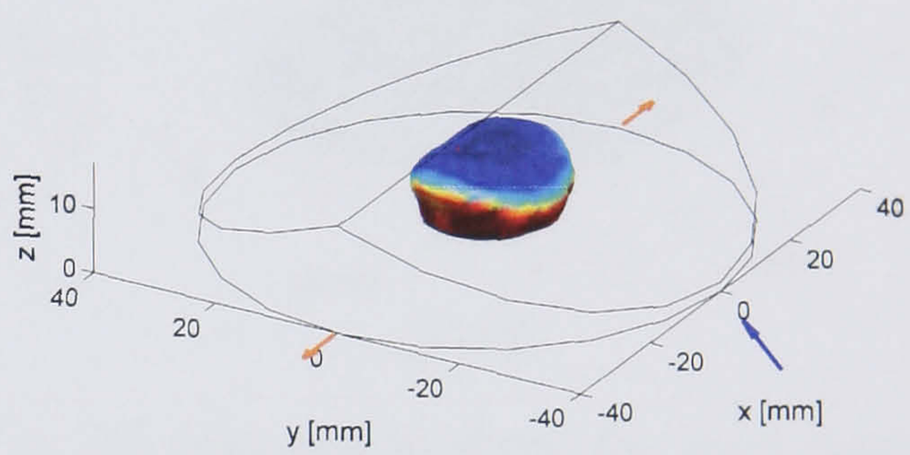

(d) 4.3° aTDC

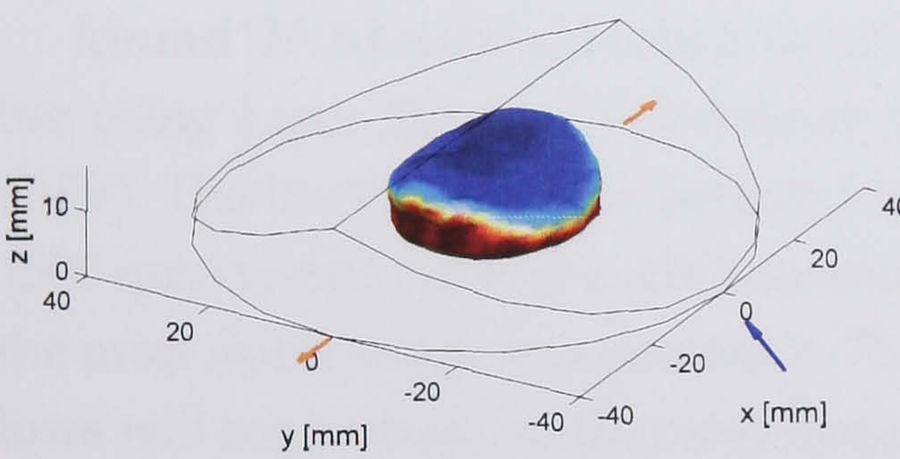

(e) 5.4° aTDC

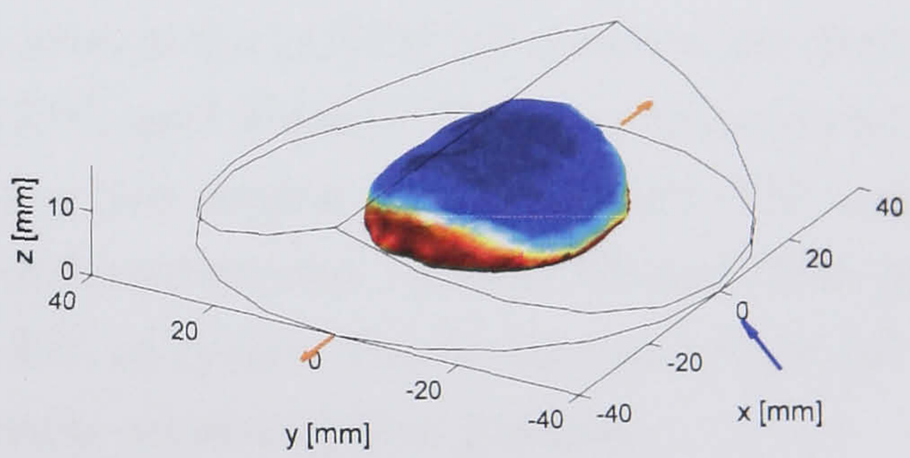

(f) 6.6° aTDC

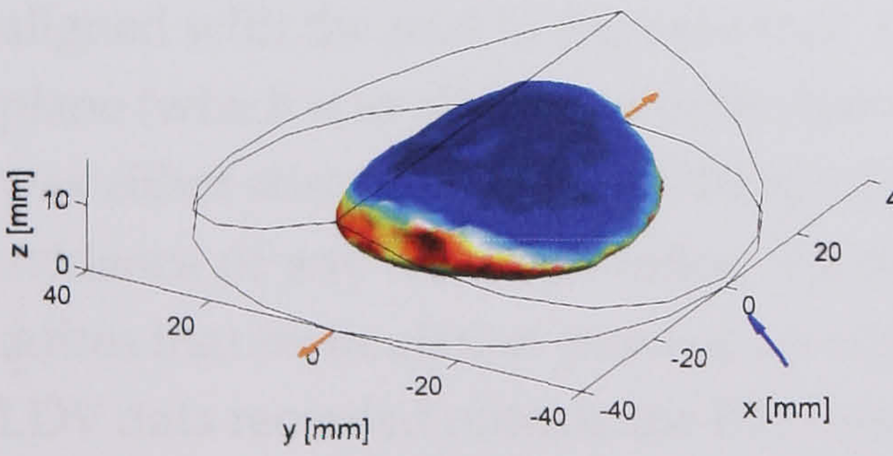

(g) 7.8° aTDC

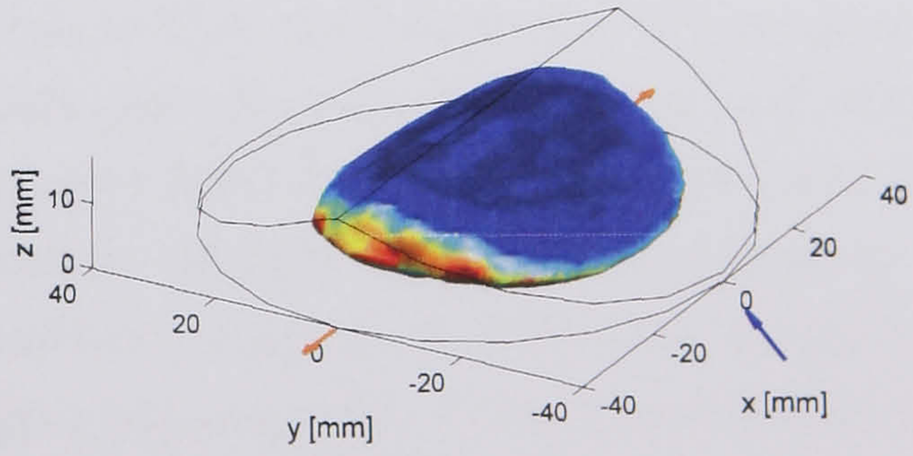

(h) 9.0

Figure 5.3: Isosurfaces of $\bar{c} = 0.5$ coloured to show the local mass burning velocity (m/s) at the 1000 rpm condition. Figure continued on page 166.

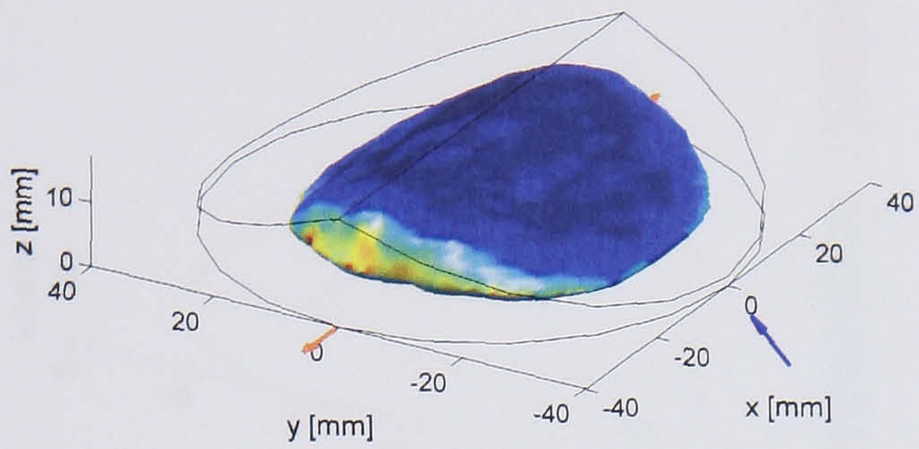

(i) 10.2° aTDC

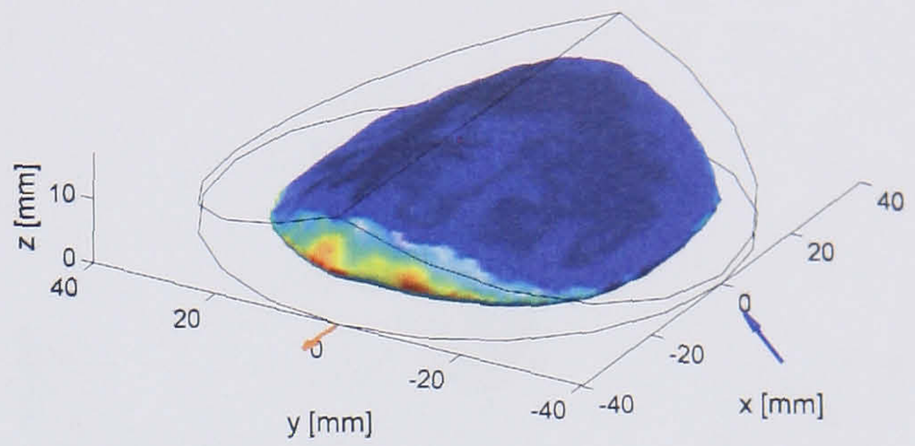

(j) 11.3

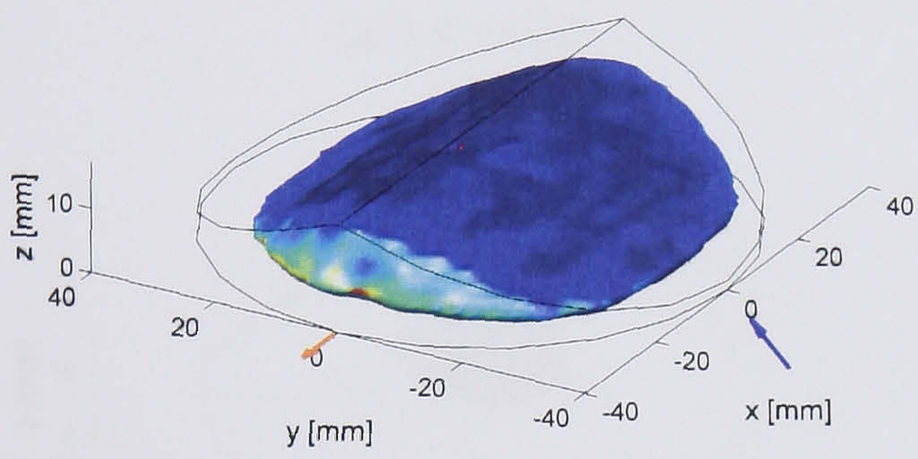

(k) 12.5

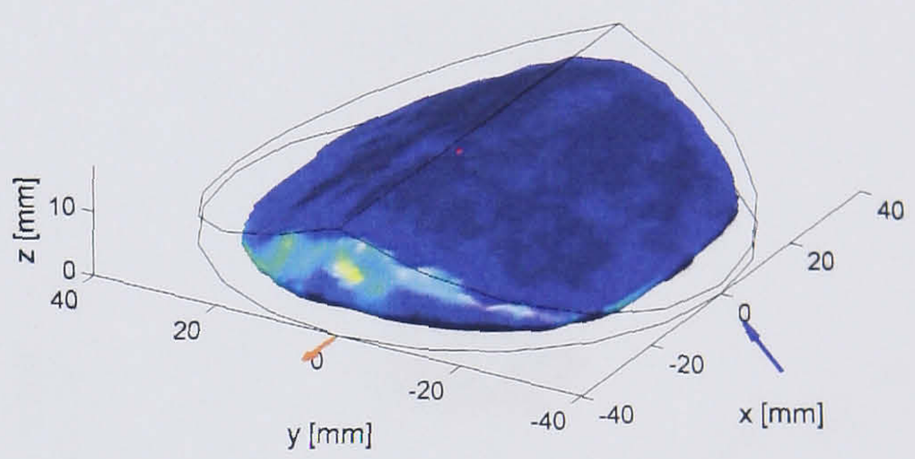

(l) 13.7

Figure 5.3: (continued) Isosurfaces of $\overline{c} = 0.5$ coloured to show the local mass burning velocity (m/s) at the 1000 rpm condition.

Murad [2006] analysed cold flow velocities in the LUPOE2-P combustion chamber using Laser Doppler Velocimetry (LDV) and Particle Tracking Velocimetry (PTV). The in-cylinder flow pattern for the two engine speeds studied (750 and 1500 rpm) varied cycle-to-cycle between different modes. At both 750 and 1500 rpm the most stable mode was present in 75–80% of cycles. The discussion which follows will concentrate on the most frequently occurring flow pattern.

During the early part of the cycle the inclined inlet caused the largest turbulent eddies, the macro scale, to form a rotating vortex whose horizontal axis was aligned with the fold in the pent roof. Close to TDC the flow in the PTV imaging plane (which was aligned with the bore axis and orthogonal to the pent roof fold) was either strongly towards (750 rpm) or away from (1500 rpm) the inlet with no evidence of any rotating vortex. As noted by Murad, conservation of mass requires that recirculation must occur somewhere within the combustion chamber. LDV data recorded outside the PTV imaging plane suggested the presence of two counter rotating vortices with axes aligned with the bore axis either side of the PTV plane. Preliminary Particle Image Velocimetry (PIV) data recorded by the author was in agreement with this observation.

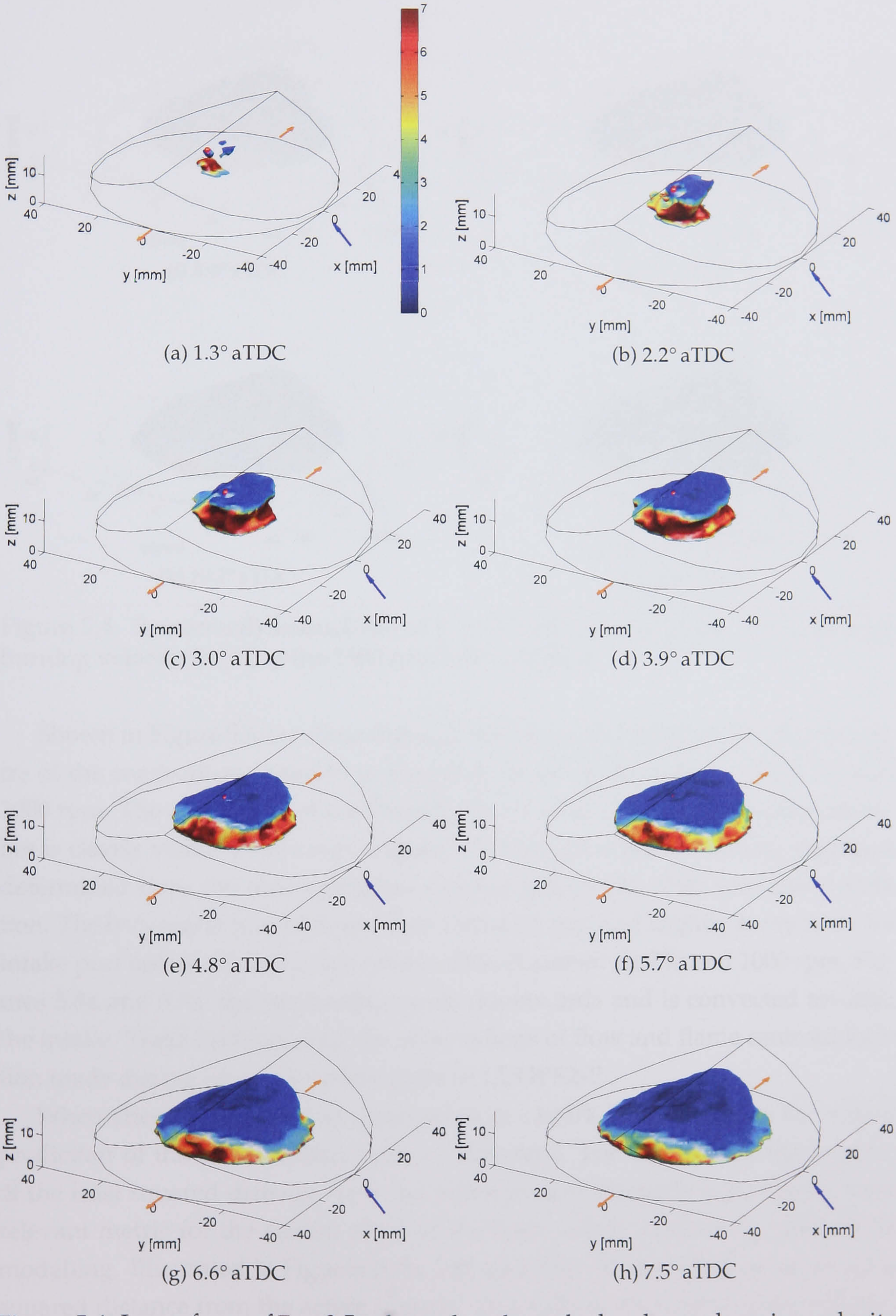

(a) 1.3° aTDC

(b) 2.2° aTDC

(c) 3.0° aTDC

(d) 3.9° aTDC

(e) 4.8° aTDC

(f) 5.7° aTDC

(g) 6.6° aTDC

(h) 7.5° aTDC

Figure 5.4: Isosurfaces of $\overline{c} = 0.5$ coloured to show the local mass burning velocity (m/s) at the 1500 rpm lean condition. Figure continued on page 168.

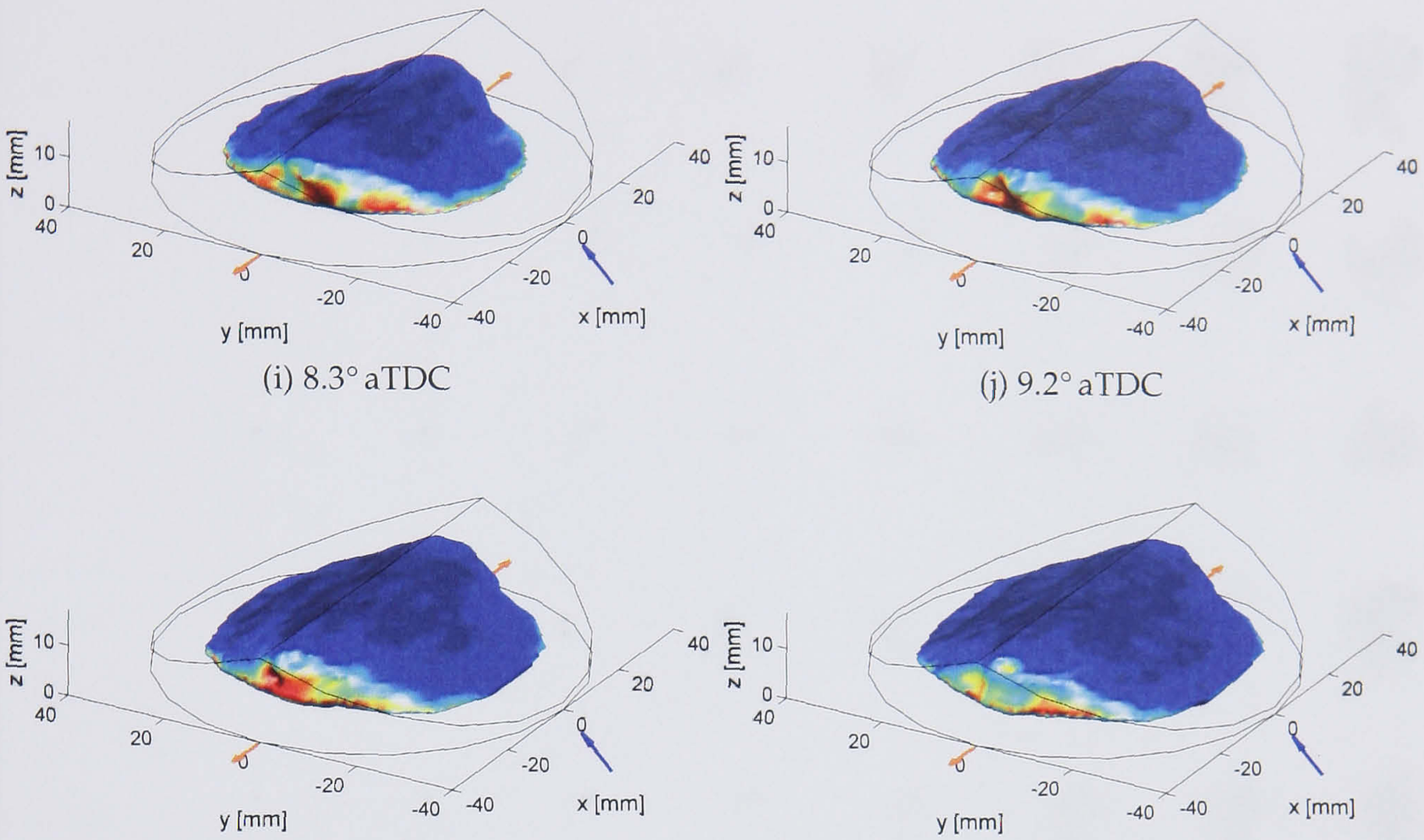

(i) 8.3° aTDC (j) 9.2° aTDC

(k) 10.1° aTDC (l) 11.0° aTDC

Figure 5.4: (continued) Isosurfaces of $\bar{c} = 0.5$ coloured to show the local mass burning velocity (m/s) at the 1500 rpm lean condition.

Shown in Figure 5.6 are slices through the mean progress variable field in centre of the combustion chamber in the plane of the intake port for 1500, 750 and 1000 rpm. The convection of the flame by the flow field in the combustion chamber is clearly visible in all cases. Figure 5.7a shows the flame centroid migration determined from the mean progress variable field at the 1500 rpm base condition. The barycentre moves down from the spark gap and slightly away from the intake port before settling in the centre of the chamber. At 750 and 1000 rpm, Figures 5.8a and 5.9a, the barycentre moves downwards and is convected towards the intake. These findings echo the observations of flow and flame centroid location made during Murad's earlier study of LUOPE2-P.

When attempting to model combustion in a spark ignition engine the correct prediction of the active surface area is important. For this reason, the location of the least squared distance from the active surface elements is perhaps a more relevant metric for the central point of the flame when conducting combustion modelling. Illustrated in Figures 5.7b, 5.8b and 5.9b are the locations of the least squared distance from the active surface. This statistic showed a similar pattern of migration to the barycentre during the early part of the cycle, albeit with the

Figure 5.5: Binary images showing the locations of burnt and unburnt gas 7.5 mm above the TDC plane in ten different cycles for the 1500 rpm lean condition. The first image (left hand side) is at -9.3° aTDC, the last image (right hand side) is at 4.8° aTDC.

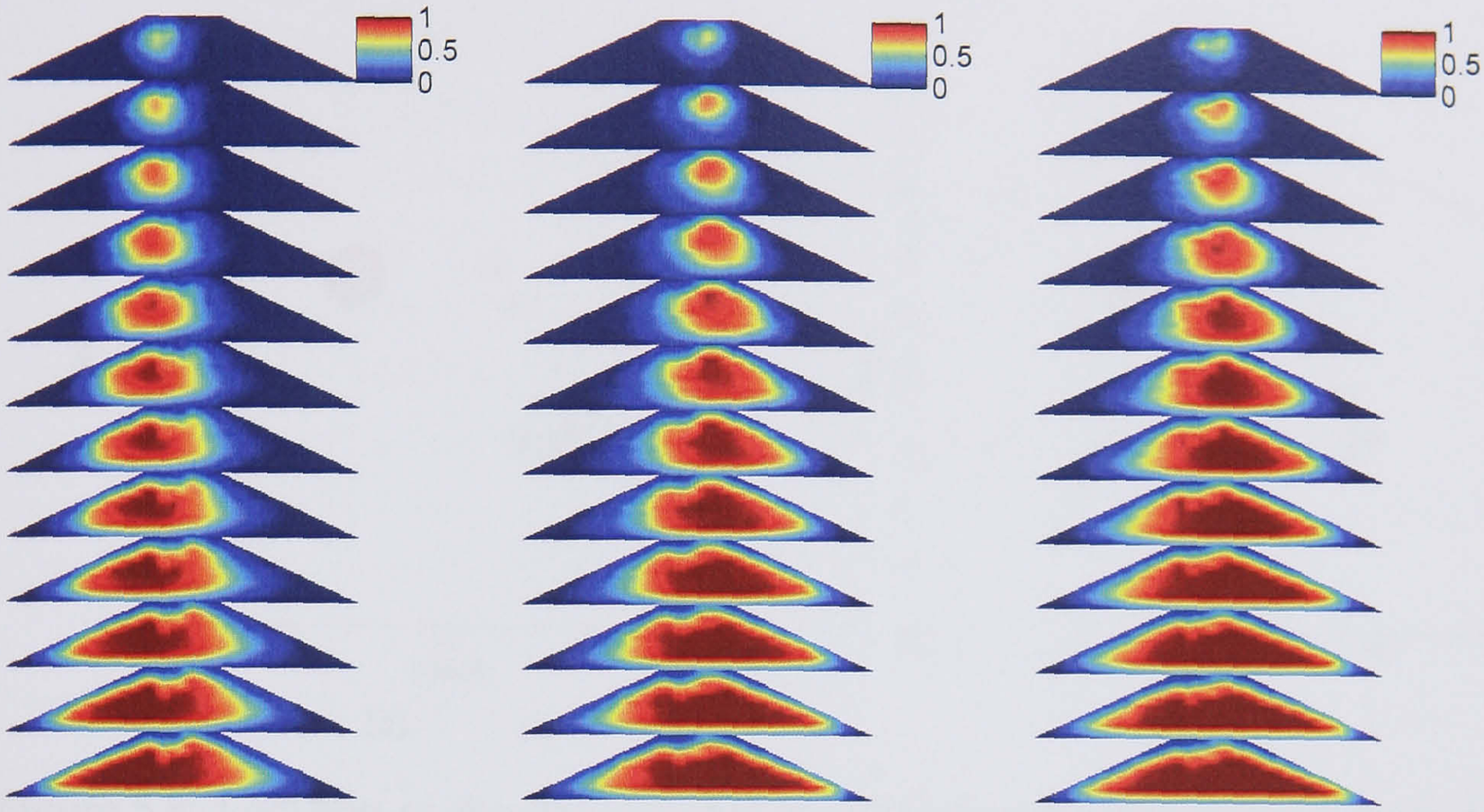

Figure 5.6: Slices showing the $\overline{c}$ field in the centre of the bore on the y-z plane. The engine conditions were: 1500 rpm base condition, -0.8–8.9° aTDC (left); 750 rpm stoichiometric, 2.0–11.8° aTDC (centre); 1000 rpm stoichiometric, -0.7–13.7° aTDC (right).

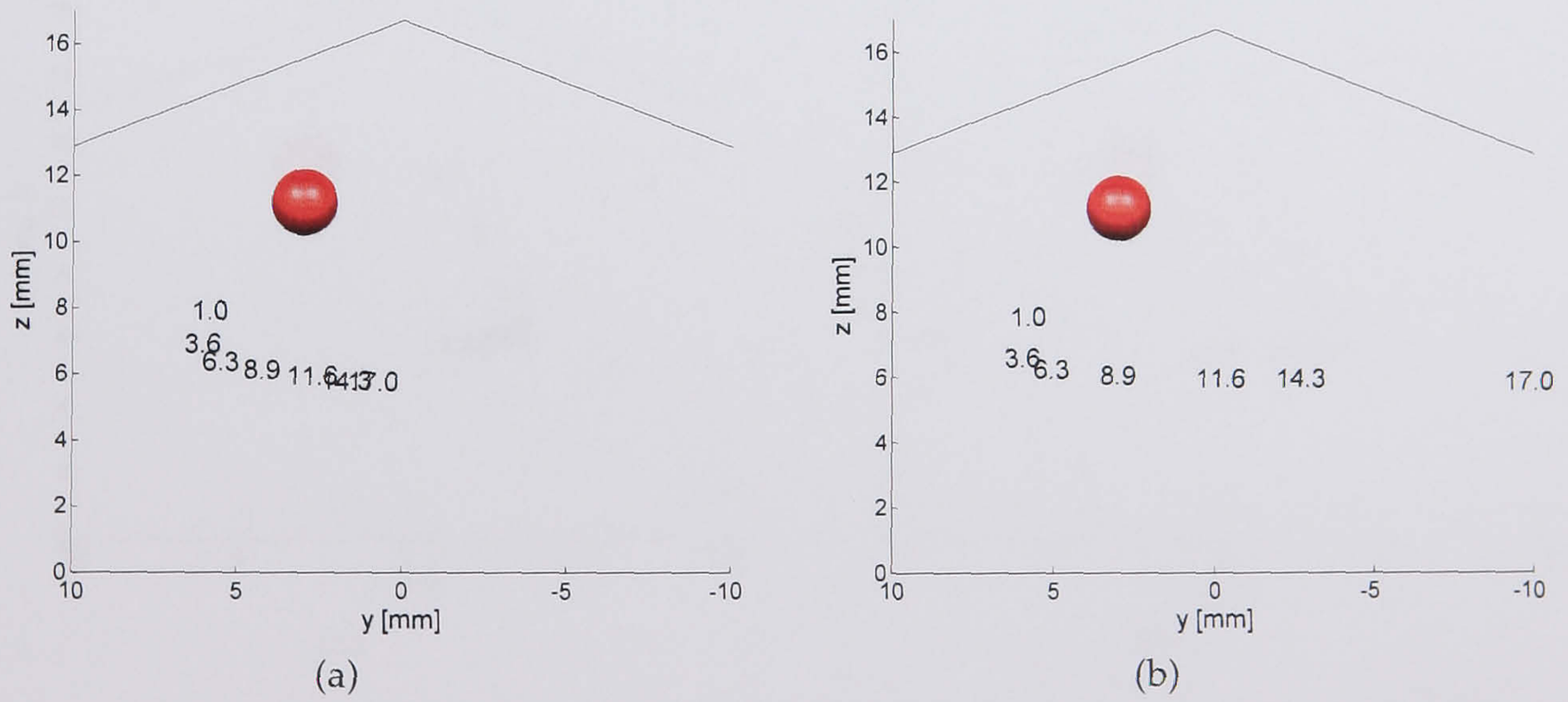

(a) (b)

Figure 5.7: Location of the flame centroid defined as the barycentre (a) and active area centre (b) at different crank angle °aTDC in the LUPOE2-P engine at 1500 rpm stoichiometric.

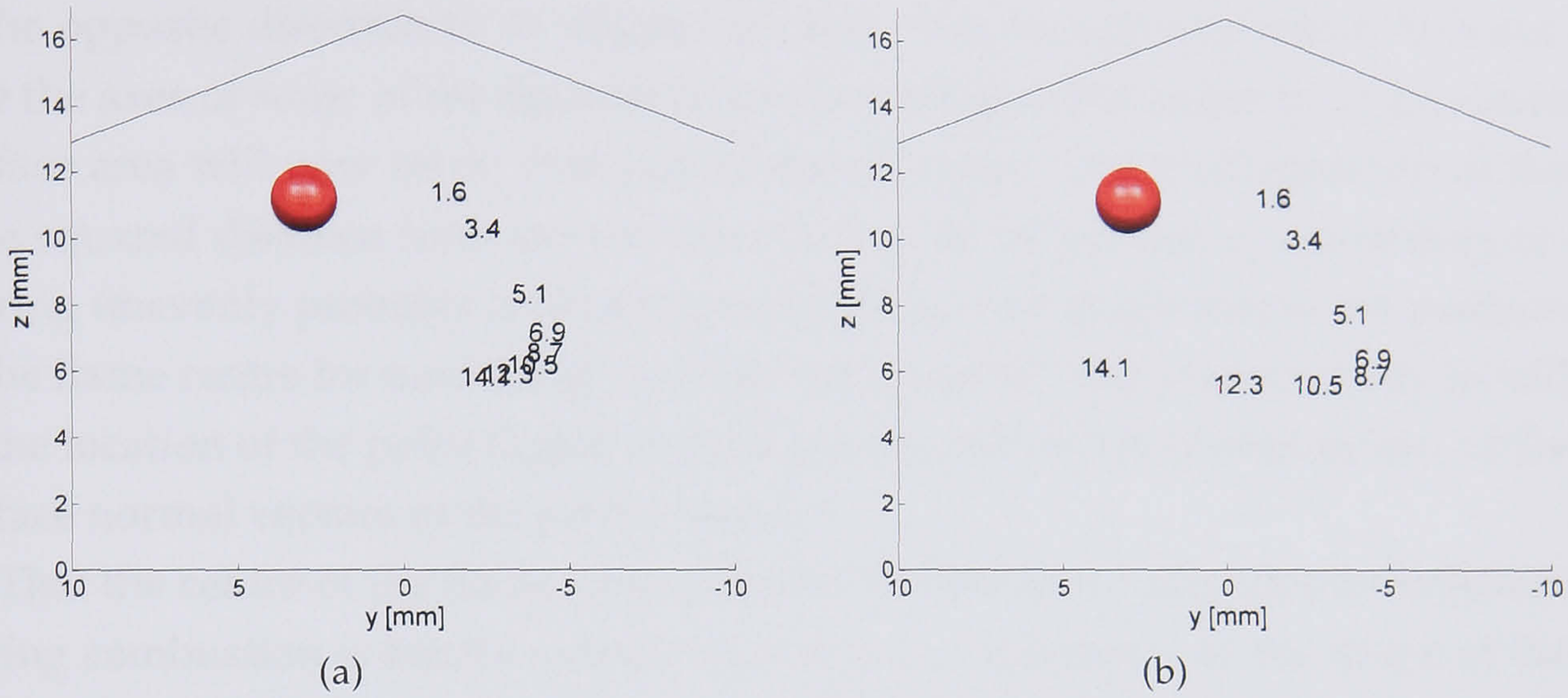

(a) (b)

Figure 5.8: Location of the flame centroid defined as the barycentre 5.8a and active area centre 5.8b at different crank angle ° aTDC in the LUPOE2-P engine at 750 rpm stoichiometric.

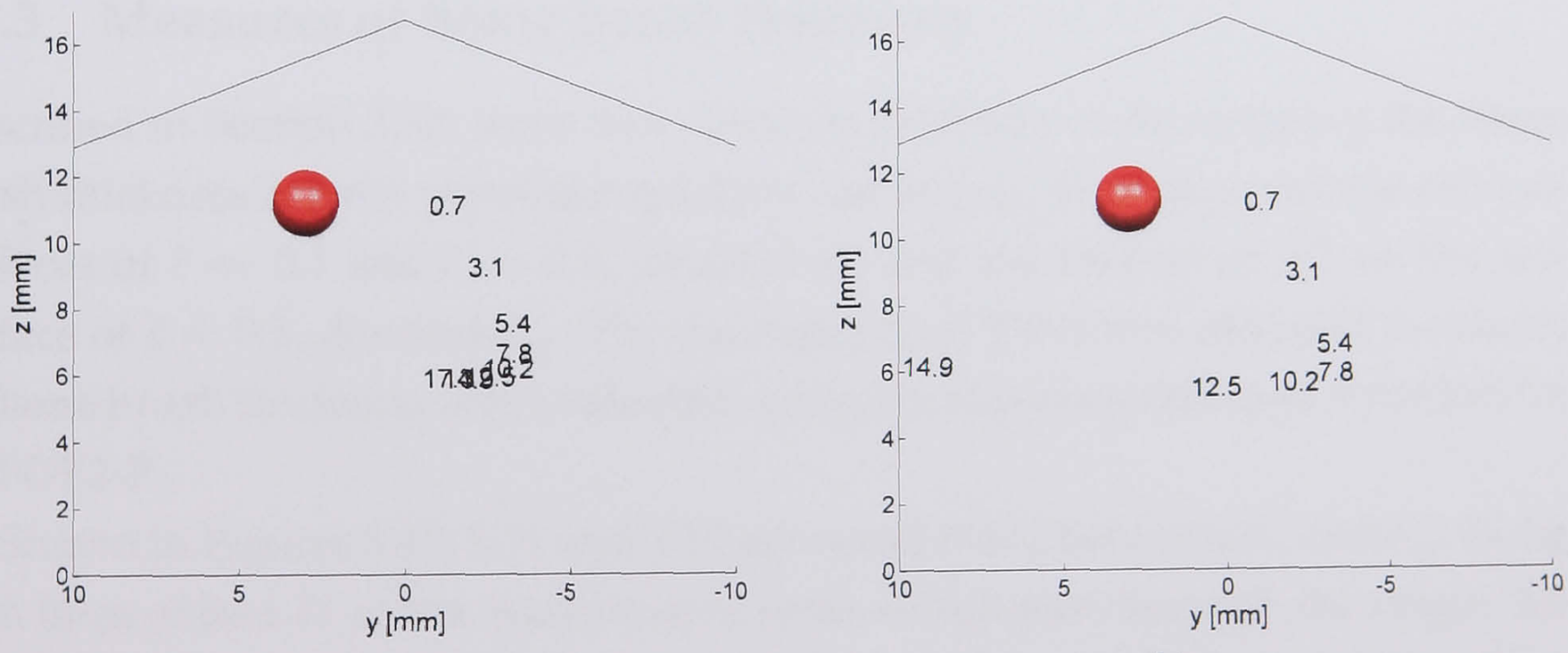

(a) (b)

Figure 5.9: Location of the flame centroid defined as the barycentre 5.9a and active area centre 5.9b at different crank angle ° aTDC in the LUPOE2-P engine at 1000 rpm stoichiometric.

movement emphasised. In the later part of the cycle, during which the majority of the flame surface had quenched on the side the flame was originally convected to, the location of the least squared distance from the active surface moved strongly in the opposite direction to its original motion. This movement (which falls outside the axes of some of the figures) is not surprising as the majority of the active surface area will now be on that side of the chamber. The predisposition of the least squared distance from the active surface to be influenced by quenching occurring unevenly probably makes it unsuitable as a measurement of the position of the flame centre for modelling. An interesting statistic for a future study would be the location of the point (again in the least squares sense) of intersection of the surface normal vectors of the active surface.

That the centre of the flame (regardless of its definition) migrates downwards during combustion is hardly surprising and is a consequence of the shape of the pent roof combustion chamber. The barycentre of a regular sphere which expands from the spark gap and is truncated by the chamber walls will naturally migrate downwards by virtue of the fact that there is less volume in the top portion of the combustion chamber because of the sloping sides of the pent roof. Migration of the flame centroid in the TDC plane, not shown here, was towards the centre of the chamber (the spark gap is slightly offset from the bore axis). In the plane orthogonal to that shown in Figures 5.7, 5.8, 5.9 and 5.6 there was little movement.

5.3.3 Measures of flame brush thickness

Described in Section 3.3.9 were two common methods of determining the flame brush thickness δ_t from experimental data: measuring the distances between iso-surfaces of $\overline{c} = 0.1$ and $\overline{c} = 0.9$, denoted δ_{ts} and the inverse of $\nabla\overline{c}$ on the iso-surface of $\overline{c} = 0.5$, denoted δ_{tg}. The equivalence of these two different measures of flame brush thickness was evaluated using the experimental data recorded for LUPOE2-P.

Shown in Figures 5.10, 5.11 and 5.12 are correlations between δ_{ts} and δ_{tg}, along with lines of best fit in the least squares sense which pass through the origin, for 1500, 750 and 1000 rpm. The figures show data for the entire flame surface from all crank angles at which burnt gas was present. There is considerable scatter in the data with many data points lying above lines of best fit. This apparent anomaly results from the majority of the data points falling close to the origin and influencing the position of the line of best fit. For all three engine speeds the

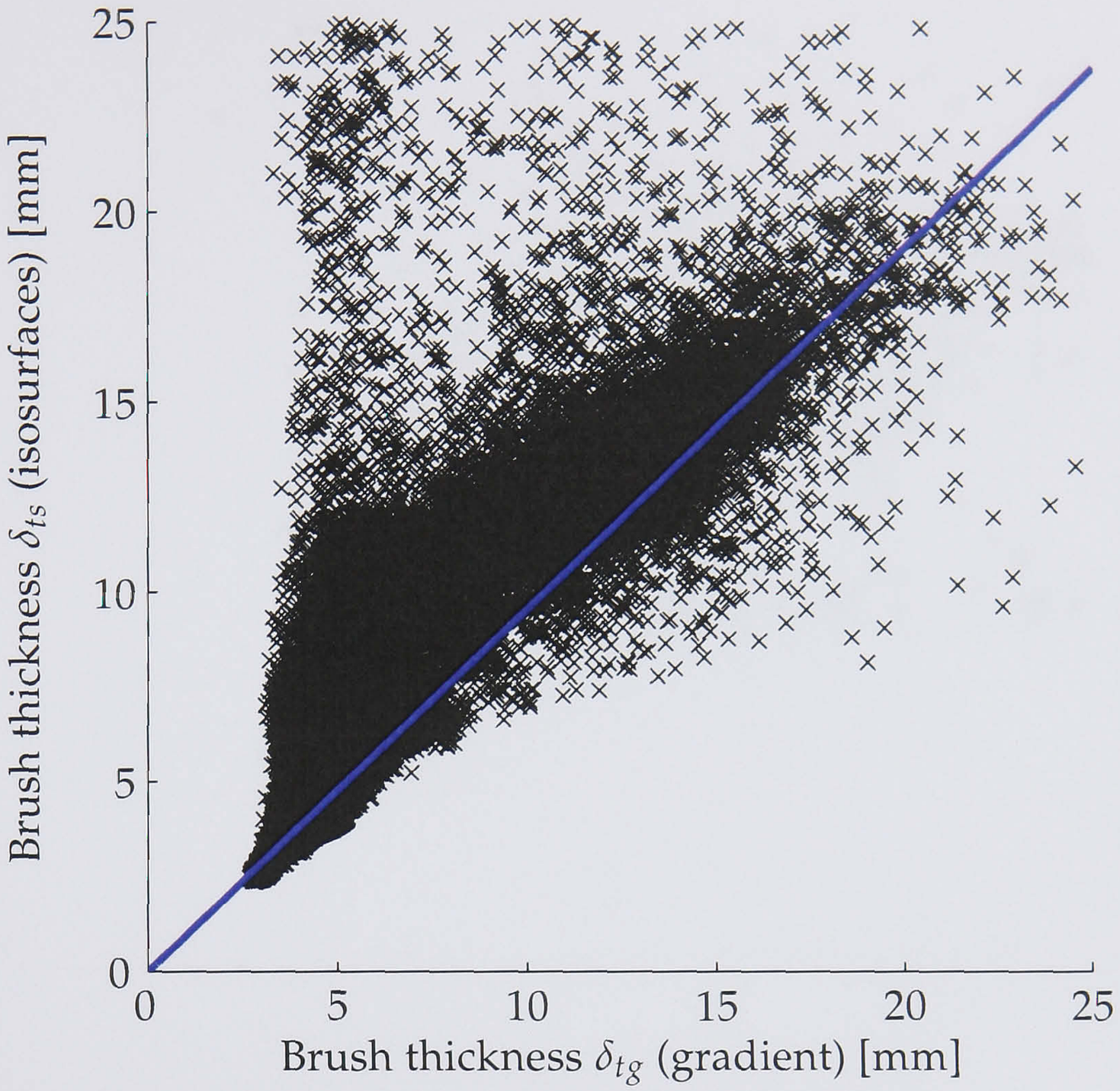

Figure 5.10: Correlation between different measures of flame thickness for all crank angles at 1500 rpm.

two measures of brush thickness, excepting the scatter in the experimental data which is discussed later, showed a reasonable correlation. The gradients of the lines of best fit were 0.97 (750 and 1500 rpm) and 0.98 (1000 rpm).

Simulated spherical flames whose profiles were generated using an error function, Equation 4.33, were processed using the same data processing procedure as applied to the real flames discussed here (Section 5.5). These simulated flames exhibited a similar correspondence between the two measures of brush thickness, albeit without the scatter found in the experimental data. It was also found when processing simulated flames that both δ_{ts} and δ_{tg} overestimated the flame brush thickness δ_t (as defined by Equation 4.33) by a factor of 1.8.

If the experimental data does conform to Equation 4.33 then it is possible to derive analytically a relationship between δ_t and δ_{tg}. For the 1-D case the inverse

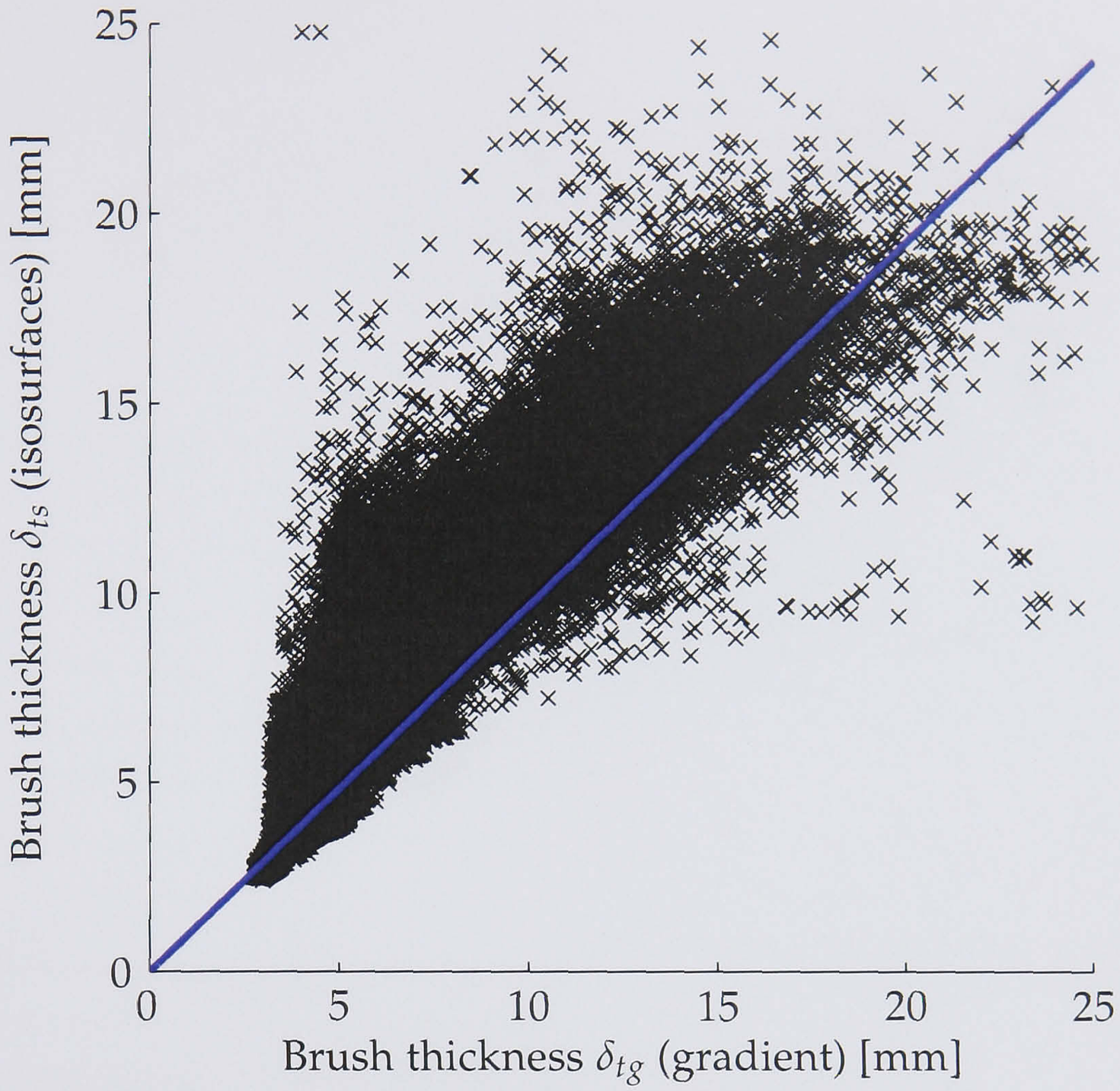

Figure 5.11: Correlation between different measures of flame thickness for all crank angles at 750 rpm.

of the space derivative of $\overline{c}$ is given by

$$\frac{\partial x}{\partial \overline{c}} = -\delta_t \sqrt{\pi} \exp\left[\frac{(x - x_0)^2}{\delta_t^2}\right] \tag{5.1}$$

where x_0 is the location of the centre of the flame, at which point $\overline{c} = 0.5$. By definition, in one dimension,

$$\delta_{tg} = \left|\frac{\partial x}{\partial \overline{c}}\right|_{\overline{c}(x)=0.5} \tag{5.2}$$

therefore

$$\delta_{tg} = \delta_t \sqrt{\pi} \tag{5.3}$$

For the flame thickness defined as the distance between isosurfaces at $\overline{c} = 0.1$ and $\overline{c} = 0.9$ a similar exercise may be undertaken. Here values of $x_{0.1}$ and $x_{0.9}$ (as defined in Figure 3.13a) are required which may be calculated algebraically from

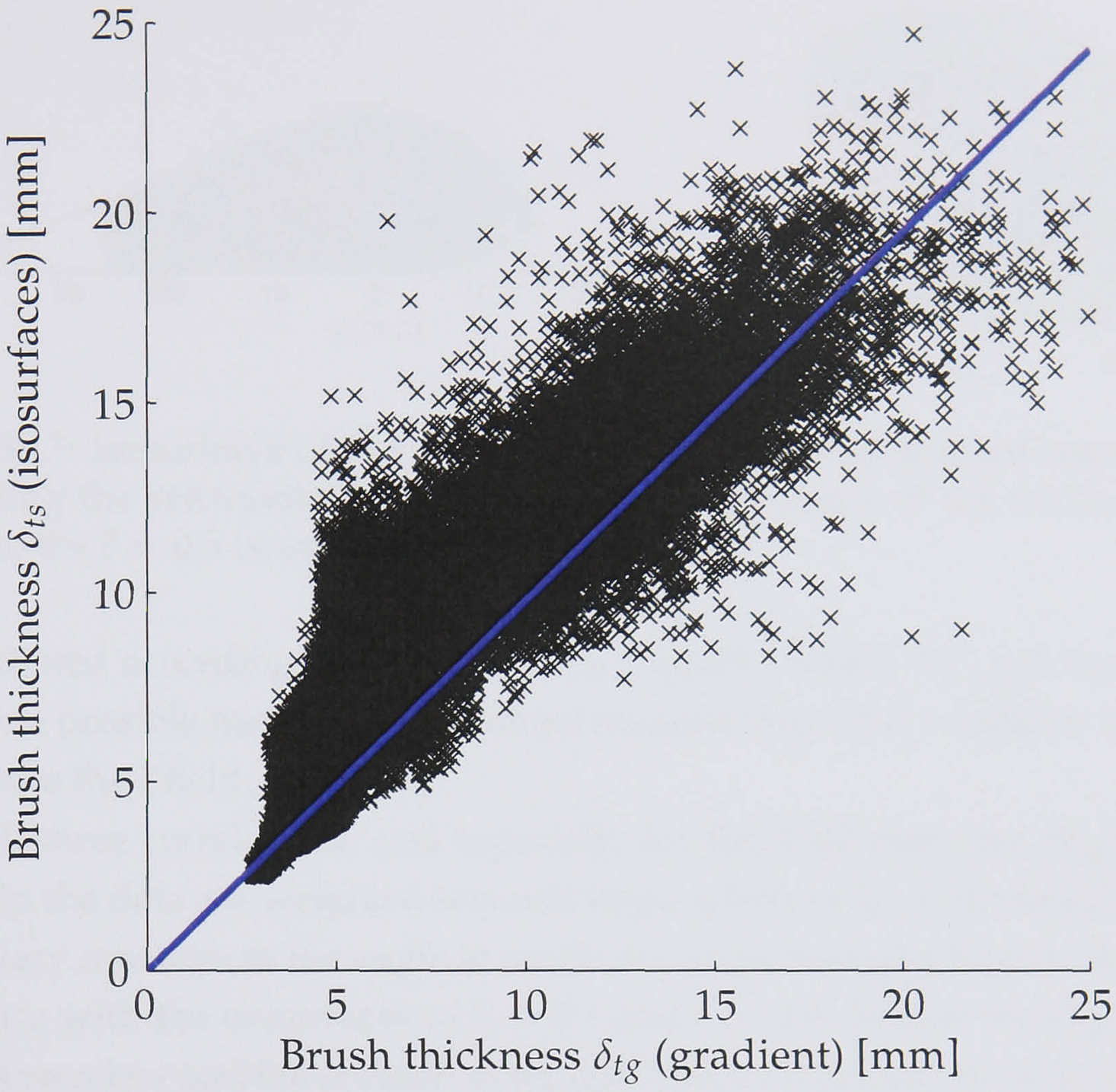

Figure 5.12: Correlation between different measures of flame thickness for all crank angles at 1000 rpm.

Equation 4.33:

$$\overline{c}(x_{0.1}) = 0.1 \Rightarrow x_{0.1} = 0.91\delta_t \tag{5.4}$$

$$\overline{c}(x_{0.9}) = 0.9 \Rightarrow x_{0.9} = -0.91\delta_t \tag{5.5}$$

therefore

$$\delta_{ts} = |x_{0.1} - x_{0.9}| = 1.82\delta_t \tag{5.6}$$

It follows from Equations 5.3 and 5.6 that

$$\delta_{ts} \approx \delta_{tg} \approx 1.8\delta_t. \tag{5.7}$$

Given the relationship between δ_{ts} and δ_{tg} which has just been established the congruence between the two measures of flame brush thickness observed in both the LUPOE2-P experimental data and the simulated flames described in Section 5.5 is hardly surprising. If anything, it suggests that the experimental $\overline{c}$ field

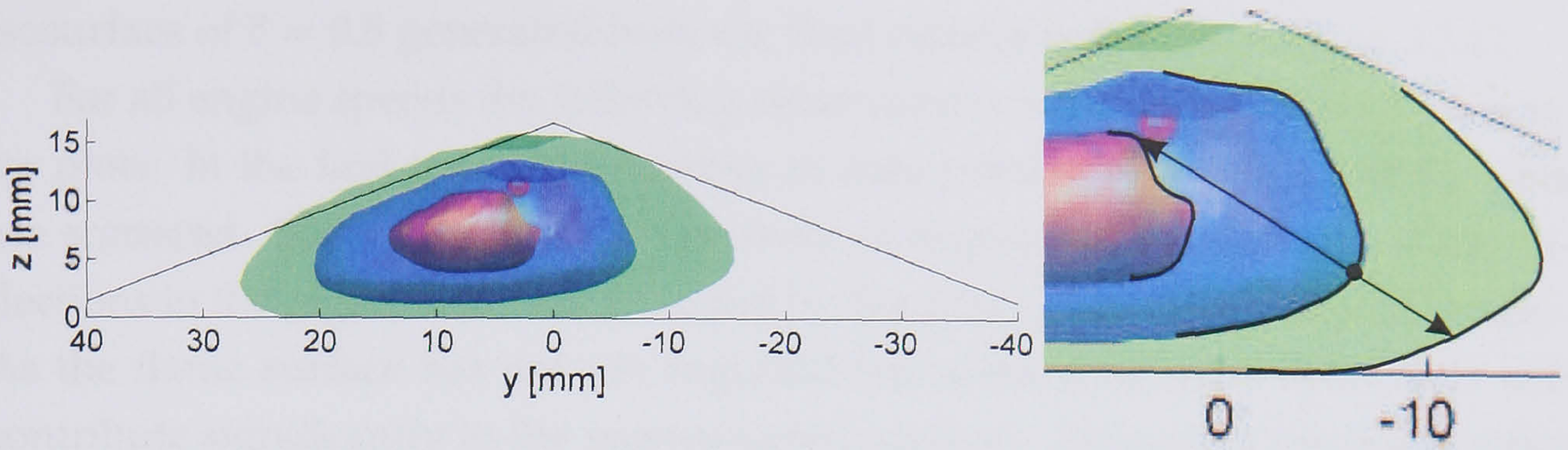

Figure 5.13: Isosurfaces of $\overline{c} = 0.1$,0.5 and 0.9 (green, blue and red respectively), illustrating the sensitivity of δ_{ts} to the angle of incidence of the surface normal vector to the $\overline{c} = 0.5$ isosurface.

is distributed according to Equation 4.33, a quality which was not investigated here. One possible method for the direct measurement of δ_t would be to apply a curve fit to the $\overline{c}$ field.

In all three correlations, and especially for the 1500 rpm case (Figure 5.10), scatter in the data are weighted towards large values of δ_{ts}. Calculated values of δ_{ts} are very sensitive to the angle of incidence of the normal vector to the $\overline{c} = 0.5$ isosurface with the isosurfaces of $\overline{c} = 0.1$ and $\overline{c} = 0.9$. Where the angle of incidence is very low and the normal vector just "grazes" the inner or outer isosurface the distance between the two isosurfaces is readily influenced by small changes to the shape of either isosurface as shown in Figure 5.13. In such cases the precision of the measurement is reduced causing scatter in the calculated values of δ_{ts}. For the current experimental dataset there were considerable areas of the flame where the isosurface at $\overline{c} = 0.5$ failed to intersect with the inner isosurface. Naturally it is not possible to calculate δ_{ts} at these points. For these reasons δ_{tg} is a more robust estimate of the flame brush thickness than δ_{ts} and is used for the remainder of the results in this chapter.

5.3.4 Flame brush thickness as flame approaches wall

The scatter plots shown in Figures 5.14, 5.15 and 5.16 show the effect of the proximity of the combustion chamber wall on the local flame brush thickness at different crank angles and engine speeds. Each plot corresponds to one of the isosurfaces displayed in Figures 5.1, 5.2 and 5.3. The local brush thickness δ_{tg} was calculated using the gradient of the $\overline{c}$ field as described in Section 3.3.9; the distance from the wall of a particular point on the $\overline{c} = 0.5$ isosurface was estimated as the distance in the direction normal to the isosurface between that point and

isosurface of $\bar{c} = 0.5$ generated from the final camera frame, see Section 3.3.11.

For all engine speeds the following observations may be drawn from the scatter plots: In the first frame the number of data points is quite low and the data are scattered. Some of this scatter is likely to originate from distortions and reflections in the region which is occluded by the spark plug in the original images. As the flame surface has not yet engulfed the spark plug these reflections will contribute significantly to the reconstructed surfaces. Because of the high scatter and low number of data points in this frame it is considered noisy and excluded from the following discussion. In later frames the flame surface is partitioned quite distinctly into two regions. In the region closest to the wall the brush thickness is influenced by the presence of the wall, the decrease in brush thickness as the flame approaches the wall appears to be linear. Where the flame is further from the wall the brush thickness is approximately constant in the mean. In some frames, see for example Figures 5.14g and 5.14h, there appears to be a small increase in brush thickness in the immediate vicinity of the wall. The reason for this is unknown but may be related to reflections or distortions close the the chamber walls in the original camera images.

The flame brush thickness δ_{tg} appears to reach a maximum (if the scatter in the data is ignored) of ~ 14 mm, at distances from the wall greater than ~ 5 mm, irrespective of engine speed. The fact that the maximum brush thickness does not change significantly with engine speed or time is indirect evidence that the integral scale of turbulence is approximately constant (the integral scale is closely related to the brush thickness, see Equation 4.36) regardless of the engine speed when the piston is close to TDC. With increasing time the scatter in the data points which are not affected by the wall increases, especially for the 1500 rpm case (Figure 5.14). This is not surprising as if the integral scale is not homogeneous and decreases in the "eaves" of the pent roof (postulated in Section 4.5.14), the flame will be thinner in the eaves of the pent than elsewhere.

It should be noted that values of δ_{tg} in the vicinity of the wall have been distorted by the smoothing procedure applied to the volume data set described in Section 3.3.5. The slices through the $\bar{c}$ field illustrated in Figure 5.6 show the effect of the smoothing procedure on regions close to the wall well. At the chamber walls the $\bar{c}$ value drops to zero over the space of a few pixels. It is more likely that $\bar{c}$ should fall abruptly from one to zero over the space of a single pixel after the flame has been in contact with the wall a short time, i.e. the brush thickness should be zero. Inspection of the unsmoothed $\bar{c}$ fields showed that a couple of

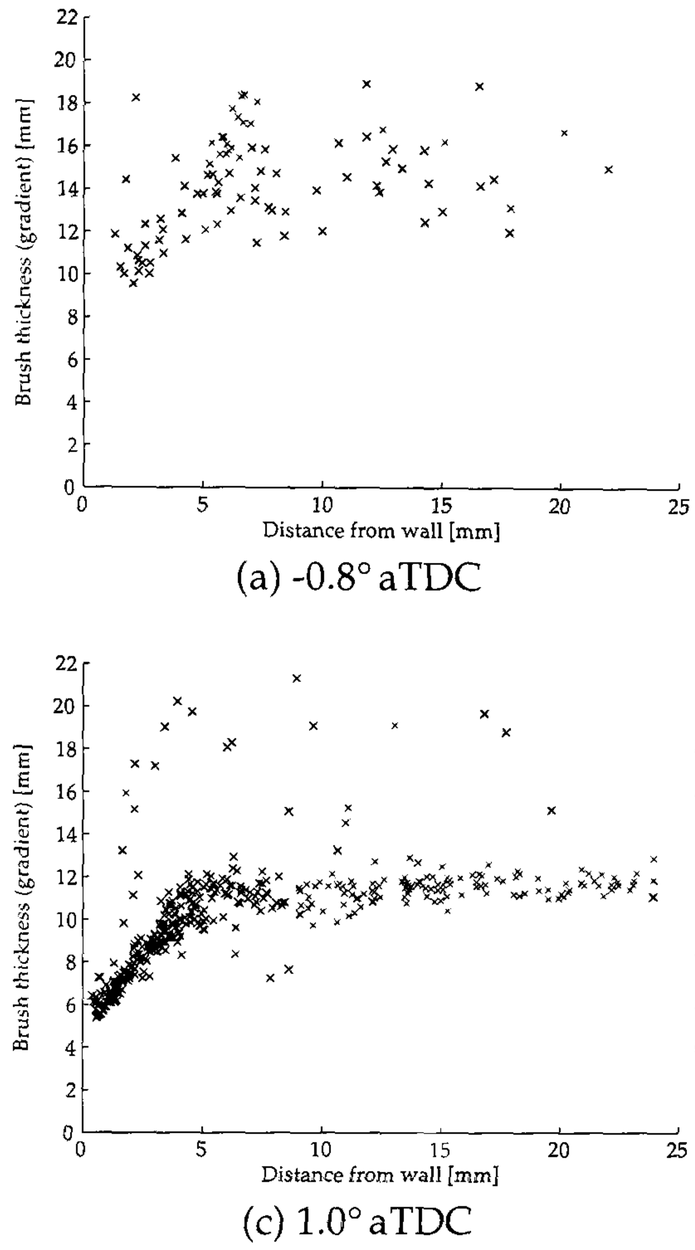

(a) -0.8° aTDC

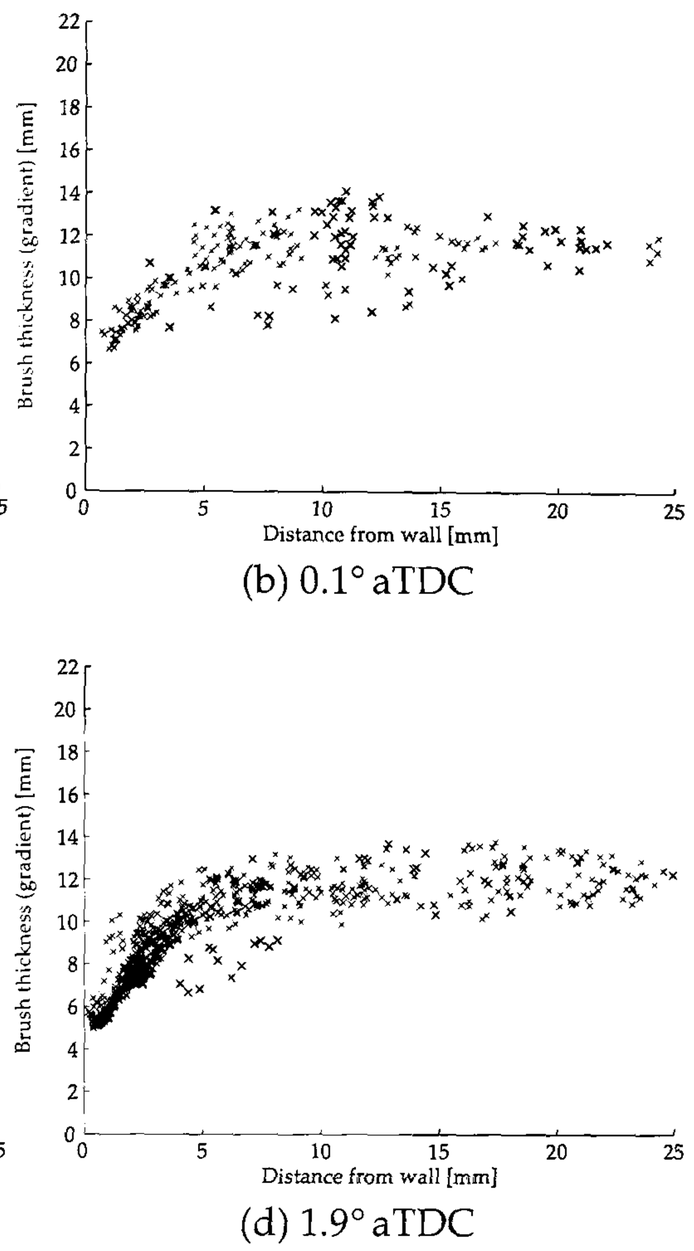

(b) 0.1° aTDC

(c) 1.0° aTDC

(d) 1.9° aTDC

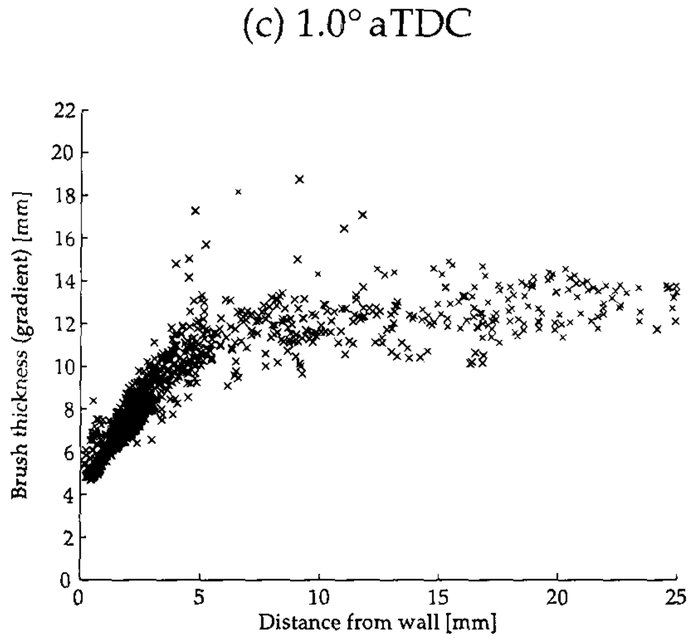

(e) 2.8° aTDC

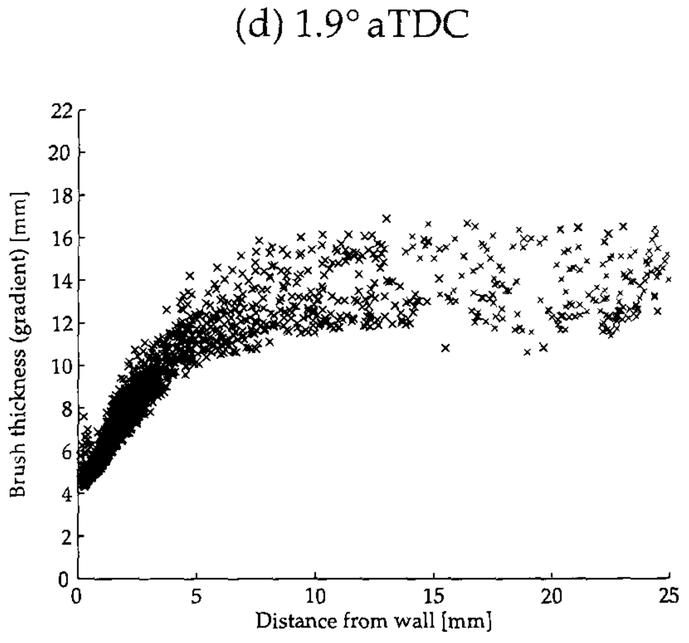

(f) 4.5° aTDC

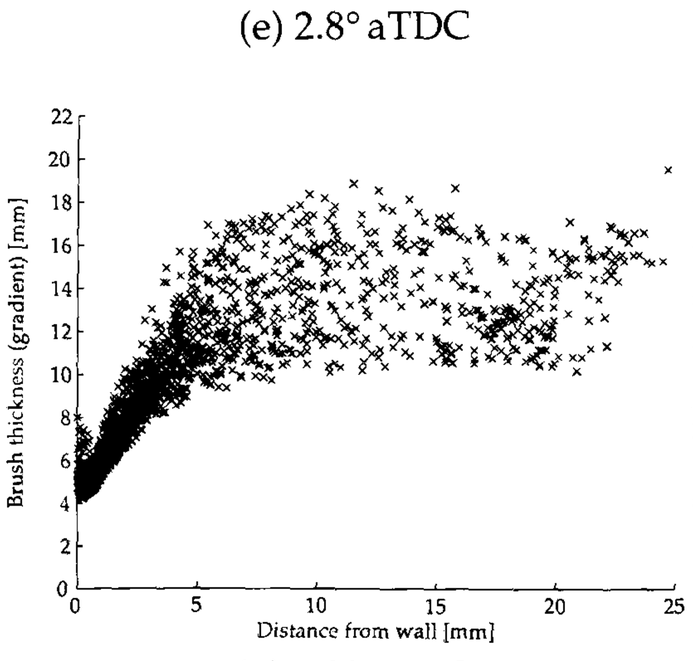

(g) 6.3° aTDC

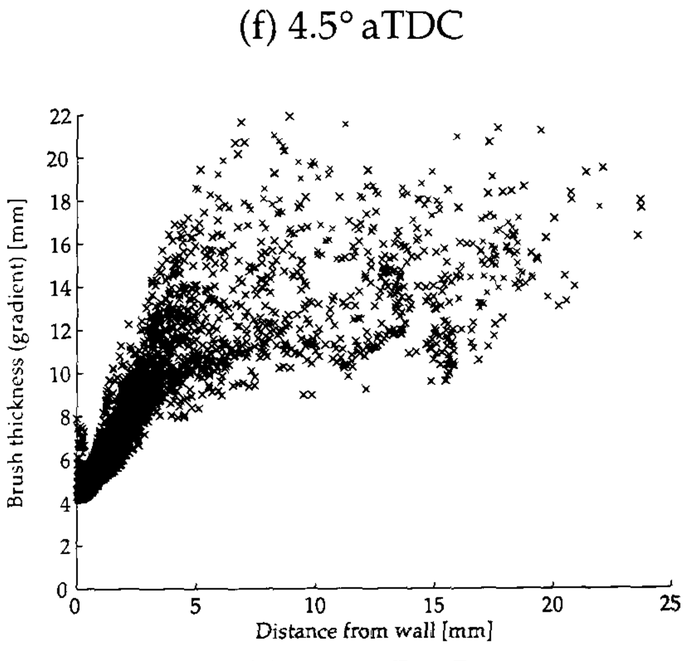

(h) 8.1° aTDC

Figure 5.14: Correlation between the distance from the wall and the flame brush thickness δ_{tg} at the 1500 rpm base condition.

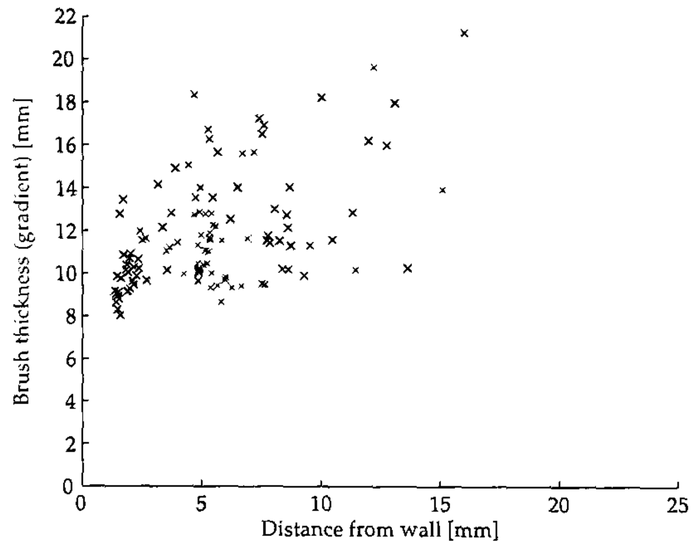

(a) 2.0° aTDC

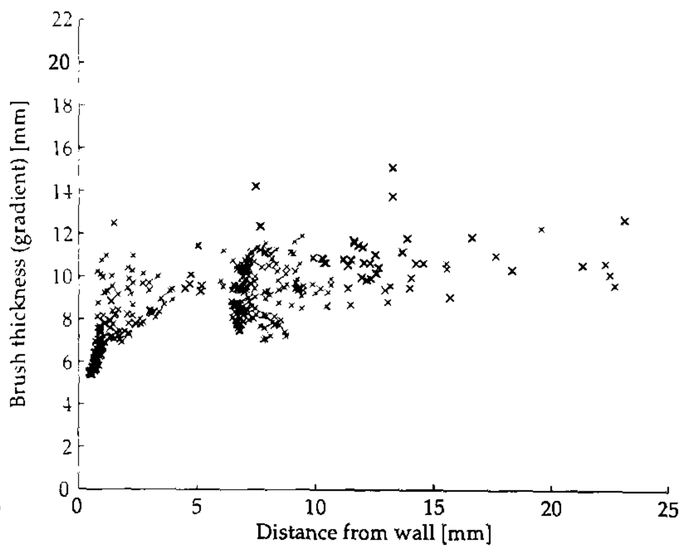

(b) 2.9° aTDC

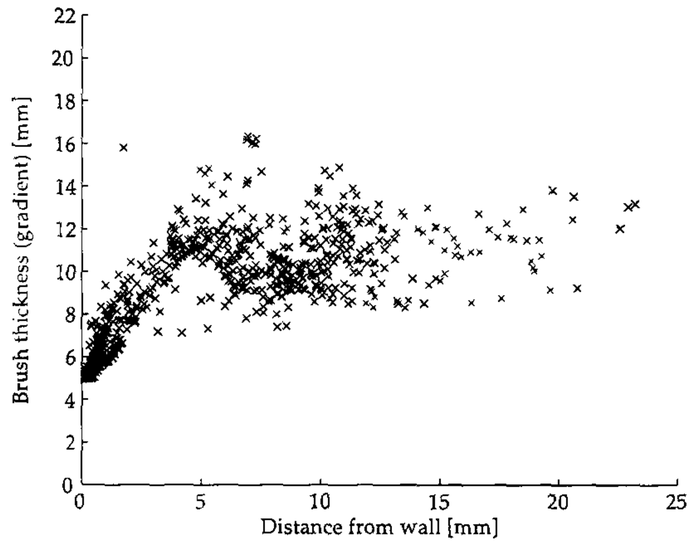

(c) 3.8° aTDC

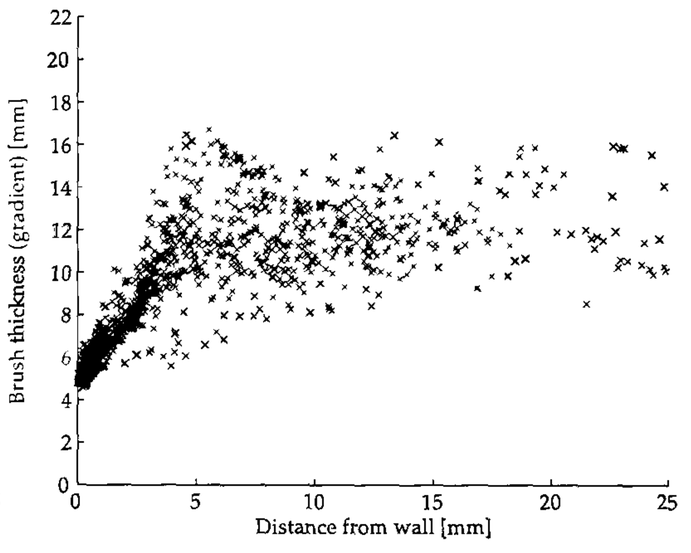

(d) 4.7° aTDC

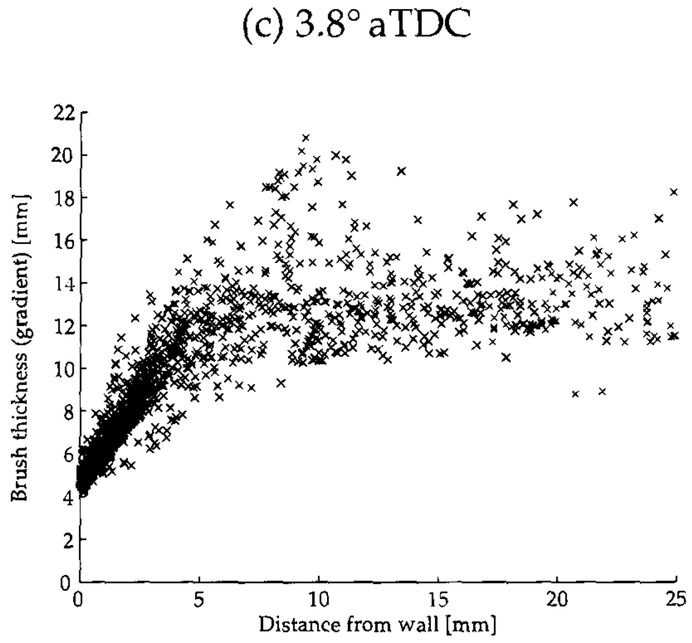

(e) 5.6° aTDC

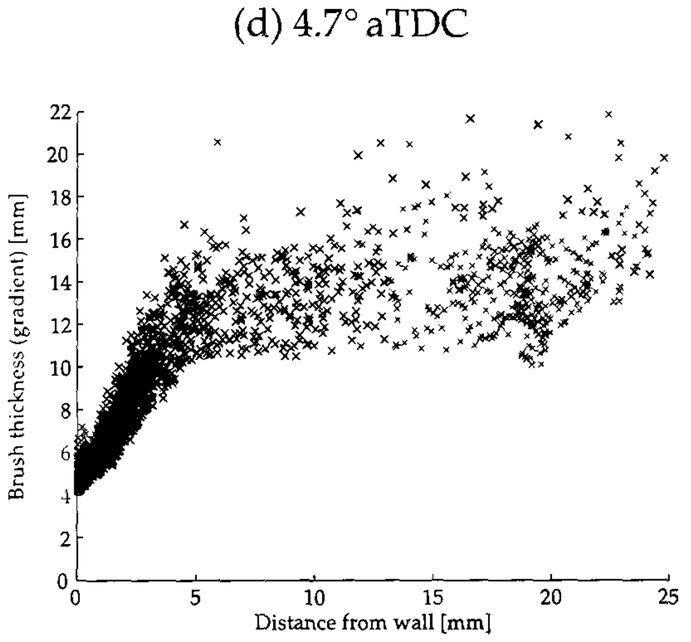

(f) 7.4° aTDC

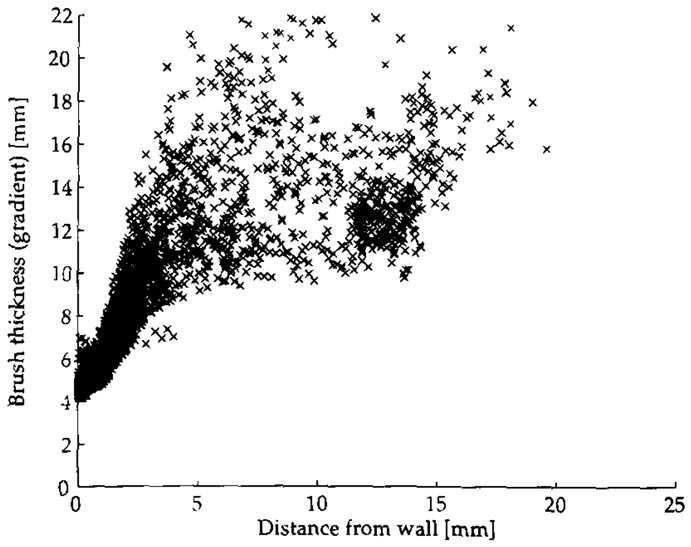

(g) 9.1° aTDC

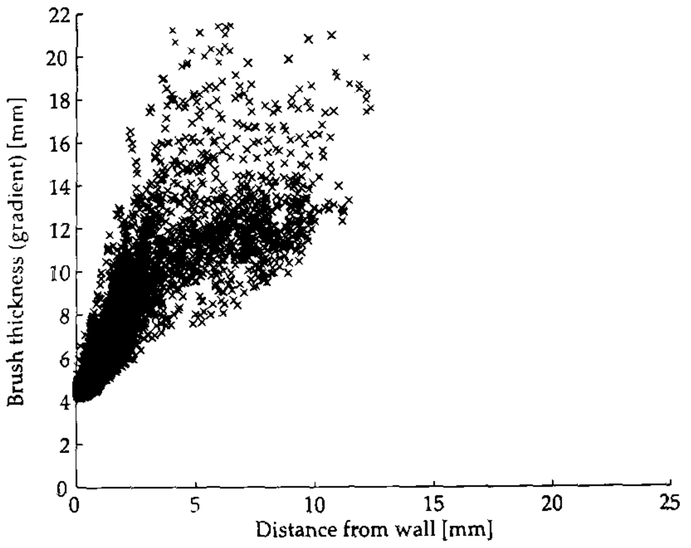

(h) 10.9° aTDC

Figure 5.15: Correlation between the distance from the wall and the flame brush thickness δ_{tg} at the 750 rpm condition.

(a) 0.7° aTDC

(b) 1.9° aTDC

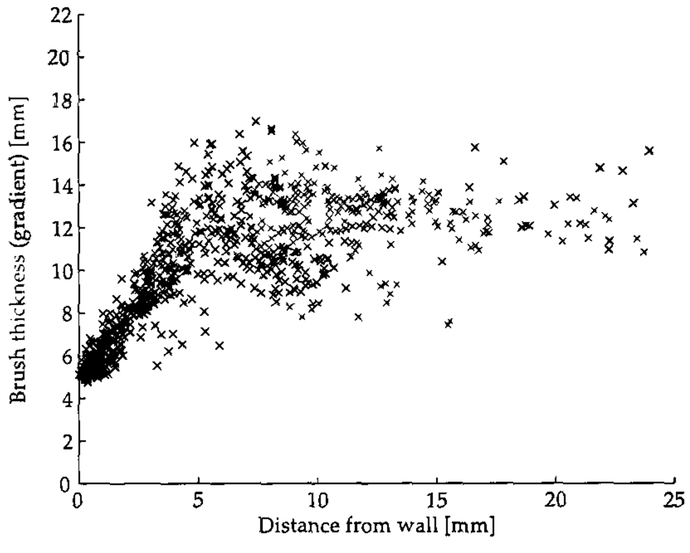

(c) 3.1° aTDC

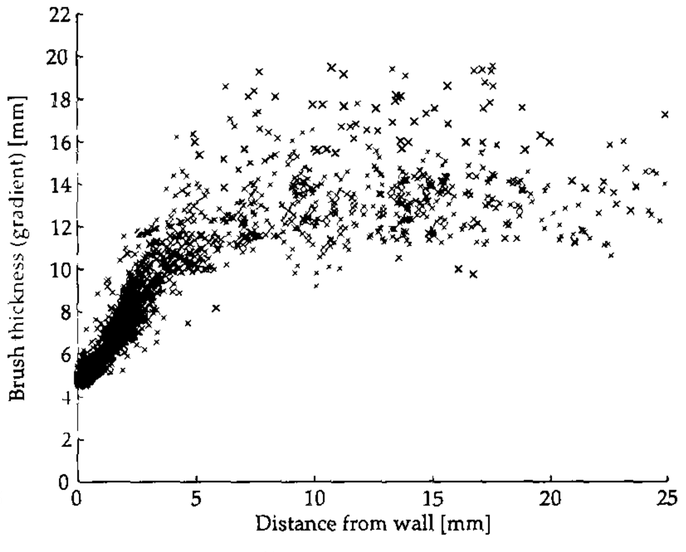

(d) 4.3° aTDC

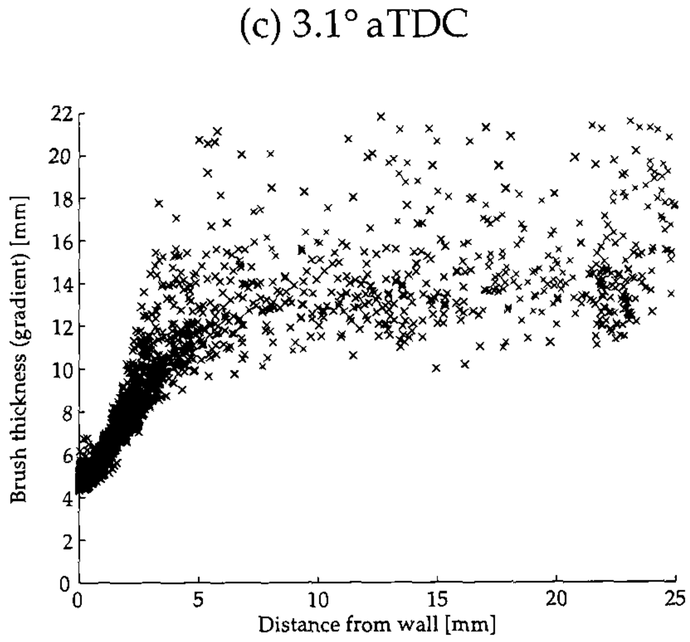

(e) 5.4° aTDC

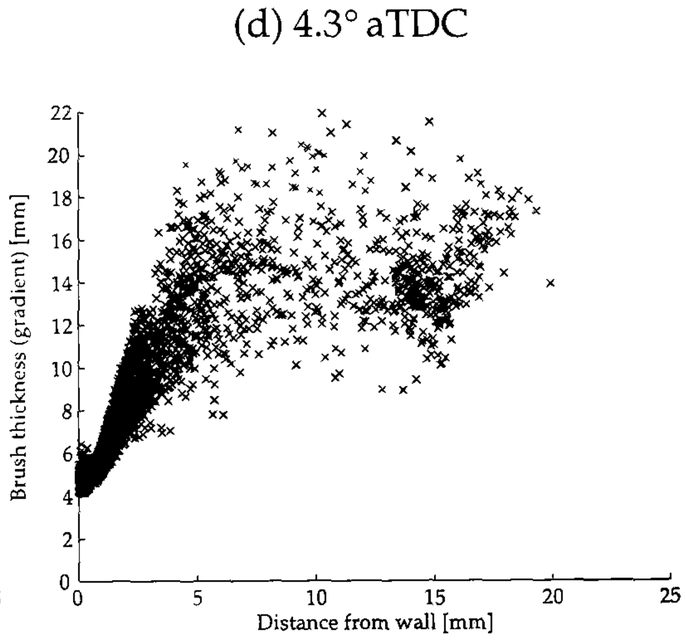

(f) 7.8° aTDC

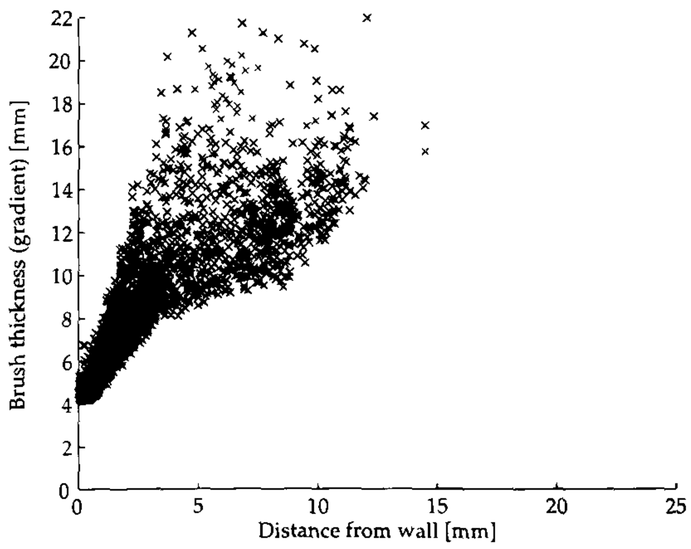

(g) 10.2° aTDC

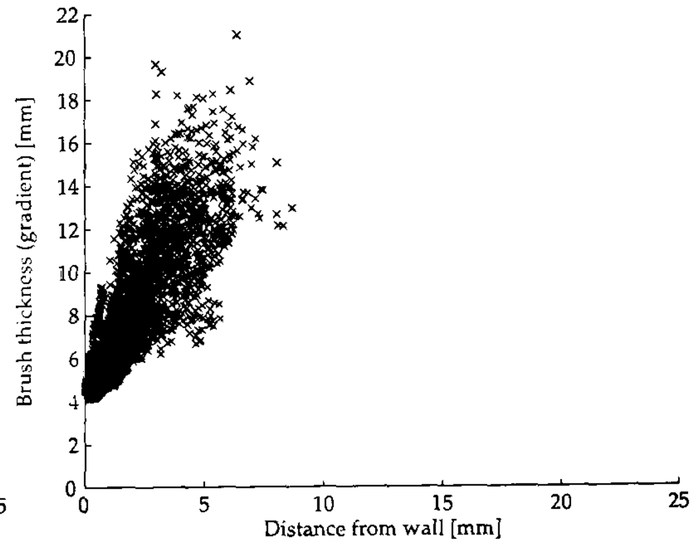

(h) 12.5

Figure 5.16: Correlation between the distance from the wall and the flame brush thickness δ_{tg} at the 1000 rpm condition.

crank angles after the flame met the wall this was indeed the case.

Simulated spherical flames of varying thickness were analysed and are reported in Section 5.5. The results presented there show that flames with a simulated brush thickness δ_t less than 1 mm were found to have a gradient brush thickness δ_{tg} of 4 mm after smoothing and processing. At the point where the flame contacts the wall in Figures 5.14, 5.15 and 5.16 the brush thickness falls to a minimum value $\sim$ 4 mm, quite comparable to the smoothed simulated flames with zero brush thickness. As there is some distortion to the calculated values of δ_{tg} close to the walls the decay in brush thickness may be closer to exponential in form than linear.

5.3.5 Burning velocity as flame approaches wall

The graphs shown in Figures 5.17, 5.18 and 5.19 depict values of the local burning velocity (calculated as described in Section 3.3.8) plotted against the distance to the chamber wall in the direction normal to the $\overline{c} = 0.5$ isosurface (calculated as described in Section 3.3.11). Similar to the data for the local flame brush thickness presented in Section 5.3.4, the data points in the early frames show considerable scatter. As discussed above, this is probably caused in part by reflections off the spark plug in the original laser sheet images when the flame is small. The flame speed, from which the burning velocity is derived, is a differential quality. Calculating the derivative of experimental data using a finite difference approximation, the method employed here, will amplify any noise present in the original data. This is also likely to have contributed to the scatter present in the early frames. More robust methods exist for calculating derivatives of noisy data, for example Cullum [1971] or the Savitzky-Golay method, implemented by Press et al. [1992], which may be useful to future investigators.

The behaviour of the local burning velocity in the presence of a wall shows similar characteristics to the local flame brush thickness near a wall (Section 5.3.4). Local burning velocities for a particular crank angle are divided into two populations. Those points on the surface which are closer than 6–8 mm have a burning velocity which is noticeably reduced compared with points further from the wall, where the local burning velocity for a given engine speed is either constant or increases slightly. Where the flame contacts the wall the burning velocity falls to zero in all cases.

In Section 4.5.9 it was suggested that, assuming that the mean progress vari-

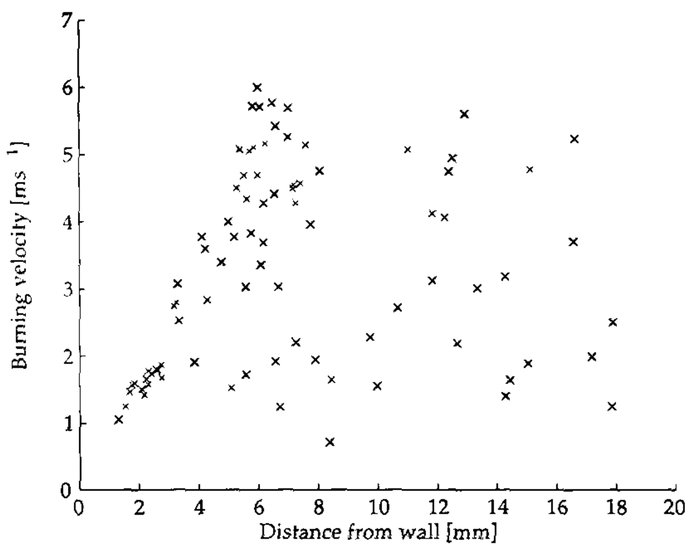

(a) -0.8° aTDC

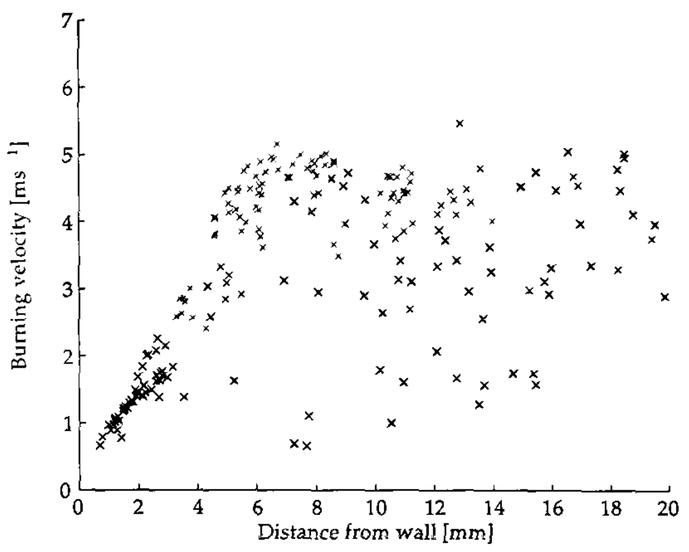

(b) 0.1° aTDC

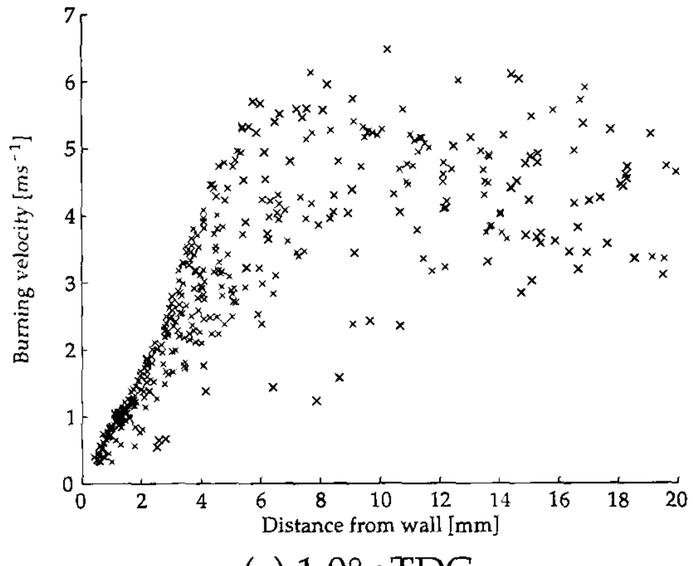

(c) 1.0° aTDC

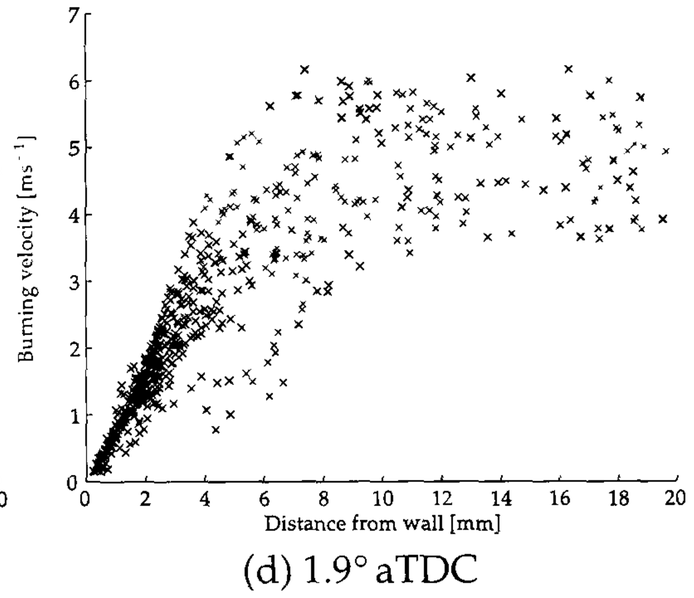

(d) 1.9° aTDC

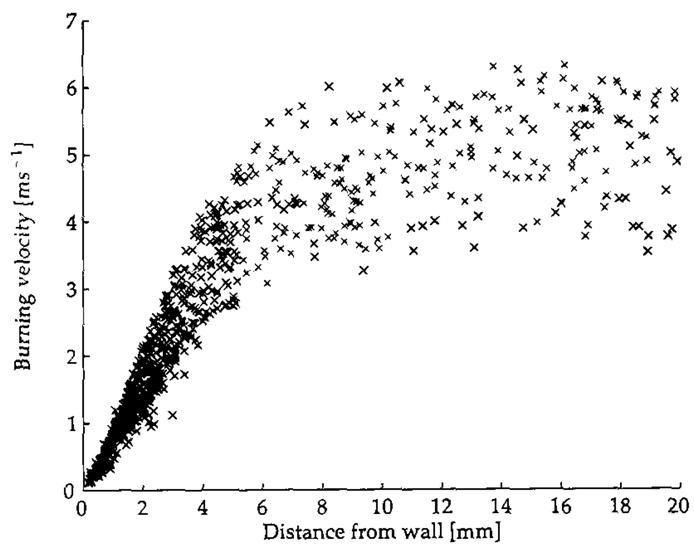

(e) 2.8° aTDC

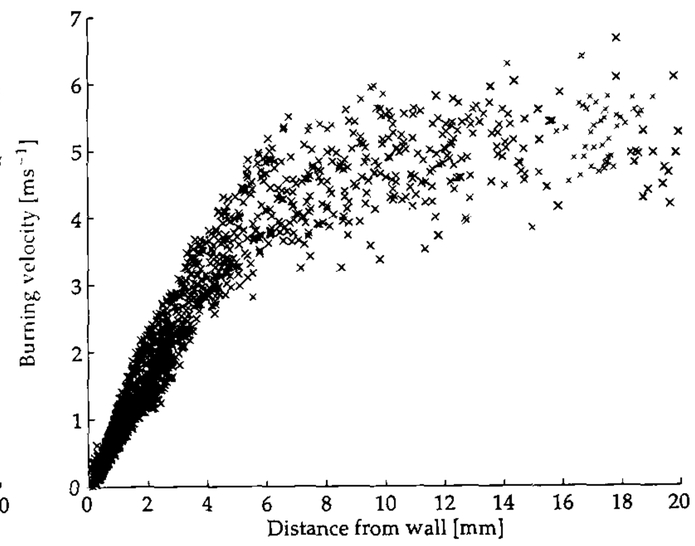

(f) 4.5° aTDC

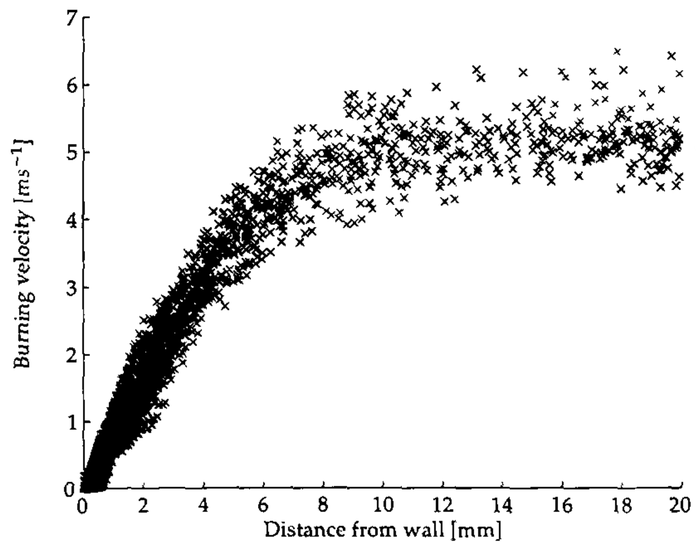

(g) 6.3° aTDC

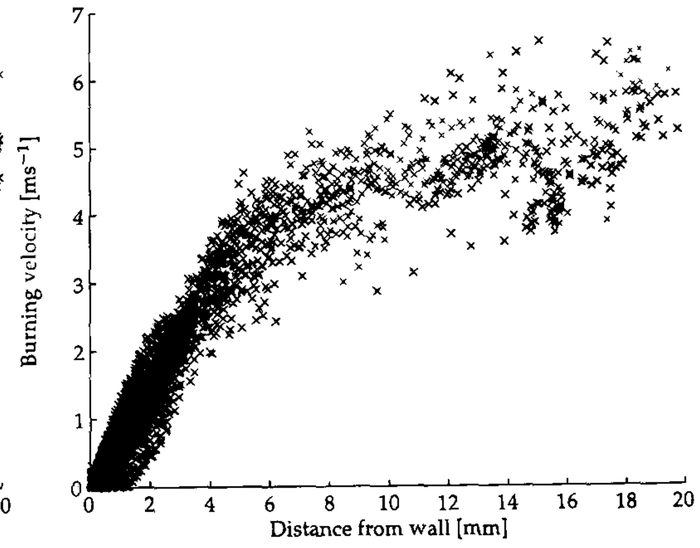

(h) 8.1° aTDC

Figure 5.17: Correlation between the distance from the wall and the burning velocity at the 1500rpm base condition.

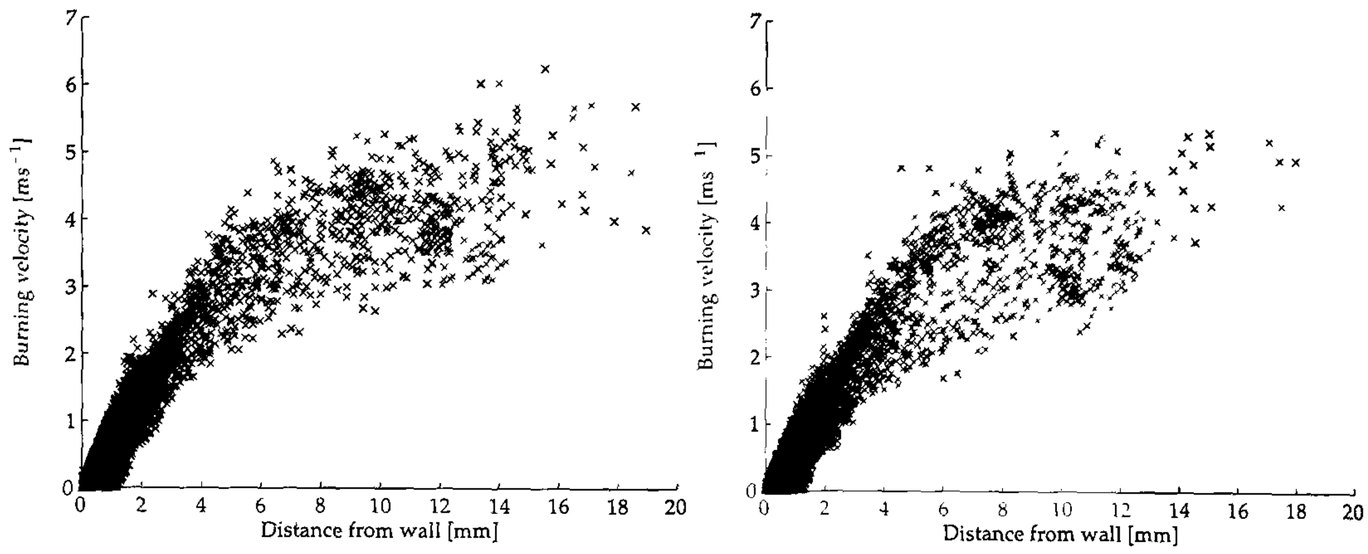

(i) 9.8° aTDC (j) 10.7° aTDC

Figure 5.17: Correlation between the distance from the wall and the burning velocity at the 1500rpm base condition.

able profile $\bar{c}$ is well described by the complimentary error function, the deceleration of the flame in the region of the wall should be a function of only the "unconstrained" flame brush thickness (i.e. the brush thickness which the flame would have if it was not affected by the wall) and the distance from the wall, Equation 4.34. The validity of this hypothesis was investigated using the experimentally calculated brush thickness for the region of the flame not in close proximity to the wall, δ_{tg0} and a value of u_{t0}, the "unconstrained" burning velocity. Both parameters were estimated by manually from the data in Figures 5.17, 5.18 and 5.19. Shown in Figure 5.20 are values of the ratio of the local burning velocity for a particular point on the surface $u_{t,i}$ to the unconstrained burning velocity u_{t0} plotted against $\mathrm{erf}(d_w/\delta_{tg0})$ where d_w is the distance to the wall. If Equation 4.34 is valid the points should fall on a straight line with a gradient of one. The points in Figure 5.20 show a significant curvature with a sharp change in gradient at high values of $u_{t,i}/u_{t0}$.

Presented in Section 5.3.3 was a relationship between values of δ_{tg}, the flame brush thickness determined from the gradient of the $\bar{c}$ field, and δ_t the flame brush thickness defined in Equation 4.33. As $\delta_{tg} \neq \delta_t$ the poor correlation shown in Figure 5.20 is hardly surprising. The same data points as plotted previously are now replotted using the correction $\delta_t = 1.8/\delta_{tg}$, shown in Figure 5.21. The correlation between the experimental data and Equation 4.34 is much improved with this correction. The points are linearly related with a gradient close to one. At 750 rpm (Figure 5.22) the correlation between $u_{t,i}/u_{t0}$ and Equation 4.34 was again linear although at this engine speed Equation 4.34 overpredicted the deceleration of the flame close to the wall by approximately 20%. At 1000 rpm (Figure 5.23) Equa-

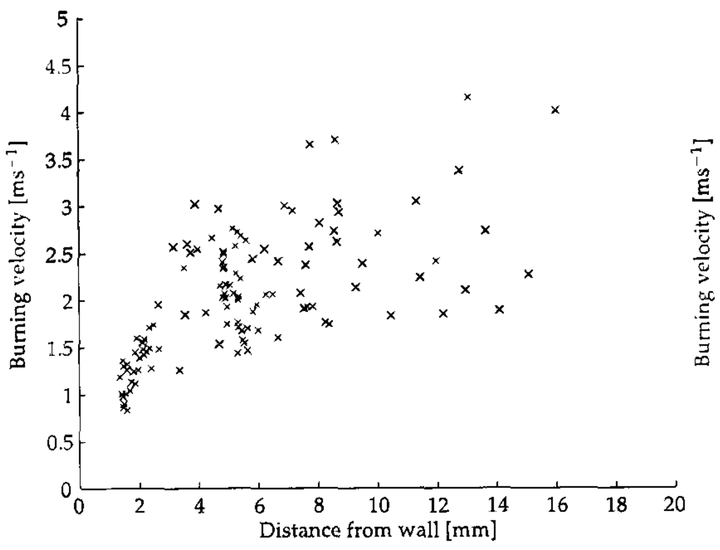

(a) 2.0° aTDC

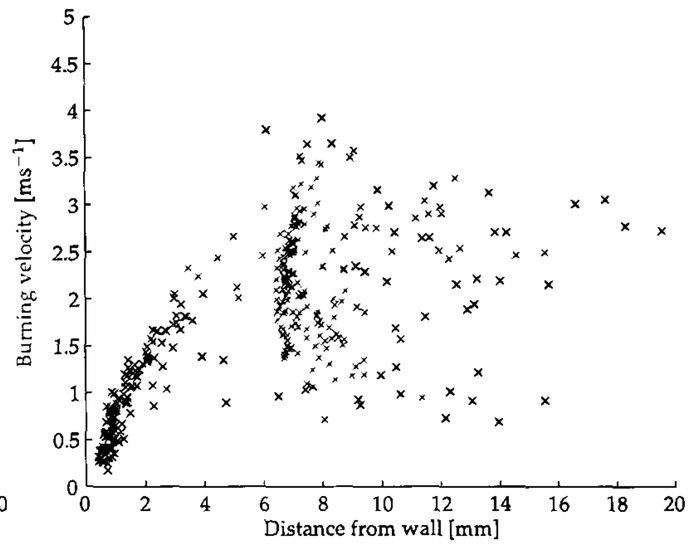

(b) 2.9° aTDC

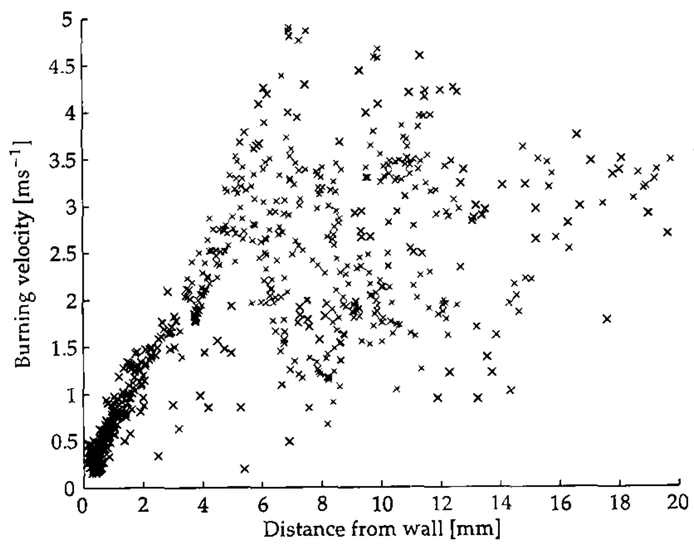

(c) 3.8° aTDC

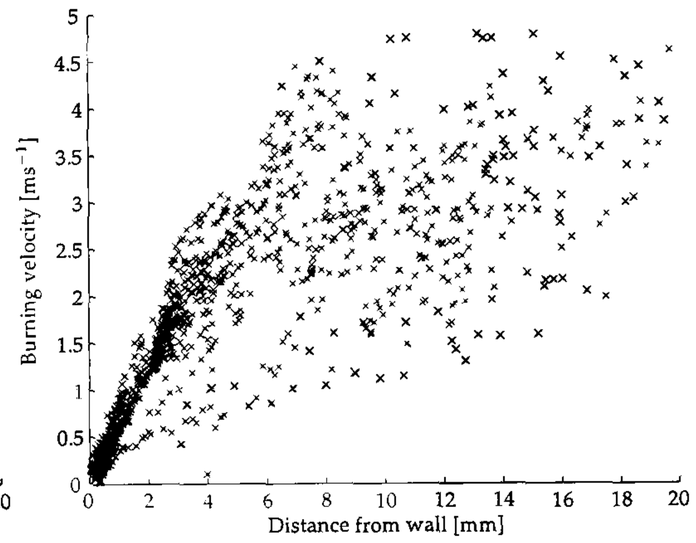

(d) 4.7° aTDC

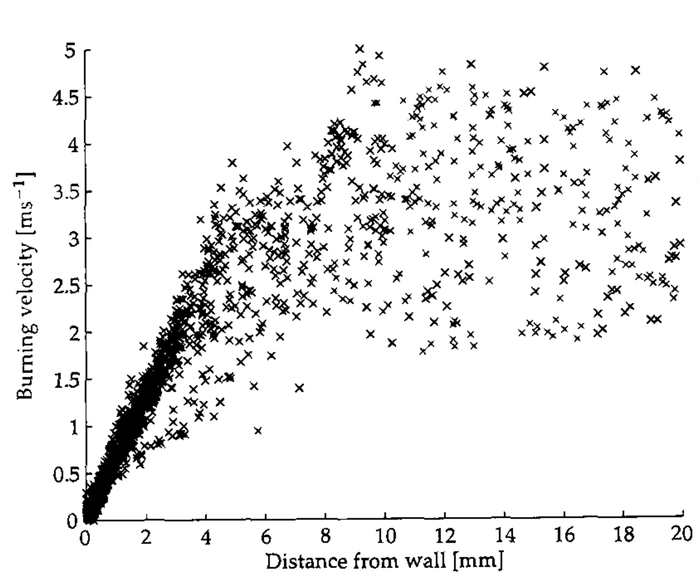

(e) 5.6° aTDC

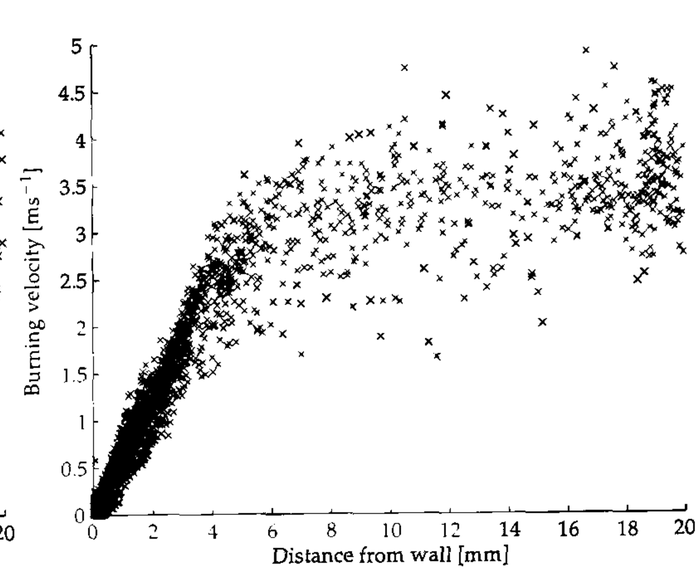

(f) 7.4° aTDC

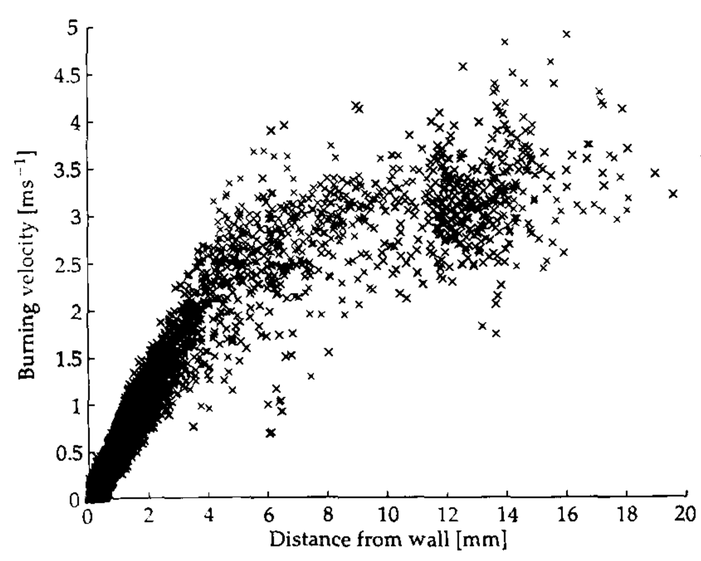

(g) 9.1° aTDC

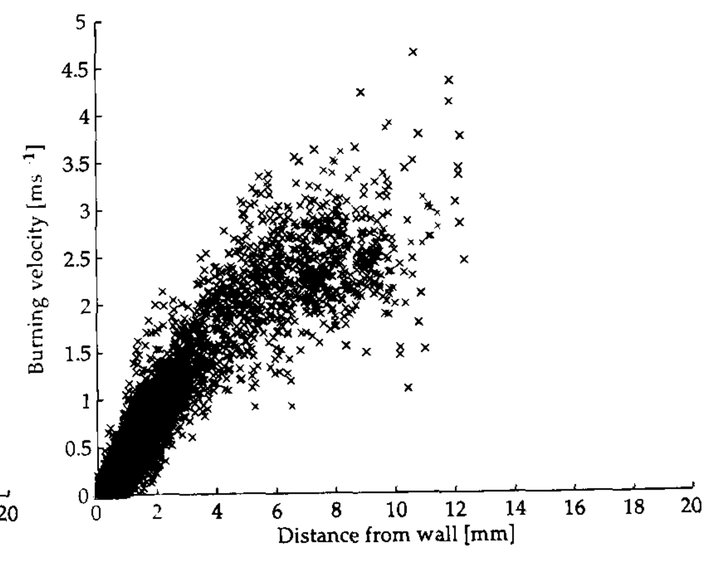

(h) 10.9

Figure 5.18: Correlation between the distance from the wall and the burning velocity at the 750rpm condition.

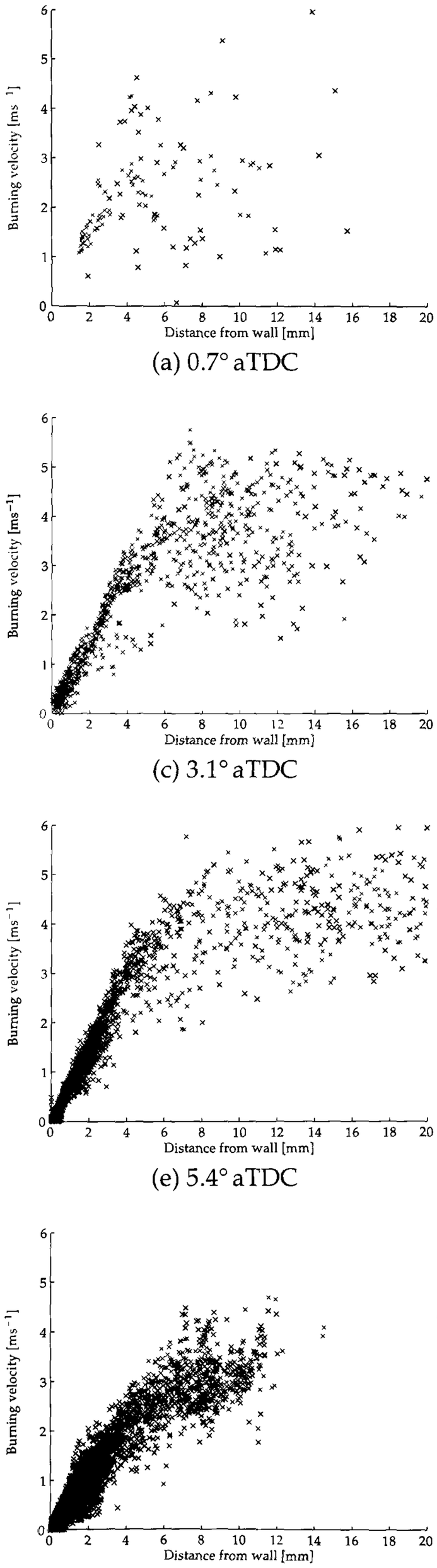

(a) 0.7° aTDC

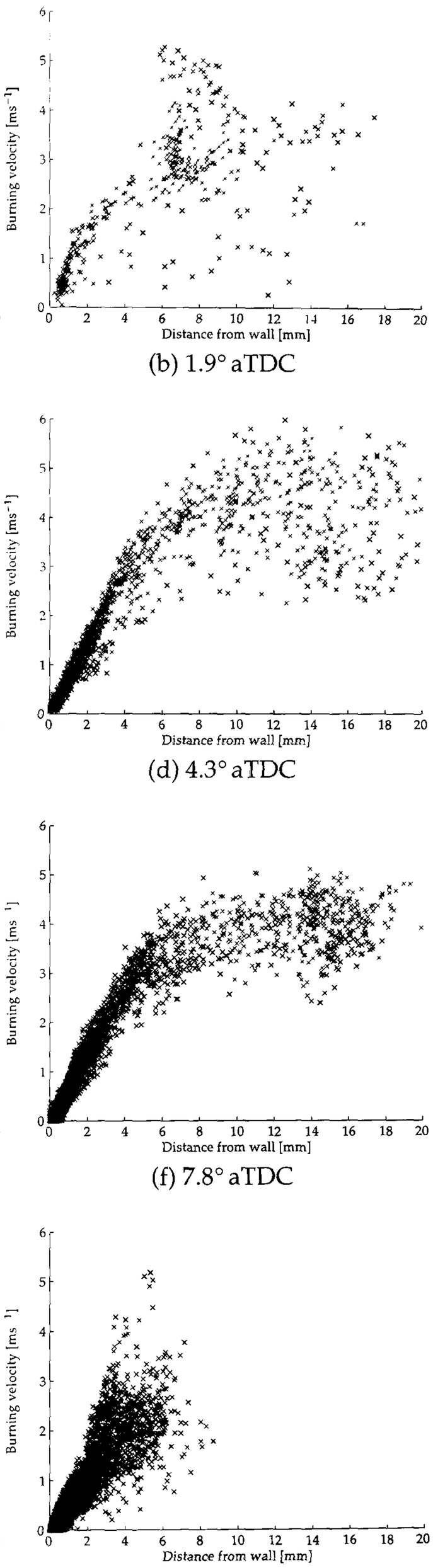

(b) 1.9° aTDC

(c) 3.1° aTDC

(d) 4.3° aTDC

(e) 5.4° aTDC

(f) 7.8° aTDC

(g) 10.2° aTDC

(h) 12.5° aTDC

Figure 5.19: Correlation between the distance from the wall and the burning velocity at the 1000rpm condition.

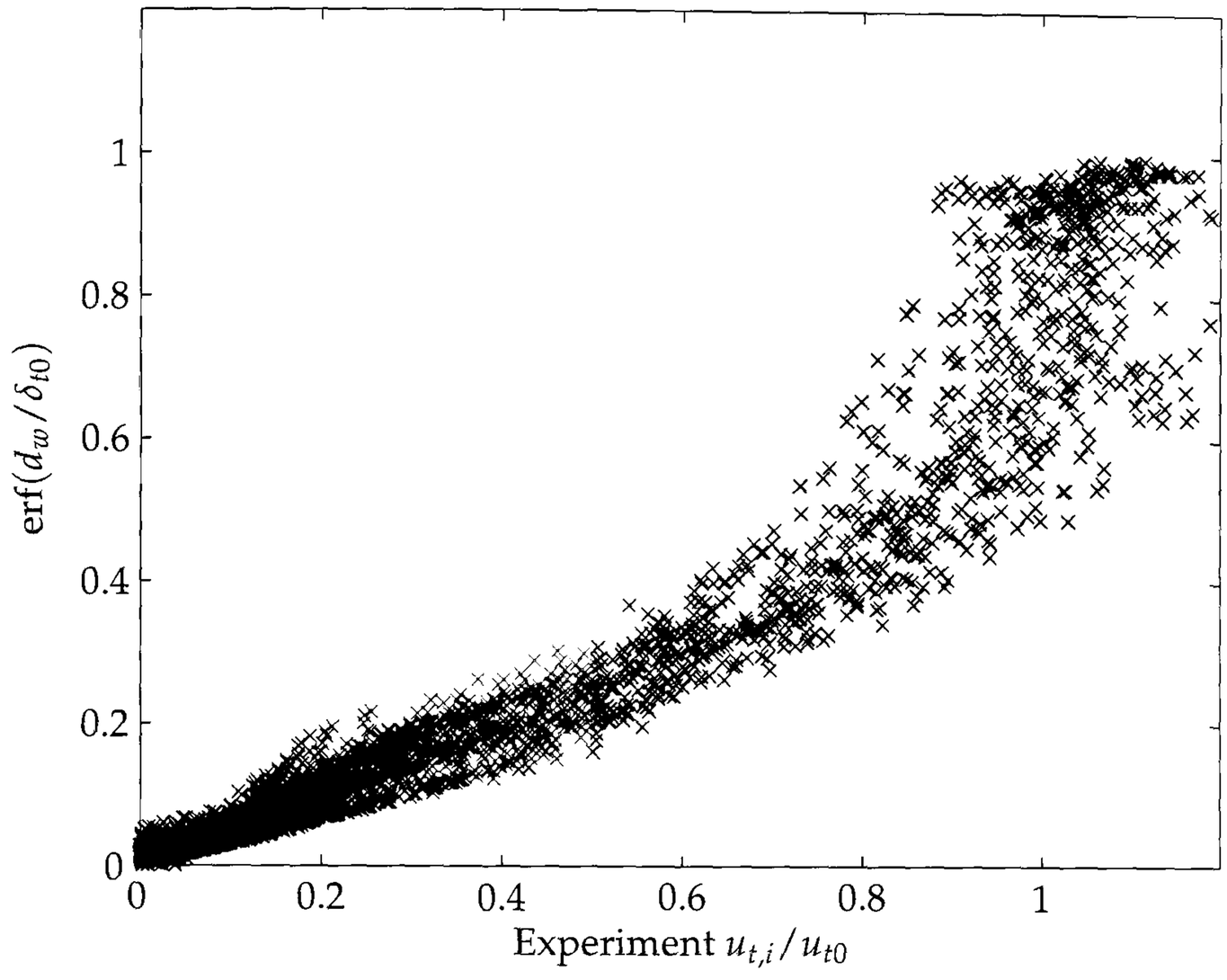

Figure 5.20: Correlation between experimental flame deceleration in the presence of a wall and Equation 4.34 at the 1500 rpm base condition, 6.3° aTDC.

tion 4.34 overpredicted the declaration by a lesser amount, close to 10%. These errors could be caused either by errors in the estimates of u_{t0} and δ_{t0} used or by some deficiency in Equation 4.34. Results for other crank angles (not shown here) were similar to those illustrated in Figures 5.21, 5.18 and 5.19.

Given the non-spherical geometry of the combustion chamber and the large scale motion of the charge different regions of the flame surface will come into contact with the walls having experienced different turbulence, pressure and temperature histories, and having been in existence for different lengths of time. This implies that the development (see Section 5.3.6) of some areas of the flame surface close to the wall will be different from other areas. This difference in development will undoubtedly have contributed to the scatter in Figures 5.21, 5.22 and 5.23. A more easily interpreted experiment to test Equation 4.34 would be the interaction of a spherical flame with spherical walls as could be observed in a fan stirred bomb, or the interaction of a flame ignited in the centre of a disc geometry combustion chamber in a spark ignition engine with the chamber walls. Such a test is easily realisable using LUPOE2-D.

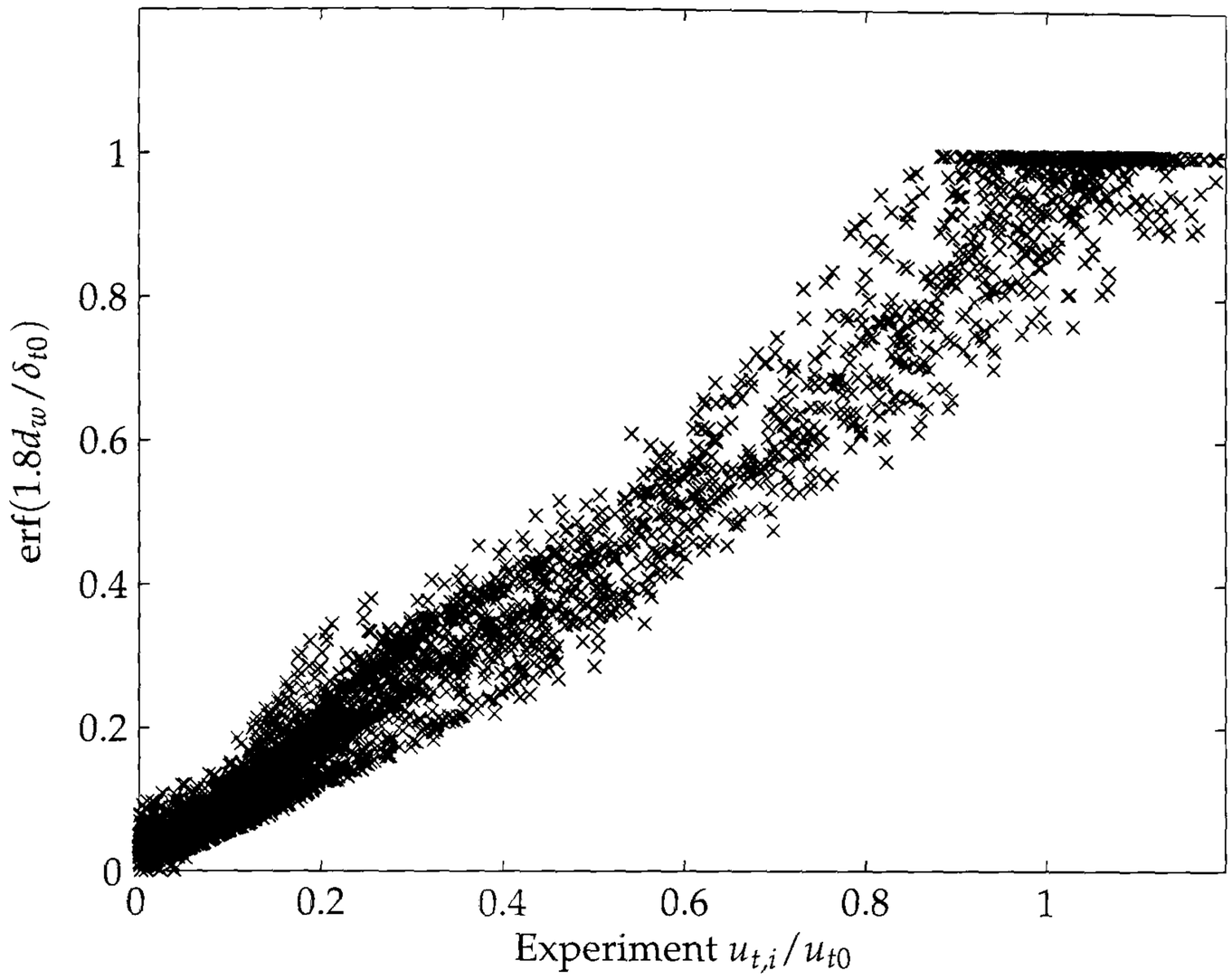

Figure 5.21: Correlation between experimental flame deceleration in the presence of a wall and Equation 4.34 calculated using $\delta_{t0} = 1.8/\delta_{tg0}$ at the 1500 rpm base condition, 6.3° aTDC.

5.3.6 Turbulent flame acceleration

The phenomenon of flame acceleration or development, whereby the burning velocity and brush thickness of the flame increase following ignition, is well known. Acceleration is typically assumed to be caused by the interaction of progressively larger turbulent eddies with the flame front as the flame grows. This increases the wrinkling, and hence active surface area, of the flame front which, in turn, increases the global reaction rate and accelerates the flame. This same mechanism of distortion by progressively large eddies is also thought to be responsible for the increase in brush thickness as the flame grows. Flame acceleration during typical cycles recorded in LUPOE1-D and LUPOE2-P is illustrated in Figures 5.24 and 5.25. A discussion of some of the more well known flame development models is given in Sections 1.5.4 and 4.5.8.

Despite the importance of flame acceleration for accurate simulation of combustion in engines there is no universally accepted model in existence. Of the expressions identified in Section 4.5.8, all predict the burning velocity to be more than 25% of its fully developed value almost immediately after ignition, shown in Figures 4.18, 4.19 and 4.20. Furthermore, following ignition, many of the models

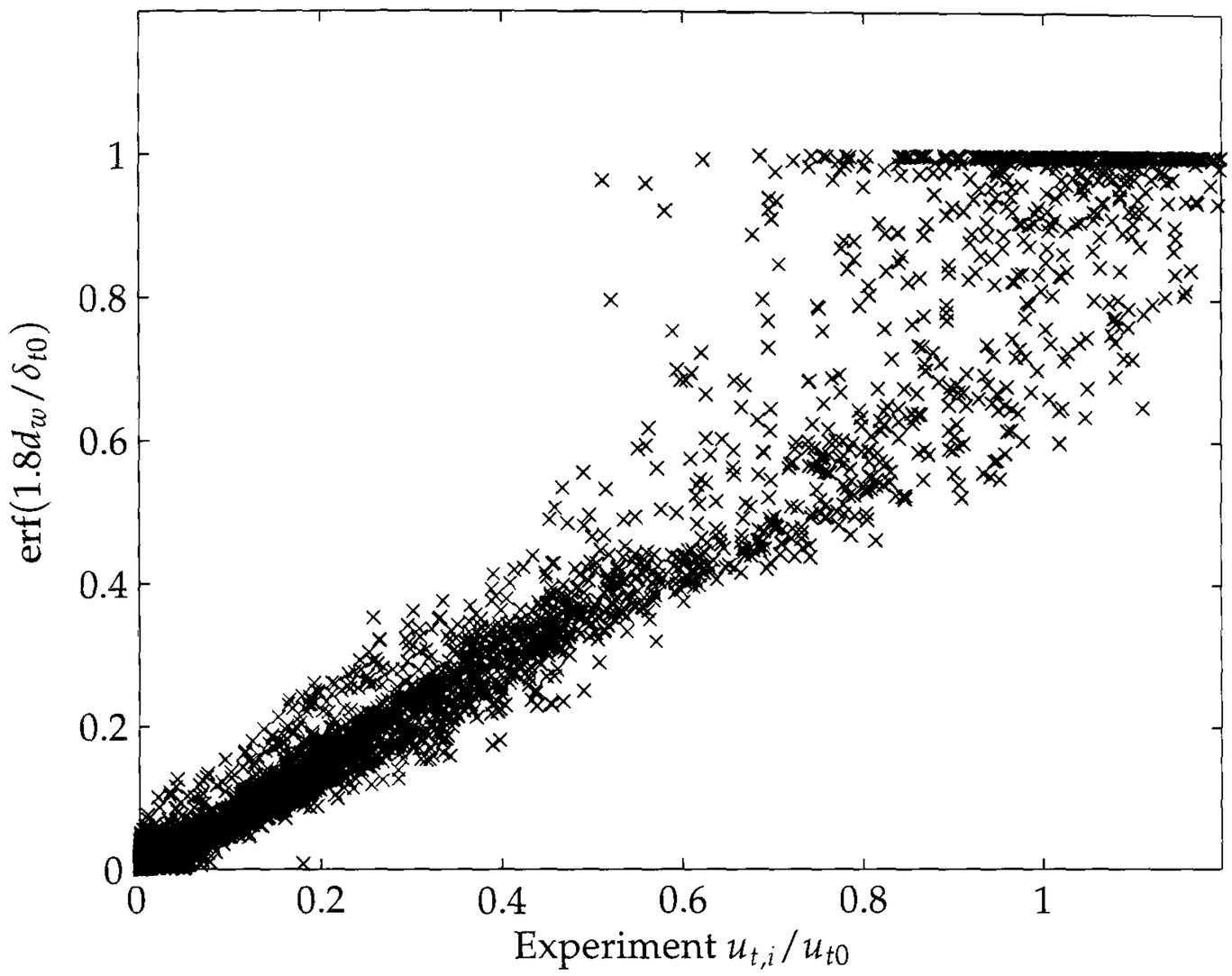

Figure 5.22: Correlation between experimental flame deceleration in the presence of a wall and Equation 4.34 calculated using $\delta_{t0} = 1.8/\delta_{tg0}$ at the 750 rpm condition, 7.4° aTDC.

predict that the transition between laminar-like and fully developed combustion occurs over $\sim 10°$ CA, quite a short period when compared to experimental data shown in Figures 5.24 and 5.25.

In order to further investigate the phenomenon of flame acceleration, data recorded on the LUPOE1-D engine [Abdi Aghdam, 2003] were postprocessed using LUSIEDA (see Section 3.2.3). The LUSIEDA analysis provided estimates of the laminar burning velocity u_l, the turbulent mass burning velocity u_{tr} and the burnt flame radius r_{fb} when supplied with a cylinder pressure trace. Given the turbulent burning velocity model formulation used in LUSIE, Equation 4.18, and the output of the LUSIEDA reverse analysis it, is possible to calculate the value of f_d, the flame development factor

$$f_d = \frac{u_{tr} - u_l}{u_{tr,\infty}} \tag{5.8}$$

For the analysis of the LUPOE1-D data, the laminar burning velocity was approximated using the correlation of Metghalchi and Keck [1982] and the fully developed turbulent mass burning velocity $u_{tr,\infty}$ estimated using the expression given

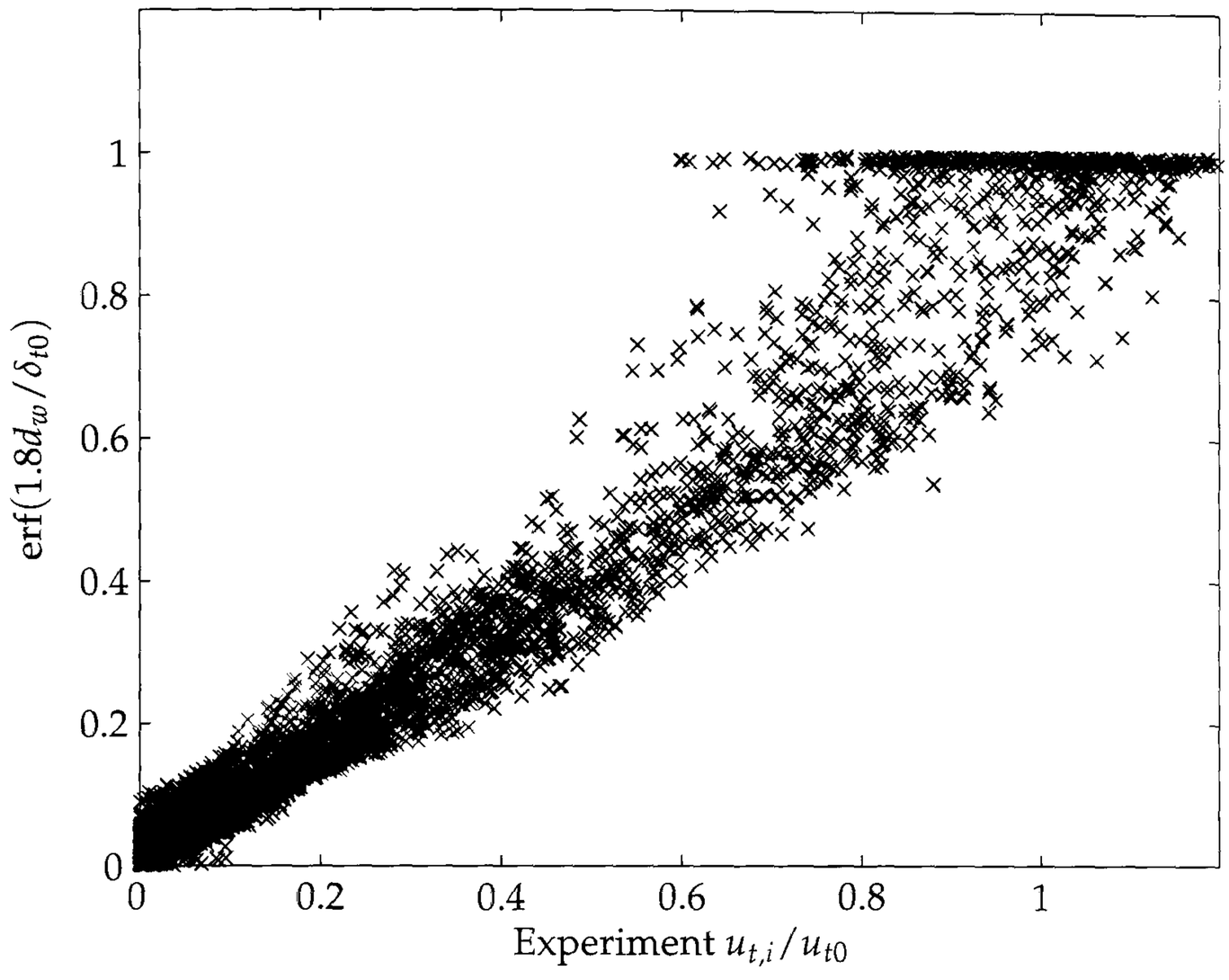

Figure 5.23: Correlation between experimental flame deceleration in the presence of a wall and Equation 4.34 calculated using $\delta_{t0} = 1.8/\delta_{tg0}$ at the 1000 rpm condition, 7.8° aTDC.

by Zimont [1979], Equation 4.17. Turbulence parameters were calculated using the standard LUSIE assumptions for this engine (Section 4.5.14) where the integral scale of turbulence L is assumed to be proportional to the clearance height with a constant of proportionality of 0.2 [Fraser and Bracco, 1989] and the rms turbulent velocity u' is calculated using the data presented by Atashkari [1997] and Jakubík [2002].

Data from the disc geometry LUPOE1-D engine were used for the analysis as the flow in this engine is close to quiescent with little large scale motion. Under these conditions it is more likely that 1) the flame has the form of a truncated sphere, which significantly improves the accuracy of the LUSIEDA reverse analysis, and 2) the integral length-scale is uniform across the combustion chamber. Values of f_d for the period before the flame contacts the cylinder bore are presented in Figure 5.26 plotted against dimensionless flame radius r_{fb}/L. The graph shows all the reported fast, middle and slow cycles (red, black and blue symbols respectively) for all engine conditions listed in Table 5.2 apart from the high compression ratio condition.[2]

[2]The data recorded at the high compression ratio condition by Abdi Aghdam [2003] may be

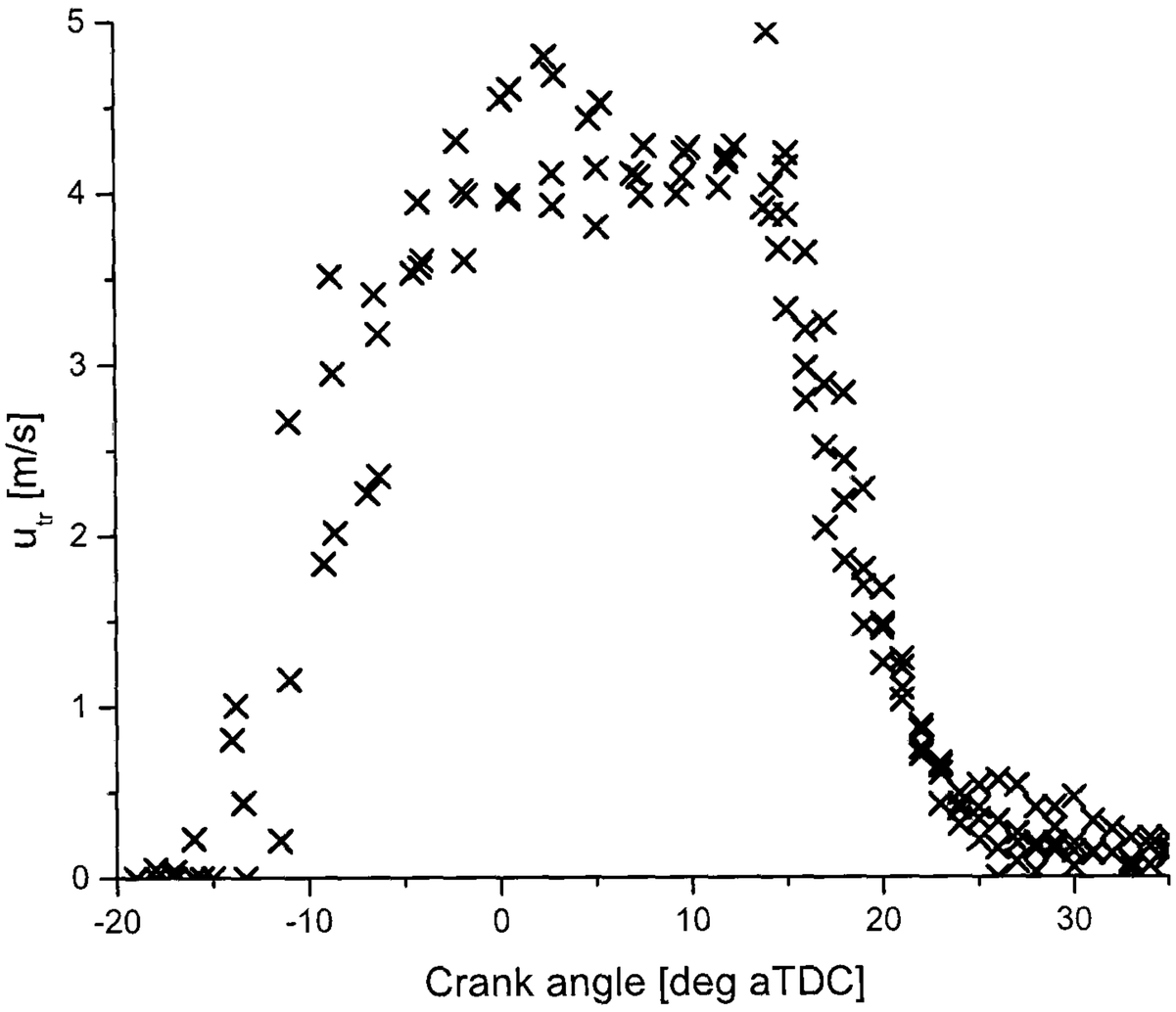

Figure 5.24: Variation in the LUSIEDA calculated turbulent mass burning velocity during three LUPOE1-D middle cycles at the 1500 rpm reference condition.

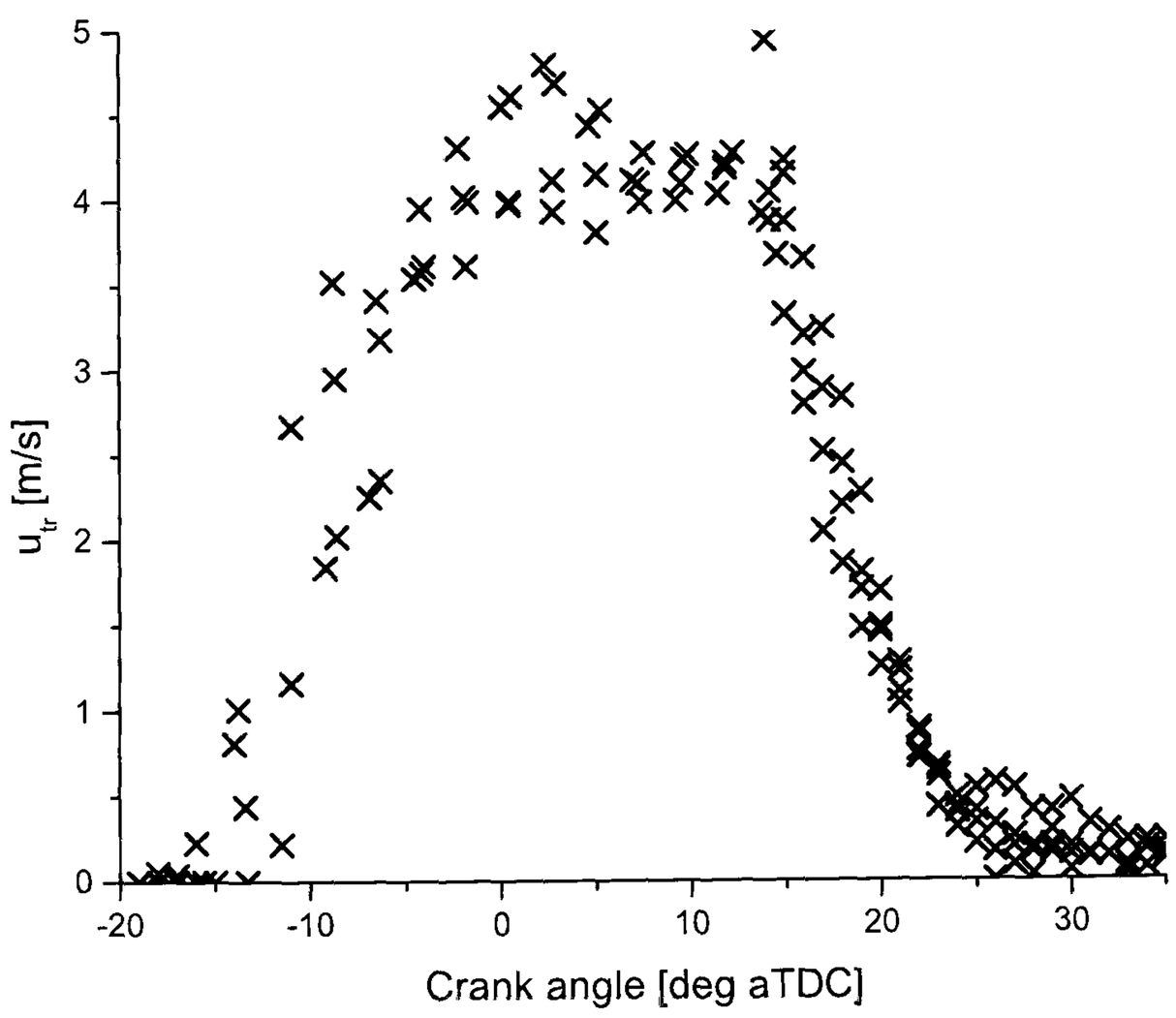

Figure 5.25: Variation in the LUSIEDA calculated turbulent mass burning velocity during three LUPOE2-P middle cycles at the 1500 rpm reference condition.

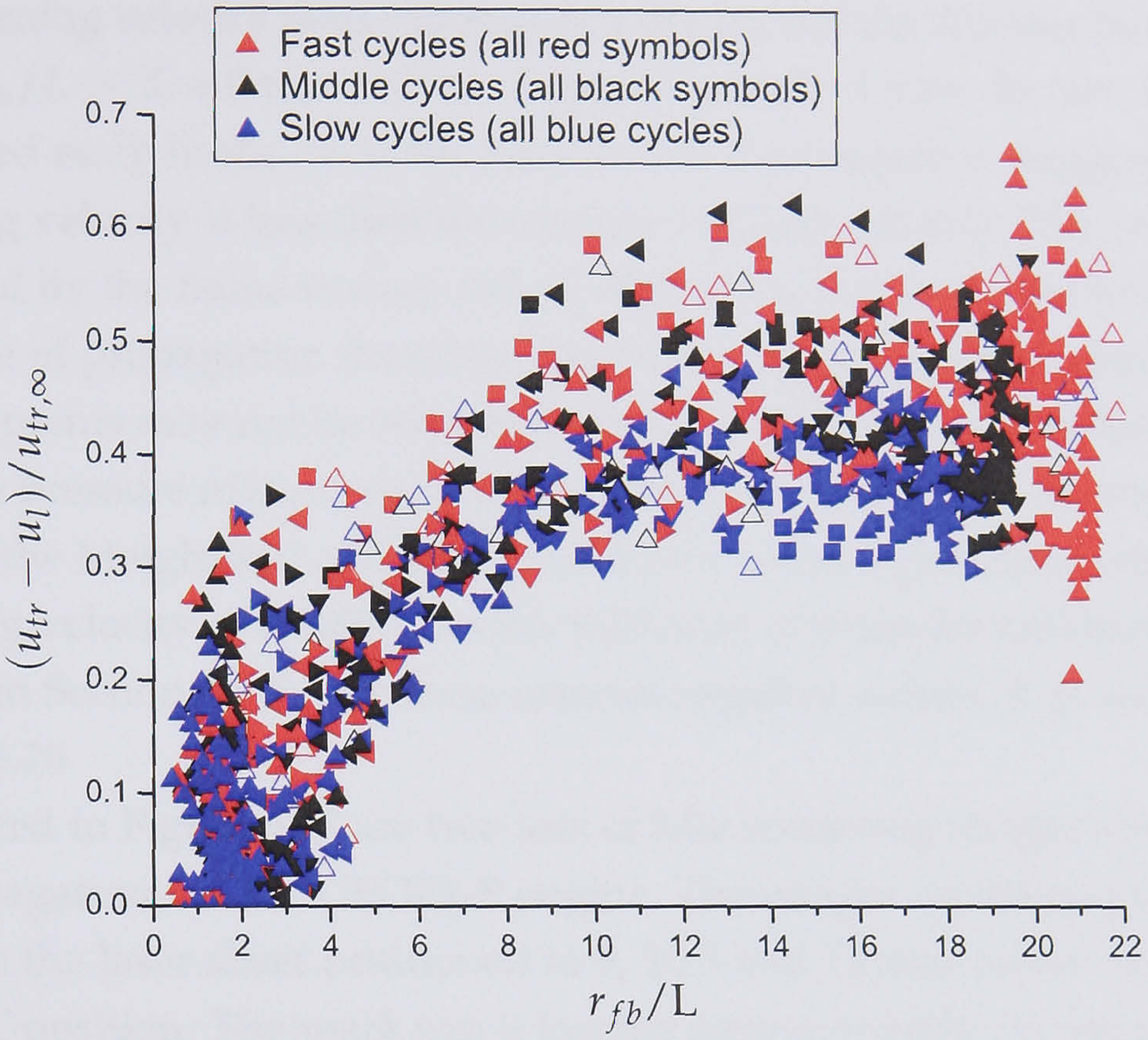

Figure 5.26: Flame acceleration during all the fast, middle and slow LUPOE1-D cycles reported by Abdi Aghdam [2003].

No correlation was observed between the engine operating condition and the location of the data points on the graph. Selected fast and middle cycles do however have a tendency to have a greater value of f_d for large values of r_{fb}/L. Following the initial combustion period the flame is observed to accelerate steadily with a fully developed burning velocity attained when the flame radius is approximately ten integral length scales. The value of f_d when the flame is fully developed is approximately 0.45. If f_d has an asymptotic value of one this implies that $A = 0.45$ (Equation 4.17), which is similar to the value found by Lipatnikov and Chomiak [1997].

Given that the data points shown in Figure 5.26 were generated using pressure data alone some caution should be attached to the interpretation of the earliest stages of combustion where the rise in pressure above the motoring pressure and the amount of mass burnt is low.[3] Nevertheless, the data presented suggests

---

unreliable, see Section 5.4.4.

[3]In most cycles, either due to spark noise corrupting the signal or errors in the data, the exper-

that the amount of burnt gas present immediately following ignition is very low and the burning velocity does not significantly exceed the laminar burning velocity until $r_{fb}/L > 2$, a flame radius of approximately 3 mm. In fact, the value of f_d calculated early in the cycle for some cycles was negative, suggesting the initial burning velocity is less than the laminar burning velocity. The rate of stretch experienced by the flame surface (see Section 1.5.1) is at a maximum during this early phase of propagation therefore this observation is entirely plausible, however these points may not be reliable because of the sensitivity of the analysis to error in the pressure measurement around the time of ignition. Furthermore, it is likely that the Metghalchi and Keck correlation used to generate values of laminar burning velocity overestimates the influence of pressure and temperature as discussed in Section 4.5.5. For these reasons negative values of f_d are not shown on Figure 5.26

Illustrated in Figure 5.27 are two sets of Mie scattering images showing early flame propagation in the LUPOE2-P engine. The images are taken from different cycles with the laser sheet positioned at 9, 10.5 and 12 mm above the flat piston crown TDC position. The spark gap is located approximately 11.2 mm above TDC hence the laser sheets cover the regions above and below the spark. The lack of burnt gas visible in the early images suggests that the conclusions drawn from the LUSIEDA analysis regarding the low speed of the early flame propagation are plausible. Certainly, in both sets of images there is no burnt gas visible until the fourth frame, 3.6° CA after ignition, at which point a small flame kernel with a radius of approximately 1.5 mm is present.

Simultaneous imaging on different laser sheet planes [Mantzaras et al., 1988, Hicks et al., 1994] was not possible with the current experimental configuration hence it is possible that for the images shown the flame kernel could have migrated out of the sheet plane. Inspection of other cycles recorded with the laser sheet in the same positions revealed that $\sim$ 3.5° CA delay between ignition and the appearance of burnt gas on any of the laser sheet planes was typical for this condition. It is possible that the temperature of the burnt gas during the initial stages of flame propagation is too low to cause the change in the seed particles necessary to indicate the presence of burnt gas in Mie scattering images. Natural light photography of combustion through the side window of the LUPOE2-P

---

imental pressure at ignition is significantly higher than the motoring pressure for a comparable cycle. In this case, LUSIEDA will "burn" an unrealistic amount of mass in the first time step after ignition and the inferred burning velocity will be erroneously high. Where this has occurred, the data point at ignition has not been plotted for clarity.

engine at a similar operating condition [Murad, 2006] indicated the presence of a flame kernel with a radius of approximately 1 mm immediately following ignition. Whether this measurement is truly reliable given the inevitable flare caused by the electrical discharge across the spark gap is debatable. Nevertheless, 4° CA after ignition the spark kernel, as imaged through the side window by Murad, was observed to have grown to a radius of 2.5 mm, suggesting that even when the flame is only just larger than the original spark kernel the entrainment and burnt gas fronts, defined by schlieren and Mie-scattering images respectively, are separated by $\sim$ 0.5mm.

As the entrainment front by definition precedes the burnt gas front it is not surprising that Murad reported slightly larger flame radii for a given crank angle. Interestingly, the results of Abdi Aghdam [2003] show that, for a stoichiometric mixture at 1500 rpm on the LUPOE1-D engine, the entrainment front took around 4° CA to reach a 3 mm radius, demonstrating the (relative) independence of the initial burn period from the chamber geometry and turbulence and the very low speed of propagation of the flame for a significant period following ignition.

Shown in Figure 5.28 are values of f_d derived from the u_{tr} results recorded in the Leeds Mk II turbulent combustion vessel by Ormsby [2005]. In this case values of u' and L were known accurately from PIV and two point LDV measurements of the turbulence in the bomb [Bradley et al., 1996, Nwagwe et al., 2000, Larsson, 2007]. Values of u_l recorded in the same vessel, tabulated by Ormsby [2005], were used as required by Equation 5.8. Again, for some conditions f_d was negative during the early stages of combustion. As the values of u_{tr} reported by Ormsby are derived from photographic measurements of flame propagation rather than measurements of pressure rise, they are likely to be more accurate during the period immediately following ignition than comparable values calculated using LUSIEDA. Turbulent burning velocities which are lower than the laminar burning velocity for the same mixture during the early stages of flame propagation have been reported elsewhere, for example [Bradley et al., 2003, Abdel-Gayed et al., 1988].

In common with values of f_d derived from engine measurements, results for different mixture strengths, turbulence and pressure show no correlation. Flame acceleration appears to be rather quicker in the bomb than in the engine, compare Figures 5.26 and 5.28, with no initial delay period and higher values of f_d for a given r_{fb}/L. The implied lack of correlation between the two data sets may be misleading as 1) the estimates of the integral scale (and hence abscissa coor-

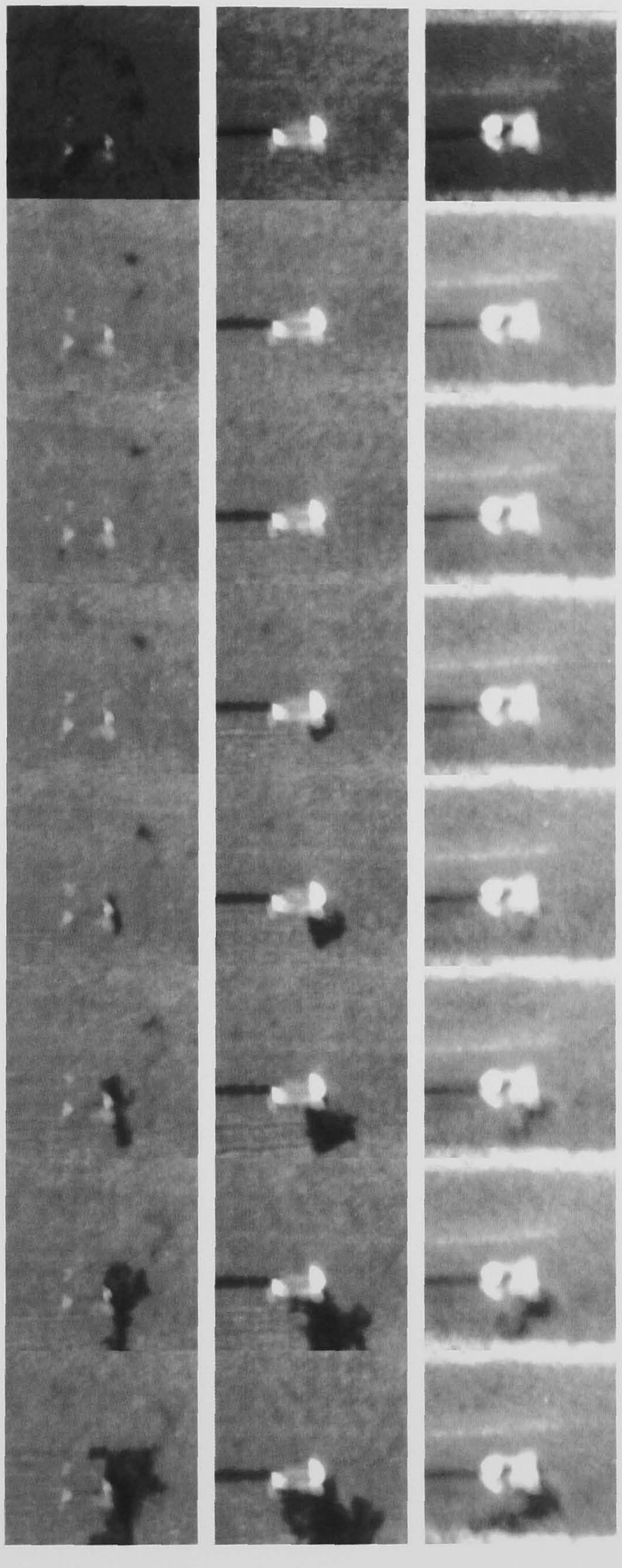

(a)

Figure 5.27: Early flame development in LUPOE2-P with a stoichiometric mixture at 1500 rpm. The laser sheets are positioned at 9 (left), 10.5 (middle) and 12 mm (right) above the TDC plane, the spark gap is approximately 11.2 mm above the TDC plane. The first frame is taken at the moment of ignition, 7° bTDC, with 0.9° CA between frames. Each frame covers an area of 20 × 20 mm. Figure continued on page 195.

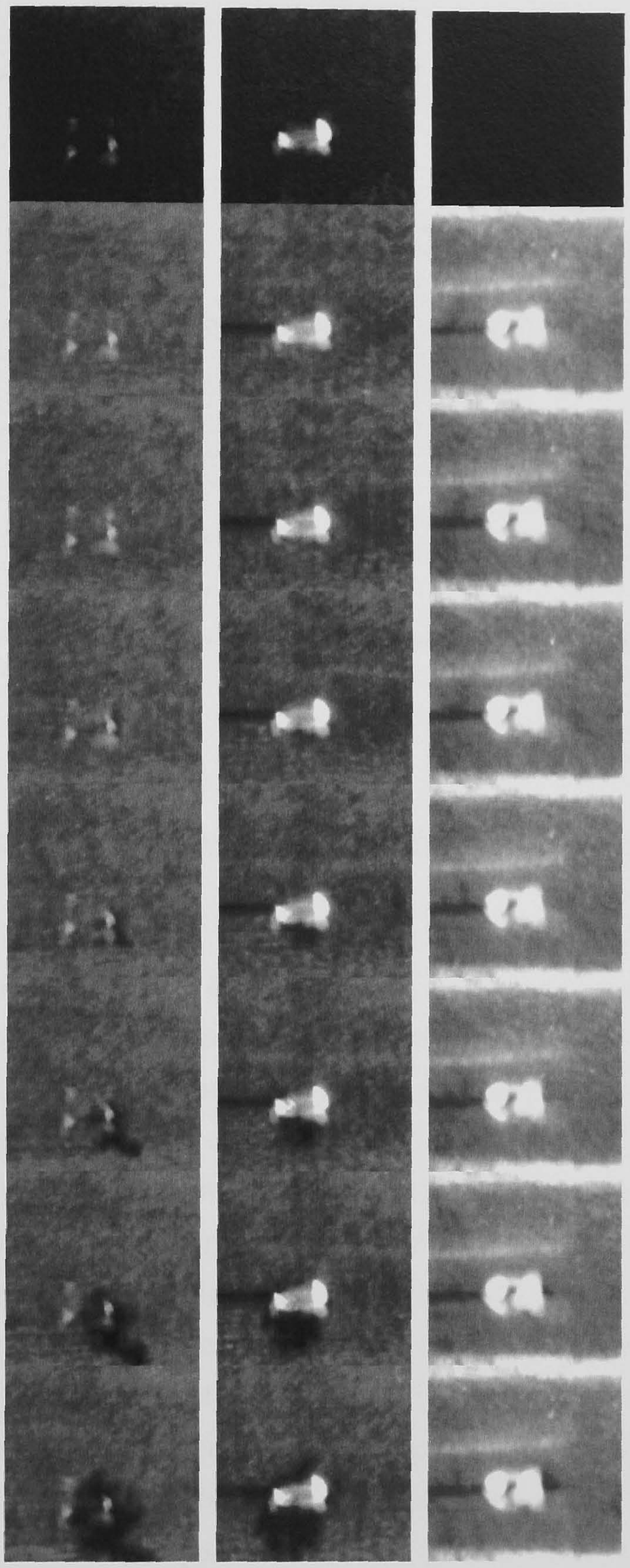

(b)

Figure 5.27: (continued) Early flame development in LUPOE2-P with a stoichiometric mixture at 1500 rpm. The laser sheets are positioned at 9 (left), 10.5 (middle) and 12 mm (right) above the TDC plane, the spark gap is approximately 11.2 mm above the TDC plane. The first frame is taken at the moment of ignition, 7° bTDC, with 0.9° CA between frames. Each frame covers an area of 20 × 20 mm.

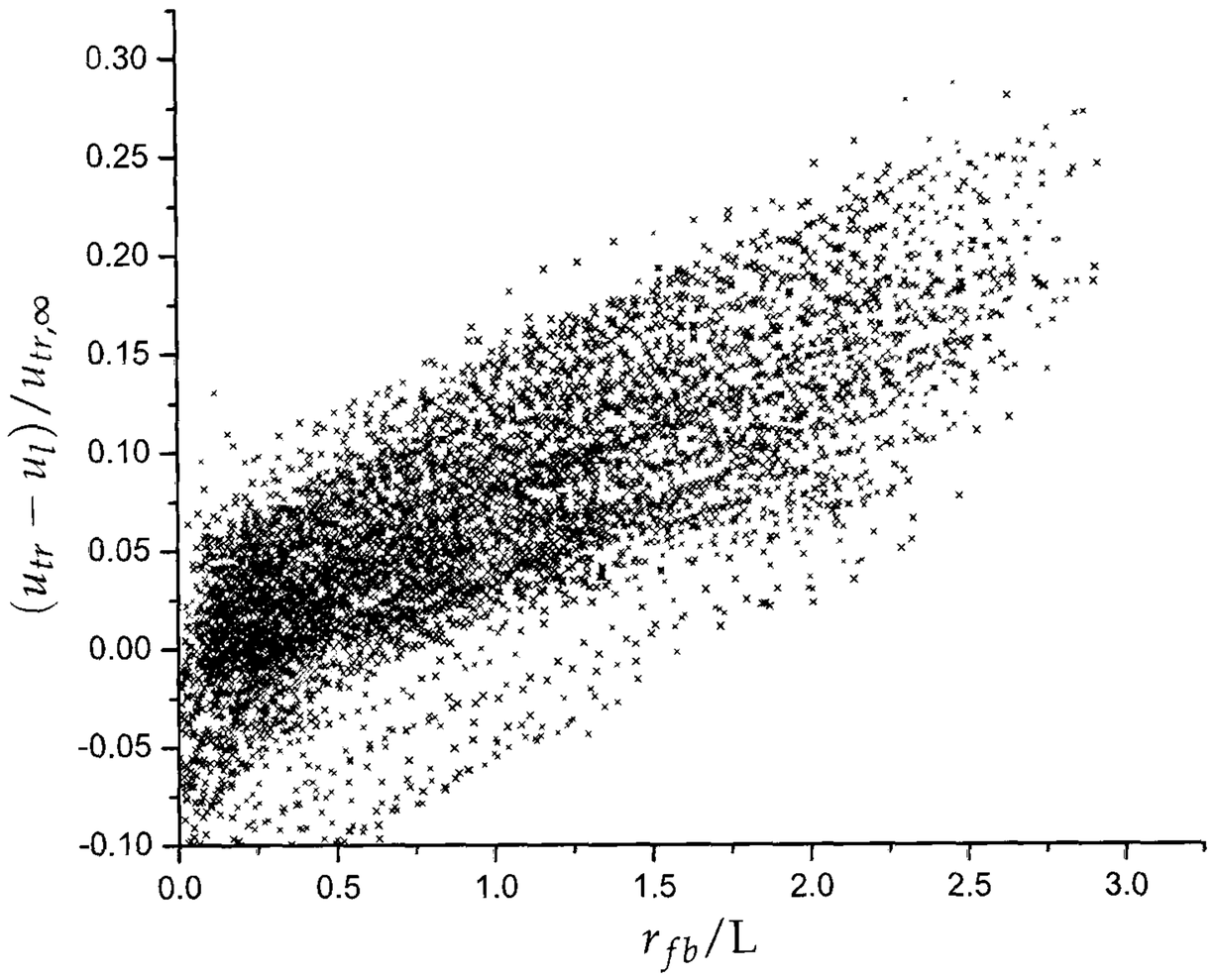

Figure 5.28: Flame acceleration during all the turbulent deflagrations reported by Ormsby [2005].

dinates) used in the analysis of the LUPOE1-D data may be inaccurate and 2) the early combustion period in an engine produces very little change in pressure therefore LUSIEDA derived values of u_{tr} during this period are subject to large error margins. That different u_l correlations were used to analyse the different data sets is possibly of some consequence as their values are quite different at higher temperatures and pressures, see Figure 4.16. However, even given the scatter in the different u_l correlations the magnitude of u_l at engine temperatures and pressures is rarely greater than 10% of u_{tr} for sensible operating conditions.

As well as plotting the estimated values of f_d against dimensionless flame radius, an attempt was made to produce similar graphs with time or dimensionless time, t/τ_L, as the abscissa. Plotting the data in this way failed to produce any useful information as the collapse of the data points onto a common curve as observed in Figures 5.26 and 5.28 did not occur.

If it is accepted that flame wrinkling is the dominant cause of flame acceleration as proposed by Abdel-Gayed et al. [1987] and others then a further discussion of the mechanism of flame wrinkling is prudent at this point. Consider a hypothetical smooth spherical surface, much larger than the largest eddies, cre-

ated instantly in a turbulent environment. If the surface is permitted to deform through contact with turbulent eddies smaller than itself the surface will change in character from smooth to wrinkled over a certain time scale determined by the characteristic rotation time of the eddies. The extent of the wrinkling on the surface will be a function of the time it has been in existence. Once the surface has been in contact with the turbulence long enough for many eddy rotations to have taken place the degree of wrinkling of the surface will reach some maximum.[4]

Now consider the same hypothetical spherical surface, this time growing from a single point. If the rate of growth of the sphere is much slower than the characteristic eddy rotation time the surface of the sphere will become wrinkled to its fullest extent almost immediately by eddies smaller than the sphere. As the sphere grows, the size of the eddies capable of wrinkling the sphere increases. The degree of wrinkling present on the surface is therefore a function of the size of the sphere and the maximum wrinkling is reached when the sphere grows larger than the largest turbulent eddies.

The above discussion may now be formalised and recast in terms of turbulent flame propagation by employing the following ratios:

$$\mathcal{R}_L = \frac{L_{\text{comb}}}{L} \tag{5.9}$$

$$\mathcal{R}_\tau = \frac{\tau_{\text{comb}}}{\tau_L} \tag{5.10}$$

where L_{comb} is the characteristic length scale over which combustion occurs, for example the bore diameter, L is the integral length scale of turbulence, τ_{comb} is the characteristic time over which combustion takes place and $\tau_L = L/u'$ is the integral time scale. Four possible combinations of $\mathcal{R}_L$ and $\mathcal{R}_\tau$ are discussed below.

$\mathcal{R}_\tau > 1, \mathcal{R}_L < 1 \rightarrow \mathcal{R}_\tau > \mathcal{R}_L$ A flame of a given size is wrinkled almost instantly by eddies smaller than itself as the eddies are rotating quicker than the flame is growing; flame development is predominantly a function of the size of the flame.

$\mathcal{R}_\tau < 1, \mathcal{R}_L < 1$ Neither the size of the flame or the time it has been in existence dominates flame development; flame development is a function of both radius and time and the flame will never become fully developed.

[4]Providing the fabric of the surface is subject to surface tension. If the surface is entirely elastic with no surface tension the degree of wrinkling will increase indefinitely.

$\mathcal{R}_\tau > 1, \mathcal{R}_L > 1$ Neither the size of the flame or the time it has been in existence dominates flame development; flame development is a function of both radius and time and the flame quickly becomes fully developed.

$\mathcal{R}_\tau < 1, \mathcal{R}_L > 1 \rightarrow \mathcal{R}_\tau < \mathcal{R}_L$ The flame quickly grows larger than the largest eddies, the rate of rotation of the eddies is smaller than the rate of propagation of the flame; flame development is predominantly a function of the elapsed time.

It is possible to estimate values of $\mathcal{R}_\tau$ and $\mathcal{R}_L$ for the bomb and the engine given their dimensions and measurements of the turbulence within them. For the LUPOE1-D engine $L_{\text{comb}} \sim 80$ mm, the bore diameter, $L \sim 2$ mm, and at 1500 rpm $u' \sim 2$ ms^{-1} and $\tau_{\text{comb}} \sim 5$ ms giving $\mathcal{R}_\tau \sim 5$ and $\mathcal{R}_L \sim 40$. For the bomb, $L_{\text{comb}} \sim 150$ mm, the diameter of the bomb window over which the measurements were taken, $L = 20$ mm, and for $u' = 5$ ms^{-1} $\tau_{\text{comb}} \sim 5$ ms giving $\mathcal{R}_\tau \sim 1$ and $\mathcal{R}_L \sim 7.5$. As, to a first approximation, τ_{comb} scales linearly with $1/u'$ ($u_t \sim u'$), and L and L_{comb} are functions of the vessel size, the values of $\mathcal{R}_\tau$ and $\mathcal{R}_L$ can be expected to remain constant for all sensible operating conditions.

The values of $\mathcal{R}_\tau$ and $\mathcal{R}_L$ calculated suggest that flames in both the bomb and engine are exposed to the full spectrum of turbulent eddy sizes much sooner than the eddies have had time to complete enough revolutions to wrinkle the flame. This places both vessels in the $\mathcal{R}_\tau < 1, \mathcal{R}_L > 1 \rightarrow \mathcal{R}_\tau < \mathcal{R}_L$ regime and implies that in this case flame acceleration should be a function of the time elapsed since ignition. It is therefore surprising that neither the bomb or engine results collapsed onto a common curve when plotted against time or dimensionless time t/τ_L and exposes the possibility that some mechanism other than the wrinkling of the flame front is influencing the rate of flame acceleration. This discussion highlights the need for more advanced flame development submodels than those currently available in the literature. In particular, the degree of flame development predicted by any proposed model should be a function of both elapsed time and the size of the flame. None of the models currently available in the literature have this feature.

5.3.7 Flame sphericity

Correct prediction of the flame active surface area is important for accurate modelling of SI engine combustion. A thermodynamic code such as LUSIE does not need to predict deformations caused by the wrinkling of the flame by small scale

turbulence, this area enhancement is incorporated in the expression for the turbulent burning velocity (see Section 4.5.7). Any larger scale distortion does need to be predicted as the active surface area directly influences the mass entrained (three-zone model) or mass burnt (two-zone model) each time step.

The LUSIE code assumes that the propagating flame has the geometry of a sphere truncated by the walls of the combustion chamber. For a disc chamber engine with a quiescent flow such as LUPOE1-D, flames observed experimentally [Gillespie, 1998, Cairns, 2001, Abdi Aghdam, 2003, and others] have been close to spherical and the assumption of sphericity is probably not a bad one. For a more conventional pent roof engine with a tumble flow such as LUPOE2-P, the flames' macro-geometry may be distorted by the largest eddies and the active surface area may be larger than that of a truncated sphere of the same volume. As a sphere is the solid with the smallest surface area for a given volume, any distortion to the flame surface will necessarily cause an increase in the surface area. Translation of the entire flame, discussed in Section 5.3.2, will also affect the active surface area by causing the flame to contact the chamber walls earlier on one side and later on the other.

The sphericity of the ensemble averaged flame surface was evaluated by calculating the Euclidian distance between the location of the spark gap and each vertex on the active part of the triangulated isosurface representing $\overline{c} = 0.5$. Per face values were calculated by averaging the contribution of the three vertices comprising each face; active surface was defined to be any face which was greater than 1.5 mm from the $\overline{c} = 0.5$ isosurface from the last frame, see Section 3.3.11. The mean and standard deviation of the distance from the spark gap was then evaluated using the methods described in Section 3.3.14. A perfectly spherical flame should have a standard deviation of zero. Non-zero standard deviations indicate either a flame which has been convected such that the spark gap is no longer located at the centre of the flame or a departure from sphericity. To try and negate the effect influence of convection of the entire flame on the mean and standard deviation calculated the procedure was repeated, this time using the distance between each vertex and the flame barycentre at that instant (Section 3.3.12).

Illustrated in Figure 5.29 is the growth in the mean distance from the spark of the active regions of the surface at the 1500 rpm base condition. The error bars indicate ± 1 standard deviation. The standard deviation grows steadily through the cycle from $\sim$ 2 mm when the flame has a radius of $\sim$ 4 mm to $\sim$ 7 mm when

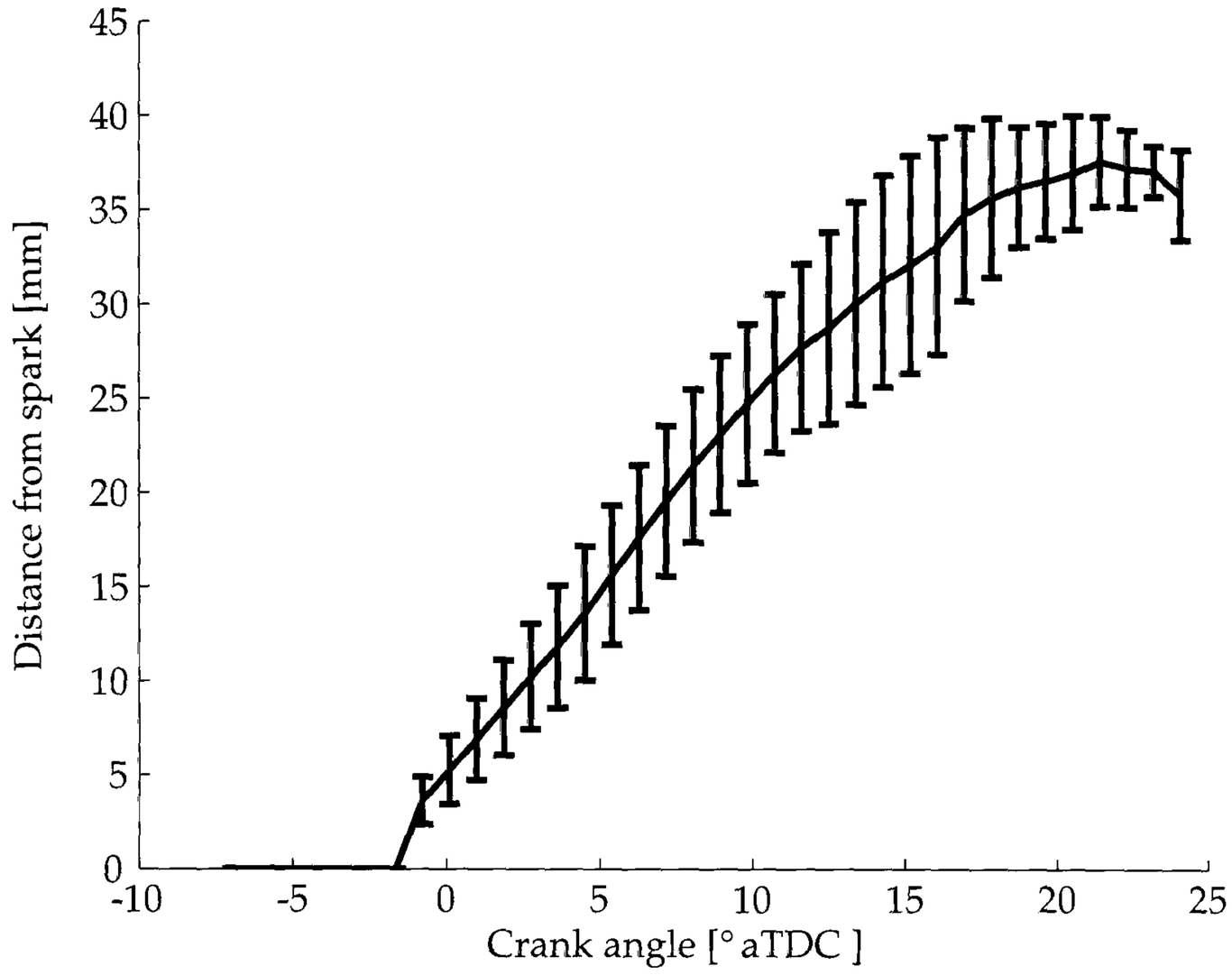

Figure 5.29: Area weighted mean and standard deviation of the distance from the spark gap to active surface elements at the 1500 rpm base condition.

the flame radius is ~ 33 mm. In relative terms the sphericity of the flame increases as the flame grows as the standard deviation grows at a slower rate than the mean flame radius. Note however that, as discussed previously (Section 5.3.1), the $\bar{c} = 0.5$ isosurface is prone to distortion caused by reflections from the spark plug during the early stages of flame propagation. The bars shown in Figure 5.30 show the probability density function (PDF) of the local distance from the spark for active surface elements at 5.4° aTDC (distributions at other crank angles were similar) for the same 1500 rpm engine condition. The probability distribution is close to constant within the range 12.5–21 mm from the spark gap with a small tail at low distances and an abrupt cutoff at large distances. The small tail suggests that as the flame surface approaches a wall it tends to conform to the wall (become "swept back") rather than quench immediately. The abrupt cutoff shows that on the mean there are no large protrusions ahead of the main flame front. As the data are ensemble averaged this is not surprising.

Figure 5.31 illustrates isosurfaces of $\bar{c} = 0.5$ at the 1500 rpm base condition. Visual inspection of the isosurfaces confirms that the ensemble averaged flame is initially spherical. As the flame approaches the walls it slows down and conforms to the shape of the combustion chamber, particularly on the side which

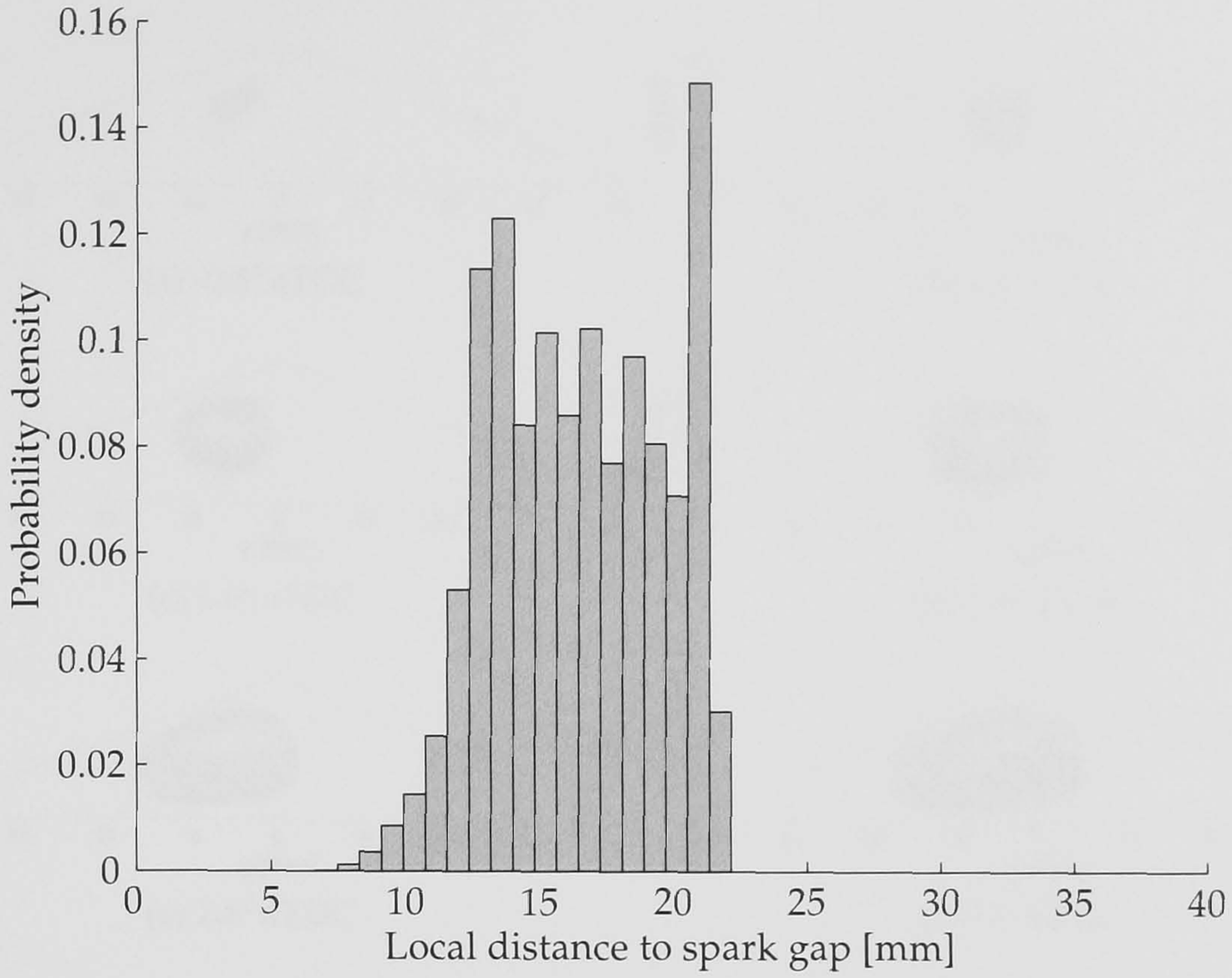

Figure 5.30: Area weighted PDF of the distance from the spark gap to active surface elements at 5.4° aTDC for the 1500 rpm base condition.

the flame is being convected away from. A similar pattern was noted for other engine speeds.

The mean and standard deviation of the distance between the flame barycentre and the active surface is depicted in Figure 5.32. The pattern of growth of the mean value is much the same as for the distance between the spark gap and the active surface however, the standard deviation is noticeably lower. A PDF of the local distance to the flame centroid at 5.4° aTDC is depicted in Figure 5.33. The spread of the distribution is much narrower than the previously discussed PDF of distance from the spark gap at the same crank angle (Figure 5.30). This indicates that the barycentre is a better measure of the position of the centre of the flame. The distribution in Figure 5.33 is clearly non-Gaussian and exhibits a negative skewness. Again, this suggests that the flame surface tends to become swept back, conforming to the chamber geometry, as it moves close to the walls. Visual inspection of $\overline{c} = 0.5$ isosurfaces as in Figure 5.31 support this supposition.

Neither the maximum value of: the mean distance from the spark gap, Figure 5.29; or the mean distance from the barycentre, Figure 5.32, ever reach the bore radius (40 mm). This occurs because 1) the spark is slightly offset from the

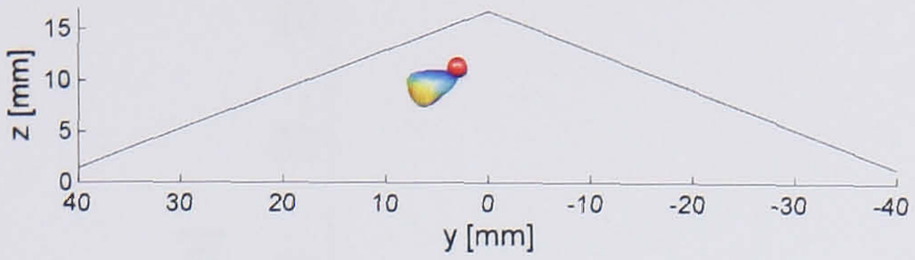

(a) -0.8° aTDC

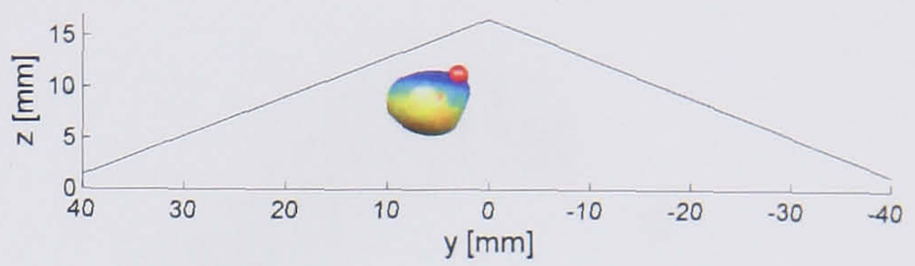

(b) 0.1° aTDC

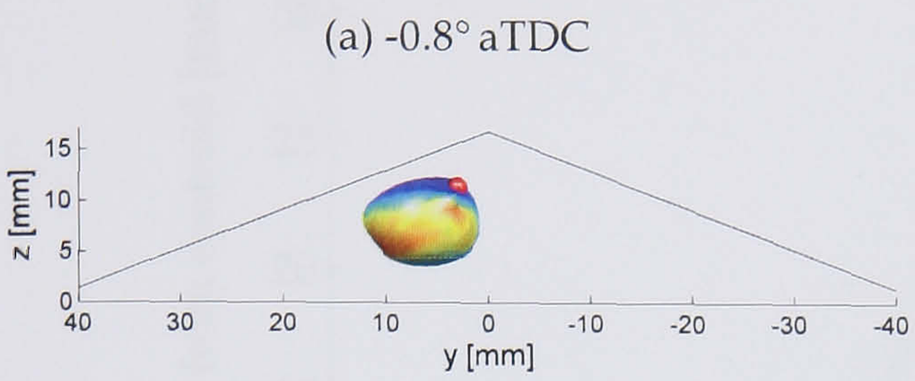

(c) 1.0° aTDC

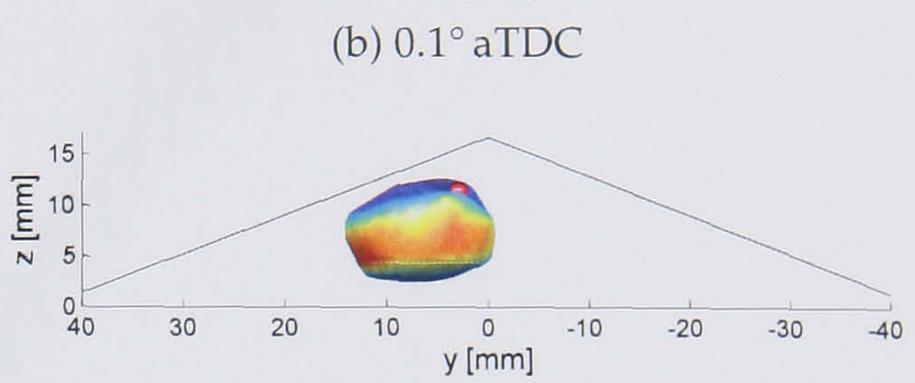

(d) 1.9° aTDC

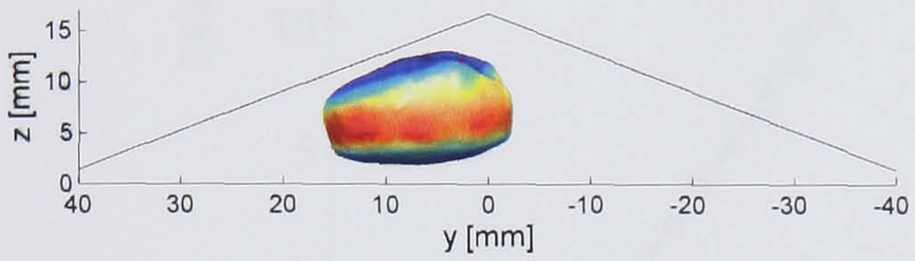

(e) 2.8° aTDC

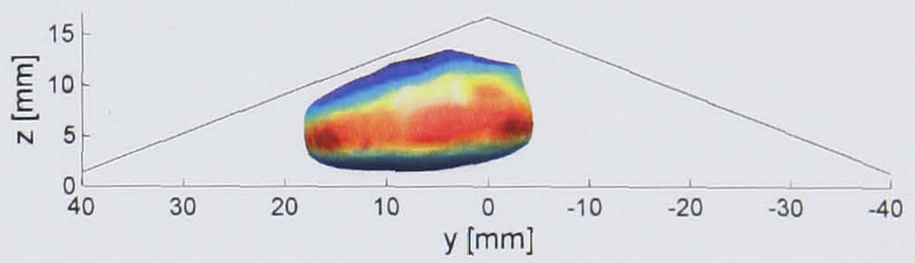

(f) 3.6° aTDC

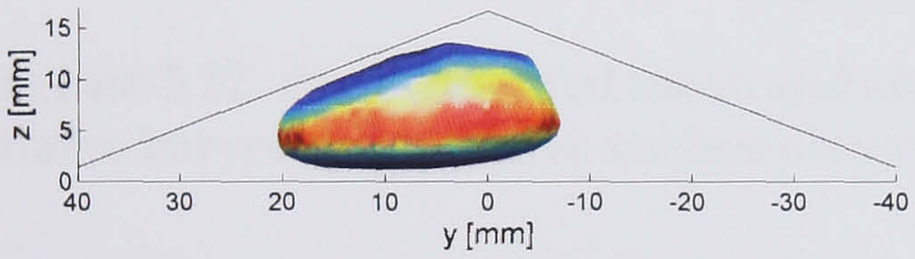

(g) 4.5° aTDC

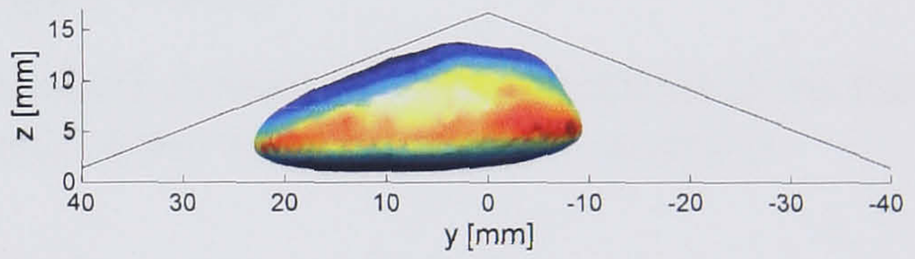

(h) 5.4° aTDC

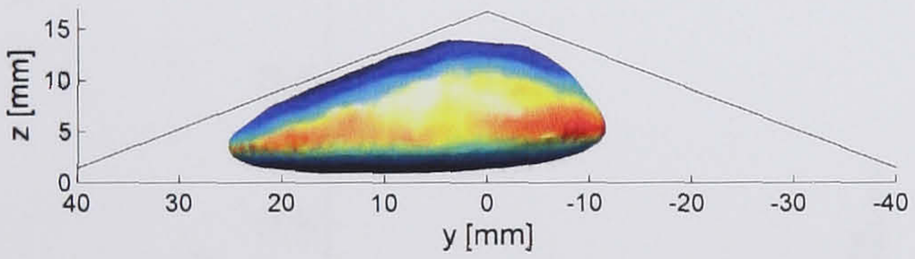

(i) 6.3° aTDC

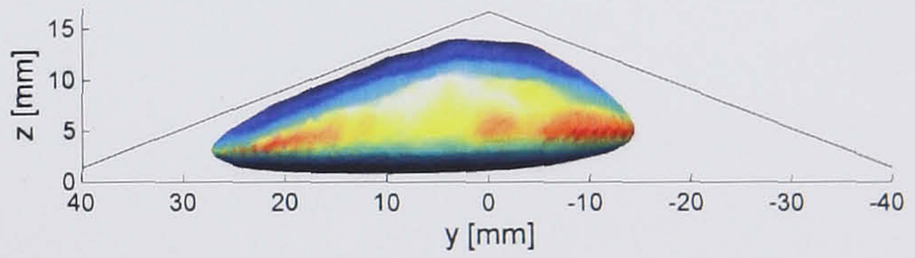

(j) 7.2° aTDC

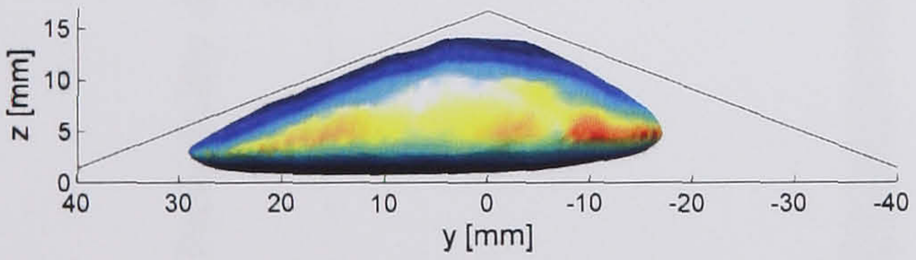

(k) 8.1° aTDC

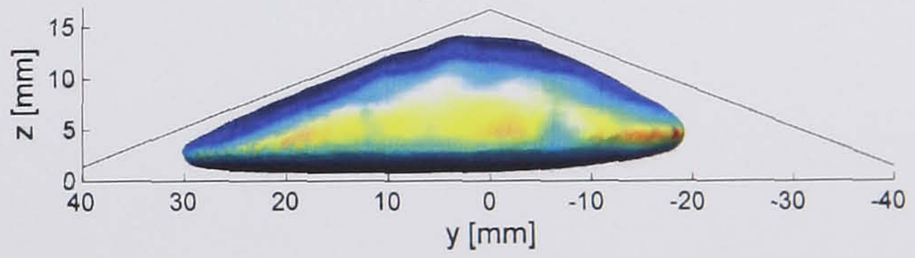

(l) 8.9° aTDC

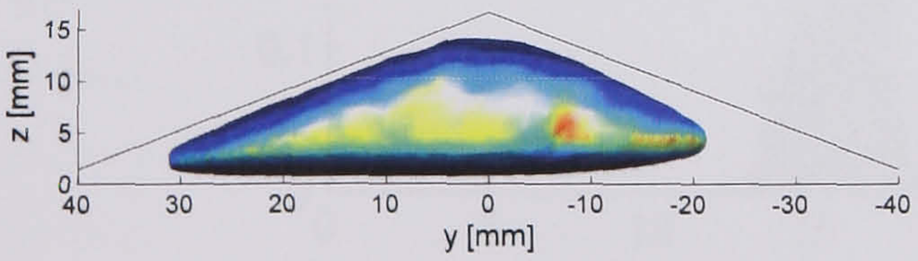

(m) 9.8° aTDC

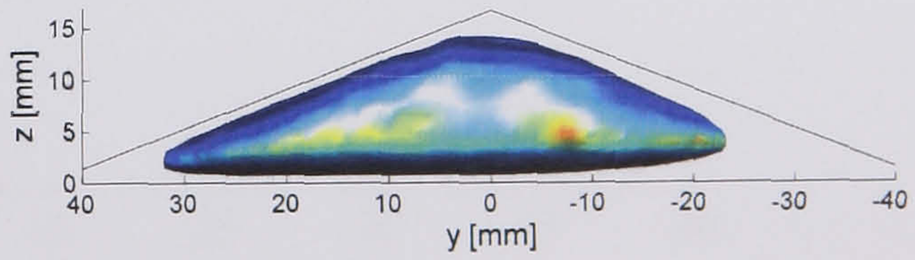

(n) 10.7° aTDC

Figure 5.31: Isosurfaces of $\overline{c} = 0.5$ coloured to show the local mass burning velocity at the 1500 rpm base condition showing the flame surface conforming the shape of the combustion chamber as it approaches the walls.

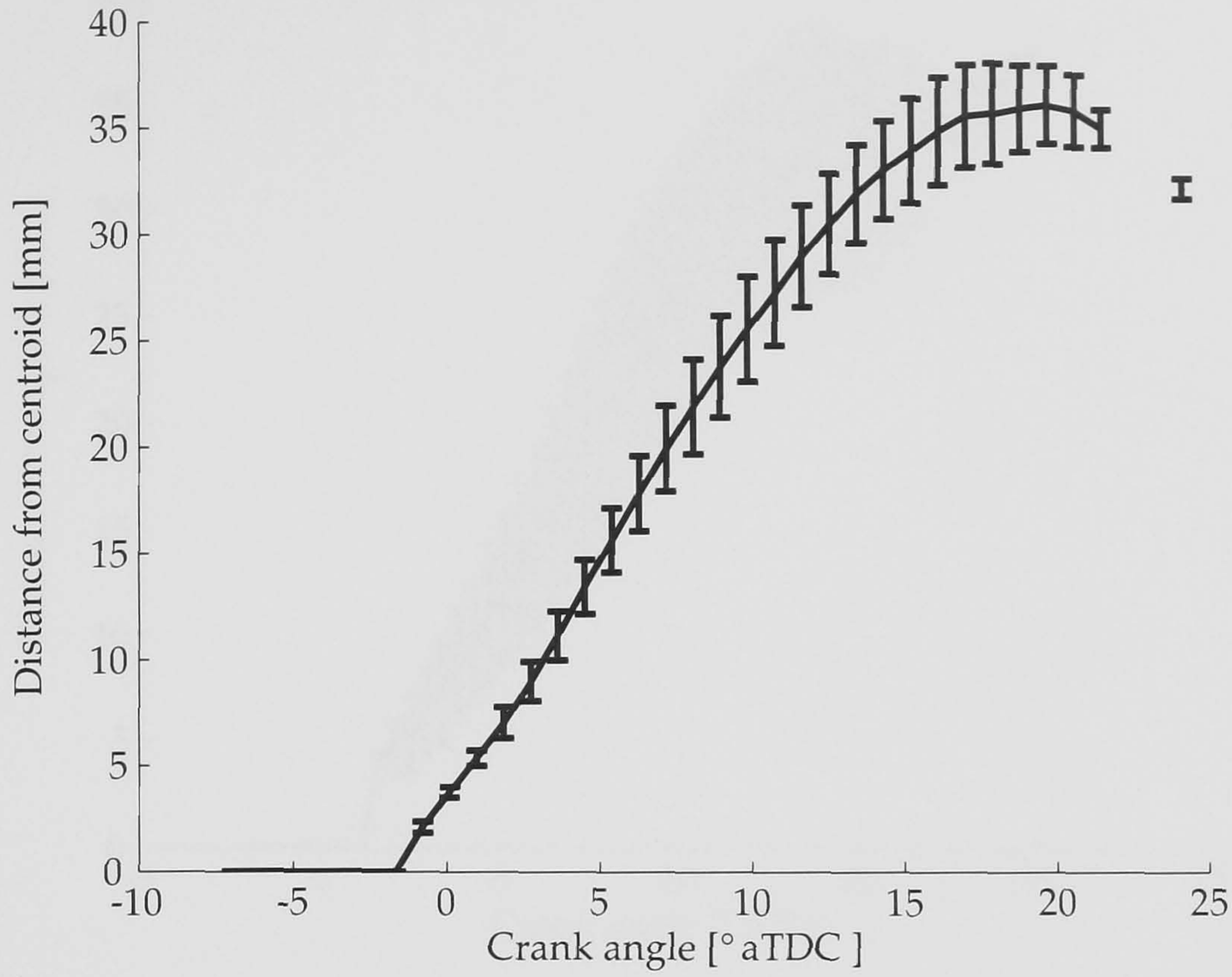

Figure 5.32: Area weighted mean and standard deviation of the distance from the flame barycentre to active surface elements at the 1500 rpm base condition.

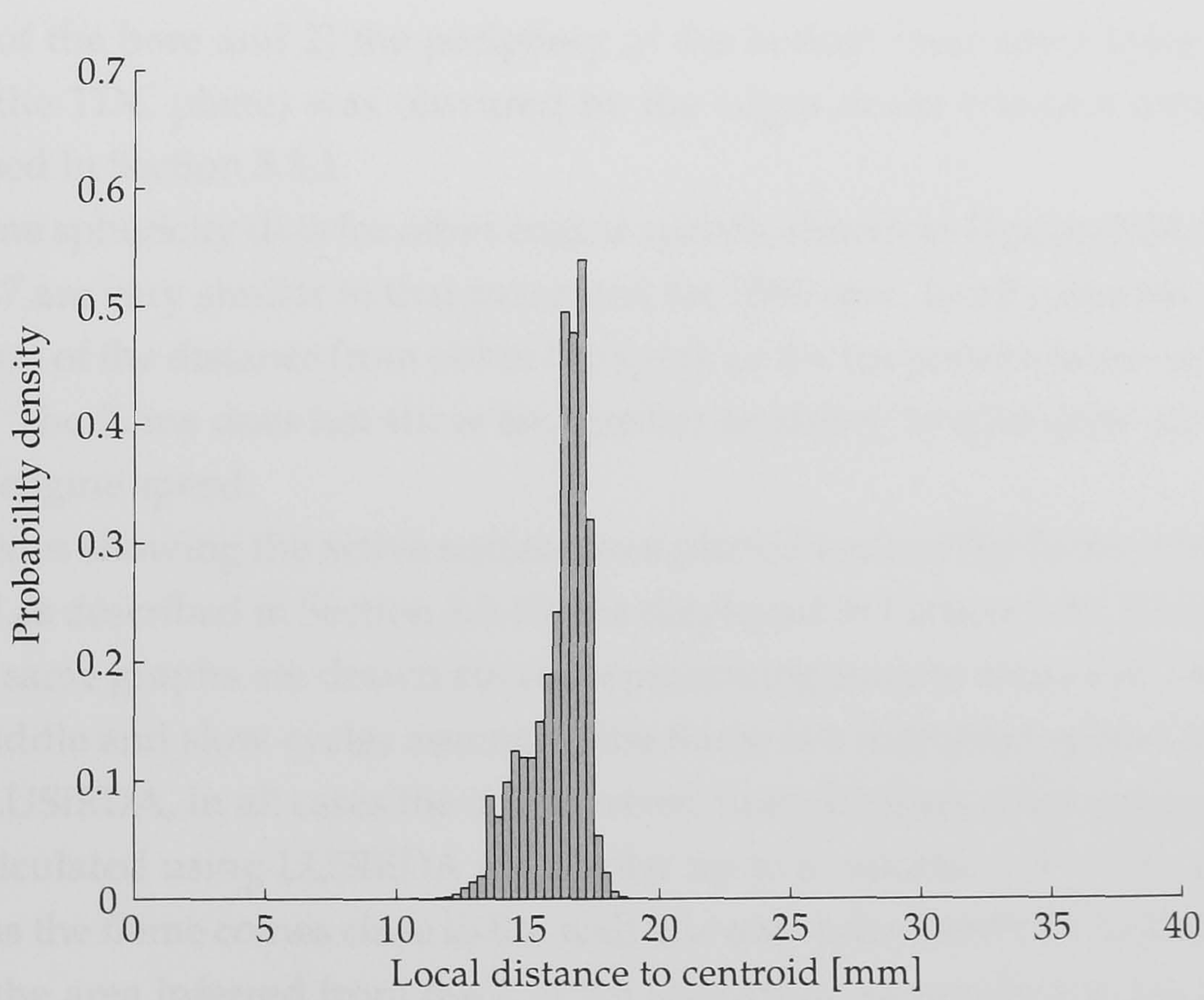

Figure 5.33: Area weighted PDF of the distance from the flame barycentre to active surface elements at 5.4° aTDC for the 1500 rpm base condition.

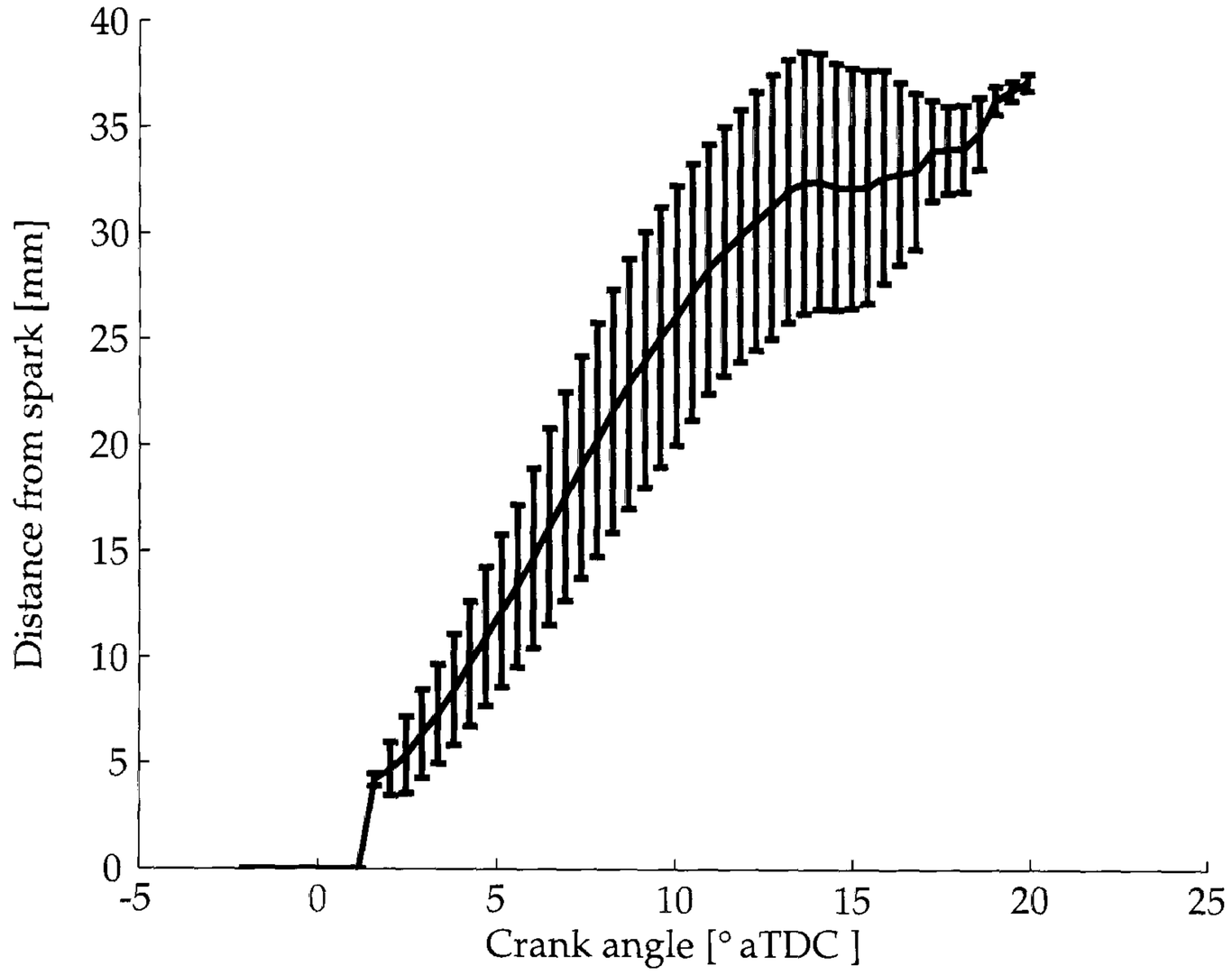

Figure 5.34: Area weighted mean and standard deviation of the distance from the spark gap to active surface elements at the 750 rpm condition.

centre of the bore and 2) the periphery of the bottom laser sheet layer (1.5 mm above the TDC plane) was obscured by the edges of the window mounting as discussed in Section 5.3.1.

Flame sphericity data for other engine speeds, shown in Figures 5.34, 5.35, 5.36 and 5.37 are very similar to that presented for 1500 rpm. In all cases the standard deviation of the distance from either the spark or the barycentre grows with flame radius. The flame does not show any greater tendency to sphericity for any particular engine speed.

Crosses showing the active surface area plotted against the flame volume (calculated as described in Section 3.3.10) are displayed in Figures 5.38, 5.39 and 5.40. On the same graphs are drawn curves representing surface areas and volumes of fast, middle and slow cycles assuming the flame is a truncated sphere calculated using LUSIEDA. In all cases the data derived from the laser sheet images and the data calculated using LUSIEDA are similar up to a volume $\sim 1 \times 10^4$. After this point, as the flame comes close to the wall, the area calculated by LUSIEDA drops below the area inferred from the $\bar{c} = 0.5$ isosurface, especially for the 1500 rpm case. This is further evidence that, for an ensemble averaged flame front, the active surface area is larger than the area of a truncated sphere. At large volumes,

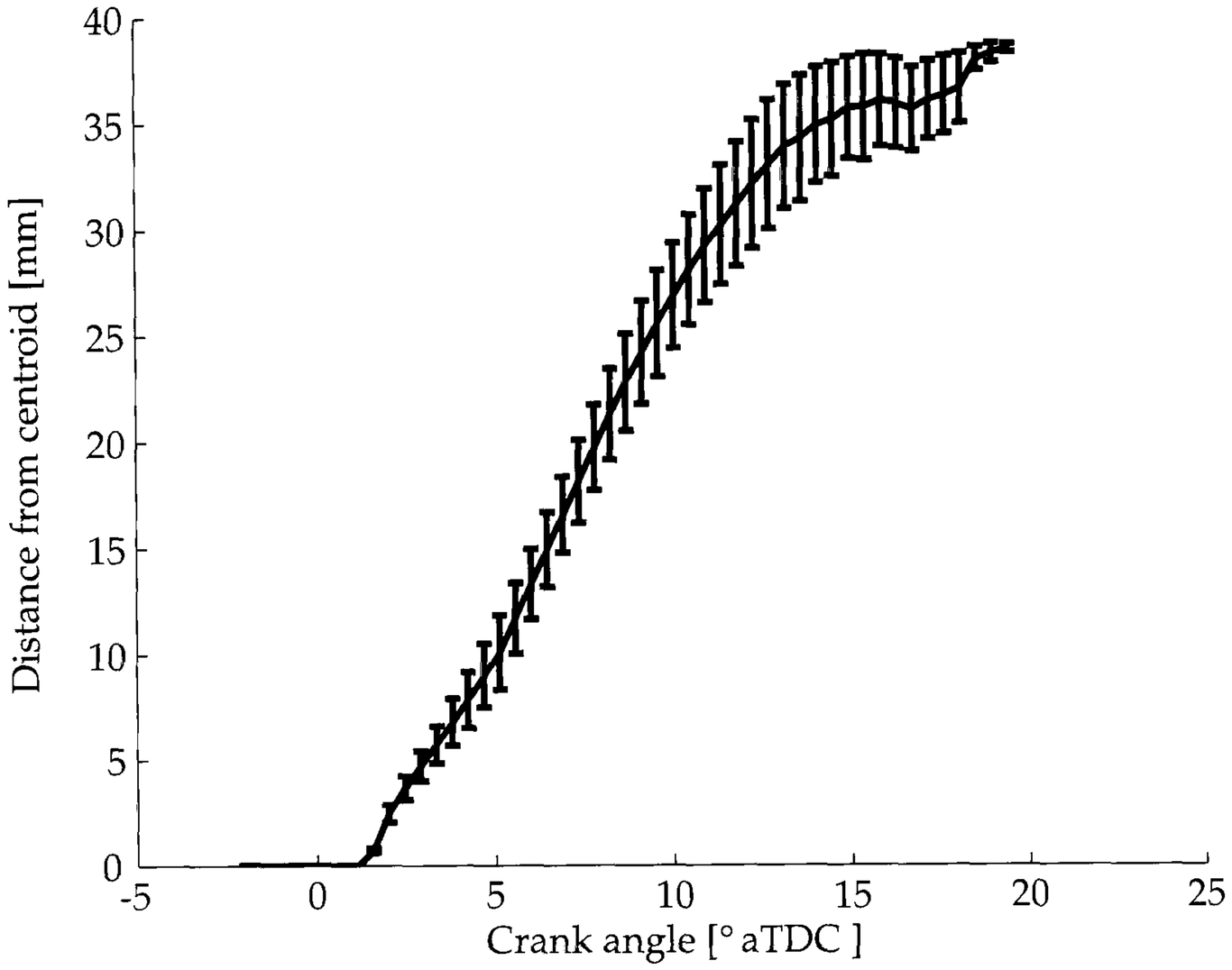

Figure 5.35: Area weighted mean and standard deviation of the distance from the flame barycentre to active surface elements at the 750 rpm condition.

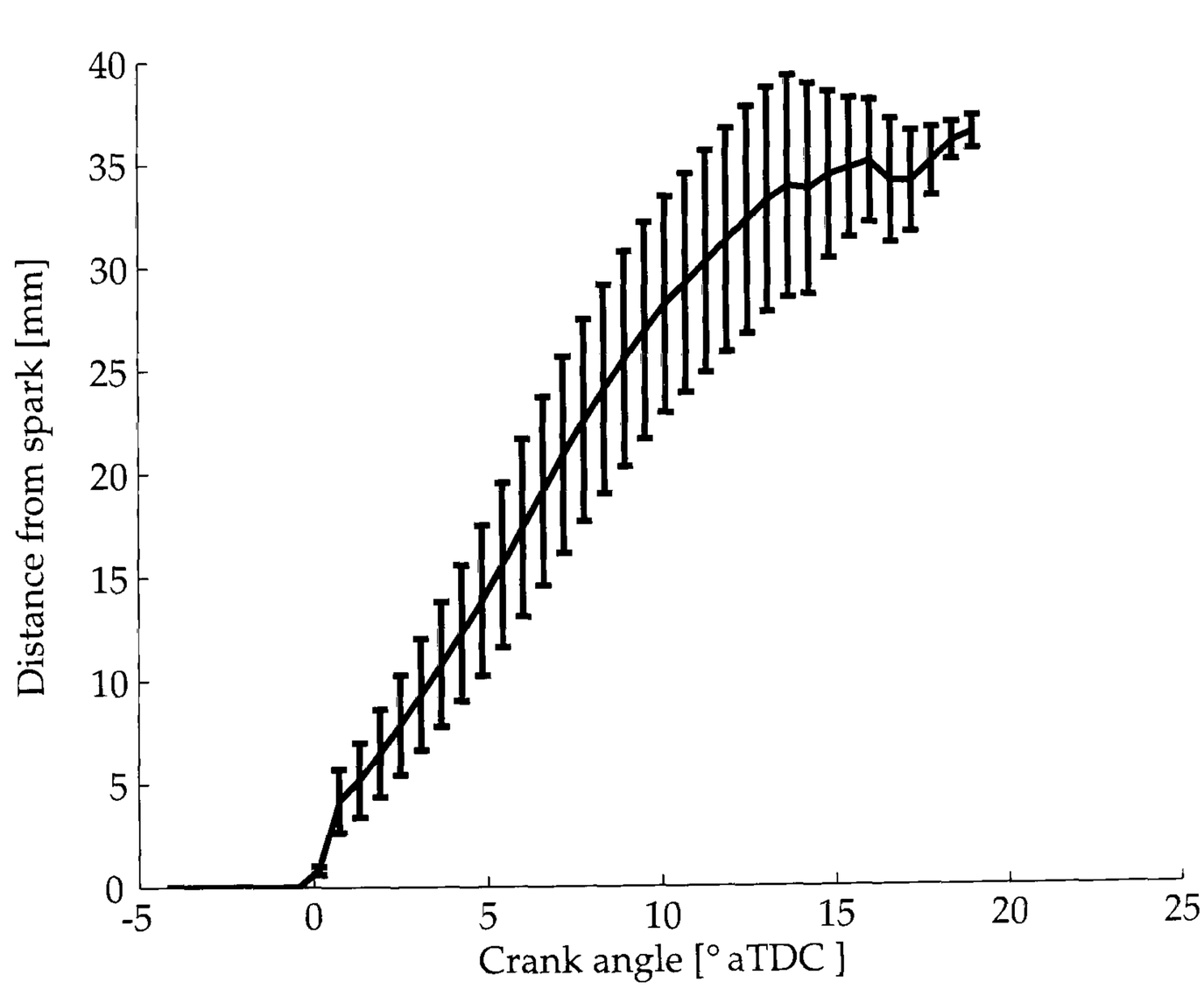

Figure 5.36: Area weighted mean and standard deviation of the distance from the spark gap to active surface elements at the 1000 rpm condition.

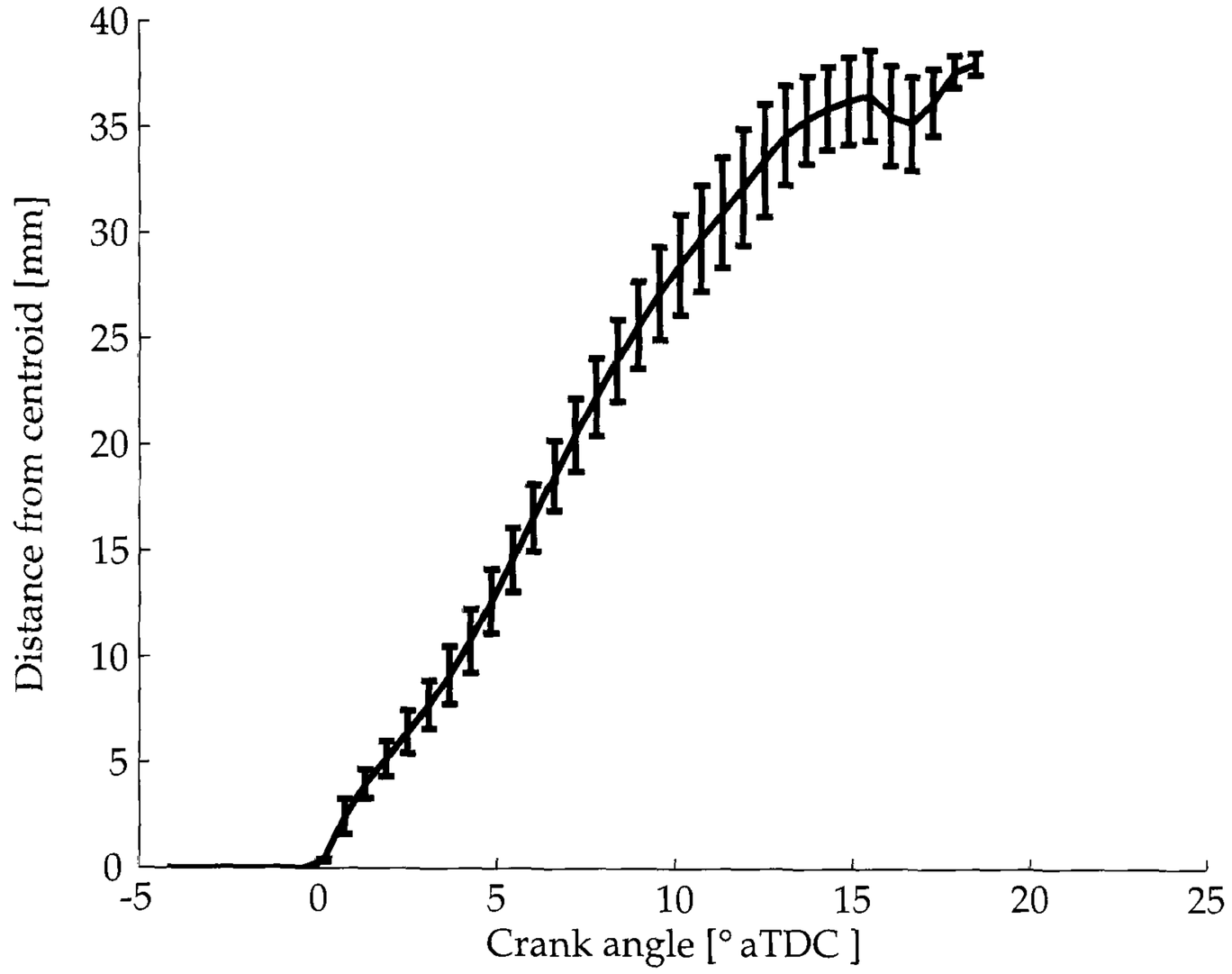

Figure 5.37: Area weighted mean and standard deviation of the distance from the flame barycentre to active surface elements at the 1000 rpm condition.

the surface areas calculated from the laser sheet images fall to zero whilst those computed by LUSIEDA continue to increase. The reasons for this discrepancy are discussed in detail in Section 5.4.7.

5.4 Combustion simulation

Ultimately, one of the main reasons for conducting experimental research into combustion is to provide data which may be used to evaluate and improve combustion models. As stated in Chapter 4, development of spark ignition engines using prototypes manufactured in small numbers is, and will remain in the future, expensive. Conversely, numerical simulations are (relatively) cheap and, if the historical downward trend in computing costs continues, will become cheaper in the future.

This section presents simulations of the LUPOE1-D and LUPOE2-P engines using the LUSIE software and the two and three-zone combustion model formulations. The section begins by describing the technique used to calibrate the blowby and combustion model constants to give good agreement with measured data. A study of the suitability of different laminar burning velocity expression

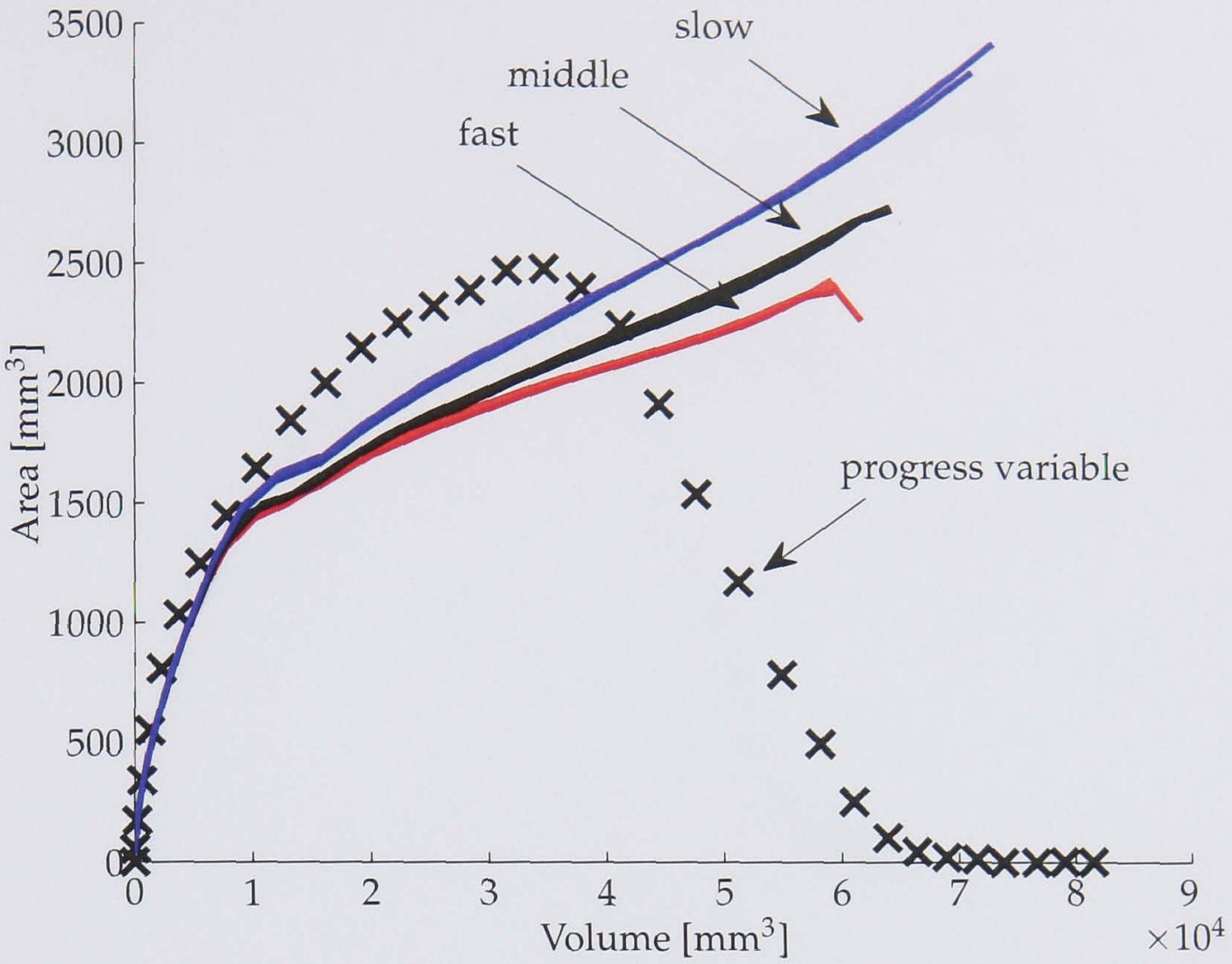

Figure 5.38: Flame active surface area plotted against flame volume derived from mean progress variable isosurfaces and LUSIEDA analysis of fast, middle and slow cycles at the 1500 rpm base condition.

for the simulation of spark ignition engine combustion is investigated by comparing predictions using the three-zone model with experimental data from the LUPOE1-D engine. Some error is present in all experimental observations. The sensitivity of the LUSIE code to small errors in input parameters which are difficult to measure accurately is explored. The predictive capability of the two-zone combustion model formulation has been greatly improved with the addition of a function which accounts for the deceleration of the flame as it approaches the cylinder walls, see Sections 4.5.9 and 5.3.5. The main source of inaccuracy in the model is now the prediction of the rate of flame acceleration. The performance, when simulating the LUPOE1-D engine, of several different flame acceleration models is assessed. Finally, the possibility of using the three-zone model formulation in a more typical pent geometry engine LUPOE2-P, as opposed to the disc chamber LUPOE1-D it has previously been tested against [Abdi Aghdam, 2003] is investigated.

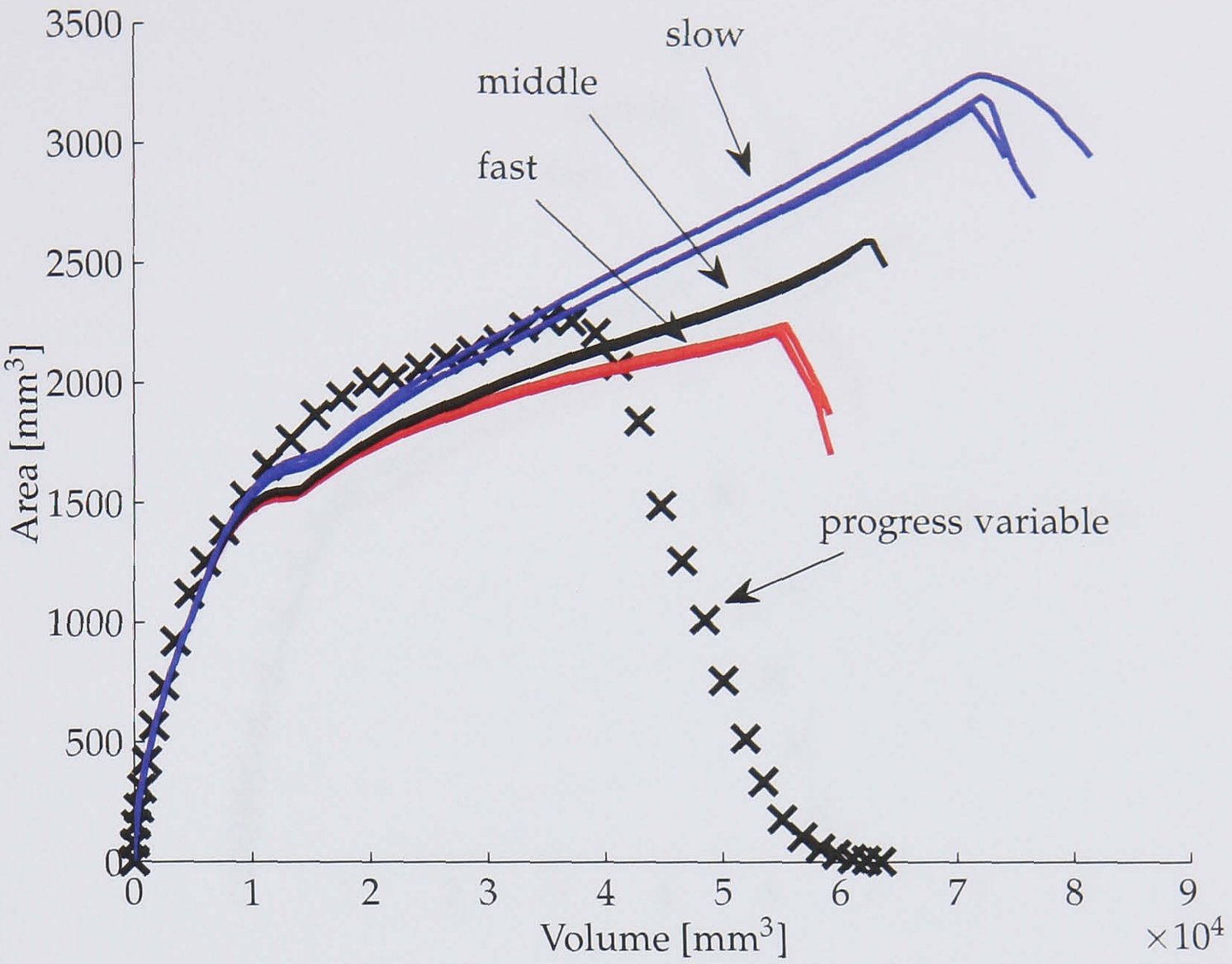

Figure 5.39: Flame active surface area plotted against flame volume derived from mean progress variable isosurfaces and LUSIEDA analysis of fast, middle, and slow, cycles at the 750 rpm condition.

5.4.1 Parameters common to all simulations

Previous studies [Abdi Aghdam, 2003, Lipatnikov and Chomiak, 2002] have identified the model proposed by Zimont [1979] as modified by Lipatnikov and Chomiak [1997] as a robust predictor of the turbulent burning velocity. This model (described in Section 4.5.7) is employed to predict values of the mass burning velocity u_{tr} and the entrainment burning velocity u_{te} for both two (u_{tr}) and three (u_{te}) zone combustion simulations. Values of the rms turbulent velocity used for simulations of LUPOE1 are taken from the measurements of Atashkari [1997] and Jakubík [2002]. For LUPOE2-P, comparable data recorded by Murad [2006] are used. The integral length scale L has not been measured in either engine. Abdi Aghdam [2003] assumed when simulating LUPOE1-D that L was equal to one fifth of the clearance height based on the results of Fraser and Bracco [1986, 1989] hence $C_L = 0.2$ (Equation 4.38). For the current study this assumption was left unchanged. For simulations of LUPOE2-P, L was assumed to decrease as the flame travelled into the "eaves" of the pent roof (Equation 4.39). Previous measurements of L reported by Fraser and Bracco [1989] (see also Sec-

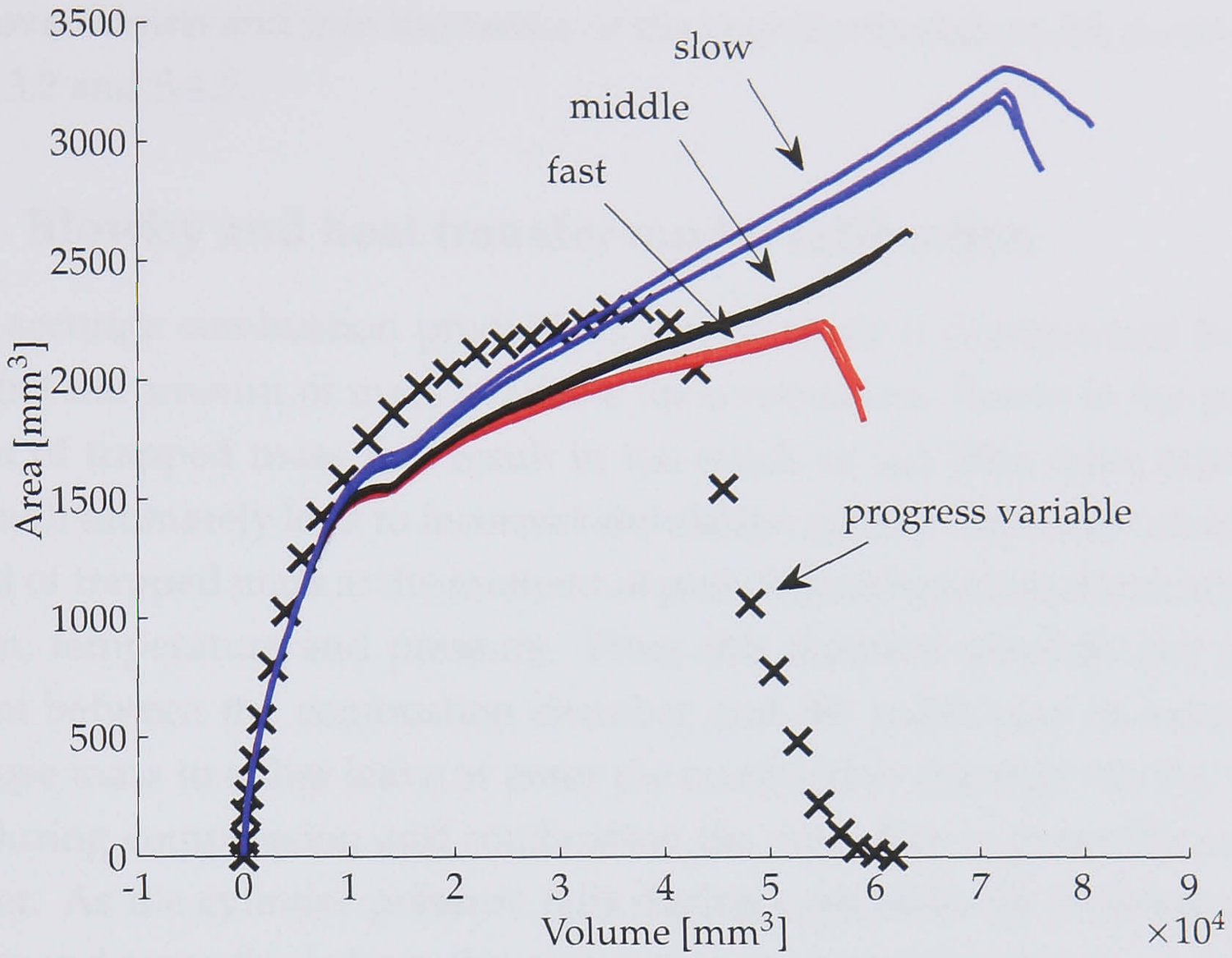

Figure 5.40: Flame active surface area plotted against flame volume derived from mean progress variable isosurfaces and LUSIEDA analysis of fast, middle and slow cycles at the 1000 rpm condition.

tion 4.5.14) showed that, whilst L is proportional to the clearance height within a cycle, changes to the compression ratio do not result in a corresponding change in L. For this reason C_L may be considered an adjustable parameter which changes from engine to engine in much the same way as the rms velocity scales approximately with mean piston speed, but with a constant of proportionality which is not universal. The constant C_L was changed to 0.15 when simulating LUPOE2-P to give a reasonable match to the measured pressure.

The temperature at the start of the cycle for all simulations of LUPOE2-P was reduced by 10° C from the set value because of the temperature drop caused by the evaporation of the fuel, see Section 5.2. As the LUPOE1 engine was decommissioned at the time of writing it was not possible to take measurements or make a similar adjustment to the intake temperature for simulations of this engine.

Combustion in all cases was initiated with a 2 mm diameter flame kernel 0.11 msec after the spark timing, with a suitable delay incorporated to allow for the response time of the ignition unit [Abdi Aghdam, 2003]. The location of the centre of the flame was positioned at the spark gap for LUPOE1-D. For simulations of LUPOE2-P, except where otherwise stated, the centre of the flame

was moved down and into the centre of the chamber based on the results of Sections 5.3.2 and 5.4.5.

5.4.2 Blowby and heat transfer model calibration

Before accurate combustion predictions can be made it is important to be able to predict the amount of mass available for combustion. Errors in the predicted amount of trapped mass will result in too much or too little mass being burnt which will ultimately lead to incorrect simulation results. The code calculates the amount of trapped mass at the moment of port closure based on the mixture composition, temperature and pressure. From this moment onwards any pressure gradient between the combustion chamber and the crank case or exhaust port will cause mass to either leave or enter the combustion chamber via the top land gap. During compression and combustion the mass flux is generally out of the chamber. As the cylinder pressure falls during expansion the pressure gradient reverses and mass flows from the piston ring pack crevices into the combustion chamber.

Although it is possible to measure the important dimensions of the ring pack accurately using a vernier micrometre it is difficult to account for changes in dimensions due to 1) thermal expansion, 2) movement of the rings within their grooves (flutter) or movement of the piston radially within the barrel and 3) imperfect sealing of the piston rings due either to ring flutter, taper, out of round or scratches to the cylinder bore. For this reason, a degree of "tuning" of the blowby model constants is always necessary to match the model motoring pressure to that recorded in the engine. In particular, it is necessary to change the volume of the top land crevice used by LUSIE to account for the crevices associated with pressure transducers, the spark plug, the crevice between the head and barrel, crevices around the quartz window housings, and any inaccuracy in the calculated value of the compression ration.[5]

In previous simulation work at Leeds involving LUSIE and LUPOE1 [Abdi Aghdam, 2003, Cairns, 2001] blowby model constants have been adjusted to provide a best fit to a single measured motoring trace. This method was initially used

[5]As the windows are seated on a thin layer of mastic it is likely that they displace outwards slightly close to TDC given the high pressure in the chamber. The surface area of the windows presented to the inside of the combustion chamber is large hence the clearance volume would change appreciably for even a small movement. Measurement of such movement, and the incorporation of a suitable submodel for it in the LUSIE code, was beyond the scope of the current study.

for LUPOE2-P but the constants determined using this technique resulted in an unrealistic over-prediction of the amount of mass lost from the chamber at firing pressures. The amount of mass expelled with these blowby constants was so large that the remaining mass was not sufficient to provide the pressure rise necessary to match the measured firing pressure.

Possible reasons for the disagreement between LUSIE and measured data were investigated. Taper in the bore was measured by resting a new piston ring on the (flat) piston crown, ensuring the ring was normal to the bore axis, with the piston at a known position between top and bottom dead centre. The piston ring gap could then be measured with a set of feeler gauges. The maximum variation in bore circumference in the region between EPC and TDC was 0.05 mm which was considered insignificant. It was discovered however that there were differences between the designed dimensions and the dimensions of the manufactured engine which were sufficient to lower the effective compression ratio significantly. This partially explains the poor performance of the blowby model; constants which were fitted to a motoring trace using a higher compression ratio in the model than the actual engine would naturally have a top land crevice volume and ring gaps which were too large in order to produce a model peak pressure which matched the experimentally observed peak pressure.

Subsequent investigations revealed that blowby model constants determined by fitting the model to just one motoring trace with a peak pressure around 20 bar did not accurately characterise the performance of the ring pack at the much higher firing pressures ($\sim$ 50 bar) of LUPOE2-P. The LUPOE1-D engine had a motoring peak pressure of $\sim$ 10 bar and a peak firing pressure of $\sim$ 30 bar. The difference in peak pressure between motoring and firing cycles is much lower for this engine.

In order to characterise the performance of the LUOPE2 ring pack at firing pressures the engine was fitted with a ball valve (hereafter referred to as a restriction so as not to confuse with ports/valves on an engine) downstream of the exhaust port which could be used to restrict the flow of air out of the engine. As the intake air is supplied from the laboratory compressed air supply, suitable adjustment of both the intake air supply pressure (at the regulator on the tower), and the exhaust restriction, enabled motoring cycles to be recorded with peak pressures up to the firing peak pressure. These motoring tests were performed at 750, 1000 and 1500 rpm with no fuel (in order to reduce any potential inaccuracy in fuel metering) and with the intake air and head/barrel temperature set to the

standard temperature of 55° C. Further experiments were conducted with the engine stationary in an attempt to calculate the discharge coefficient for the piston ring gaps. It was found that the static performance of the ring pack was much worse than the dynamic performance. This is probably because 1) the pressure gradient applied was not sufficient to force the rings down onto their seats and 2) the small amount of oil in the ring grooves and on the bore walls which aid sealing will have been blown out and not replenished with the engine stationary. For these reasons the results of this test were discarded.

A GT-Power model of the piston ring pack was used to calibrate the LUPOE2-P blowby model. The ring pack model was built in GT-Power using the same volume and orifice assumptions as used in LUSIE, see Section 4.2.7 and Abdi Aghdam [2003], and included provisions for the covering and uncovering of the exhaust port by the ring pack. GT-Power and the LUSIE blowby model both have their foundations in one dimensional gas dynamics hence parameters used in one code are readily interchangeable with the other. This assumption has been verified previously, see Figures 4.29 and 4.30. The Design of Experiments (DoE) feature of GT-Power was used to run a matrix of different simulations each with a different ring pack geometry and inlet pressure. The results of the simulations were then fitted to a hyper-surface with one dimension for every model parameter varied. Best fit constants to the experimental data for all recorded intake pressures at a given engine speed were then selected using a genetic algorithm to find the point on the surface which best fit the experimental data. Experimental motoring tests for a variety of intake pressures and engine speeds along with LUSIE simulated pressures using the model constants determined with GT-Power are shown in Figures 5.41, 5.42 and 5.43.

When determining blowby model constants the top land crevice volume was constrained to the same value for all engine speeds. The volumes of the inter-ring crevices was set to their measured values and the ring gap orifice areas allowed to vary with engine speed. Variations in the ring gap orifice areas are justified because at different engine speeds: the torsion on the rings is different; the rings will lift at different points in the cycle; the piston will move on a different axial path in the bore (piston slap or wobble); and the rings will have a different propensity to flutter[6] [Tian, 2002a,b]. For all engine speeds the ring gap orifice areas found were within the limits where 1) the rings seal perfectly, the only flow is

[6]The author is indebted to Dr Richard Chittenden of the Tribology group in the School of Mechanical Engineering, University of Leeds for informative discussions on the performance of piston rings.

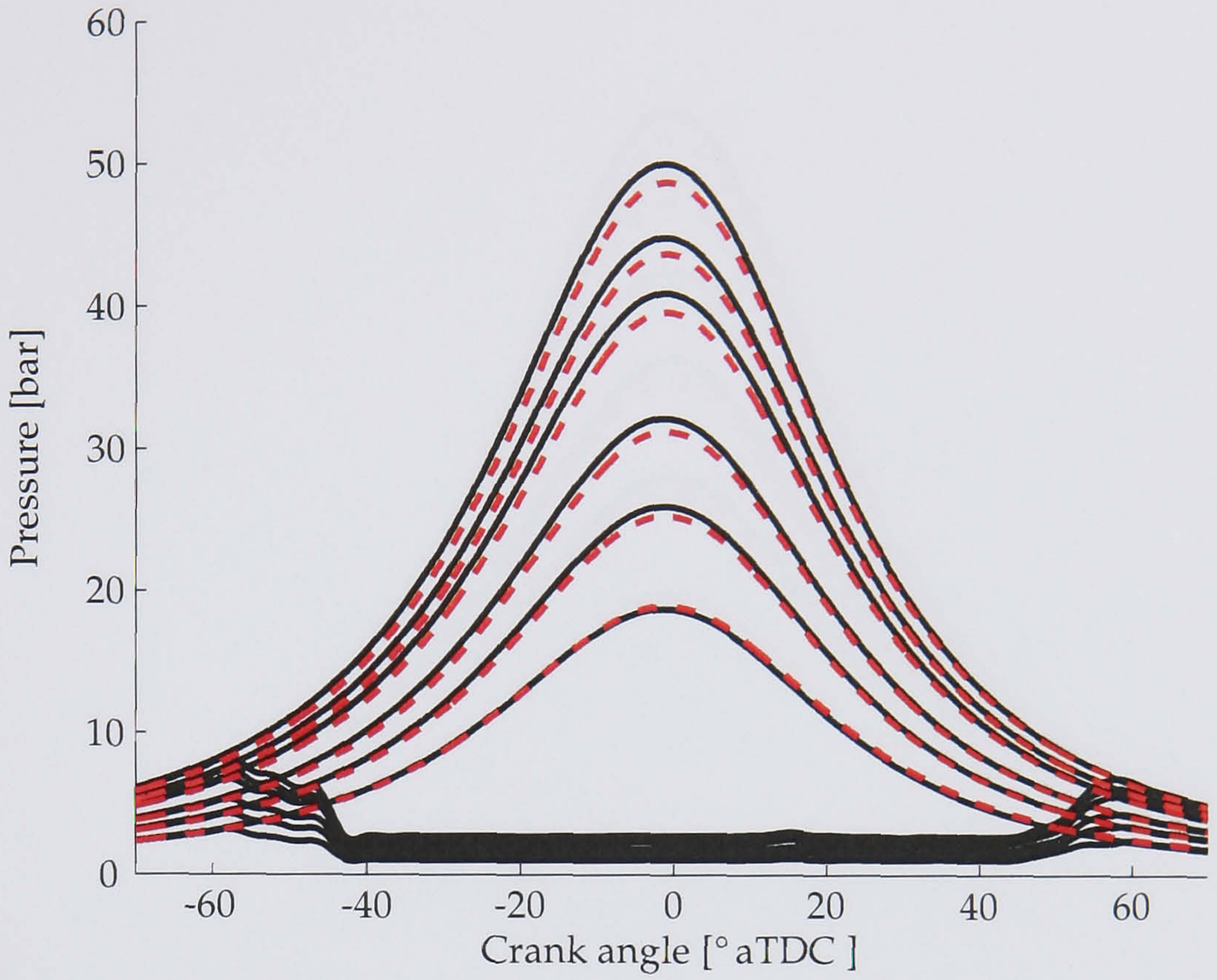

Figure 5.41: Experimental (black) and LUSIE calculated (red) motoring pressure traces for the LUPOE2-P engine at 750 rpm with different intake pressures. The bottom pressure trace is the signal recorded by the absolute pressure transducer.

through the ring gap and 2) the rings are lifted and gas can flow both through the ring gap and behind the ring. To improve the blowby model such that it properly encapsulates ring lift, flutter and other phenomena, a more detailed model of the ring pack is required such as that proposed by Namazian and Heywood [1982].

The LUSIE software includes the heat transfer models proposed by Annand [1963] and Woschni [1967]. For the currently reported simulations, the model of Woschni was employed with the heat flux predicted by the standard Woschni heat transfer model multiplied by 1.25. This value is recommended in the GT-Power literature [Gam, 2004] and has been found by colleagues at Mahle Powertrain to describe well the rate of heat transfer in typical engines. It may be argued that LUPOE2 is anything but a typical engine; given the lack of reliable data either way this value was used for the want of a better alternative. Further, it is likely that the value of the heat transfer model "constant" varies for different engine conditions [Guezennec and Hamama, 1999]. Again, given the lack of heat transfer data available for LUPOE2 it is not possible to account for this.

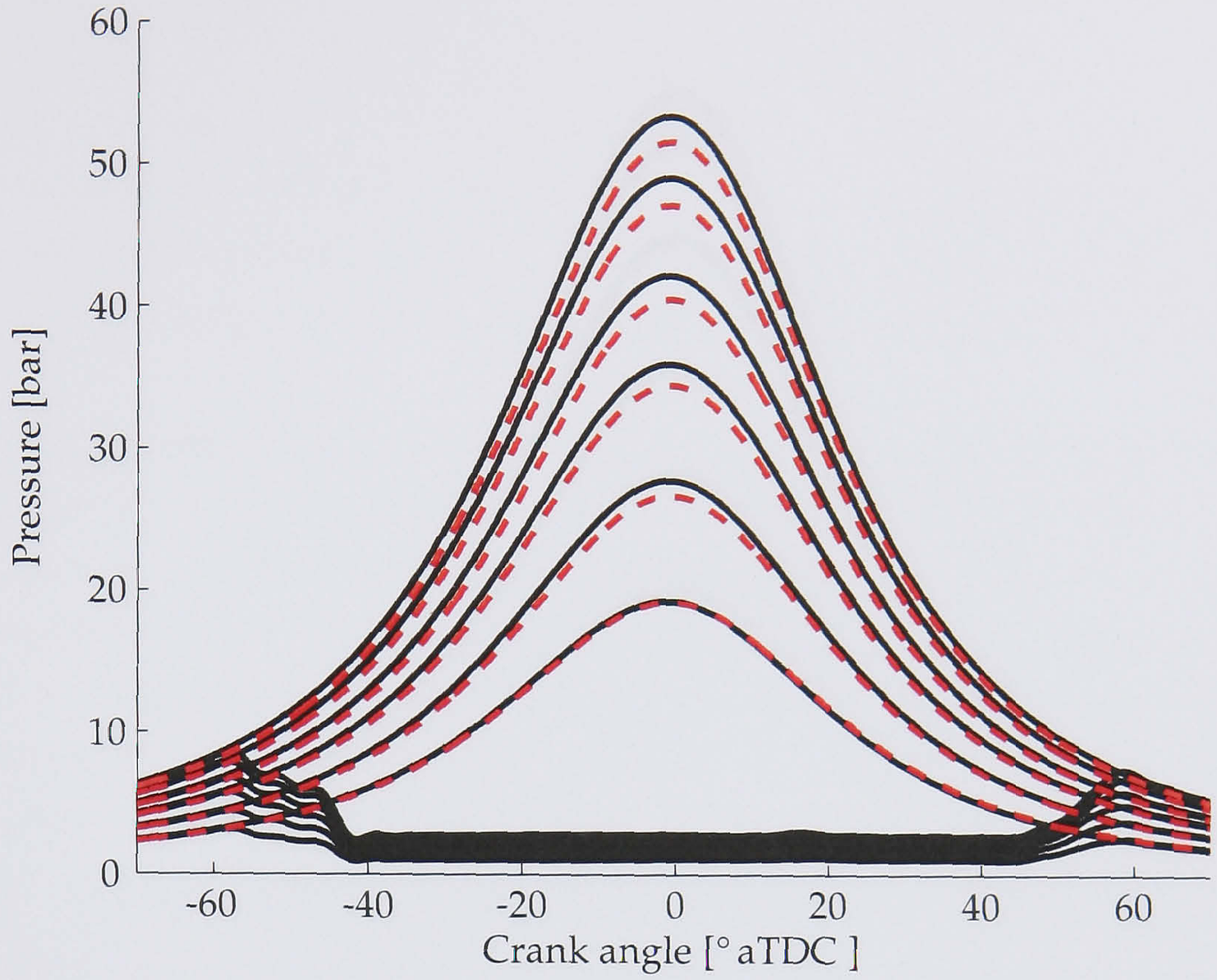

Figure 5.42: Experimental (black) and LUSIE calculated (red) motoring pressure traces for the LUPOE2-P engine at 1000 rpm with different intake pressures. The bottom pressure trace is the signal recorded by the absolute pressure transducer.

5.4.3 Combustion model calibration

Accurate model predictions from LUSIE require as a prerequisite the correct determination of the combustion model constant(s). In the case of the two-zone model there is only one constant to adjust, A (see Equation 4.17), whose value may be found by successive approximation. For the three-zone model there are two constants to adjust, A and C_{τ_b} (see Equation 4.5). Determining the correct values for the constants in this case is more difficult as there are many combinations of A and C_{τ_b} which give similar model predictions.

To overcome this difficulty, a full factorial design of experiments technique was used. A matrix of LUSIE simulations was run covering all the possible values of A and C_{τ_b} within a sensible range. The goodness of fit of each of these simulations with experimental pressure and flame radius data were then evaluated using Matlab to automate the post processing. For the purpose of finding the model constants, pressure and entrainment flame radius data from middle cycles at the base condition on the LUOPO1-D engine [Abdi Aghdam, 2003] was used as reference experimental data. This data set was selected as 1) the combustion

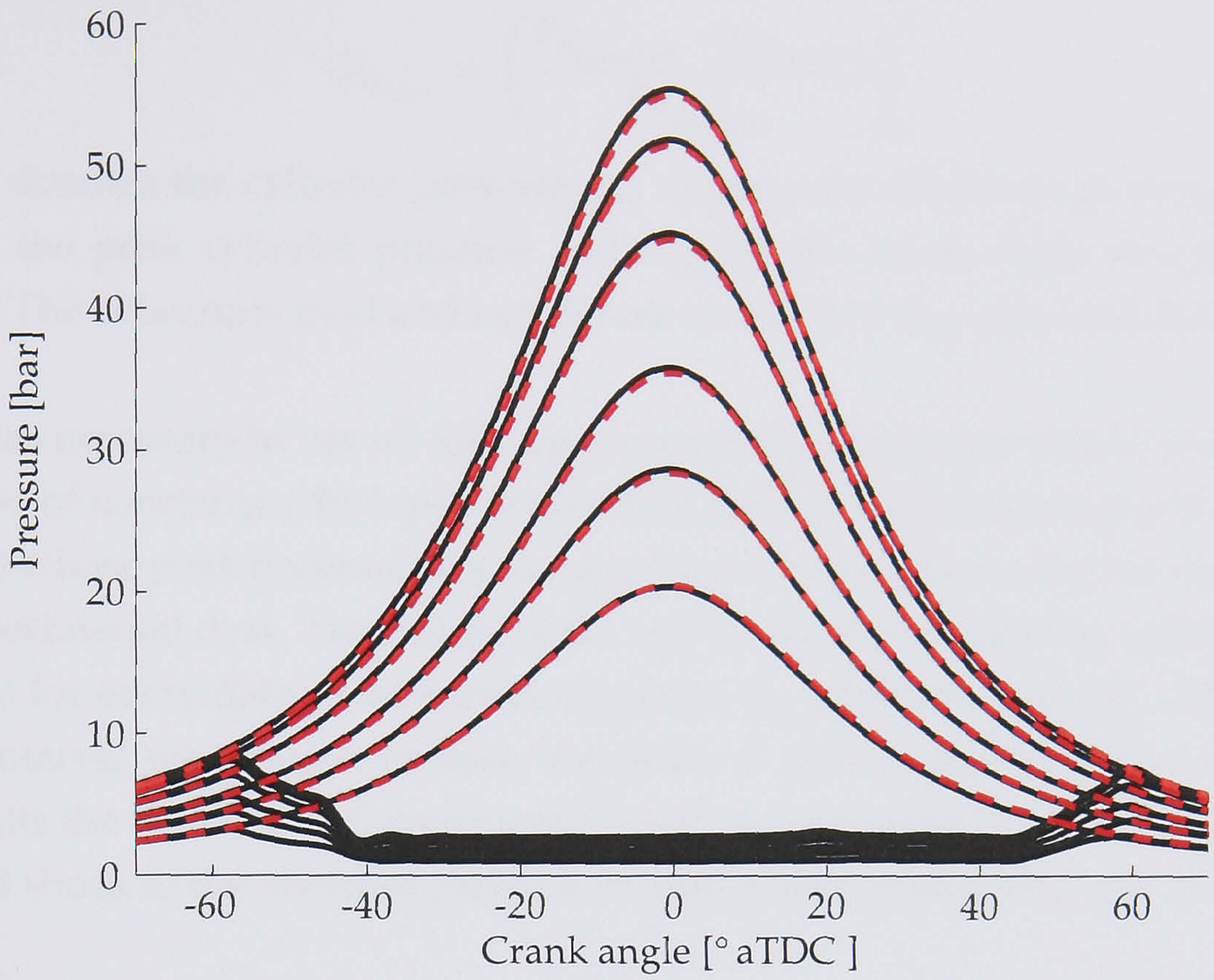

Figure 5.43: Experimental (black) and LUSIE calculated (red) motoring pressure traces for the LUPOE2-P engine at 1500 rpm with different intake pressures. The bottom pressure trace is the signal recorded by the absolute pressure transducer.

chamber has a disc geometry with a quiescent flow hence the flame is likely to be close to spherical, one of LUSIE's assumptions and 2) two independent variables, for example pressure and *entrainment* flame radius (rather than burnt radius) are required to ensure the system of equations is consistent. The goodness of fit G of the model data for a particular combination of constants to the reference data was determined in the least squares sense according to the following equation

$$G = G_P + G_r + G_{P_{\max}} + G_{\theta_{P_{\max}}} \tag{5.11}$$

where

$$G_P = \sum_{\theta=\theta_{\mathrm{sp}}}^{\theta_{P_{\max}}} \left(\frac{P_{\mathrm{exp}}(\theta) - P_{\mathrm{mod}}(\theta)}{P_{\mathrm{exp}}(\theta)} \right)^2 \tag{5.12}$$

$$G_r = \sum_{\theta=\theta_{\mathrm{sp}}}^{\theta_{P_{\max}}} \left(\frac{r_{fe,\mathrm{exp}}(\theta) - r_{fe,\mathrm{mod}}(\theta)}{r_{fe,\mathrm{exp}}(\theta)} \right)^2 \tag{5.13}$$

$$G_{P_{\max}} = \left(\frac{P_{\max,\mathrm{exp}} - P_{\max,\mathrm{mod}}}{P_{\max,\mathrm{exp}}} \right)^2 \tag{5.14}$$

$$G_{\theta_{P_{max}}} = \left(\frac{\theta_{P_{max,mod}} - \theta_{P_{max,exp}}}{\theta_{P_{max,mod}}} \right)^2 \tag{5.15}$$

Here P denotes the cylinder pressure, r_{fe} denotes the entrainment flame radius, P_{max} is the peak cylinder pressure and $\theta_{P_{max}}$ is the crank angle at which P_{max} occurs. The subscripts mod and exp denote model and experimental data respectively.

It was necessary to use all four measures of the goodness of fit to prevent the selection of constants which performed well during the initial stages of combustion but whose peak pressure and crank angle at peak pressure did not match well the experimental data. The values of G_P and G_r were calculated by summing the residual for every data point between ignition θ_{sp} and peak pressure. This crank angle interval was chosen because the point of peak pressure occurs when the flame hits the bore walls. Experimental pressure data were typically distorted by thermal shock to the pressure transducer after peak pressure [Kuratle and Marki, 1992].

An example of the change in G with different values of A and C_{τ_b} is shown in Figure 5.44. The G surface forms a valley along which different combinations of A and C_{τ_b} give very similar model predictions for a given engine condition. The optimum model constants were selected as those which gave the lowest value of G when compared with the LUPOE1-D reference condition experimental data. Once constants for a particular model configuration were determined they were left unchanged for all simulations using that model, regardless of the engine or operating condition.

5.4.4 Laminar burning velocity model calibration

The laminar burning velocity u_l is a physico-chemical parameter which encapsulates the reaction rate of a mixture with a given temperature, pressure and composition [Gillespie et al., 2000]. The difficulty of measuring u_l at the temperatures and pressures commonly encountered in engines, where laminar flames have a propensity to become unstable, are well known and have been discussed in Section 4.5.5. The predictions of LUSIE simulations are very sensitive to changes in u_l as shown in Section 5.4.5. Traditionally, LUSIE has used the Metghalchi and Keck [1982] laminar burning velocity correlations. The suitability of alternative u_l expressions, described in Section 4.5.5, for engine simulations was investigated by running tests for different engine conditions and comparing the re-

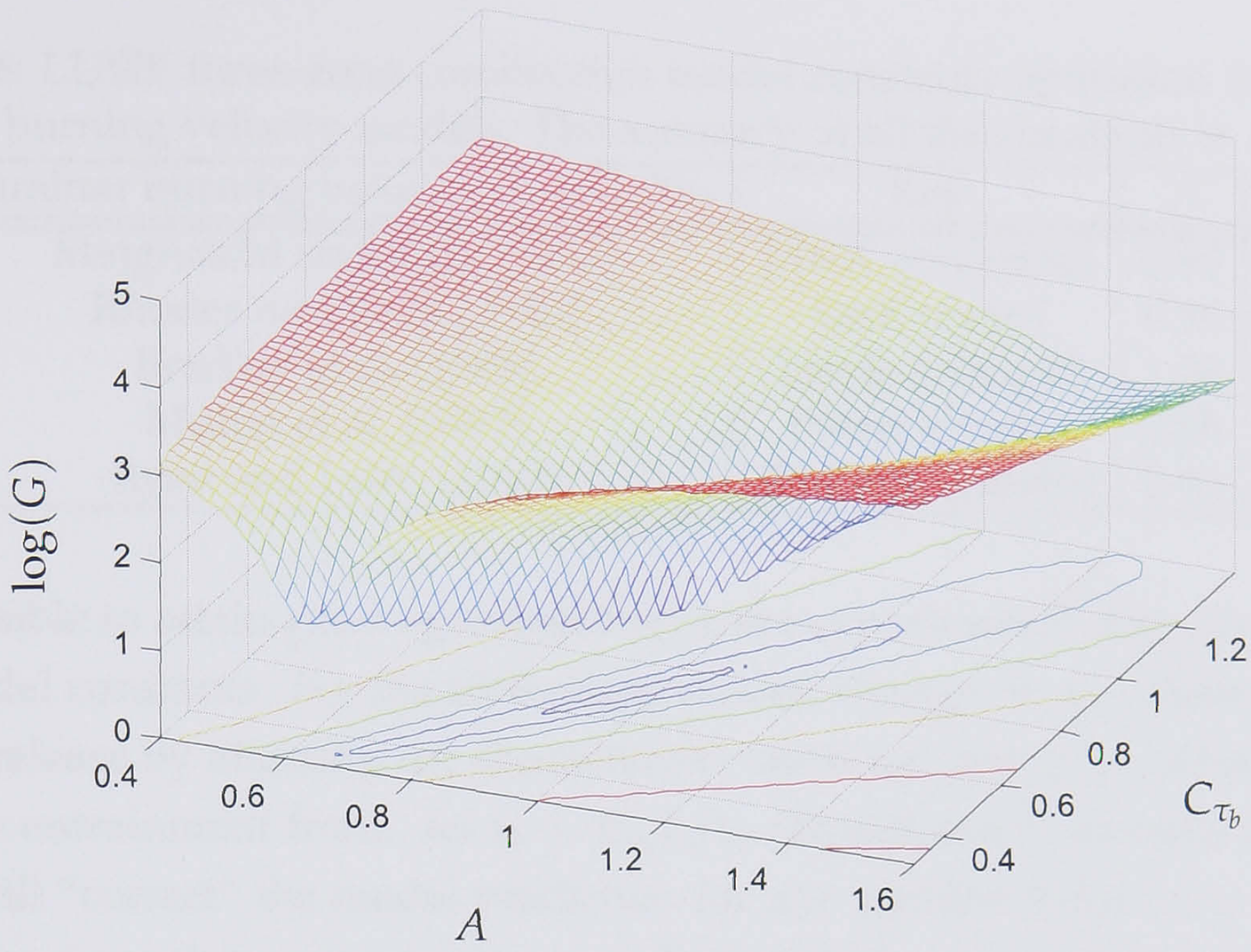

Figure 5.44: Surface showing the variation in G for different values of the combustion model constants A and C_{τ_b}.

sults with experimental data. For this purpose data recorded on the LUPOE1-D engine [Abdi Aghdam, 2003] was used as it includes both pressure and entrainment flame radius data for a wide range of conditions. The combustion chamber of LUPOE1-D has a disc geometry with a quiescent flow close to TDC [Atashkari, 1997, Jakubík, 2002]. Simulations of this engine can therefore be readily compared with experimental data as the flame geometry in both cases is close to a truncated sphere. Only the three-zone model formulation was tested as this model is more sensitive to changes in u_l than the two-zone model, see Section 5.4.5.

Combustion model constants for each of the laminar burning velocity expressions given in Secion 4.5.5 were determined using the least-squares method described in Secion 5.4.3. The correlations to the data recorded by Ormsby and Al-Shahrany were excluded from the study as they are very similar to the previously published Leeds iso-octane correlation [Bradley et al., 1998] as shown in Figure 4.16. Table 5.6 lists the model constants found for the different u_l expressions.

The curves illustrated in Figures 5.45 and 5.46 compare the model predicted pressure, entrainment front radius and laminar burning velocity with selected middle experimental cycles at the base condition for each of the u_l models. Despite the substantially different values of u_l predicted by the different expressions

Table 5.6: LUSIE three-zone combustion model constants optimised for different laminar burning velocity models. The accuracy of all the constants is ±0.1.

Laminar burning velocity correlation	Key	A	C_{τ_b}
Metghalchi and Keck [1982]	M&K (magenta)	0.94	0.62
Rhodes and Keck [1985]	R&K (cyan)	0.96	0.54
Bradley et al. [1998]	Leeds (orange)	1.26	0.20
Muller et al. [1997]	Peters (green)	0.98	0.44
Ryan and Lestz [1980]	R&L (burgundy)	0.90	1.04

it is possible to attain good agreement with the experimental data given the correct model constants. For the three-zone model, changes to u_l influence the rate of heat release by affecting the characteristic burn-up time τ_b of unburnt gas behind the entrainment front. As $\tau_b = C_{\tau_b} L/u_l$ (Equation 4.5) suitable adjustment of C_{τ_b} will "correct" the model prediction for any sensible value of u_l used. This is obvious from the constants shown in Table 5.6; the correlations which predict the extremum values of u_l, Ryan and Lestz [1980] and Bradley et al. [1998], have the largest and smallest values of C_{τ_b}.

Simulations where the engine speed was varied (not shown here) did not produce a significant difference in the model output when comparing the different u_l models. This is because, for the skip-fired LUPOE1-D engine, u_l is a function solely of temperature, pressure and equivalence ratio ϕ. In order to elucidate any difference between the u_l models the engine must therefore move into a different temperature, pressure or ϕ regime: a change in engine speed is not sufficient to do this.

Fuel lean simulations ($\phi = 0.8$), compared with experimental middle cycles, are depicted in Figure 5.47. The simulation results show that for a change in equivalence ratio of this magnitude there is little difference between the different u_l correlations.[7] In all cases, the pressure rise is advanced and the predicted peak pressure slightly too low. The entrainment front radius is significantly over predicted, the simulations of Abdi Aghdam [2003] show a similar deficiency. It is possible that either the camera was poorly synchronised or, with the lean mixture, the luminosity of the flame was insufficient to properly determine the flame radius.

The results of simulations at an increased compression ratio of 10.2 are compared with experimental middle cycles in Figure 5.48. Under these conditions

[7]The correlation of Ryan and Lestz is not available at this equivalence ratio and is therefore excluded from the comparison.

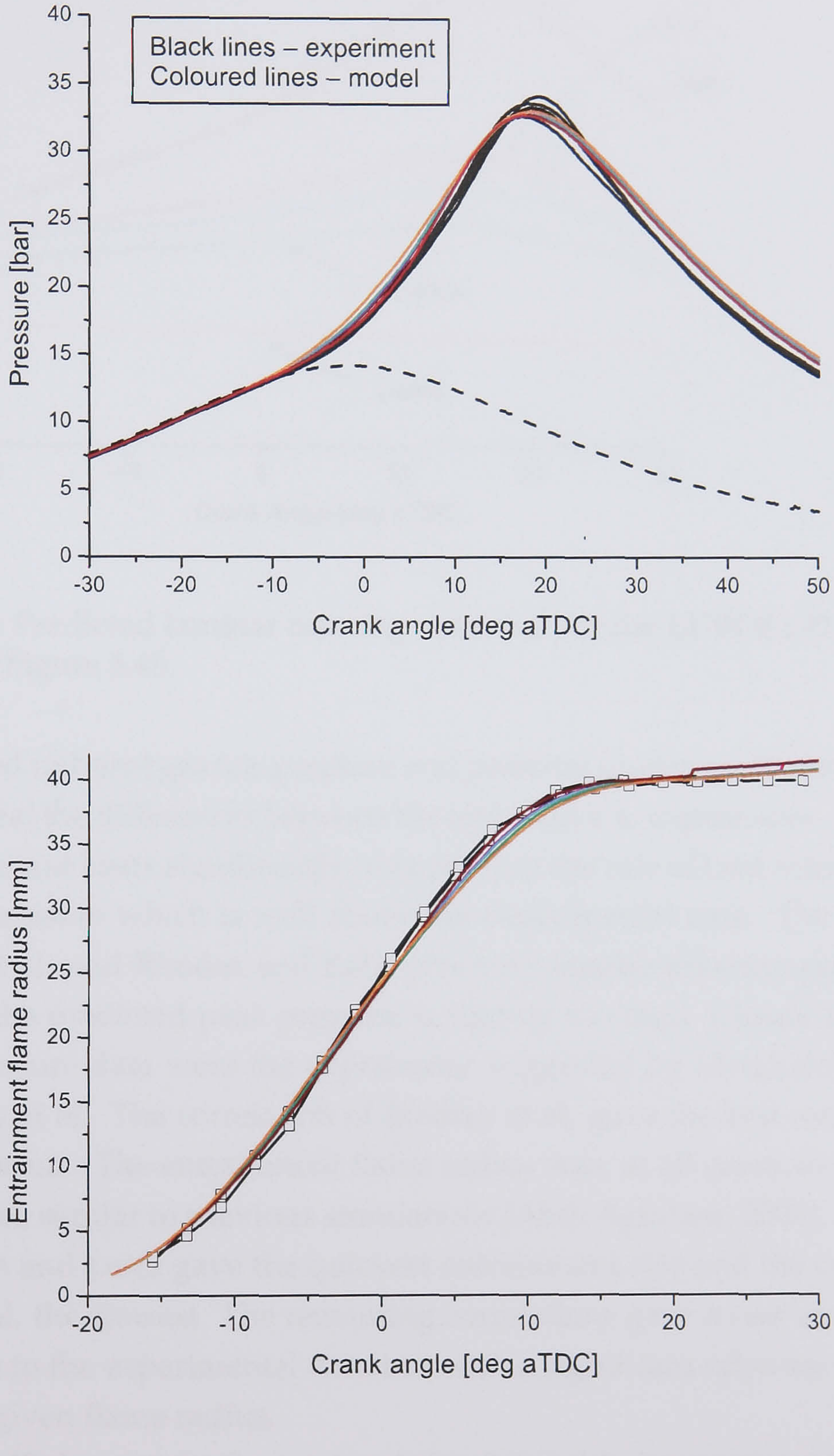

Figure 5.45: Predicted (coloured lines) and experimental (black lines) pressure (top) and entrainment flame radius (bottom) for LUPOE1-D using different laminar burning velocity expressions at the base condition. The key to the coloured lines is given in Table 5.6.

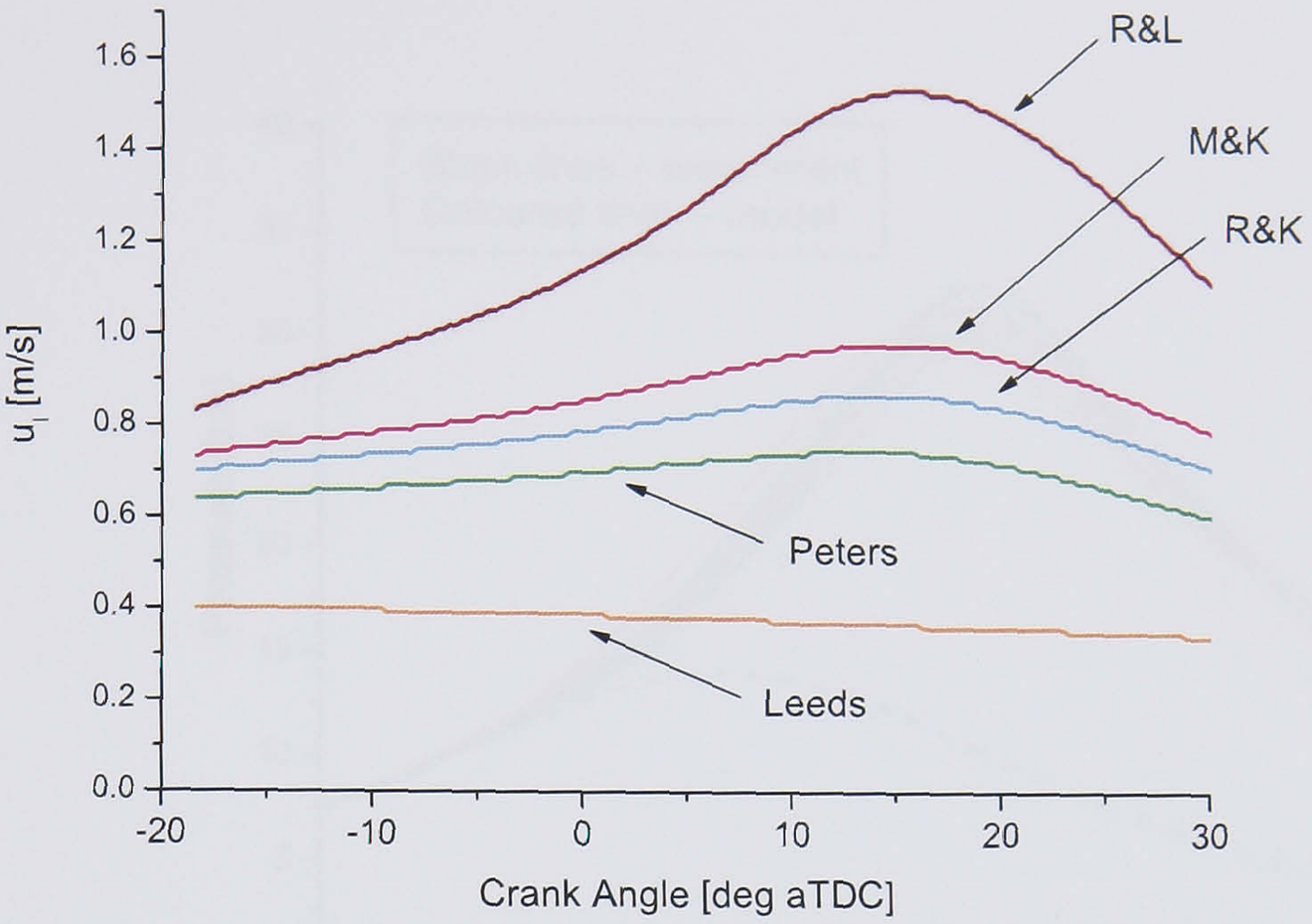

Figure 5.46: Predicted laminar burning velocities for the LUPOE1-D simulations depicted in Figure 5.45.

the increased unburnt gas temperature and pressure during combustion are sufficient to reveal the differences between the alternative u_l expressions. The correlation of Ryan and Lestz significantly over predicts the rate of heat release resulting in a peak pressure which is well above the experimental data. The expressions of Muller et al. and Rhodes and Keck give very similar pressure predictions, in both cases the predicted peak pressure is slightly too high. Closest to the experimental pressure data were the expressions suggested by Metghalchi and Keck and Bradley et al.. The correlation of Bradley et al. gave the best match in terms of peak pressure. The entrainment flame radius was, in all cases, over predicted by the model, similar to previous simulations [Abdi Aghdam, 2003]. The correlation of Ryan and Lestz gave the quickest entrainment rate and the correlation of Bradley et al. the slowest. The remaining correlations gave a rate of entrainment comparable to the experimental data but with a significant advance in the crank angle for a given flame radius.

Figure 5.49 shows experimental and simulated data for a compression ratio of 12.4.[8] At this compression ratio the differences between the u_l models are much

[8]It was previously found that the pressure transducer may have developed a fault during testing at this compression ratio. For this reason the experimental pressures should be considered suspect, however the flame radii should be correct. See Abdi Aghdam [2003] for a complete description of the problems with the pressure transducer.

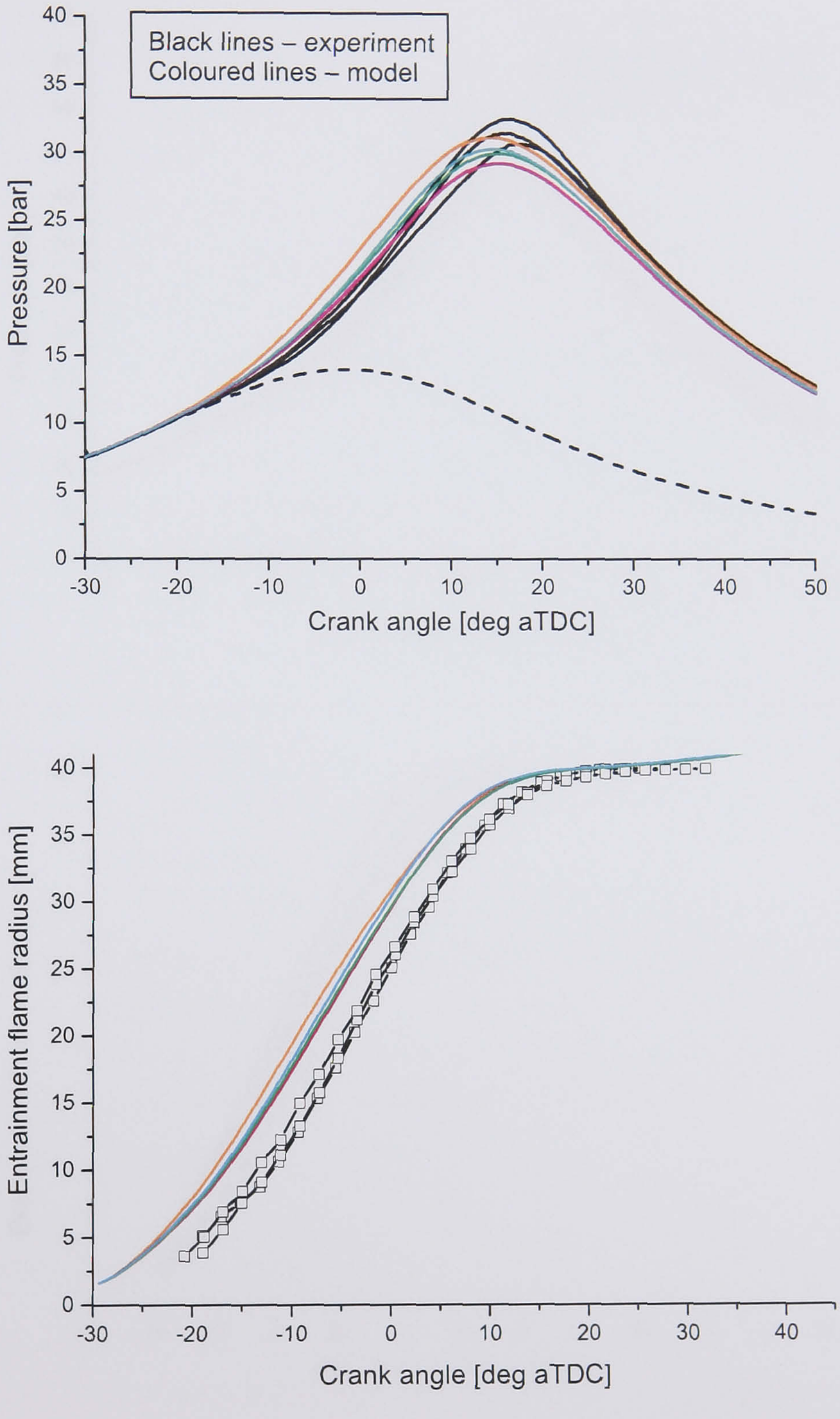

Figure 5.47: Predicted (coloured lines) and experimental (black lines) pressure (top) and entrainment flame radius (bottom) for LUPOE1-D using different laminar burning velocity expressions at the 1500 rpm $\phi = 0.8$ condition. The key to the coloured lines is given in Table 5.6.

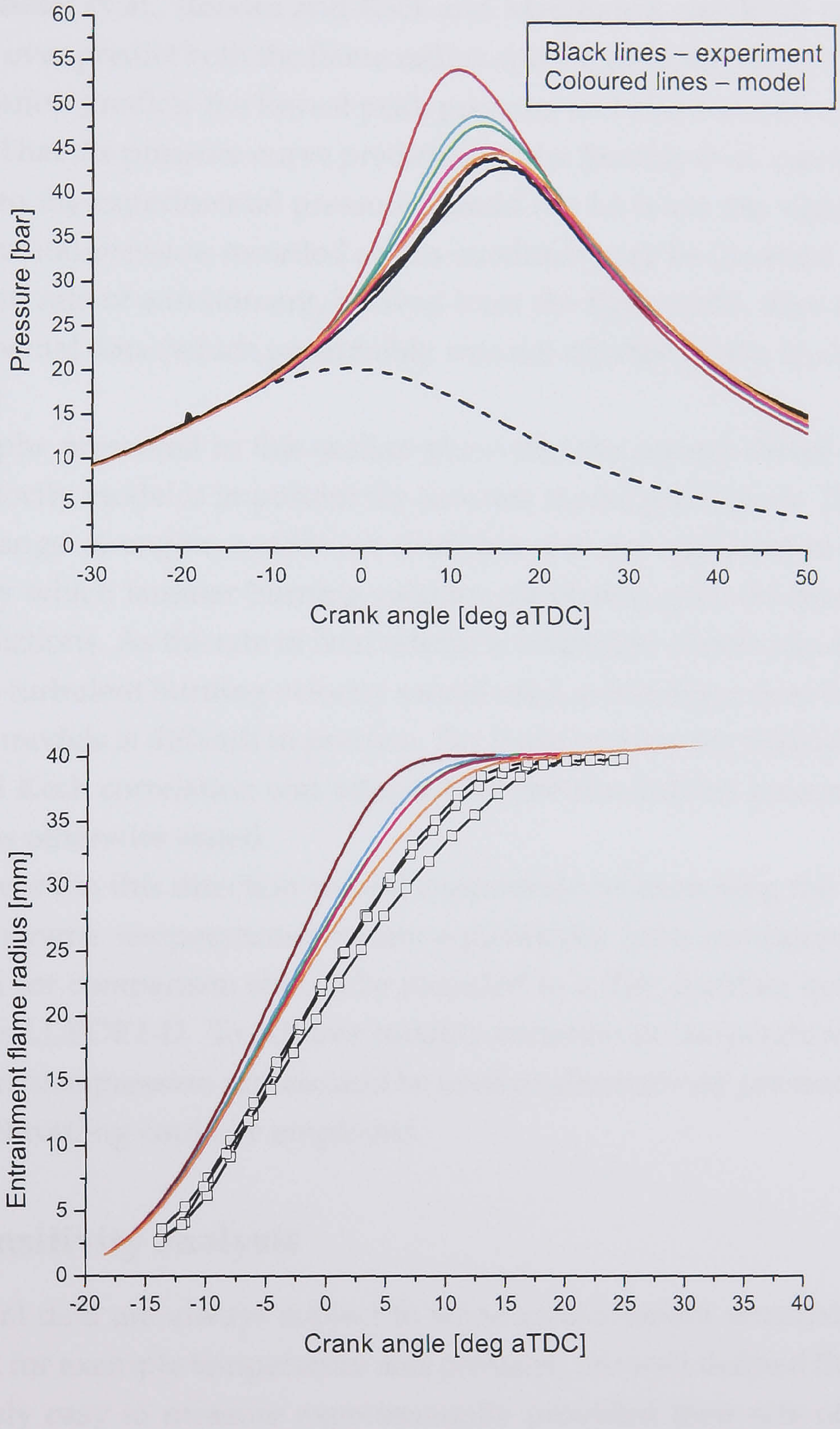

Figure 5.48: Predicted (coloured lines) and experimental (black lines) pressure (top) and entrainment flame radius (bottom) for LUPOE1-D using different laminar burning velocity expressions at 1500 rpm with a compression ratio of 10.2. The key to the coloured lines is given in Table 5.6.

more apparent. The Ryan and Lestz correlation does not give good predictions either for pressure or flame radius. Of the other correlations, the expressions proposed by Muller et al., Rhodes and Keck and Metghalchi and Keck fall close together, and over predict both the flame radius and the peak pressure. The Bradley et al. correlation predicts the lowest peak pressure and also the lowest rate of entrainment. That the pressure curve predicted by the Bradley et al. correlation falls the closest to the experimental pressure should not be taken too significantly as the experimental pressure recorded at this condition may be incorrect. However, the predicted rate of entrainment, derived from the flame radii, does match well the experimental data (which presumably was not affected by the faulty pressure transducer).

The graphs presented in this section show that the correct choice of laminar burning velocity model is important for accurate model predictions. Disappointingly, the range of engine conditions available was not sufficient to determine conclusively which laminar burning velocity correlation gave the most accurate model predictions. As the rate of heat release is a function of not only the laminar but also the turbulent burning velocity model used, achieving a clear comparison between u_l models is difficult in practice. For these reasons the widely used Metghalchi and Keck correlation was adopted for the simulations presented in this thesis unless otherwise stated.

Future work in this direction should concentrate on exercising the model under more extreme temperature-pressure-equivalence ratio conditions. Experimental data for comparison should be recorded in a disc chamber quiescent engine such as LUPOE1-D. To achieve suitable variation in temperature and pressure different compression ratios could be used or alternatively pressure charging and intake throttling could be employed.

5.4.5 Sensitivity analysis

Experimental data are always subject to some measurement uncertainty. Some parameters, for example temperature and pressure, are well defined theoretically and relatively easy to measure experimentally provided their rate of change is not too large. Other parameters, for example the laminar burning velocity, the integral length scale of turbulence or the rms turbulent velocity, are difficult to measure experimentally under engine conditions. In the case of turbulence parameters a consensus on how they can be measured, or even how they should be

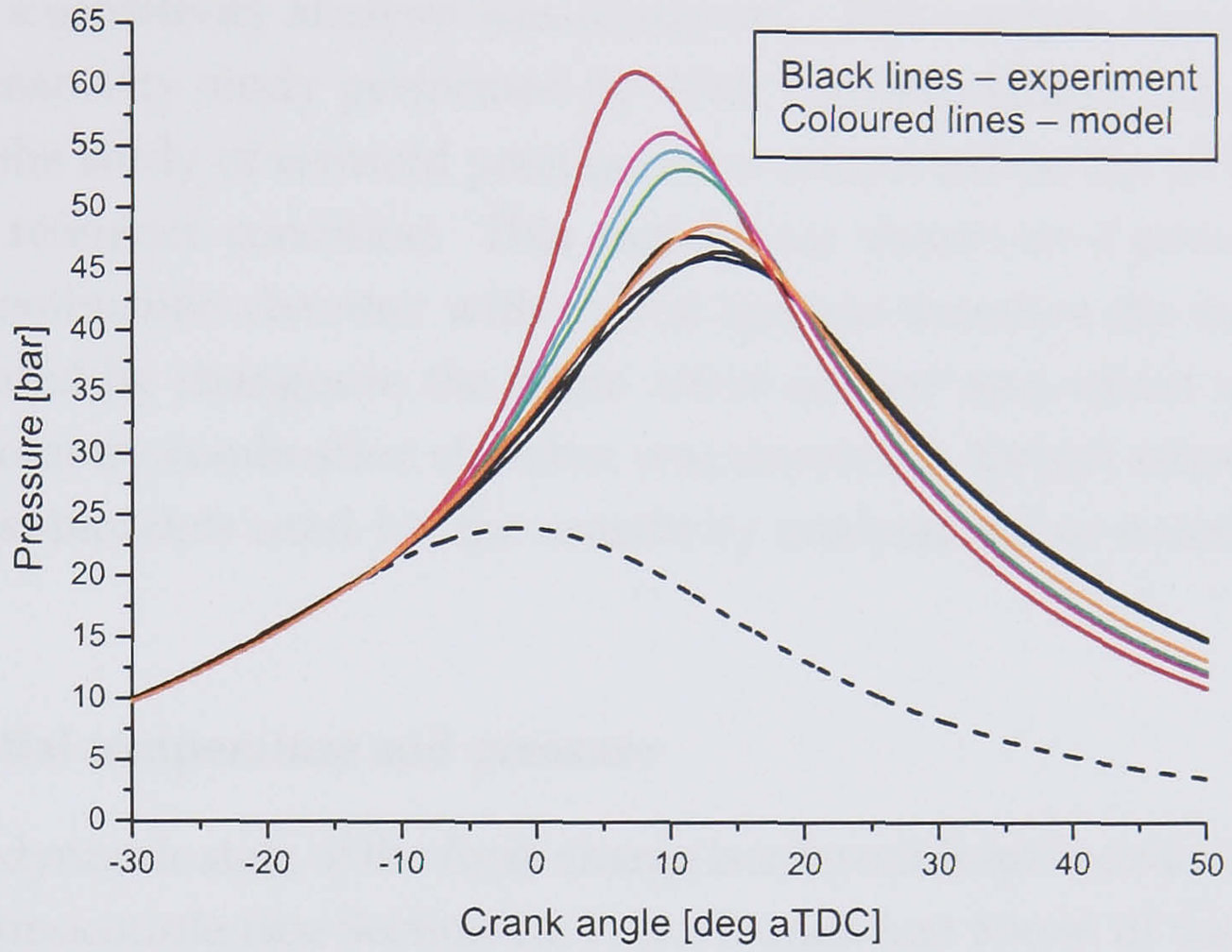

Figure 5.49: Predicted (coloured lines) and experimental (black lines) pressure (top) and entrainment flame radius (bottom) for LUPOE1-D using different laminar burning velocity expressions at 1500 rpm with a compression ratio of 12.4. The key to the coloured lines is given in Table 5.6.

defined, has yet to be reached for the case of an engine.

To investigate the sensitivity of the LUSIE code to small changes in the input parameters a sensitivity analysis was conducted. This analysis compliments the previous sensitivity study performed by Abdi Aghdam [2003]. All simulations apart from the study of centroid position were conducted on the LUPOE1-D engine at the reference condition. This engine was chosen as it possesses a disc geometry combustion chamber with central ignition therefore the model output is not obscured by changes in the flame active surface area which would occur if a pent-geometry combustion chamber was simulated. Except where otherwise stated, the submodels used for the sensitivity analysis are as described in Section 5.4.

5.4.5.1 Initial temperature and pressure

The thermodynamic state of the fresh charge is inferred from measurements taken using a thermocouple (see Section 2.2.2) positioned just ahead of the intake port and an "absolute" pressure transducer (see Section 2.2.6) which is mounted part way down the barrel. Mounting the transducer part way down the barrel ensures that it is only uncovered by the piston during the period where the cylinder contents are (relatively) cool and the pressure is low. Both of these measurements are subject to errors. In the case of the charge temperature, the intake air is subject to cooling by the evaporation of the fuel spray. Although this cooling is noticeable as a change in the thermocouple readout, its exact magnitude is difficult to quantify as the system is no longer in a steady state and the thermocouple readout is influenced by the thermal inertia of the thermocouple housing. In the case of the pressure transducer, the transducer is prone to long term drift and must be zeroed at the start of the day. The sensitivity of the three-zone model to changes in the charge state was therefore investigated.

Illustrated in Figure 5.50 is the variation in model output for $\pm$50 mbar change in intake pressure. The most obvious effect of varying the intake pressure is to change the mass of trapped gas by changing the charge density. Neither the laminar or turbulent burning velocities are particularly strongly influenced by the pressure of the unburnt mixture hence the rate of heat release is very similar for these small changes in pressure. The change in peak pressure is greater than the $\pm$50 mbar variation which would be expected for a non-reacting mixture undergoing isentropic compression. Combustion of the different masses of fuel-air mixture causes the peak pressure to vary by $\pm$1.2 bar.

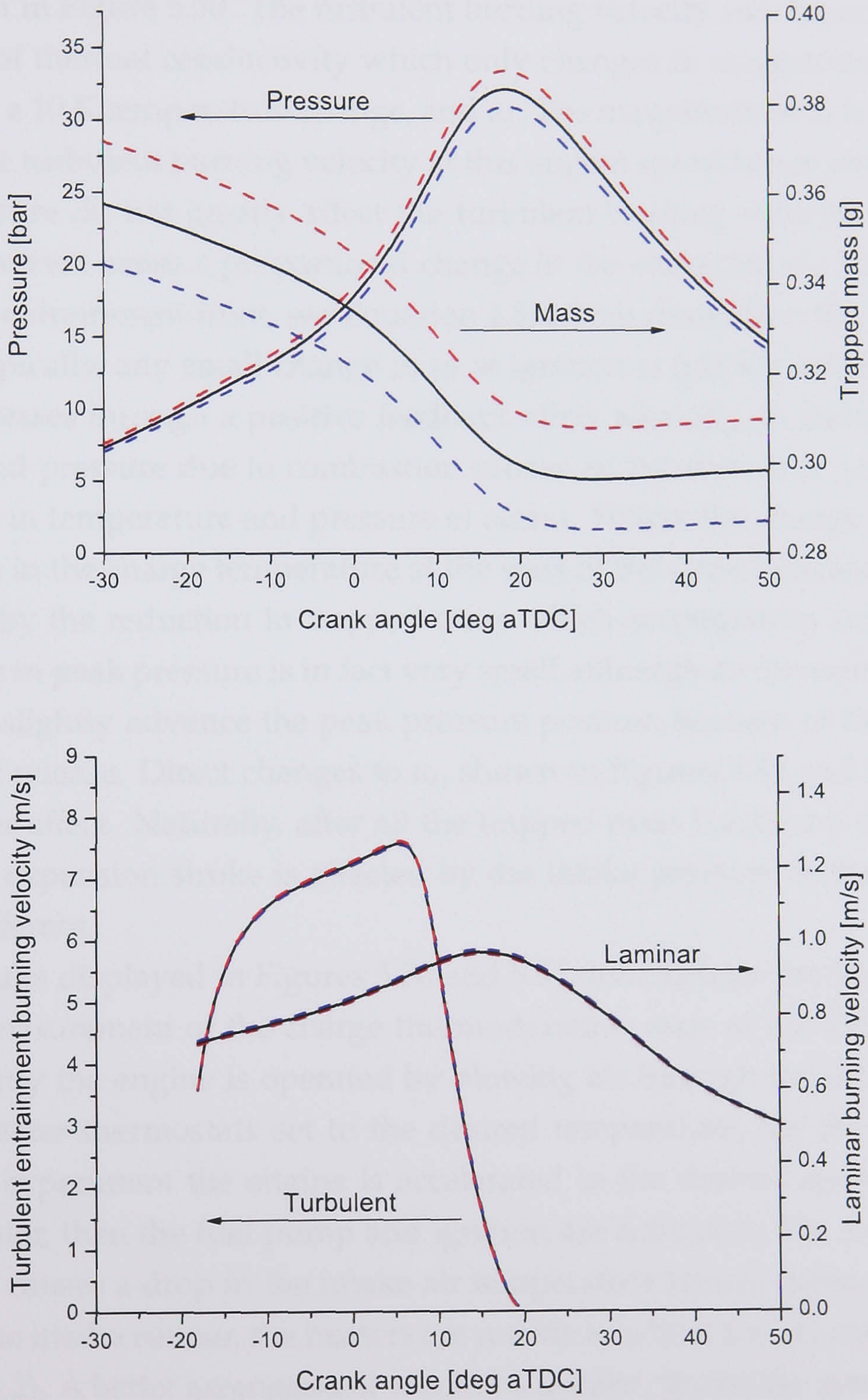

Figure 5.50: Sensitivity of the three-zone LUSIE model to small changes in intake pressure.

A variation of ±10 K in intake temperature was simulated, shown in Figure 5.51. The change in charge density causes an obvious change in the trapped mass, and also a change in the laminar burning velocity u_l, in contrast to the results shown in Figure 5.50. The turbulent burning velocity (see Equation 4.17) is a function of thermal conductivity which only changes in magnitude by a small amount for a 10 K temperature change, and u_l. The magnitude of u_l is small compared to the turbulent burning velocity at this engine speed hence small changes in temperature do not greatly affect the turbulent burning velocity. Variations in u_l do however cause a proportional change in the characteristic burn-up time behind the entrainment front, see Equation 4.5, which does affect the rate of heat release. Typically, any small change in u_l at ignition is quickly amplified as the cycle progresses through a positive feedback effect whereby an increase in temperature and pressure due to combustion causes an increase in u_l which causes an increase in temperature and pressure et cetera. Where the change in u_l is due to a change in the charge temperature at the start of the cycle this feedback effect is negated by the reduction in trapped mass which accompanies any rise in u_l. The change in peak pressure is in fact very small although an increase in temperature does slightly advance the peak pressure position because of the increased rate of heat release. Direct changes to u_l, shown in Figures 5.52 and 5.53, have a much larger effect. Naturally, after all the trapped mass has burnt, the pressure during the expansion stroke is affected by the intake pressure as the total mass burnt is different.

The results displayed in Figures 5.50 and 5.51 demonstrate the importance of accurate measurement of the charge thermodynamic state at the start of the cycle. Currently the engine is operated by blowing air through the intake system, with the heater thermostats set to the desired temperature, for the whole day. During an experiment the engine is accelerated to the desired speed using the dynamometer, then the fuel pump and ignition are activated. The sudden addition of fuel causes a drop in the intake air temperature which, given the thermal inertia of the intake runner, the heaters are unable to adjust for (discussed further in Section 5.2). A better arrangement would be to allow the intake system to come to a steady state whilst fuel is being added. This would generate a large volume of potentially explosive fuel-air mixture which would have to be safely ventilated but would give a more accurate intake temperature, something which will be of even greater importance given the planned use LUPOE2 for HCCI (homogenous charge compression ignition) studies.

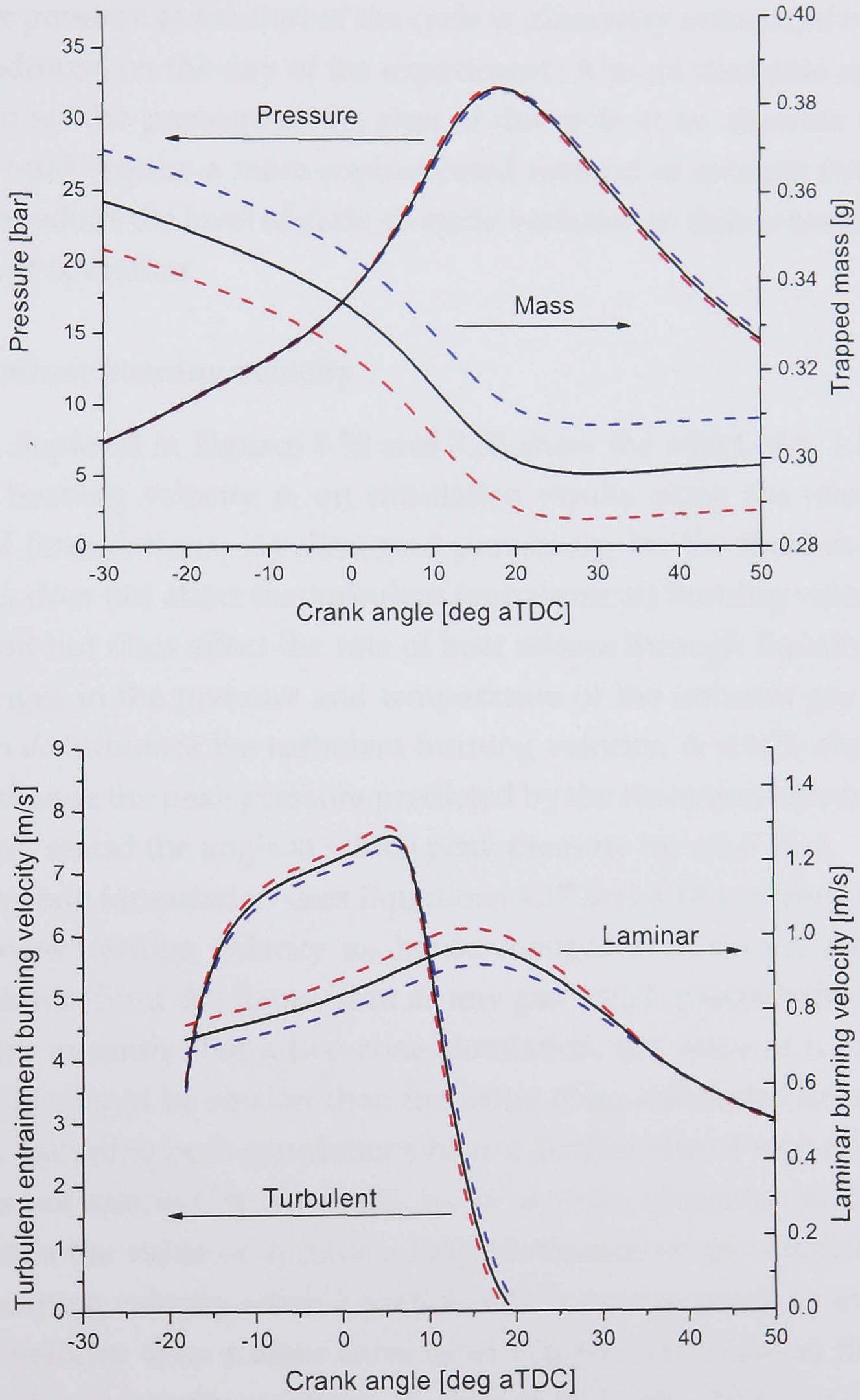

Figure 5.51: Sensitivity of the three-zone LUSIE model to small changes in intake temperature.

The pressure of the charge at the start of the cycle is determined by the pressure in the exhaust port (the last port to close). As the laboratory exhaust extraction system is evacuated using a blower which is working against atmospheric pressure the pressure at the start of the cycle is ultimately influenced by the atmospheric conditions on the day of the experiment. A more desirable arrangement would be to set the pressure at the start of the cycle at an absolute level. Such a system would require a more sophisticated method of exhaust extraction but may help to reduce the level of cycle-to-cycle variation in data sets recorded over many days of operation.

5.4.5.2 Laminar burning velocity

The curves depicted in Figures 5.52 and 5.53 show the effect of a $\pm 10\%$ change in laminar burning velocity u_l on simulation results using the two and three-zone model formulations. As discussed previously, for the three-zone model a change in u_l does not affect the turbulent (entrainment) burning velocity u_{te} by a large amount but does affect the rate of heat release through Equation 4.5. This causes changes in the pressure and temperature of the unburnt gas later in the cycle which *do* influence the turbulent burning velocity. A $\pm 10\%$ change in u_l is enough to change the peak pressure predicted by the three-zone model by ± 3 bar and advance/retard the angle at which peak pressure by $\pm 1.6\,^{\circ}$CA.

The two-zone formulation uses Equations 4.17 and 4.18 to directly predict the turbulent mass burning velocity u_{tr} hence changes in u_l do not affect the rate of combustion behind the flame front as any gas which passes behind the flame front is burnt instantly. For a two-zone simulation, the value of u_{tr} supplied by Equation 4.18 should be smaller than the value of u_{te} calculated for a three-zone simulation, assuming both simulations have a similar rate of heat release. When the flame is not affected by the walls, $u_{tr} = u_l + u_{t0}$ (Equation 4.18). As $u_{tr} < u_{te}$, changes in the value of u_l have a larger influence on the predicted value of turbulent burning velocity when Equation 4.18 is used to predict a mass burning (two-zone) velocity than a mass entrainment (three-zone) rate as the predicted value of u_{t0} is necessarily smaller.[9] A change in u_l of $\pm 10\%$ caused a change in peak pressure of ± 2.1 bar with a corresponding change in the crank angle at peak pressure of $\pm 1.2^{\circ}$ CA. For the engine studied therefore, the two-zone model appears to be less sensitive to small changes to u_l than the three-zone model.

[9]The square root of the laminar burning velocity also appears in the expression for u_{t0}, Equation 4.17.

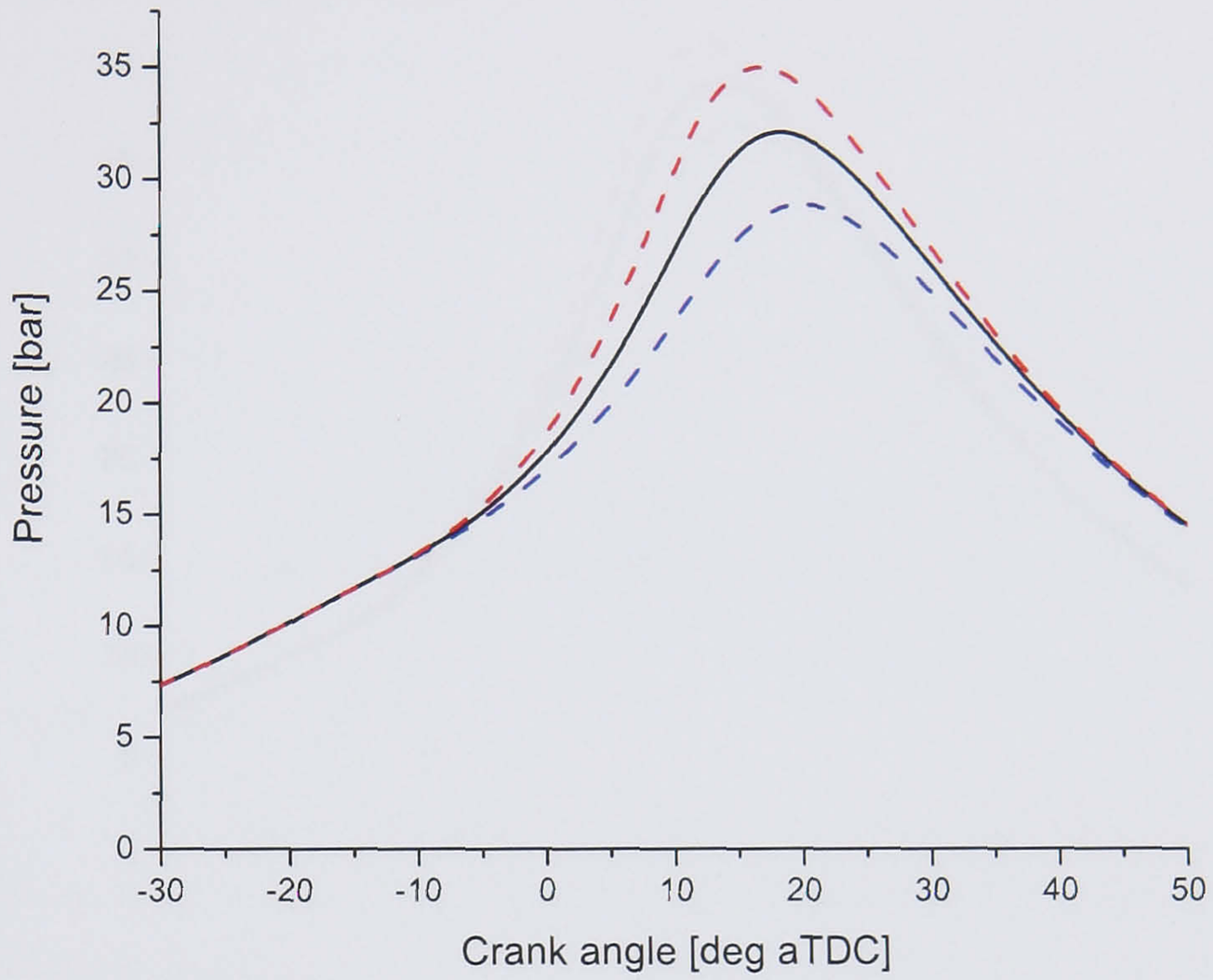

Figure 5.52: Sensitivity of the three-zone LUSIE model to small changes in laminar burning velocity.

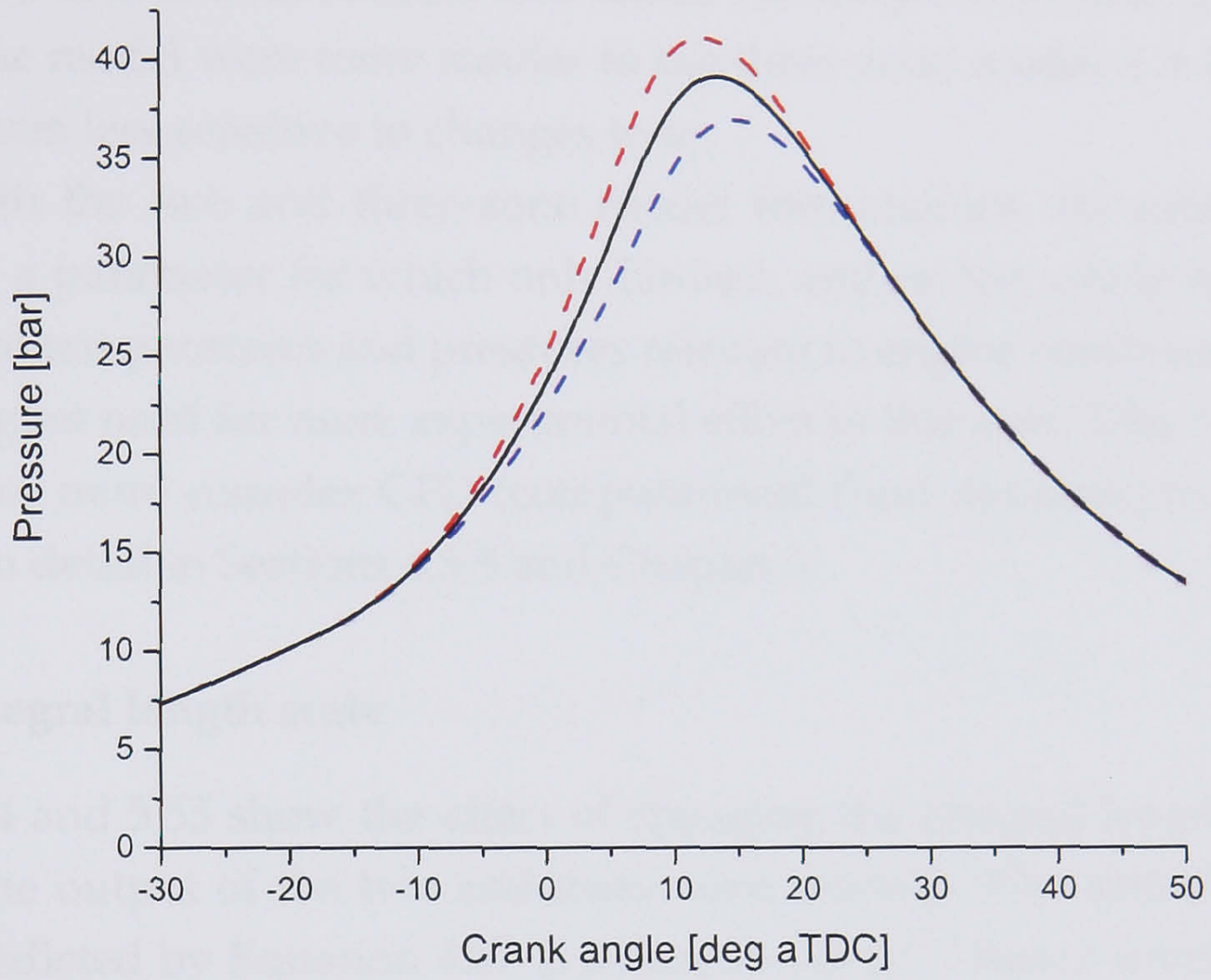

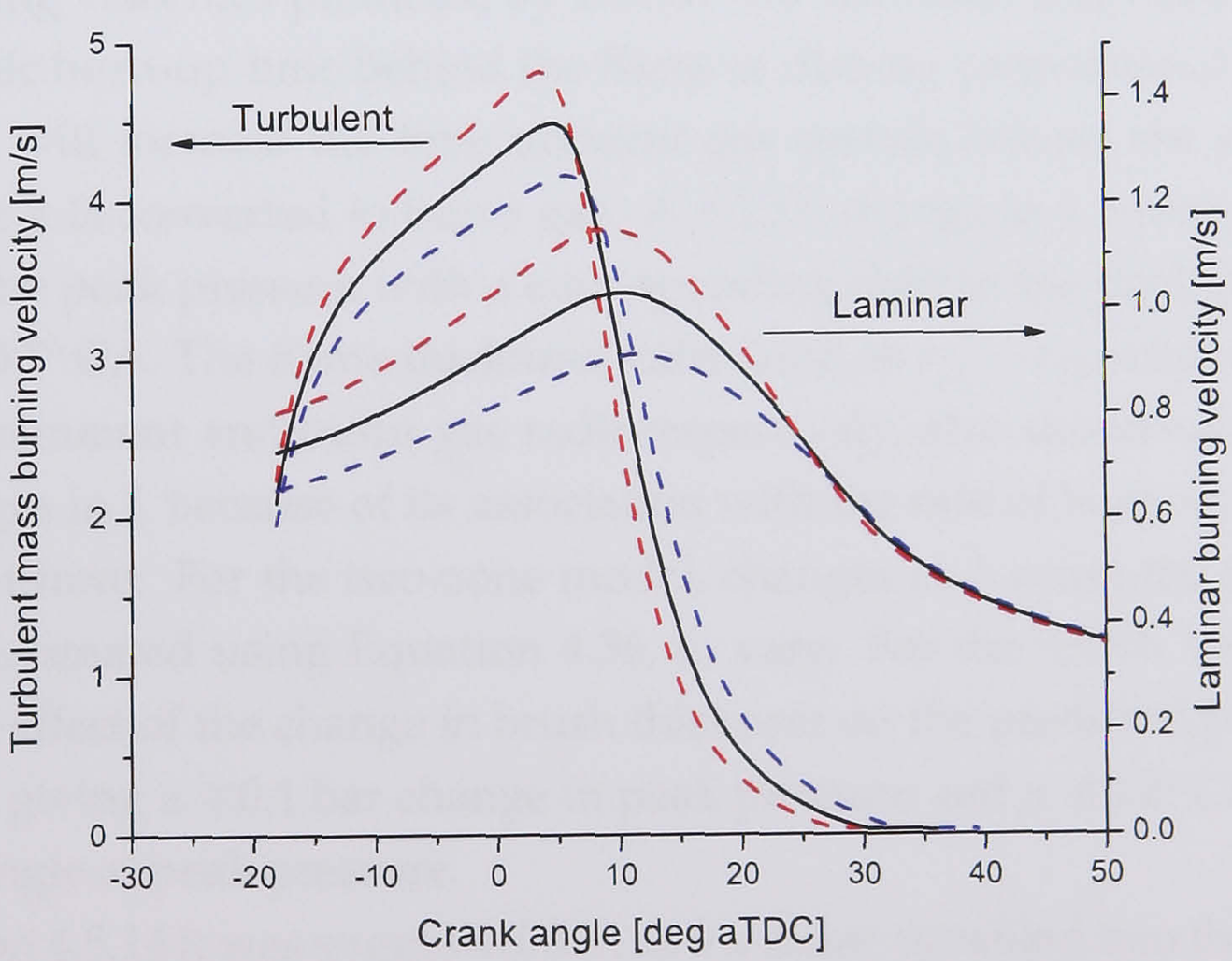

Figure 5.53: Sensitivity of the two-zone LUSIE model to small changes in laminar burning velocity.

Note however that this is not truly a "like-for-like" test as the rate of heat release predicted by the two-zone model was lower than that predicted by the three-zone model. If the rate of heat release, and hence the temperature rise, predicted by the two-zone model were more similar to the three-zone model it is likely that it would be even less sensitive to changes to u_l.

That both the two and three-zone model formulations are sensitive to the value of u_l, a parameter for which only limited, and on the whole inconclusive, data exists at temperatures and pressures relevant to engine combustion, emphasises the urgent need for more experimental effort in this area. This conclusion is valid also for more complex CFD (computational fluid dynamic) models and is discussed in detail in Sections 4.5.5 and Chapter 6

5.4.5.3 Integral length scale

Figures 5.54 and 5.55 show the effect of changing the integral length scale L by $\pm 10\%$ on the output of the two and three-zone models. The turbulent burning velocity predicted by Equation 4.17 is a function of $L^{1/4}$ hence small changes in L have little direct effect on the turbulent entrainment (three-zone) or mass (two-zone) burning velocities predicted by LUSIE. For the three-zone formulation the characteristic burn-up time behind the flame is directly proportional to L: an increase in L will increase the time unburnt gas spends behind the entrainment front before it is converted to burnt gas. A $\pm 10\%$ change in L causes a ∓ 1.5 bar change in the peak pressure with a corresponding shift in the peak pressure position of $\mp 0.5°$ CA. The flame thickness, calculated as $r_{fe} - r_{fb}$ where r_{fe} and r_{fb} are the entrainment and burnt gas radii respectively, also shows some sensitivity to changes in L because of its association with the rate of burn-up behind the entrainment front. For the two-zone model, changes in L cause the flame brush thickness, estimated using Equation 4.36, to vary. For the $\pm 10\%$ variation in L studied the effect of the change in brush thickness on the predicted pressure was very small, giving a ∓ 0.1 bar change in peak pressure and a $\mp 0.2°$ CA change in the crank angle at peak pressure.

In Section 4.5.14 it was suggested that as the flame travelled into the "eaves" of the pent, the integral length scale would decrease because of the reduced clearance height. The curves in Figure 5.56 illustrate the effect of including or otherwise this assumption in a three-zone simulation of LUPOE2-P. Without any decrease in L in the eaves of the pent the burn-up behind the flame front at the end of the cycle is very slow giving a low peak pressure. The effect of including a

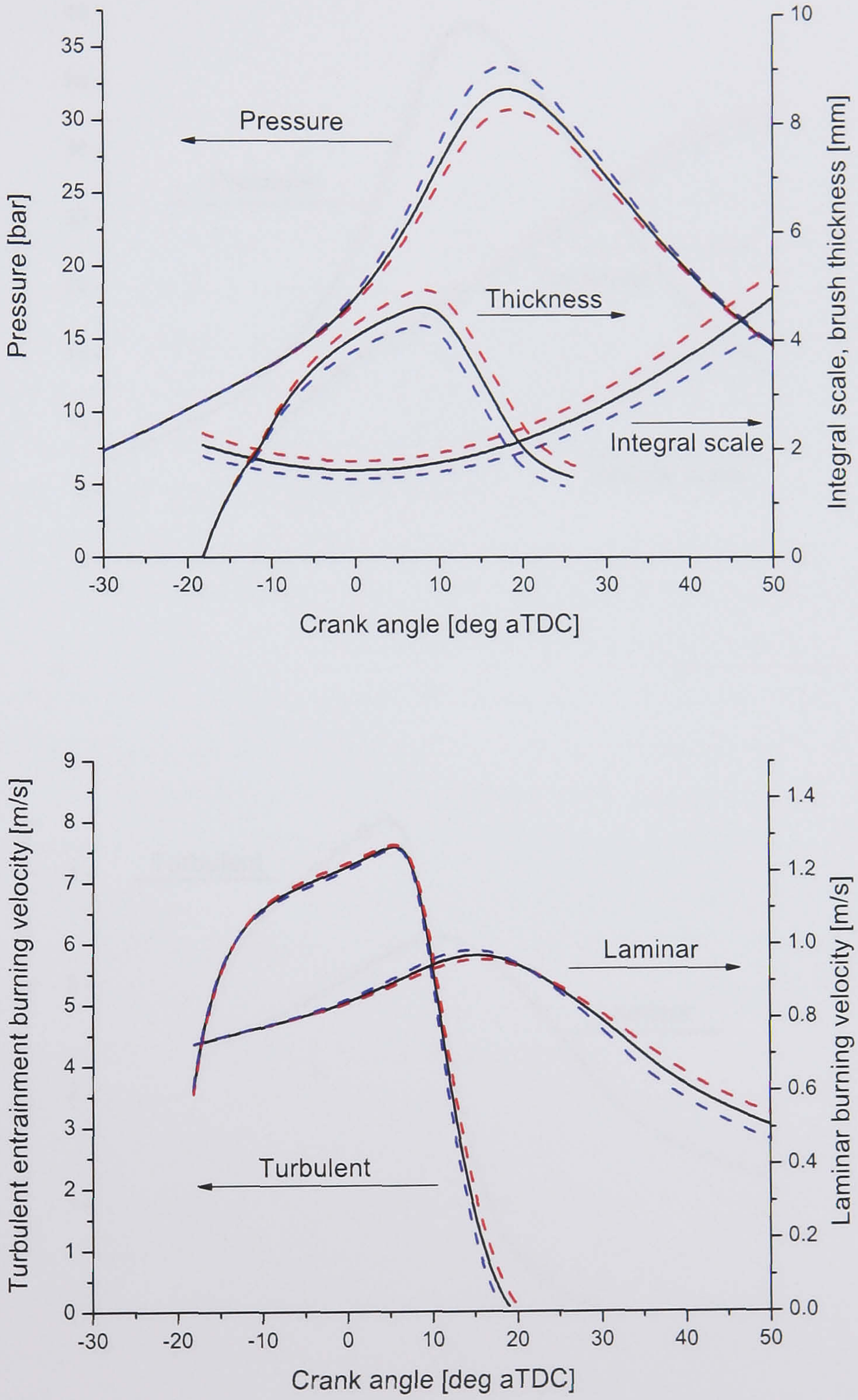

Figure 5.54: Sensitivity of the three-zone LUSIE model to small changes in integral length scale.

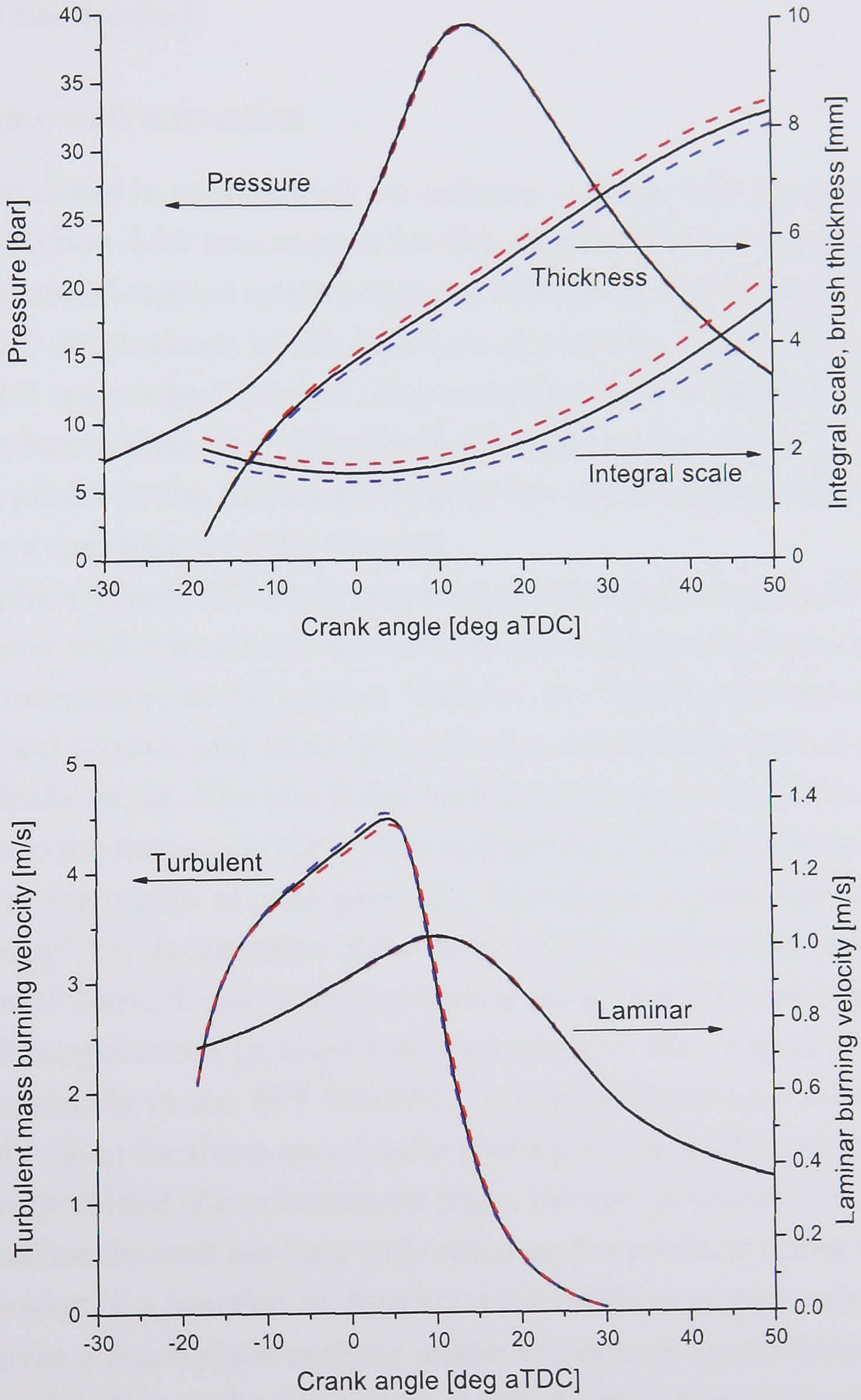

Figure 5.55: Sensitivity of the two-zone LUSIE model to small changes in integral length scale.

decrease in L is to decrease the characteristic burn-up time at the end of the cycle. This leads to a much more rapid burn-up as the flame comes close to the wall and ultimately results in a greater proportion of the trapped mass being burnt when combustion has finished.

5.4.5.4 Flame-wall interaction

As the flame comes in contact with the cylinder walls its rate of propagation decreases. In Section 4.5.9 two models for this deceleration were described. One, an empirical model termed active perimeter fraction (APF) [Abdi Aghdam, 2003] was based on observations of the active, as opposed to quenched, perimeter of the flame as it approached the wall. The second model was based on the hypothesis that the heat release rate as the flame impinges on the wall is reduced as the self similar profile of the turbulent flame brush, approximated using a complementary error function, is cut by the wall.

The graphs in Figure 5.57 show two-zone simulations using the APF and error function flame-wall interactions submodels, and a third simulation in which no flame-wall interaction model is used. Without any flame-wall interaction model the rate of heat release, and hence pressure rise, towards the end of combustion is unrealistically rapid. The two flame-wall interaction models both slow down combustion as the flame approaches the wall giving a rounded shape to the pressure curve in the region of peak pressure. The shape of both functions is quite similar although the deceleration of the flame begins earlier when using the error function based flame deceleration function leading to a reduced peak pressure. Some small irregularities (presumably an artifact of the original experimental data) are noticeable in the APF function. A similar flame-wall interaction sensitivity study using the three-zone model (not shown here) showed that, because of the burn-up behind the entrainment front, the rate at which the entrainment front approaches the wall has very little effect on the predicted pressure trace.

The inclusion of a function to decelerate the flame as it approaches the cylinder walls gives a much more realistic shape to pressure traces predicted by the two-zone model. Coupled with a more detailed ignition or flame development model (see Sections 5.3.6 and 5.4.6) the two-zone formulation could well provide a more robust frame work for SI engine combustion simulations due to its reduced dependency on accurate values of laminar burning velocity and integral length scale. It is likely that the error function based deceleration model is more general than the empirical APF model as it includes a term which accounts for

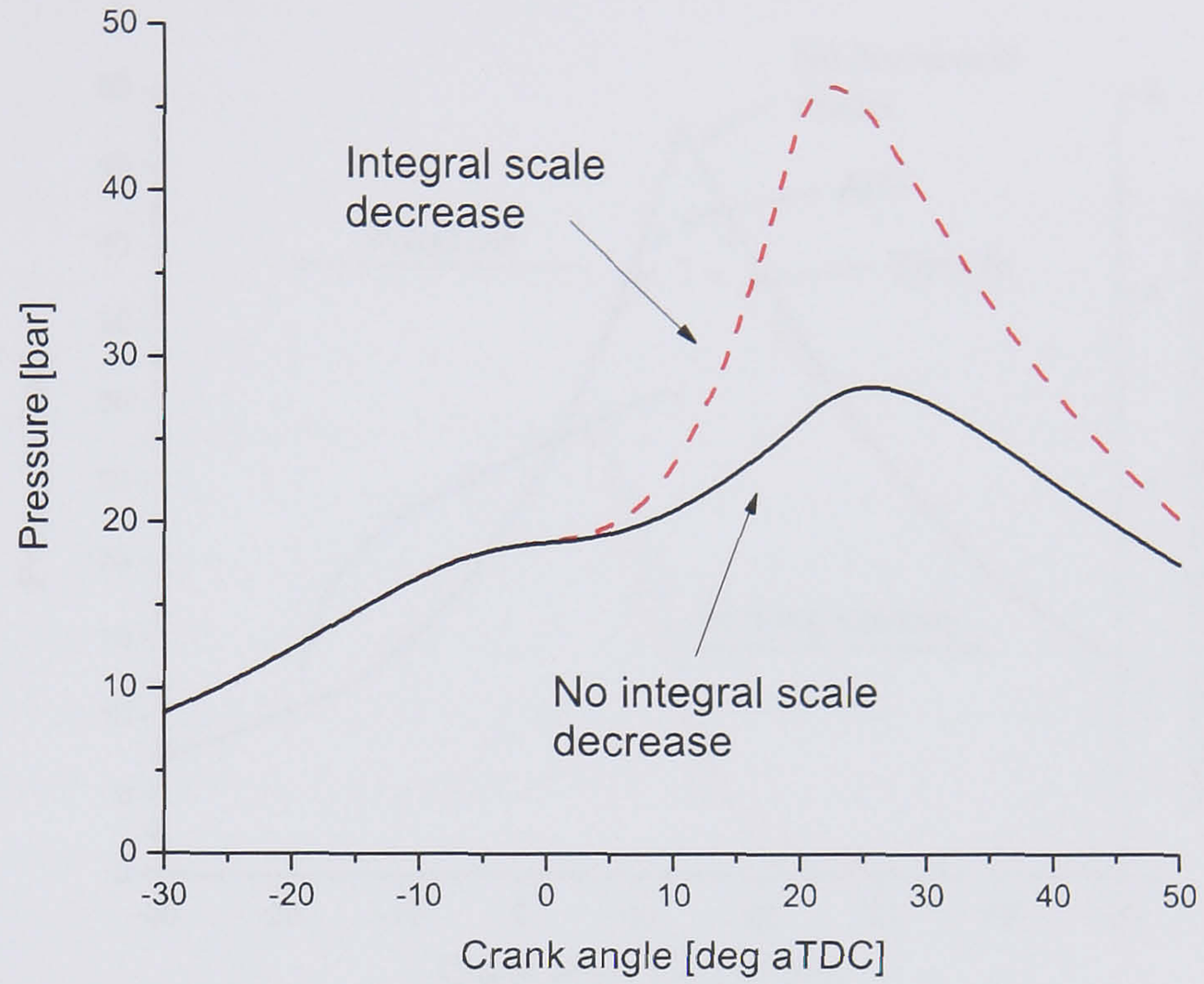

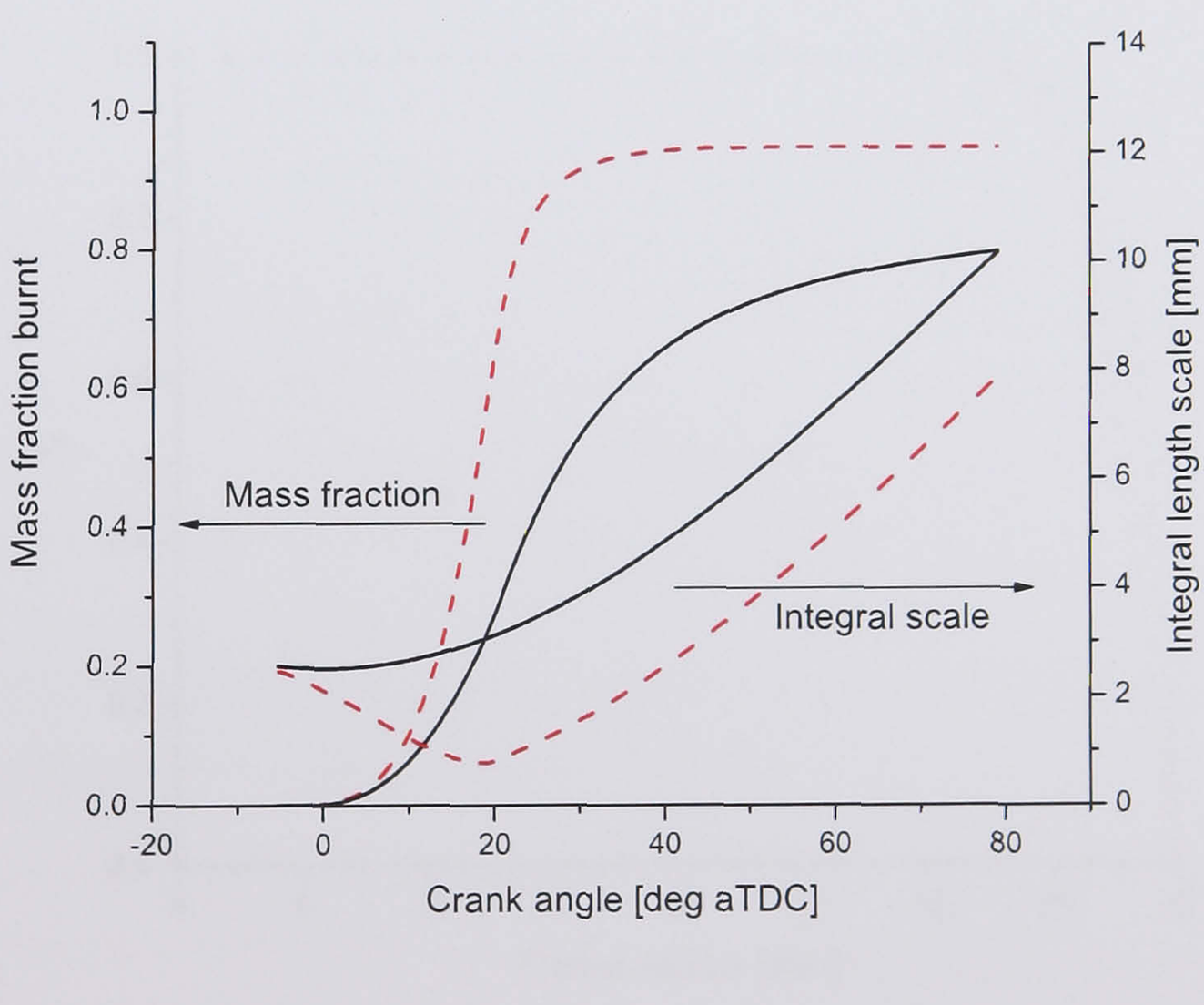

Figure 5.56: Sensitivity of the three-zone LUSIE model for a pent roof engine to changes in integral length scale model. Red lines show the integral scale decreasing in the eaves of the pent, Equation 4.39; black lines show no decrease, Equation 4.38

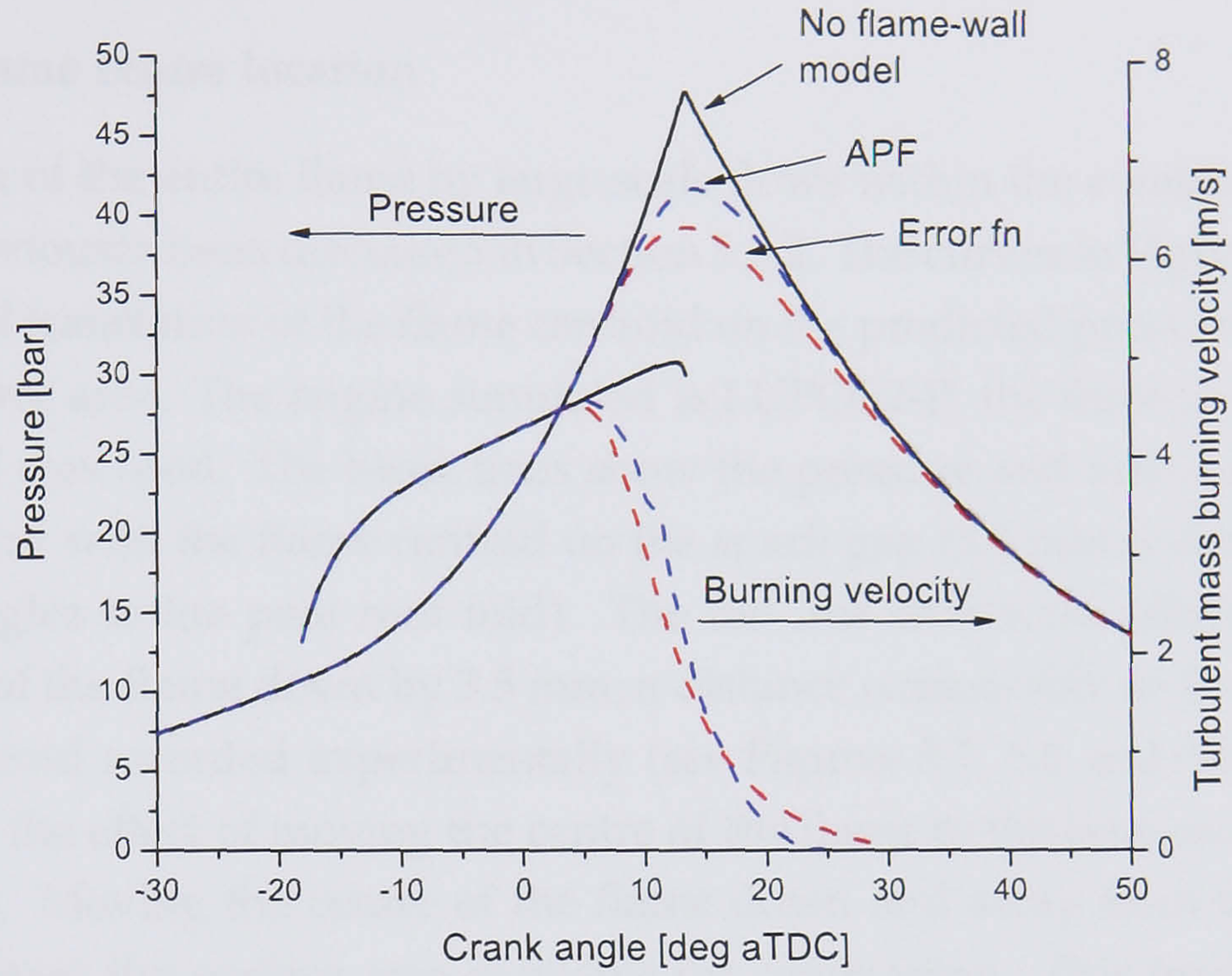

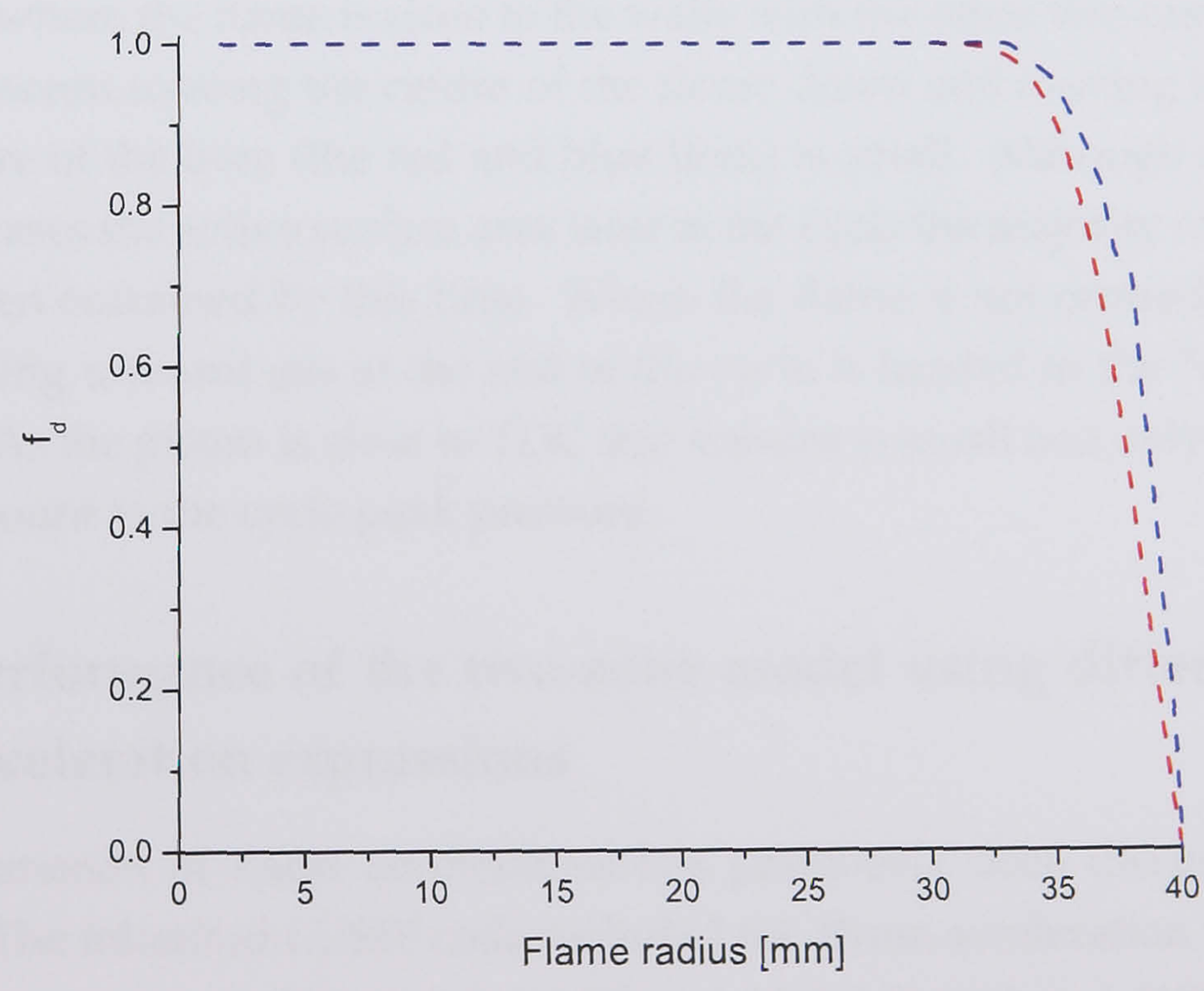

Figure 5.57: Sensitivity of the two-zone LUSIE model to different flame-wall interaction models.

the flame brush thickness. For this reason it was used for the other simulations reported in this thesis.

5.4.5.5 Flame centre location

Convection of the entire flame by large scale flows within the combustion chamber has previously been discussed in Section 5.3.2. The curves in Figure 5.58 show the effect of translation of the flame centroid on the predicted pressure and active flame surface area. The engine simulated is LUPOE2-P, the three-zone combustion model was used. The black lines show the pressure and active surface area development with the flame centred on the spark gap (5.5 mm down and 3 mm at right angles to the pent roof fold). The red line shows the effect of moving the centre of the flame down by 3.5 mm, a distance comparable to the movement of the centroid recorded experimentally (see Figures 5.7, 5.8 and 5.9). The blue line shows the effect of moving the centre of the flame to the bore axis and down by 3.5 mm. Moving the centre of the flame down and away from the chamber walls increases the surface area available for combustion. This leads in turn to an increased rate of heat release and faster pressure development (compare the black line, where the flame is close to the walls with the other two cases). The difference between moving the centre of the flame down and moving it down and to the centre of the bore (the red and blue lines) is small. Although centring the flame increases the active surface area later in the cycle the majority of the gas has already been entrained by this time. Where the flame is not centred in the bore the remaining unburnt gas at the end of the cycle is located in the "eave" of the pent roof. As the piston is close to TDC this volume is small and only contributes a small amount to the cycle peak pressure.

5.4.6 Performance of the two-zone model using different flame acceleration expressions

The phenomenon of flame acceleration has previously been discussed in Section 5.3.6. The inherited LUSIE code included the flame acceleration models proposed by Lipatnikov and Chomiak [1997] and Abdel-Gayed et al. [1987]. In order to investigate the influence of the choice of flame acceleration model a number of alternative flame acceleration models were added to the LUSIE code as described in Section 4.5.8.

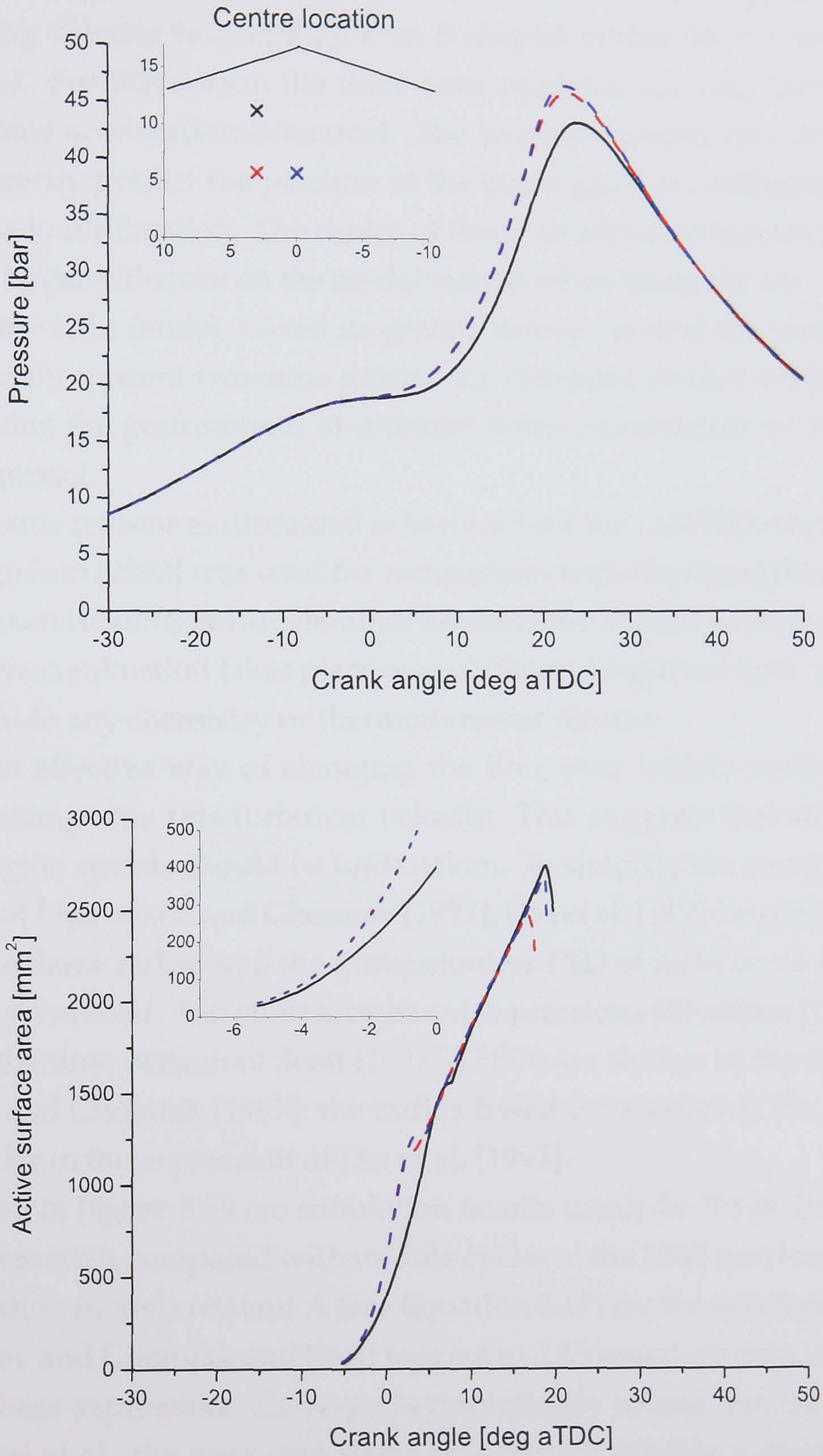

Figure 5.58: Sensitivity of the three-zone LUSIE model to changes in ignition position when simulating a pent roof engine. Lines of different colours correspond to the ignition positions shown in the inset of the top graph.

The differential nature of the governing equations of LUSIE's three-zone combustion model (Equations 4.4 and 4.5) tend to smooth any change in the entrainment burning velocity (u_{te}) and give an S-shaped profile for the mass burning velocity (u_{tr}). For this reason the three-zone model is not very sensitive to the choice of flame acceleration submodel. The two-zone model uses an expression for u_{tr} to directly predict the position of the burnt gas front and hence the pressure rise due to combustion. The choice of flame acceleration submodel therefore has a much larger influence on the model output when using the two-zone model than the three-zone model. Given its greater sensitivity and the poor predictive capability of the current two-zone model, the two-zone model is a better candidate for testing the performance of different flame acceleration models than the three-zone model.

For the same reasons as discussed in Section 5.4.4 the LUPOE1-D data recorded by Abdi Aghdam [2003] was used for comparison with the simulation results. To effectively exercise different acceleration models they should be tested under conditions where combustion takes place over different lengths of time. (None of the models include any chemistry or thermodynamic terms.)

The most effective way of changing the time over which combustion takes place is to change the rms turbulent velocity. This suggests that simulations at different engine speeds should be undertaken. To simplify the comparison, only the models of Lipatnikov and Chomiak [1997], Dai et al. [1995] and the expression based on the flame radius and the dimensionless PSD of turbulence proposed by Scott [1992] were used. The other time based expressions (Merdjani [1996], Cairns [2001] and the time version of Scott [1992]'s PSD) are similar to the expression of Lipatnikov and Chomiak [1997]; the radius based expression of Wu et al. [1993] is very similar to the expression of Dai et al. [1995].

Displayed in Figure 5.59 are simulation results using the three different flame acceleration models compared with middle cycles at the 1500 rpm base condition. The combustion model constant A (see Equation 4.17) for the acceleration models of Lipatnikov and Chomiak and Scott was set to 0.45 based on data in Figure 5.26 as both of these expressions converge asymptotically to one. For the model proposed by Dai et al. the predicted flame acceleration reaches a maximum of 2.5 hence $A = 0.45/2.5 = 0.18$. None of the models produce a particularly good correspondence between predicted and model results. The rapid initial acceleration predicted by the expression of Lipatnikov and Chomiak results in a very rapid pressure rise following ignition and the highest peak pressure being predicted by

this model. The other two models are quite similar, they both give a lower rate of flame acceleration and consequently lower peak pressures.

At 750 rpm the three acceleration expressions result in very similar model predictions as illustrated in Figure 5.60. As the engine speed is much slower the time based model of Lipatnikov and Chomiak develops at roughly the same rate as the radius based models of Dai et al. and Scott. Again, none of the models match the experimental data particularly well because of the rapid initial acceleration they predict. With an increase in engine speed to 2000 rpm, Figure 5.61 the difference between the time and radius based models is again apparent. In all cases the flame acceleration is much too fast giving a peak pressure which is larger, and more advanced than, the experimental data.

The data presented in this section indicates that, whilst the correspondence between the model and experimental data is not particularly encouraging, the two-zone model, combined with an appropriate expression for flame deceleration in the presence of a wall, could give realistic combustion predictions if coupled with the correct flame acceleration model. Certainly, the addition of a function to slow the flame as it approaches the walls makes improves the predictive capability of the model greatly as shown in Figure 5.57. Regardless of the flame acceleration model used, the predicted flame acceleration immediately after ignition was much too rapid. The experimental flame acceleration results presented in Section 5.3.6 show that in the period following ignition the burning velocity remains close to the laminar burning velocity for quite some time. If, as proposed by many authors (e.g. Beretta et al. [1983], Lancaster et al. [1976] and Abdel-Gayed et al. [1987]) the initial flame propagation is laminar, the time elapsed during this initial period should be a function of the laminar burning velocity. None of the flame acceleration models described in Section 4.5.8 included a chemical term which could account for this.

One of the advantages of the two-zone model over the three-zone model is its simplicity. Simulation predictions are not so readily influenced by the (difficult to measure) integral scale as shown in Section 5.4.5 and the model has only one tunable constant (A). In a sense, the concept of entrainment and burn-up used in the three-zone model obscures the actual combustion process which, as evidenced by the Mie scattering laser sheet imaging presented in this thesis, is a distinctly binary process. The results presented in this section suggest that, given a more detailed treatment of the ignition process and initial flame acceleration, predictions using the two-zone model could be comparable in accuracy

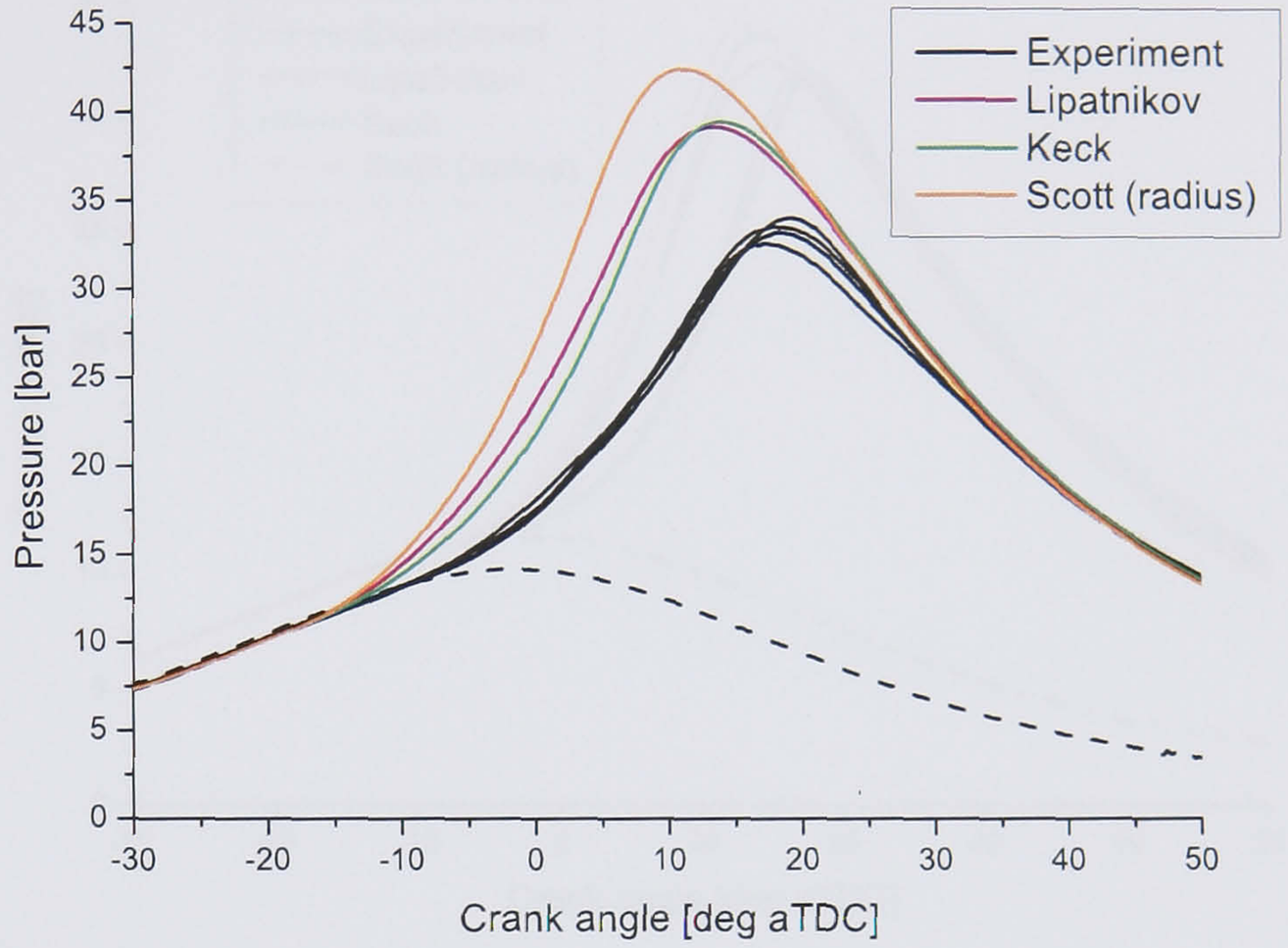

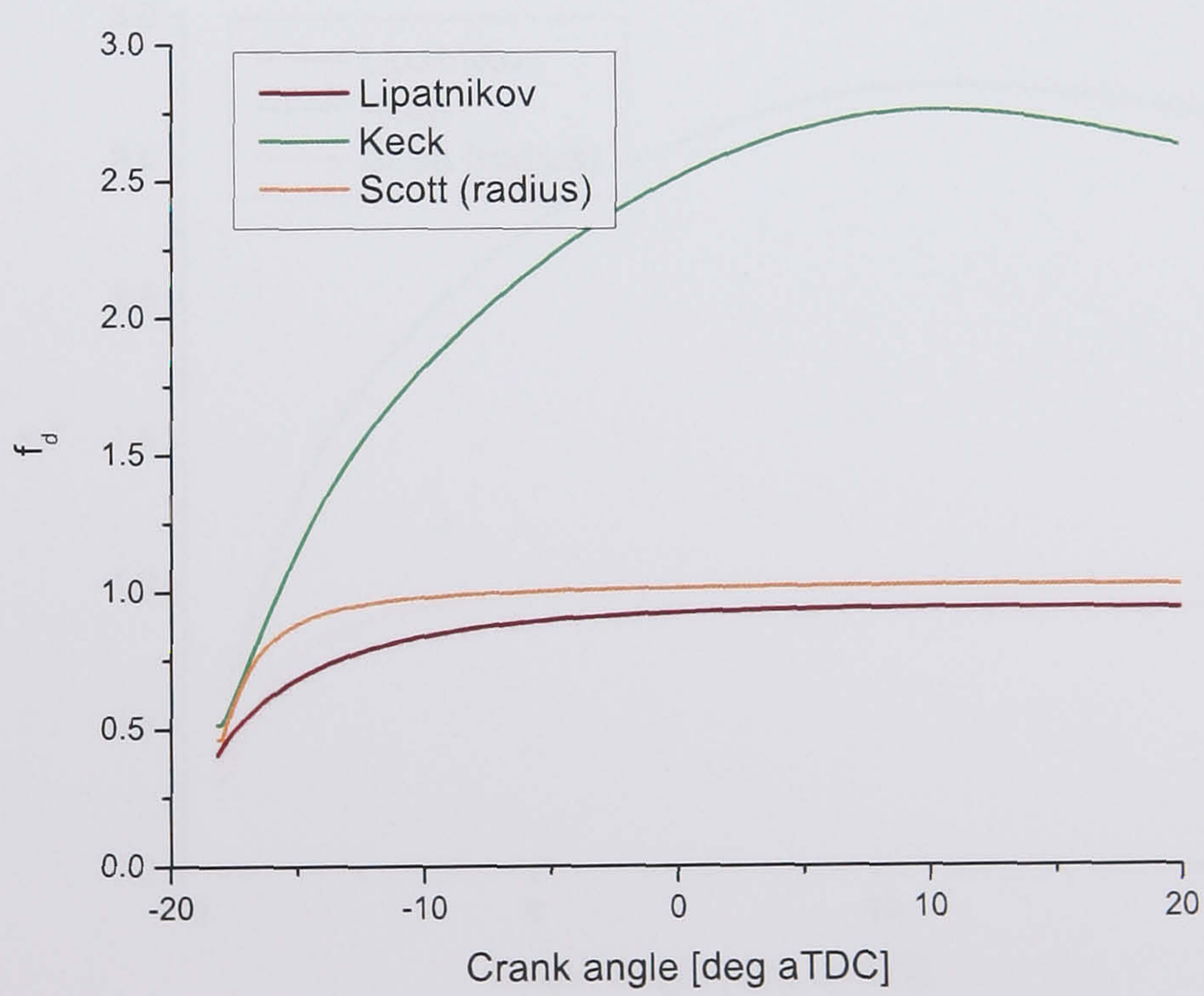

Figure 5.59: LUSIE simulations of LUPOE1-D using different flame acceleration models at the 1500 rpm base condition.

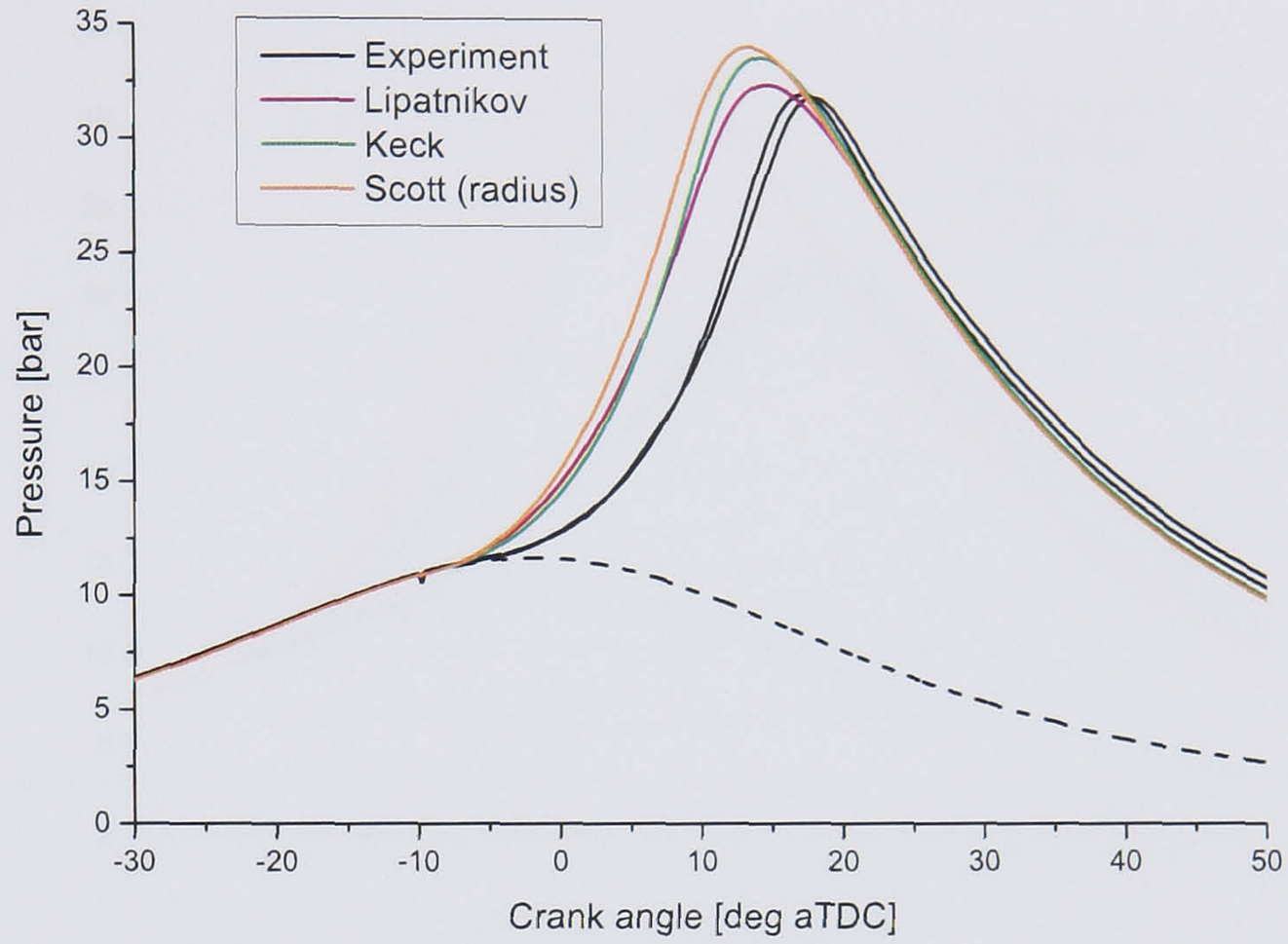

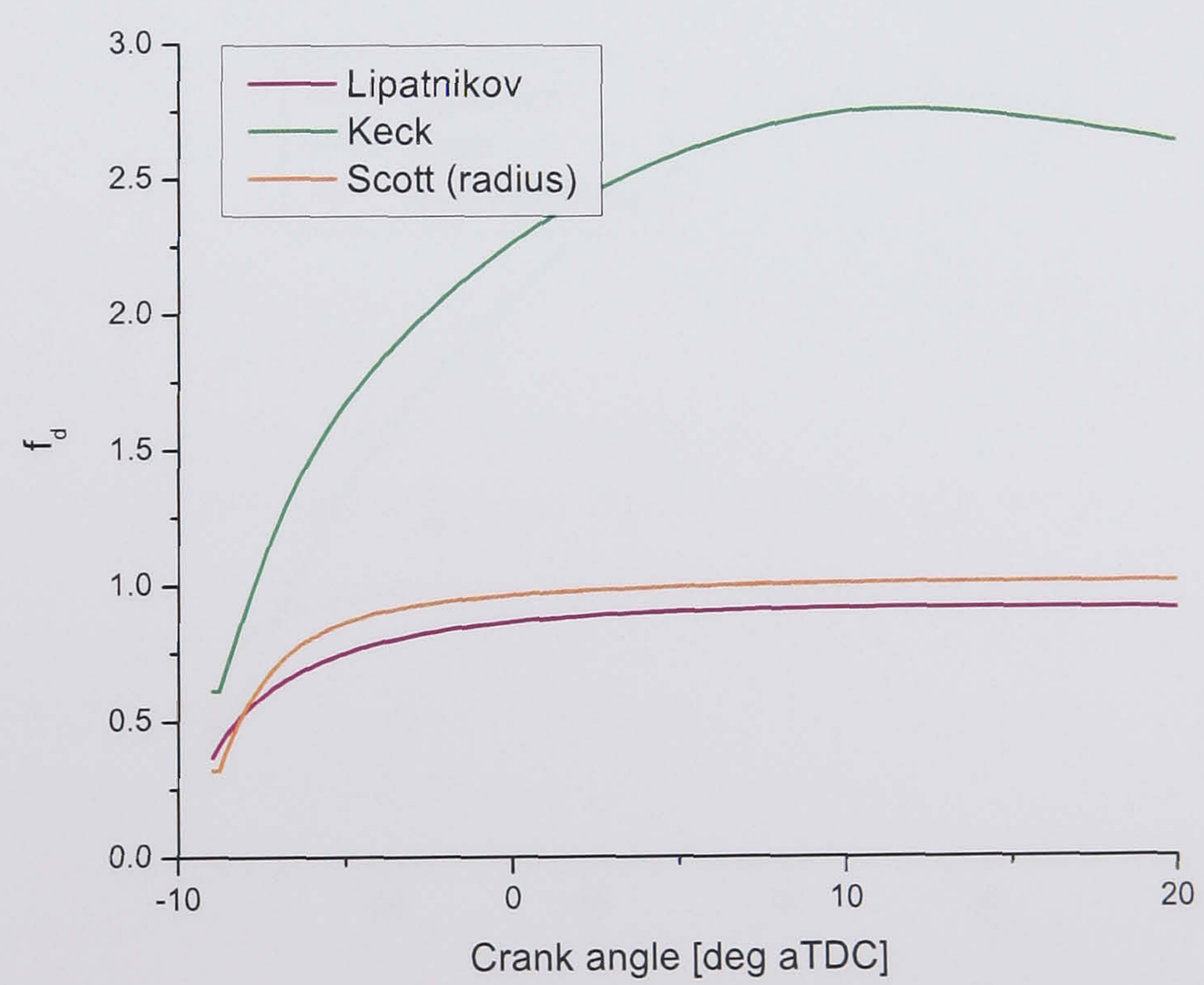

Figure 5.60: LUSIE simulations of LUPOE1-D using different flame acceleration models at the 750 rpm operating condition.

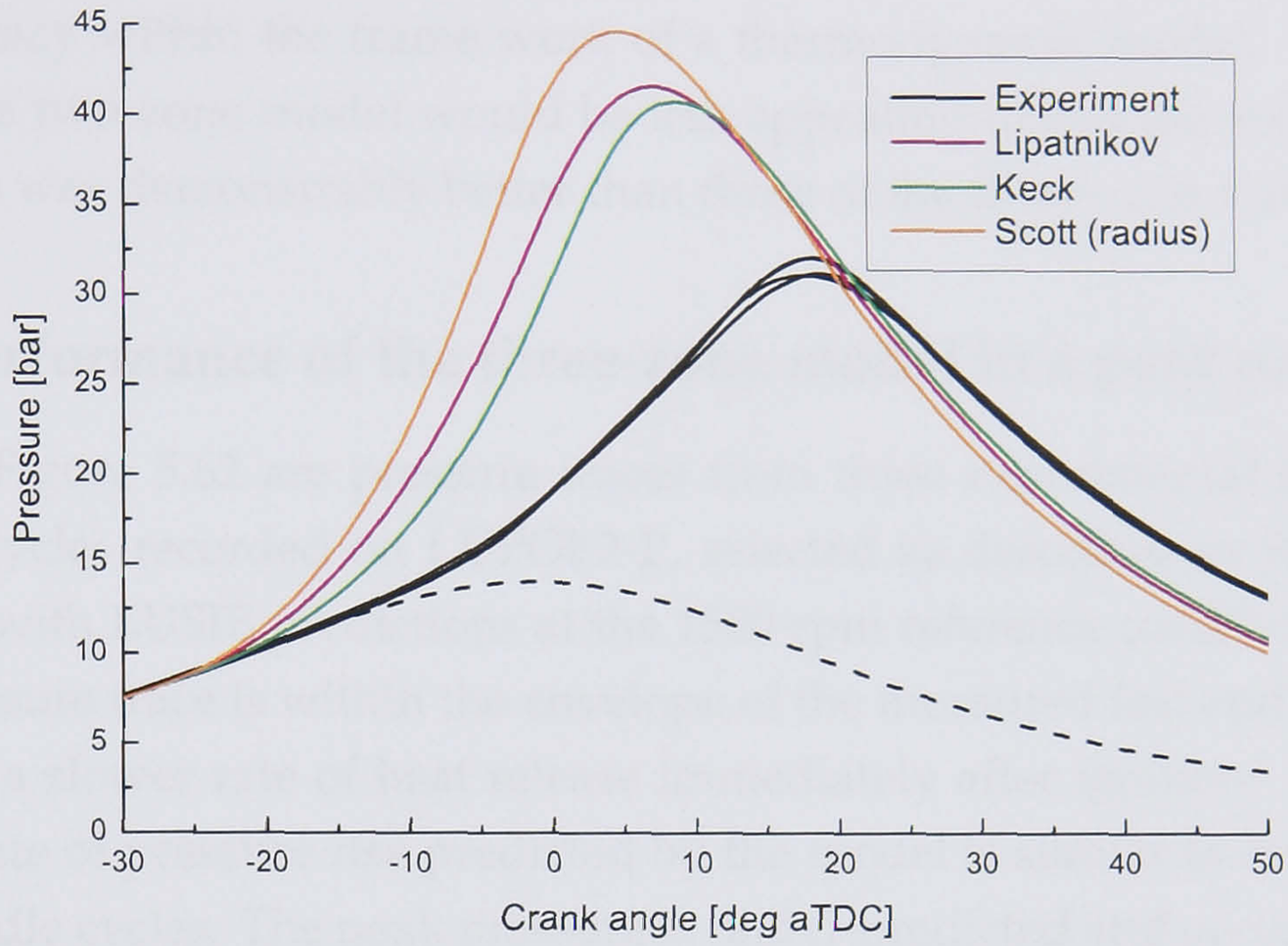

Figure 5.61: LUSIE simulations of LUPOE1-D using different flame acceleration models at the 2000 rpm operating condition.

to the three-zone model. This may come at a price however: the introduction of more complex models will quite possibly introduce additional model parameters to adjust or dependencies on quantities which are hard to predict with any great accuracy within the frame work of a thermodynamic model. If this were the case the two-zone model would be less appealing unless the accuracy of its predictions was demonstrably better than those of the three-zone model.

5.4.7 Performance of the three-zone model in a pent roof engine

Shown in Figure 5.62 are pressure traces from three experimental fast, middle and slow cycles recorded on LUPOE2-P, selected as described in Section 3.2.2, compared with LUSIE predictions at the 1500 rpm reference condition. The predicted pressure trace is within the envelope of the measured fast and slow cycles but shows a slower rate of heat release immediately after ignition. Later in the cycle the rate of pressure rise predicted by the model is similar to that exhibited by the middle cycles. The peak pressure is under-predicted and occurs later than the middle cycles, this is likely to have been caused by the low initial burn rate.

The burnt flame radius predicted by LUSIE, along with and LUSIEDA derived experimental fast, middle and slow burnt flame radii and the flame silhouette radius calculated from the laser sheet images (Section 3.3.13) are illustrated in Figure 5.63. The flame radii of the middle cycles and the laser sheet radius show good agreement. LUSIE predicts a flame radius which is larger than all but the experimental fast cycles in the first part of the cycle. After $\sim 5°$ aTDC the LUSIE flame radius is close to the flame radii of the slow cycles. The experimental flame radii data immediately after ignition may be inaccurate for reasons discussed below.

The data in Figure 5.64 show the active burnt flame surface area predicted by LUSIE alongside burnt areas derived from a LUSIEDA reverse analysis (Section 3.2.3) of three fast middle and slow cycles and the active area of the $\overline{c} = 0.5$ isosurface (Section 3.3.11). The burnt gas area is used for comparison with the experimental results which, being derived from the $\overline{c} = 0.5$ isosurface of laser sheet images, are closer to the burnt gas surface than the entrainment front surface. Areas calculated by LUSIE and LUSIEDA assume the flame has the geometry of a truncated sphere. In the period immediately following ignition there is no isosurface of $\overline{c} = 0.5$ as 1) random convection of the flame kernel by turbulent eddies reduces the likelihood of finding burnt gas in any one area, 2) the laser

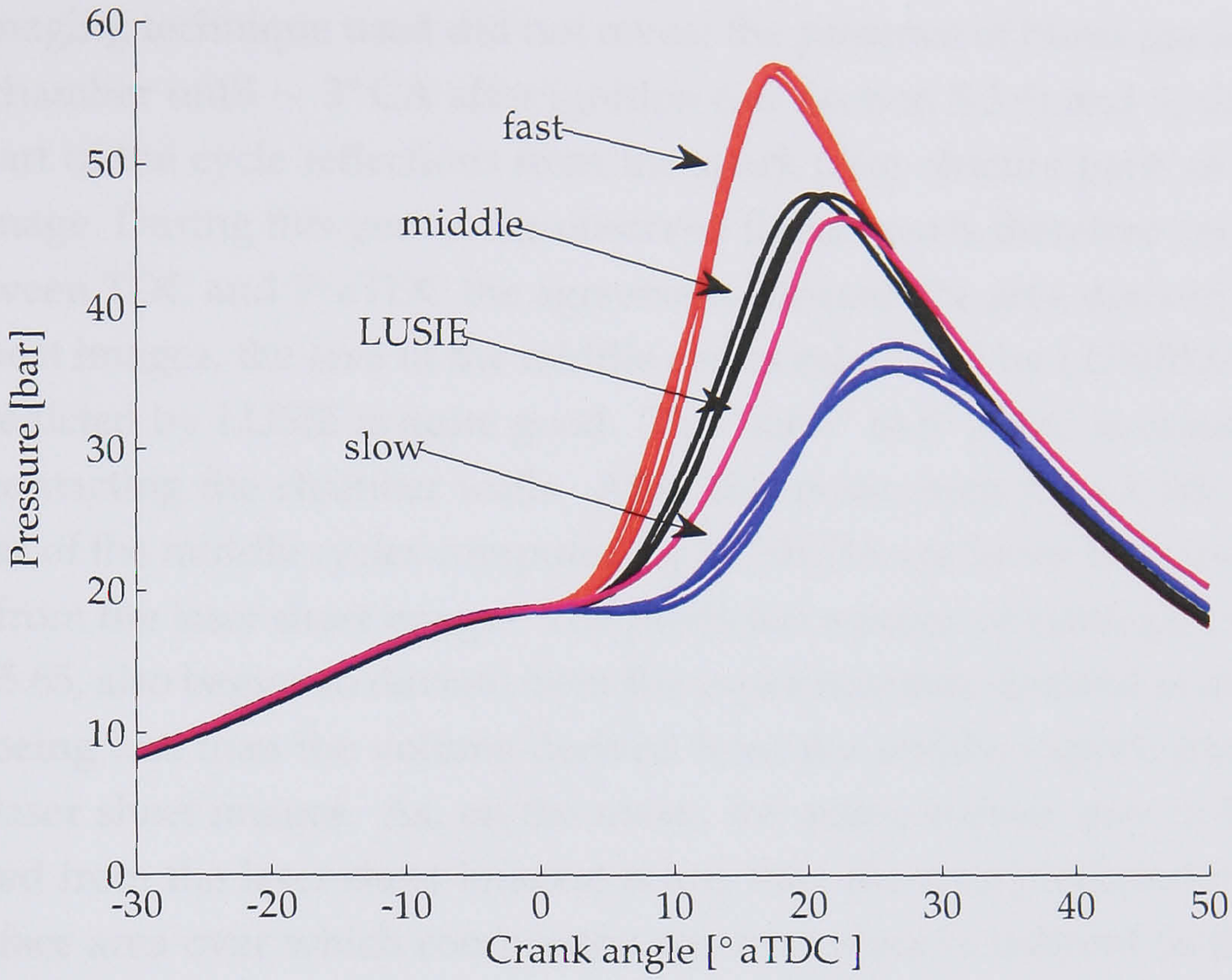

Figure 5.62: Cylinder pressure recorded in selected fast, middle and slow cycles compared with the LUSIE predicted pressure for LUPOE2-P at the 1500 rpm base condition.

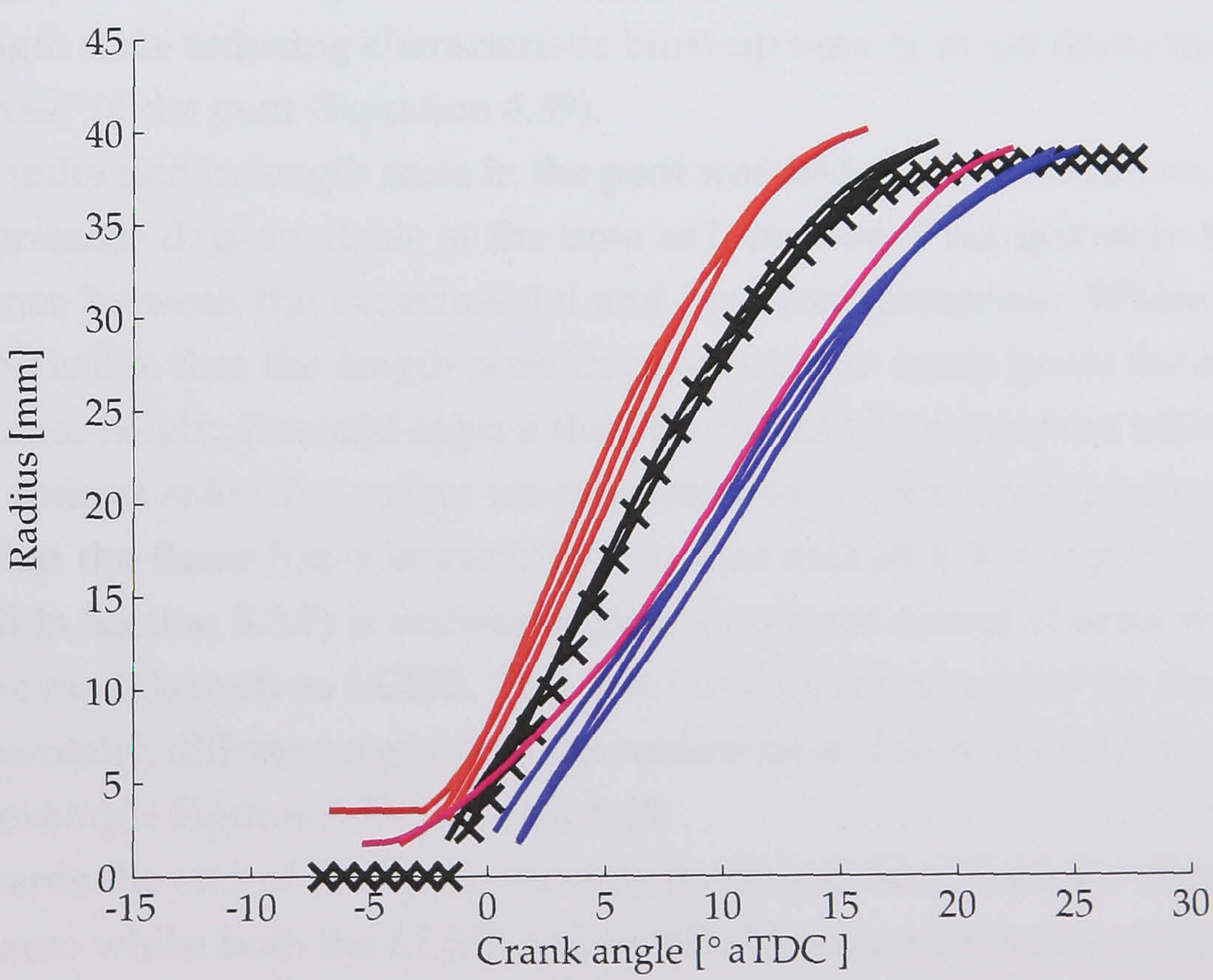

Figure 5.63: Flame radius derived from mean progress variable isosurfaces (black crosses) compared with LUSIEDA calculated burnt flame radii for fast, middle and slow cycles, and the LUSIE predicted burnt flame radius for LUPOE2-P at the 1500 rpm base condition. Line colours correspond with those used in Figure 5.62.

sheet imaging technique used did not reveal the presence of burnt gas anywhere in the chamber until $\sim 3°$ CA after ignition (see Section 5.3.6) and 3) during the early part of the cycle reflections from the spark plug obscure parts of the laser sheet image. During this period the observed flame area is therefore zero.

Between TDC and 5° aTDC the agreement between the area derived from the laser sheet images, the area of the middle cycles calculated by LUSIEDA and the area predicted by LUSIE is quite good. The "kink" at 5° aTDC is caused by the flame contacting the chamber walls. After this point, both the LUSIE area and the areas of the middle cycles computed by LUSIEDA are lower than the area obtained from the laser sheet images. The predicted volume of burnt gas, shown in Figure 5.65, also begins to deviate from the experimentally derived values at this point, being less than the volume derived from the middle experimental cycles or the laser sheet images. As, on the mean, the active surface area of the flame (obtained from the laser sheet images) is less than the area predicted by LUSIE, the surface area over which combustion can take place is reduced in the model later in the cycle. Given this discrepancy, it is rather surprising that the rate of production of burnt gas predicted by LUSIE shows a clear increase later in the cycle compared to the experimental results. This is a result of the decreasing integral length scale reducing characteristic burn-up time τ_b as the flame travels into the "eaves" of the pent (Equation 4.39).

The reduction in length scale in the pent was added to the model on the basis of the pressure data available at the time as it improved considerably the correspondence between the experimental and predicted pressures. Whilst it is certainly plausible that the length scale decreases in the eaves given the reduction in clearance height, it would appear that the reduced burn-up time which results merely compensates in a rather un-physical way for the underpredicted flame area. That the flame has a larger active surface area in a real engine (discussed in detail in Section 5.3.7) is undoubtedly a significant source of error in thermodynamic models such as LUSIE. This error will be compounded by the fact that experimentally, different regions of the surface have different burning velocities, see for example Figures 5.38, 5.39 and 5.40.

Towards the end of the cycle, the area measured from the laser sheet images falls to zero whilst both the LUSIE and LUSIEDA areas continue to grow. In reality, none of the areas should be regarded as accurate as once the majority of gas has been burnt, any further combustion is likely to occur as remaining pockets of unburnt gas mix with burnt gas and oxidise slowly, rather than through con-

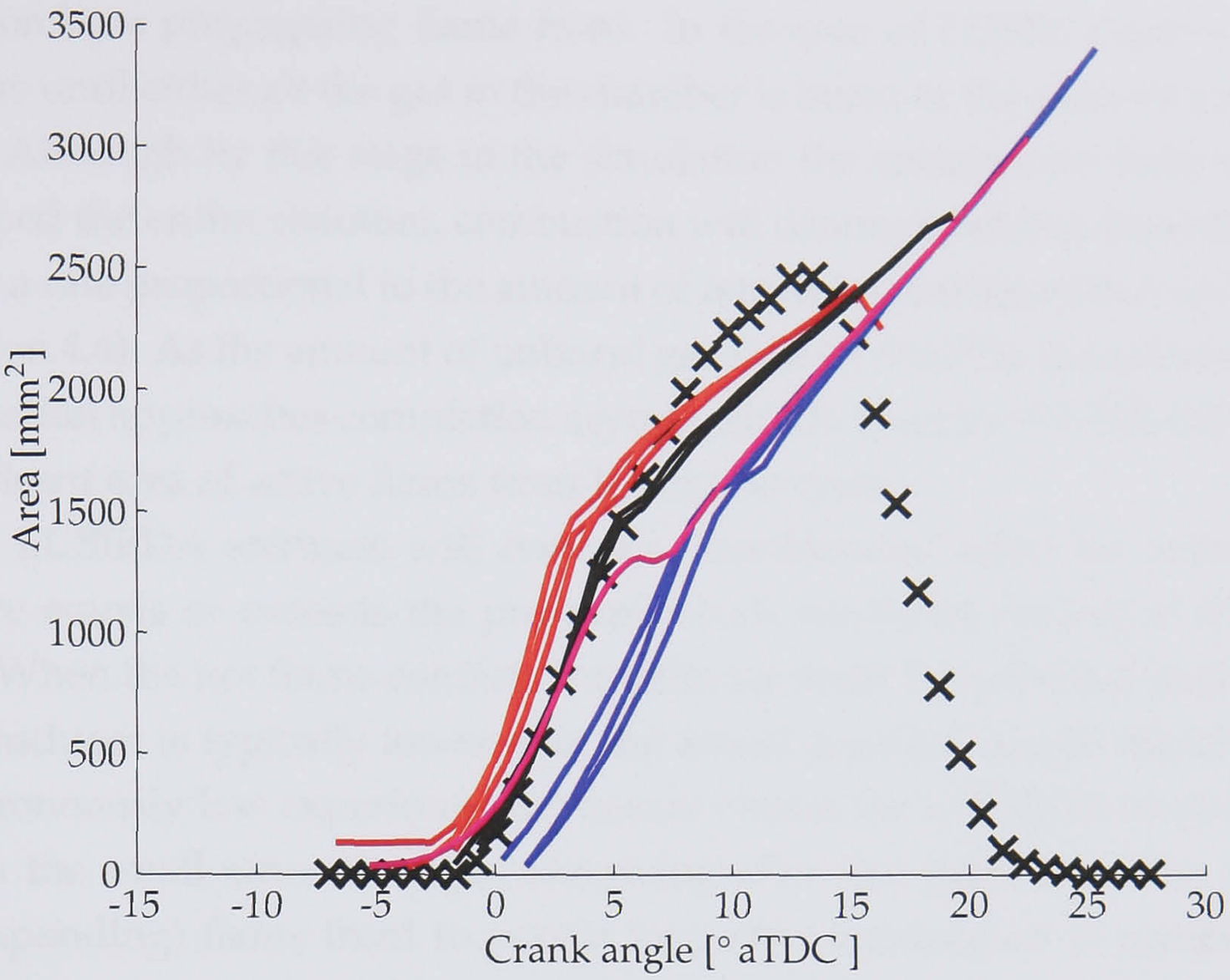

Figure 5.64: Flame active surface area derived from mean progress variable iso-surfaces (black crosses) compared with LUSIEDA calculated active surface areas for fast, middle and slow cycles, and the LUSIE predicted active surface area for LUPOE2-P at the 1500 rpm base condition. Line colours correspond with those used in Figure 5.62.

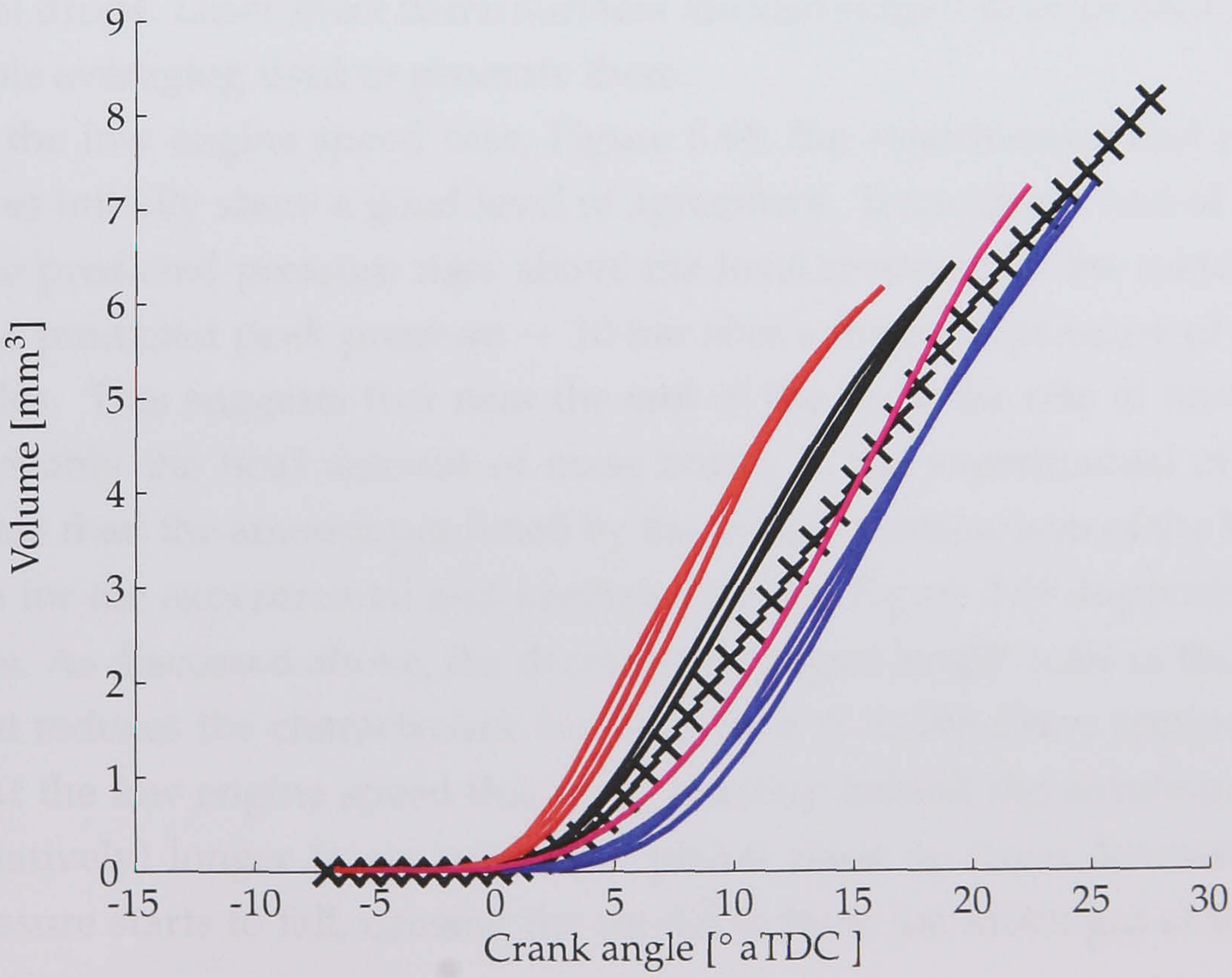

Figure 5.65: Flame volume derived from mean progress variable isosurfaces (black crosses) compared with LUSIEDA calculated burnt gas volumes for fast, middle and slow cycles, and the LUSIE predicted burnt gas volume for LUPOE2-P at the 1500 rpm base condition. Line colours correspond with those used in Figure 5.62.

sumption by a propagating flame front. In the case of LUSIE, combustion will continue until either all the gas in the chamber is burnt or the exhaust port/valve opens. Although by this stage in the simulation the entrainment front will have enveloped the entire chamber, combustion will continue behind the entrainment front at a rate proportional to the amount of remaining entrained but unburnt gas (Equation 4.4). As the amount of unburnt gas falls so does the rate of combustion. Combustion approaches completion asymptotically therefore LUSIE still predicts a significant area of active flame front late in the cycle.

The LUSIEDA software will continue "combustion" until the experimental pressure equals or exceeds the pressure which would be present if all the gas burnt. When the hot flame contacts the cylinder walls the pressure reading from the transducer is typically lower than the actual pressure due to thermal shock. This erroneously low experimental pressure causes the LUSIEDA analysis to fail to burn the small amount of gas remaining after this point allowing an active (and expanding) flame front to persist long after combustion is complete. The active area measured from the laser sheet images falls to zero as any region of the $\overline{c} = 0.5$ isosurface closer than 1.5 mm to the isosurface generated from the last camera frame (Section 3.3.11) is counted as inactive. Images were only taken inside the clearance volume whereas any combustion still happening is most likely occurring near the top land gap where gas will be returning to the chamber as the pressure drops. Laser sheet flame surfaces are also subject to error because of the ensemble averaging used to generate them.

For the low engine speed case, Figure 5.66, the experimental and predicted pressures initially show a good level of agreement. Towards the end of combustion, the predicted pressure rises above the level observed in the middle cycles with the predicted peak pressure $\sim$ 10 bar above the peak pressure of the middle cycles. This suggests that near the end of the cycle the rate of heat release, and probably the final amount of mass burnt, in the experimental cycles was much less than the amount predicted by the model. Comparison of the burnt gas volume for the experimental and predicted cycles, Figure 5.69 supports this hypothesis. As discussed above, the decreasing integral length scale in the eaves of the pent reduces the characteristic burn-up time τ_b as the flame approaches the wall. At the low engine speed this rapid burn-up behind the entrainment front has (relatively) longer to act before the piston starts to move downwards and the pressure starts to fall, causing the model to burn too much gas at the end of combustion.

The predicted flame radius, Figure 5.67, was very close to the flame radius derived from the mean progress variable field and the flame radii of the middle cycles estimated by LUSIEDA indicating that the bulk dimensions of the flame were similar in the model and the experiment. The predicted active surface area at a given crank angle, displayed in Figure 5.68, is underestimated and falls below the area calculated from the $\overline{c} = 0.5$ isosurface. As discussed above, this is related to the spherical flame assumption used by LUSIE.

The experimental middle cycles and predicted pressure trace for the medium engine speed (1000 rpm) case show a similar rate of pressure rise and combustion phasing. The predicted peak pressure is greater than the peak pressure of the middle cycles. Some rounding of experimental pressure traces close to the moment of peak pressure is known to occur due to thermal shock to the pressure transducer from flame front [Kuratle and Marki, 1992]. This causes a reduction in the experimental peak pressure which could explain the difference between the two peak pressure values. The predicted flame radius (discounting the very early stages where the experimental flame radii are unreliable) is close to the flame radius derived from the laser sheet data and the LUSIEDA calculated middle cycle flame radii until $\sim 7°$ aTDC. After this crank angle the experimental flame radii grow faster than the model predicts. Active flame areas predicted by LUSIE are lower than the area derived from the laser sheet images for a given crank angle indicating again that the truncated sphere flame geometry assumed by LUSIE under predicts the active surface area. The burnt gas volume of the middle cycles, laser sheet derived volume and predicted volume of burnt gas, depicted in Figure 5.73, are very similar. Given the good agreement between the experimental and predicted pressure traces this is to be expected.

5.5 Error analysis

Inevitably, any attempt to measure physical quantities will be subject to some error. Some sources of error can be minimised by good experiment design and careful work on the part of the operator. Other sources of error are random and caused by test-to-test variability in measurements. Finally, errors can be introduced by processing raw experimental data. This section attempts a simple analysis of the most obvious sources of error in the results presented above.

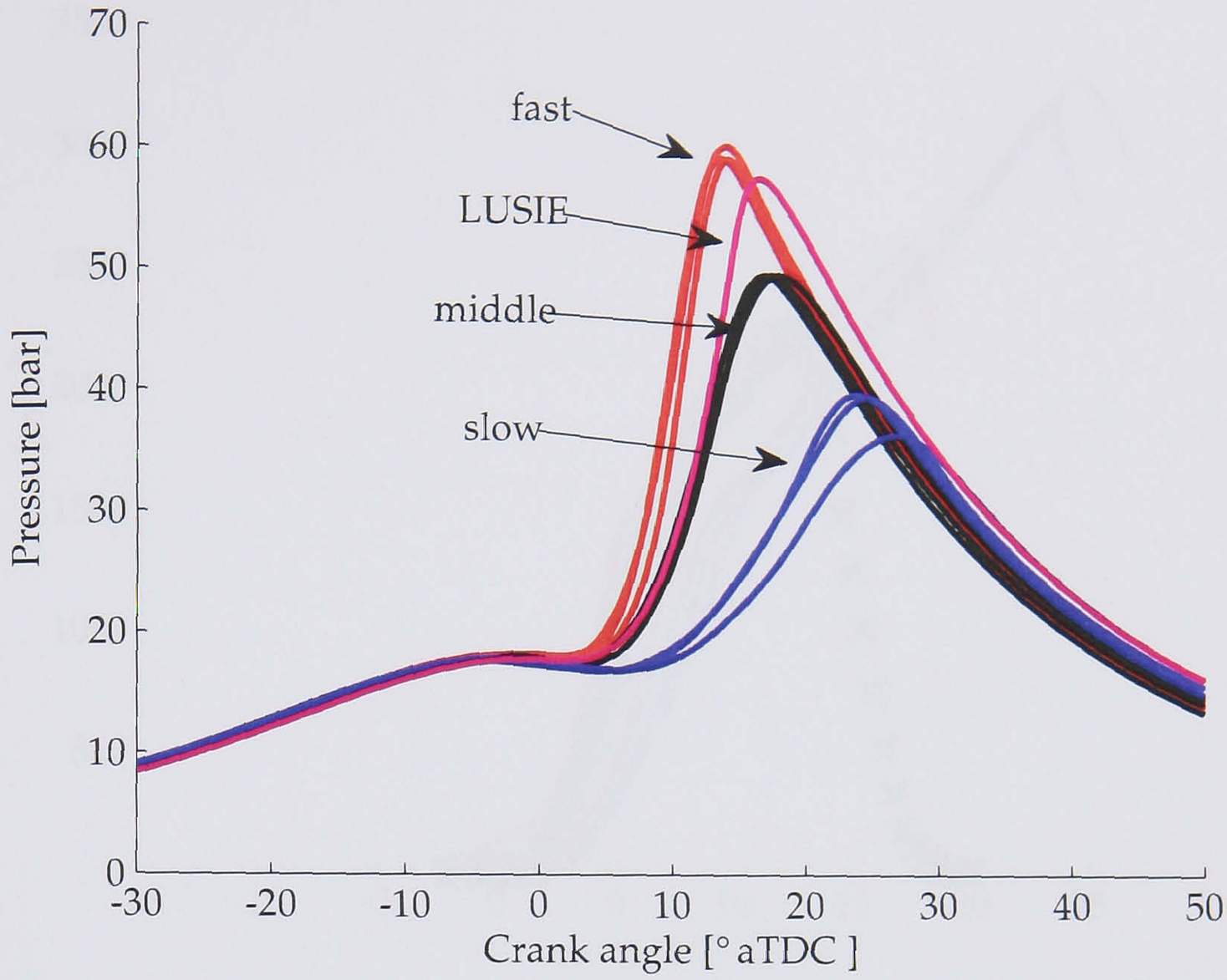

Figure 5.66: Cylinder pressure recorded in selected fast, middle and slow cycles compared with the LUSIE predicted pressure for LUPOE2-P at the 750 rpm operating condition.

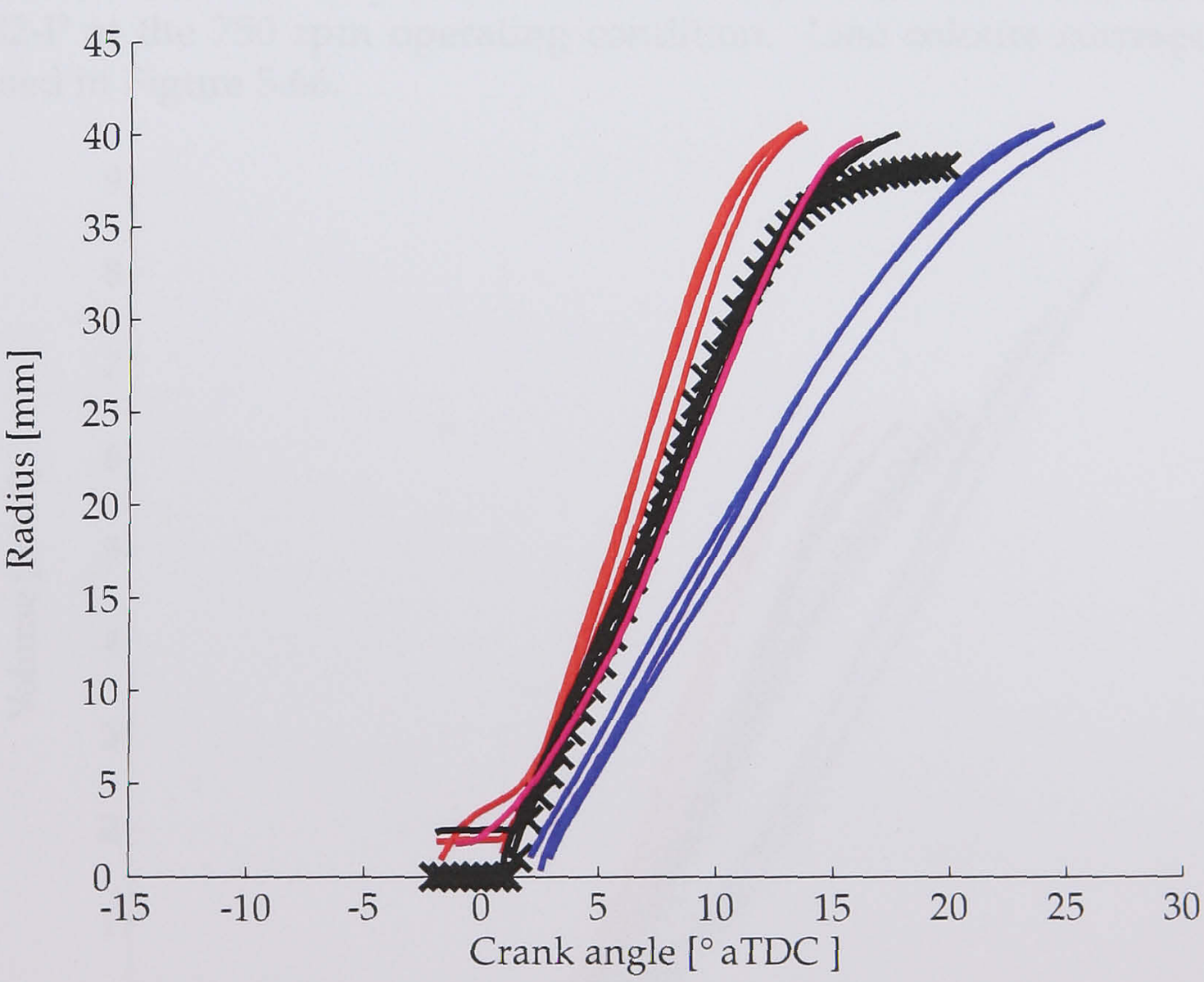

Figure 5.67: Burnt flame radius derived from mean progress variable isosurfaces (black crosses) compared with LUSIEDA calculated burnt flame radii for fast, middle and slow cycles, and the LUSIE predicted burnt flame radius for LUPOE2-P at the 750 rpm operating condition. Line colours correspond with those used in Figure 5.66.

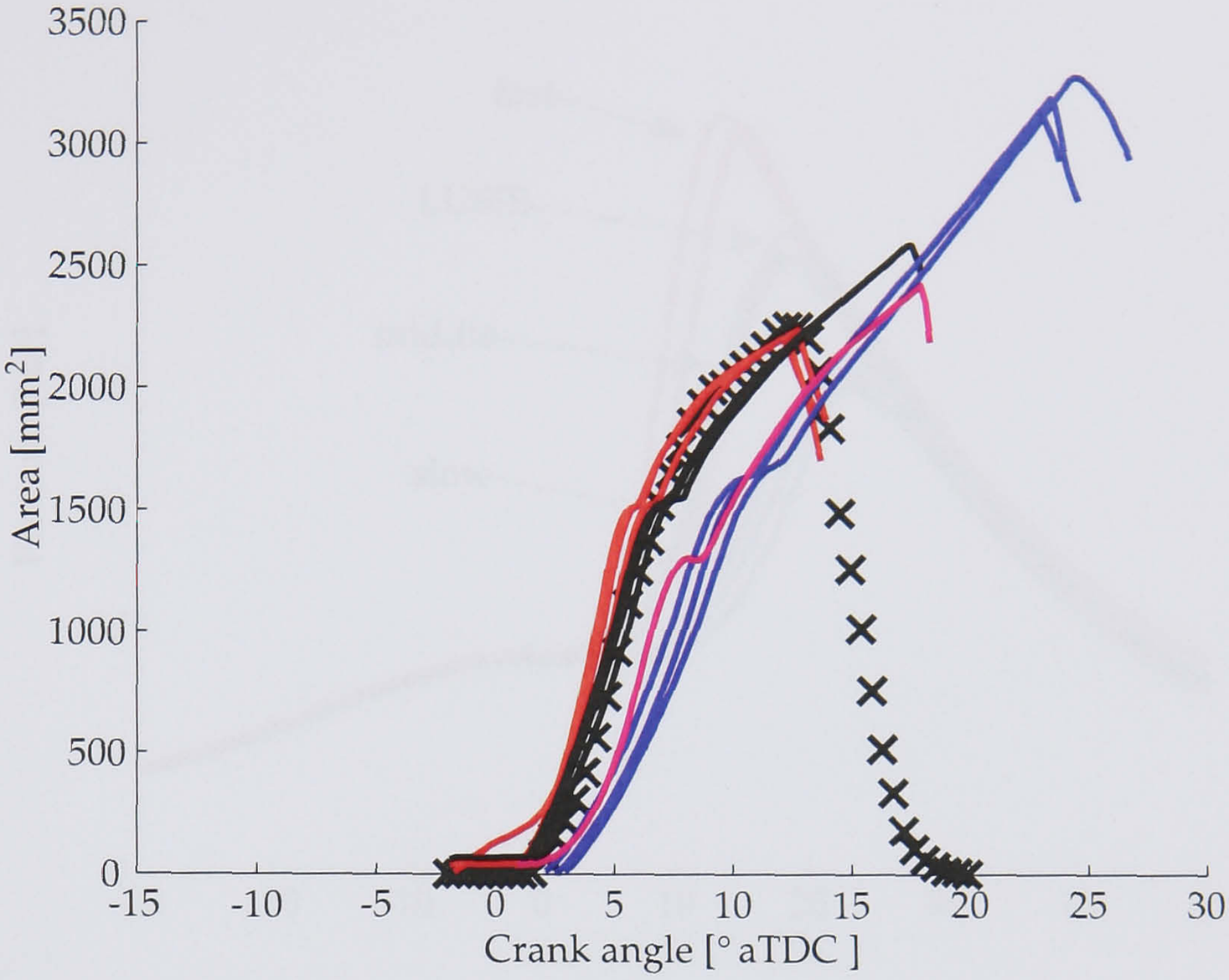

Figure 5.68: Flame active surface area derived from mean progress variable iso-surfaces (black crosses) compared with LUSIEDA calculated active surface areas for fast, middle and slow cycles, and the LUSIE predicted active surface area for LUPOE2-P at the 750 rpm operating condition. Line colours correspond with those used in Figure 5.66.

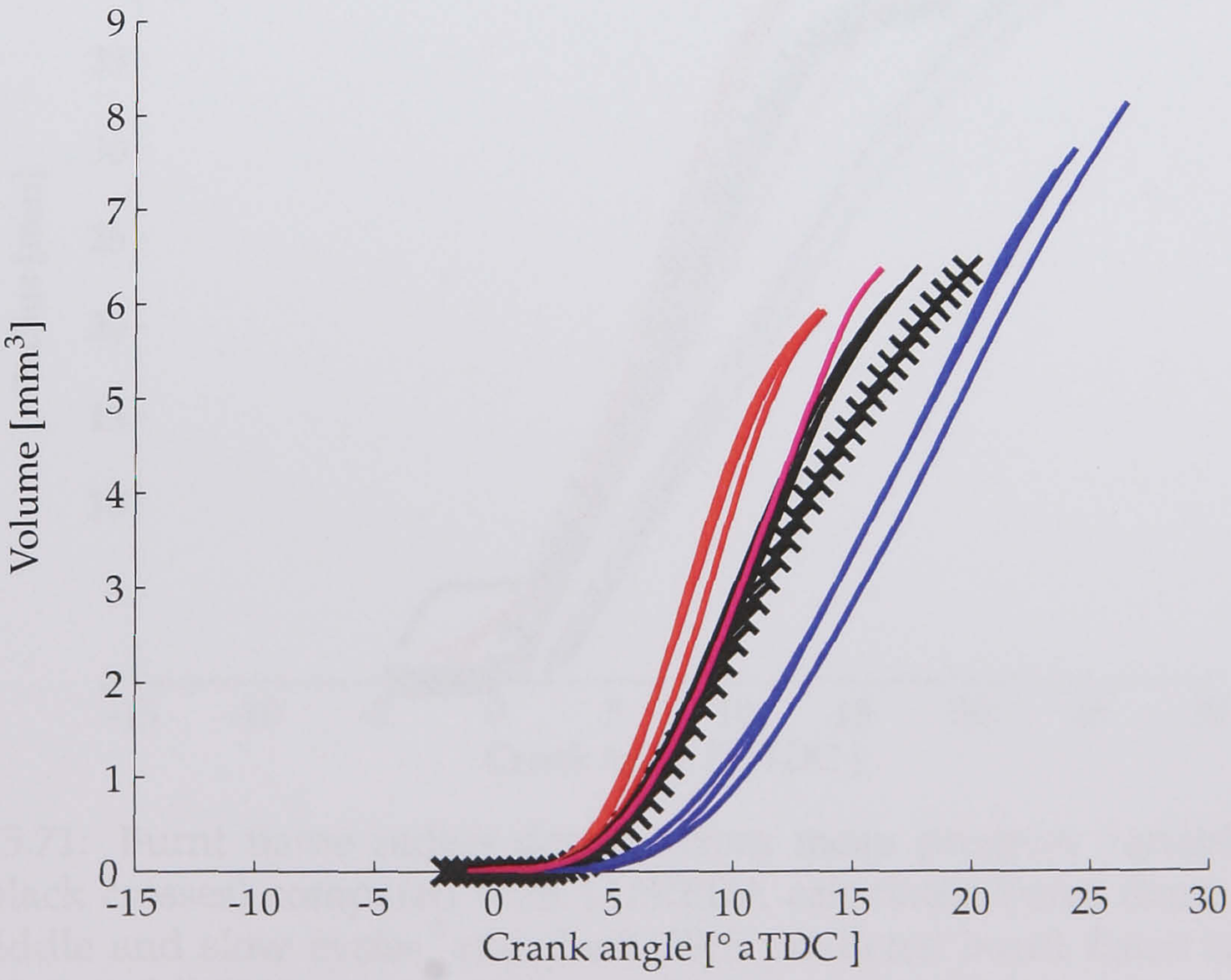

Figure 5.69: Flame volume derived from mean progress variable isosurfaces (black crosses) compared with LUSIEDA calculated burnt gas volumes for fast, middle and slow cycles, and the LUSIE predicted burnt gas volume for LUPOE2-P at the 750 rpm base condition. Line colours correspond with those used in Figure 5.66.

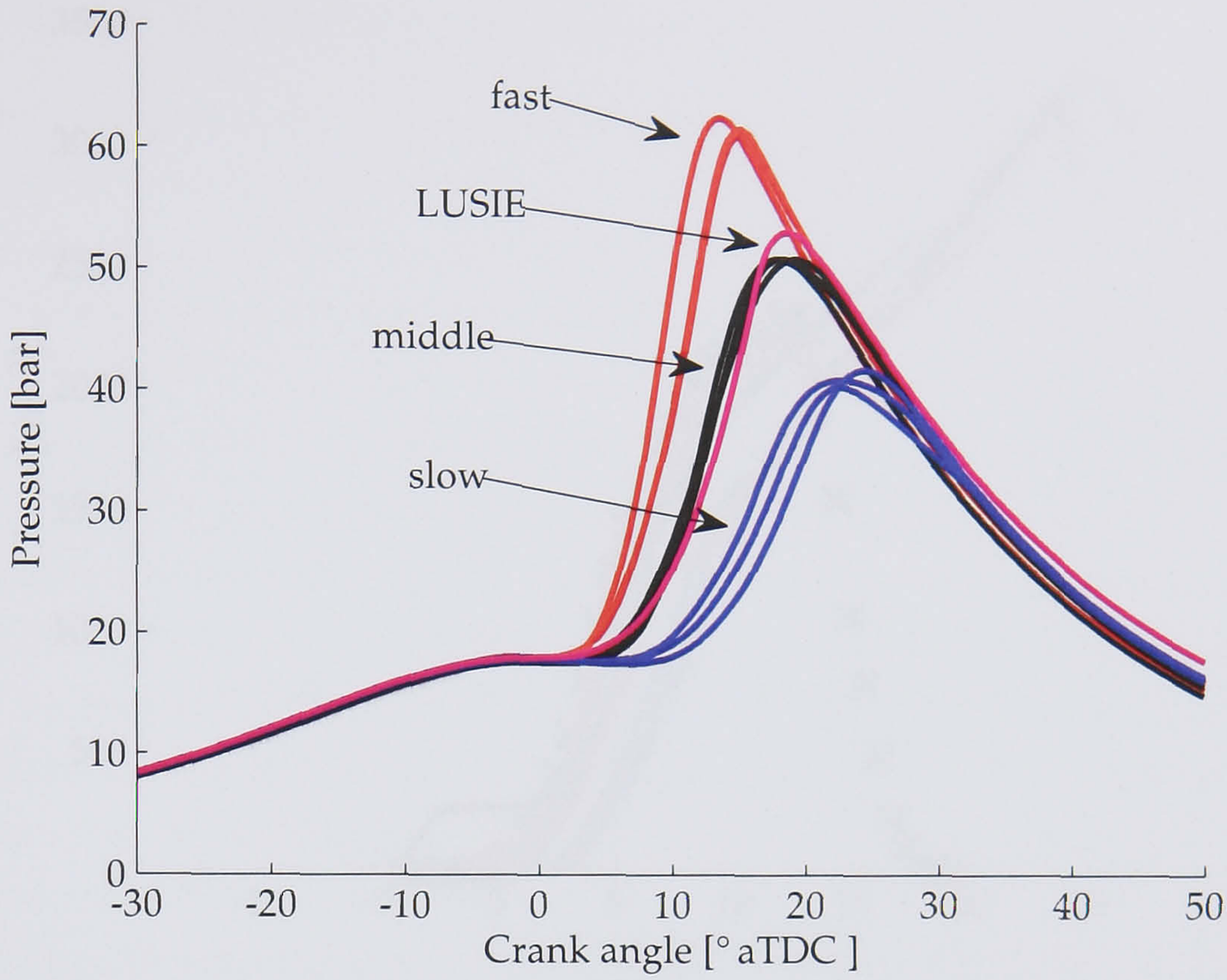

Figure 5.70: Cylinder pressure recorded in selected fast, middle and slow cycles compared with the LUSIE predicted pressure for LUPOE2-P at the 1000 rpm operating condition.

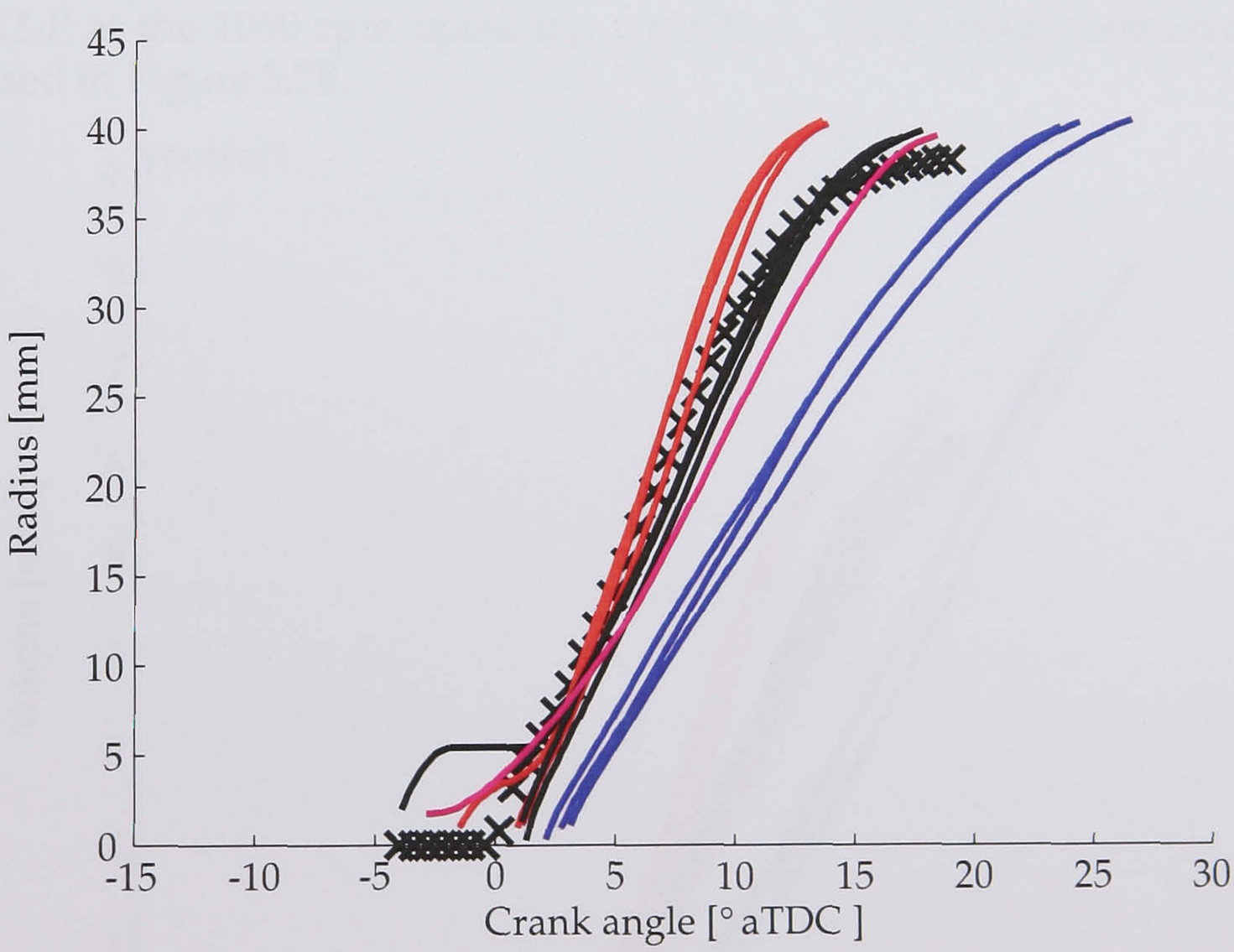

Figure 5.71: Burnt flame radius derived from mean progress variable isosurfaces (black crosses) compared with LUSIEDA calculated burnt flame radii for fast, middle and slow cycles, and the LUSIE predicted burnt flame radius for LUPOE2-P at the 1000 rpm operating condition. Line colours correspond with those used in Figure 5.70.

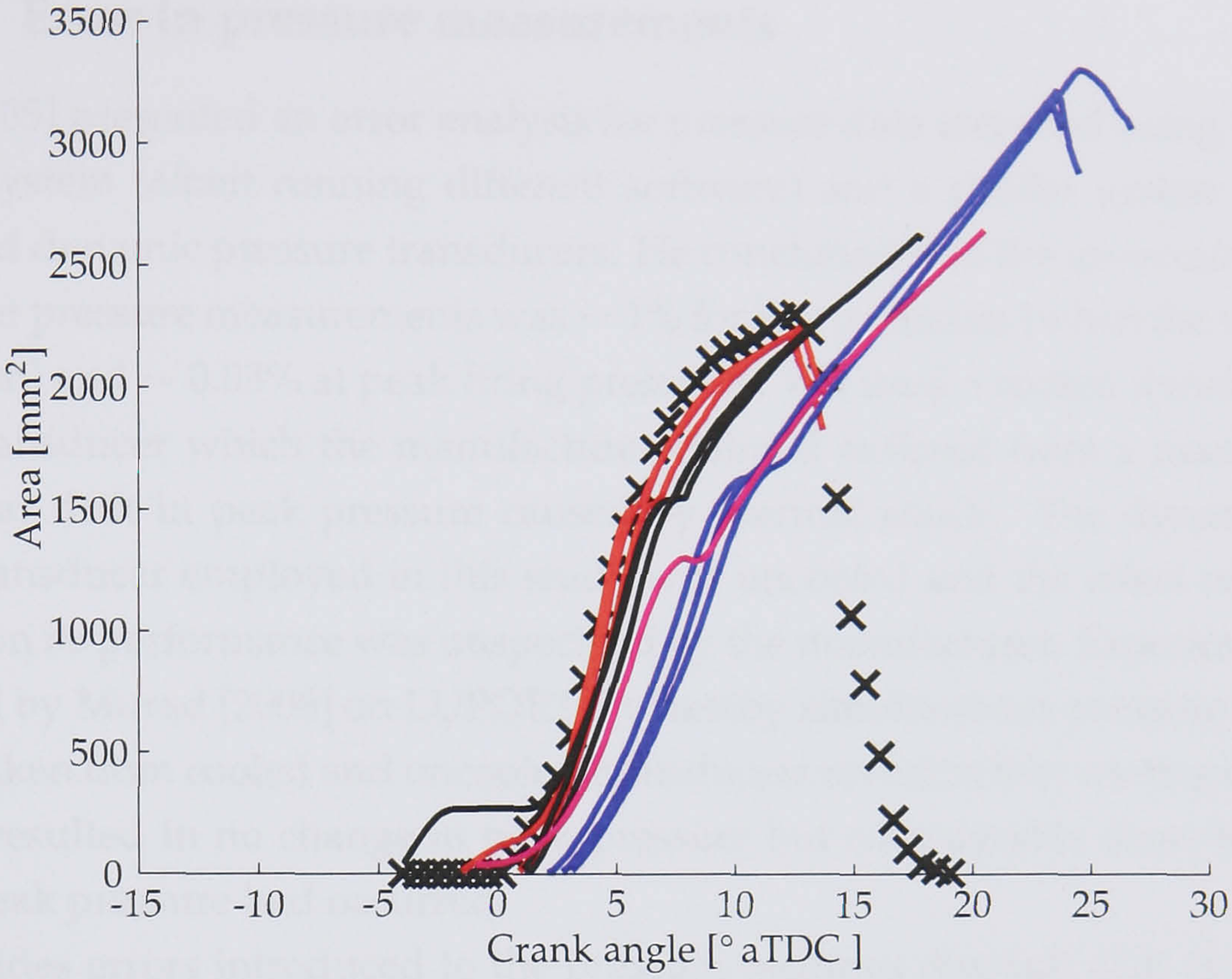

Figure 5.72: Flame active surface area derived from mean progress variable iso-surfaces (black crosses) compared with LUSIEDA calculated active surface areas for fast, middle and slow cycles, and the LUSIE predicted active surface area for LUPOE2-P at the 1000 rpm operating condition. Line colours correspond with those used in Figure 5.70.

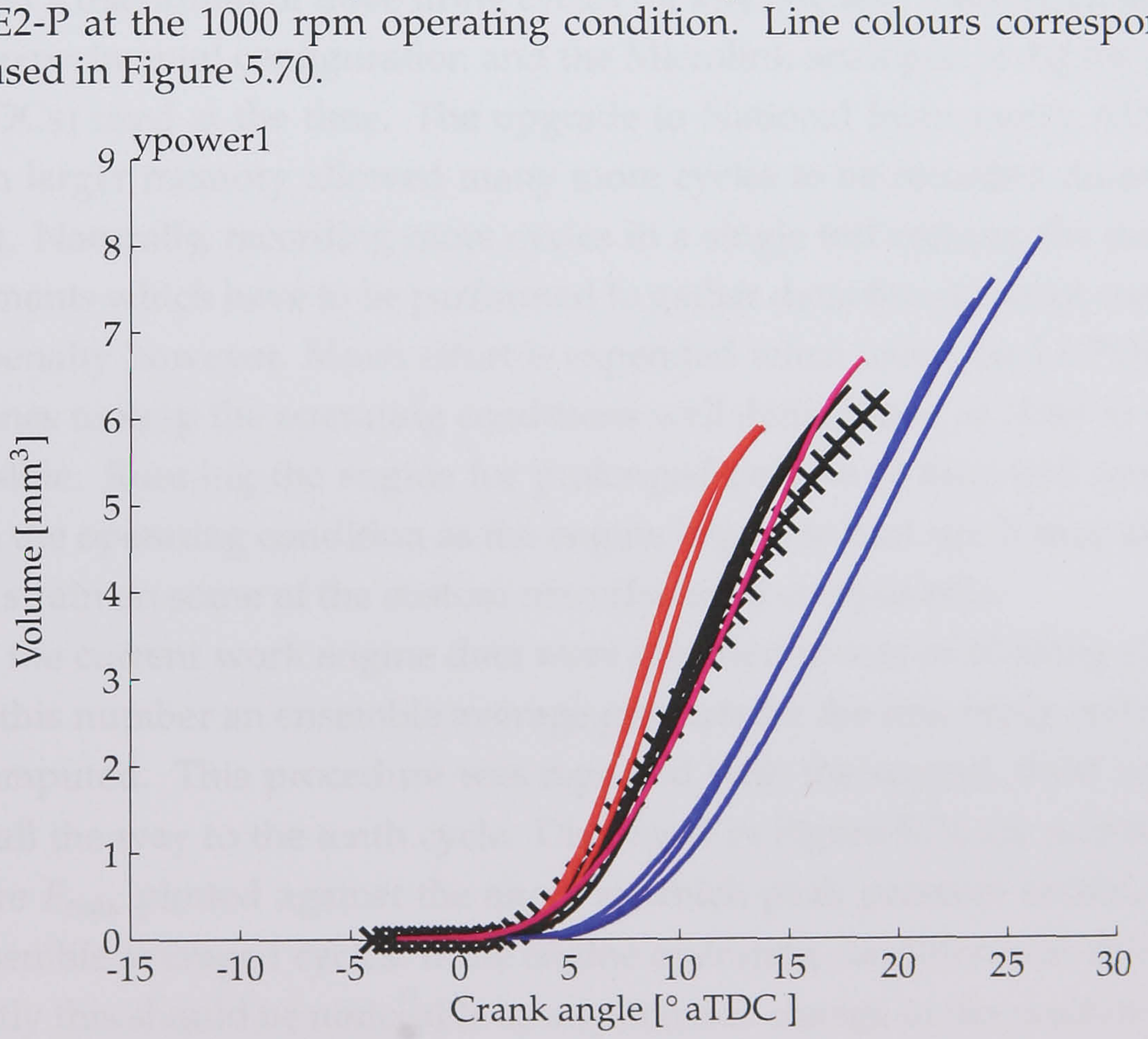

Figure 5.73: Flame volume derived from mean progress variable isosurfaces (black crosses) compared with LUSIEDA calculated burnt gas volumes for fast, middle and slow cycles, and the LUSIE predicted burnt gas volume for LUPOE2-P at the 1000 rpm operating condition. Line colours correspond with those used in Figure 5.70.

5.5.1 Error in pressure measurements

Wu [2005] presented an error analysis for pressure data recorded using the same DAQ system (albeit running different software) and a similar system of absolute and dynamic pressure transducers. He concluded that the uncertainty in the cylinder pressure measurements was $\sim 1\%$ for low pressures (when the valves/ports are open) and $\sim 0.03\%$ at peak firing pressures. Wu used a cooled dynamic pressure transducer which the manufacturer claimed suffered from a maximum of ± 0.2 bar drift in peak pressure caused by thermal shock. The dynamic pressure transducer employed in this study was uncooled and the effect of thermal shock on its performance was unspecified by the manufacturer. Experiments performed by Murad [2006] on LUPOE2-P whereby simultaneous pressure readings were taken from cooled and uncooled transducers revealed that cooling the transducer resulted in no change in peak pressure but considerable short term drift after peak pressure had occurred.

Besides errors introduced to the pressure readings through drift in the pressure transducers, an additional source of error is drift in the engine operating condition. The previous LUPOE2-P experiments reported by Murad [2006] had recorded a maximum of three firing cycles for any one test. This was a limitation of the experimental configuration and the Microlink analogue to digital converters (ADCs) used at the time. The upgrade to National Instruments ADCs with a much larger memory allowed many more cycles to be recorded during a single test. Naturally, recording more cycles in a single test reduces the number of experiments which have to be performed to gather data; this does not come without a penalty however. Much effort is expended when using the LUPOE family of engines to keep the operating conditions well defined and as close to constant as possible. Running the engine for prolonged periods of time will cause some drift in the operating condition as the engine begins to heat up. It may also place undue strain on some of the custom manufactured components.

For the current work engine data were recorded in sets of 10 firing cycles. To justify this number an ensemble average pressure for the first firing cycle per test was computed. This procedure was repeated with the second, third and so on cycles all the way to the tenth cycle. Displayed in Figure 5.74 are points of peak pressure P_{max} plotted against the angle at which peak pressure occurs $\theta_{P_{\text{max}}}$ for the ensemble averaged cycles. If the engine operating condition was drifting significantly this should be noticeable as a systematic change in the position of these points. That there was no significant movement in their position, nor any differ-

ence in the pressure traces for the complete ensemble averaged cycles (not shown here) indicates that the engine operating condition does not change significantly over 10 firing cycles. It is recommended that future workers continue this investigation as collecting larger numbers of cycles in fewer tests would enable either 1) full experimental programs to be conducted in shorter periods of time or 2) greater numbers of cycles, with an associated increase in the confidence interval for any statistics derived from them, to be collected.

5.5.2 Error in optical measurements

The Mie scattering images of combustion recorded with the high speed digital camera are limited to a certain finite spatial resolution. With the camera operating at 10 kHz the maximum number of pixels available was 512×512 giving an approximate spatial resolution of 0.16 mm per pixel assuming the entire 80 mm bore was imaged. The resolution of the camera optics was quantified using a United States Air Force resolution test chart purchased from Edmund Optics and found to be 2 line pairs per millimetre, 0.5 mm resolution, in the worst case. The resolution of the camera system therefore significantly exceeds the 1.5 mm resolution[10] of the volume data space the images were subsequently transferred to.

Following their recording, the captured images were averaged to yield mean progress variable $\bar{c}$ contours. With the averaging of an infinite number of images the calculated $\bar{c}$ contours will be stable. Obviously for any real experiment it is only possible to collect a finite number of images hence some compromise must be made between the accuracy of the final result and the amount of time taken to complete the experiment. If it is assumed that the sample size is large enough that the progress variable deviation from its mean can be approximated by the normal distribution then for an average of n images a 95% confidence interval is given by

$$\bar{c} \pm 1.96 \frac{\sigma}{\sqrt{n}} \tag{5.16}$$

The population standard deviation σ is necessarily greatest where $\bar{c} = 0.5$, here exactly half the pixels have the value zero and half one hence $\sigma = 0.5$. Taking this figure as a worst case estimate of the population standard deviation, in order to be 95% confident that $\bar{c} = 0.5 \pm 0.05$, an estimate of $\bar{c}$ should be calculated using a minimum of 385 images. In other words, if a set of 385 images are averaged the

[10]The spacing between the laser sheets was 1.5 mm, limiting the maximum resolution of the data in post processing.

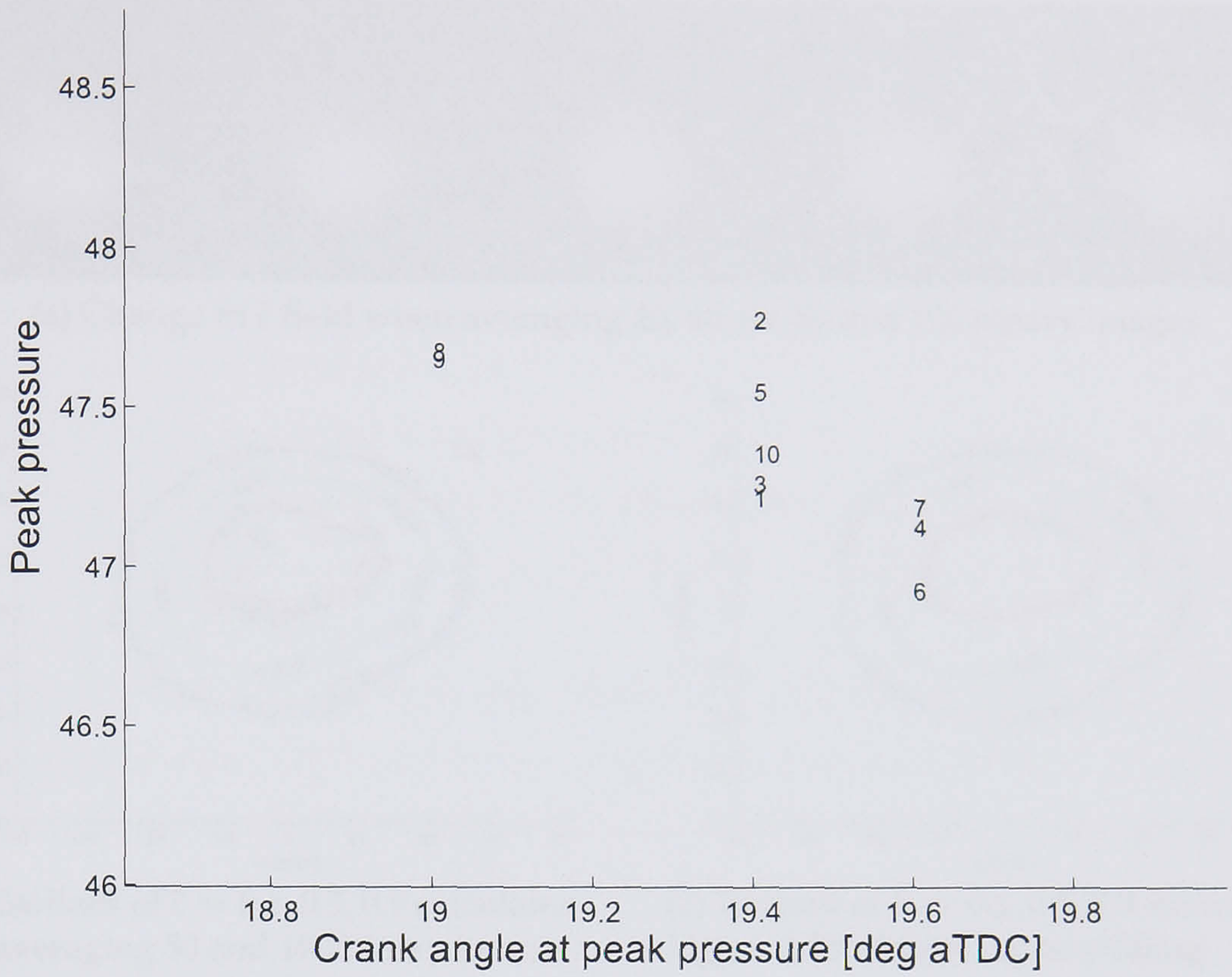

(a) Individual ensemble averaged cycles.

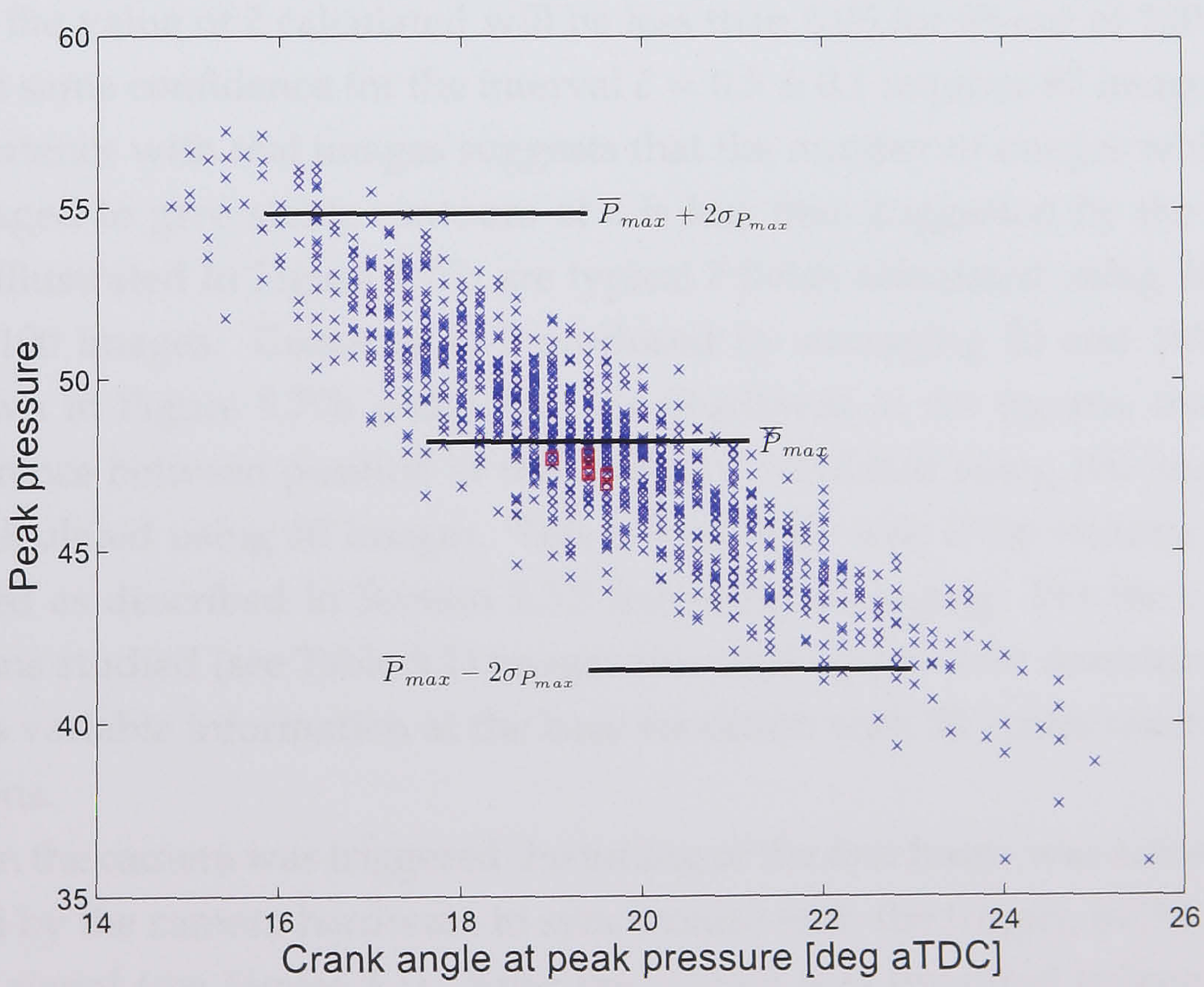

(b) Individual ensemble averaged cycles compared with the entire data set.

Figure 5.74: Positions of $P_{\max}$ plotted against $\theta_{P_{\max}}$ for ensemble averaged first, second, third etc. cycles from individual data sets recorded on LUPOE2-P at the 1500 rpm base condition. Numbers in Figure 5.74a denote the cycle number to which each point relates. Red points in Figure 5.74b correspond to the numbers in Figure 5.74a whilst blue points show the position of $P_{\max}$ against $\theta_{P_{\max}}$ for all of the cycles in the data set.

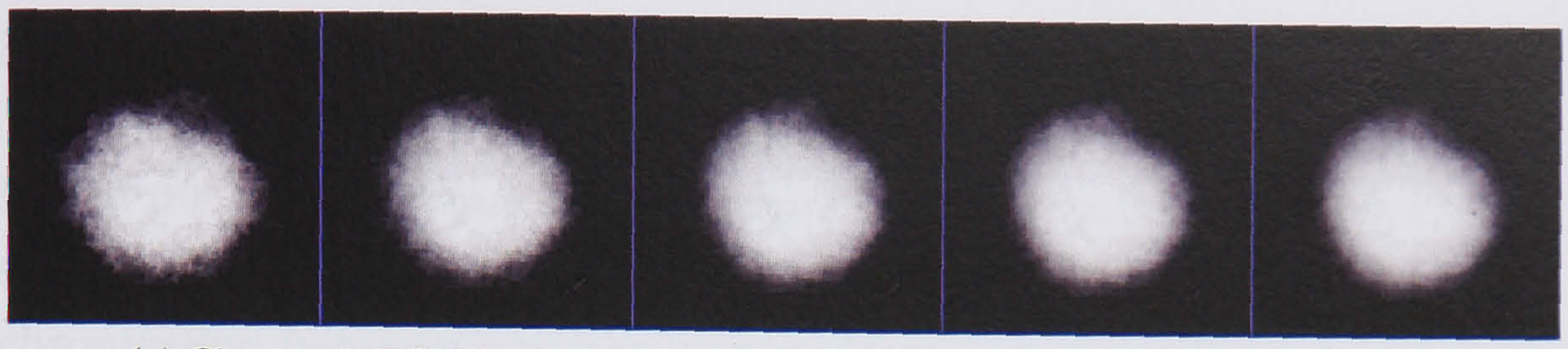

(a) Change in $\overline{c}$ field when averaging 20, 40, 60, 80 and 100 binary images.

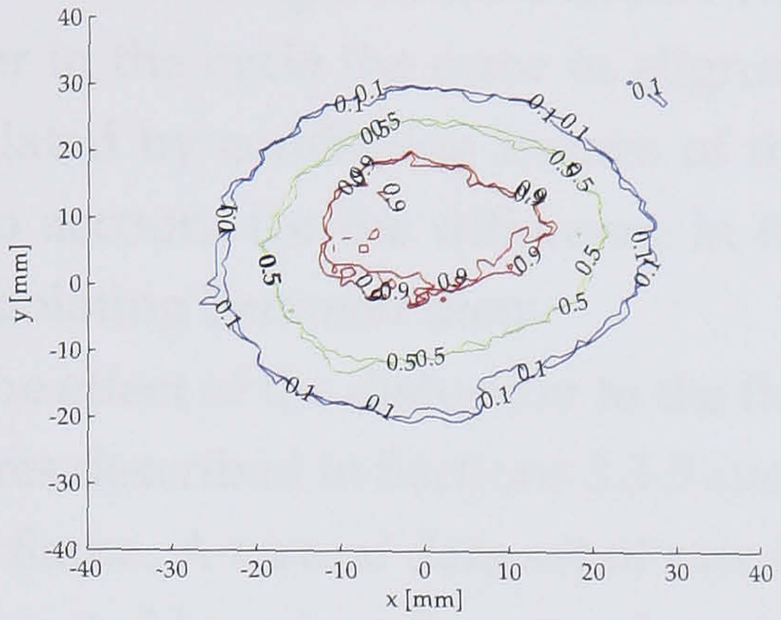

(b) Isolines of $\overline{c} = 0.1, 0.5, 0.9$ calculated by averaging 50 and 100 binary images.

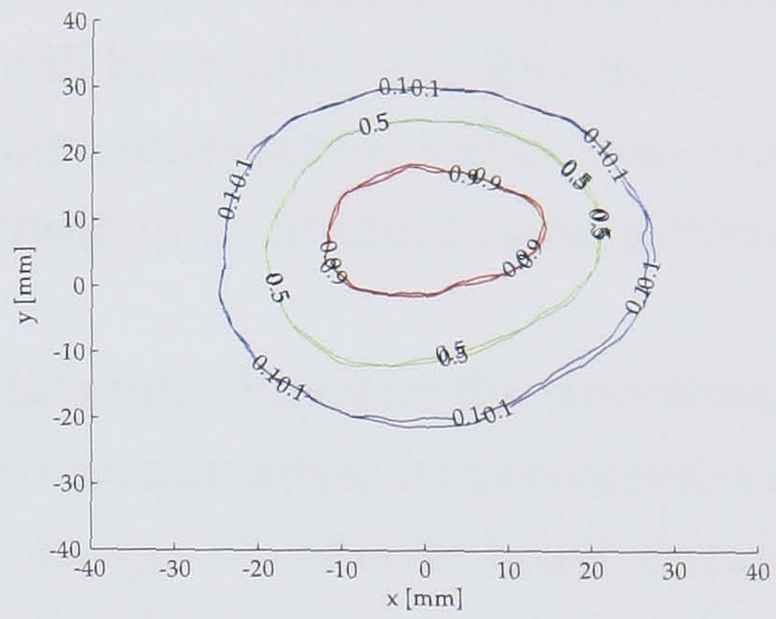

(c) Isolines of $\overline{c} = 0.1, 0.5, 0.9$ shown in Figure 5.75b following smoothing.

Figure 5.75: Change in $\overline{c}$ calculated using increasing numbers of binary images

error in the value of $\overline{c}$ calculated will be less than 0.05 for 95 out of 100 sets. To have the same confidence for the interval $\overline{c} = 0.5 \pm 0.1$ requires 97 images.

Experience with real images suggests that the number of images which must be averaged to give stable contours of $\overline{c}$ is less than suggested by the analysis above. Illustrated in Figure 5.75a are typical $\overline{c}$ fields calculated using 20, 40, 60, 80 and 100 images. Contours of $\overline{c}$ produced by averaging 50 and 100 images are shown in Figure 5.75b and 5.75c. As illustrated in the figures, there is little difference between position of the contours calculated using 100 images and those calculated using 50 images. This is especially true if the volume data are smoothed as described in Section 3.3.5 following averaging. For the operating conditions studied (see Table 5.1) images from 100 cycles were combined to give progress variable information at the base condition with 50 cycles taken at other conditions.

When the camera was triggered the timing of the first frame was automatically adjusted by the camera hardware to synchronise with the trigger, in this case the ignition signal (see Figure 3.1). After the camera was triggered subsequent images were recorded at 10 kHz hence small cycle-to-cycle and intra-cycle variations in engine speed and test-to-test variations in the dynamometer set speed could cause the relative timing of the camera frames to drift. Post processing of the

data recorded by the DAQ system revealed that, for the worst case, close to the end of combustion when the engine was running at 750 rpm, the standard deviation in the timing of individual camera frames was less than 0.6° CA. As the time between frames is approximately 0.45° CA at this engine speed the error in synchronisation between any two camera frames at the end of combustion is of the order of a single camera frame. For higher engine speeds or frames recorded earlier in the cycle the error in alignment will be smaller. For this reason, $\overline{c}$ was calculated by combining frames of the same enumeration rather than attempting to account for the difference in the timing of individual camera frames by interpolating between them.

The effect of the distortion to the flame data introduced by the smoothing procedures described in Sections 3.3.5 and 3.3.6 was quantified by processing a simulated flame. A virtual data set of raw flame images of different brush thicknesses was created based on the error function profile thought to govern the $\overline{c}$ distribution of turbulent flames (Equation 4.33). These virtual flame then expanded over five time steps at a rate of 1 mm per step and the "images" were processed to give the flame speed, surface area, volume and brush thickness as described in Chapter 3. The processing was performed once in full and once with the smoothing steps omitted.

The influence of the data smoothing techniques on the calculated flame speed, surface area and volume were minimal. All of these parameters were underestimated fractionally because of the triangulation of the convex isosurface but whether the data were smoothed before processing or not made little difference to the calculated values.

The flame brush thickness was not affected by smoothing providing the flame was significantly thicker than the 1.5 mm resolution of the measurement volume, shown in Figure 5.76. At flame thicknesses below 3 mm the relationship between the specified thickness δ_t (i.e. the thickness used when generating the flame using the error function) of the simulated flame, and the thickness defined by the gradient δ_{tg} and isosurface δ_{ts} methods measured using the processing procedures in Section 3.3.9, departed from linearity.[11] This occurred regardless of whether the simulated flames were smoothed or not although, as would be expected, where the flame was smoothed the effect was greater due to the "smudging" caused by the smoothing algorithms. For values of δ_t greater than 3 mm the difference

[11]Note that the flame thicknesses determined by both the gradient and slope methods are 1.8 times greater than the thickness specified by an error function. This relationship is derived in Section 5.3.3.

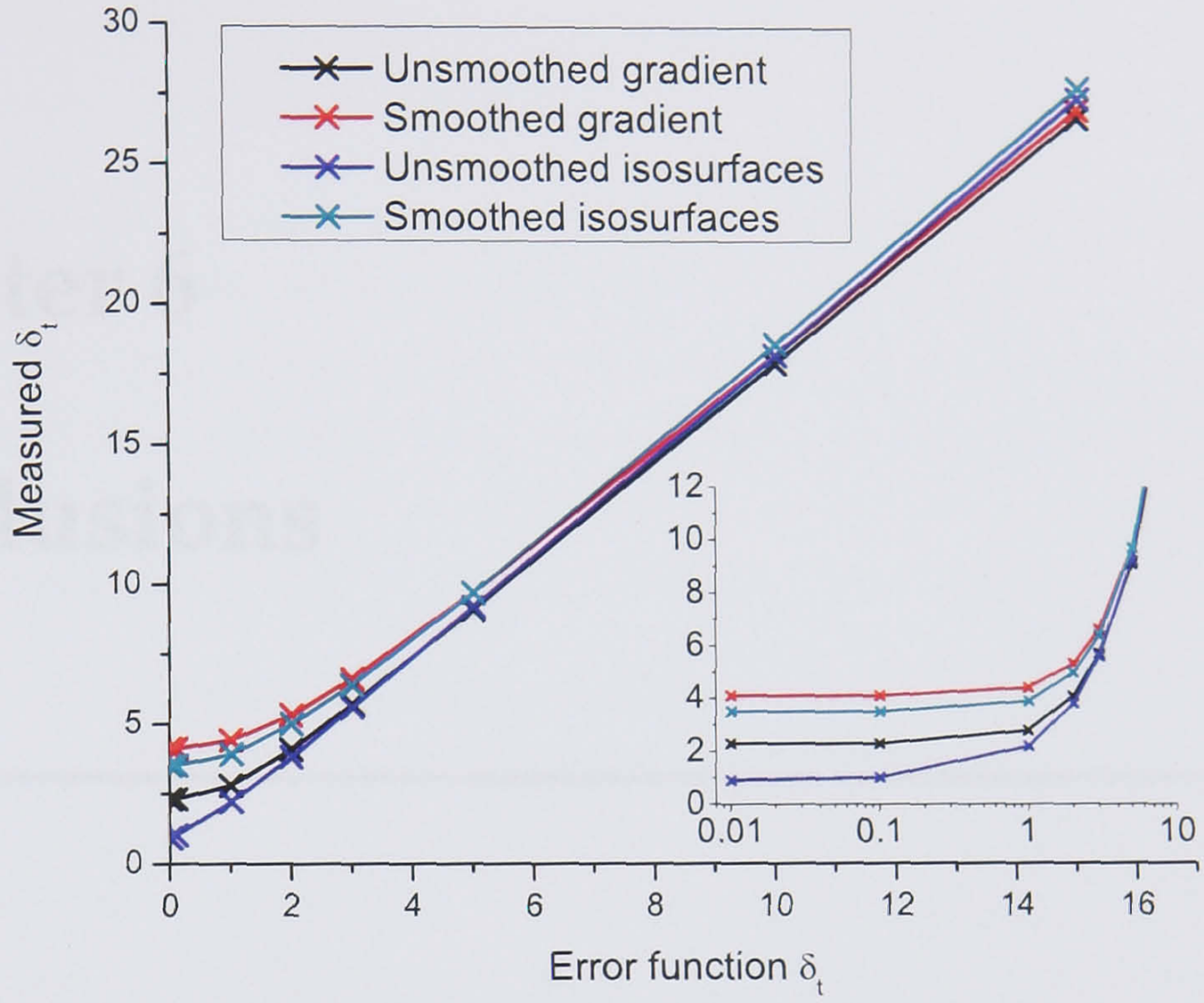

Figure 5.76: Flame thicknesses calculated from simulated spherical flames with and without data smoothing.

between δ_{tg} and δ_{ts} calculated with and without smoothing was very small.

Chapter 6

Conclusions

6.1 Conclusions to the current work

As a result of the experimental investigations presented in Chapter 5 the three-dimensional time varying mean progress variable field in a spark ignition engine has, to the authors knowledge, been directly measured for the first time. If nothing else, this dataset provides a valuable resource against which spark ignition engine combustion simulation software can be evaluated. In particular, Reynolds averaged Navier-Stokes simulations produce an output of this form and the comparison of such a simulation with the presented experimental data would be a beneficial exercise. Preliminary particle imaging velocimetry experiments performed by the author in conjunction with Mr A. Dawood [2007] suggest that simultaneous measurements of flame position and fluid flow in the unburnt gas are possible. Prediction of three-dimensional ensemble averaged flame position and gas flow measurements would be a formidable test for any computational fluid dynamic model and this avenue should be pursued in the future.

From the experimental results themselves some interesting conclusions can be drawn, see Chapter 5. These are presented in abridged format below.

- The flame was observed to be convected by the flow field in the combustion chamber. The direction of convection was observed to change with engine speed suggesting that the direction of tumble rotation is influenced by the

engine speed (also noted by Murad [2006]). Some problems with the use of the barycentre to define the position of the centre of the flame were discussed and two alternative definitions were suggested for future study.

- A relationship between two different measures of flame brush thickness was derived mathematically and confirmed experimentally. A definition of brush thickness based on the spatial derivative of the mean progress variable field is recommended for future work. The local flame brush thickness was observed to grow to a maximum of around 14 mm independent of the engine speed and decrease in the vicinity of the combustion chamber walls.

- The local turbulent burning velocity derived from the movement of iso-surfaces of the mean progress variable was observed to have a maximum value for a given engine speed and decrease as the flame approached the combustion chamber walls. A theoretical explanation for this decrease was suggested and a mathematical relationship between the burning velocity of an unconstrained flame and a flame in the vicinity of the wall was derived which showed good agreement with the experimental results.

- The flame acceleration in a turbulent combustion vessel and an engine was found to collapse onto a common curve when plotted against normalised flame radius but not when plotted against normalised time since ignition. This finding was surprising as dimensional arguments suggest that, given the characteristics of the turbulence and vessels, flame acceleration should primarily be a function of the time elapsed since ignition.

  Several published models of flame acceleration were incorporated into the LUSIE code and their performance evaluated using the two-zone combustion model. All of the models were found to predict an initial rate of flame acceleration which significantly exceeded the acceleration of the measured engine flames.

- The ensemble averaged flame surface recorded in LUPOE2-P appears to be close to spherical during the period immediately after ignition. As combustion progresses and the flame comes into the vicinity of the combustion chamber walls the profile of the advancing flame front becomes "swept back" and the flame geometry conforms to the shape of the combustion chamber. The previously discussed decrease in burning velocity in the vicinity of a wall is likely to be at least partially responsible for this phenomenon.

The purpose of gathering the experimental data discussed above was not only as a fundamental research exercise into spark ignition engine combustion but also to provide a database against which the LUSIE combustion simulation code could be compared. Previous research at the University of Leeds [Abdi Aghdam, 2003] attempted to use the LUSIE software to simulate combustion in a quiescent flow disc chamber engine, LUPOE1-D. One of the aims of this research was to apply the same code, with improvements and modifications where necessary, to simulate combustion in a pent-roof engine. The ultimate motivation is the prospect of using a code such as GT-LU for virtual engine development in a commercial environment. The main points arising from the comparison between the experimental data, subsequent pressure reverse analysis using LUSIEDA, and LUSIE predicted qualities are summarised below:

- Given the great range of laminar burning velocity measurements reported in the literature and the importance of this parameter as a fundamental model input, an attempt was made to determine the suitability of the different laminar burning velocity correlations for use in simulations of spark ignition engines. It was found that, given a suitable choice of the combustion model constants, all of the laminar burning velocity expressions used gave good agreement with pressure and flame radius data measured on the LUPOE1-D engine at the reference condition. With changes in engine operating condition the quality of this agreement deteriorated. It proved impossible to draw definite conclusions as to the "best" laminar burning velocity model as the variation in end gas temperature and pressure history was small over the range of engine operating conditions for which experimental data were available.

- In order that future research efforts may be focused in the most effective direction a sensitivity study was conducted to determine which model inputs had the greatest bearing on the simulation results. The three-zone combustion model was most sensitive to changes in the laminar burning velocity and the integral length scale, both quantities which are difficult to measure accurately in conditions which are relevant for engine combustion. In contrast, the two-zone model was found to be greatly influenced by the choice of expression used to determine the deceleration of the flame in the vicinity of a wall.

- Realistic predictions using the LUSIE software have only previously been

obtained using the three-zone combustion model. The introduction of a robust expression for the deceleration of a turbulent flame as it approaches a wall greatly improved the two-zone model predictions. In order to make the two-zone model a viable option for spark ignition engine simulations an alternative flame acceleration model is required as the rate of flame acceleration predicted by the Zimont-Lipatnikov expression was much larger than that observed experimentally.

A number of different flame acceleration expressions reported in the literature were added to the LUSIE code and predictions using them were compared with experimental data recorded at different operating conditions on the disc chamber LUPOE1-D engine. It was found that all of the evaluated expressions predicted an initial rate of flame acceleration which was in excess of the experimental data.

- The three-zone combustion model was used to simulate combustion in the pent-roof LUPOE2-P with combustion model constants determined as a best fit in the least squares sense to pressure and flame radius data recorded at one operating condition on LUPOE1-D. For the three engine speeds for which data were collected during the current study the simulation results matched well the experimental pressure. After the initial period of propagation, flame active areas predicted by LUSIE and calculated using LUSIEDA were lower than the active area determined using the Mie scattering laser sheet images. This is most probably due to the departure of the flame from the form of a truncated sphere, as assumed by LUSIE and LUSIEDA, caused by the deceleration of the flame as it approaches the wall. Convection of the entire flame by the flow inside the combustion chamber will also alter the active flame area.

- Two assumptions were used when modelling the pent-roof LUPOE2-P. These were that 1) the integral length scale of turbulence decreased as the flame travelled into the "eaves" of the pent and 2) the flame centroid was convected towards the centre of the combustion chamber early in the cycle. The use of the second of these assumptions was justified by the experimental measurements presented in this thesis and also the work of Murad [2006]. The use of the first of the assumptions is not supported by any experimental measurements of the turbulence in the LUPOE2-P combustion chamber but was found to significantly improve the model predictions. Given the

observation that the active flame area is quite significantly underestimated by the LUSIE code late in the cycle it is likely that the reduced burn-up time which results from decreasing the integral length scale as the flame travels into the eaves of the pent roof merely compensates for the under predicted active surface area. Analysis of the Mie scattering images recorded as part of the current work to determine whether the integral scale of flame wrinkling (see, for example, Hicks et al. [1994], Gillespie [1998], Cairns [2001]) does indeed decrease as the flame travels into the eaves of the pent would provide much needed experimental support for the continued use of this assumption.[1]

6.2 The future of SI engine combustion simulation and directions for further research

In concluding a similar study four years previously, Abdi Aghdam [2003] asked the question "do thermodynamic engine models with turbulent entrainment burning models have a future?" He concluded that, whilst their capability as a truly predictive model paradigm was perhaps limited their strength lay "trend prediction". Given the advances in computing power and computational fluid dynamic (CFD) simulations which have taken place since 2003 it is perhaps time to reexamine that conclusion.

In the near term, quasi-dimensional models and CFD will probably continue to have complementary roles. Reynolds averaged Navier Stokes (RANS) type formulations are restricted by their limited predictive capability and the more promising large eddy simulation (LES) type models require prohibitively large computational resources. Satisfactory simulations of two very different engines have been obtained during the current study and the previous study by Abdi Aghdam [2003] using a simple quasi-dimensional model, demonstrating that such models are still useful. That the model will complete a simulation in under twenty seconds with no need for complex meshing or other preprocessing steps is in marked contrast to even the most basic CFD models, the predictive capa-

[1] It is probable that the turbulence is anisotropic in the eaves of the pent therefore it is possible that any subsequent analysis of flame wrinkling in images from a plane normal to the bore axis may not reveal a decrease in its integral scale. A better experiment would be to examine (directly if possible, rather than inferred from flame wrinkling) the spatial variation in the integral scale in the axis of the cylinder bore.

bility of which are arguably no better. Parametric studies such as Abdi Aghdam et al. [2007] are impossible using RANS models and will remain impractical using CFD for a long time to come.

In the long term, the future of quasi-dimensional models is probably not good. Just as in the discipline of solid mechanics finite element analysis has displaced the more traditional analytical stress analysis in all but the simplest of cases, so computational fluid dynamics is likely to displace thermodynamics as the predictive tool of choice for generations to come. Certainly, the level of detail provided by CFD simulations simply cannot be provided by quasi-dimensional models. However, for all their mathematical and computational complexity the accuracy of the current generation of CFD models is still no better than the predictions of a simple quasi-dimensional model when comparing predicted and experimental pressures. Ultimately, it is the rise in pressure due to combustion which produces torque and this is the quality an engine designer will be most interested in knowing. For this reason, it is probably safe to say, as Abdi Aghdam concluded, that at least in the near term, quasi-dimensional models do have a future in providing trend prediction and parametric studies with a minimum of computational effort.

It is worth considering for a moment whether the two or three-zone quasi-dimensional model formulation is the most promising. The two-zone formulation requires the direct prediction of the rate of production of burnt gas. For this to take place the model must correctly predict the turbulent burning velocity, its acceleration with time and deceleration as it approaches the wall, as well as the active flame surface area over which it acts. The three-zone model indirectly predicts the rate of production of burnt gas by invoking an entrainment front at the leading edge of the flame. The entrainment front travels at the turbulent burning velocity and is followed by a burnt gas front which lags behind the entrainment front by a characteristic time proportional to the quotient of the integral scale of turbulence and the mixture laminar burning velocity.

The differential form of the governing equations of the three-zone model guarantee that the mass fraction burnt curve will follow a smooth profile with a steady take off and exponential decay (similar to a "Wiebe" function) as the flame reaches the cylinder walls. Whilst this may appear to be an advantage, the end result is that the model is unduly sensitive to the choice of laminar burning velocity and integral scale models as these are the parameters which govern the characteristic burn-up time; the action of the governing equations is to smear out small changes in turbulent burning velocity, flame acceleration and active flame

area. In a real engine these are undoubtedly more important parameters. The turbulent burning velocity is primarily a function of rms turbulent velocity and a real engine is most sensitive to changes in turbulent burning velocity, flame acceleration and active flame area.

The use of an entrainment front by the three-zone model is essentially a mathematical convenience. The Mie scattering images of combustion presented in this thesis clearly show that combustion takes place in the flamelet regime and that the interface between unburnt and burnt gas is very small for the operating conditions studied. Whilst it can be argued that the leading edge of a flame recorded using schlieren photography does define an entrainment front, it should be remembered that this is simply an integration of the Mie scattering (burnt gas) flame front along the line of sight.

For the reasons discussed above, despite the comparatively poor results using the two-zone model (compared to the three zone model) reported in the current work, it is recommended that future efforts are concentrated on refining the two-zone model, in particular the flame acceleration submodel. Any future researchers should however bear in mind that reliable predictions with any quasi-dimensional model require the properties of the turbulent flow within the combustion chamber to be properly characterised, either through cold CFD simulations or (preferably) direct measurements.

Specific impediments to progress using quasi-dimensional models (and in many cases CFD) are as follows: Firstly, there is a lack of a robust definition of what exactly constitutes turbulence in an engine and how best to measure it. All quasi-dimensional models take as an input the rms turbulent velocity u' as the turbulent burning velocity is very strongly influenced by turbulence. Ultimately, in the confined environment of a spark ignition engine combustion chamber, the flame (under normal circumstances) expands to fill the entire volume therefore all the scales of fluid flow influence how that flame propagates. Whether it is possible to make a precise distinction between what constitutes "turbulence" and what is merely gas motion which will convect the flame is undecided at this time. This must be resolved to enable serious progress.

Secondly, any successful quasi-dimensional (or CFD) model must be universal. Simulations of turbulent combustion in the Leeds Mk II turbulent combustion vessel (not reported here) have revealed that the LUSIE code in its current configuration, with model constants adjusted to give a good fit to data from an engine, is a very poor predictor of combustion when the environment in which is takes

place is radically altered. Whether this is due to some fundamental limitation of the model, or whether the lack of a rigourous definition of what constitutes turbulence in an engine is hampering the setting of the model constants, is unknown. Likewise, there are, to the authors best knowledge, no studies reported in the literature using CFD codes where combustion is simulated, using the same model constants, in vessels of very different characteristics. If a rigourous study of this type was undertaken (using any predictive model) with successful results it would be a good indication of that model's universality.

Thirdly, given a value of the "fully developed" turbulent burning velocity, if such a quality exists, some mechanism must be invoked which controls flame acceleration/development. If it assumed that one of the many existing turbulent burning velocity models is accurate enough to be used in a quasi-dimensional model, and the true test of accuracy can only be made when u' is successfully defined, much effort must be expended to properly investigate the parameters governing flame development. The current lack of understanding in this area not only restricts the development of turbulent combustion models but also makes the comparisons between turbulent burning velocity data recorded by different research groups very difficult. The two-zone combustion model simulations and the analysis of the data presented by Ormsby [2005] reported in the current work highlight both the large differences between the currently available models and their disagreement with experimental data.

Finally, the question of whether the concept of a fully developed turbulent burning velocity is useful has not yet been properly answered. In a very comprehensive review of published turbulent burning velocities, Lipatnikov and Chomiak [2002] reasoned that as data reported by many research groups showed the same qualitative trends the turbulent burning velocity was a physically meaningful local quality. Most of the turbulent burning velocity models published (including the Zimont-Lipatnikov model employed in the current work [Lipatnikov and Chomiak, 1997]) are based on the assumption that, after an initial period of growth, the turbulent flame brush thickness and burning velocity will reach some asymptotic value. Experimental data measured in well controlled environments, for example turbulent combustion vessels or burners, supporting this assumption are scarce.[2]

A real flame, fully developed or otherwise, will be wrinkled by all scales of

[2]Note that the measurements of local burning velocity and flame speed reported in Chapter 5 do appear to reach a maximum.

fluid flow. The turbulent burning velocity, by definition, is a macroscale property and not valid at the smallest scales. Over what "length" of flame front a turbulent burning velocity should be considered to act, and where the cutoff lies between large distortions to the overall flame geometry, and small scale turbulent wrinkling, is not yet satisfactorily defined. This problem is similar in nature to the proper distinction between turbulence and mean flow discussed elsewhere in this chapter.

The impediments to further progress in the field of turbulent combustion simulation as a whole are a lack of: understanding of turbulent flow; chemistry at high temperatures and pressures; and experimental data. Despite centuries of effort and much progress, especially over the last fifty years, turbulence remains a poorly understood phenomenon. Mathematically, the problem does not lend itself to simple analysis because of the range of length and time scales involved. Most problems may be simplified by assuming certain details to be unimportant. For example, when calculating the bending of a beam the order of the atoms within the beam is generally considered unimportant. Turbulence resists attack by this type of approach because the transport of heat and mass is a product of all scales. The cascade of energy from the largest to the smallest scales means that none can be neglected.

In the future, improved understanding will probably come from direct numerical simulation and further experimentation. Because of the shear size of the computational resources required however it is likely to remain the case that engine combustion cannot be modelled using direct numerical simulation for many years to come. Whether large eddy simulation, whereby the largest scales of turbulence are solved for directly and a submodel is used for the smaller scales, will prove to be a simulation tool useful enough to justify its enormous demand for computational resources will no doubt be answered in the next ten years.

In the field of chemistry some progress has been made and measurements of laminar burning velocities of hydrocarbon fuels at atmospheric temperature and pressure made by different research groups have converged. These measurements provide a simple test against which chemical kinetic models may be evaluated. Where progress must still be made is at the much higher temperatures and pressures relevant to engine combustion. Under these conditions flames become unstable and the determination of an unstretched laminar burning velocity from measured stretched laminar burning velocity is complex. It is important to note that the laminar burning velocity is a key input parameter for many CFD

type combustion models as well as quasi-dimensional models. Where the laminar burning velocity is not a direct input parameter the model must rely on a chemical reaction mechanism, the rate constants of which have typically been adjusted to provide a good fit to measured laminar burning velocity data. Examination of the various laminar burning velocity data reported in the literature at high temperatures and pressures showed that, despite the importance of this parameter, measurements are a long way from agreement under these conditions. Before further progress can be made it is essential that some agreement on how best to determine the laminar burning velocity from a cellular flame is made. Only then can any combustion model, CFD or otherwise, hope to produce accurate prediction of engine combustion.

For a model of turbulent premixed combustion in a spark ignition engine to be declared accurate it must first be tested against experimental data. Experimental measurements of cylinder pressure are relatively straightforward with modern experimental equipment and may be found in the open literature at a great range of engine operating conditions. Direct optical measurements of flame position or in-cylinder flow are much more difficult and the majority of the data reported in the literature and, to the authors knowledge, all of the data recorded by previous students at the University of Leeds, are recorded at or below 2000 rpm. If a typical engine idles at 1000 rpm and has a maximum usable speed of 5000 rpm the currently available measurements cover only 25% of that range.

Whilst the engine speed primarily determines the characteristics of the turbulence present in the charge, the compression ratio or degree of throttling or pressure charging determines the range of temperatures and pressures the charge will experience. The LUPOE family of ported engines are operated without any intake throttling which restricts the range of temperature and pressure variation in the charge gas. For serious evaluation of potential models accurate and detailed measurements must be taken at much higher engine speeds and at a greater range of temperatures and pressures. As the simulations using different laminar burning velocity expressions reported in Section 5.4.4 revealed, widely different submodels can be coaxed to give seemingly accurate predictions given the correct choice of model constants provided that the range over which they are tested is not too large.

6.3 Recommended improvements to experimental and numerical facilities

The LUPOE2 engine and LUSIE/LUSIEDA software is the result of much development work by former students at the University of Leeds. Despite this previous effort there remain a number of weak points, some of which have only become apparent with the prolonged experimental programme conducted by the current author. The following paragraphs describe a number of proposed improvements to the experimental and computational facilities. The advice is mostly of a practical nature; suggestions as to directions for future research may be found in the preceding sections.

- The system of fuel delivery and metering using an automotive fuel pump and regulator to pressurise the system and rotameters with needle valves to measure and control the flow rate, is difficult to control and does not provide repeatable fuel delivery. Replacement of the pump with a system pressurised using a gas bottle would provide a near constant pressure. The use of a more accurate metering/control system would be a great improvement.[3]

- Over the year when experimental data were recorded atmospheric pressure varied between 0.98 and 1.04 bar.[4] As the exhaust blower, which evacuates the laboratory exhaust ducting, is working against atmospheric pressure and the pressure in the exhaust manifold ultimately determines the pressure at the start of the cycle (the exhaust port closes last) this implies a 6% variation in pressure at cycle start. This variability in pressure at the start of the cycle could be removed by throttling or pressure charging the engine and using an absolute pressure transducer to monitor the pressure in the intake manifold. Such measures may help to reduce the amount of cyclic variability present in data sets recorded over prolonged periods of time.

- The seeding system employed for the reported experiments used solid TiO_2 particles. This seed has been shown to have good light scattering properties in previous studies [Scott, 1992] but has two disadvantages:

[3]At the time of writing the rotameters have been replaced with a closed loop coriolis flow metering and control system.

[4]Data recorded at Leeds airport available on the internet.

1. The seed has a tendency to foul the windows of the engine, requiring the cylinder head to be removed and cleaned regularly. This not only slows down the experimental work but also increases the likelihood of damage to the head and fragile custom made spark plug.
2. The seed must be fluidised before it can be introduced to the intake air-fuel mixture. The seed concentration, and therefore image contrast, using the current fluidised bed system was found to vary significantly test-to-test.

Two potential solutions exist to these problems. Either a commercially available smoke generator could be used to seed the flow (smoke has been used successfully in previous studies, for example Hicks et al. [1994] or Bradley et al. [2003]) or TiO_2 could be prepared in a slurry with a suitable solvent, atomised and introduced into the intake air. A seeder with Laskin nozzles capable of dealing with TiO_2 slurry has recently been purchased however finding a suitable solvent which does not affect combustion may be difficult and this technique will not prevent fouling of the windows. If the current system is retained it may be beneficial to run the fluidised bed with a dedicated metered air supply (this configuration was used by Cairns [2001]) to try and eliminate test-to-test variability in seed concentration.

- Some effort should be made to investigate and reduce the amount of blowby and mass transfer into and out of the top land crevice. The piston crown is screwed into the piston on the LUPOE2 engine to allow it to be replaced with a crown with a mirrored surface to facilitate schlieren photography. For this reason, the first piston ring groove, which is in the piston itself rather than the removable piston crown, is further from the piston crown than on a typical automotive engine with a larger top land crevice volume as a consequence.

  Blowby is significant at the start of the cycle during the period when the piston crown has moved past the top of the port but the first piston ring has yet to seal the combustion chamber. At this point in the cycle gas flows with very little resistance from the cylinder into the top land crevice and out of the exhaust port. From a modelling point of view this is important as the amount of mass lost during this period is not easily quantified experimentally and hence model predictions cannot be verified. An appropriate first step would be to measure the discharge coefficient between the cylinder

and the exhaust port for different crank angles during this period using a simple flow bench with the engine stationary. Data derived from these tests could then be included in the LUSIE blowby model. Moving the first piston ring closer to the piston crown would have the dual benefits of reducing the top land crevice volume and shortening the period at the start of the cycle where blowby is significant.

- As discussed in Section 5.2, the addition of fuel to the intake air stream immediately[5] before firing causes the temperature of the resulting mixture to drop below the value set on the heater thermostats. The thermal inertia of the intake system is large enough that the heaters can not respond quickly to this drop, with the result that the experiment is conducted with a small but unquantified temperature error. It would be beneficial for future researchers to reduce this error, either by preparing the air-fuel mixture in a different way or perhaps by adding additional heaters to the intake system and reducing its thermal inertia.

- The experimental data from LUPOE2-P presented in this thesis was recorded in runs of ten firing cycles. In between runs the engine was dismantled and the cylinder head windows cleaned to remove deposits of TiO_2 seed and oil. Subsequent analysis of the recorded cycles revealed that the engine operating condition did not drift significantly over ten firing cycles therefore it may be possible to run the engine for longer periods without compromising the quality of the recorded data. This possibility should be investigated thoroughly as, if a similar experimental programme is conducted again, it would allow a greater number of cycles to be recorded and a consequent reduction in the spacing between laser sheets.

- The current method of aligning the shaft encoder on the crankshaft with TDC requires that the cylinder head be removed and a capacitive proximity sensor placed above the piston. As discussed in Section 2.2.5, piston rock close to TDC can cause problems when attempting to align the shaft encoder dynamically. The method suggested by Douglas et al. [1997], whereby motoring pressure traces are recorded with the engine rotating in each direction and the difference between them is bisected to find a true TDC position,

[5] Although it is possible to turn the fuel supply on well before the start of the experiment and allow the system to reach thermal equilibrium, the resulting large volume of fuel-air mixture presents problems from a health and safety perspective.

should be used in future.

Techniques and software for processing multiple Mie scattering images of combustion have been developed extensively during the course of the study and the opportunity to use these to study combustion in different environments should not be lost. In particular, time should be taken to record similar data sets in the much simpler LUPOE2-D[6] and Leeds Mk II turbulent combustion vessel. Much more is known about combustion in these environments, having been characterised extensively in previous experiments. Comparison between the ensemble averaged three-dimensional flame surfaces generated using the current experimental technique and images recorded using schlieren photography or natural light (chemiluminescence) would provide confirmation of the validity of the flame surface generated and help to relate the position of the flame surface to the flame radii generated using the more traditional schlieren and natural light methods. In terms of the data acquisition and processing techniques specifically, the following recommendations are given:

- The current ignition and data acquisition trigger system is built from hard wired electrical logic circuits. Although the system was obviously designed with flexibility in mind a number of time consuming changes to the circuitry had to be made in order to provide the trigger pattern required by the laser, camera and data acquisition (DAQ) system. There now exist commercially available "counter-timer" cards which can be controlled using the LabVIEW programming language in a similar fashion to the DAQ system. Use of these cards would provide a more flexible system that could be reconfigured using software rather than hardware changes.

- Data recorded by the DAQ system were stored on the computer hard disk as ASCII text files in keeping previous experiments conducted in the School of Mechanical Engineering. Although text files have the advantage that they are easily accessed using a text editor, encoding text in the ASCII format requires far more storage space than if the data were stored as raw binary numbers. Consequently, given the large experimental programme conducted, the time taken to read and write the data was much longer than it might otherwise have been and processing the final data set took around one week of continuous CPU time on a personal computer. Storage of the

[6] A disc chamber version of the LUPOE2-P pent roof engine used in the current study.

data recorded by the DAQ system in a binary format would have allowed this processing to take place in a much shorter time.

- The image processing techniques used built on previous work in the School of Mechanical Engineering and used a simple threshold to determine the interface between burnt and unburnt gas. Although the accuracy of this technique was improved significantly by normalising the image in question using the first and last recorded images of each cycle, spatial and temporal variations in seed level remained problematic. Some effort should be made to investigate other edge detection techniques with the review of Russ [1995] providing a good starting point. Software which implements a number of these techniques is distributed with the Matlab image processing toolbox.

A significant amount of effort was expended on maintaining the LUSIE simulation software, LUSEIDA reverse analysis software and their derivatives during the course of the study. Maintenance involved not just the addition of new submodels but also, where necessary, restructuring of the code and rewriting to take advantage of the new language features offered by Fortran 90/95. In addition, a number of small numerical errors were rectified bringing the thermodynamics of the code in-line with the commercially available GT-Power software. During maintenance of the code a number of further shortcomings were identified which are as follows:

- Both LUSIE and LUSIEDA use fixed time steps with the magnitude specified by the user. Using this method inexperienced users can specify a time step size which is too large resulting in inaccurate calculations. A more robust system would be to have the user specify the largest possible time step size and implement some form of adaptive step size control.

  The simplest form of adaptive step size control is step doubling. Here each time step is taken twice, once as one large time step and then again with two smaller time steps. The error in the calculated solution may be estimated as the difference between the calculation result using one large step and the result using two smaller steps. If the error is below some specified tolerance the large step is considered adequate and the calculation proceeds to the next time step. If the error is too large each half step is subdivided and the procedure repeated until the error falls below the specified tolerance. Such a system is often implemented when solving problems numerically

(see for example Press et al. [1992]) and is already used by LUSIE in the Runge-Kutta solution of the blowby equations. The computational overhead incurred is insignificant and would probably be reduced as the code would be able to take larger time steps where rates of change are not too large. The potential increase in solution accuracy, especially when using LUSIEDA where the experimental data may not be smooth, would justify the effort required to rewrite the software.

- Many of the thermodynamics subroutines used by LUSIE and LUSIEDA, and the procedure used by LUSIEDA to find the amount of mass burnt in a given time step, employ the bisection method to find the root of an equation. Although guaranteed to converge, the bisection method is inefficient and could easily be replaced by a more modern algorithm, for example Brent's method [Brent, 1973], source code for which may be found either in Press et al. [1992] or Netlib. This should be employed as a stand alone solver module to which the function to be solved is passed as an argument rather than by writing individual implementations for different subroutines, the style by which the bisection method is currently implemented.

Appendix A

Summary of PProc routines

A.1 PProc data structure

A.1.1 Data fields

`Data.Var` Stores data points as real numbers.

`Data.Var(sample,cycle,variableNumber) = sampleValue`

`Data.VarTitle` Stores a title string for the data in `Data.Var`.

`Data.VarTitle{variableNumber} = 'variableTitleString'` where `'variableTitleString'` is one of the following strings: `'External Clock'`, `'TDC Marker'`, `'BDC Marker'`, `'Spark Marker'`, `'Crank Angle'`, `'Absolute Pressure`, `'Dynamic Pressure Transducer'`, `'Cylinder Pressure'`, `'Cylinder Volume'`, `'Instantanious RPM'`, `'Camera Frame Signal'`

`Data.VarUnit` Stores a unit string for each dataset.

`Data.VarUnit{variableNumber} = 'variableUnitString'`

`Data.VarType` Stores a type string for each dataset.

`Data.VarType{variableNumber} = 'variableType'` where `'variableType'` is one of the following strings: `'discreet'` (i.e. Camera frame numbers, digital data), `'continuous'` (i.e. Smooth analogue data such as elapsed time from trigger generated from knowledge of sample rate or data generated by simulations) or `'ADC'` (i.e. Analogue data recorded in the lab with ADC's). The value of `Data.VarType` affects the way data is resampled to the crank angle domain. Discreet data is resampled by looking for the nearest neighbour to the resample point.

Continuous data is resampled by a linear approximation. ADC Data is resampled by taking the mean of the nearest data points. This reduces the rms noise in the ADC signal.

`Data.VarLogic` Stores a logic level designation for each dataset.
`Data.VarLogic{variableNumber} = logicLevel` where `logicLevel = 0` indicates that negative going edges are significant and `logicLevel = 1` indicates that positive going edges are significant. This only applies to signals for which `Data.VarType = 'discreet'` and where the data is digital.

`Data.CName` Stores a name string for each cycle. `Data.CName{cycle} = 'cycleName'`.

A.1.2 Cycle statistics

`Data.CStat` Statistics which are calculated every cycle.
`Data.CStat(cycle,statisticNumber) = statisticValue`.

`Data.CStatTitle` Title string for statistics calculated every cycle.
`Data.CStatTitle{statisticNumber} = 'statisticTitleString'`.

`Data.CStatUnit` Unit string for statistics which are calculated every cycle.
`Data.CStatUnit{statisticNumber} = 'statisticUnitString'`.

A.1.3 Dataset statistics

`Data.OStat` Statistics which are calculated using the entire dataset.
`Data.OStat(statisticNumber) = statisticValue`.

`Data.OStatTitle` Title string for statistics which are calculated using the entire dataset. `Data.OStatTitle{statisticNumber} = 'statisticTitleString'`.

`Data.OStatUnit` Unit string for statistics which are calculated using the entire dataset. format `Data.OStatUnit{statisticNumber} = 'statisticUnitString'`

A.1.4 Cycle lists

`Data.List` Array defining lists of data related to each cycle.
`Data.List{cycle,listNumber} = listArray`.

`Data.ListTitle` Title string for lists of data related to each cycle.
`Data.ListTitle{listNumber} = 'listTitleString'`.

`Data.ListColHeading` Column heading strings for lists of data related to each cycle. `Data.ListColHeading{columnNumber,listNumber} = 'listColHeadingString'`.

`Data.ListColUnit` Column unit strings for lists of data related to each cycle.
`Data.ListColUnit{columNumber,listNumber} = 'listUnitString'`.

A.1.5 Dataset lists

`Data.OList` Array defining lists of data calculated using the entire dataset.
`Data.OList{listNumber} = listArray`.

`Data.OListTitle` Title string for lists of data calculated using the entire dataset.
`Data.OList{listNumber} = 'listTitleString'`.

`Data.OListColHeading` Column heading strings for lists of data calculated using the entire dataset.
`Data.OListColHeading{columNumber,listNumber} = 'listColHeadingString'`.

`Data.OListColUnit` Column unit strings for lists of data calculated using the entire dataset. `Data.OListColUnit{columNumber,listNumber} = 'listUnitString'`.

A.1.6 Dataset parameters

`Data.Cycle` True if the dataset is split into individual cycles.

`Data.Cont` True if the dataset is continuous, i.e. not split into individual cycles.

`Data.Sample` True if data is sample (i.e. time) based.

`Data.SampleFreq` Data sample frequency [Hz].

`Data.Crank` True if data has been resampled to the crank angle domain.

`Data.CrankDTheta` Crank angle increment [° CA].

`Data.Filename` Filename string for the dataset.

`Data.Pathname` Pathname string for the dataset.

A.1.7 Engine parameters

`Data.EngineName` Name string for engine.

`Data.EngineBore` Bore of engine [mm].

`Data.EngineStroke` Stroke of engine [mm].

`Data.EngineConRdLn` Connecting rod length for engine [mm].

`Data.EngineVolCl` Clearance volume of engine [mm^3].

`Data.EngineNStrokes` Number of strokes of engine, i.e. two or four.

`Data.EngineCARefPoint` Crank angle at which the dynamic pressure transducer should be pegged to the absolute pressure transducer [° aTDC].

A.2 PProc routines

`Chop` Separates raw data sets into individual cycles.

`DecodePulseTrain` Utility function which takes a digital pulse train, such as that produced by the camera or shaft encoder, and decodes it to produce a series of numbers.

`ExtractCameraFrameNumber` Extracts the camera frame number given the camera frame signal using `DecodePulseTrain`.

`ExtractCrankAngle` Extracts the crank angle given the shaft encoder signal using `DecodePulseTrain`.

`FilterAnalogue` Low-pass filters an analogue signal to remove glitches and noise caused by electrical interference.

`LoadTxt` Loads raw text files saved by LabVIEW into the Matlab workspace.

`NewDataSet` Creates an empty engine dataset.

`Reference` Pegs the signal from the dynamic pressure transducer to either a known reference pressure or the signal from the absolute pressure transducer.

`ResampleData` Re-samples data, usually used to convert the original 200 kHz signal recorded by the DAQ system to 0.2° CA suitable for postprocessing.

`TrimCycles` Removes motoring cycles from a skip-fired dataset.

`VariabilityStats` Calculates some standard cycle-to-cycle variability statistics.

Appendix B

Summary of IProc routines

`adaptive_threshold` Implements an adaptive thresholding operation using the first and last images of each cycle to normalise the image which is being thresholded.

`alternating_sequential_filter` Alternating sequential open close filtering to remove high frequency noise (graininess) from images.

`apply_mask` Masks an image to remove peripheral noise using a mask created in Adobe Photoshop.

`closevolume` Closes a volume dataset by padding all edges with null data.

`distance_between_isosurfaces` Calculates the local distance between concentric triangulated surfaces.

`filter_and_adaptive_threshold` Implements a combined filtering (using `alternating_sequential_filter`) and thresholding (using `adaptive_threshold`) operation.

`flame_thickness` Calculates the local flame thickness using `distance_between_isosurfaces`.

`imreadraww` Reads an image saved in the `raww` file format used by the camera.

`local_flame_speed` Calculates the local flame speed using `distance_between_isosurfaces`.

`LUPOE2PWindowCalcs` Script to calculate the overlap in the view from the two top windows in LUPOE2-P.

`merge_windows` Takes two images, one from each top window in LUPOE2-P and fades them into each other give a single image.

`polyarea3` Calculates the surface area of a three dimensional triangulated surface.

`polyvolume3` Calculates the volume enclosed by a three dimensional triangulated surface.

`split_rot_trim` Takes a raw image from the LUPOE2-P engine, splits it into two separate images, one from each window in the pent roof, trims the images and rotates them so that they are aligned.

`sum_and_combine_layers` Takes a series of images from the same laser sheet position, averages them to give a mean progress variable and then combines images from different laser sheet positions to give a three-dimensional progress variable volume field.

`surfmean` Calculates the area weighted mean of a surface property.

`surfpdf` Displays an area weighted probability density function of a surface property.

`surfstd` Calculates the area weighted standard deviation of a surface property.

`taubin_smoothing` Smooths a triangulated surface.

Bibliography

R. G. Abdel-Gayed and D. Bradley. Criteria for turbulent propagation limits of premixed flames. *Combustion and Flame*, 62(1):61–68, 1985.

R. G. Abdel-Gayed, D. Bradley, and M. Lawes. Turbulent burning velocities: A general correlation in terms of straining rates. *Proceedings of the Royal Society of London Series A, Mathematical and Physical Sciences*, 414(1847):389–413, December 1987.

R. G. Abdel-Gayed, D. Bradley, M. Lawes, and Lung F.K-K. Premixed turbulent burning during the early stages of an explosion. In *Twenty-First Symposium (International) on Combustion*, pages 497–504, Pittsburgh, 1988. The Combustion Institute.

H. A. Abdel-Salam. *Modelling and Experimental Validation of Turbulent Flame Propagation in Spark Ignition Engines*. PhD thesis, Mechanical Engineering Department, El-Mansoura University, 1992.

E. Abdi Aghdam. *Improvement and Validation of a Thermodynamic SI Engine Simulation Code*. PhD thesis, School of Mechanical Engineering, The University of Leeds, 2003.

E. Abdi Aghdam, A. A. Burluka, T. Hattrell, K. Liu, C. G. W. Sheppard, J. Neumeister, and N. Crundwell. Study of cyclic variation in an SI engine using quasi-dimensional combustion model. *SAE Technical Paper* 2007-01-0939, Society of Automotive Engineers, 2007.

F. N. A. A. Al-Mamar. *Combustion in a dual chamber spark ignition engine*. PhD thesis, Department of Mechanical Engineering, The University of Leeds, 1983.

A. S. Al-Shahrany. *Experimental and theoretical studies of combustion rates at high pressure*. PhD thesis, School of Mechanical Engineering, The University of Leeds, 2004.

A. S. Al-Shahrany, D. Bradley, M. Lawes, and R. Woolley. Measurement of unstable burning velocities of iso-octane-air mixtures at high pressure and the derivation of laminar burning velocities. *Proceedings of the Combustion Institute*, 30:225–232, 2005.

E. L. Allgower and P. H. Schmidt. Computing volumes of polyhedra. *Mathematics of Computation*, 46(173):171–174, January 1986.

W. J. D. Annand. Heat transfer in the cylinder of reciprocating internal combustion engines. *Proceedings of the Institution of Mechanical Engineers*, 177(36): 973–990, 1963.

C. Arcoumanis, Z. Hu, C. Vafidis, and J. H. Whitelaw. Tumbling motion: A mechanism for turbulence enhancement in spark-ignition engines. *SAE Technical Paper* 900060, Society of Automotive Engineers, 1990.

C. Arcoumanis, C. S. Bae, and Z. Hu. Flow and combustion in a four-valve, spark-ignition engine. *SAE Technical Paper* 940475, Society of Automotive Engineers, 1994.

K. Atashkari. *Experimental study of flow and turbulence in a V-flame burner and a S.I. engine*. PhD thesis, School of Mechanical Engineering, The University of Leeds, 1997.

N. Aubry, P. Holmes, J. Lumley, and E. Stone. The dynamics of coherent structures in the wall region of a turbulent boundary layer. *Journal of Fluid Mechanics*, 192: 115–173, 1988.

X. Baby, A. Dupont, A. Ahmed, W. Deslandes, G. Charnay, and M. Michard. A new methodology to analyze cycle-to-cycle aerodynamic variations. *SAE Technical Paper* 2002-01-2837, Society of Automotive Engineers, 2002.

M. Baratta, A. E. Catania, E. Spessa, and A. Vassallo. Development and assessment of a multizone combustion simulation code for SI engines based on a novel fractal model. *SAE Technical Paper* 2006-01-0048, Society of Automotive Engineers, 2006.

T. A. Baritaud and R. Green. A 2-D flame visualisation technique applied to the IC engine. *SAE Technical Paper* 860025, Society of Automotive Engineers, 1986.

G. K. Batchelor. *The Theory of Homogeneous Turbulence*. Cambridge University Press, Cambridge, England, 1953.

J. K. Bechtold and M. Matalon. Hydrodynamic and diffusion effects on the stability of spherically expanding flames. *Combustion and Flame*, 67:77–90, 1987.

G. P. Beretta, M Rashidi, and J. C. Keck. Turbulent flame propagation and combustion in spark ignition engines. *Combustion and Flame*, 52:217–245, 1983.

P. S. Bernard and J. M. Wallace. *Turbulent Flow: analysis, measurement and prediction*. Wiley, 2002.

R. B. Bird, W. E. Stewart, and Lightfoot E. N. *Transport phenomena*. J. Wiley & Sons, Inc., N. Y., 1960.

N. C. Blizard and J. C. Keck. Experimental and theoretical investigation of turbulent burning model for internal combustion engines. *SAE Technical Paper* 740191, Society of Automotive Engineers, 1974.

P. N. Blumberg, G. A. Lavoie, and R. J. Tabaczynski. Phenomenological models for reciprocating internal combustion engines. *Progress in Energy and Combustion Science*, 5(23):123–167, 1979.

R. Borghi and M. Destriau. *Combustion and flames: chemical and physical principles*. Editions Technip, Paris, 1st edition, 1998.

G. Borman and K. Nishiwaki. Internal-combustion engine heat transfer. *Progress in Energy and Combustion Science*, 13(1):1–46, 1987.

F. W. Bowditch. A new tool for combustion research – a quartz piston engine. *SAE Technical Paper* 610002, Society of Automotive Engineers, 1961.

D. Bradley. Instabilities and flame speeds in large-scale premixed gaseous explosions. *Philosophical Transactions: Mathematical, Physical and Engineering Sciences*, 357(1764):3567–3581, December 1999.

D. Bradley. Flame propagation in a tube: The legacy of henri guenoche. *Combustion Science and Technology*, 158(1):15–33, 2000.

D. Bradley, J. Hynes, M. Lawes, and C. G. W. Sheppard. Limitations to turbulence-enhanced burning rates in lean burn engines. *Proceedings of the Institution of Mechanical Engineers*, C46/88:17–24, 1988.

D. Bradley, A. K. C. Lau, and Lawes M. Flame stretch rate as a determinant of turbulent burning velocity. *Philosophical Transactions of the Royal Society: Physical and Engineering Sciences*, 338(1650):359–387, February 1992.

D. Bradley, R. A. Hicks, M. Lawes, and C. G. W. Sheppard. Study of turbulence and combustion interaction: Measurement and prediction of the rate of turbulent burning. Technical report, Department of Mechanical Engineering, The University of Leeds, 1996.

D. Bradley, R. A. Hicks, M. Lawes, C. G. W. Sheppard, and R. Woolley. The measurement of laminar burning velocities and markstein numbers for iso-octaneair and iso-octanen-heptaneair mixtures at elevated temperatures and pressures in an explosion bomb. *Combustion and Flame*, 115:126–144, 1998.

D. Bradley, C. G. W. Sheppard, R. Woolley, D. A. Greenhalgh, and R. D. Lockett. The development and structure of flame instabilities and cellularity at low markstein numbers in explosions. *Combustion and Flame*, 122:195–209, 2000.

D. Bradley, M. Z. Haq, R. A. Hicks, T. Kitagawa, M. Lawes, C. G. W. Sheppard, and R. Woolley. Turbulent burning velocity, burned gas distribution, and associated flame surface definition. *Combustion and Flame*, 133:415–430, 2003.

R. P. Brent. *Algorithms for minimization without derivatives*, chapter 3–4. Prentice-Hall, 1973.

S. Breuer, M. Oberlak, and N. Peters. Non-isotropic lengthscales during the compression stroke of a motored piston engine. *Flow, Turbulence and Combustion*, 74:145–167, 2005.

D. Buran. *Turbulent Flame Propagation in a Methane Fuelled Spark Ignition Engine*. PhD thesis, Department of Mechanical Engineering, The University of Leeds, 1998.

G. R. Butler. *The effects of swirl on combustion in spark ignition engines*. PhD thesis, School of Mechanical Engineering, The University of Leeds, 1999.

A. Cairns. *Turbulent Flame Development in a Spark Ignition Engine*. PhD thesis, School of Mechanical Engineering, The University of Leeds, 2001.

S. Candel, D. Thévenin, N. Darabiha, and D. Veynante. Progress in numerical combustion. *Combustion Science and Technology*, 149:297–337, 1999.

R. K. Cheng and I. G. Shepherd. The influence of burner geometry on premixed turbulent flame propagation. *Combustion and Flame*, 85(1):7–26, 1991.

T. C. Chew, K. N. C. Bray, and R. E. Britter. Spatially resolved flamelet statistics for reaction rate modeling. *Combustion and Flame*, 80(1):65–82, 1990.

W. C. Choi and Y. G. Guezennec. Measurement of cycle-to-cycle variations and cycle-resolved turbulence in an IC engine using a 3-D particle tracking velocimetry. *JSME International Journal Series B-Fluids and Thermal Engineering*, 41(4):991–1003, 1998.

J. Chomiak. *Combustion: a study in theory, fact and application*. Gordon and Breach Science Publishers, 1989.

F. E. Corcione and G. Valentino. Analysis of in-cylinder flow processes by LDA. *Combustion and Flame*, 99(2):387–394, 1994.

J. Cullum. Numerical differentiation and regularisation. *SIAM Journal of Numerical Analysis*, 8:254–265, 1971.

W. Dai, C. D. Davis, M. J. Hall, and R. D. Matthews. Diluents and lean mixture combustion modelling for SI engines with a quasi-dimensional model. *SAE Technical Paper* 952382, Society of Automotive Engineers, 1995.

G. Damköhler. The effect of turbulence on the flame velocity in gas mixtures. Technical Report Technical Memorandum 1112, National Advisory Committee for Aeronautics, April 1947. Originally published in German as "Der Einfluss der Turbulenz auf die Flammengeschwindigkeit in Gasgemischen" in Zeitschrift für Elektrochemie und angewandte Physikalische Chemie, vol. 46 no. 11, November 1940, pp. 601–626.

A. Dawood. *In preparation*. PhD thesis, School of Mechanical Engineering, The University of Leeds, 2007.

A. R. A. A. Desoky. *An experimental and theoretical study of the combustion process in a divided chamber spark-ignition engine*. PhD thesis, Department of Mechanical Engineering, The University of Leeds, 1981.

R. Douglas, R. J. Kee, and B. P. Carberry. Analysis of in-cylinder pressure data in two-stroke engines. *SAE Technical Paper* 972792, Society of Automotive Engineers, 1997.

J. M. Duclos, D. Veynante, and T. Poinsot. A comparison of flamelet models for turbulent premixed combustion. *Combustion and Flame*, 95:101–118, 1993.

J. D. Foley, A. van Dam, S. Feiner, and J. F. Hughes. *Computer Graphics: principals and practice*. Addison-Wesley, Reading, Mass., 2nd edition, 1996.

R. A. Fraser and F. V. Bracco. Preliminary turbulence length scale measurements in a motored IC engine. *SAE Technical Paper* 860021, Society of Automotive Engineers, 1986.

R. A. Fraser and F. V. Bracco. Cycle-resolved LDV integral length scale measurements investigating clearance height scaling, isotropy, and homogeneity in an IC engine. *SAE Technical Paper* 890615, Society of Automotive Engineers, 1989.

S. Furuhama and T. Tada. On the flow of gas through the piston-rings (1st report, the discharge coefficient and temperature of leakage gas. *Bulletin of the Japan Society of Mechanical Engineers*, 4(16):684–690, 1961.

GT-Power User's Manual. Gamma Technologies, Inc., 601 Oakmont Lane, Suite 220, Westmont, IL 60559, USA, 2004.

A. G. Gaydon and H. G. Wolfhard. *Flames: Their structure, radiation and temperature*. Chapman & Hall, London, 1953.

L. Gillespie. *Imaging and Analysis of Turbulent Flame Development in SI Engines*. PhD thesis, School of Mechanical Engineering, The University of Leeds, 1998.

L. Gillespie, M. Lawes, C. G. W. Sheppard, and R. Woolley. Aspects of laminar and turbulent burning velocity relevant to SI engines. *SAE Technical Paper* 2000-01-0192, Society of Automotive Engineers, 2000.

R. C. Gonzalez, R. E. Woods, and S. L. Eddins. *Digital Image processing using MATLAB*. Pearson/Prentice Hall, Upper Saddle River, NJ, 2004.

F. C. Gouldin and P. C. Miles. Chemical closure and burning rates in premixed turbulent flames. *Combustion and Flame*, 100:202–210, 1995.

A. B. Greene and G. G. Lucas. *The Testing of Internal Combustion Engines*. The English Universities Press Limited, London, 1969.

J. F. Griffiths and J. A. Barnard. *Flame and Combustion*. Blackie Academic & Professional, Glasgow, 3rd edition, 1995.

E. G. Groff. The cellular nature of confined spherical propane-air flames. *Combustion and Flame*, 48:51–62, 1982.

E. G. Groff and F. A. Matekunas. The nature of turbulent flame propagation in a homogeneous spark-ignited engine. *SAE Technical Paper* 800133, Society of Automotive Engineers, 1980.

GTS. Gnu triangulated surface library. URL `http://gts.sourceforge.net/`.

Y. G. Guezennec and W. Hamama. Two-zone heat release analysis of combustion data and calibration of heat transfer correlation in an IC engine. *SAE Technical Paper* 1999-01-0218, Society of Automotive Engineers, 1999.

M. J. Hall and F. V. Bracco. A study of velocities and turbulence intensities measured in firing and motored engines. *SAE Technical Paper* 870453, Society of Automotive Engineers, 1987.

M. N. Hamid. *Fundamental turbulent combustion problems related to gasoline engines*. PhD thesis, Department of Mechanical Engineering, The University of Leeds, 1986.

M. Z. Haq. *Fundamental Studies of Turbulent Combustion*. PhD thesis, School of Mechanical Engineering, University of Leeds, 1998.

M. Harker, T. Hattrell, M. Lawes, and R. Woolley. Local curvature of three dimensional flame surfaces captured using laser tomography. article in preparation.

T. Hattrell, C. G. W. Sheppard, A. A. Burluka, J. Neumeister, and A. Cairns. Burn rate implications of alternative knock reduction strategies for turbocharged SI engines. *SAE Technical Paper* 2006-01-1110, Society of Automotive Engineers, 2006.

Donald D. Hearn and M. Pauline Baker. *Computer graphics with OpenGL*. Pearson Prentice Hall, Upper Saddle River, NJ, 3rd edition, 2004.

W. Heisenberg. On the theory of statistical and isotropic turbulence. *Proceedings of the Royal Society of London. Series A, Mathematical and Physical Sciences*, 195 (1042):402–406, December 1948.

J. Heywood. *Internal Combustion Engine Fundamentals*. McGraw-Hill series in mechanical engineering, 1988.

J. B. Heywood. Combustion and its modeling in spark-ignition engines. In *The Third International Symposium on Diagnostics and Modeling of Combustion in Internal Combustion Engines, COMODIA 94*, pages 1–15, Yokohama, Japan, 1994.

R. A. Hicks, M. Lawes, C. G. W. Sheppard, and B. J. Whitaker. Multiple laser sheet imaging investigation of turbulent flame structure in a spark ignition engine. *SAE Technical Paper* 941992, Society of Automotive Engineers, 1994.

R. Hilbert, F. Tap, H. El-Rabii, and D. Thévenin. Impact of detailed chemistry and transport models on turbulent combustion simulations. *Progress in Energy and Combustion Science*, 30:61–117, 2004.

F. S. Hill. *Computer graphics using OpenGL*. Prentice-Hall International, London, 2nd edition, 2001.

P. G. Hill and D. Zhang. The effects of swirl and tumble on combustion in spark-ignition engines. *Progress in Energy and Combustion Science*, 20:373–429, 1994.

A. D. M. Hilton, J. B. Roberts, and O. Hadded. Autocorrelation based analysis of ensemble averaged LDA engine data for bias-free turbulence estimates: A unified approach. *SAE Technical Paper* 910479, Society of Automotive Engineers, 1991.

J. O. Hinze. *Turbulence: an Introduction to its Mechanism and Theory*. McGraw-Hill series in Mechanical Engineering, 1959.

J. O. Hirschfelder, C. F. Curtiss, and R. B. Bird. *Molecular theory of gases and liquids*. John Wiley and sons, 1964.

C. W. Hong and S. D. Tarng. Direct measurement and computational analysis of turbulence length scales of a motored engine. *Experimental and Thermal Fluid Science*, 16:277–285, 1998.

D. T. Hountalas, G. C. Mavropoulos, and G. Kourbetis. Experimental investigation to develop a methodology for estimating the compression condition of DI diesel engines. *ENERGY CONVERSION AND MANAGEMENT*, 47(1):1–18, January 2006.

J. C. R. Hunt. A review of the theory of rapidly distorted turbulent flows and its applications. In W. Fiszdon, editor, *Proceedings of the 13th Biennial Fluid Mechanics Symposium*, pages 121–152, Poland, September 1978.

J. Hynes. *Turbulence effects on combustion in spark ignition engines.* PhD thesis, Department of Mechanical Engineering, The University of Leeds, 1986.

Y. Ikeda, A. Nishiyama, N. Kawahara, E. Tomita, S. Arimoto, and A. Takeuchi. In-spark-plug sensor for analyzing the initial flame and its structure in an SI engine. *SAE Technical Paper* 2005-01-0644, Society of Automotive Engineers, 2005.

N. S. Jackson, J. Stokes, M. Heikal, and J. Downie. A dynamic water flow visualization rig for automotive combustion system development. *SAE Technical Paper* 950728, Society of Automotive Engineers, 1995.

T. Jakubík. Engine LDA technique progress report. Technical report, School of Mechanical Engineering, The University of Leeds, 2002.

B. Johansson and K. Olsson. Combustion chambers for natural gas SI engines part 1: Fluid flow and combustion. *SAE Technical Paper* 950469, Society of Automotive Engineers, 1995.

K. Y. Kang and J. H. Baek. Turbulence characteristics of tumble flow in a four-valve engine. *Experimental and Thermal Fluid Science*, 18(3):231–243, 1998.

A. R. Kerstein. *Proceedings of the Combustion Institute*, 21:1281, 1988.

W. T Kim, K. Y Huh, J. W Lee, and Kang K. Y. Numerical simulation of intake and compression flow in a four-valve pent-roof spark ignition engine and validation with LDV data. *Proceedings of the IMechE Part D*, 214(4):361–372, 2000.

J. Klingmann and B. Johansson. Interaction between turbulence and flame in an SI engine and in a stationary burner. *SAE Technical Paper* 1999-01-0569, Society of Automotive Engineers, 1999.

D. A. Knause, F. C. Gouldin, P. C. Hinze, and P. C. Miles. Measurement of instantaneous flamelet surface normals and the burning rate in a SI engine. *SAE Technical Paper* 1999-01-3543, Society of Automotive Engineers, 1999.

D. E. Knuth. *Seminumerical Algorithms*, volume 2 of *The Art of Computer Programming*. Addison-Wesley, Boston, 3rd edition, 1998.

A. N. Kolmogorov. The local structure of turbulence in incompressible viscous fluid for very large reynolds numbers. *C. R. (Doklady) Acad. Sci. SSSR (English*

translation available in Proceedings of the Royal Society of London A 434 pp15 (1991)), 30:301–305, 1941. Kolmogorov scale.

L. S. G. Kovasznay. A comment on turbulent combustion. *Jet Propulsion*, 26(6): 485, 1956.

R. H. Kuratle and B. Marki. Influencing parameters and error sources during indication on internal combustion engines. *SAE Technical Paper* 920233, Society of Automotive Engineers, 1992.

D. R. Lancaster, R. B. Krieger, S. C. Sorenson, and W. L. Hull. Effects of turbulence on spark ignition engine combustion. *SAE Technical Paper* 760160, Society of Automotive Engineers, 1976.

S. Langridge. *Imaging and thermodynamic analysis of autoignition and knock in SI engines*. PhD thesis, Department of Mechanical Engineering, The University of Leeds, 1995.

G. Larsson. *In preparation*. PhD thesis, School of Mechanical Engineering, The University of Leeds, 2007.

B. E. Launder and D. B. Spalding. *Mathematical Models of Turbulence*. Academic Press Inc., 1972.

G. A. Lavoie. Correlations of combustion data for SI engine calculations—laminar flame speed, quench distance and global reaction rates. *SAE Technical Paper* 780229, Society of Automotive Engineers, 1978.

C. K. Law. Dynamics of stretched flames. In *Twenty-Second Symposium (International) on Combustion*, pages 1381–1402. The Combustion Institute, 1988.

M. Lawes, M. P. Ormsby, C. G. W. Sheppard, and R. Woolley. Variation of turbulent burning rate of methane, methanol, and iso-octane air mixtures with equivalence ratio at elevated pressure. *Combustion Science and Technology*, 177 (7):1273–1289, July 2005.

A. P. Lee. *The Effects of Bulk Motions and Turbulence on Combustion in SI Engines*. PhD thesis, Department of Mechanical Engineering, The University of Leeds, 1995.

K. H. Lee and C. S. Lee. Effects of tumble and swirl flows on turbulence scale near top dead centre in a four-valve spark ignition engine. *Proceedings of the Institution of Mechanical Engineers Part D: Journal of Automotive Engineering*, 217: 607–615, 2003.

S. Lee, C. Bae, R. Prucka, G. Fernandes, Z. S. Filipi, and D. N. Assanis. Quantification of thermal shock in a piezoelectric pressure transducer. *SAE Technical Paper* 2005-01-2092, Society of Automotive Engineers, 2005.

B. Leisenheimer and W. Leuckel. Self-generated acceleration of confined deflagrative flame fronts. *Combustion Science and Technology*, 118:147–164, 1996.

Y. Li, H. Zhao, Z. Peng, and N. Ladommatos. Particle image velocimetry measurement of in-cylinder flow in internal combustion engines—experiment and flow structure analysis. *Proceedings of the Institution of Mechanical Engineers Part D*, 216:65–81, 2002.

A. N. Lipatnikov and J. Chomiak. A simple model of unsteady turbulent flame propagation. *SAE Technical Paper* 972993, Society of Automotive Engineers, 1997.

A. N. Lipatnikov and J. Chomiak. Modeling of pressure and non-stationary effects in spark-ignition engine combustion: A comparison of different approaches. *SAE Technical Paper* 2000-01-2034, Society of Automotive Engineers, 2000.

A. N. Lipatnikov and J. Chomiak. Turbulent flame speed and thickness: phenomenology, evaluation, and application in multi-dimensional simulations. *Progress in Energy and Combustion Science*, 28:1–74, 2002.

K. Liu. LUSIE manual. Technical report, School of Mechanical Engineering, The University of Leeds, 2004.

R.-L. Liu, W. Liu, L.-Q. Wu, and C.-L. Zhao. LDV measurements of velocities and turbulence intensities in a production SI engine under motored and firing conditions. *SAE Technical Paper* 1999-01-0955, Society of Automotive Engineers, 1999.

W. E. Lorensen and H. E. Cline. Marching cubes: A high resolution 3D surface construction algorithm. *Computer Graphics*, 21(4), July 1987.

J. Lumley. *Engines: an Introduction*. Cambridge University Press, 1999.

J. Mantzaras, P. G. Felton, and F. V. Bracco. 3-D visualisation of premixed charge engine flames: Islands of reactants and products; fractal dimensions and homogeneity. *SAE Technical Paper* 881635, Society of Automotive Engineers, 1988.

G. H. Markstein. *Nonsteady flame propagation*. Permagon, Oxford, 1964.

R. Matthews, M. J. Hall, W. Dai, and G. C. Davis. Combustion modeling in SI engines with a peninsula fractal combustion model. *SAE Technical Paper* 960072, Society of Automotive Engineers, 1996.

S. Merdjani. *LUSIE: Leeds University Spark Ignition Engine Computer Model version 6.1 User Manual*. School of Mechanical Engineering, The University of Leeds, 1996.

S. Merdjani and C. G. W. Sheppard. Gasoline engine cycle simulation using the leeds turbulent burning velocity correlations. *SAE Technical Paper* 932640, Society of Automotive Engineers, 1993.

M. Metghalchi and J. C. Keck. Burning velocities of mixtures of air with methanol, isooctane, and indolene at high pressure and temperature. *Combustion and Flame*, 48:191–210, 1982.

M. Meyer, M. Desrun, P. Schr oder, and A. H. Barr. Discrete differential-geometry operators for triangulated 2-manifolds. In *Proceedings of International Workshop on Visualization and Mathematics (VisMath '02)*, 2002.

B. Mihura. *LabVIEW for data acquisition*. Prentice Hall, London, 2001.

U. C. Muller, M. Bollig, and N. Peters. Approximations for burning velocities and markstein numbers for lean hydrocarbon and methanol flames. *Combustion and Flame*, 108:349–356, 1997.

Ahmad E. M. A. Murad. *Flow and Combustion in Disc and Pent-Roof SI Engines*. PhD thesis, School of Mechanical Engineering, The University of Leeds, 2006.

M. Namazian and J. B. Heywood. Flow in the piston-cylinder-ring crevices of a spark-ignition engine: Effect on hydrocarbon emissions, efficiency and power. *SAE Technical Paper*, Society of Automotive Engineers, 1982.

M. Namazian, I. G. Shepherd, and L. Talbot. Characterization of the density fluctuations in turbulent V-shaped premixed flames. *Combustion and Flame*, 64: 299–308, 1986.

Netlib. The netlib repository. URL `http://www.netlib.org/`.

Y. Nilsson and L. Eriksson. Determining TDC position using symmetry and other methods. *SAE Technical Paper* 2004-01-1458, Society of Automotive Engineers, 2004.

H. Nordgren, L. Hildingsson, B. Johansson, L. Dahlén, and D. Konstanzer. Comparison between in-cylinder PIV measurements, CFD simulations and steady-flow impulse torque swirl meter measurements. *SAE Technical Paper* 2003-01-3147, Society of Automotive Engineers, 2003.

K. Nwagwe, H. G. Weller, G. R. Tabor, A. D. Gosman, M. Lawes, C. G. W. Sheppard, and R. Woolley. Measurements and large eddy simulations of turbulent premixed flame kernel growth. *Proceedings of the Combustion Institute*, 28:59–65, 2000.

M. P. Ormsby. *Turbulent flame development in a high-pressure combustion vessel*. PhD thesis, School of Mechanical Engineering, The University of Leeds, 2005.

N. Peters. *Turbulent Combustion*. Cambridge University Press, Cambridge, 2000.

N. Peters and F. A. Williams. The asymptotic structure of stoichiometric methane-air flames. *Combustion and Flame*, 68:185–207, 1987.

FASTCAM-ultima APX Hardware Manual. Photron Limited, Fujimi-cho 1-1-8, Chiyoda-ku, Tokyo 102-0071, Japan, 1.05 edition, April 2003.

M. A. Plint and A. Martyr. *Engine Testing: Theory and Practice*. Butterworth-Heinemann Ltd., Oxford, 1995.

T. Poinsot, D. Veynante, and S. Candel. Diagrams of premixed turbulent combustion based on direct simulation. In *In Twenty Third Symposium (International) on Combustion*, Pittsburgh, 1990. The Combustion Institute.

W. H. Press, S. A. Teukolsky, W. T. Vetterling, and B. P. Flannery. *Numerical Recipies in FORTRAN: The Art of Scientific Computing*. Cambridge University Press, Cambridge, 2nd edition, 1992.

A. Prothero. Computing with thermochemical data. *Combustion and Flame*, 13(4): 399–408, August 1969.

G. M. Rassweiler and L. Withrow. Motion pictures of engine flames correlated with pressure cards. *SAE Technical Paper* 380139, Society of Automotive Engineers, 1938.

B. Renou, A. Mura, E. Sampson, and A. Boukhalfa. Characterization of the local flame structure and the flame surface density for freely propagation premixed flames at various lewis numbers. *Combustion Science and Technology*, 174:143–179, 2002.

O. Reynolds. On the dynamical theory of incompressible viscous fluids and the determination of the criterion. *Philosophical Transactions of the Royal Society of London, Series A*, 186:123, 1895.

D. B. Rhodes and J. C. Keck. Laminar burning speed measurements of indolene-air-diluent mixtures at high pressures and temperatures. *SAE Technical Paper* 850047, Society of Automotive Engineers, 1985.

G. Rogers and Y. Mayhew. *Engineering Thermodynamics: work and heat transfer*. Longman Scientific & Technical, Harlow, Essex, 4th edition, 1992.

B. L. Ruddy, D. Dowson, and P. N. Economou. The prediction of gas pressures within the ring packs of large bore diesel engines. *Journal of Mechanical Engineering Science (IMechE)*, 23(6):295–304, 1981.

L. Rui-Lin, Z. Chun-Run, W. Liang-Qin, A. Xiang-Bi, Y. Yi-Kun, L. Shu-Min, F. Ming-Zhi, and S. Chong-Lin. A study on the mechanism of in-cylinder tumble generation by directed intake ports. *SAE Technical Paper* 962089, Society of Automotive Engineers, 1996.

J. C. Russ. Thresholding images. *Journal of Computer Assisted Microscopy*, 7(3): 141–164, 1995.

T. W. III Ryan and S. S. Lestz. The laminar burning velocity of isooctane, n-heptane, methanol, methane, and propane at elevated temperatures and pressures in the presence of a diluent. *SAE Technical Paper* 800103, Society of Automotive Engineers, 1980.

O. P. Salvat, A. S. Cheng, W. K. Cheng, and J. B. Heywood. Flame shape determination using an optical-fiber sparkplug and a head-gasket ionization probe. *SAE Technical Paper* 941987, Society of Automotive Engineers, 1994.

M. J. Scott. *Distributions of strain rate and temperature in turbulent combustion*. PhD thesis, Department of Mechanical Engineering, University of Leeds, 1992.

E. S. Semenov. Device for measuring the turbulence in piston engines. *Instruments and Experimental Techniques*, 1(26):102–111, 1958. Russian translation.

E. S. Semenov. Studies of turbulent gas flow in piston engines. In L. N. Khitrin, editor, *Combustion in turbulent flow: proceedings of the Moscow seminar on combustion held at the Energetics Institute of the U.S.S.R. Academy of Sciences*, pages 122–147. Israel program for scientific translations, Jerusalem, 1963. Originally published in Russian as "Gorenie v turbulentom potoke", Moskva, Izdatel'stvo Akademii Nauk SSSR, 1959.

C. G. W. Sheppard, A. A. Burluka, M. Lawes, R. Woolley, K. Liu, E. Abdi Aghdam, A.J. Smallbone, A. Murad, and C. H. Wu. Gasoline engine turbo-charging: Advanced gasoline powertrain for reduced fuel consumption and CO2 emissions. GET-CO2 Project Final Report European Union project number: GRDA-2000-25618, European Union contract number: G3RD-CT-2000-00364, School of Mechanical Engineering, The University of Leeds, 2005.

L. Sirovich. Turbulence and the dynamics of coherent structures part i: coherent structures. *Quarterly of applied mathematics*, 45(3):561–571, October 1987.

A. Smallbone. *Fuel and residual effects on knock onset in SI engines*. PhD thesis, School of Mechanical Engineering, The University of Leeds, 2004.

D. A Soltis. Evaluation of cylinder pressure transducer accuracy based upon mounting style, heat shields, and watercooling. *SAE Technical Paper* 2005-01-3750, Society of Automotive Engineers, 2005.

J. A. Stratton. *Electromagnetic Theory*. McGraw Hill, 1941.

R. J. Tabaczynski. Turbulence and turbulent combustion in spark-ignition engines. *Progress in Energy and Combustion Science*, 2:143–165, 1976.

G. Taubin. A signal processing approach to fair surface design. In *SIGGRAPH '95: Proceedings of the 22nd annual conference on Computer graphics and interactive*

techniques, pages 351–358, New York, NY, USA, 1995a. ACM Press. ISBN 0-89791-701-4. doi: http://doi.acm.org/10.1145/218380.218473.

G. Taubin. Curve and surface smoothing without shrinkage. In *ICCV '95: Proceedings of the Fifth International Conference on Computer Vision*, page 852, Washington, DC, USA, 1995b. IEEE Computer Society. ISBN 0-8186-7042-8.

G. I. Taylor. Eddy motion in the atmosphere. *Philosophical Transactions of the Royal Society of London, Series A*, 215:1, 1921.

G. I. Taylor. Statistical theory of turbulence. *Proceedings of the Royal Society of London, Series A*, 151:421–444, 1935.

G. I. Taylor. The spectrum of turbulence. *Proceedings of the Royal Society of London, Series A*, 164:476–490, 1938.

H. Tennekes and J. Lumley. *A First Course in Turbulence*. M. I. T. Press, 1972.

D. Thévenin. Three-dimensional direct simulations and structure of expanding turbulent methane flames. *Proceedings of the Combustion Institute*, 30:629–637, 2005.

T. Tian. Dynamic behaviours of piston rings and their practical impact. part 1: ring flutter and ring collapse and their effects on gas flow and oil transport. *Proceedings of the Institute of Mechanical Engineers Part J: Journal of Engineering Tribology*, 216(4):209–227, 2002a.

T. Tian. Dynamic behaviours of piston rings and their practical impact. part 2: oil transport, friction and wear of ring/liner interface and the effects of piston and ring dynamics. *Proceedings of the Institute of Mechanical Engineers Part J: Journal of Engineering Tribology*, 216(4):229–247, 2002b.

L. L. Ting and J. E. Mayer. Piston ring lubrication and cylinder bore wear analysis. *ASME Journal of Lubrication Technology*, 96:305–314, 1974.

S. R. Turns. *An Introduction to Combustion: Concepts and Applications*. McGraw-Hill, 1996.

S. Verhelst. *A Study of the Combustion in Hydrogen-Fuelled Internal Combustion Engines*. PhD thesis, Department of Flow, Heat and Combustion Mechanics (Vakgroep Mechanica van Stroming, Warmte en Verbranding), Ghent University, 2005.

O. Vermorel, S. Richard, O. Colin, C. Angelberger, A. Benkenida, and D. Veynante. Multi-cycle LES simulations of flow and combustion in a PFI SI 4-valve production engine. *SAE Technical Paper* 2007-01-0151, Society of Automotive Engineers, 2007.

Volkswagon. VWSE CFD simulations. Private Communications, approx. 2004.

T. von Karman. The fundamentals of the statistical theory of turbulence. *Journal of Aeronautical Science*, 4(131), 1937.

VTK. Visualization ToolKit (VTK). URL `http://public.kitware.com/VTK/index.php`.

J. Wallesten, A. N. Lipatnikov, and J. Nisbet. Turbulent flame speed closure model: Further development and implimentation for 3-D simulation of combustion in SI engine. *SAE Technical Paper* 982613, Society of Automotive Engineers, 1998.

J. T. R. Watson. *Viscosity of gases in metric units*. H. M. Stationary Office, National Engineering Laboratory, Edinburgh, 1972.

B. P. Welford. Note on a method for calculating corrected sums of squares and products. *Technometrics*, 4(3):419–420, 1962.

V. W. Wong and D. P. Hoult. Rapid distortion theory applied to turbulent combustion. *SAE Technical Paper* 790357, Society of Automotive Engineers, 1979.

G. Woschni. A universally applicable equation for the instantaneous heat transfer coefficient in the internal combustion engine. *SAE Technical Paper* 670931, Society of Automotive Engineers, 1967.

C.-H. Wu. *Turbulence and combustion studies in a naturally aspirated and pressure charged spark ignition engine*. PhD thesis, School of Mechanical Engineering, The University of Leeds, 2005.

C. M. Wu, C. E. Roberts, R. D. Matthews, and M. J. Hall. Effects of engine speed on combustion in SI engines: Comparison of predictions of a fractal burning model with experimental data. *SAE Technical Paper* 932714, Society of Automotive Engineers, 1993.

Y. B. Zeldovich, G. I. Barenblatt, Librovich V. B., and Makhviladze G. M. *The Mathematical Theory of Combustion and Explosion*. Consultants Bureau, 1st edition, 1985.

H. Zhao and N. Ladommatos. *Engine combustion instrumentation and diagnostics*. Society of Automotive Engineers, Inc., 2001.

V. L. Zimont. Theory of turbulent combustion of a homogeneous fuel mixture at high reynolds numbers. *Combustion, Explosions & Shockwaves*, 15:305–311, 1979.